

Complexity in the AdS/CFT correspondence

by

Hugo Cangussu Marrochio

A thesis
presented to the University of Waterloo
in fulfillment of the
thesis requirement for the degree of
Doctor of Philosophy
in
Physics

Waterloo, Ontario, Canada, 2019

© Hugo Cangussu Marrochio 2019

Examining Committee Membership

The following served on the Examining Committee for this thesis. The decision of the Examining Committee is by majority vote.

External Examiner: Simon Ross
 Professor, Durham University

Supervisor: Robert Myers
 Professor, Perimeter Institute for Theoretical Physics

Internal Member: Robert Mann
 Professor, University of Waterloo

Internal-External Member: Eduardo Martin-Martinez
 Professor, University of Waterloo

Committee Member: Luis Lehner
 Professor, Perimeter Institute for Theoretical Physics

This thesis consists of material all of which I authored or co-authored: see Statement of Contributions included in the thesis. This is a true copy of the thesis, including any required final revisions, as accepted by my examiners.

I understand that my thesis may be made electronically available to the public.

Statement of contributions

This thesis is based on the following published articles.

- Chapters 2 and 3 are based on:
 - S. Chapman, H. Marrochio and R.C. Myers, “Complexity of Formation in Holography”, arXiv:1610.08063, JHEP 1701, 062 (2017)
- Chapter 4 is based on:
 - D. Carmi, S. Chapman, H. Marrochio, R.C. Myers and S. Sugishita, “On the Time Dependence of Holographic Complexity”, arXiv:1709.10184, JHEP 1711, 188 (2017)
- Chapters 5 is based on:
 - S. Chapman, H. Marrochio, R.C. Myers, “Holographic Complexity in Vaidya spacetimes. Part I”, arXiv:1804.07410, JHEP 1806, 046 (2018)
- Chapter 6 is based on:
 - S. Chapman, H. Marrochio, R.C. Myers, “Holographic Complexity in Vaidya spacetimes. Part II”, arXiv:1805.07262, JHEP 1806, 114 (2018)
- Contributions not included in the thesis:
 - S. Chapman, M. P. Heller, H. Marrochio and F. Pastawski, “Towards Complexity for Quantum Field Theory States”, arXiv:1707.08582, Phys. Rev. Lett 120, no.12, 121602 (2018)
 - P.A.Cano, R.A. Hennigar, H. Marrochio, “Complexity Growth in Lovelock Gravity”, arXiv:1803.02795, Phys. Rev. Lett 121, no.12, 121602 (2018)
 - S. Chapman, J. Eisert, L. Hackl, M.P. Heller, R. Jefferson, H. Marrochio, R.C. Myers, “Complexity and entanglement for thermofield double states”, arXiv:1810.05151, SciPost Physics 6 (2019) 034
 - K. Goto, H. Marrochio, R.C. Myers, L. Queimada, B. Yoshida, “Holographic complexity equals which action?”, arXiv:1901.00014, JHEP 1902, 160 (2019)

Abstract

The main goal of this thesis is to carefully analyze aspects of the gravitational quantities conjectured to be dual to quantum complexity in the AdS/CFT correspondence. The two most promising candidates for such holographic proposals are known as the complexity=volume (CV) and complexity=action (CA) proposals, which will be the main objects of study in this thesis. The latter involves the evaluation of the gravitational action in a region of spacetime known as the Wheeler-DeWitt patch, whose boundary includes null hypersurfaces and null codimension-two joints. There are several subtleties when evaluating the action in a region bounded by null surfaces, and a major part of the work presented here is based on a careful treatment of the boundary contributions to the gravitational action.

We start by evaluating the complexity of formation in holography, which is the additional complexity required to build the thermofield double state (TFD) in comparison to the complexity of building two copies of the vacuum. From the gravitational perspective, such quantity is interesting as it involves geometries with black holes. We find that for AdS-Schwarzschild black holes, both the CA and CV proposals yield a UV finite complexity of formation, and at large temperatures it becomes proportional to the thermodynamic entropy for boundary spacetime dimensions $d > 2$.

In addition, we investigate dynamical properties of the holographic duals of complexity. We study the time evolution of the thermofield double state for AdS-Schwarzschild and AdS-Reissner-Nordstrom black holes. In the AdS/CFT correspondence, this time evolution corresponds to time slices that cover the interior region of the black hole. We find the striking result that the late time rate of change of complexity in the CA proposal is approached from above, which implies that the originally proposed connection to the conjectured Lloyd's bound on computation rate is violated. In contrast, the CV proposal growth rate is approached from below at late times for these geometries.

Next, we investigate the time evolution of holographic complexities when the bulk spacetime has non-trivial dynamics. We investigate both one-sided and two-sided Vaidya geometries, which are sourced by the collapse of an infinitesimally thin layer of null dust. In order to evaluate the complexity in the CA proposal, we construct a null fluid action that sources the Vaidya geometry. Our main result is that the inclusion of a surface counterterm that ensures reparametrization invariance to the null normals at the null boundaries of the Wheeler-DeWitt patch is necessary in order to reproduce desired properties of complexity, such as the switchback effect. In addition, we find that for one-sided black holes, the late time rate of change is approached from below in the CA approach, in contrast to what was found in two-sided geometries.

Acknowledgements

And then I reach the final stretch of my graduate years!

I want to start by expressing my gratitude to my supervisor Rob Myers. Thank you for always making an effort to be available to discuss, and for the patience and trust in my scientific growth. You have shaped the scientist that I have become, and your kindness and commitment to hard work are lessons I hope to carry with me to the future as well. I am privileged that I have had you as a mentor in these formative years!

In addition to working with Rob, I also had the chance to collaborate with many exciting minds. My gratitude to Pablo Cano, Dean Carmi, Shira Chapman, Jens Eisert, Kanato Goto, Lucas Hackl, Robie Hennigar, Michal Heller, Ro Jefferson, Leonel Queimada, Fernando Pastawski, Sotaro Sugishita and Beni Yoshida. I want to particularly thank Michal and Beni, two bright physicists from whom I have learned much, and also I really appreciate the conversations and career advice. I also want to thank Robie for reading a draft of this thesis and for his very helpful feedback. In addition, I want to thank Luis Lehner and Guifre Vidal for many useful conversations and my committee members for being part of the defense and following my progress in the past years. Also, Ronaldo Fogo and Jorge Noronha are two past mentors I would like to acknowledge who were very important in different stages of my story with physics.

I want to thank the people around Perimeter Institute that made these past years so enjoyable! In particular, I want to thank Tibra Ali, Evan Andrews, Gal Bahar, Alvaro Ballon, Matt Beach, Yoni Bentov, Alice Bernamonti, Krista Blake, Lenka Bojdová, Pablo Bosch, Adam Chapman, Lucia Cordova, Frank Coronado, Lorenzo di Pietro, Adrián Franco-Rubio, Zach Fisher, Thomas Galley, Federico Galli, Daniel Guariento, Debbie Guenther, Anna Golubeva, Juan Hernandez, Matthijs Hogervorst, Qi Hu, Nick Hunter-Jones, Pavel Kovtun, David Kubiznak, Dan Lynch and the Bistro staff, Fiona Mccarthy, Jonah Miller, Andre Pereira, Djordje Radicevic, Miroslav Rapcak, Shan-Ming Ruan, Andres Schlieff, Jamie Sikora, Barbara Soda, Antony Speranza and Bruno Umbert.

Being far from home and family can certainly be quite challenging, so I am fortunate to have had great friends around. I have enjoyed the conversations about cinema and music with Lorenzo, not to mention the always inspiring discussions about physics. Also, I want to add that I am grateful for all the help I got from my most frequent collaborator Shira. In addition, I want to thank Robie for being such a supportive friend, and I hope there will be many opportunities in the next years to have healthy granola breakfasts and to make dubious choices at karaokes.

My past friends have been a very important source of enjoyment despite the distance. I want to thank Nayara Fonseca, Giuliano Giacaglia, Illan Halpern, Kamena Kostova, Carol Lewin, César Lima, Jessica Niide, Henrique Pondé, Bianca Ricci, Márcia Shimabukuro, Shoshana Vasserman and Karine Yuki. In addition, I would like to thank Gabriel Bujokas and Carolina Yamate, with whom we shared so many stories and that through the years got to know me so well. Also, I want to thank my supersymmetric partner Camila Machado: it has been 12 years since we were listening to some of the finest friendship-forming podcasts! I really appreciate the support through these years.

I am very grateful for my family, and I would like to start by thanking my cousin Matheus and my sister-in-law Camila. To my older brother and best friend Eduardo, who has always been an inspiration since my childhood, thank you for your love and for awakening in me the appreciation for knowledge. They say the PhD years change you: in my case I have become an uncle! Sofia and Benicio, even though I have been far, you were always in my heart and seeing you grow always made my days lighter. To my grandma Maria, who was very loved and is always missed. Finally, to my parents David and Solange, who loved me unconditionally from the very beginning of my life, I am eternally grateful for your love, understanding and support. Despite the distance, you were, are and will always be loved.

Thank you Canada for being a second home for these past years and until next time!

Table of Contents

List of Figures	xii
1 Introduction	1
1.1 A lightning review of AdS/CFT	2
1.2 The concept of quantum complexity	11
1.3 Complexity in AdS/CFT	17
1.4 Organization of the thesis	22
2 Preliminaries	24
2.1 General framework in higher dimensions ($d > 2$)	24
2.1.1 Evaluating the Action	29
2.2 Framework for the BTZ black hole	37
3 Complexity of Formation	40
3.1 Complexity of Formation	41
3.1.1 $d = 4$	42
3.1.2 $d = 3$	44
3.1.3 Planar Case for General d	47
3.1.4 Complexity of BTZ Black Holes	50
3.2 Comparison with Complexity=Volume	52
3.2.1 Planar Geometry	54

3.2.2	Spherical and Hyperbolic Geometries	56
3.3	Discussion	60
4	The Growth Rate of Holographic Complexity	65
4.1	Evaluating the Time Dependent Action	67
4.2	Time Dependence of Complexity	73
4.2.1	Examples	79
4.3	Complexity=Volume	82
4.3.1	Late Time Behaviour	87
4.3.2	General Time Dependence	91
4.4	Charged Black Holes	92
4.4.1	Complexity=Action	98
4.4.2	Complexity=Volume	105
4.5	Discussion	106
5	Holographic Complexity in Vaidya Spacetimes: One-sided black holes	114
5.1	Null Fluid and the Vaidya Geometry	115
5.1.1	Action for a Null Fluid	116
5.1.2	Null Fluids & Complexity=Action	119
5.1.3	Counterterm for Null Boundaries	125
5.2	Complexity in Black Hole Formation	127
5.2.1	Complexity=Action	130
5.2.2	Complexity=Volume	144
5.3	Discussion	153
6	Holographic Complexity in Vaidya Spacetimes: Two-sided black holes	161
6.1	Background Geometry	162
6.2	Complexity = Action	167

6.2.1	Time Evolution	168
6.2.2	Complexity of Formation	189
6.2.3	‘Complexity’ without the Counterterm	197
6.3	Discussion	203
7	Final remarks	229
7.1	Lessons from quantum field theory models	230
7.2	Holographic complexity is equal to which action?	235
7.3	Future directions	237
	References	240
	APPENDICES	259
A	Appendices to chapter 3	260
A.1	Fefferman-Graham near Boundary Expansions	260
A.1.1	Relating the Cutoffs	260
A.1.2	Cutoff Independence of the Action	262
A.2	Details for Vacuum AdS Actions	265
A.3	Small Hyperbolic Black Holes	269
A.3.1	$d = 4$	271
A.3.2	$d = 3$	272
A.3.3	Late-Time Growth of Complexity	275
A.4	Ambiguities in the Action Calculations	275
A.4.1	Redefinition of the Function Defining the Null Hypersurface	277
A.4.2	Reparameterizations	278
A.4.3	Changing the Normalization Condition at the Boundary	280
A.4.4	A Comment on the Cutoff Choice	281

B	Appendices to chapter 4	283
B.1	Details of Complexity=Action for BTZ Black Holes	283
B.1.1	General Boundary Times	283
B.1.2	Boundary Counterterm	287
B.2	Additional Examples of Time Dependence of Complexity	290
B.2.1	CA Results in $d = 3$	290
B.3	Complexity of Formation for Charged Black Holes	294
B.3.1	Complexity=Action	295
B.3.2	Small Hyperbolic Black Holes	301
B.4	Ambiguities in the Action Calculations	302
B.4.1	Influence of a Constant a_0	302
B.4.2	Boundary Counterterm	303
C	Appendices to chapter 6	305
C.1	Counterterm for the Null Boundaries	305
C.2	Complexity=Action in Higher Dimensions	311

List of Figures

1.1	Excitations in the AdS/CFT correspondence	6
1.2	Eternal AdS black hole and the Einstein-Rosen bridge	9
1.3	Euclidean preparation of the thermofield double state	10
1.4	The conjectured behaviour of the time evolution of quantum complexity	14
1.5	The precursor operator as a circuit	16
1.6	The saturation of entanglement for the time evolution of the TFD wormholes	18
1.7	Penrose diagrams for the CA and CV proposals.	19
2.1	Penrose diagram and the WDW patch at $t_L = t_R = 0$	26
2.2	Penrose diagrams and the Wheeler-DeWitt patch in vacuum AdS	28
2.3	The top of the WDW patch for AdS black holes	34
2.4	Penrose diagram and the WDW patch for zero angular momentum BTZ	38
3.1	Complexity of formation in $d = 4$ using the CA proposal	45
3.2	Complexity of formation in $d = 3$ using the CA proposal	48
3.3	Ratio of the complexity of formation to the entropy for the CA proposal	51
3.4	Penrose diagram of the wormhole passing through the bifurcation surface	53
3.5	The two ratios R_{form} and R_{rate} as a function of d	56
3.6	Complexity of formation in $d = 4$ using the CV proposal	57
3.7	Complexity of formation in $d = 3$ using the CV proposal	58

4.1	Penrose diagram of the WDW patch of an eternal AdS black hole, moving forward in time in a symmetric way ($t_L = t_R$).	68
4.2	Time dependence of complexity in $d = 2$ using the CA proposal	81
4.3	Critical time t_c as a function of the horizon radius for $d = 4$ for the various horizon geometries	83
4.4	Time dependence of complexity in $d = 4$ using the CA proposal	83
4.5	Penrose diagram of the maximal wormhole connecting the two boundaries anchored at times t_L and t_R	84
4.6	Time dependence of complexity in $d = 3$ and $d = 4$ using the CV proposal	89
4.7	Late time rate of change of complexity for planar black holes in the CV proposal	92
4.8	Penrose diagrams for a charged AdS-Reissner-Nordstrom black hole	96
4.9	Complexity of formation divided by the entropy for the planar charged black hole in $d = 4$	98
4.10	The time derivative of complexity with $d = 4$, $k = 1$ and non-zero chemical potential using CA	101
4.11	The time derivative of complexity with $d = 4$, $k = 0$ and non-zero chemical potential using CA	101
4.12	The time derivative of complexity with $d = 4$, $k = 1$ with non-zero chemical potential using CV	106
4.13	The time derivative of complexity with $d = 4$, $k = 0$ with non-zero chemical potential using CV	107
4.14	The averaged rate of growth of complexity	109
4.15	Phase structure of hyperbolic black holes	113
5.1	Evaluating the gravitational action across a null shell	120
5.2	Penrose-like diagrams for the thin shell collapsing in one-sided geometries	129
5.3	The growth rate for the complexity in $d = 2$ one-sided Vaidya geometry using CA	141
5.4	The growth rate for the complexity in $d = 3$ and $d = 4$ one-sided Vaidya geometries using CA	143

5.5	Penrose-like diagram of maximal volume surfaces in a one-sided Vaidya geometry	144
5.6	Potential energy for determining the extremal surfaces	147
5.7	The growth rate for the complexity in $d = 2$ one-sided Vaidya geometry using CV	152
5.8	The growth rate for the complexity in $d = 3$ and $d = 4$ one-sided Vaidya geometries using CV	153
6.1	Penrose-like diagram for one shock wave on a two-sided black hole geometry	165
6.2	Time derivative of complexity evolving both boundary times symmetrically for one light shock in a two-sided geometry	183
6.3	Time derivative of complexity evolving both boundary times symmetrically for one heavy shock in a two-sided geometry	184
6.4	Dependence of the critical time t_{c1} on the energy carried by the shock wave	187
6.5	Dependence of the critical time t_{c0} on the energy carried by the shock wave	188
6.6	Penrose-like diagram for one shock wave sent from the right boundary at $v_s = -t_w$ on an eternal black hole geometry, with the Wheeler-DeWitt patch anchored at $t_L = t_R = 0$	190
6.7	The complexity of formation for BTZ black holes in a two-sided geometry with one shock wave	193
6.8	The derivative of the complexity of formation with respect to t_w	195
6.9	The ‘delay’ time (6.105) as a function of the energy carried by the shock wave	195
6.10	Rate of change of “complexity” for BTZ ($d = 2$) black hole without the addition of the counterterm	201
6.11	Comparison of rate of change of complexity evolving both boundary times symmetrically with and without the inclusion of the counterterm	224
6.12	Complexity of Formation for BTZ black holes with no counterterm	225
6.13	Complexity evolution in $d = 2$ for light shock waves	225
6.14	The time evolution of complexity evolving the left and right boundary times independently	226
6.15	Complexity evolution in $d = 2$ for heavy shock waves	226

6.16	A representation of the insertion of a simple perturbation at an early time $-t_w$ for the thermofield double state	227
6.17	Illustration of the spread of infected qubits in the epidemic model when $t_L + t_R > 0$ and $t_w - t_L > 0$	228
6.18	The derivative of the complexity of formation for BTZ black holes with respect to the insertion time t_w	228
7.1	The time evolution of complexity with varying reference scale for the massless scalar in $d = 2$	234
7.2	The rate of change of complexity for the dyonic black hole varying the ratio between electric and magnetic charges	236
A.1	The future caustic of the Wheeler-DeWitt patch in the vacuum global AdS geometry	266
A.2	Penrose diagram for the vacuum hyperbolic AdS space.	268
A.3	Penrose diagram for small hyperbolic black holes with $r_h < L$	270
A.4	The meeting point of the two ingoing null rays as a function of r_h	272
A.5	Meeting point of the two ingoing null rays for hyperbolic black holes in AdS ₄ as a function of the horizon radius	274
A.6	Various possible null junctions appearing in our action calculations	276
A.7	Complexity of formation for the small hyperbolic black holes in $d = 4$ for different choices of a_0	278
A.8	Penrose diagram of a black hole in $d > 2$ representing a different way of regularizing the WDW patch	281
B.1	The WDW patches in the BTZ black hole background	284
B.2	Integrated complexity as a function of time for $d = 2$ using CA	289
B.3	The rate of change of complexity for $d = 2$ using CA	289
B.4	Critical time as a function of the horizon radius for $d = 3$ for the various geometries	292
B.5	Time dependence of complexity in $d = 3$ using the CA proposal	292

B.6	Time dependence of complexity in $d = 3$ for hyperbolic geometry using the CA proposal	293
B.7	Integrated complexity as a function of time in $d = 3$ using the CA proposal	293
B.8	Integrated complexity as a function of time in $d = 3$ for hyperbolic geometry using the CA proposal	294
B.9	Complexity of formation for planar $d = 4$ charged black hole	298
B.10	Complexity of formation for spherical charged black holes in $d = 4$	300
B.11	The rate of change of the complexity for different values of the constant a_0	303
C.1	The growth rate of the holographic complexity at $t = 0$ for $d = 4$ spherical black hole as a function of the perturbation time t_w	314
C.2	Complexity growth rate for $d = 4$ spherical black hole	316
C.3	The complexity of formation for planar $d = 4$ black hole as a function of the shock wave time t_w	319
C.4	The delay time as a function of the energy carried by the shock wave . . .	321
C.5	The derivative of the complexity of formation with respect to the insertion time t_w , for planar $d = 4$	322
C.6	The “complexity” of formation for planar $d = 4$ black hole as a function of the shock wave time t_w , without the inclusion of the counterterm	324

Chapter 1

Introduction

One of the biggest challenges of modern theoretical physics is to fully understand the unification of gravity with quantum theory. On the one hand, physical phenomena on the large scales of the cosmos are all very well described by general relativity. However, in order to comprehend the nature of the early universe, as well as the fate of old black holes, a quantum description of gravity is imperative. Quantum theory itself is a backbone of modern physics, as it provides the description of elementary particles and their interactions through quantum field theory, as well as a variety of phenomena related to the quantum structure of matter. Because gravity is by many orders of magnitude a weaker force at low energies, the quantum description of particles is possible without resorting to a theory of quantum gravity.

There is one surprising development to the previous discussion: at least for certain examples of quantum gravity in negatively curved spacetimes, the description is rather “ordinary”, and yet extraordinary at the same time. In fact, it is equivalent to a conformal field theory, without gravitational degrees of freedom, in a spacetime with one less dimension. This duality between quantum gravity and conformal field theory is generally known as the AdS/CFT correspondence, or as holographic duality, since it explicitly makes the holographic [1, 2] nature of gravity manifest [3–6].

The AdS/CFT correspondence has been an active research field for the past twenty years, for some relevant reviews see [7–11]. Recently, there has been a focus on investigating how the quantum structure of the field theory manifests in the emergence of spacetime [12–29]. The long term hope is that by understanding how quantum information (QI) concepts are realized in AdS/CFT, then one can ask sharp questions about longstanding problems in theoretical physics. For instance, how the black hole interior in a quantum

theory of gravity is encoded in the properties of the boundary, which can shed light on questions about firewalls and the information loss problem, *e.g.*, [8, 20, 30]. In this sense, we could describe a variety of complicated problems by using definitions that depend only on quantum information theoretic notions in the boundary CFT!

There has been a recent suggestion that the concept of quantum complexity of boundary states should be included in the AdS/CFT dictionary [31–34]. In quantum information theory, quantum complexity is an important concept used to characterize algorithms that can be realized by quantum computers and it creates an important hierarchy of problems ordered by how “easy” it is to find a solution [35–37]. We are interested in a slightly different notion of complexity, one that deals with quantum circuits that realize a particular task optimally or most efficiently. From the point of view of quantum field theory, quantum complexity is still a new research subject that has only started to be developed [38–62], and there is still much to be explored, in particular for interacting field theories and for QFTs with holographic duals. In addition, from the point of view of AdS/CFT, the proposals of holographic complexity point at novel gravitational observables that are sensitive to the physics deep into the black hole geometry [33, 34] and to chaotic dynamics as well [32]. For some additional references to recent works in holographic complexity, see [63–89].

The goal of this thesis is to concretely and carefully evaluate the conjectured holographic proposals of complexity in AdS/CFT, with the goal of checking whether these quantities have properties consistent with the quantum complexity of the boundary state. We organize this introductory chapter in the following manner: in section 1.1, we provide a brief overview of the AdS/CFT duality, describing the properties that are most relevant for the work in this thesis. Next, we introduce the concept of quantum complexity in section 1.2, as well as the key properties that the holographic proposals should obey in order to be good candidates of duals to complexity. We describe the two main holographic proposals of complexity in section 1.3, in particular focusing on black hole spacetimes. Finally, we make an overview of the rest of the chapters in this thesis in section 1.4.

Throughout the thesis, we will use natural units where $\hbar = c = k_B = 1$, unless explicitly stated otherwise.

1.1 A lightning review of AdS/CFT

The AdS/CFT correspondence was originally derived in the context of string theory, where its most precise and tested form exists: type IIB string theory in $AdS_5 \times S^5$ is equivalent to $\mathcal{N} = 4$ super Yang-Mills in four dimensions [3–6].

In general, the string theory side of the duality can have a very complicated structure, but there is a simple limit where it essentially becomes general relativity coupled to a few quantum field excitations. On the field theory side, this is equivalent to a limit where the theory has many degrees of freedom and is strongly coupled. We will follow mostly the discussion of the reviews [7–9, 11, 90] for this section of the introduction.

We start by writing the simple metric of vacuum planar AdS_{d+1} , which makes manifest the conformal invariance of the duality. The conformal group for a field theory in d space-time dimensions is $SO(d, 2)$, and the AdS_{d+1} is a spacetime that has the isometry given by the same group $SO(d, 2)$. The metric function takes the form

$$ds^2 = \frac{L^2}{z^2} (dz^2 - dt^2 + d\vec{x}_{d-1}^2) , \quad (1.1)$$

where the vector \vec{x}_{d-1} indicates the $(d - 1)$ spatial directions, t the time coordinate for the CFT. The coordinate z is associated to the “bulk” direction in AdS and L is the AdS radius of curvature. The above coordinate chart is useful in order to make manifest the scale invariance of the metric under the transformation $(z, t, \vec{x}_{d-1}) \rightarrow \lambda(z, t, \vec{x}_{d-1})$.

The expectation is that, as a classical gravitational spacetime, the metric in eq. (1.1) is a solution of Einstein’s equation in the presence of a negative cosmological constant. The field equations are obtained from the Einstein-Hilbert action,

$$I_{EH} = \frac{1}{16\pi G_N} \int d^{d+1}x \sqrt{-g} (\mathcal{R} - 2\Lambda) + \dots , \quad (1.2)$$

where the dots indicate a variety of possible boundary terms, which will be discussed extensively in this thesis, as well as various matter fields. By plugging in the metric function in the equations of motion, the cosmological constant gets related to the AdS curvature scale L as $\Lambda = -\frac{d(d-1)}{2L^2}$.

The coupling of the gravitational constant in the action in eq. (1.2) has dimensions of length ^{$d-1$} , which can be directly associated with Planck’s length as $G_N \equiv \ell_{pl}^{d-1}$ in natural units. In addition, the action in eq. (1.2) can be understood as a low energy limit of string theory models, where higher derivative interactions (*e.g.*, $R_{abcd}R^{abcd}$) would be neglected in perturbation theory if $\ell_{pl}/L \ll 1$.

Let us discuss a simple example to illustrate how this ratio manifests a dependence on the degrees of freedom for both sides of the duality, based on an argument in [7]. Let us consider an analog of the Bekenstein-Hawking entropy [91–93], where the area enclosed is the area at the regulating surface of AdS spacetime. Since AdS space has infinite volume, as one can see from the metric function in eq. (1.1) for $z \rightarrow 0$, one needs to introduce a

cutoff such that the boundary is located at $z_b = \delta$. From the CFT perspective, naturally the theory is UV divergent, so in order to calculate regulated quantities one needs to introduce a UV cutoff. It turns out that it is possible to identify the UV regulator of the CFT with δ as well.

We will explain later in this section how areas are connected to quantum entanglement in the boundary theory via the Ryu-Takayanagi formula [12, 13]. For the simplicity of the argument, let us assume the holographic principle for theories containing gravitational degrees of freedom here [1, 2]. It relates the maximum entropy in a region of space with the area of the boundary as

$$S_g = \frac{A}{4G_N}. \quad (1.3)$$

Therefore, we can calculate a regularized expression for eq. (1.3) taking into account the area at the boundary of AdS which yields

$$S_g = \frac{A(z_b)}{4G_N} = \frac{L^{d-1} \text{vol}}{\delta^{d-1} 4G_N}, \quad (1.4)$$

where vol is a (regularized) volume of the spatial dimensions in which the CFT is defined.

Now, suppose that we introduce a lattice regulator for the CFT at the boundary, with spacing given by δ . A simple counting argument implies that the total entropy of the CFT should essentially scale as

$$S_{CFT} \sim \frac{\text{vol}}{\delta^{d-1}} \times N_d, \quad (1.5)$$

where N_d indicates the degrees of freedom per lattice site. For instance, for a class of CFTs the central charge is a quantity that is directly related to the degrees of freedom of the theory. In the example of gauge theory $SU(N_c)$, the degrees of freedom become the square of the number of colours as $N_d = N_c^2$.

The exact coefficient is theory-dependent, but eqns. (1.5) and (1.4) both scale similarly with respect to the δ cutoff and the spatial volume of the theory. Therefore, the number of degrees of freedom becomes associated with the ratio on the gravitational side as

$$\frac{L^{d-1}}{G_N} \sim N_d. \quad (1.6)$$

As a consequence, the condition $\ell_{pl}/L \ll 1$ translates to a CFT dual with many degrees of freedom as

$$\frac{L^{d-1}}{G_N} \sim N_d \gg 1. \quad (1.7)$$

Let us note that large number of degrees of freedom is not a sufficient condition in order to have a simple gravitational dual. For instance, the large N critical vector model $\mathcal{O}(n)$ in $d = 3$ is conjectured to be dual to a complicated theory of higher spin gravity in AdS_4 [94]. In contrast, there was an early hint that certain gauge theories could have large N limit that is related to perturbative string theory. The famous construction of t'Hooft [6, 95] realizes this for gauge theories, containing matter fields such as Φ_j^i with $i, j \in 1, \dots, N_c$ transforming in the adjoint of the gauge group $SU(N_c)$. Essentially the large N limit in this case is non-trivial in the field theory side because a large number of Feynman diagrams grows carries a factor of N_c^2 , while the perturbative coupling grows to zero, such that the t'Hooft coupling $\lambda \equiv N_c g_{YM}^2$ remains finite. In fact, only planar diagrams contribute to the perturbative expansion in the large N limit, which ends up with a structure reminiscent of a perturbative string expansion with string coupling $1/N_c$. The original Maldacena construction of AdS/CFT [3] in a sense makes this connection precise, including non-perturbative ingredients and specifying the contents of the theories on each side of the correspondence. In fact, it is understood that for large N_c , the gravity side reduces to perturbative string theory, and for large λ , which signals strong coupling, the string theory reduces to a supergravity regime [6, 11].

The previous discussion is relevant for constructing and testing exact examples of the holographic duality. However, we will use a reverse engineering argument for AdS/CFT in this thesis: given a classical gravitational background with some excitations of quantum fields, this defines a strongly coupled CFT at the boundary with many degrees of freedom. By studying excitations of the geometry, we will be able to analyze non-trivial properties of the duality, such as the existence of black holes in the bulk.

Since we are often interested in describing excited states of the CFT, one can construct local gauge invariant single trace operators by turning on a source in the field theory and calculating expectation values. On the gravitational side, this is equivalent to turning on a fundamental field in the bulk, with the boundary condition near the AdS boundary acting as the source for the field operators. In the case of a scalar field, the mass is directly related to the dimension of the operator as $m^2 L^2 = \Delta(\Delta - d)$. We depict such excitation in figure 1.1, where the dynamics of the fields in asymptotically AdS spacetimes is connected to turning on various sources of the CFT. This fact can be summarized in the fundamental equation that defines AdS/CFT, which relates the partition function on both sides and we write in the Euclidean signature in order to avoid time ordering complications

$$\left\langle \exp \left(\int d^d x \mathcal{O} \phi_{(0)} \right) \right\rangle_{CFT} = \exp(-I_{grav}) \Big|_{\lim_{z \rightarrow 0} \phi(z, x^\mu) z^{\Delta-d} = \phi_{(0)}(x^\mu)}. \quad (1.8)$$

The partition function in the gravitational side can be evaluated in a saddle point ap-

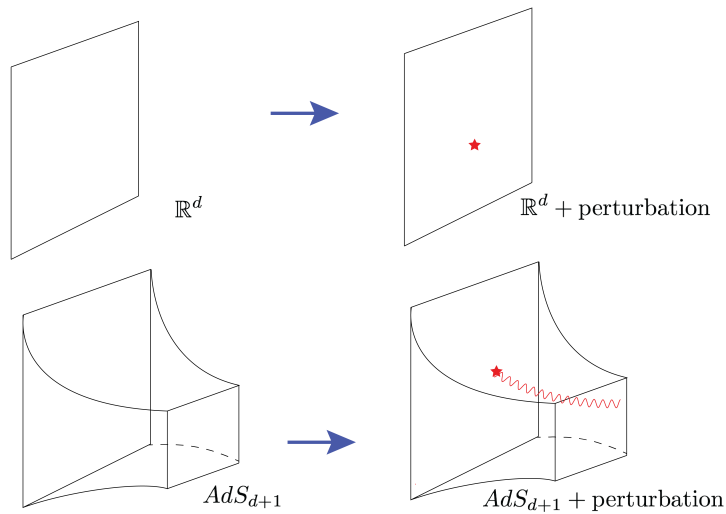


Figure 1.1: A pictorial representation of the AdS/CFT correspondence. Left - The vacuum of a CFT in the Euclidean plane is dual to the vacuum of the Poincaré patch in one more dimension, AdS_{d+1} . Right - A source in the CFT is dual to a field perturbation in AdS, which propagates into the bulk. This connects perturbed geometries that are asymptotically AdS to excitations of CFT when certain sources are turned on. Further, the boundary condition of the field in AdS acts as the source of the operator in the CFT. For instance, if the field is a scalar field, its mass is related to the dimension of the operator in the CFT as $m^2 L^2 = \Delta(\Delta - d)$.

proximation when the CFT is strongly coupled and have many degrees of freedom, and this approximation is the essence of the power of the AdS/CFT correspondence. In fact, understanding exactly which states have simple geometric duals is still an active research topic in AdS/CFT. Another example that will be the main focus of this thesis is the description of thermal states in the holographic duality. In this case, the geometry can be quite different from the vacuum, as it generically involves spacetimes with black holes [30].

Next, we want to study the quantum information properties of the AdS/CFT correspondence. The natural place to start is from entanglement entropy, which has been the most well studied QI probe in holography, and has provided many powerful results through the years, *e.g.*, see the recent review [96]. Entanglement can shed light on important phenomena such as the area law [97], quantum phase transitions [98, 99], dynamics of strongly correlated systems [100, 101] and probe the degrees of freedom for a variety of field theories [102–104]. The holographic dual of entanglement entropy, as described by the celebrated Ryu-Takayanagi (RT) formula, states that the entanglement entropy of a spatial region \mathcal{A} in the boundary theory is given by [12, 13]

$$S_{\mathcal{A}} = \min \frac{A(\mathcal{E}_{\mathcal{A}})}{4G_N}, \quad (1.9)$$

where the bulk surface $\mathcal{E}_{\mathcal{A}}$ is homologous to \mathcal{A} in the boundary. In case there are multiple surfaces that obey these conditions and extremize the area functional, the one of minimum area should be chosen. Of course there have been several important milestones in the study of entanglement for CFTs as well as holographic entanglement entropy, reviewing all of them is outside the scope of this thesis. In addition, holographic entanglement entropy has an important property with respect to locality: the duality has a high degree of non-locality, as a consequence of eq. (1.8), however entanglement entropy associates a subregion in the boundary to a subregion in the bulk. Notice that the Bekenstein-Hawking formula for black hole entropy in eq. (1.3) hints how areas in gravitational theories might play an important role in describing entropic quantities, and the RT formula makes this connection precise.

There is an exact sense in which the entanglement entropy is connected to the Bekenstein-Hawking entropy of black holes. In order to understand such examples, we need to introduce an important state in the context of the AdS/CFT correspondence, which is the thermofield double (TFD) state [30, 105–107]. Suppose we have two copies of a system, which we will denote left and right for reasons that will become clear, and we want to generate a pure state that entangles the energy eigenstates in a particular way, by summing

in the energy eigenbasis [30]

$$|TFD\rangle \equiv Z^{-1/2} \sum_{n=0}^{\infty} e^{-\frac{1}{2}\beta E_n} |E_n\rangle_L \otimes |E_n\rangle_R. \quad (1.10)$$

Upon tracing out either the left or the right theory, the remaining density matrix is of a thermal state with inverse temperature β , for instance

$$\begin{aligned} \rho_R &= \text{tr}_L |TFD\rangle \langle TFD| \\ &= \sum_n e^{-\beta E_n} |E_n\rangle_R \langle E_n|_R = e^{-\beta H_R} \end{aligned} \quad (1.11)$$

The thermofield double is therefore a purification of the thermal state, where the auxiliary system is chosen to be an exact copy of the original theory. In holography, the thermofield double is dual to the two-sided (or eternal) black hole geometry [30], as represented in figure 1.2, where the two copies of the CFT can be interpreted as living in the left and right boundaries. In figure 1.3, we show how one constructs the TFD state by an Euclidean time evolution. It consists of half of the Euclidean-AdS-Schwarzschild black hole, represented in part (a) of figure 1.3. It is understood that the path integral prepares the vacuum state of quantum fields in the Euclidean black hole geometry, which originally is a construction known as the Hartle-Hawking state [106, 107]. Because the geometry of the time slices at Euclidean and Lorentzian times agree at $t_E = 0$ and $t = 0$ (and the conjugate momenta vanish, *i.e.*, $\partial_{t_E} g_{ab} = 0 = \partial_t g_{ab}$), one can glue the Euclidean sector as initial data to the wave functional in the Lorentzian picture.

We can now compare the partition function on both sides of the AdS/CFT correspondence given by eq. (1.8). The path integral for the boundary CFT in part (b) of figure 1.3 is the representation of a path integral that prepares the TFD state, with geometry $I_{\beta/2} \times S^{d-1}$, where $I_{\beta/2}$ is simply the interval with length $\beta/2$ and S^{d-1} is the spatial $(d-1)$ -dimensional sphere. In the saddle point approximation of eq. (1.8), we see that the TFD path integral in part (b) of 1.3 is at the conformal boundary of half of the Euclidean black hole disk in part (a), which equates both states via the AdS/CFT correspondence.

The bulk geometry connecting the left and right boundaries contains a spacelike wormhole. If we interpret the sum of the energy eigenstates in eq. (1.10) as summing disconnected geometries, it is quite striking that by entangling the left and right theories in a particular way results in a geometry connected by a (non-traversable) wormhole. This is a manifestation of the ER = EPR proposal [22]. Notice that the blue time slices in figure 1.2 depict the boost invariance of the state with respect to the Hamiltonian time evolution at the

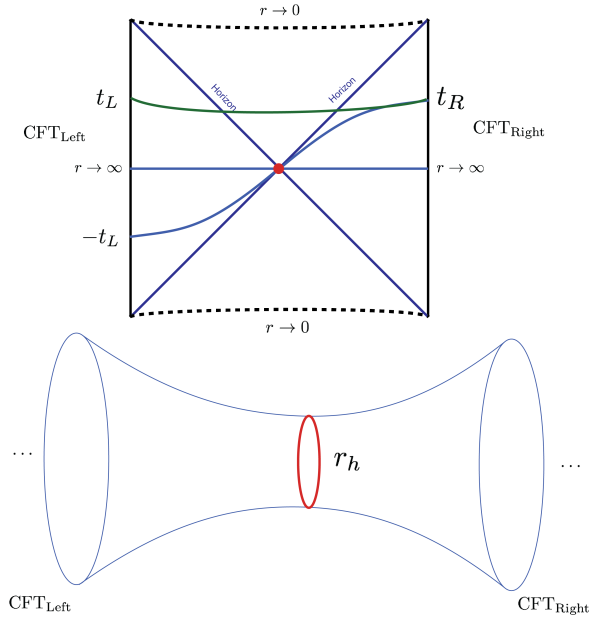


Figure 1.2: The eternal black hole geometry, dual to the thermofield double state in AdS/CFT. The top figure is a Penrose diagram, which is a two-dimensional representation that captures the causal structure of the spacetime. The blue slices that pass through the bifurcation point (red dot) are equivalent due to the boost invariance of the geometry. The spacelike wormhole represented by the blue slice is depicted below, with the horizon radius being the minimum radius of the wormhole. From the perspective of the RT formula, the area of the horizon that separates the left and right CFTs becomes the Bekenstein-Hawking entropy $S_{BH} = \frac{A(r_h)}{4G_N}$, as indicated by eq. (1.12). The wormhole depicted in the green slice has a non-trivial time evolution and will be the focus of section 1.3.

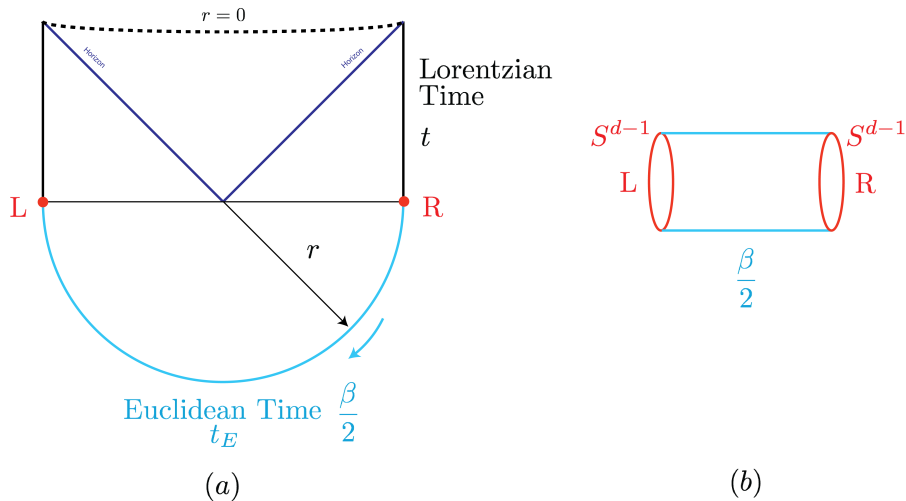


Figure 1.3: (a) The upper half of the Penrose diagram for the eternal black hole glued to half of the Euclidean black hole in the bottom. The Euclidean time evolution of $\beta/2$ corresponds to half of the circle of the Euclidean black hole solution. Because the time slices at Euclidean and Lorentzian times match at the origin ($t_E = t = 0$), one can glue both geometries, where the Euclidean time evolution prepares the state as initial data for the Lorentzian time evolution. This construction is also known as the Hartle-Hawking state [106, 107] (b) The path integral representation in the boundary theory that prepares the TFD state. This geometry consists of an interval $\beta/2$ times the sphere S^{d-1} , which corresponds to the spatial geometry on which the boundary theory lives [8, 30, 90]. The saddle-point approximation in the equivalence of partition functions of AdS/CFT in eq. (1.8) connects the path integral that prepares the TFD state in the boundary with the gravitational solution of the Euclidean half-disk, as the picture in (b) is equivalent to the conformal boundary in (a).

boundaries. That is, since the theories are equivalent, time evolving upwards on the right boundary and downwards by an equal amount on the left side leaves the state invariant, as we will explore further in section 1.3.

Let us close this introductory section by making an observation about the entanglement entropy associated with the left and right degrees of freedom. Consider for instance the constant time slice that passes through the bifurcation point, connecting the two boundaries. When the interval \mathcal{A} is taken to be either the entire left (or right) system, the extremal surface that is homologous to the boundary is the bifurcation surface of the black hole (red circle in figure 1.2). Hence, the RT formula connects the von Neumann entropy of the density matrix of the TFD state in eq. (1.10) with the Bekenstein-Hawking entropy

$$S_{L/R} = S_{BH} = \frac{A(r_h)}{4G_N}. \quad (1.12)$$

In this sense, entanglement entropy is the black hole entropy!

1.2 The concept of quantum complexity

We now turn our attention to a brief introduction to quantum complexity which we expect the holographic proposals studied in this thesis to capture. Only recently quantum complexity started being explored in the context of high energy theoretical physics, which has turned into a research program of its own. For some references into this growing field of research, look into [38–62].

We start by analyzing finite dimensional quantum mechanical systems. Given a reference state, which we denote $|R\rangle$ and a set of elementary gates $\{U_{g,1}, U_{g,2}, \dots, U_{g,n}\}$, we want to investigate which quantum circuit prepares (at least approximately) a target state, $|T\rangle$, such that a certain distance measure is minimized. In summary, we want to find an optimal unitary such that

$$|T\rangle = U_T |R\rangle, \quad (1.13)$$

to a tolerance ϵ with respect to some norm, *i.e.*,

$$\|U_T |R\rangle - |T\rangle\|^2 \leq \epsilon. \quad (1.14)$$

A geometric construction relevant to study this problem was suggested by Michael Nielsen [108, 109], where the circuit complexity can be framed as a ‘‘Hamiltonian’’ control

problem, where the circuits are described in a continuous fashion with [38, 108, 109]

$$U_c(t) = \tilde{\mathcal{P}} \exp \left[-i \int_0^t dt' H(t') \right] \quad \text{and} \quad H(t') = \sum_I Y^I(t') K_I, \quad (1.15)$$

where K_I stands for the Hermitian generators that form a basis for the Hamiltonian $H(t')$. The boundary conditions are associated to the unitary in eq. (1.13) as

$$U_c(0) = \mathbb{I} \quad \text{and} \quad U_c(1) = U_T. \quad (1.16)$$

The path ordering $\tilde{\mathcal{P}}$ indicates that the circuit is built from right to left with increasing value of t . It is natural to assign a cost to different paths in this framework. As a consequence, determining the complexity involves the study of geodesics, associating a cost function $F(U_c(t), Y^I(t))$ to each path, such that the circuit depth is given by

$$D(U_c) = \int_0^1 dt F(U_c(t), Y^I(t)). \quad (1.17)$$

Let us add that in general the complexity for building a unitary operator and the one for building a state are different. In many systems, however, there should be a simple and efficient operation that translates from one quantity to the other [36]. Since we expect the complexities in both approaches to be comparable in many situations, we will often talk interchangeably about both, unless the situation demands a distinction between both notions.

In the case of free field theories, such a formalism was recently employed to investigate some general properties of complexity, such as the UV dependence [38, 39], excited states [47, 48], the additional complexity for building the thermofield double state from the vacuum, and the time dependence under the time evolution [49]. Despite not being directly applicable to theories where there is a simple holographic dual geometry, some of the properties analyzed seem to connect with the holographic results, and we will describe this a bit more in chapter 7. Also, the discussion of circuit complexity so far indicates that the concept of complexity naturally contains ambiguities. For instance, there are ambiguities associated to the reference state, the gate set, the cost function and the list goes on. Therefore, as we will see further, there is more than one holographic proposal that seem to capture some important properties of complexity. A goal of the work of this thesis is to try to investigate which properties seem to be universal, and whether it is possible to connect some of the ambiguities on either side of the AdS/CFT duality.

One puzzling observation for complexity that has an interesting consequence for the holographic proposals is that it can keep increasing for long times. For instance, for a spin

chain of N_q qubits, the complexity is conjectured to keep increasing for times exponential in the degrees of freedom $\sim 2^{N_q}$ [41]. This reflects the fact that the Hilbert spaces for quantum many-body systems are exponentially big: as a simple exercise, for a linear chain with $N_q \sim 265$ sites, or a square lattice with 16×16 sites, the Hilbert space is of size comparable to the number of atoms in the observable universe!

In practice, this translates to the fact that for chaotic systems, many states built by circuits involving Hamiltonian evolution look approximately thermal in a few circuit steps. By approximately thermal we mean the following: even though the full density matrix of the system remains in a pure state, if we consider a small subsystem we can evaluate the entanglement entropy with respect to its complement. This will be approximately thermal (in a regime near infinite temperature) if the entanglement entropy approaches its maximal value [110–112]. When every subsystem smaller than half of the whole system has maximal entanglement entropy, the system has “scrambled” the information enough such that one has to have access to at least half of the system in order to recover precisely any perturbation.

Suppose the quantum system contains a Hamiltonian with interaction terms such that a local perturbation spreads through the whole system quickly, we then expect the scrambling time to scale as the logarithm of the degrees of freedom, $\sim \log N_q$. On the other hand, complexity can still increase for exponential times $\sim 2^{N_q}$, as the group $SU(2^{N_q})$ contains exponentially large number of possible unitaries.

Therefore, we expect the circuit complexity to increase for very long times, even after perturbations have effectively thermalized, in the sense discussed above.¹ We reproduce these behaviour in figure 1.4 (adapted from [41]), with the complexity increasing for times of the order of the exponential of the degrees of freedom of the system, when it saturates. For much longer times, doubly exponential in N_q , we expect quantum recurrences to occur, such that the system returns to its initial state [113].

In this regime of linear growth, the conjecture is that the complexity should increase proportionally to the energy of the system E , such that [41]

$$\left. \frac{d\mathcal{C}}{dt} \right|_{t \lesssim 2^{N_q}} \sim E \quad \text{or} \quad \left. \frac{d\mathcal{C}}{d(tT)} \right|_{t \lesssim 2^{N_q}} \sim S, \quad (1.18)$$

where S is the entropy and T the temperature of the system. Equivalently, we could say that the derivative with respect to the time in units of the temperature should increase

¹In [85], it is presented an argument with random walks in graph theory in order to understand how the complexity should keep approximately increasing. Each node in the graph is a matrix in the space of unitaries in $SU(2^{N_q})$, and the center of the graph is the identity operator, with nodes representing a simple k -local gate.

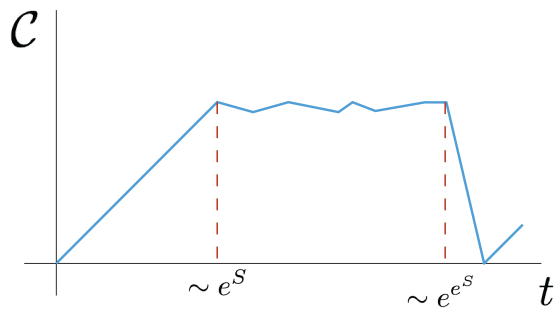


Figure 1.4: A pictorial expectation of the time evolution of complexity, based on [41]. The complexity is expected to grow linearly for times of the order of the exponential of the degrees of freedom of the system, when it saturates. We also depict much longer times, double exponential, where quantum recurrences are expected to occur and the complexity could go back to its initial small values. In the context of AdS/CFT, because the field theories under consideration have very large number of degrees of freedom, we expect that while the geometry has a good classical approximation, the complexity should keep increasing.

with a rate of the order of the entropy. One simple example where the complexity rate of change is related to the degrees of freedom of the system can be seen in an epidemic quantum circuit model, described in [86] (see also section 6.3).

Another important property of complexity, which is relevant for the discussion in shock wave geometries in chapter 6, is the study of the complexity of the precursor operator. It is defined as [32, 68]

$$V(t_w) \equiv U(t_w)\mathcal{O}_R U(-t_w) = U(t_w)\mathcal{O}_R U^\dagger(t_w), \quad U(t) = \exp(-iHt) \quad (1.19)$$

where U is the time evolution operator, and \mathcal{O}_R is a small perturbation to the system. Our interest in chapter 6 will be to apply this operator to the TFD state, such that at an earlier time t_w , one of the copies of the system in eq. (1.21) (chosen to be the right one in this notation) is slightly perturbed by \mathcal{O}_R . Since the system is evolved forward to t_w in eq. (1.19), the precursor operator is related to how a system would evolve in time in case it was slightly perturbed in the past.

Let us revisit how we should expect a circuit for N_q qubits with an interacting Hamiltonian such that every qubit is connected to one another after a few steps of time evolution. By the previous discussion, if all we wanted was a circuit that builds the time evolution unitary, we would argue that the complexity of the precursor operator should be at most $\mathcal{C}(V(t_w)) \sim 2Et_w$, as we could simply build the unitaries $U(t_w)$ and $U(-t_w)$ separately. Complexity, however, should contain a sense of optimality: we want the minimum circuit that prepares a certain unitary. For such, there is a simple argument from quantum circuits that suggests an optimal way to build the operator in eq. (1.19).

Consider for instance the schematic representation in figure 1.5 of a circuit that prepares eq. (1.19). If the perturbation only touches a small number of qubits, we expect on average that it takes $\log N_q$ for the perturbation to have propagated throughout the system. We will define more precisely this quantity in section 6, but this is essentially proportional to a quantity known as the scrambling time t_{scr}^* . In fact, if the size of the time evolution t_w is smaller than the scrambling time, we expect a great deal of cancelation in the multiplication of the unitaries $U(t_w)$ and $U^\dagger(t_w)$, such that the precursor should have a low complexity. For time evolution of times greater than the scrambling time, we do expect that the complexity of the precursor grows with t_w , but we have to take into account that there is a good cancellation of gates until the scrambling time. This can be summarized in the following [32, 68]:

$$\begin{aligned} \mathcal{C}(V(t_w)) &\sim 0 && \text{for } t_w < t_{scr}^*, \\ \mathcal{C}(V(t_w)) &\sim 2E(t_w - t_{scr}^*) && \text{for } t_w > t_{scr}^*. \end{aligned} \quad (1.20)$$

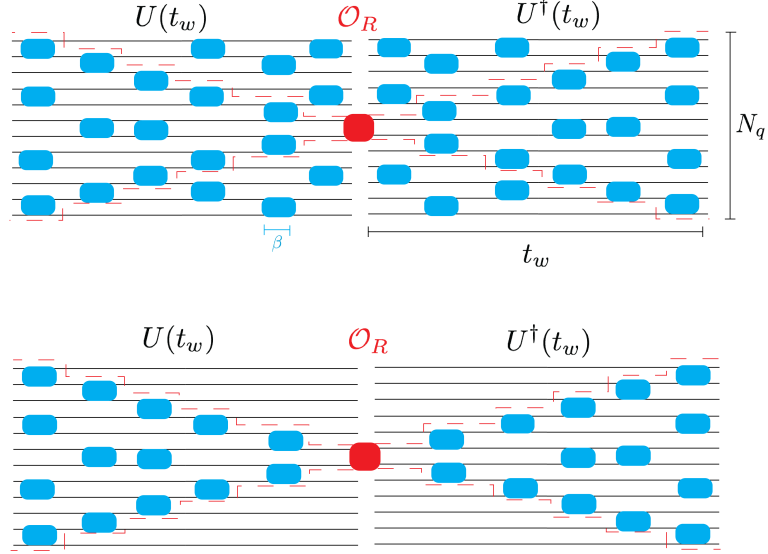


Figure 1.5: A pictorial depiction of the precursor circuit in eq. (1.19). Due to the nature of the quantum systems under consideration, it is assumed that in a time step of the order of the inverse temperature β , most of the qubits in the system interact with each other. Due to non-trivial commutation relation, we see in the lower diagram that the influence of the small perturbation grows approximately exponentially throughout the circuit, until it reaches all the degrees of freedom N_q when t_w is of the order of the scrambling time t_{scr}^* . If the time evolution unitaries are evolved for a short period of time t_w , then there is a good cancelation of gates between U^\dagger and U , and we expect a low complexity for these regimes. In fact, the subtraction of the scrambling times in the complexity, given by eq. (1.20), is known as the switchback effect.

The subtraction of the scrambling time is known as the switchback effect [32, 87]. Both linear time growth for long times, and the switchback effect are important general properties that the holographic proposals of complexity should reproduce, and a major part of the work in this thesis is to test carefully how the proposed gravitational observables of action and volume capture such properties.

1.3 Complexity in AdS/CFT

Now, we have all the ingredients needed to discuss the two holographic proposals in AdS/CFT for quantum complexity. We turn our attention back to the eternal black hole geometry dual to the thermofield double state in figure 1.2. The two boundaries are connected through the spacelike non-traversable wormhole, and we associate the “connectedness” of the spacetime to the entanglement structure of the two theories through the TFD state. One natural question is what happens with the TFD state once there is some dynamics, such as a non-trivial time evolution [114]. Since the CFTs are identical, they share the same Hamiltonian, so the time evolution in the left and right boundary reads

$$|TFD(t_L, t_R)\rangle = Z^{-1/2} \sum_{n=0}^{\infty} e^{-iE_n(t_L+t_R) - \frac{1}{2}\beta E_n} |E_n\rangle_L \otimes |E_n\rangle_R, \quad (1.21)$$

where we have defined t_L and t_R such that both are increasing towards the top part of the diagram in figure 1.2. The boost symmetry of the state is manifest: if we take the time slice to be the blue curves in figure 1.2, which represents time shifts such as

$$t_R \rightarrow t_R + \Delta t \quad \text{and} \quad t_L \rightarrow t_L - \Delta t, \quad (1.22)$$

which leaves the state in eq. (1.21) invariant. However, when the time for both CFTs evolve upwards, there is non-trivial dynamics, as there are the non-trivial complex phases that appear in eq. (1.21). From the point of view of the geometry, these are described by the green lines in figure 1.2, which are surfaces that probe the region behind the black hole horizon and with overall proper length that increases with time. In fact, as long as the geometry is well described classically, the length of the wormhole increases forever [115]!

The dynamics described by eq. (1.21) could be seen as a toy model to understand thermalization. Consider the entanglement structure between the left and right CFTs. Let us suppose that we are in a system with spherical CFTs with radius R and inverse temperature β , and let’s assume that the temperature is high. We want to study the correlation between the union of half of the sphere in one side with half of the sphere in

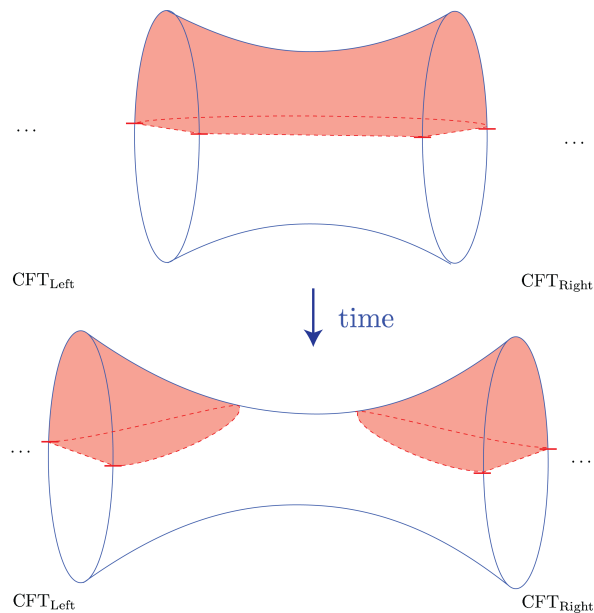


Figure 1.6: A pictorial representation of the minimal surface for the wormhole connecting the left and right CFTs under the non-trivial time evolution in eq. (1.21). If we study the entanglement structure between the union of half of the left and right CFTs with their complement, there is a critical time such that the minimal surface becomes disconnected, as the wormhole stretches. Because the entanglement saturates after a finite time to the thermal value, of the order of the system size, this model has been studied in the context of thermalization. The fact that the wormhole size keeps increasing forever, even after this saturation, has led to the conjecture that it is associated with the increase of complexity.

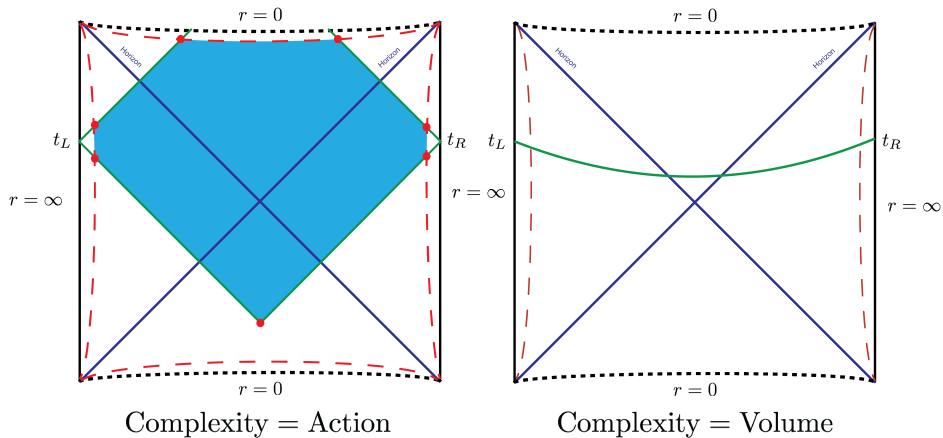


Figure 1.7: The Penrose diagram for the eternal AdS-Schwarzschild black hole and the two main holographic proposals of complexity, complexity=action (left) and complexity=volume (right). Left- We depict the Wheeler-DeWitt patch, which is bounded by null hypersurfaces, null joints and the spacelike hypersurface right above future singularity. In order to regulate the action, we represent in dashed red lines the regulator near the boundary, with $r_{max} = L^2/\delta$ being related to the UV cutoff of the CFT δ . Right - We represent the maximal volume connecting the two sided geometries, which is the ingredient of the CV proposal.

the other side with the complements of these regions. The minimum surface that separates these regions at early time is a surface that connects the left and right boundaries, as shown in figure 1.6. However, as the time increases, the wormhole “stretches”, such that there is a critical time that the minimum surface becomes disconnected, and the entanglement saturates to the thermal value [114]. Therefore, the wormhole keeps increasing for long times - classically forever - but this measure of the correlations between the left and right theories saturates at a finite time.

The fact that even though the entanglement has thermalized, but there is a property of the bulk geometry that keeps increasing for much longer times is what motivated Susskind to argue that the growth of the wormhole is capturing properties of the complexity of the time evolution [115]. In this sense, entanglement would not be an appropriate probe to

describe this very late time dynamics in the boundary, which translates to the hypersurfaces probing a region in the interior of the black hole. Since complexity for the boundary theory should increase for times exponential in N_c , as long as $N_c \rightarrow \infty$ and the geometry is well-described classically, the holographic dual of complexity should increase forever in this regime! Therefore, it was conjectured [115] that the increase of the wormhole size could be encoding properties about the complexity of the state. It was then proposed at first that the volume of the extremal/maximal time slice anchored at the boundaries at t_L and t_R (see figure 1.7) should be associated with the complexity, which is known as Complexity=Volume (CV) [31, 32], as

$$\mathcal{C}_V(\Sigma) = \max_{\Sigma=\partial\mathcal{B}} \left[\frac{\mathcal{V}(\mathcal{B})}{G_N l} \right], \quad (1.23)$$

where l is a certain arbitrary length scale in order to make the complexity dimensionless. One usual choice of l is simply to use the AdS radius L .²

Next, it was suggested that not only the maximal time slice should contribute to the complexity, but the whole domain of dependence of this surface should be taken into account. This gives rise to a region of spacetime bounded by null hypersurfaces known as the Wheeler-DeWitt (WDW) patch, as represented in the Penrose diagram in figure 1.7. The proposal is that the full action should be evaluated in this region of spacetime, which gives rise to the proposal known as Complexity=Action (CA) [33, 34], which states that

$$\mathcal{C}_A(\Sigma) = \frac{I_{\text{WDW}}}{\pi \hbar}. \quad (1.24)$$

At first glance, the CA proposal has the advantage of not depending on an overall arbitrary dimensionful multiplicative factor in its definition. In addition, for a large class of AdS-Schwarzschild black holes, the late time rate of change was simply proportional to the black hole mass, independent of the the geometry of the horizon, as well as the number of dimensions.³ The factor of $1/\pi$ was a choice for the authors of [33, 34] in an attempt to connect to a suggestion that computation rates are bounded, a conjecture known as Lloyd's bound [116]. We prove, however, that this bound is generically violated in the CA proposal in chapter 4, and in fact a generic applicability of Lloyd's bound has its own subtleties [117].

The object in eq. (1.24) is an interesting quantity from the point of view of gravitational theories. First, since it is bounded by null hypersurfaces and null joints, codimension 2

²It was suggested in [79] a more sophisticated approach in order to determine this overall scale l .

³We will analyze the rate of change of holographic complexity in chapter 4.

regions at the intersection of these null hypersurfaces, one must be careful in writing a consistent well-posed gravitational action. Recall that the Einstein-Hilbert action with a negative cosmological constant in eq. (1.2) reads

$$I_{EH} = \frac{1}{16\pi G_N} \int_{\mathcal{M}} d^{d+1}x \sqrt{-g} \left(R + \frac{d(d-1)}{L^2} \right), \quad (1.25)$$

and variations of the action naturally involve the variation of the Ricci scalar R , which depends on second derivatives of the spacetime metric. We can rewrite the variation of the Ricci tensor with derivatives of the Christoffel symbols as

$$\begin{aligned} \delta R_{\mu\nu} &= \nabla_\lambda (\delta \Gamma_{\mu\nu}^\lambda) - \nabla_\nu (\delta \Gamma_{\mu\lambda}^\lambda), \\ \text{where } \Gamma_{\mu\nu}^\alpha &= \frac{1}{2} g^{\alpha\lambda} (\partial_\nu g_{\mu\lambda} + \partial_\mu g_{\nu\lambda} - \partial_\lambda g_{\mu\nu}). \end{aligned} \quad (1.26)$$

The variation of the action in eq. (1.25) gives

$$\begin{aligned} 16\pi G_N \delta I_{EH} &= \int_{\mathcal{M}} d^{d+1}x \sqrt{-g} \left(G_{\mu\nu} - \frac{d(d-1)}{2L^2} g_{\mu\nu} \right) \delta g^{\mu\nu} + \\ &+ \oint_{\partial\mathcal{M}} d\Sigma_\mu \left(g^{\alpha\beta} \delta \Gamma_{\alpha\beta}^\mu - g^{\alpha\mu} \delta \Gamma_{\alpha\beta}^\beta \right). \end{aligned} \quad (1.27)$$

The first line leads to the equations of motion for the metric $g_{\mu\nu}$, while the second surface term still contains variations of the first derivative of the metric. Therefore, in order to have a well-posed variational principle, one must add boundary terms in order to compensate such contributions. This is the origin of the Gibbons-Hawking-York surface term [118, 119], which one must add to spacelike/timelike boundaries when evaluating a gravitational action. Due to the nature of the holographic CA proposal, we need a rigorous prescription to evaluate the gravitational action bounded by null surfaces and joints, which was recently developed in [63].⁴

Despite not having an overall multiplicative dimensionful ambiguity as the CV proposal in eq. (1.23), there are a number of ambiguities in evaluating the action bounded by null surfaces, and a major part of the work in this thesis is to understand how they affect the properties of holographic complexity, and if so whether there are any counterparts in the complexity models for the field theories defined at the boundary.

Another interesting property from the point of view of the gravitational side of the AdS/CFT duality is that both CV and CA proposals depend non-trivially on the physics

⁴See also [120] for a discussion of null boundaries, [121, 122] for alternative discussions and [123] for an earlier related construction.

behind the black hole horizon even at very late times, probing degrees of freedom in the interior. In addition, the WDW patch in the CA proposal can effectively probe very small distances, as it involves the evaluation of the action bounded by a regulating hypersurface very close to the curvature singularity, in case it is a spacelike singularity such as in AdS-Schwarzschild black holes. The fact that such proposals are sensitive to the physics of the interior, as well as the causal structure of the black hole spacetimes, makes them novel gravitational probes that could reveal surprising properties in the context of AdS/CFT.

In addition, both CA and CV proposals can reproduce the main desired properties discussed in the last section given some assumptions. For instance, after a few time steps in units of the inverse temperature, the complexity grows linearly to a very good approximation for a large class of black holes, and it is proportional to the mass, consistent with the proposal in eq. (1.18). Also, as we will show carefully in chapter 6, the gravitational observables exhibit a behaviour consistent with the switchback effect, which translates to studying geometries perturbed by shock waves. In fact, we use the switchback effect in order to argue that imposing reparametrization invariance of the null normals to null boundaries of the WDW patch in the CA proposal is necessary, which is achieved by the addition of a surface counterterm to the action [67, 68].

1.4 Organization of the thesis

This thesis is organized as follows: we start in chapter 2 with general considerations about the black hole geometries, describing the relevant parameters and trying to unify the notation that will be relevant for the remainder of the thesis. In addition, we discuss some general properties of evaluating the different contributions to the gravitational action in the Wheeler-DeWitt patch, since we will mostly examine the CA proposal in the rest of the chapters.

Next, we evaluate the complexity of formation in holographic theories in chapter 3, where we compare the additional complexity of building the thermofield double state in comparison to building two copies of the vacuum. This observable is of interest as the subtraction between the complexities provide a possible way to regulate them, as we will show that the complexity of formation is UV-finite, and proportional to the entropy of the thermal system (plus curvature corrections). We will evaluate AdS-Schwarzschild black holes with different horizon geometries, for both the CA and CV proposals.

In chapter 4, we study the time evolution of the holographic complexity in the AdS-Schwarzschild eternal black hole, and in particular we want to evaluate how the late time

growth rate is reached. We find a generic feature that for the CA proposal in the eternal black hole geometry, the late time limit is reached from above. For the CV proposal, we find the opposite behaviour, and the late time growth rate is reached from below. We also evaluate the full time evolution for charged black holes, and show that the approach of the late time limit is also from above in the CA proposal. In this situation, we conclude that using Lloyd's bound does not appear to be an appropriate approach to constrain the holographic duals of complexity.

We study shock wave geometries in the next chapters, we focus on one-sided geometries in chapter 5 and two-sided ones in chapter 6. We start by constructing a null fluid action in chapter 5, showing how one can evaluate the action in the limit that the collapsing null shell has zero thickness. Next, we investigate the complexity rate of change for geometries connecting the AdS vacuum to a black hole geometry, and we find that it is necessary to include a surface counterterm to the null boundaries of the WDW patch that ensures reparametrization invariance. In addition, in contrast to the results of chapter 4, the CA proposal has the late time limit reached from below, while for the CV proposal it is reached from above.

Next, we investigate the switchback effect for shock waves in two-sided black hole geometries in chapter 6. We find once again that the addition of the reparametrization invariance counterterm is necessary in order to reproduce the switchback effect. Since we construct the Vaidya geometry for all energies of shock waves, we also investigate how the switchback effect extends to and is matched for heavier shocks. For brevity, we will present only the results of the CA proposal in this chapter.

Finally, we discuss other developments and provide some future outlook in chapter 7.

Chapter 2

Preliminaries

In this chapter we introduce some common notation and assumptions in order to evaluate the holographic complexity in the remainder of the thesis. This chapter is an extended version of section 2 of [64].

2.1 General framework in higher dimensions ($d > 2$)

In this section, we describe the evaluation of the (regulated) gravitational action for the Wheeler-DeWitt (WDW) patch in various asymptotically locally AdS spacetimes. In particular, we focus on the AdS black holes in $d+1$ dimensions, whose metric takes the general form:¹

$$ds^2 = -f(r) dt^2 + \frac{dr^2}{f(r)} + r^2 d\Sigma_{k,d-1}^2, \quad (2.1)$$

with

$$f(r) = \frac{r^2}{L^2} + k - \frac{\omega^{d-2}}{r^{d-2}}. \quad (2.2)$$

Here, L denotes the AdS curvature scale while $k = \{+1, 0, -1\}$ indicates the curvature of the $(d-1)$ -dimensional line element $d\Sigma_{k,d-1}^2$, which is given by

$$d\Sigma_{k,d-1}^2 = \begin{cases} d\Omega_{d-1}^2 & = d\theta^2 + \sin^2 \theta d\Omega_{d-2}^2 & \text{for } k = +1, \\ d\ell_{d-1}^2 & = \sum_{i=1}^{d-1} dx_i^2 / L^2 & \text{for } k = 0, \\ d\Xi_{d-1}^2 & = d\theta^2 + \sinh^2 \theta d\Omega_{d-2}^2 & \text{for } k = -1. \end{cases} \quad (2.3)$$

¹Here, we will assume that the boundary dimension satisfies $d > 2$. The special case of the BTZ black hole [124, 125] with $d = 2$ will be treated in section 2.2.

Hence, with $k = +1$, we have $d\Omega_{d-1}^2$, the standard round metric on a unit $(d-1)$ -sphere; while for $k = 0$, $d\ell_{d-1}^2$ is the flat metric on R^{d-1} (normalized by $1/L^2$); and for $k = -1$, $d\Xi_{d-1}^2$ is the metric on a $(d-1)$ -dimensional hyperbolic ‘plane’ with unit curvature. In particular then, the black holes corresponding to $k = \{+1, 0, -1\}$ have spherical, planar, and hyperbolic horizons, respectively. The position of the horizon r_h is determined by the ‘mass’ parameter ω with

$$\omega^{d-2} = r_h^{d-2} \left(\frac{r_h^2}{L^2} + k \right). \quad (2.4)$$

Each of these solutions (2.1) of the $(d+1)$ -dimensional Einstein equations can be represented by the same Penrose diagram shown in figure 4.1.² Of course, these geometries are also static with the Killing vector ∂_t .

In the context of the AdS/CFT correspondence, these AdS black holes provide a holographic description of a uniform thermal bath in the dual CFT in the corresponding d -dimensional boundary geometry:

$$ds_{\text{boundary}}^2 = -dt^2 + L^2 d\Sigma_{k,d-1}^2. \quad (2.5)$$

The temperature of the thermal ensemble is given by

$$T = \frac{1}{4\pi} \left. \frac{\partial f}{\partial r} \right|_{r=r_h} = \frac{1}{4\pi r_h} \left(d \frac{r_h^2}{L^2} + (d-2)k \right), \quad (2.6)$$

where we have used eq. (2.4) to substitute for ω^{d-2} in the above expression. The total energy is given by [126, 127]

$$M = \frac{(d-1)\Omega_{k,d-1}}{16\pi G_N} \omega^{d-2}, \quad (2.7)$$

where $\Omega_{k,d-1}$ denotes the dimensionless volume of the relevant spatial geometry in eq. (2.3). For instance, for $k = +1$, we have the volume of a $(d-1)$ -dimensional unit sphere: $\Omega_{1,d-1} = 2\pi^{d/2}/\Gamma(d/2)$. For the hyperbolic and planar geometries, we must introduce an infrared regulator to produce a finite volume, *e.g.*, for $k = 0$, we could simply identify the spatial coordinates with $x_i \sim x_i + R_i$.³ The entropy of the system is determined by the usual Bekenstein-Hawking entropy of the event horizon:

$$S = \frac{\mathcal{A}_{\text{horizon}}}{4G_N} = \frac{\Omega_{k,d-1}}{4G_N} r_h^{d-1}. \quad (2.8)$$

²‘Small’ hyperbolic black holes (with $k = -1$) require some extra consideration — see comments below, as well as appendix A.3.

³This choice then yields the dimensionless volume $\Omega_{0,d-1} = \prod_{i=1}^{d-1} R_i/L^{d-1}$, while the dimensionful spatial volume of the boundary geometry (2.5) would be simply $\mathcal{V}_{0,d-1} = L^{d-1} \Omega_{0,d-1} = \prod_{i=1}^{d-1} R_i$.

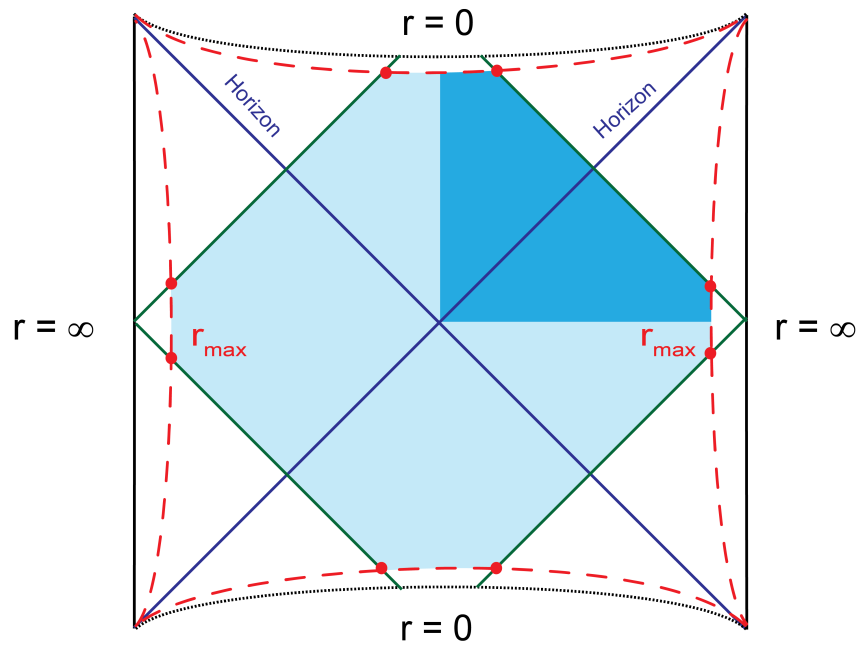


Figure 2.1: Penrose diagram for black holes in more than three bulk dimensions ($d > 2$). We define surfaces of constant r to regulate the action both near the asymptotic boundary ($r = r_{\max}$) and near the past and future singularities ($r = \epsilon_0$). We identify the Wheeler-DeWitt patch as the area of the bulk bounded by the four null sheets which originate from the boundary at $t = 0$. The joints between the null sheets and the regulating surfaces are indicated by red dots.

In using the language of a thermal ensemble, we are describing the physics of the CFT dual to a single asymptotic boundary of the black hole geometry (2.1). As described in the introduction, the full geometry illustrated in figure 4.1 can be interpreted as the dual of the thermofield double state (1.10), which provides a purification of the thermal ensemble with the second asymptotic boundary being dual to the thermofield double of the original CFT [30]. Now the central question, which we wish to address here, is what is the additional complexity involved in forming this entangled thermofield double state (1.10) compared to preparing each of the two individual CFTs in their vacuum state. In the nomenclature of [33, 34], we wish to evaluate the ‘complexity of formation.’

Hence applying the complexity=action proposal [33, 34], we begin by evaluating the action of the WDW patch with $t_L = 0 = t_R$, shown in figure 4.1, to determine the complexity of the thermofield double state (1.10). Then for comparison, we evaluate the action of the WDW patch in the vacuum AdS spacetime, corresponding to the metric (2.1) with $\omega = 0$, *i.e.*, replacing $f(r)$ with

$$f_0(r) = \frac{r^2}{L^2} + k. \quad (2.9)$$

While the evaluation of the action in the black hole backgrounds is essentially the same for the three different geometries corresponding to $k = \{+1, 0, -1\}$, there are small differences for the vacuum geometries which should be accounted for. We will describe these subtleties here, *i.e.*, various singularities in the geometry. However, we defer evaluating their contributions to the gravitational action to appendix A.2, because our final conclusion will be that in fact these singularities do *not* affect the final value of the WDW action in the vacuum spacetimes. The WDW patches for the AdS vacua are shown in figure 2.2.

a) Spherical geometry: With $k = +1$, the vacuum metric in the bulk is the AdS geometry in global coordinates. In particular then, these coordinates cover the entire AdS spacetime. Choosing a constant time slice, the corresponding WDW patch is the causal diamond shown in figure 2.2a. The only point to note here is that the past and future tips of the causal diamond are caustics, *i.e.*, all of the null rays in the associated null boundaries cross each other at these points. Singular features like this were not considered in the recent discussion of boundary terms for the gravitational action [63] and so will require some special attention.

b) Planar geometry: With $k = 0$, the vacuum bulk metric is the AdS space in Poincaré coordinates, which only cover a portion of the full AdS geometry. We note that in these coordinates, the $t = 0$ time slice covers the entire Cauchy surface at $t = 0$ in global coordinates.⁴ In the present context, however, we are compactifying the spatial coordinates

⁴We must include an extra point at infinity, *i.e.*, at $x_i, r \rightarrow \infty$.

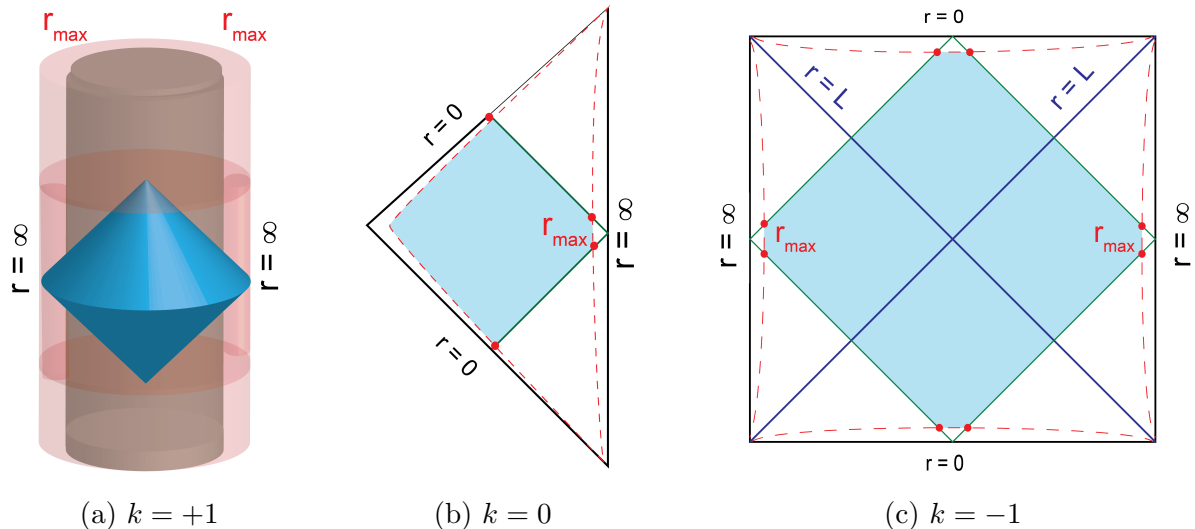


Figure 2.2: Penrose diagrams of the Wheeler-DeWitt patch in vacuum AdS for the different values $k = \{+1, 0, -1\}$.

— as described below eq. (2.7) — and as a result, the Poincaré horizon becomes a null orbifold or ‘conical’ singularity. That is, the proper volume of the spatial geometry shrinks to zero along this null line. Further, the null generators of the corresponding WDW patch all intersect when they hit this null spacetime singularity, as shown in figure 2.2b. Hence both this caustic and the null singularity will require special attention in evaluating the action of the WDW patch.

c) Hyperbolic geometry: With $k = -1$, the vacuum bulk metric is AdS space in the so-called ‘AdS-Rindler’ coordinates. Again these coordinates only cover a portion of the full AdS geometry, and in particular, the infinite hyperbolic geometry only covers a portion of the boundary time slice at $t = 0$ and $r \rightarrow \infty$ — see figure 2 in [26]. Examining $f_0(r)$ in eq. (2.9) with $k = -1$, we see that there is still a horizon at $r_h = L$ even when $\omega = 0$. Further, eq. (2.6) then yields a finite temperature $T = 1/(2\pi L)$ in this case. Hence the vacuum metric still has the form of an AdS black hole and it can be interpreted in terms of an entangled state of two copies of the CFT on a hyperbolic hyperplane. This curious interpretation of the ‘AdS vacuum’ can be understood from the discussion of [128]. The hyperbolic boundary geometry, *i.e.*, eq. (2.5) with $k = -1$, can be mapped to the spherical or planar boundary geometry with a conformal transformation. However, this mapping

takes the $t = 0$ time slice in the $k = -1$ geometry to the interior of a finite spherical region in either of the other two geometries. While the CFT vacuum is a pure state on the global time slice of either of the latter backgrounds, it becomes a mixed state when reduced to this spherical region. The entangled state of two copies of the CFT on a hyperbolic plane appearing above can then be understood as a conformally transformed description of the global vacuum state which entangles the CFT degrees of freedom on the interior with those on the exterior of the sphere. Since the vacuum already contains two copies of the CFT in the hyperbolic case, we only need to consider a single copy of the vacuum AdS geometry when evaluating the complexity of formation.

We should also add that since we are compactifying the spatial geometry, the volume of the spatial sections shrinks to zero at $r = 0$ producing an orbifold singularity. However, for $k = -1$, this singularity lies behind the horizon and as shown in figure 2.2c, the tips of the WDW patch just touch this singular surface. Again this singularity requires special attention in evaluating the action of the WDW patch.

At this point, we might also mention that with $k = -1$, the event horizon persists when ω^{d-2} takes on negative values and the black hole mass (2.7) becomes negative [129, 130]. In this case, eq. (2.4) yields two real positive solutions for r_h and the causal structure of the geometry takes a form similar to that of a charged black hole — see figure A.3. Hence the evaluation of the action in this case demands some extra attention, as described in appendix A.3.

Finally, let us close here by observing that we can follow the procedure outlined below to evaluate the complexity of formation for any value of r_h . However, in the case of spherical horizons, we should recall the Hawking-Page phase transition [131–133], which occurs for small black holes.⁵ That is, when $r_h < L$, the saddle point which dominates the bulk partition function is still vacuum AdS space. This implies then that the complexity of formation is only an order one quantity in the large N (or large central charge) expansion of the boundary CFT — see section 3.3.

2.1.1 Evaluating the Action

Next, we describe in detail the evaluation of the gravitational action for the Wheeler-DeWitt patch. Including all of the various boundary terms, the gravitational action can

⁵Recall that there is no analogous phase transition for the planar or hyperbolic black holes [133].

be written as [63],⁶

$$\begin{aligned}
I = & \frac{1}{16\pi G_N} \int_{\mathcal{M}} d^{d+1}x \sqrt{-g} \left(R + \frac{d(d-1)}{L^2} \right) + \frac{1}{8\pi G_N} \int_{\mathcal{B}} d^d x \sqrt{|h|} K \\
& + \frac{1}{8\pi G_N} \int_{\mathcal{B}'} d\lambda d^{d-1}\theta \sqrt{\gamma} \kappa + \frac{1}{8\pi G_N} \int_{\Sigma} d^{d-1}x \sqrt{\sigma} \eta + \frac{1}{8\pi G_N} \int_{\Sigma'} d^{d-1}x \sqrt{\sigma} a.
\end{aligned} \tag{2.10}$$

The various terms include: the Einstein-Hilbert and cosmological constant terms (with $\Lambda = -d(d-1)/(2L^2)$) integrated over the $d+1$ -dimensional volume \mathcal{M} ; the Gibbons-Hawking-York extrinsic curvature term [118, 119] integrated over the timelike and spacelike boundary surfaces, denoted by \mathcal{B} ; the κ boundary contribution [63] (see also [120]) integrated over d -dimensional null boundary surfaces, denoted by \mathcal{B}' ; the Hayward joint terms [134, 135] which are included at the intersections Σ of two boundaries which are either timelike or spacelike; and finally the a joint terms [63] which are included at the intersections Σ' of two boundary surfaces where either or both are null surfaces. In the following, we consider the contribution of each of these terms to the action of the WDW patch in the static black hole background (2.1) at $t_L = 0 = t_R$, as well as in the corresponding AdS vacuum geometries. We will examine the full time evolution of the complexity in chapter 4. There is also a possible addition of a counterterm to the action in eq. (2.10), which was constructed in [63] in order to impose reparametrization invariance of the null normals to the boundary of \mathcal{M} . This counterterm reads

$$I_{\text{ct}} = \frac{1}{8\pi G_N} \int_{\mathcal{B}'} d\lambda d^{d-1}\theta \sqrt{\gamma} \Theta \log(\ell_{\text{ct}} \Theta), \tag{2.11}$$

with ℓ_{ct} being an arbitrary (constant) length scale and Θ is the expansion scalar of the null boundary generators, *i.e.*,

$$\Theta = \partial_\lambda \log \sqrt{\gamma}. \tag{2.12}$$

The expansion Θ only depends on the intrinsic geometry of the null boundaries and so this additional surface term (2.11) is not required to ensure that the gravitational action (2.10) produces a well-defined variational principle. However, this counterterm was constructed to eliminate the dependence of the action on the parametrization of the null generators. The properties discussed in chapters 3 and 4 do not depend significantly on the addition of such term to the action, however it is essential to consider such term in shock wave geometries, as we discuss in chapters 5 and 6.

⁶We will be using slightly modified conventions from those given in [63] — see [65]. In addition, we noticed a typo in the null surface contribution to the action, proportional to κ , in [63, 65]. Correcting for this mistake, we have flipped the sign of the κ term above. We comment further on this issue below where this sign becomes important — see eq. (5.21) in chapter 5.

However, before proceeding with these calculations, we first observe that the action of the WDW patch is divergent because this spacetime region extends all the way to the asymptotic boundary of the bulk geometry. This divergence would naturally be associated with a UV divergence in the complexity related to establishing correlations between the CFT degrees of freedom at arbitrarily short distance scales, *e.g.*, see [65]. Hence to make sense of the calculation, we regulate with the standard approach of truncating the region on which the action is evaluated by a cutoff surface at $r = r_{\max}$, see, *e.g.*, [127, 136–139].⁷ A potential subtlety here is that we wish to compare the WDW actions in the two different spacetimes (*i.e.*, the AdS black hole and vacuum AdS space) and so we need to choose our cutoff surfaces in a consistent way. As described in appendix A.1, we do so by describing both geometries with the corresponding metric in the canonical form given by the Fefferman-Graham expansion [140, 141] and then we set the radial cutoff surface at $z = \delta$ in both cases. As usual, δ plays the role of a short-distance cutoff in the dual boundary theory. The final result is given by

$$r_{\max}^{\text{BH}} - r_{\max}^{\text{vac}} = \frac{\omega^{d-2}}{2dL^{2(d-2)}} \delta^{d-1} + \mathcal{O}(\delta^{d+1}) . \quad (2.13)$$

It turns out that this difference appears at a sufficiently high order that, in fact, the complexity of formation is not affected — see appendix A.1. Note that the (timelike) UV cutoff surfaces at $r = r_{\max}$ are shown in the Penrose diagrams in figures 4.1 and 2.2.⁸

Next we need to define the (null) boundaries of the WDW patch. For this purpose, it will be useful to define the tortoise coordinate,

$$r^* = \int \frac{dr}{f(r)} , \quad (2.14)$$

with which we construct the Eddington-Finkelstein outgoing and infalling coordinates,

$$u = t - r^*(r) \quad \text{and} \quad v = t + r^*(r) , \quad (2.15)$$

⁷The standard approach is to eliminate the corresponding divergences in the regulated action by adding surface counterterms, *e.g.*, [127, 136–139]. The ‘renormalized’ action is then evaluated by taking the limit $r_{\max} \rightarrow \infty$ (or $\delta \rightarrow 0$). We do not apply this approach here in evaluating the action of the WDW patch for two reasons: First, the same surface counterterms simply do not remove the divergences in the WDW action [65]. Second, the UV divergences have a physical interpretation in terms of the complexity, as described above. Note, however, that the UV divergences will cancel below in the difference of the WDW actions for the black hole and vacuum, and hence the complexity of formation is finite, *i.e.*, independent of the details of the UV regulator.

⁸We have also shown various other regulator surfaces, *e.g.*, near the spacetime singularity in the black hole geometry. These will appear in the discussion below and in appendix A.2.

respectively. In terms of these coordinates, the metric (2.1) becomes

$$\begin{aligned} ds^2 &= -f(r) du^2 - 2 du dr + r^2 d\Sigma_{k,d-1}^2 \\ &= -f(r) dv^2 + 2 dv dr + r^2 d\Sigma_{k,d-1}^2, \end{aligned} \quad (2.16)$$

which are well-behaved on the past and future event horizons, respectively. Now let us focus our attention on the right-hand side of the Penrose diagram in figure 4.1. We are interested in the WDW patch corresponding to the time slice $t = 0$ (*i.e.*, $t_R = 0$) and so the past null boundary can be defined as

$$u = u_\infty \quad \text{with} \quad u_\infty = - \lim_{r \rightarrow \infty} r^*(r). \quad (2.17)$$

Similarly, the future null boundary is given by

$$v = v_\infty \quad \text{with} \quad v_\infty = \lim_{r \rightarrow \infty} r^*(r). \quad (2.18)$$

Note that the two constants are the same up to a sign, *i.e.*, $u_\infty = -v_\infty$.

Analogous boundaries can be constructed for the left-hand side of the Penrose diagram, however, the details for these will not be needed. In particular, there is a four-fold symmetry in the case of interest (*i.e.*, the WDW patch corresponding to $t_R = 0 = t_L$) consisting of the left-right symmetry in the Penrose diagram and the time reflection symmetry, *i.e.*, $t \rightarrow -t$. Hence for simplicity, our calculations of the action focus only on the upper right quadrant in figure 4.1, *i.e.*, the region between $t = 0$ and $v = v_\infty$.

As a final note here, it will be useful for the following calculations to evaluate the tortoise coordinate (2.14). In general, the blackening factor can be written in the form:

$$f(r) = (r - r_h) F(r) \quad (2.19)$$

where $F(r)$ has no positive real roots.⁹ Hence the inverse of $f(r)$ can be decomposed as:

$$\frac{1}{f(r)} = \frac{1}{F(r_h)(r - r_h)} + \frac{F(r_h) - F(r)}{F(r)F(r_h)(r - r_h)}. \quad (2.20)$$

Note that while the first term contains a pole at $r = r_h$, the second term above is regular at the horizon. Integrating with respect to r , we obtain the tortoise coordinate:

$$r^*(r) = \frac{\log|r - r_h|}{F(r_h)} + G(r) \quad \text{where} \quad G(r) = \int \frac{F(r_h) - F(r)}{F(r)F(r_h)(r - r_h)} dr. \quad (2.21)$$

⁹The only exception is the case of small hyperbolic black holes, where the blackening factor has two positive real roots. We will deal with this case separately in appendix A.3.

Again, the function $G(r)$ is completely regular at $r = r_h$. Eq. (2.21) will be useful to explicitly evaluate the tortoise coordinate (2.14) for the specific examples presented in the following section.

We now turn to the evaluation of each of the contributions in the gravitational action (2.10) for the WDW patch shown in figure 4.1.

Bulk Contribution

We start by evaluating the Einstein-Hilbert and cosmological constant terms in eq. (2.10):

$$I_{\text{bulk}} = \frac{1}{16\pi G_N} \int_{\mathcal{M}} d^{d+1}x \sqrt{-g} \left(R + \frac{d(d-1)}{L^2} \right). \quad (2.22)$$

Einstein's equations yield $R = -d(d+1)/L^2$ and so the above can be written as¹⁰

$$I_{\text{bulk}} = -\frac{\Omega_{k,d-1} d}{2\pi G_N L^2} \int_0^{r_{\text{max}}} dr r^{d-1} (v_{\infty} - r^*(r)), \quad (2.23)$$

where v_{∞} is the constant defining the null boundary for this quadrant, as in eq. (2.18). Further, as described above, we have multiplied by a factor of 4 and we are only performing the integral over the upper right quadrant of the WDW patch.

We might note that the same expression can be applied for the vacuum AdS spacetime. The latter only requires that we replace $f(r)$ by $f_0(r)$ from eq. (2.9), which is used in the definition of $r^*(r)$ in eq. (2.14) — as well as v_{∞} then in eq. (2.18). In this case, the factor of 4 in eq. (2.23) automatically includes the contribution of two vacuum AdS geometries.

Surface Contributions

Next we have the GHY extrinsic curvature term [118, 119], which is integrated over the timelike or spacelike boundary surfaces,

$$I_{\text{GHY}} = \frac{1}{8\pi G_N} \int_B d^d x \sqrt{|h|} K. \quad (2.24)$$

There are two pairs of such surfaces for the WDW patch in figure 4.1: the timelike surfaces at $r = r_{\text{max}}$, which are introduced in both of the asymptotic regions to provide a UV cutoff,

¹⁰We are evaluating eq. (2.22) using the original (t, r) coordinates in eq. (2.1). For the upper right quadrant described above, we integrate over the time coordinate as: $\int_0^{v_{\infty} - r^*(r)} dt = v_{\infty} - r^*(r)$.

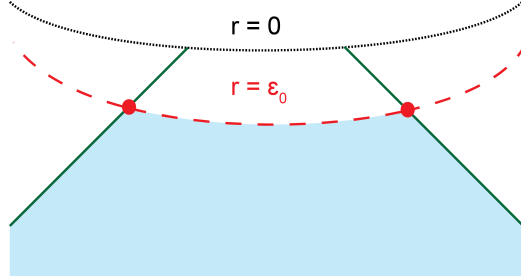


Figure 2.3: The top of the WDW patch for black holes in $d > 2$. The GHY surface term evaluated on the regulator surface at $r = \epsilon_0$ makes a finite contribution to the action.

as discussed above eq. (2.13); and the spacelike surfaces at $r = \epsilon_0$, which are inserted to regulate the geometry of the WDW patch where it touches the future and past curvature singularities behind the horizon, following [34] — see figure 2.3. As described above, we will only focus on the contribution of the GHY terms in the upper right quadrant. We can write the unit normal vectors to these surfaces as

$$\begin{aligned}
 r = r_{\max} : \quad \mathbf{s} &= s_\mu dx^\mu = \frac{dr}{\sqrt{f(r_{\max})}}, \\
 r = \epsilon_0 : \quad \mathbf{t} &= t_\mu dx^\mu = -\frac{dr}{\sqrt{-f(\epsilon_0)}}.
 \end{aligned}
 \tag{2.25}$$

Note that our convention here is that these normals (as one-forms) point outward from the spacetime volume of interest. The trace of the extrinsic curvature is then given by

$$K = \frac{n_r}{2} \left(\partial_r f(r) + \frac{2(d-1)}{r} f(r) \right),
 \tag{2.26}$$

where n_μ denotes the unit normal of interest. Substituting the appropriate normals from eq. (2.25) into this expression then yields for (2.24):

$$I_{\text{GHY}}(r = \epsilon_0) = -\frac{\Omega_{k,d-1} r^{d-1}}{4\pi G_N} \left(\partial_r f(r) + \frac{2(d-1)}{r} f(r) \right) \left(v_\infty - r^*(r) \right) \Big|_{r=\epsilon_0},
 \tag{2.27}$$

$$I_{\text{GHY}}(r = r_{\max}) = \frac{\Omega_{k,d-1} r^{d-1}}{4\pi G_N} \left(\partial_r f(r) + \frac{2(d-1)}{r} f(r) \right) \left(v_\infty - r^*(r) \right) \Big|_{r=r_{\max}},
 \tag{2.28}$$

where we have included an additional factor of 4 to include the contributions from all four quadrants of the Penrose diagram.

Note that eq. (2.28) for the contribution of the UV cutoff surface can also be used for the vacuum AdS spaces upon replacing $f(r)$ with $f_0(r)$ from eq. (2.9). Recall that there is a small difference in the value of r_{\max} for the black hole and vacuum AdS geometries, as shown in eq. (2.13). However, a detailed analysis shows that the difference between these surface contributions in the two geometries vanishes. That is, when the corresponding contribution for vacuum AdS is subtracted from eq. (2.28) for the black hole geometry, the result is proportional to a single power of δ and so vanishes in the limit $\delta \rightarrow 0$ — see appendix A.1.2 for details.

On the other hand, the contribution (2.27) coming from the singularity has no counterpart in the vacuum AdS geometry. Examining this expression in more detail, we find that the black hole geometry yields a finite result,

$$I_{\text{GHY}}(r = \epsilon_0) = \frac{d \Omega_{k,d-1} \omega^{d-2}}{4\pi G_N} (v_\infty - r^*(0)) + O(\epsilon_0). \quad (2.29)$$

Hence this is the only contribution which the GHY surface terms make to the complexity of formation.¹¹

We also have the surface term introduced in [63] for null boundary surfaces,

$$I_{\text{null surface}} = -\frac{1}{8\pi G_N} \int_{\mathcal{B}'} d\lambda d^{d-1}\theta \sqrt{\gamma} \kappa, \quad (2.30)$$

where the hypersurface is described parametrically by $x^\mu = x^\mu(\lambda, \theta^A)$ with λ , the parameter along the null generators spanning the boundary surface and θ^A constant on each generator. Then κ measures the failure of λ to be an affine parameter on the null generators of the surface, *i.e.*,

$$k^\mu \nabla_\mu k_\nu = \kappa k_\nu \quad \text{with} \quad k^\mu = \frac{\partial x^\mu}{\partial \lambda}. \quad (2.31)$$

Hence this contribution can be easily dismissed by using the ambiguity in the null normals to choose them to be affinely parameterized and so setting $\kappa = 0$, as discussed in [63].¹² This is easily achieved here using the definition of the null boundaries in terms of the Eddington-Finkelstein coordinates (2.17) and (2.18). In particular for the null boundary in the upper right quadrant, we set

$$\mathbf{k} = dv|_{v=v_\infty} = \left(dt + \frac{dr}{f(r)} \right) \Big|_{v=v_\infty}. \quad (2.32)$$

¹¹We note that the computation for small hyperbolic black holes is slightly different and there is no contribution from the spacetime singularity inside the event horizon — see appendix A.3 for details.

¹²In appendix A.4, we consider a different parameterization of the null surfaces yielding $\kappa = \text{constant}$ and we find that our results for the complexity of formation do not change.

Implicitly, we have normalized this null normal at the asymptotic AdS boundary such that $\mathbf{k} \cdot \hat{\mathbf{t}} = 1$ where $\hat{\mathbf{t}} = \partial_t$, as suggested in [63].

Joint Contributions

This leaves the joint terms in the gravitational action (2.10) which are needed where two of the boundary surfaces intersect. First, we have the Hayward terms [134, 135]

$$I_{\text{Hay}} = \frac{1}{8\pi G_N} \int_{\Sigma} d^{d-1}x \sqrt{\sigma} \eta, \quad (2.33)$$

but these are not relevant here since all of the joints in figure 4.1 involve at least one null surface. Hence we only need to consider the last term in the gravitational action (2.10)

$$I_{\text{jnt}} = \frac{1}{8\pi G_N} \int_{\Sigma'} d^{d-1}x \sqrt{\sigma} a, \quad (2.34)$$

where a is defined as [63],

$$a = \begin{cases} \epsilon \log |k \cdot t| & \text{for spacelike-null joint with } \epsilon = -\text{sign}(k \cdot t) \text{sign}(k \cdot \hat{s}), \\ \epsilon \log |k \cdot s| & \text{for timelike-null joint with } \epsilon = -\text{sign}(k \cdot s) \text{sign}(k \cdot \hat{t}). \end{cases} \quad (2.35)$$

and \hat{s} and \hat{t} are auxiliary unit *vectors* in the tangent space of the spacelike/timelike boundary surface, which are orthogonal to the junction and point outwards from the boundary region of interest — see figure A.6 and reference [65].

Again focusing our attention on the upper right quadrant of the WDW patch, we have a spacelike-null joint where the null boundary (2.18) meets the regulator surface $r = \epsilon_0$.¹³ Using the corresponding normals in eqs. (2.25) and (2.32) and $\hat{\mathbf{s}} = \hat{s}^\mu \partial_\mu = \partial_t / \sqrt{-f(r)}$, the null joint term (2.34) yields

$$\begin{aligned} I_{\text{jnt,sing}} &= -\frac{\Omega_{k,d-1}}{4\pi G_N} r^{d-1} \log |f(r)| \Big|_{r=\epsilon_0} \\ &\simeq \frac{\Omega_{k,d-1}}{4\pi G_N} \epsilon_0^{d-1} \log(\epsilon_0^{d-2} / \omega^{d-2}), \end{aligned} \quad (2.36)$$

where as usual we have included a factor of 4 to include the contributions of all of the joints near the future and past singularities. However, the key observation about this result is that this contribution vanishes in the limit $\epsilon_0 \rightarrow 0$.

¹³Again, we note that the computation for small hyperbolic black holes is slightly different — see appendix A.3 for details.

We also have a timelike-null joint where the null boundary (2.18) meets the cut-off surface $r = r_{\max}$. In this case $\hat{\mathbf{t}} = \hat{t}^\mu \partial_\mu = \partial_t / \sqrt{f(r)}$ and the corresponding contribution (including the usual factor of 4) is

$$I_{\text{jnt,cut}} = \frac{\Omega_{k,d-1}}{4\pi G_N} r^{d-1} \log f(r) \Big|_{r=r_{\max}}. \quad (2.37)$$

Again, this contribution from the UV cutoff surface appears in the vacuum AdS calculation as well but with $f(r)$ replaced by $f_0(r)$, given in eq. (2.9). Further analysis shows that the difference between these contributions in the black hole and vacuum AdS geometries again vanishes in the limit $\delta \rightarrow 0$ — see appendix A.1.2 for details.

At this point, let us reiterate that there are certain subtleties, *e.g.*, caustics and orbifold singularities, in the case of the AdS vacua, which should be accounted for in evaluating the gravitational action. However, as described in appendix A.2, we find that in fact they do not produce any additional nonvanishing contributions to the gravitational action of the vacuum WDW patch.

2.2 Framework for the BTZ black hole

The case of two dimensions in the boundary theory is special. In this situation, the corresponding BTZ black hole [124, 125] can be seen as an orbifold of the vacuum AdS₃ solution. The corresponding calculation of the complexity of formation is slightly different from that for its higher dimensional counterparts. The main difference is that the null surfaces from the two asymptotic boundaries now meet each other at a joint precisely on the (orbifold) singularity, instead of ending separately on the singularity. The metric can still be written in the form given in eq. (2.1) with $d\Sigma_{k,d-1}^2$ replaced by $d\phi^2$ and with the blackening factor

$$f(r) = \frac{r^2 - r_h^2}{L^2}. \quad (2.38)$$

For the vacuum solution, we take eq. (2.9) with $k = +1$,¹⁴ *i.e.*,

$$f_0(r) = \frac{r^2}{L^2} + 1. \quad (2.39)$$

¹⁴We could also choose $k = -1$ or 0. However, the $k = -1$ solution is precisely the BTZ black hole with $r_h = L$ and the $k = 0$ vacuum will be discussed at the end of this section.

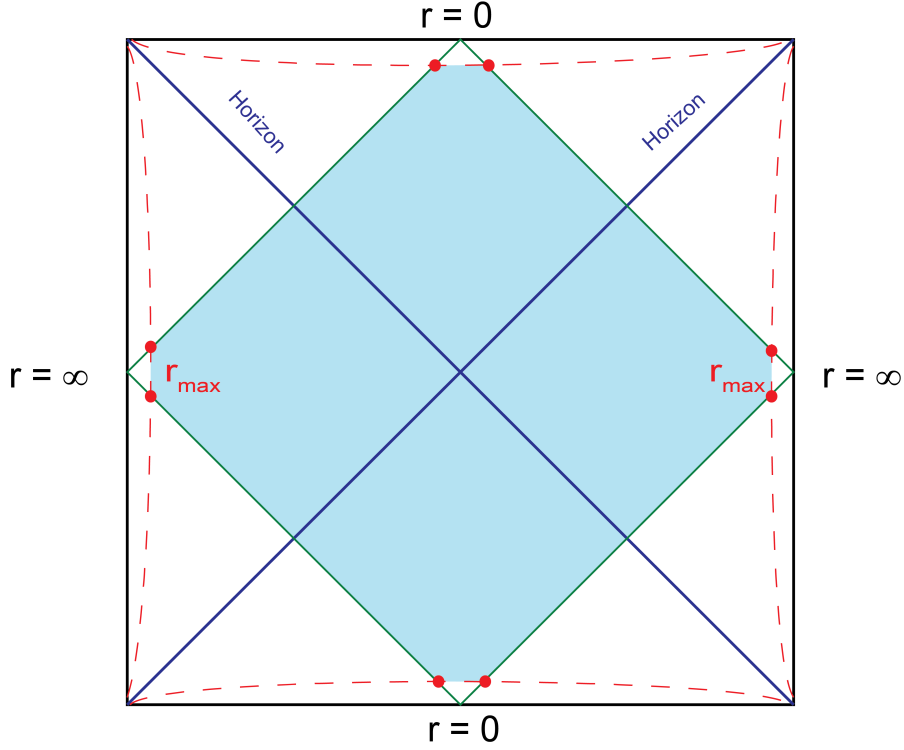


Figure 2.4: Penrose diagram of the WDW patch in the BTZ black hole background (with zero angular momentum). Note that unlike the higher dimensional case, the null sheets originating from the $t = 0$ slices on the left and right boundaries meet with each other in a joint, precisely at $r = 0$.

The Penrose diagram representing the BTZ black hole is shown in figure 2.4. The corresponding mass, temperature and entropy are given by

$$M = \frac{r_h^2}{8G_N L^2}, \quad T = \frac{r_h}{2\pi L^2}, \quad \text{and} \quad S = \frac{\pi r_h}{2G_N}. \quad (2.40)$$

The cutoff surfaces follow again from the near boundary expansion in appendix A.1,

$$r_{\text{max}}^{\text{BTZ}} = \frac{L^2}{\delta} + \frac{r_h^2}{4L^2}\delta \quad \text{and} \quad r_{\text{max}}^{\text{vac}} = \frac{L^2}{\delta} - \frac{\delta}{4}. \quad (2.41)$$

The vacuum AdS calculation follows immediately from previous examples and the bulk

integral (2.23) becomes for $d = 2$:

$$I_{\text{bulk}}^{\text{vac}} = -\frac{L^2}{G_N \delta} + \frac{\pi L}{4G_N} + \mathcal{O}(\delta). \quad (2.42)$$

Next, we evaluate the action for the BTZ black hole. The tortoise coordinate (2.14) is

$$r^*(r) = \frac{L^2}{2r_h} \log \frac{|r - r_h|}{r + r_h}, \quad (2.43)$$

and from eq. (2.18), $v_\infty = 0$.

We have now established some of the conventions necessary in order to evaluate the complexity in the CA in the following chapters.

Chapter 3

Complexity of Formation

In this chapter we will evaluate the complexity of formation of the thermofield double state in eq. (1.10), *i.e.*, the additional complexity of preparing the TFD state with respect to two copies of the vacuum. We will analyze both holographic proposals of complexity=volume and complexity=action. We find that this quantity is interesting as it provides a possible way to regularize the holographic complexity, since the complexity of formation does not depend on the UV divergences, and is essentially proportional to the entropy of the system for AdS-Schwarzschild black holes.

The chapter is organized as follows: In section 3.1, we evaluate the complexity of formation for black holes in five and four bulk dimensions, where we consider various possible horizon geometries – spherical, planar and hyperbolic, and the special case of $d = 2$, where the bulk geometry is described by a BTZ black hole. Section 3.2 compares our results for the complexity of formation using the complexity=action duality to those found with the complexity=volume approach. Finally, we close with a brief discussion in section 3.3. A number of technical details are left to four appendices: Appendix A.1 presents some details about the choice of the UV cutoff surfaces, which are needed to regulate the action. In appendix A.2, we describe certain subtle differences in the calculation of the vacuum complexity that arise for the different spatial geometries. Appendix A.3 describes the calculation of the complexity of formation for ‘small’ hyperbolic black holes, *i.e.*, with a negative mass. Appendix A.4 demonstrates that our results for the complexity of formations are robust against ambiguities in the definition of the gravitational action found in [63].

This chapter is adapted from [64].

3.1 Complexity of Formation

We discussed in the previous chapter the setup for evaluating the action in the eternal black hole geometry, as well as the possible subtleties involved in the evaluation of the action for the vacuum spacetimes. The complexity of formation can then be defined as the difference of complexities as

$$\Delta\mathcal{C} = \frac{1}{\pi} [I(\text{BH}) - 2I(\text{AdS})]. \quad (3.1)$$

We already established that the surface and joint contributions associated with the cutoff surface at $r = r_{\text{max}}$ precisely cancel between the two geometries. Hence the only non-vanishing contributions that need to be considered are the bulk contributions (2.23) for both geometries and the GHY surface contribution (2.29) at the black hole singularity. Combining the various results above then, we arrive at

$$\Delta\mathcal{C} = \frac{1}{\pi} [\Delta I_{\text{bulk}} + I_{\text{GHY}}^{\text{BH,sing}}] \quad (3.2)$$

where

$$\begin{aligned} \Delta I_{\text{bulk}} &= -\frac{\Omega_{k,d-1} d}{2\pi G_N L^2} \int_0^{r_{\text{max}}} dr r^{d-1} [v_\infty - v'_\infty - (r^*(r) - r_0^*(r))], \\ I_{\text{GHY}}^{\text{BH,sing}} &= \frac{\Omega_{k,d-1} d}{4\pi G_N} \omega^{d-2} (v_\infty - r^*(0)). \end{aligned} \quad (3.3)$$

In the expression for ΔI_{bulk} , we use $r_0^*(r)$ and v'_∞ to denote the tortoise coordinate and the null boundary in the AdS vacuum — see eq. (3.11) below.

As mentioned previously, the computation for “small” hyperbolic black holes with $k = -1$ and $r_h < L$ is slightly different. The full details are described in appendix A.3. The essential difference is that $f(r)$ has two positive real roots and the Penrose diagram resembles that of a charged black hole — see figure A.3. In this case, the null boundaries from the two asymptotic regions meet between the two horizons at $r^*(r_{\text{meet}}) = v_\infty$ and hence the surface term near the singularity is replaced by a null joint term (2.34). The complexity of formation then becomes:

$$\text{small hyperbolic BH:} \quad \Delta\mathcal{C} = \frac{1}{\pi} [\Delta I_{\text{bulk}} + I_{\text{jnt}}] \quad (3.4)$$

where

$$\begin{aligned} \Delta I_{\text{bulk}} &= -\frac{\Omega_{-1,d-1} d}{2\pi G_N L^2} \left[\int_{r_{\text{meet}}}^{r_{\text{max}}} dr r^{d-1} [v_\infty - r^*(r)] - \int_0^{r_{\text{max}}} dr r^{d-1} [v'_\infty - r_0^*(r)] \right], \\ I_{\text{jnt}} &= -\frac{\Omega_{-1,d-1}}{4\pi G_N} r_{\text{meet}}^{d-1} \log |f(r_{\text{meet}})|. \end{aligned} \quad (3.5)$$

However, we should add that this result will change with redefinitions allowed by the ambiguities in the definition of the gravitational action [63] — for further discussion, see section 3.3 and appendix A.4.

We now evaluate the above results for some specific examples:

3.1.1 $d = 4$

For $d = 4$, *i.e.*, a five-dimensional AdS black hole, the blackening factor (2.2) becomes

$$f(r) = \frac{r^2}{L^2} + k - \frac{r_h^2}{r^2} \left(\frac{r_h^2}{L^2} + k \right), \quad (3.6)$$

while for vacuum AdS, we have $f_0(r)$ in eq. (2.9). From the results in appendix A.1, we fix the UV cutoff surface at

$$r_{\max} = \frac{L^2}{\delta} - \frac{k}{4} \delta + \frac{r_h^2(r_h^2 + k L^2)}{8L^6} \delta^3 + \mathcal{O}(\delta^5). \quad (3.7)$$

Setting $r_h = 0$ in the above expression yields the cutoff for the vacuum spacetime, but in accord with eq. (2.13), we see the difference is $O(\delta^3)$. To evaluate the tortoise coordinate (2.14), we use eq. (2.20) to first write:

$$\frac{1}{f(r)} = \frac{L^2 r_h}{2(2r_h^2 + k L^2)(r - r_h)} - \frac{L^2}{2r_h^2 + k L^2} \left(\frac{r_h}{2(r + r_h)} - \frac{r_h^2 + k L^2}{r^2 + r_h^2 + k L^2} \right). \quad (3.8)$$

Eq. (2.14) then yields

$$r^*(r) = \frac{L^2 \sqrt{r_h^2 + k L^2}}{(2r_h^2 + k L^2)} \tan^{-1} \left[\frac{r}{\sqrt{r_h^2 + k L^2}} \right] + \frac{L^2 r_h}{2(2r_h^2 + k L^2)} \log \frac{|r - r_h|}{r + r_h}, \quad (3.9)$$

which leads to:¹

$$v_\infty = \frac{\pi L^2}{2} \frac{\sqrt{r_h^2 + k L^2}}{2r_h^2 + k L^2}. \quad (3.10)$$

For $k = +1$, it is straightforward to substitute $r_h = 0$ into the above expressions to recover the vacuum results, *i.e.*, $r_0^*(r)$ and v'_∞ as given in eqs. (A.27) and (A.28). Unfortunately,

¹Note that we have chosen an (arbitrary) integration constant in eq. (3.9) but this choice cancels in the difference $v_\infty - r^*(r)$ appearing, *e.g.*, in eq. (3.3).

this substitution is more subtle for $k = 0$ and -1 but one can calculate the desired quantities directly. From appendix A.2, the results are

$$\begin{aligned}
k = +1 & : & r_0^*(r) &= L \tan^{-1}(r/L) , & v'_\infty &= L \pi/2 , \\
k = 0 & : & r_0^*(r) &= -L^2/r , & v'_\infty &= 0 , \\
k = -1 & : & r_0^*(r) &= \frac{L}{2} \log \frac{|r-L|}{r+L} , & v'_\infty &= 0 .
\end{aligned} \tag{3.11}$$

Now it is straightforward to evaluate the expressions in eq. (3.3):

$$\Delta I_{\text{bulk}} = -\frac{\Omega_{k,3}}{4G_N} \left[\frac{(r_h^2 + kL^2)^{5/2}}{2r_h^2 + kL^2} - L^3 \delta_{k,1} \right] , \tag{3.12}$$

$$I_{\text{GHY}}^{\text{BH,sing}} = \frac{\Omega_{k,3}}{2G_N} \frac{r_h^2 (r_h^2 + kL^2)^{3/2}}{2r_h^2 + kL^2} . \tag{3.13}$$

Combining these results in eq. (3.2) then yields

$$\Delta \mathcal{C} = \frac{\Omega_{k,3}}{4\pi G_N} \left[\frac{(r_h^2 + kL^2)^{3/2} (r_h^2 - kL^2)}{(2r_h^2 + kL^2)} + L^3 \delta_{k,1} \right] . \tag{3.14}$$

With an expansion in large horizon radius, this result becomes

$$\Delta \mathcal{C} = \frac{\Omega_{k,3} L^3}{8\pi G_N} \left[\frac{r_h^3}{L^3} + 2\delta_{k,1} - \frac{9k^2}{8} \frac{L}{r_h} + \frac{k^3}{8} \frac{L^3}{r_h^3} + \mathcal{O}(L^5/r_h^5) \right] . \tag{3.15}$$

or expressed as a function of entropy (2.8):

$$\Delta \mathcal{C} = \frac{S}{2\pi} + \frac{\Omega_{k,3} \pi^2}{20} C_T \delta_{k,1} - 9\pi^3 k^2 \left(\frac{\Omega_{k,3}}{160} \right)^{4/3} \frac{C_T^{4/3}}{S^{1/3}} + \pi^5 k \left(\frac{\Omega_{k,3}}{80} \right)^2 \frac{C_T^2}{S} + \mathcal{O}(S^{-5/3}) . \tag{3.16}$$

where we have introduced the central charge in the boundary theory [142]: $C_T = \frac{5}{\pi^3} \frac{L^3}{G_N}$. Hence we see that to leading order in this large entropy expansion (*i.e.*, implicitly a high temperature expansion), the complexity of formation grows linearly with the entropy. Further, eq. (3.16) shows that this expansion is an expansion for large values of S/C_T . Finally, the coefficient of the leading behavior in $\Delta \mathcal{C}$ is independent of the spatial geometry. In section 3.1.3, we derive an analytic expression for this leading coefficient as a function of the boundary dimension d .

The “small” hyperbolic black holes are discussed in detail in appendix A.3. Using the results presented there, eq. (3.4) yields the following complexity of formation

$$\Delta\mathcal{C} = -\frac{\Omega_{-1,3}}{4\pi^2 G_N} \left(r_2 \frac{r_{\text{meet}}^4 - r_2^4}{2r_h^2 - L^2} \log \left[\frac{r_{\text{meet}} + r_2}{r_{\text{meet}} - r_2} \right] + r_h \frac{r_h^4 - r_{\text{meet}}^4}{2r_h^2 - L^2} \log \left[\frac{r_h + r_{\text{meet}}}{r_h - r_{\text{meet}}} \right] - \frac{2}{3} r_{\text{meet}} (3L^2 + r_{\text{meet}}^2) + r_{\text{meet}}^3 \log |f(r_{\text{meet}})| \right). \quad (3.17)$$

for small hyperbolic black holes, with

$$r_2 = \sqrt{L^2 - r_h^2} \quad \text{and} \quad r^*(r_{\text{meet}}) = 0. \quad (3.18)$$

Here, r_2 is the second root of $f(r) = 0$, which defines the position of the inner horizon — see figure A.3. Further, r_{meet} is the coordinate radius where the null surfaces from the left and right asymptotic regions meet behind the horizon. Since r_{meet} is the solution to a transcendental equation, evaluating the expression in eq. (3.17) requires some numerical treatment. Finally, as we mentioned above, this result is also ambiguous — see further discussion in section 3.3 and appendix A.4.

Figure 3.1 summarizes the results of this subsection.

3.1.2 $d = 3$

For $d = 3$ (four-dimensional bulk), the blackening factor (2.2) becomes

$$f(r) = \frac{r^2}{L^2} + k - \frac{r_h}{r} \left(\frac{r_h^2}{L^2} + k \right), \quad (3.19)$$

and as before for vacuum AdS, we have $f_0(r)$ in eq. (2.9). In appendix A.1, the UV cutoff surface is set at

$$r_{\text{max}} = \frac{L^2}{\delta} - \frac{k}{4} \delta + \frac{r_h}{6L^2} \left(\frac{r_h^2}{L^2} + k \right) \delta^2 + \mathcal{O}(\delta^4), \quad (3.20)$$

which also fixes the vacuum cutoff with $r_h = 0$. To evaluate the tortoise coordinate (2.14), we first use eq. (2.20) to write

$$\frac{1}{f(r)} = \frac{L^2 r_h}{(r - r_h)(3r_h^2 + kL^2)} + \frac{L^2 (r_h^2 - r r_h + kL^2)}{(r^2 + r r_h + r_h^2 + kL^2)(3r_h^2 + kL^2)}. \quad (3.21)$$

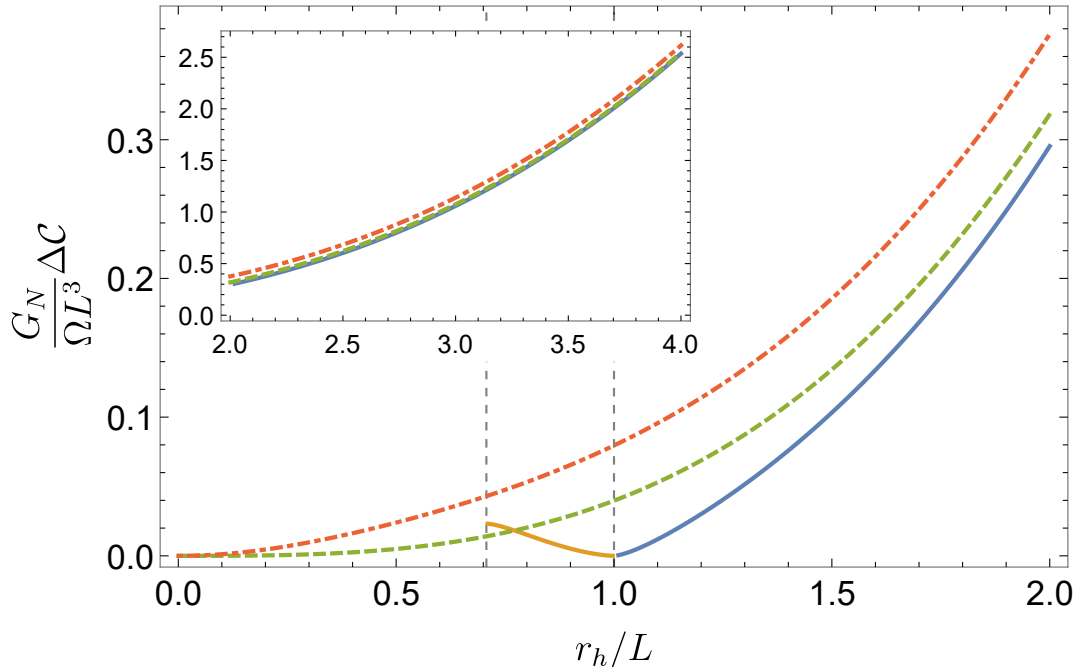


Figure 3.1: Complexity of formation for the different geometries in four boundary (five bulk) dimensions: large hyperbolic (blue), small hyperbolic (orange), planar (dashed green) and spherical (dot-dashed red). In the inset, a larger range of horizon radii is presented demonstrating that the leading behavior at large r_h is the same for the three different horizon geometries. The two vertical dashed lines are: (1) $r_h = L/\sqrt{2}$, where the (small) hyperbolic black holes become extremal; (2) $r_h = L$, where the Hawking-Page phase transition takes place for the spherical black holes (planar and hyperbolic black holes do not admit a similar transition).

Eq. (2.14) then yields²

$$r^*(r) = \frac{L^2 r_h}{3r_h^2 + kL^2} \left(\log \left[\frac{|r - r_h|}{\sqrt{r^2 + rr_h + r_h^2 + kL^2}} \right] + \frac{3r_h^2 + 2kL^2}{r_h \sqrt{3r_h^2 + 4kL^2}} \tan^{-1} \left[\frac{2r + r_h}{\sqrt{3r_h^2 + 4kL^2}} \right] \right), \quad (3.22)$$

which in eq. (2.18) yields

$$v_\infty = \frac{\pi L^2 (3r_h^2 + 2kL^2)}{2(3r_h^2 + kL^2) \sqrt{3r_h^2 + 4kL^2}}. \quad (3.23)$$

The vacuum results, $r_0^*(r)$ and v'_∞ , are identical to those shown in eq. (3.11).

Using these results to evaluate the expressions in eq. (3.3), the complexity of formation (3.2) becomes

$$\begin{aligned} \Delta\mathcal{C} = & \frac{\Omega_{k,2}}{8\pi^2 G_N (3r_h^2 + kL^2) \sqrt{3r_h^2 + 4kL^2}} \\ & \times \left[2r_h (3r_h^4 + 5kL^2 r_h^2 + 4k^2 L^4) \left(\frac{\pi}{2} - \tan^{-1} \left[\frac{r_h}{\sqrt{3r_h^2 + 4kL^2}} \right] \right) + \right. \\ & \left. \sqrt{3r_h^2 + 4kL^2} \left((r_h^4 - 3kL^2 r_h^2 - 2k^2 L^4) \log \left[\frac{r_h^2}{L^2} + k \right] - 2(r_h^4 + 3kL^2 r_h^2) \log \frac{r_h}{L} \right) \right]. \end{aligned} \quad (3.24)$$

An expansion in large r_h/L then yields

$$\Delta\mathcal{C} = \frac{\Omega_{k,2} L^2}{8\pi^2 G_N} \left[\frac{2\pi}{3\sqrt{3}} \frac{r_h^2}{L^2} - 4k \log \frac{r_h}{L} + \frac{2k(9 + 2\sqrt{3}\pi)}{27} - \frac{4k^2}{27} (9 - \sqrt{3}\pi) \frac{L^2}{r_h^2} + \mathcal{O}(r_h^{-4}) \right], \quad (3.25)$$

or alternatively, an expansion for large entropy (2.8) gives

$$\begin{aligned} \Delta\mathcal{C} = & \frac{S}{3\sqrt{3}\pi} - \frac{k\pi \Omega_{k,2}}{12} C_T \log \left[\frac{12}{\Omega_{k,2} \pi^3} \frac{S}{C_T} \right] + \\ & + \frac{k\pi \Omega_{k,2}}{324} C_T (9 + 2\sqrt{3}\pi) - \frac{k^2 \pi^4 \Omega_{k,2}^2}{1944} \frac{C_T^2}{S} (9 - \sqrt{3}\pi) + \mathcal{O}(S^{-2}), \end{aligned} \quad (3.26)$$

²Here and below, we assume $r_h > 2L/\sqrt{3}$ for the hyperbolic case with $k = -1$. In the range $L \leq r_h \leq 2L/\sqrt{3}$, $f(r)$ has two additional negative real roots. While these do not signify the presence of additional horizons, this case has some similarities to that of small hyperbolic black holes, *i.e.*, $r_h < L$. Hence it will be treated separately in appendix A.3.

where we used $C_T = 3L^2/(\pi^3 G_N)$ for the boundary central charge. As in the previous case, the coefficient of the leading order term matches with the general d argument in section 3.1.3.

The “small” hyperbolic black holes for $d = 3$ are discussed in detail in appendix A.3, and the complexity of formation is given by

$$\begin{aligned} \Delta\mathcal{C} = & \frac{\Omega_{-1,2}}{4\pi^2 G_N (r_2 - r_3)(r_h - r_2)(r_h - r_3)} \left[2r_h (r_2 - r_3) (r_h^3 - r_{\text{meet}}^3) \log \left(\frac{r_h - r_{\text{meet}}}{L} \right) \right. \\ & \left. + 2r_2 (r_h - r_3) (r_{\text{meet}}^3 - r_2^3) \log \left(\frac{r_{\text{meet}} - r_2}{L} \right) - 2r_3 (r_h - r_2) (r_{\text{meet}}^3 - r_3^3) \log \left(\frac{r_{\text{meet}} - r_3}{L} \right) \right] \\ & + \frac{\Omega_{-1,2}}{4\pi^2 G_N} \left[r_{\text{meet}} (2r_h + 2r_2 + 2r_3 + r_{\text{meet}}) - r_{\text{meet}}^2 \log |f(r_{\text{meet}})| \right] \end{aligned} \quad (3.27)$$

where

$$r_2 = \frac{1}{2} \left(\sqrt{4L^2 - 3r_h^2} - r_h \right) \quad \text{and} \quad r_3 = -\frac{1}{2} \left(\sqrt{4L^2 - 3r_h^2} + r_h \right). \quad (3.28)$$

Here r_2 denotes the second positive root of $f(r) = 0$, which specifies the position of the inner horizon, while r_3 is a third real but negative root (which does not correspond to the location of a horizon). As before, r_{meet} is the radius of the meeting point of the null surfaces behind the horizon, which satisfies $r^*(r_{\text{meet}}) = 0$.

We show the results of this subsection in figure 3.2.

3.1.3 Planar Case for General d

In the previous subsections, we saw that our results for $d = 4$ and 3 reduce to a single term proportional to r_h^{d-1} for the planar black holes. Therefore, up to an overall coefficient, the complexity of formation is given by the horizon entropy in these cases. Further, for hyperbolic and spherical black holes this same term appears as the leading behavior for large black holes, irrespective of the sign of k . In this section, we compute the complexity of formation for planar black holes in general dimension ($d > 2$) and find a similar result, *i.e.*, $\Delta\mathcal{C} = k_d S$ where the proportionality constant k_d is a relatively simple function of the dimension d .

With $k = 0$, the blacking factor (2.2) reduces to

$$f(r) = \frac{r^2}{L^2} - \frac{r_h^d}{L^2 r^{d-2}}, \quad (3.29)$$

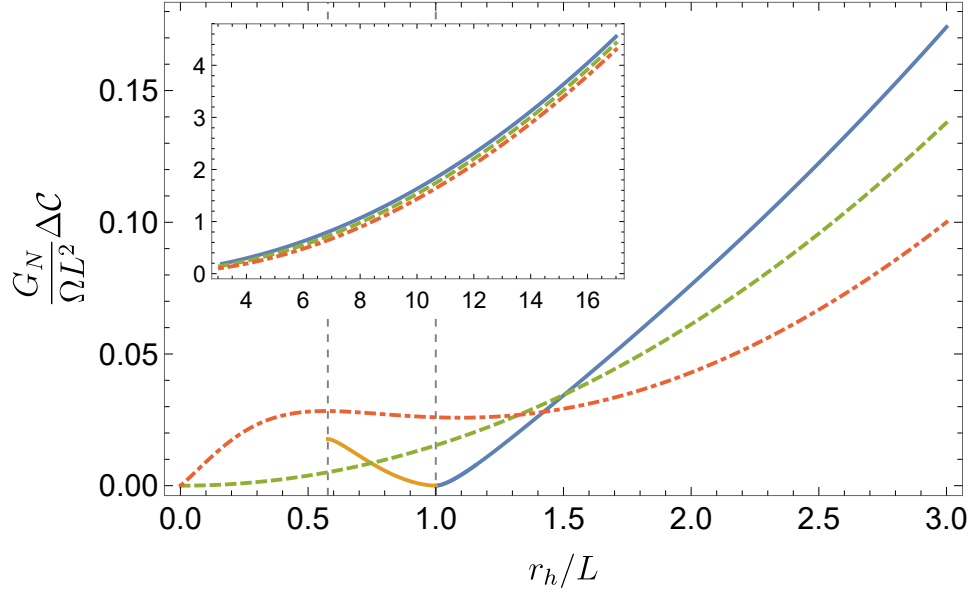


Figure 3.2: Complexity of formation for the different geometries in three boundary (four bulk) dimensions: large hyperbolic (blue), small hyperbolic (orange), planar (dashed green) and spherical (dot-dashed red). In the inset, a larger range of horizon radii is presented demonstrating that the leading behavior at large r_h is the same for the three different horizon geometries. The two vertical dashed lines are: (1) $r_h = L/\sqrt{3}$, where the (small) hyperbolic black holes become extremal; (2) $r_h = L$, where the Hawking-Page phase transition takes place for the spherical black holes (planar and hyperbolic black holes do not admit a similar transition).

and for vacuum AdS, we have $f_0(r) = r^2/L^2$. Following the calculations from appendix A.1, the UV cutoff surface is

$$r_{\max} = \frac{L^2}{\delta} + \frac{r_h^d \delta^{d-1}}{2dL^{2(d-1)}} + O(\delta^{d+1}), \quad (3.30)$$

while the cutoff for vacuum AdS is given by taking the limit $r_h \rightarrow 0$ in this expression. As usual, the tortoise coordinate is given by integrating $1/f(r)$ with the result³

$$\begin{aligned} r_{\text{in}}^*(r) &= \frac{L^2}{r} \left[{}_2F_1 \left(1, -\frac{1}{d}; 1 - \frac{1}{d}; \left(\frac{r}{r_h} \right)^d \right) - 1 \right], \\ r_{\text{out}}^*(r) &= \frac{L^2}{r_h} \left[\frac{\pi}{d} \cot \left(\frac{\pi}{d} \right) - \left(\frac{r_h^d}{r^d - r_h^d} \right)^{1/d} {}_2F_1 \left(\frac{1}{d}, \frac{1}{d}; 1 + \frac{1}{d}; \frac{r_h^d}{r^d - r_h^d} \right) \right]. \end{aligned} \quad (3.32)$$

where the subscripts in/out indicate inside ($r < r_h$) and outside ($r > r_h$) of the horizon, respectively. Note that we have to impose that the nonlogarithmic part of these functions is continuous across the horizon, *i.e.*,

$$\lim_{r \rightarrow r_h^+} \left(r_{\text{out}}^*(r) - \frac{L^2}{dr_h} \log(r - r_h) \right) = \lim_{r \rightarrow r_h^-} \left(r_{\text{in}}^*(r) - \frac{L^2}{dr_h} \log(r_h - r) \right) \quad (3.33)$$

to fix the relative integration constant between the two hypergeometric functions. This condition is responsible for the appearance of the constant $(L^2\pi)/(dr_h) \cot(\pi/d)$ in $r_{\text{out}}^*(r)$. This also yields:

$$v_\infty = \frac{\pi L^2}{dr_h} \cot \left(\frac{\pi}{d} \right). \quad (3.34)$$

The vacuum expressions are the same as in eq. (3.11). Now, the bulk contribution in

³Note that the inverse blackening factor can be decomposed as follows:

$$\frac{1}{f(r)} = \frac{L^2}{dr_h} \left(\frac{1}{r - r_h} + \frac{-r^{d-2} + \sum_{n=0}^{d-3} (n+1)r^n r_h^{d-2-n}}{\sum_{m=0}^{d-1} r^m r_h^{d-1-m}} \right), \quad (3.31)$$

where all of the terms in the sum are regular at the location of the horizon and the first term leads to a contribution in the tortoise coordinate of the form $r^*(r) = L^2/(dr_h) \log|r - r_h| + \dots$.

eq. (3.3) yields

$$\begin{aligned}
\Delta I_{\text{bulk}} &= -\frac{\Omega_{0,d-1}}{2\pi G_N} \frac{d}{d-1} \left[(r^d - r_h^d)^{\frac{d-1}{d}} {}_2F_1 \left(\frac{1}{d} - 1, \frac{1}{d}; 1 + \frac{1}{d}; \frac{r_h^d}{r^d - r_h^d} \right) \right]_{r_h}^{r_{\text{max}}} \\
&\quad + r^{d-1} \left[\frac{\pi(d-1)}{d^2} \frac{r}{r_h} \cot \left(\frac{\pi}{d} \right) - {}_2F_1 \left(1, -\frac{1}{d}; 2 - \frac{1}{d}; \left(\frac{r}{r_h} \right)^d \right) + 1 \right]_0^{r_h} - r_{\text{max}}^{d-1} \\
&= -\frac{\Omega_{0,d-1}}{2d G_N} \cot \left(\frac{\pi}{d} \right) r_h^{d-1}.
\end{aligned} \tag{3.35}$$

The corresponding surface contribution is also easily evaluated

$$I_{\text{GHY}}^{\text{BH,sing}} = \frac{\Omega_{0,d-1}}{4G_N} \cot \left(\frac{\pi}{d} \right) r_h^{d-1}, \tag{3.36}$$

and the total complexity of formation becomes

$$\Delta \mathcal{C} = \frac{1}{\pi} [\Delta I_{\text{bulk}} + I_{\text{GHY}}^{\text{BH,sing}}] = \frac{d-2}{d} \cot \left(\frac{\pi}{d} \right) \frac{\Omega_{0,d-1} r_h^{d-1}}{4\pi G_N}. \tag{3.37}$$

Therefore, the complexity of formation has a simple form in terms of the horizon entropy (2.8)

$$\Delta \mathcal{C} = \frac{d-2}{d\pi} \cot \left(\frac{\pi}{d} \right) S \equiv k_d S. \tag{3.38}$$

Note that for large d , the coefficient k_d approaches a linear function of d , *i.e.*,

$$k_d \simeq \frac{d-2}{\pi^2} + \mathcal{O}(1/d). \tag{3.39}$$

In figure 3.3, we plot the coefficient k_d as a function of the dimension and show that it rapidly approaches the linear approximation above. Note that k_d vanishes for $d = 2$. Strictly speaking, however, our calculations above only apply for $d > 2$ and $d = 2$ is a special case which we discuss in the next section. Nevertheless, we will confirm there that the complexity of formation is independent of the entropy for $d = 2$.

3.1.4 Complexity of BTZ Black Holes

We can simply follow the previous discussion and the BTZ parameters in chapter 2 in order to evaluate the complexity of formation for BTZ black holes.

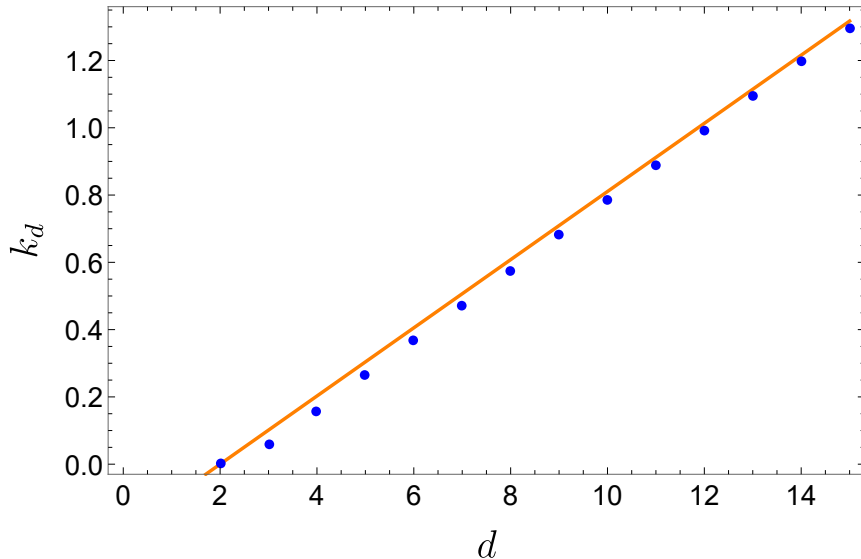


Figure 3.3: Coefficient of entropy in eq. (3.38), $k_d \equiv \Delta\mathcal{C}/S$, plotted as a function of the boundary dimension d , for planar AdS black holes. The orange line shows the linear approximation in eq. (3.39).

The bulk integral result is

$$I_{\text{bulk}}^{\text{BTZ}} = -\frac{2L^2}{G_N \delta} + \mathcal{O}(\delta). \quad (3.40)$$

Of course, the divergence cancels when subtracting twice the action of vacuum AdS. There is no contribution from a surface term near the singularity, as the null boundaries meet as described above, and the joint contribution there vanishes. Therefore, the complexity of formation is simply given by

$$\Delta\mathcal{C} = \frac{1}{\pi} [I_{\text{bulk}}^{\text{BTZ}} - 2I_{\text{bulk}}^{\text{vac}}] = -\frac{L}{2G_N} = -\frac{c}{3}, \quad (3.41)$$

where we have introduced the central charge of the boundary theory $c = 3L/(2G_N)$ [143]. Hence $\Delta\mathcal{C}$ is a fixed constant, independent of the temperature or horizon radius.

One notable fact about the above expression is that it does not vanish when the mass (or r_h) vanishes. At a pragmatic level, this occurs because in the limit $r_h \rightarrow 0$, the blackening factor (2.38) does not become $f_0(r)$ in eq. (2.39) for the vacuum AdS₃ spacetime. Implicitly, in choosing eq. (2.39), we are choosing to consider the Neveu-Schwarz vacuum

of the boundary theory [144]. Alternatively, we could have chosen $f_0(r) = r^2/L^2$ (*i.e.*, the $r_h \rightarrow 0$ limit of the BTZ blackening factor), but this choice would correspond to the Ramond vacuum of the boundary theory. In this case, we find that the complexity of formation vanishes, *i.e.*, $\Delta\mathcal{C} = 0$.

3.2 Comparison with Complexity=Volume

In the previous sections, we were investigating the conjectured duality between complexity and action (CA) [33, 34]. However, it was previously conjectured that the complexity of states in a holographic theory should be dual to the volume of the extremal codimension-one bulk hypersurface which meets the asymptotic boundary on the desired time slice [32].⁴ More precisely, the complexity = volume (CV) duality states that the complexity of the state on a time slice denoted Ω is given by:

$$\mathcal{C}_V(\Omega) = \max_{\Omega=\partial\mathcal{B}} \left[\frac{\mathcal{V}(\mathcal{B})}{G_N \ell} \right], \quad (3.42)$$

where \mathcal{B} is the corresponding bulk surface and ℓ is some length scale associated with the bulk geometry, *e.g.*, the AdS radius for large black holes and r_h for small black holes, see, *e.g.*, [34]. The ambiguity in defining the latter is somewhat unsatisfactory and provided some motivation for developing the CA duality, since this choice is naturally eliminated in this framework. For simplicity, we will set $\ell = L$ in all of the following calculations. In this section, we compare our previous results for the complexity of formation obtained from the CA duality to those obtained by the CV duality.

We are interested in evaluating the complexity for the thermal state defined on the time slice at $t_L = t_R = 0$. By symmetry, the maximal volume is given by the bulk $t = 0$ slice, *i.e.*, the straight line connecting the two boundaries through the bifurcation surface in the Penrose diagram shown in figure 3.4. The volume integral then simplifies to:

$$\mathcal{V} = 2\Omega_{k,d-1} \int_{r_h}^{r_{\max}} \frac{r^{d-1}}{\sqrt{f(r)}} dr. \quad (3.43)$$

To evaluate the complexity of formation, we will subtract from this integral, the corre-

⁴An alternative proposal related to complexity=volume was recently put forward by [145], which is denoted complexity=volume 2.0, associating the complexity with the spacetime volume of the WDW patch.

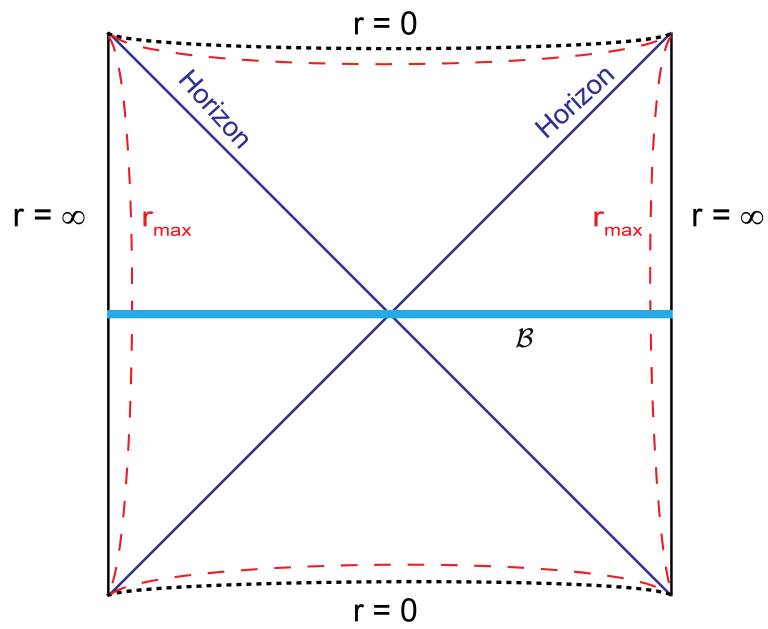


Figure 3.4: The maximal volume slice \mathcal{B} connecting the two boundaries at $t_L = t_R = 0$ through the Einstein-Rosen bridge.

sponding contribution from (two copies of) the vacuum AdS background:

$$\mathcal{V}_0 = 2\Omega_{k,d-1} \int_{r_{\min}}^{r_{\max}} \frac{r^{d-1}}{\sqrt{f_0(r)}} dr. \quad (3.44)$$

Here we have introduced the minimum radius r_{\min} because while the integration starts at $r_{\min} = 0$ for $k = +1$ and 0 , we must set $r_{\min} = L$ for $k = -1$. Hence in this framework, the complexity of formation becomes⁵

$$\Delta\mathcal{C}_V = \frac{2\Omega_{k,d-1}}{G_N L} \left[\int_{r_h}^{r_{\max}} \frac{r^{d-1} dr}{\sqrt{f(r)}} - \int_{r_{\min}}^{r_{\max}} \frac{r^{d-1} dr}{\sqrt{f_0(r)}} \right]. \quad (3.45)$$

3.2.1 Planar Geometry

It is easiest to evaluate this expression (3.45) for planar black holes with $k = 0$. The volume integral (3.43) can be evaluated analytically for any d :

$$\mathcal{V} = \frac{4\Omega_{0,d-1} L}{d} r_h^{\frac{d}{2}-1} \sqrt{r^d - r_h^d} {}_2F_1\left(\frac{1}{2}, \frac{1}{d} - \frac{1}{2}; \frac{3}{2}; 1 - (r/r_h)^d\right) \Big|_{r_h}^{r_{\max}}. \quad (3.46)$$

The cutoff r_{\max} is given in appendix A.1 — see eq. (A.13). In the limit of a small short distance cutoff δ , the volume integral becomes

$$\mathcal{V} = \frac{2\Omega_{0,d-1} L^{2d-1}}{(d-1)\delta^{d-1}} + \frac{2\Omega_{0,d-1} \sqrt{\pi} \Gamma(-1 + \frac{1}{d})}{d \Gamma(-\frac{1}{2} + \frac{1}{d})} L r_h^{d-1} + \mathcal{O}(\delta). \quad (3.47)$$

The leading (divergent) term above is exactly canceled when subtracting the volume of the maximal slice in the vacuum AdS geometry. The complexity of formation (3.45) can be written as

$$\Delta\mathcal{C}_V = \frac{\sqrt{\pi} \Omega_{0,d-1}}{G_N} \frac{(d-2) \Gamma(1 + \frac{1}{d})}{(d-1) \Gamma(\frac{1}{2} + \frac{1}{d})} r_h^{d-1}. \quad (3.48)$$

Again, this result for the complexity of formation can be expressed in terms of the entropy (2.8)

$$\Delta\mathcal{C}_V = 4\sqrt{\pi} \frac{(d-2) \Gamma(1 + \frac{1}{d})}{(d-1) \Gamma(\frac{1}{2} + \frac{1}{d})} S \equiv \tilde{k}_d S. \quad (3.49)$$

⁵Using the methods of appendix A.1, we confirmed that the difference between r_{\max} evaluated for the vacuum AdS and the black hole backgrounds will not contribute to $\Delta\mathcal{C}_V$ when we send $\delta \rightarrow 0$.

Note that in this case, the coefficient \tilde{k}_d approaches a constant for large d , *i.e.*,

$$\tilde{k}_d \simeq 4 + O(1/d). \quad (3.50)$$

It is interesting, of course, to compare these results to the analogous results found using the CA duality — see eqs. (3.38) and (3.39). It is perhaps notable that in both approaches, the coefficient vanishes for $d = 2$. However, otherwise the coefficients k_d and \tilde{k}_d seem to bear little resemblance to each other. For example, we saw that for large d , the coefficient \tilde{k}_d approaches a constant for the CV duality while k_d grows linearly with d for the CA duality. The two coefficients are roughly equal in the vicinity of $d = 42$.

However, one should be aware that the definition of complexity is not completely precise and different choices of, *e.g.*, the universal gate set may lead to changing the complexity of a given family of states by a multiplicative constant — see discussions in [34, 63]. Hence an interesting approach is to combine the above comparison with a comparison of the late time growth of complexity from the CV and CA dualities. In particular, examining the growth of complexity for an uncharged AdS black hole using the two conjectures yields [32–34]⁶

$$\left. \frac{d\mathcal{C}_V}{dt} \right|_{t \rightarrow \infty} = \frac{8\pi}{d-1} M \quad \text{and} \quad \left. \frac{d\mathcal{C}_A}{dt} \right|_{t \rightarrow \infty} = \frac{2M}{\pi}. \quad (3.51)$$

We note that the late time growth rate above from the CV duality is only valid in the limit of large temperatures for $k = \pm 1$ [32]. Of course, our results for the complexity of formation $\Delta\mathcal{C}_{A,V}$ only apply for high temperatures, as well. Now let us compare the two ratios⁷

$$\begin{aligned} R_{\text{form}} &= \frac{\Delta\mathcal{C}_A}{\Delta\mathcal{C}_V} = \frac{d-1}{4\pi^{3/2}} \frac{\Gamma\left(1 - \frac{1}{d}\right)}{\Gamma\left(\frac{1}{2} - \frac{1}{d}\right)}, \\ R_{\text{rate}} &= \frac{d\mathcal{C}_A/dt}{d\mathcal{C}_V/dt} = \frac{d-1}{4\pi^2}. \end{aligned} \quad (3.52)$$

Now it is straightforward to see that in the limit of large d , both ratios grow linearly with d and further we may write

$$R_{\text{rate}} - R_{\text{form}} = \frac{\log 2}{2\pi^2} + O(1/d). \quad (3.53)$$

⁶Recall that it was suggested in [33, 34] that the late time limit of $d\mathcal{C}_A/dt$ was related to Lloyd’s bound for the rate of computation for a system of energy M [116]. Recently, ref. [146] considered conditions under which this bound is compatible with the CA duality conjecture.

⁷We have simplified the first ratio using $\cot(\pi x) = \frac{\Gamma(1-x)\Gamma(x)}{\Gamma(\frac{1}{2}-x)\Gamma(\frac{1}{2}+x)}$.

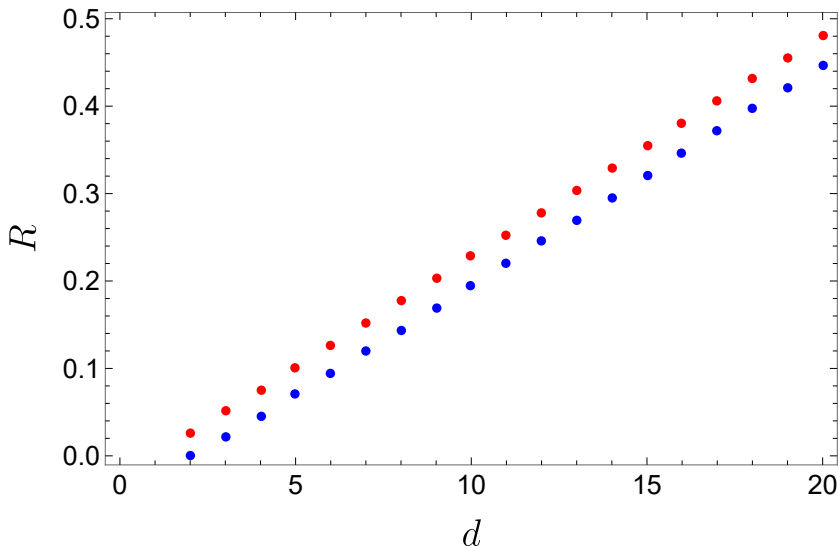


Figure 3.5: The two ratios R_{form} (blue) and R_{rate} (red) as a function of d .

However, from figure 3.5, we can see that apart from the constant shift in eq. (3.53), the two ratios agree very well for all values of d . This comparison then suggests that the two holographic approaches to complexity are more or less consistent up to an overall multiplicative factor.

3.2.2 Spherical and Hyperbolic Geometries

Here we evaluate the complexity of formation (3.45) using the CV duality for the spherical and hyperbolic black holes. In the following, it is convenient to define the dimensionless coordinate $x \equiv r/L$, as well as $x_h \equiv r_h/L$ and $x_{\min} = 0$ or 1 for $k = +1$ or -1 , respectively. Then eq. (3.45) may be expressed as

$$\Delta\mathcal{C}_V = 2\Omega_{k,d-1} \frac{L^{d-1}}{G_N} \left[\int_{x_h}^{\infty} \left(\frac{x^{d-1}}{\sqrt{f(x)}} - \frac{x^{d-1}}{\sqrt{x^2+k}} \right) dx - \int_{x_{\min}}^{x_h} \frac{x^{d-1} dx}{\sqrt{x^2+k}} \right], \quad (3.54)$$

where $f(x)$ is the usual blackening factor (2.2), *i.e.*, $f(x) = x^2 + k - (x_h/x)^{d-2}(x_h^2 + k)$. Note that in extending the upper limit of integration to infinity in the first integral, we have allowed for the cancellation of the divergences which appear individually in eqs. (3.43) and (3.44). Again, the small hyperbolic black holes are a special case and eq. (3.54) must

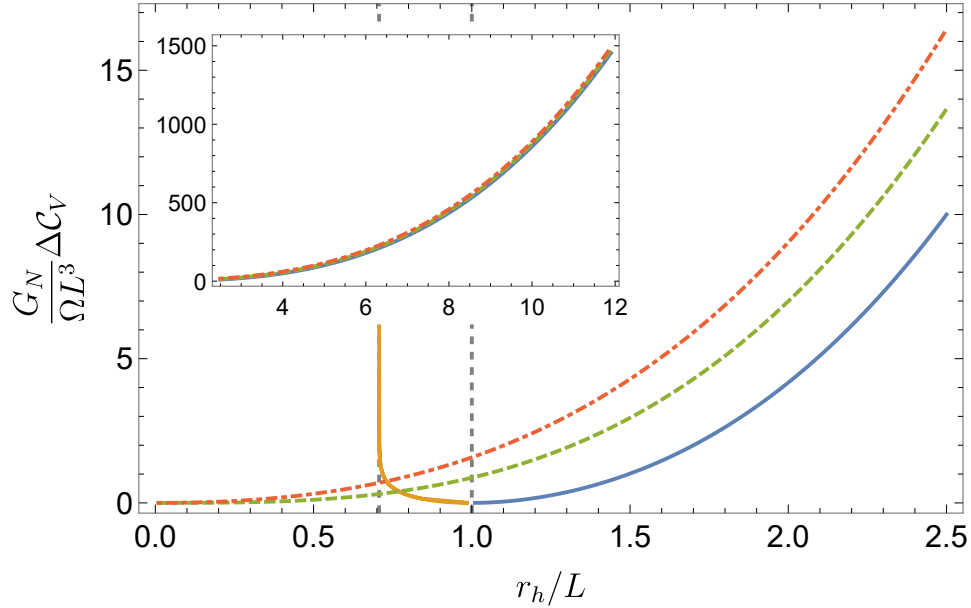


Figure 3.6: Complexity calculated from the CV duality for the three different geometries in $d = 4$ – large hyperbolic (blue), small hyperbolic (orange), planar (dashed green) and spherical (dot-dashed red). In the inset, a larger range of horizon radii is presented demonstrating that the leading behavior at large r_h is the same for the three different horizon geometries. The dashed vertical line at $r_h = L$ denotes the position of the Hawking-Page transition for the spherical black holes, while the one at $r_h = L/\sqrt{2}$ indicates where the (small) hyperbolic black holes become extremal. The volume, and hence the complexity of formation, diverges for these extremal black holes.

be modified slightly in this situation since with $\omega^{d-2} < 0$, one finds that $x_h < x_{\min} = 1$. Hence for small hyperbolic black holes, we write instead

$$\Delta\mathcal{C}_V = 2\Omega_{-1,d-1} \frac{L^{d-1}}{G_N} \left[\int_1^\infty \left(\frac{x^{d-1}}{\sqrt{f(x)}} - \frac{x^{d-1}}{\sqrt{x^2-1}} \right) dx + \int_{x_h}^1 \frac{x^{d-1} dx}{\sqrt{f(x)}} \right], \quad (3.55)$$

The above expressions can be evaluated in terms of elliptic integrals (at least for certain dimensions), however, these are not particularly enlightening. Therefore, we evaluate these expressions numerically instead to study their behavior. Figures 3.6 and 3.7 show the results for $\Delta\mathcal{C}_V$ in $d = 4$ and $d = 3$, respectively. There are many features found in common with the CA results shown in figures 3.1 and 3.2, but there are some differences as well.

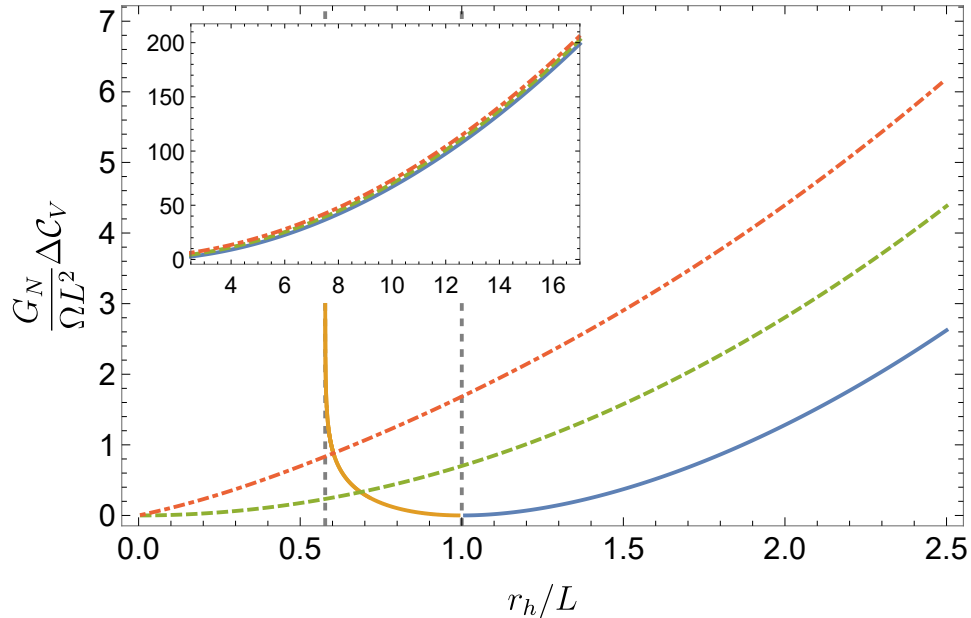


Figure 3.7: Complexity calculated from the CV duality for the three different geometries in $d = 3$ – large hyperbolic (blue), small hyperbolic (orange), planar (dashed green) and spherical (dot-dashed red). In the inset, a larger range of horizon radii is presented demonstrating that the leading behavior at large r_h is the same for the three different horizon geometries. The dashed vertical line at $r_h = L$ denotes the position of the Hawking-Page transition for the spherical black holes, while the one at $r_h = L/\sqrt{3}$ indicates where the (small) hyperbolic black holes become extremal. The volume, and hence the complexity of formation, diverges for these extremal black holes.

For instance, for large horizon radius, the result for the spherical and hyperbolic geometries approaches eq. (3.48) for the planar case, as expected, *i.e.*, $\Delta\mathcal{C}_V \simeq \tilde{k}_d S$ as in eq. (3.49). We can subtract this leading behavior and fit the residual numerical result to

find

$$\begin{aligned}
d = 4, \quad k = +1 : \quad & \frac{G}{\Omega_{1,3}L^3} \left(\Delta\mathcal{C}_V - \tilde{k}_4 S \right) = 1.55 \frac{r_h}{L} - 1.33 + 0.55 \frac{L}{r_h} + \dots, \\
d = 4, \quad k = -1 : \quad & \frac{G}{\Omega_{-1,3}L^3} \left(\Delta\mathcal{C}_V - \tilde{k}_4 S \right) = -1.55 \frac{r_h}{L} + 0.00 + 0.55 \frac{L}{r_h} + \dots, \\
d = 3, \quad k = +1 : \quad & \frac{G}{\Omega_{1,2}L^2} \left(\Delta\mathcal{C}_V - \tilde{k}_3 S \right) = 1.00 \log\left(\frac{r_h}{L}\right) + 0.865 + 0.14 \frac{L^2}{r_h^2} + \dots, \\
d = 3, \quad k = -1 : \quad & \frac{G}{\Omega_{-1,2}L^2} \left(\Delta\mathcal{C}_V - \tilde{k}_3 S \right) = -1.00 \log\left(\frac{r_h}{L}\right) - 0.865 + 0.14 \frac{L^2}{r_h^2} + \dots.
\end{aligned} \tag{3.56}$$

We observe that in many respects, the structure here is very similar to that found in eqs. (3.15) and (3.25) for the CA duality. For example, there are clearly factors of k multiplying the various terms; a special $\delta_{k,1}$ constant contribution appears in $d = 4$; and a logarithmic contribution appears in $d = 3$. Note, however, that the first term for $d = 4$ is proportional to r_h/L above, whereas the term at this order vanishes for $\Delta\mathcal{C}_A$ in eq. (3.15). Further, note that the first term for $d = 3$ above seems to be $k \log(r_h/L)$ whereas the first subleading contribution in eq. (3.25) has the same form but the opposite sign. As a result, the curves in figure 3.2 cross in the vicinity of $r_h/L \sim 1.4$, but no such crossing appears in figure 3.7.

Another interesting difference is that in both figures, $\Delta\mathcal{C}_V$ diverges as T approaches zero for $k = -1$, *i.e.*, as the small hyperbolic black holes approach the extremal limit.⁸ This divergence arises because the throat of the black hole grows to have infinite (proper) length in this limit. In contrast with the CA duality, $\Delta\mathcal{C}_A$ remains finite in this limit, but recall that the results for small hyperbolic black holes are ambiguous in this approach — see appendix A.4.

Special Case of $d = 2$:

Recall that $d = 2$ is a special case, which is described by the BTZ black hole in the bulk. In this case, it is possible to evaluate the complexity of formation for the CV duality analytically. We use the blackening factors $f(r)$ and $f_0(r)$ given by eqs. (2.38) and (2.39), respectively, as well as r_{\max} given by eq. (2.41) and $r_{\min} = 0$. The required volumes in

⁸Note that choosing $\ell = r_h$ (rather than $\ell = L$) in eq. (3.42) for these ‘small’ hyperbolic black holes does not remedy this divergence, since r_h remains finite in the extremal limit, *e.g.*, $r_h = L/\sqrt{2}$ for $d = 4$.

eqs. (3.43) and (3.44) are then given by

$$\mathcal{V} = \frac{4\pi L^3}{\delta} + \mathcal{O}(\delta), \quad \mathcal{V}_0 = \frac{4\pi L^3}{\delta} - 4\pi L^2 + \mathcal{O}(\delta). \quad (3.57)$$

Hence the complexity of formation for the BTZ black hole becomes

$$\Delta\mathcal{C}_V = \frac{4\pi L}{G_N} = \frac{8\pi}{3} c, \quad (3.58)$$

where $c = 3L/(2G_N)$ is the boundary central charge. As before, we are implicitly considering the Neveu-Schwarz vacuum in choosing $f_0(r)$ in eq. (2.39). If instead we consider the Ramond vacuum with $f_0(r) = r^2/L^2$, we find $\Delta\mathcal{C} = 0$.

In any event, we find that the complexity of formation is a fixed constant, independent of the temperature. Of course, this result for $d = 2$ agrees with that found in section 3.1.4 using the CA duality. One curious difference is that the sign of $\Delta\mathcal{C}_V$ in eq. (3.58) is positive while the corresponding result for $\Delta\mathcal{C}_A$ in eq. (3.41) is negative.

3.3 Discussion

In this chapter, we considered the conjectured duality between complexity and action [33, 34] to evaluate the complexity of formation, *i.e.*, the additional complexity involved in preparing an entangled thermofield double state between two boundary CFTs compared to preparing each of the individual CFTs in their vacuum state. Using the results of [63] to account for the contributions of null hypersurfaces and joints to the gravitational action, we were able to evaluate the action of the WDW patch for the dual AdS black holes and vacuum spacetimes. While the individual actions need to be regulated because of divergences coming from the asymptotic boundary, these divergences cancel in the difference of the actions in eq. (3.1) and hence the complexity of formation remains finite in the $\delta \rightarrow 0$ limit.

We evaluated $\Delta\mathcal{C}$ for three horizon geometries (*i.e.*, for the three different spatial geometries (2.5) in the boundary theory) — spherical, planar and hyperbolic. For high temperatures, this geometry is unimportant and as indicated in eq. (3.38), the leading contribution is proportional to the entropy, *i.e.*,

$$\Delta\mathcal{C} = k_d S + \dots \quad \text{with} \quad k_d = \frac{d-2}{d\pi} \cot\left(\frac{\pi}{d}\right). \quad (3.59)$$

The ellipsis indicates the presence of subleading terms for $k = \pm 1$. From the explicit examples in eqs. (3.16) and (3.26), we can see that for curved horizons, eq. (3.59) is the leading term in an expansion for large values of S/C_T where C_T is the central charge in the boundary theory. Above, we referred to this as a high temperature expansion because up to numerical factors, $S/C_T \sim \mathcal{V} T^{d-1}$ at high temperatures, where \mathcal{V} is the spatial volume in the boundary theory. This explains why the spatial curvature was unimportant in this limit and the leading result in eq. (3.59) is independent of the parameter k . Let us note that more generally, the results for $d = 4$ and 3 show that we can write $\Delta\mathcal{C} = C_T f(S/C_T)$.

Hence at least for high temperatures, the additional complexity required in preparing the entangled thermofield double state is proportional to the entanglement entropy between the two boundary CFTs in this state. It is perhaps useful to think of the description of analogous CFT states with MERA tensor networks [147–149] to gain some insight into this result. The interested reader may find a more detailed discussion in appendix E of our work [64], however, we describe some of the salient points here. If we compare the tensor networks describing the individual ground states and the entangled thermofield double state, a large portion of the circuits are in fact identical and prepare the short range entanglements in the final UV state from a coarse-grained IR state. In the holographic context, this is reflected in the fact that the asymptotic AdS regions are nearly identical in both cases and make the same UV divergent contributions to the individual WDW actions. The difference between the MERA tensor networks at high temperatures is that the IR portion of the two vacuum circuits is removed and replaced with a layer of distinct tensors which entangles the two CFTs and introduces the appropriate thermal spectrum of eigenvalues — see figure 2c in [150]. Of course, this central layer of tensors can be thought of as representing the Einstein-Rosen bridge connecting the two asymptotic AdS regions [150]. Hence in considering the complexity of formation, there is a competition between the additional complexity of preparing these bridge tensors and the simplification coming from removing the IR components of the vacuum circuits. At high temperatures, our holographic results indicate that the former dominates since $\Delta\mathcal{C} > 0$. Examining the corresponding MERA circuits in appendix E of [64], we argue that the complexity of the bridge tensors and of the corresponding IR vacuum circuits should both be proportional to the entanglement entropy between the two copies of the CFT. Hence the complexity of formation should be proportional to this entropy, in accord with our holographic results in higher dimensions — see comments on $d = 2$ below. Unfortunately, these arguments do not allow us to determine the sign of $\Delta\mathcal{C}$, which requires a more detailed knowledge of the precise tensors appearing in these constructions. Let us add that recently the complexity of formation was evaluated in free bosonic field theory [49], we will comment on this connection in chapter 7.

In section 3.2, a similar result was obtained for the complexity of formation using the previously proposed duality relating complexity to the volume of an extremal bulk surface [32]. For high temperatures, the leading contribution is independent of the geometry and given by eq. (3.49),

$$\Delta\mathcal{C}_V = \tilde{k}_d S + \dots \quad \text{with} \quad \tilde{k}_d = 4\sqrt{\pi} \frac{(d-2) \Gamma(1 + \frac{1}{d})}{(d-1) \Gamma(\frac{1}{2} + \frac{1}{d})}. \quad (3.60)$$

Again this leading term is the complete result of the planar case while the ellipsis indicates subleading terms which appear with a spherical or hyperbolic horizon. Comparing eqs. (3.59) and (3.60) shows that both of the proposed dualities yield more or less the same complexity of formation up to an overall multiplicative factor. In fact, comparing the growth of complexity at late times found with the two different approaches yields essentially the same multiplicative factor — see eq. (3.52). Now as emphasized in [33, 34], the circuit complexity of a given quantum state can only be assigned a precise value once the algorithm for constructing the state is defined. For example, the value will depend on the choice of an initial reference state and the specific set of quantum gates with which one acts to construct the desired state. In particular, the complexity would be expected to change by an overall multiplicative factor with different gate choices. This may then provide an explanation of the multiplicative factor relating the complexities found using the CA and CV dualities. For example, as shown in eq. (3.39) and figure 3.3, the coefficient k_d appearing in $\Delta\mathcal{C}_A$ (see eq. (3.59)) grows linearly with the boundary dimension d , while the corresponding coefficient \tilde{k}_d appearing in $\Delta\mathcal{C}_V$ (see eq. (3.60)) quickly saturates to a constant with growing d , as shown in eq. (3.50). One can imagine that the former behavior would arise if one chose gates which only act on, *e.g.*, pairs of neighboring qubits.⁹ On the other hand, the latter behaviour might emerge if the gate set was expanded to include $(d-1)$ -local gates as d increases. In any event, our holographic results suggest that the CA and CV dualities may both provide a consistent description of the complexity of holographic boundary states, however, the microscopic details of the algorithms used to define the complexity differs in each case.

As noted previously, the coefficients k_d and \tilde{k}_d both vanish for $d = 2$. Hence in the case of two boundary dimensions, the complexity of formation is a fixed constant, independent of the temperature. Referring back to the discussion of MERA above, this result indicates that the complexity associated with constructing the layer of bridge tensors is essentially the same as for the IR portion of the vacuum network. This result is likely related to

⁹For example, with a simple square lattice filling $d-1$ spatial dimensions, one would have to act with $2(d-1)$ two-qubit gates to simply establish correlations between a particular qubit and all of its nearest neighbors.

the recent discussion of MERA tensor networks in the context of kinematic space [151–153]. In particular, it was found that for the special case of $d = 2$, the bridge tensors can be constructed from the standard isometries and disentanglers appearing in the UV portion of the MERA [152]. In the holographic context, the fact that $\Delta\mathcal{C}$ is independent of the temperature is related to the fact that in three bulk dimensions, the BTZ black hole geometry is still locally the same as the vacuum AdS_3 space [124, 125]. Comparing to the Neveu-Schwarz vacuum in the boundary theory [144], our holographic results in eqs. (3.41) and (3.58) indicated that the complexity of formation is

$$d = 2 : \quad \Delta\mathcal{C}_A = -\frac{c}{3} \quad \text{and} \quad \Delta\mathcal{C}_V = +\frac{8\pi}{3} c, \quad (3.61)$$

where c is the central charge of the boundary theory. Further, considering the Ramond vacuum instead, we find $\Delta\mathcal{C} = 0$ with both the CA and CV dualities. Naively, the difference in the sign of the two results in eq. (3.61) might indicate some tension between the two holographic approaches to evaluating complexity. However, it seems more likely that the different microscopic details in the definition of the complexity, *e.g.*, the reference state, for the two approaches is simply producing different results at this fine-grained level. That is, the precise value (or even sign) of the complexity of formation is not robust against the ambiguities appearing in the definition of the complexity.

At this point, we note that, as discussed in [63], the boundary terms on the null boundary surfaces (2.30) and null joints (2.34) are ambiguous. That is, evaluating the gravitational action for a particular spacetime geometry generally produces different numerical values depending on different choices that can be made in constructing the boundary terms. However, we show in appendix A.4 that our results for the complexity of formation are not effected by these ambiguities. The one exception to this statement is for the small hyperbolic black holes, *i.e.*, with $k = -1$ and $\omega^{d-2} < 0$. In this case, we find that the complexity of formation is ambiguous due to the possibility of shifting a in the joint contributions (2.34) by an extra (arbitrary) function [63]. In particular, $\Delta\mathcal{C}$ is modified by such a shift through the joint terms where the null sheets from the opposite asymptotic boundaries meet between the inner and outer horizons — see appendix A.4 for a detailed discussion. Hence our results for the complexity of formation are not universal in this case. It is interesting that in this regime, we observed a discrepancy between the CA and CV approaches. Namely, $\Delta\mathcal{C}_V$ diverges as T approaches zero for $k = -1$, while $\Delta\mathcal{C}_A$ remains finite. The CA duality also yields the curious result $d\mathcal{C}_A/dt = 0$ for small hyperbolic black holes — see appendix A.3. All of these results highlight the exotic nature of these states, as was first commented by [130].

We also observe that the complexity of formation appears well-behaved, for small spherical black holes, *i.e.*, with $k = +1$ and $r_h < L$, as shown in figures 3.1 and 3.2. However,

these black holes are thermodynamically unstable [131, 132] and the correct saddle point which dominates the bulk partition function is actually still the vacuum AdS space. Of course, with this saddle to represent the thermofield double, our calculations would yield a vanishing complexity of formation. However, this simply indicates that there is no leading order contribution to $\Delta\mathcal{C}$ in the large central charge (or large N) expansion of the boundary CFT. That is, there is no contribution to $\Delta\mathcal{C}$ of the magnitude of the central charge C_T , just as there is no entropy of this order. However, the thermofield double state still entangles the two CFTs and it is simply that the entanglement entropy is an order one quantity. Hence we expect that the complexity of formation is also nonvanishing but only an order one quantity. It would be interesting to understand how to evaluate this contribution to $\Delta\mathcal{C}$.

Chapter 4

The Growth Rate of Holographic Complexity

We now turn our attention to the analysis of the full time dependence of holographic complexity in the TFD state in eq. (1.21). For the complexity=action proposal, the time evolution with both times evolving up is represented in the Penrose diagrams of figure 4.1.

One striking result found with the CA proposal is that the late time growth rate is proportional to $2M/\pi$, independent of the boundary curvature and the spacetime dimension [33, 34]. Further it was suggested that this saturation of the growth rate is related to Lloyd's bound on the rate of computation by a system with energy M [116]. Using the CV conjecture, the late time growth rate of the complexity also saturates, but this final rate is only proportional to the mass at high temperatures and with a coefficient that depends on the spacetime dimension [32]. Despite extensive discussions of this late time limit for the time dependence of the holographic complexity, the question of its full time evolution and in particular the rate of change at early times had not been thoroughly investigated.¹ Therefore, in the present chapter, we study the full time evolution of holographic complexity, for both the CV and the CA proposals, in static two-sided eternal black holes. We consider black holes in various dimensions and with spherical, planar and hyperbolical horizon geometries. We also investigate the properties of complexity for charged black holes (for $d \geq 3$, where d is the spacetime dimension of the boundary theory). The full time profile in all cases except $d = 2$ requires some numerical treatment. We are, however, able to identify certain general features.

For the CA proposal (and in $d \geq 3$), we find that the complexity remains unchanged

¹However, see [154] and section 8 of [34]

for some critical time, which is of the order of the thermal scale. Immediately after this time, the rate of change of the complexity is negatively divergent and we observe a short transient period during which the complexity is decreasing. At late times, the rate of change in complexity approaches a constant, previously understood to be associated with Lloyd’s bound on the rate of computation. However we observe a violation of this late time bound since the rate approaches the late time limit from above.² We also comment on the role of the arbitrary length scale in the boundary theory associated with the holographic normalization of null-normals and its influence on the rate of change of complexity. For the CV proposal, the rate of change of complexity is a monotonically increasing function of time, and it saturates to a constant at late times. While at high temperatures this late time rate is proportional to the mass, the precise value depends on the boundary curvature for spherical and hyperbolic horizons at finite temperatures. For either conjecture, we find that the rate of change of complexity approaches its late time limit with an exponential decay where the characteristic time scale is proportional to the inverse temperature. For both conjectures (and in $d \geq 3$), we also examined the rate of change of complexity for charged black holes, as well as their complexity of formation. In either case, we find that the holographic complexity smoothly approaches to that of the neutral black holes in the limit of zero charge. With the CA approach, adding a charge washes out the curious early time behaviour, *i.e.*, complexity immediately begins increasing with sufficient charge, but the late time violation is essentially the same as in the neutral case. Further, the complexity of formation for charged extremal black holes is divergent in either case, implying that the holographic states at finite chemical potential and zero temperature are infinitely more complex than their finite temperature counterparts.

The remainder of this chapter is organized as follows: We start in section 4.1 by setting up the evaluation of the action anchored at general boundary times. In section 4.2 we investigate the full time evolution of complexity for the thermofield double state (1.21), dual to an eternal AdS black hole, using the CA conjecture. We consider different boundary geometries and different dimensions, and investigate how the holographic complexity approaches the late time limit. In section 4.3, we study the time evolution of complexity using the CV conjecture. We consider various geometries and dimensions, and prove that it approaches its late time limit from below. In section 4.4, we analyze Reissner-Nordstrom AdS charged black holes, their complexity of formation and how they violate a proposed generalization of Lloyd’s bound. Finally, we discuss some implications of our results, as well as possible future directions, in section 4.5. We relegate certain details of the calcu-

²Earlier works have investigated possible violations of Lloyd’s bound in the context of Reissner-Nordstrom black holes [34, 145, 155]. In this chapter we find a generic violation of this bound appearing even for uncharged AdS-Schwarzschild black holes.

lations to the appendices. In appendix B.1, we present additional details for the action calculation for BTZ black holes. Extra examples of the time dependence of complexity for uncharged black holes in $d = 3$ using the CA conjecture are presented in appendix B.2. In appendix B.3, we show the details of the calculation of the complexity of formation for charged black holes using the CA proposal. In appendix B.4, we discuss the influence of ambiguities associated with the presence of null boundaries on the CA proposal results.

This chapter is adapted from [66].

4.1 Evaluating the Time Dependent Action

The causal structure of the black holes described by the metric (2.1) is illustrated by the Penrose diagram in figure 4.1.³ We are considering the holographic complexity of the boundary state on the constant time slices, denoted by t_L and t_R , on the two asymptotic boundaries. The corresponding WDW patch (also depicted in figure 4.1) is then bounded by the light sheets sent from these two asymptotic time slices. We will be interested in the time dependence of the complexity and therefore in the time dependence of the gravitational action evaluated on this patch as the boundary time increases.⁴ The result depends only on $t = t_L + t_R$ and not on each of the boundary times separately due to the invariance of the system under boosts in Kruskal coordinates, *i.e.*, under shifts $t_L \rightarrow t_L + \Delta t$ and $t_R \rightarrow t_R - \Delta t$. In terms of the boundary theory, this corresponds to the invariance of the thermofield double state (1.21) under an evolution with the Hamiltonian $H = H_L - H_R$. In any event, we can therefore deduce the rate of change of the holographic complexity for a general choice of time slices from the result for the symmetric configuration with times $t_L = t_R \equiv t/2$.

For our calculations, there are two different regimes to be considered with respect to the position of the WDW patch. The first, illustrated in the left panel of figure 4.1, is when the WDW patch is in contact with the past singularity. In the second regime, shown in the right panel, the past light sheets from the left and right boundaries intersect before hitting the past singularity. The critical time t_c separating the two regimes is easily found to be

$$t_c = 2(r_\infty^* - r^*(0)), \quad (4.1)$$

³Small hyperbolic black holes are an exception since their causal structure resembles that of charged black holes. We will comment on this case at the end of appendix B.3, where we discuss further properties of charged black holes.

⁴The geometry is symmetric under $t \rightarrow -t$ and we only consider the behaviour of the complexity for $t > 0$. We briefly comment on the decrease of the complexity found for $t < 0$ in section 4.2.

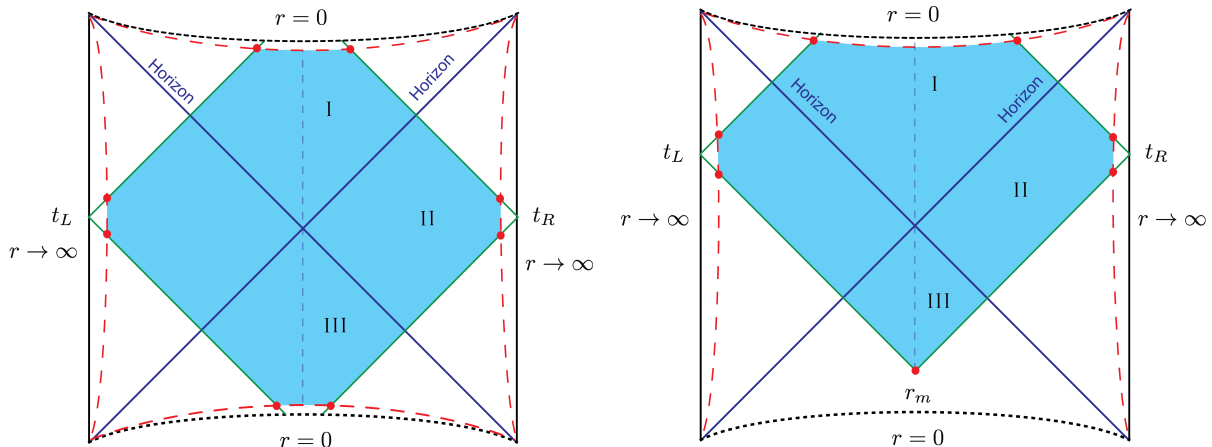


Figure 4.1: Penrose diagram of the WDW patch of an eternal AdS black hole, moving forward in time in a symmetric way ($t_L = t_R$).

for the symmetric scenario (*i.e.*, $t_L = t_R = t/2$). Generally, we can only find closed form expression for t_c in specific dimensions. However, for planar black holes (*i.e.*, $k = 0$ in eq. (2.2)), the solution can be written in a closed form for any d as:

$$t_c = \frac{2\pi}{d} \frac{L^2}{r_h} \cot\left(\frac{\pi}{d}\right) = \frac{1}{2T} \cot\left(\frac{\pi}{d}\right), \quad (4.2)$$

where $T = dr_h/(4\pi L^2)$ is the boundary temperature (2.6) in this case.

In the following, we evaluate the various contributions to the gravitational action for both the $0 < t < t_c$ and $t > t_c$ regimes. We use these results to compute the rate of change of the holographic complexity using eq. (1.24) and the action in eq. (2.10).

Initial times: $t < t_c$

For times before t_c , the action (2.10) contains three nonvanishing contributions: the bulk contribution; the GHY surface contributions from the regulator surfaces at the past and future singularities, as well as from the UV cutoff surfaces; and the null joint terms where the null boundaries of the WDW patches intersect the regulator surfaces at the past and future singularities, as well as the intersections with the UV cutoff surface. We will evaluate all these contributions in turn and demonstrate that the total action is independent of time in the interval $t_c \geq t (\geq -t_c)$.⁵ Due to the symmetry of the configuration that we have

⁵See comment about negative times around eq. (4.36).

chosen, we can evaluate the contributions for the right side of the Penrose diagram (in the left panel of figure 4.1) and then simply multiply the result by a factor of two.

Bulk contribution: We divide the WDW patch into three regions: I, the region behind the future horizon; II, the region outside both horizons; and III, the regions behind the past horizon — see figure 4.1. The corresponding bulk contributions to the action read:

$$\begin{aligned}
I_{\text{bulk}}^{\text{I}} &= -\frac{d\Omega_{k,d-1}}{8\pi G_N L^2} \int_{\epsilon_0}^{r_h} r^{d-1} \left(\frac{t}{2} + r_\infty^* - r^*(r) \right) dr \\
I_{\text{bulk}}^{\text{II}} &= -\frac{d\Omega_{k,d-1}}{4\pi G_N L^2} \int_{r_h}^{r_{\text{max}}} r^{d-1} \left(r_\infty^* - r^*(r) \right) dr \\
I_{\text{bulk}}^{\text{III}} &= -\frac{d\Omega_{k,d-1}}{8\pi G_N L^2} \int_{\epsilon_0}^{r_h} r^{d-1} \left(-\frac{t}{2} + r_\infty^* - r^*(r) \right) dr
\end{aligned} \tag{4.3}$$

where r_{max} is a UV cutoff. Summing these three contributions, we are left with:

$$I_{\text{bulk}}^0 = -\frac{d\Omega_{k,d-1}}{2\pi G_N L^2} \int_{\epsilon_0}^{r_{\text{max}}} r^{d-1} (r_\infty^* - r^*(r)) dr, \tag{4.4}$$

where an extra factor of two was included to account for the two sides of the Penrose diagram in figure 4.1. We see that the time dependences in $I_{\text{bulk}}^{\text{I}}$ and $I_{\text{bulk}}^{\text{III}}$ precisely cancel and hence the total bulk contribution is time independent.

GHY surface contributions: There are three different GHY surface contributions to be considered: those coming from the regulator surfaces at the future and past singularities, and the surface contribution at the UV cutoff surface.⁶ We use the following (outward-directed unit) normal vectors to evaluate the corresponding extrinsic curvatures

$$\begin{aligned}
r = r_{\text{max}} : \quad \mathbf{s} &= s_\mu dx^\mu = \frac{dr}{\sqrt{f(r_{\text{max}})}} \\
r = \epsilon_0 : \quad \mathbf{t} &= t_\mu dx^\mu = -\frac{dr}{\sqrt{-f(\epsilon_0)}}
\end{aligned} \tag{4.5}$$

where the second normal applies for both regulator surfaces next to the past and future singularities. For a constant r surface in the metric (2.1), the trace of the extrinsic curvature is given by

$$K = \frac{n_r}{2} \left(\partial_r f(r) + \frac{2(d-1)}{r} f(r) \right), \tag{4.6}$$

⁶Recall that we chose the null normals to be affinely parametrized and hence the null surface contributions vanish, *i.e.*, $\kappa = 0$.

and as a result, we obtain

$$\begin{aligned}
I_{\text{surf}}^{\text{future}} &= -\frac{r^{d-1}\Omega_{k,d-1}}{8\pi G_N} \left(\partial_r f(r) + \frac{2(d-1)}{r} f(r) \right) \left(\frac{t}{2} + r_\infty^* - r^*(r) \right) \Big|_{r=\epsilon_0}, \\
I_{\text{surf}}^{\text{past}} &= -\frac{r^{d-1}\Omega_{k,d-1}}{8\pi G_N} \left(\partial_r f(r) + \frac{2(d-1)}{r} f(r) \right) \left(-\frac{t}{2} + r_\infty^* - r^*(r) \right) \Big|_{r=\epsilon_0}, \\
I_{\text{surf}}^{\text{cutoff}} &= \frac{r^{d-1}\Omega_{k,d-1}}{8\pi G_N} \left(\partial_r f(r) + \frac{2(d-1)}{r} f(r) \right) (r_\infty^* - r^*(r)) \Big|_{r=r_{\text{max}}}.
\end{aligned} \tag{4.7}$$

We see that the surface contribution $I_{\text{surf}}^{\text{cutoff}}$ at the UV cutoff surface is independent of time. Further we note that this contribution is identical in the regime $t > t_c$. Therefore, the UV surface terms do not contribute to the time dependence of holographic complexity and we will ignore them both here and in the next section. For $t < t_c$, we see that the time dependence of the GHY surface contributions from the past and future singularities precisely cancels leaving:

$$I_{\text{surf, sing}}^0 = -\frac{r^{d-1}\Omega_{k,d-1}}{4\pi G_N} \left(\partial_r f(r) + \frac{2(d-1)}{r} f(r) \right) (r_\infty^* - r^*(r)) \Big|_{r=\epsilon_0}. \tag{4.8}$$

We note again that this contribution is independent of time for all $t < t_c$.

Null joint contributions: There are a number of null joint contributions to be considered. In particular, we have the joint contributions at the intersections of the null boundaries of the WDW patch with the regulator surfaces at the past and future singularities and those at their intersections with the UV cutoff surface. These contributions were carefully evaluated in chapter 2 — see eqs. (2.36) and (2.37)— and they are not modified in the present case. However, two key observations are that the null joint contributions at the singularities vanish, while those at the UV cutoff surface have no time dependence. Hence neither of these terms contribute to the time rate of change of holographic complexity.

Total Action: Hence as our calculations above demonstrate, the total gravitational action of the WDW patch is independent of time for the initial time period $t < t_c$. If we denote its value by I_0 ,⁷ then in this early time interval, we have

$$0 \leq t \leq t_c : \quad \frac{d\mathcal{C}_A}{dt} = \frac{1}{\pi} \frac{dI_0}{dt} = 0. \tag{4.9}$$

⁷Note that $I_0 = I_{\text{WDW}}(t_L = t_R = 0)$ and so this result is identical to the action evaluated in chapter 3. In particular, the complexity of formation of the thermofield double state in the boundary is given by I_0 minus twice the corresponding action of the WDW patch in vacuum AdS.

Later times: $t > t_c$

For times $t > t_c$, the same three sets of terms make nonvanishing contributions to the action of the WDW patch, *i.e.*, the bulk term, the GHY surface terms and the null joint terms, and so we again evaluate each of these contributions in turn. We again use the symmetry of the configuration to only explicitly evaluate the contributions for the right side of the Penrose diagram (in the right panel of figure 4.1) and then simply multiply the result by a factor of two.

Bulk contribution: As before, we split the WDW patch into three regions which we denote as I, II and III — see figure 4.1. The corresponding bulk contributions to the gravitational action become:

$$\begin{aligned} I_{\text{bulk}}^{\text{I}} &= -\frac{d\Omega_{k,d-1}}{8\pi G_N L^2} \int_0^{r_h} r^{d-1} \left(\frac{t}{2} + r_\infty^* - r^*(r) \right) dr \\ I_{\text{bulk}}^{\text{II}} &= -\frac{d\Omega_{k,d-1}}{8\pi G_N L^2} \int_{r_h}^{r^{\text{max}}} r^{d-1} 2 \left(r_\infty^* - r^*(r) \right) dr \\ I_{\text{bulk}}^{\text{III}} &= -\frac{d\Omega_{k,d-1}}{8\pi G_N L^2} \int_{r_m}^{r_h} r^{d-1} \left(-\frac{t}{2} + r_\infty^* - r^*(r) \right) dr \end{aligned} \quad (4.10)$$

where r_m is the radius behind the past horizon where the null boundary sheets from the left and right boundaries intersect. This position is determined by the following equation:

$$\frac{t}{2} - r_\infty^* + r^*(r_m) = 0. \quad (4.11)$$

Generally, this is a transcendental equation and we can only determine r_m numerically. Combining the above results, we obtain the total bulk contribution

$$I_{\text{bulk}} = I_{\text{bulk}}^0 - \frac{d\Omega_{k,d-1}}{4\pi G_N L^2} \int_0^{r_m} r^{d-1} \left(\frac{t}{2} - r_\infty^* + r^*(r) \right) dr, \quad (4.12)$$

where we have again included a factor of two to account for the equal contributions coming from the two sides of the WDW patch shown in figure 4.1. We have also introduced I_{bulk}^0 , which was defined in eq. (4.4) and which is time independent.

GHY surface contributions: For $t > t_c$, the WDW patch does not reach the past singularity and so only the regulator surface at the future singularity contributes here. The expression takes the same form as in eq. (4.7) and as a result we obtain

$$I_{\text{surf}}^{\text{future}} = -\frac{f(r)r^{d-1}\Omega_{k,d-1}}{8\pi G_N} \left(\frac{\partial_r f(r)}{f(r)} + \frac{2(d-1)}{r} \right) \left(\frac{t}{2} + r_\infty^* - r^*(r) \right) \Big|_{r=\epsilon_0}. \quad (4.13)$$

We also have the GHY contribution from the UV cutoff surface as in eq. (4.7). However, this contribution is time independent and so we ignore it here.

Using eq. (4.8), the above expression can be rewritten as follows

$$I_{\text{surf}} = I_{\text{surf, sing}}^0 - \frac{r^{d-1}\Omega_{k,d-1}}{8\pi G_N} \left(\partial_r f(r) + \frac{2(d-1)}{r} f(r) \right) \left(\frac{t}{2} - r_\infty^* + r^*(r) \right) \Big|_{r=\epsilon_0}. \quad (4.14)$$

The difference $I_{\text{surf}} - I_{\text{surf, sing}}^0$ encodes the change in the GHY contribution to the holographic complexity after $t = t_c$.

Null Joint Contribution: There are null joint contributions from the intersection of the null boundaries with the regulator surface at the future singularity and with the UV cutoff surface. However, as in the previous section, the former vanish while the latter are independent of time. Therefore neither of these contribute to $d\mathcal{C}_A/dt$. The last joint contribution to consider when $t > t_c$ is that from the intersection of the two past null boundaries at $r = r_m$. To evaluate this term, we use the following outward-directed null normal vectors:

$$\text{Right : } \mathbf{k}_R = -\alpha dt + \alpha \frac{dr}{f(r)}; \quad \text{Left : } \mathbf{k}_L = \alpha dt + \alpha \frac{dr}{f(r)}. \quad (4.15)$$

Here we have assumed that the Killing vector ∂_t describes a flow from right to left for the region behind the past horizon in figure 4.1. The joint term can then be evaluated as

$$I_{\text{jnt}} = -\frac{\Omega_{d-1} r_m^{d-1}}{8\pi G_N} \log \frac{|f(r_m)|}{\alpha^2}, \quad (4.16)$$

This term depends on t through the implicit time dependence of r_m , as determined by eq. (4.11). We would like to stress that this contribution is sensitive to the ambiguities discussed in [63], *i.e.*, through its dependence on the normalization constant α . We discuss this issue further in appendix B.4.

Total Action: The total action for $t > t_c$ is given by the sum of eqs. (4.12), (4.14) and (4.16) plus some time independent contributions from the UV cutoff surfaces and the null junctions. It is sometimes convenient to express our various contributions in terms of $\delta t = t - t_c$. As a consequence, the equation for the position r_m of the past null junction becomes

$$\frac{\delta t}{2} + r^*(r_m) - r^*(0) = 0. \quad (4.17)$$

The total gravitational action can then be expressed as

$$I = I_0 + \delta I \quad \text{with} \quad \delta I = \delta I_{\text{bulk}} + \delta I_{\text{surf}} + I_{\text{jnt}}. \quad (4.18)$$

where

$$\delta I_{\text{bulk}} \equiv I_{\text{bulk}} - I_{\text{bulk}}^0 = -\frac{d\Omega_{k,d-1}}{4\pi G_N L^2} \int_0^{r_m} dr r^{d-1} \left(\frac{\delta t}{2} + r^*(r) - r^*(0) \right), \quad (4.19)$$

$$\delta I_{\text{surf}} \equiv I_{\text{surf}} - I_{\text{surf}}^0 = -\frac{r^{d-1}\Omega_{k,d-1}}{8\pi G_N} \left(\partial_r f(r) + \frac{2(d-1)}{r} f(r) \right) \frac{\delta t}{2} \Big|_{r=\epsilon_0}, \quad (4.20)$$

$$I_{\text{jnt}} = -\frac{\Omega_{d-1} r_m^{d-1}}{8\pi G_N} \log \frac{|f(r_m)|}{\alpha^2}. \quad (4.21)$$

We note that δI is finite, *i.e.*, independent of the UV cutoff δ . Further it vanishes in the limit $\delta t \rightarrow 0$, which can be seen by explicitly substituting the blackening factor (2.2) into eqs. (4.19)-(4.21). However, we will show below that the rate of change of the holographic complexity is discontinuous at $t = t_c$.

4.2 Time Dependence of Complexity

Here we examine the time dependence of the holographic complexity. As we already noted above in eq. (4.9), initially, we have

$$0 \leq t \leq t_c : \quad \frac{d\mathcal{C}_A}{dt} = \frac{1}{\pi} \frac{dI_0}{dt} = 0, \quad (4.22)$$

where t_c was defined in eq. (4.1).

For later times $t > t_c$, we obtain the time derivative of complexity by differentiating eqs. (4.17)-(4.21) with respect to time. From eq. (4.17), we find the time dependence of the meeting point r_m to be

$$\frac{dr_m}{dt} = -\frac{f(r_m)}{2}. \quad (4.23)$$

Differentiating eq. (4.19) yields

$$\frac{dI_{\text{bulk}}}{dt} = \frac{d\delta I_{\text{bulk}}}{dt} = -\frac{\Omega_{k,d-1}}{8\pi G_N L^2} r_m^d, \quad (4.24)$$

where in obtaining this result, we used eq. (4.17) to demonstrate that the contribution coming from differentiating the upper limit of integration vanishes. Evaluating the GHY surface term (4.20) at $r = \epsilon_0$ and then taking the $\epsilon_0 \rightarrow 0$ limit yields

$$\frac{dI_{\text{surf}}}{dt} = \frac{d\delta I_{\text{surf}}}{dt} = \frac{\omega^{d-2} d\Omega_{k,d-1}}{16\pi G_N}. \quad (4.25)$$

Finally, differentiating the null joint term (4.21) gives

$$\frac{dI_{\text{jnt}}}{dt} = \frac{\Omega_{k,d-1} r_m^{d-2}}{16\pi G_N} \left[(d-1) f(r_m) \log \frac{|f(r_m)|}{\alpha^2} + r_m \partial_r f(r_m) \right]. \quad (4.26)$$

where we have used eq. (4.23). Using the explicit form of the blackening factor (2.2) and summing the three terms above, eq. (1.24) yields the rate of growth of holographic complexity as

$$t > t_c : \quad \frac{d\mathcal{C}_A}{dt} = \frac{1}{\pi} \left(2M + \frac{\Omega_{k,d-1} (d-1) r_m^{d-2}}{16\pi G_N} f(r_m) \log \frac{|f(r_m)|}{\alpha^2} \right). \quad (4.27)$$

Of course, this result reproduces the expected rate of growth at late times [33, 34], *i.e.*, $d\mathcal{C}_A/dt = 2M/\pi$, since in this limit r_m approaches r_h and so the second term on the right vanishes with $f(r_m \rightarrow r_h) \rightarrow 0^-$. We provide further comments on the properties of our result (4.27) below.

Comments

As already noted above, this result (4.27) reproduces the expected rate of growth at late times since in this limit r_m approaches r_h and so $f(r_m \rightarrow r_h) \rightarrow 0^-$. We also note that at late times with r_m approaching r_h from below, $f(r_m)$ is small and negative and therefore the correction to $d\mathcal{C}_A/dt = 2M/\pi$ in eq. (4.27) is positive! That is, $d\mathcal{C}_A/dt$ approaches the late time limit from above. Recall that [33, 34] suggested that the late time limit of $d\mathcal{C}_A/dt$ may be related to Lloyd's bound $2M/\pi$ for the rate of computation for a system of energy M [116]. Therefore we see here a (small) violation of Lloyd's bound in the eternal black hole.

Late time expansion: To get a better understanding of the late time behaviour, it is possible to solve the equation for r_m in a late time expansion. We do this by defining the regular part of the blackening factor $F(r)$:

$$f(r) \equiv F(r)(r - r_h) \quad (4.28)$$

and decomposing the inverse blackening factor as

$$\frac{1}{f(r)} = \frac{1}{F(r_h)(r - r_h)} + \frac{F(r_h) - F(r)}{F(r_h)F(r)(r - r_h)}. \quad (4.29)$$

This leads to the following form of the tortoise coordinate

$$r^*(r) = \frac{1}{F(r_h)} \log \frac{|r - r_h|}{\tilde{\ell}} + \int^r \frac{F(r_h) - F(\tilde{r})}{F(r_h)F(\tilde{r})(\tilde{r} - r_h)} d\tilde{r} \quad (4.30)$$

where $\tilde{\ell}$ is an unspecified integration constant. Using eqs. (2.6) and (4.17), we can solve for r_m at late times as

$$r_m = r_h \left(1 - c_1 e^{-2\pi T(t-t_c)}\right) + \dots \quad (4.31)$$

with

$$c_1 = \exp \left[- \int_0^{r_h} dr \frac{F(r_h) - F(r)}{F(r)(r - r_h)} \right] > 0, \quad (4.32)$$

and where the ellipsis stands for corrections which are higher order in $(r_h - r_m)$, *i.e.*, which would decay at least as fast as $e^{-4\pi T t}$. Substituting this expression (4.31) into eq. (4.27), we obtain the first corrections to the rate of change in complexity in the $t \rightarrow \infty$ limit

$$\frac{d\mathcal{C}_A}{dt} = \frac{2M}{\pi} + 2(d-1)c_1 S T^2 e^{-2\pi T(t-t_c)} \left(t - t_c - \frac{1}{2\pi T} \log \left[\frac{4\pi c_1 T r_h}{\alpha^2} \right] \right) + \dots \quad (4.33)$$

We see that the final factor will always become positive for sufficiently late times and hence the bound conjectured by [33, 34] will be violated.

Early times: It is also interesting to look at an early time expansion of the expression (4.27). At very early times after t_c , r_m is very close to the past singularity, *i.e.*, as $\delta t = t - t_c \rightarrow 0$, $r_m \rightarrow 0$. As a consequence, $f(r_m) \sim -\omega^{d-2}/r_m^{d-2}$ and the second term in eq. (4.27) diverges to minus infinity (as long as $d \geq 3$). More explicitly, one can show that this leading divergence as $\delta t \rightarrow 0$ is logarithmic with

$$\left. \frac{d\mathcal{C}_A}{dt} \right|_{\delta t \rightarrow 0} \longrightarrow -\frac{(d-2)M}{(d-1)\pi} \log \left(\frac{2\omega}{\alpha^{2(d-1)/(d-2)}(d-1)\delta t} \right) \quad \text{for } d \geq 3. \quad (4.34)$$

Despite this divergence, we note again that the complexity itself remains finite as $\delta t \rightarrow 0$ and it is only its derivative which is divergent. We would also like to stress again, that these results are influenced by the ambiguities in the corner term mentioned in [63]. We explore this issue further in appendix B.4. We also examine the case $d = 2$, *i.e.*, BTZ black holes, in detail in the following section.

Averaging: The discussion above indicates that the action changes very rapidly in the vicinity of $\delta t = 0$ — see also the examples in section 4.2.1. However, one might argue that the holographic complexity does not have a good definition on time scales smaller than

$\beta = 1/T$ in the context of the eternal black hole.⁸ Hence we might average the rate of change in complexity over time scales which are longer than the thermal time scale. We can define a simple averaged rate of change in complexity as follows:

$$\left[\frac{d\mathcal{C}_A}{dt} \right]_{\gamma; \text{avg}} = \frac{1}{\gamma\beta} \int_{t-\gamma\beta/2}^{t+\gamma\beta/2} \frac{d\mathcal{C}_A}{dt'} dt' = \frac{\mathcal{C}_A(t + \gamma\beta/2) - \mathcal{C}_A(t - \gamma\beta/2)}{\gamma\beta}, \quad (4.35)$$

where γ is some numerical factor of order one. In the second expression, we see that we have essentially constructed a discrete time derivative on a time step $\Delta t = \gamma/T$.

Let us comment on the properties of this averaged rate: First, we note that $\left[\frac{d\mathcal{C}_A}{dt} \right]_{\gamma; \text{avg}}$ remains continuous at all times. However, its time derivative will be discontinuous at $|t \pm \frac{\gamma\beta}{2}| = t_c$ because of the discontinuity in $d\mathcal{C}_A/dt$ noted above. When $\gamma\beta/2 < t_c$ there will generically be a short period of time right after $t = t_c - \gamma\beta/2$ for which this averaged rate will be negative. After this period, the rate will rise quickly to positive values. Note that this averaging does not remove the (small) violation of Lloyd's bound, discussed above. We will return to discuss this time averaging in more detail in section 4.5.

Negative Times: In our setup, the complexity is a symmetric function of time $\mathcal{C}_A(t) = \mathcal{C}_A(-t)$. Of course, this implies that the time derivative is anti-symmetric

$$\frac{d\mathcal{C}_A}{dt}(t) = -\frac{d\mathcal{C}_A}{dt}(-t). \quad (4.36)$$

Our system therefore admits a regime of decreasing complexity, at least for large negative times. This situation is unstable — an arbitrary small perturbation would cause the complexity to start increasing again. A discussion of this issue can be found in subsection [2.1] of [86].

Dependence on the boundary curvature: Given the black hole metric in eqs. (2.1) and (2.2), it is clear that L is the AdS curvature scale. However, implicitly, L also plays the role of the curvature of the boundary metric in the cases $k = \pm 1$. Hence when we express our results in terms of quantities of the boundary theory, it is perfectly consistent for the final answer to depend on L . However, if we introduce a separate curvature scale R for the boundary metric, it becomes a consistency test to demonstrate that we can eliminate the AdS scale from our expressions.

Hence let us consider the AdS black hole metric

$$ds^2 = -f(r) \frac{L^2}{R^2} d\tau^2 + \frac{dr^2}{f(r)} + r^2 d\Sigma_{k,d-1}^2, \quad (4.37)$$

⁸We thank Lenny Susskind, Dan Roberts and Brian Swingle for correspondence on this point.

where $f(r)$ is still given by eq. (2.2). Now scaling the metric in the asymptotic region $r \rightarrow \infty$ by R^2/r^2 yields the boundary metric

$$ds_{bdy}^2 = -d\tau^2 + R^2 d\Sigma_{k,d-1}^2, \quad (4.38)$$

where the curvature of the spatial geometry is now set by R .⁹ Of course, the only real change between eqs. (2.1) and (4.37) is that we have rescaled the time variable, *i.e.*, $\tau = (R/L)t$. So essentially all of our computations follow identically for the ‘new’ geometry to those that were performed above. However, the scaling of the time coordinate appears in various places, such as the definition of the null coordinates in eq. (2.15) or of the null normals in eq. (4.15). Another important difference is in the definition of various quantities which characterize the boundary state in terms of the geometric parameters appearing in the bulk. In particular, eqs. (2.7), (2.8) and (2.6) are replaced with the following

$$\begin{aligned} M &= \frac{(d-1)\Omega_{k,d-1}}{16\pi G_N} \frac{L}{R} \omega^{d-2}, & S &= \frac{\Omega_{k,d-1}}{4G_N} r_h^{d-1}, \\ T &= \frac{L}{4\pi R} \frac{\partial f}{\partial r} \Big|_{r=r_h} = \frac{L}{4\pi R r_h} \left(d \frac{r_h^2}{L^2} + (d-2)k \right), \end{aligned} \quad (4.39)$$

and the spatial volume of boundary becomes $V = \Omega_{k,d-1} R^{d-1}$. Given these changes, the critical time is given by

$$\tau_c = \frac{2R}{L} (r_\infty^* - r^*(0)) \quad (4.40)$$

and our result (4.27) for the rate of change of the complexity becomes

$$\tau > \tau_c : \quad \frac{d\mathcal{C}_A}{d\tau} = \frac{1}{\pi} \left(2M + \frac{\Omega_{k,d-1}(d-1)r_m^{d-2}}{16\pi G_N} \frac{L}{R} f(r_m) \log \frac{L^2 |f(r_m)|}{R^2 \alpha^2} \right), \quad (4.41)$$

where the equation for the meeting point can be written as

$$\delta\tau = -\frac{2R}{L} (r^*(r_m) - r^*(0)). \quad (4.42)$$

Now we would like to recast this result (4.41) in terms of boundary quantities. We do so by first defining a dimensionless radial coordinate $x = r/r_h$. Next we note that

⁹Notice that for the planar geometry, *i.e.*, $k = 0$, there is no curvature scale and hence R becomes some arbitrary length scale in the boundary theory. Further, for $k = 0$ in eq. (2.1), we implicitly had chosen the boundary metric $d\Sigma_{0,d-1}^2 = \sum_{i=1}^{d-1} dx_i^2/L^2$, following chapter 2. Normalizing with the AdS curvature scale L was required to ensure that the line element was dimensionless. Here, it is more natural to set $d\Sigma_{0,d-1}^2 = \sum_{i=1}^{d-1} d\tilde{x}_i^2/R^2$, so that the boundary metric (4.38) is independent of R (and L). Of course, this is equivalent to rescaling the (spatial) boundary coordinates as $\tilde{x}_i = (R/L)x_i$.

from eq. (4.39), we see that the dimensionless ratio of geometric scales r_h/L in the bulk is determined by the dimensionless product of boundary quantities RT . In particular, we find

$$\frac{r_h}{L} = \frac{2\pi RT}{d} \left(1 + \sqrt{1 - \frac{d(d-2)k}{(2\pi RT)^2}} \right) \equiv 2\pi RT \tilde{g}(RT). \quad (4.43)$$

Now examining the blackening factor, we can write:

$$\begin{aligned} f(r) &= \frac{r^2}{L^2} + k + \frac{r_h^{d-2}}{r^{d-2}} \left(\frac{r_h^2}{L^2} + k \right) \\ &= \frac{r_h^2}{L^2} \left(x^2 + \frac{kL^2}{r_h^2} - \frac{1}{x^{d-2}} \left(1 + \frac{kL^2}{r_h^2} \right) \right) \equiv \frac{r_h^2}{L^2} \tilde{f}(x, RT). \end{aligned} \quad (4.44)$$

Further, combining the above expressions in eq. (4.42), we have

$$\pi \tilde{g}(RT) T \delta\tau = - \int_0^{x_m} \frac{dx}{\tilde{f}(x, RT)}, \quad (4.45)$$

which demonstrates that x_m is implicitly a function of the (dimensionless) boundary quantities, $T\delta\tau$ and RT . Further, these results allow us to translate the rate of change in complexity (4.41) for $\tau > \tau_c$ to the form¹⁰

$$\frac{d\mathcal{C}_A}{d\tau} = \frac{1}{\pi} \left(2M + ST(d-1) \tilde{g}(RT) x_m^{d-2} \tilde{f}(x_m, RT) \log \left[\frac{2\pi LT}{\alpha} \tilde{g}(RT) |\tilde{f}(x_m, RT)|^{1/2} \right] \right). \quad (4.46)$$

Here we see that the right-hand side is expressed in terms of boundary quantities, except for a single factor of L appearing in the argument of the logarithm. Of course, this argument also contains a factor of the (dimensionless) normalization constant α , which is arbitrary. Precisely, the same situation arose in [65] in investigating the structure of the UV divergences in holographic complexity. Following [65], it is natural to choose $\alpha = L/\ell$ which eliminates the errant factor of L but introduces some new scale ℓ in the boundary theory. Hence this choice raises the question of what the most appropriate choice for ℓ would be. For simplicity in the following, we will set $\ell = R$, the curvature scale in the $k = \pm 1$ boundary geometries (4.38). As noted in the planar case (see footnote 9), R remains an arbitrary length scale in the boundary theory. We return to discuss this point in section 4.5.

¹⁰Let us note that for planar horizons, *i.e.*, for $k = 0$, eq. (4.43) yields $\tilde{g} = 2/d$ while eq. (4.44) simply gives $\tilde{f}(x_m, RT) = (x^d - 1)/x^{d-2}$. Hence $d\mathcal{C}_A/d\tau$ does not actually depend on RT for $k = 0$.

4.2.1 Examples

In this subsection, we present two specific examples in which we solve explicitly for the meeting point and evaluate the rate of change in complexity for all times $t > t_c$. First, we will consider BTZ black holes ($d = 2$) for which analytic results can be obtained. Further details of the results for this special case are given in appendix B.1. Next, we consider numerical solutions for $d = 4$ with various horizon geometries. As a further example we consider the case $d = 3$ in appendix B.2.

BTZ Black Holes

For BTZ black holes, most of the expressions can be evaluated analytically. The evaluation of the action given in section 4.1 strictly applies only to $d > 2$ and so we must derive the results separately here for the BTZ case. While we review the salient calculations below, further details are also given for this special case in appendix B.1. Following eq. (4.37), we write the BTZ metric as

$$ds^2 = -f(r) \frac{L^2}{R^2} d\tau^2 + \frac{dr^2}{f(r)} + r^2 d\phi^2, \quad (4.47)$$

where the blackening factor, mass, temperature and entropy are then given by

$$f(r) = \frac{r^2 - r_h^2}{L^2}, \quad M = \frac{r_h^2}{8G_N L R}, \quad T = \frac{r_h}{2\pi L R}, \quad S = \frac{\pi r_h}{2G_N}. \quad (4.48)$$

As described in section 4.2, with the coordinates in eq. (4.47), the boundary geometry is fixed by a new independent scale R . In particular, the boundary metric is given by

$$ds^2 = -d\tau^2 + R^2 d\phi^2, \quad (4.49)$$

and hence a constant τ slice is a circle with the circumference $2\pi R$.¹¹

We can evaluate the tortoise coordinate (2.14) analytically as

$$r^*(r) = \frac{L^2}{2r_h} \log \frac{|r - r_h|}{r + r_h}, \quad \implies \quad r_\infty^* = r_0^* = \tau_c = 0. \quad (4.50)$$

¹¹Note that $\beta = 1/T$ should satisfy $\beta < 2\pi R$ so that the BTZ black hole solution is the dominant saddle point in the gravitational path integral. Further note that, R is associated with the spatial size of the boundary here, rather than a curvature scale as in eq. (4.38).

The latter, *i.e.*, $\tau_c = 0$, means that the action of the BTZ black hole starts changing right away for $\tau > 0$. This is due to the fact that for the boundary time slice at $\tau = 0$, *i.e.*, $\tau_R = \tau_L = 0$, the null rays coming from the left and right boundaries to define the past and future boundaries of the WDW patch meet at the singularity at $r = 0$. Given eq. (4.50), the meeting point relation in eq. (4.17) can be solved analytically for general times,

$$r_m = r_h \tanh\left(\frac{r_h \tau}{2LR}\right). \quad (4.51)$$

Now in evaluating the action, eqs. (4.19)–(4.21) are not modified up to some factors of L/R coming from rescaling the time coordinate — see the details in appendix B.1 — and their sum still reflects the change in complexity from what it was at $\tau = 0$. The growth rate (4.41) is then not modified for $d = 2$ and substituting in the BTZ blackening factor (4.48) and the meeting point (4.51) then yields

$$\frac{d\mathcal{C}_A}{d\tau} = \frac{r_h^2}{4\pi G_N LR} \left(1 + \operatorname{sech}^2\left(\frac{r_h \tau}{2LR}\right) \log\left[\frac{R\alpha}{r_h} \cosh\left(\frac{r_h \tau}{2LR}\right)\right] \right), \quad (4.52)$$

where we have also used $\Omega_{+1,1} = 2\pi$ above. Further using the expressions for the mass and temperature in eq. (4.48), this result can be expressed in terms of boundary quantities as

$$\frac{d\mathcal{C}_A}{d\tau} = \frac{2M}{\pi} \left(1 + \operatorname{sech}^2(\pi T\tau) \log\left[\frac{\alpha}{2\pi LT} \cosh(\pi T\tau)\right] \right). \quad (4.53)$$

Of course, the above expression is evaluated for $\tau > 0$. One simple consistency check on our result is that in the limit $\tau \rightarrow \infty$, we recover the expected late time result of [33, 34], *i.e.*, $d\mathcal{C}_A/dt = 2M/\pi$. As in eq. (4.46), we see the appearance of both L and α in the argument of the logarithm. Hence there is some ambiguity about the interpretation of this result in the boundary theory.

Now we can also rewrite eq. (4.53) in the following form

$$\frac{d\mathcal{C}_A}{d\tau} = \frac{2M}{\pi} \left(\tanh^2(\pi\tau/\beta) + \frac{\log \cosh(\pi\tau/\beta)}{\cosh^2(\pi\tau/\beta)} + \frac{\log\left[\frac{\beta e}{2\pi L} \alpha\right]}{\cosh^2(\pi\tau/\beta)} \right) \quad (4.54)$$

where we have introduced $\beta = 1/T$ and e is simply Euler’s number, *i.e.*, $\log(e) = 1$. This form facilitates a comparison to the analogous result in [34] evaluated with a regulator based on timelike radial geodesics in the bulk, which is

$$\frac{d\mathcal{C}_A}{d\tau} = \frac{2M}{\pi} \left(\tanh^2(\pi\tau/\beta) + \frac{\log \cosh(\pi\tau/\beta)}{\cosh^2(\pi\tau/\beta)} - \frac{\log \epsilon}{\cosh^2(\pi\tau/\beta)} \right) + \mathcal{O}(\epsilon). \quad (4.55)$$

where ϵ is a dimensionless UV regulator, *i.e.*, $\epsilon \sim \delta/\beta$ and δ is the short-distance cut-off in the boundary theory.¹² Interestingly, we see that eqs. (4.54) and (4.55) will be in complete

¹²We thank Ying Zhao for explaining this point.

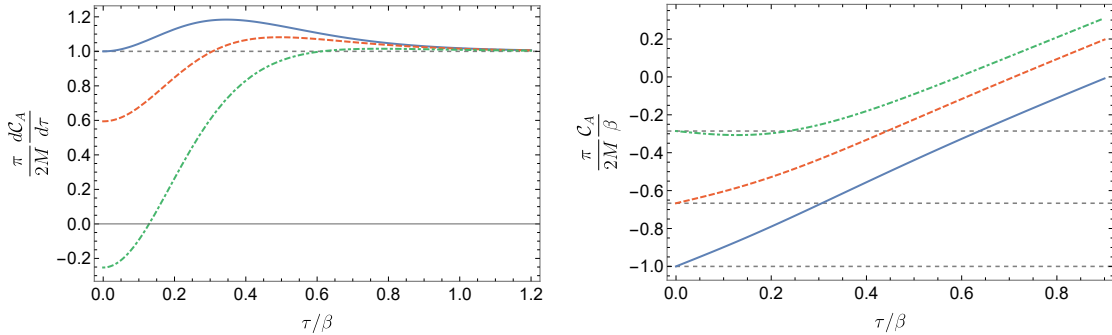


Figure 4.2: Left panel: time derivative of the complexity for the BTZ black hole ($d = 2$) from eq. (4.53) with $\alpha = L/R$. Right panel: ‘total’ complexity found by integrating $d\mathcal{C}_A/d\tau$. Results are shown for several values of the horizon radius — $r_h/L = 1$ (blue), $r_h/L = 1.5$ (dashed red) and $r_h/L = 3.5$ (dot-dashed green).

agreement if we choose $\alpha \sim L/\delta$. We return to a discussion of this point in section 4.5.

To close this section, we plot both the rate of change of the complexity (4.53) and the total complexity in figure 4.2 for several values of r_h/L . In the figure, we have chosen $\alpha = L/R$ and then in the argument of the logarithmic factor, we have $2\pi RT = r_h/L$ using eq. (4.48). Note that all of the curves for $d\mathcal{C}_A/d\tau$ in the left panel exceed the Lloyd bound and further the violation increases for smaller black holes, *i.e.*, smaller r_h/L , or equivalently smaller temperatures. The right panel shows the complexity itself, found by integrating $d\mathcal{C}_A/d\tau$. The integration constant is chosen there so that the result of $\mathcal{C}_A(\tau = 0) = \mathcal{C}_{\text{form}} = -\frac{L}{2G_N}$ — see eq. (3.41).¹³ After dividing by βM , all of these become functions of r_h/L . We provide further details of the calculations and a more extensive discussion of the special case of BTZ black holes in appendix B.1.

$d = 4$

To study the case where the boundary theory lives in $d = 4$, in principle, we simply substitute this value into eqs. (4.41) or (4.46) for $d\mathcal{C}_A/d\tau$, with the blackening factor given by eq. (2.2). Of course, we must evaluate the meeting point r_m , or alternatively the dimensionless x_m , numerically. For the latter, we introduce the dimensionless radius

¹³This corresponds to comparing the complexity of the thermofield double state to that of (two copies of) the Neveu-Schwarz vacuum in the boundary theory [144]. Comparing to the Ramond vacuum would instead yield $\mathcal{C}_{\text{form}} = 0$ as discussed in chapter 3

$x = r/r_h$, as well as $\tilde{f}(x, RT) = L^2/r_h^2 f(r)$ from eq. (4.44). Then following eq. (4.45), we can then define a dimensionless tortoise coordinate

$$\begin{aligned} x^*(x, RT) &\equiv \int \frac{dx}{\tilde{f}(x, RT)} = \frac{r_h}{L^2} r^*(r) \\ &= \frac{r_h^2}{2r_h^2 + kL^2} \left(\frac{1}{2} \log \frac{|1-x|}{1+x} + \frac{\sqrt{r_h^2 + kL^2}}{r_h} \tan^{-1} \left[\frac{r_h x}{\sqrt{r_h^2 + kL^2}} \right] \right), \end{aligned} \quad (4.56)$$

which yields

$$x_\infty^* \equiv x^*(\infty, RT) = \frac{\pi}{2} r_h \frac{\sqrt{r_h^2 + kL^2}}{2r_h^2 + kL^2} \quad \text{and} \quad x^*(0, RT) = 0. \quad (4.57)$$

It is clear from eq. (4.56) that x^* is a function of the ratio r_h/L , however, as our notation indicates the latter is implicitly fixed in eq. (4.43) by RT in the boundary theory. Combining these results with eq. (4.40) yields the critical time, at which the complexity begins to change,

$$\tau_c = \frac{2LR}{r_h} (x_\infty^* - x^*(0)) = \pi LR \frac{\sqrt{r_h^2 + kL^2}}{2r_h^2 + kL^2} = \frac{1}{2T} \left(1 + k \left(\frac{L}{r_h} \right)^2 \right). \quad (4.58)$$

Note that for $k = 0$, we have $\tau_c = 1/(2T)$, *i.e.*, the critical time does not depend on R for the planar geometry. Figure 4.3 shows a plot of τ_c as a function of r_h/L for the various horizon geometries.

Now solving numerically for the meeting point x_m using eq. (4.45), we can evaluate $d\mathcal{C}_A/d\tau$ in eq. (4.46), as shown in figure 4.4 for spherical ($k = 1$) and planar ($k = 0$) horizons. As commented above, we have set $\alpha = L/R$ for simplicity in these plots. Note that for a fixed r_h/L , the planar geometries seem to violate the $2M/\pi$ bound more strongly. We also note that the violation of the bound is stronger for smaller black holes, *i.e.*, smaller values of r_h/L . A more careful examination shows that generally $d\mathcal{C}_A/d\tau$ is larger for $k = 0$ than for $k = +1$ and that this difference between the rate of growth for these two cases grows as the size of the black hole shrinks. Similar results apply for hyperbolic horizon geometries and for other boundary dimensions. We describe our results for the case of $d = 3$ for all three horizon geometries in appendix B.2.

4.3 Complexity=Volume

In this section, we study the time dependence of the complexity for eternal AdS black holes using the complexity=volume conjecture [31, 32]. Applying eq. (3.42), we must evaluate

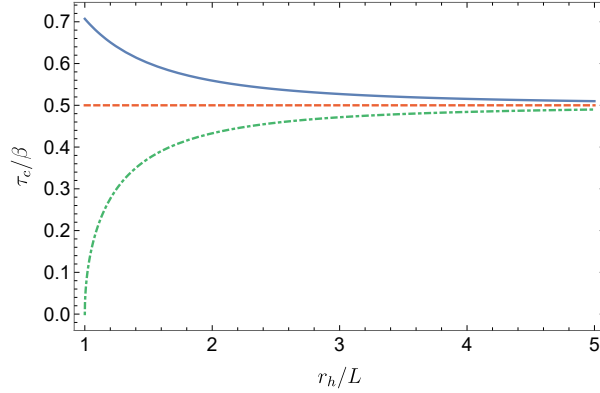


Figure 4.3: Critical time t_c as a function of the horizon radius for $d = 4$ for the various horizon geometries, *i.e.*, spherical $k = 1$ (blue), planar $k = 0$ (dashed-red) and large hyperbolic $k = -1$ (dot-dashed green). Note that we only consider $r_h > L$.

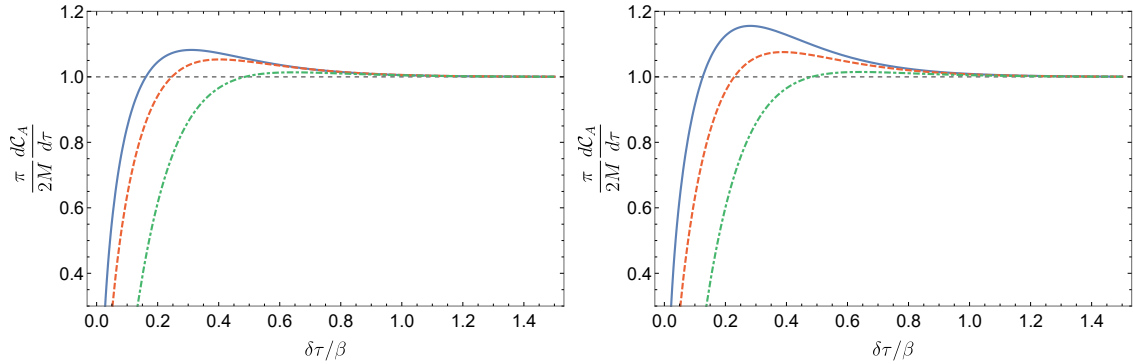


Figure 4.4: Time derivative of complexity as a function of time for spherical ($k = +1$, left) and planar ($k = 0$, right) horizons with $d = 4$ boundary dimensions for various values of the horizon radius, *i.e.*, $r_h/L = 1$ (blue), $r_h/L = 1.5$ (dashed red) and $r_h/L = 3.5$ (dot-dashed green). We present the plots as a function of $\delta\tau = \tau - \tau_c$ to allow for a meaningful comparison between the different cases. We stress again that each of the curves has a different value of τ_c — see figure 4.3.

the volume of the extremal codimension-one bulk surface, whose boundaries correspond to the desired time slices in the two asymptotic boundaries, as shown in figure 4.5. As in the previous section, the symmetry of our setup implies that the volume depends only on

the total boundary time $t = t_L + t_R$. Thus, it is enough to consider the symmetric case $t_L = t_R$, as we assume from now on. Further, in eq. (3.42), we will simply set $\ell = L$, the AdS radius, to eliminate the ambiguity associated with the choice of the scale ℓ .

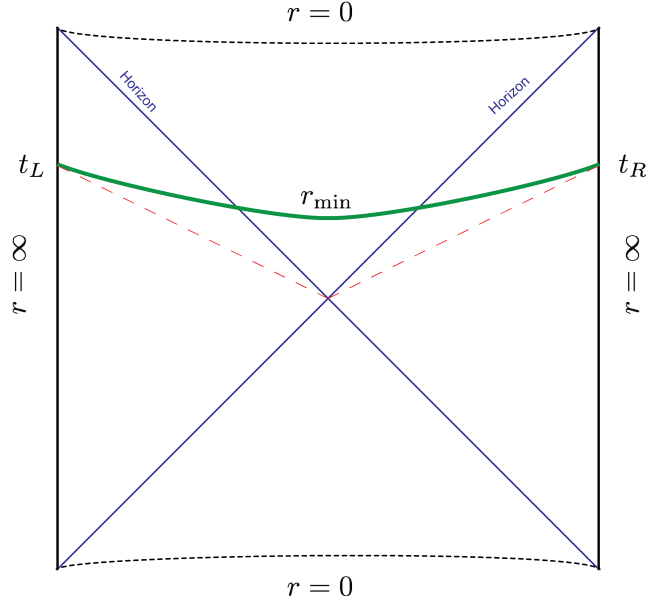


Figure 4.5: A representation of the maximal wormhole connecting the two boundaries anchored at times t_L and t_R (depicted at symmetric times in the figure). The bridge reaches the minimum distance inside the future horizon at r_{min} , and approaches each boundary tangent to constant time slices.

First, we review the computation of the maximal volume following [32] and then evaluate its time derivative. We will see that the time derivative of the extremal volume is determined by a conserved quantity E . With the infalling Eddington-Finkelstein coordinates (2.15), the metric (2.1) becomes

$$v = t + r^*(r); \quad ds^2 = -f(r) dv^2 + 2 dv dr + r^2 d\Sigma_{k,d-1}^2. \quad (4.59)$$

Now, assuming that the extremal surface is ‘spherically’ symmetric,¹⁴ its profile will be determined by an embedding $r(\lambda)$ and $v(\lambda)$, where λ is some radial coordinate intrinsic to

¹⁴That is, the extremal surface has the same symmetry as the spatial slices described by $d\Sigma_{k,d-1}^2$, e.g., it is spherically symmetric for $k = +1$.

the surface. The maximal volume is then obtained by extremizing

$$\mathcal{V} = \Omega_{k,d-1} \int d\lambda r^{d-1} \sqrt{-f(r)\dot{v}^2 + 2\dot{v}\dot{r}} \equiv \Omega_{k,d-1} \int d\lambda \mathcal{L}(\dot{v}, r, \dot{r}), \quad (4.60)$$

where the dots indicate derivatives with respect to λ . Since the integrand \mathcal{L} does not depend explicitly on v , we have a conserved quantity E defined as

$$E = -\frac{\partial \mathcal{L}}{\partial \dot{v}} = \frac{r^{d-1}(f\dot{v} - \dot{r})}{\sqrt{-f\dot{v}^2 + 2\dot{v}\dot{r}}}. \quad (4.61)$$

We will refer to this quantity as the energy. Since the expression in eq. (4.60) is reparametrization invariant, we are free to choose λ to keep the radial volume element fixed, *i.e.*,

$$r^{d-1} \sqrt{-f\dot{v}^2 + 2\dot{v}\dot{r}} = 1. \quad (4.62)$$

The equations determining $r(\lambda)$ and $v(\lambda)$ then simplify to

$$E = r^{2(d-1)} (f(r)\dot{v} - \dot{r}), \quad (4.63)$$

$$r^{2(d-1)} \dot{r}^2 = f(r) + r^{-2(d-1)} E^2, \quad (4.64)$$

and further, the maximal volume can be written as

$$\mathcal{V} = 2\Omega_{k,d-1} \int_{r_{min}}^{r_{max}} \frac{dr}{\dot{r}} = 2\Omega_{k,d-1} \int_{r_{min}}^{r_{max}} dr \frac{r^{2(d-1)}}{\sqrt{f(r)r^{2(d-1)} + E^2}}. \quad (4.65)$$

Here, we are assuming a symmetric configuration where $t_L = t_R$, as described above, and so the integral only runs from a minimum radius r_{min} to the cutoff surface at $r = r_{max}$. The minimal radius is determined by setting $\dot{r} = 0$ in eq. (4.64), *i.e.*,

$$f(r_{min}) r_{min}^{2(d-1)} + E^2 = 0. \quad (4.66)$$

Further we note that this turning point is inside the horizon (see figure 4.5) and hence we have $f(r_{min}) < 0$, $\dot{r}|_{r=r_{min}} = 0$ and $\dot{v}|_{r=r_{min}} > 0$. Therefore we may conclude that $E < 0$ by evaluating eq. (4.63) at this point. Now using eqs. (4.63) and (4.64), we have

$$t_R + r_\infty^* - r^*(r_{min}) = \int_{v_{min}}^{v_\infty} dv = \int_{r_{min}}^{r=\infty} dr \left[\frac{E}{f(r)\sqrt{f(r)r^{2(d-1)} + E^2}} + \frac{1}{f(r)} \right], \quad (4.67)$$

where the symmetry of our configuration determines $t = 0$ at the turning point, *i.e.*, $v_{min} = r^*(r_{min})$. One may verify that the integrand in the final expression is well-behaved

at the horizon, using the fact that the energy is negative. The integrand also decays as L^2/r^2 with $r \rightarrow \infty$ and so in the following, we will replace the upper limit of the integral by $r = r_{max}$ because the difference produced by this replacement vanishes as the short-distance cutoff is taken to zero. We will make use of this several times in the derivation below.

Using eq. (4.67), we can rewrite eq. (4.65) as follows:

$$\frac{\mathcal{V}}{2\Omega_{k,d-1}} = \int_{r_{min}}^{r_{max}} dr \left[\frac{\sqrt{f(r)r^{2(d-1)} + E^2}}{f(r)} + \frac{E}{f(r)} \right] - E(t_R + r_\infty^* - r^*(r_{min})). \quad (4.68)$$

Next, we would like to take the time derivative of this equation, however, we would like to use the time coordinate introduced in eq. (4.37), *i.e.*, $\tau = Rt/L$. We use eq. (4.66) to simplify the contribution from the derivative acting on r_{min} in the lower limit of the integral to obtain

$$\begin{aligned} \frac{1}{2\Omega_{k,d-1}} \frac{d\mathcal{V}}{d\tau_R} &= \frac{dE}{d\tau_R} \int_{r_{min}}^{r_{max}} dr \left[\frac{E}{f(r)\sqrt{f(r)r^{2(d-1)} + E^2}} + \frac{1}{f(r)} \right] \\ &\quad - \frac{dE}{d\tau_R} \left(\frac{L}{R} \tau_R + r_\infty^* - r^*(r_{min}) \right) - \frac{L}{R} E. \end{aligned} \quad (4.69)$$

Note that $dE/d\tau_R$ is a constant that characterizes the entire surface and so it was brought outside of the integral in the first term. However, the remaining integral is identical to that appearing in eq. (4.67) and so we may further simplify the result to

$$\frac{d\mathcal{V}}{d\tau_R} = -2\Omega_{k,d-1} \frac{L}{R} E. \quad (4.70)$$

Since we set $\tau_R = \tau_L$, the derivative with respect to $\tau = \tau_R + \tau_L$ is given by simply multiplying the result by a factor of 1/2. Hence our final result for the rate of growth of the complexity becomes

$$\frac{d\mathcal{C}_V}{d\tau} = \frac{1}{G_N L} \frac{d\mathcal{V}}{d\tau} = -\frac{\Omega_{k,d-1}}{G_N R} E = \frac{\Omega_{k,d-1}}{G_N R} \sqrt{-f(r_{min})} r_{min}^{d-1}. \quad (4.71)$$

Therefore, the time derivative of complexity is completely determined by computing either E or r_{min} , with eq. (4.66).

However, as in eq. (4.46), we would like to show that eq. (4.71) can be expressed entirely in terms of boundary quantities. After some work, the final result takes the form

$$\frac{d\mathcal{C}_V}{d\tau} = \frac{8\pi M}{(d-1)} \frac{8\pi^2 R^2 T^2 \tilde{g}^2(RT)}{4\pi^2 R^2 T^2 \tilde{g}^2(RT) + k} \sqrt{-\tilde{f}(x_{min}, RT)} x_{min}^{d-1}, \quad (4.72)$$

where the functions $\tilde{g}(RT)$ and $\tilde{f}(x, RT)$ were defined in eqs. (4.43) and (4.44), respectively. Further, as above, we have introduced the dimensionless radial coordinate $x = r/r_h$. Then defining the corresponding tortoise coordinate $x^*(x) \equiv \int dx/\tilde{f}(x, RT)$ and also $x_E \equiv E/r_h^{d-1}$, x_{min} is determined by the boundary versions of eqs. (4.66) and (4.67):

$$0 = 4\pi^2 R^2 T^2 \tilde{g}^2(RT) \tilde{f}(x_{min}, RT) x_{min}^{2(d-1)} + x_E^2, \quad (4.73)$$

$$\frac{\tau_R}{\beta} + \frac{x_\infty^* - x^*(x_{min})}{2\pi} = \int_{x_{min}}^{x=\infty} \frac{dx \left[x_E + \sqrt{4\pi^2 R^2 T^2 \tilde{g}^2(RT) \tilde{f}(x, RT) x^{2(d-1)} + x_E^2} \right]}{2\pi \tilde{f}(x, RT) \sqrt{4\pi^2 R^2 T^2 \tilde{g}^2(RT) \tilde{f}(x, RT) x^{2(d-1)} + x_E^2}}.$$

4.3.1 Late Time Behaviour

Before examining the full time-dependence of $d\mathcal{C}_V/d\tau$, we would like to study its late time behaviour. At late times, the maximal surface is (almost) tangent to a special slice of constant $r = \tilde{r}_{min}$ inside the black hole [32].¹⁵ To evaluate \tilde{r}_{min} , we first define the function $W(r)$ as appeared in eq. (4.71),

$$W(r) \equiv \sqrt{-f(r)} r^{d-1}, \quad (4.74)$$

and observe that eq. (4.66) can be rewritten as $-W(r_{min})^2 + E^2 = 0$. The latter generally has two positive roots, with the larger root corresponding to r_{min} . However, in the late time limit, $|E|$ increases until the two roots meet at the extremum of $-W(r)^2$, which also corresponds to the extremum of $W(r)$. Hence \tilde{r}_{min} is both a root of eq. (4.66) and the extremum of $W(r)$. Then \tilde{r}_{min} can be computed as

$$0 = W'(\tilde{r}_{min}) = (d-1)\tilde{r}_{min}^{d-2} \sqrt{-f(\tilde{r}_{min})} - \frac{\tilde{r}_{min}^{d-1} f'(\tilde{r}_{min})}{2\sqrt{-f(\tilde{r}_{min})}}. \quad (4.75)$$

Since $d\mathcal{C}_V/d\tau$ in eq. (4.71) only depends on the time τ through r_{min} , at late times, we have

$$\frac{d\mathcal{C}_V}{d\tau} = \frac{\Omega_{k,d-1}}{G_N R} \left[W(\tilde{r}_{min}) + \frac{1}{2} W''(\tilde{r}_{min}) (r_{min} - \tilde{r}_{min})^2 + \mathcal{O}((r_{min} - \tilde{r}_{min})^3) \right]. \quad (4.76)$$

Hence asymptotically, $d\mathcal{C}_V/d\tau$ approaches the constant value

$$\lim_{\tau \rightarrow \infty} \frac{d\mathcal{C}_V}{d\tau} = \frac{\Omega_{k,d-1}}{G_N R} W(\tilde{r}_{min}) = \frac{\Omega_{k,d-1}}{G_N R} \sqrt{-f(\tilde{r}_{min})} \tilde{r}_{min}^{d-1}. \quad (4.77)$$

¹⁵Similar behaviour appears in computing the time dependence of holographic entanglement entropy for regions with components in both asymptotic boundaries [114]. However, the special (codimension-two) surface appearing there extremizes the area rather than the volume.

Further, we observe that $d\mathcal{C}_V/d\tau$ approaches this limit from below because $W''(\tilde{r}_{min})$ is negative. The latter conclusion is easily produced by noting from eq. (4.74), that $W(r)$ vanishes at both $r = r_h$ and 0 and that $W(r) > 0$ inside the horizon. Hence the extremum (4.75) must be a maximum, *i.e.*, $W''(\tilde{r}_{min}) < 0$.¹⁶ In appendix C of our work [66], we examine the leading correction to the late time limit (4.77) and show that $d\mathcal{C}_V/d\tau$ approaches this asymptotic value with an exponential decay in τ . Next we turn to computing the asymptotic value (4.77).

Planar horizons: With $k = 0$, eq. (4.75) can be solved analytically for \tilde{r}_{min} and we find

$$\tilde{r}_{min} = \left(\frac{\omega^{d-2} L^2}{2} \right)^{\frac{1}{d}} = \frac{r_h}{2^{\frac{1}{d}}}, \quad (4.78)$$

which then leads to

$$\sqrt{-f(\tilde{r}_{min})} \tilde{r}_{min}^{d-1} = \frac{\omega^{d-2} L}{2}. \quad (4.79)$$

Thus, using eq. (4.39), the asymptotic value (4.77) becomes

$$\lim_{\tau \rightarrow \infty} \frac{d\mathcal{C}_V}{d\tau} = \frac{8\pi M}{d-1}, \quad (4.80)$$

for any planar black hole. Of course, this reproduces the result first found in [32].

Curved horizons: Figure 4.6a shows a plot of the late time limit (4.77) for spherical black holes (with $k = 1$) for $d = 3$ and 4. We can see that $d\mathcal{C}_V/d\tau$ approaches the value $8\pi M/(d-1)$ in the limit $r_h \gg L$, *i.e.*, $RT \gg 1$.

Since the mass of hyperbolic black holes (*i.e.*, $k = -1$) can take negative values, $\frac{d-1}{8\pi M} \lim_{t \rightarrow \infty} d\mathcal{C}_V/dt$ would diverge at $M = 0$ before reaching the minimal mass. Hence, we instead present numerical plots of

$$\frac{d-1}{8\pi(M - M_{min})} \lim_{\tau \rightarrow \infty} \frac{d\mathcal{C}_V}{d\tau}, \quad (4.81)$$

¹⁶The case of small hyperbolic black holes, *i.e.*, $k = -1$ and $r_h < L$, is slightly more complicated since there is an inner horizon — see appendix B.3.2. However, implicitly r_{min} lies in between the two horizons and so one reaches the same conclusion.

where M_{min} is the minimal value of mass

$$M_{min} = -\frac{(d-1)\Omega_{-1,d-1}}{8\pi G_N d} \left(\frac{d-2}{d}\right)^{\frac{d-2}{2}} \frac{L^{d-1}}{R}. \quad (4.82)$$

This corresponds to the mass of the extremal small hyperbolic black holes — see appendix B.3.2. Figure 4.6b presents the late time limit results for $d = 3$ and $d = 4$ as a function of r_h/L . Hence we can see that eq. (4.81) approaches to 1 from above, in the limit $r_h/L \gg 1$. The divergence in these curves where r_h/L approaches its minimal value, *i.e.*, $M \rightarrow M_{min}$, is interesting because $d\mathcal{C}_V/d\tau$ actually vanishes in the extremal limit. The horizon radius of the extremal black hole can be written as $r_h^{ext} = \frac{\sqrt{d-2}L}{\sqrt{d}}$. Then we would readily find in the extremal limit that $d\mathcal{C}_V/d\tau \sim (r - r_h^{ext})$ while $M - M_{min} \sim (r - r_h^{ext})^2$. As a consequence, while both the numerator and denominator vanish in this limit, we still obtain a divergent result.

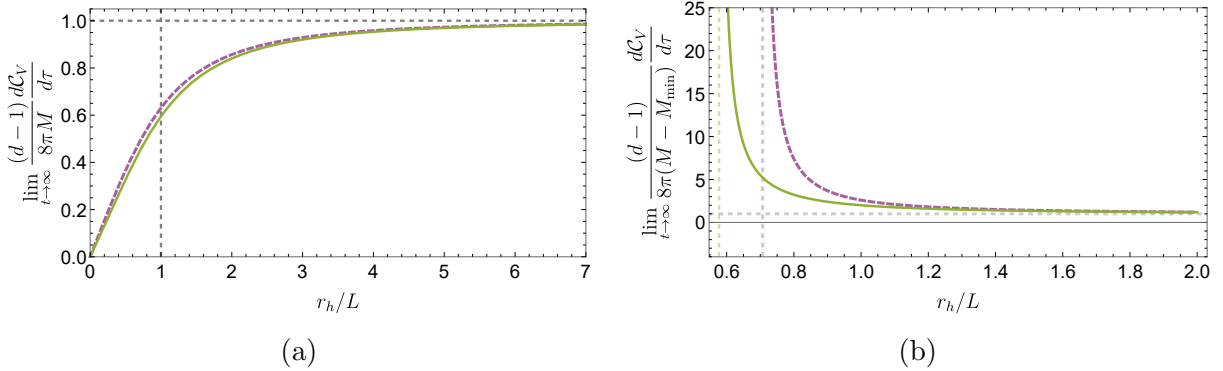


Figure 4.6: (a) Late time rate of change in complexity $\frac{d-1}{8\pi M} \lim_{t \rightarrow \infty} d\mathcal{C}_V/d\tau$ as a function of r_h/L for spherical black holes ($k = 1$) in $d = 3$ (green) and $d = 4$ (dashed purple) dimensions. The vertical dashed line at $r_h/L = 1$ indicates the Hawking-Page phase transition below which the dominant saddle point in the bulk partition function is vacuum AdS rather than a (small) spherical black hole. (b) Plots of $\frac{(d-1)}{8\pi(M-M_{min})} \lim_{t \rightarrow \infty} d\mathcal{C}_V/d\tau$ as a function of r_h/L for hyperbolic black holes ($k = -1$) in $d = 3$ (green) and $d = 4$ (dashed purple) dimensions. The vertical lines indicate the minimal values of r_h/L corresponding to extremal small hyperbolic black holes. The gray dashed horizontal line indicates 1, which is approached in the large black hole limit ($r_h \gg L$).

Now we proceed to examine the late time behaviour analytically in the limit of large temperatures, *i.e.*, for large black holes. First, we expand eq. (4.75) in the limit $r_h \gg L$

to find the leading corrections to \tilde{r}_{min} compared to its planar value (4.78),

$$\tilde{r}_{min} = \frac{r_h}{2^{\frac{1}{d}}} \left[1 - \frac{(2^{2/d}(d-1) - d) L^2}{d^2} \frac{L^2}{r_h^2} k \right. \\ \left. + \frac{(d-1) \left(-d^2 + 2^{\frac{2}{d}+1} d + 2^{4/d} (d-3)(d-1) \right) L^4}{2d^4} \frac{L^4}{r_h^4} k^2 + \mathcal{O} \left(\frac{L^6}{r_h^6} \right) \right]. \quad (4.83)$$

Using this expression, the asymptotic value of $d\mathcal{C}_V/d\tau$ can be written in terms of the following expansion¹⁷

$$\lim_{t \rightarrow \infty} \frac{(d-1)}{8\pi M} \frac{d\mathcal{C}_V}{d\tau} = \left(1 - \frac{M_{min}}{M} \delta_{k,-1} \right) \left(1 - 2^{\frac{2}{d}-1} k \frac{L^2}{r_h^2} + \frac{2^{\frac{2}{d}} (\gamma + d) k^2 L^4}{d^2 r_h^4} + \dots \right) \\ = \left(1 + \frac{2d(d-2)^{\frac{d-2}{2}}}{(4\pi)^d (RT)^d} \delta_{k,-1} + \dots \right) \\ \times \left(1 - \frac{2^{\frac{2}{d}-1} d^2 k}{(4\pi)^2 (RT)^2} + \frac{2^{\frac{2}{d}} (\gamma - d(d-3)) d^2 k^2}{(4\pi)^4 (RT)^4} + \dots \right) \quad (4.84)$$

where to reduce the clutter in the above expressions, we have defined the coefficient:

$$\gamma = 2^{\frac{2}{d}-3} (3d-2)(d-2). \quad (4.85)$$

Let us first focus our attention on the second factor on the right-hand side of eq. (4.84). Here the corrections involve (integer) powers of k/R^2 and hence we expect that these terms can be expressed as simple powers of the boundary curvature. Of course, these curvature corrections become important when the temperature is comparable to the curvature scale, *i.e.*, $RT \sim 1$. However, for high temperatures where the characteristic thermal wavelength is much shorter than the curvature scale, these terms become vanishingly small and the asymptotic growth rate approaches the flat space limit $8\pi M/(d-1)$, as in eq. (4.80).

The above discussion overlooks the first factor on the right-hand side of eq. (4.84). This factor only appears for the case of the hyperbolic horizons (*i.e.*, $k = -1$) and is related to the fact that the minimal mass is actually negative (rather than zero) for these black holes. Further, we observe that when the boundary dimension d is odd, the first correction in this factor involves an odd power of $1/R$. Therefore while the corrections in this factor

¹⁷This expansion can also be expressed in terms of central charge over the entropy — see chapter 3.

are appearing because of the negative curvature in the boundary metric (4.38), they will not generally be expressed in terms of geometric factors involving powers of the curvature tensor.

We also note that the expression in eq. (4.84) only holds for $d \geq 3$ and so the leading correction for $RT \gg 1$ always comes from the second factor, *i.e.*, the term proportional to $k/(RT)^2$. Therefore we can conclude that for spherical black holes, the asymptotic value (4.77) approaches the planar value (4.80) from below as $RT \rightarrow 0$. Of course, this is in agreement with the results shown in figure 4.6a, where we see that for all values of RT ,

$$\lim_{\tau \rightarrow \infty} \frac{d\mathcal{C}_V}{d\tau} \leq \frac{8\pi M}{d-1} \quad \text{for } k = +1. \quad (4.86)$$

Similarly for hyperbolic black holes, the asymptotic value (4.77) approaches the planar value (4.80) from above in the limit $RT \rightarrow 0$. Again, this agrees with the results shown in figure 4.6b, where we see that for all values of RT ,

$$\lim_{t \rightarrow \infty} \frac{d\mathcal{C}_V}{d\tau} \geq \frac{8\pi}{d-1} (M - M_{min}) \quad \text{for } k = -1. \quad (4.87)$$

4.3.2 General Time Dependence

To close this section, we present plots of $d\mathcal{C}_V/d\tau$ for planar black holes in various dimensions for general values of the time. We explore further examples with spherical and hyperbolic horizon geometries in appendix B.2.

In the case that $k = 0$ (and $d \geq 3$), if we define $a \equiv \frac{d-1}{8\pi M} d\mathcal{C}_V/d\tau$, eq. (4.71) can be recast in the form

$$a = 2s_{min}^{d/2} \sqrt{1 - s_{min}^d}, \quad (s_{min} \equiv r_{min}/r_h). \quad (4.88)$$

Inverting this equation, we can represent s_{min} as a function of a ,

$$s_{min} = \left(\frac{1 + \sqrt{1 - a^2}}{2} \right)^{\frac{1}{d}}. \quad (4.89)$$

Then rewriting eq. (4.67) in terms of dimensionless quantities, one can find the relation between $a = \frac{d-1}{8\pi M} d\mathcal{C}_V/d\tau$ and τ/β

$$\tau/\beta = \frac{da}{4\pi} \int_{s_{min}}^{\infty} ds \frac{s^{d-2}}{(1-s^d) \sqrt{s_{min}^d(1-s_{min}^d) - s^d(1-s^d)}}. \quad (4.90)$$

Since this relation and eq. (4.89) do not depend on r_h/L , the plot of a as a function of τ/β has the same form for all values r_h/L . Figure 4.7 shows the plot and we see that at late times, it approaches one from below, as discussed above in section 4.3.1.

Figure 4.7 shows $\frac{d-1}{8\pi M} d\mathcal{C}_V/dt$ for the case of $d = 2$, *i.e.*, BTZ black holes. A similar derivation to the one presented for planar black holes holds in this case. Again, the result does not depend on the value of r_h/L and approaches to one at late times.

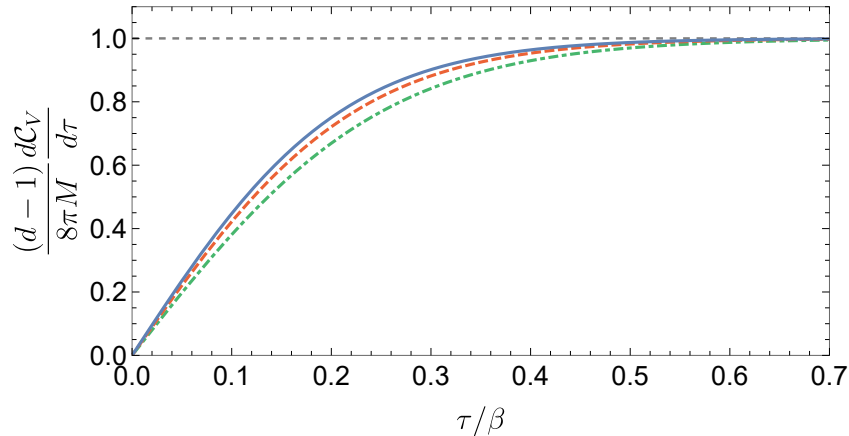


Figure 4.7: Plot of $\frac{d-1}{8\pi M} \frac{d\mathcal{C}_V}{d\tau}$ for planar $d = 4$ (blue), planar $d = 3$ (dashed-red) and $d = 2$ (dot-dashed green) black holes. All three curves are independent of r_h/L and approach to one at late times.

4.4 Charged Black Holes

In this section, we study the growth rate of the complexity for charged black holes with $d \geq 3$ using both the CA and CV conjectures. Charged black holes are solutions to Einstein gravity coupled to a Maxwell field with the following action:

$$I = I_{\text{grav}} - \frac{1}{4g^2} \int d^{d+1}x \sqrt{-g} F_{ab} F^{ab} \quad (4.91)$$

where I_{grav} is the gravitational action given in eq. (2.10). Note that the gauge coupling g has dimensions of length $\frac{d-3}{2}$.

The black hole metric takes the form (4.37) with blackening factor given by, *e.g.*, [156, 157]:¹⁸

$$f(r) = \frac{r^2}{L^2} + k - \frac{\omega^{d-2}}{r^{d-2}} + \frac{q^2}{r^{2(d-2)}}, \quad (4.92)$$

and the Maxwell potential can be written as:¹⁹

$$A_\tau = \frac{g}{2\sqrt{2\pi G_N}} \frac{L}{R} \sqrt{\frac{d-1}{d-2}} \left(\frac{q}{r_+^{d-2}} - \frac{q}{r_-^{d-2}} \right). \quad (4.93)$$

The new blackening factor (4.92) has two real roots, r_+ and r_- (where $r_+ \geq r_-$) corresponding to the outer and inner horizons, respectively. Figure 4.8 shows the Penrose diagrams for these charged black holes. We note that the integration constant in A_τ was chosen such that it vanishes at the outer horizon, which ensures that it is a well behaved differential form at the corresponding bifurcation surface [156]. It will typically be convenient to write our results in terms of r_+ and r_- by expressing ω^{d-2} and q^2 in terms of r_+ and r_- using the equations $f(r_+) = f(r_-) = 0$ — see below.

Of course, the Maxwell field in the bulk is dual to a conserved current corresponding to a global $U(1)$ symmetry in the boundary theory *e.g.*, [157]. Hence the charged black hole geometry extends the thermofield double state (1.21) to the entangled state where, as well as a temperature T , we have a chemical potential μ which distinguishes the boundary states by their $U(1)$ charges. We will refer to this as the charged thermofield double state,

$$|\text{cTFD}(t_L, t_R)\rangle = Z^{-1/2} \sum_{\alpha, \sigma} e^{-(E_\alpha - \mu Q_\sigma)/(2T)} e^{-iE_\alpha(t_L + t_R)} |E_\alpha, -Q_\sigma\rangle_L |E_\alpha, Q_\sigma\rangle_R, \quad (4.94)$$

where L and R label the quantum states (and times) at the left and right boundaries. Notice that tracing out the states in either boundary produces the density matrix corresponding to the grand canonical ensemble characterized by T and μ — see further discussion below.

The thermodynamic quantities describing the black hole are the same as those given in eq. (4.39) with the replacement $r_h \rightarrow r_+$ *i.e.*,

$$M = \frac{(d-1)\Omega_{k,d-1}}{16\pi G_N} \frac{L}{R} \omega^{d-2}, \quad S = \frac{\Omega_{k,d-1}}{4G_N} r_+^{d-1}, \quad T = \frac{L}{R} \frac{1}{4\pi} \frac{\partial f}{\partial r} \Big|_{r=r_+}. \quad (4.95)$$

¹⁸We work with the rescaled time $\tau = Rt/L$ throughout the following.

¹⁹Our conventions compare to those of [156] (denoted with tildes) as follows: $A_t = \tilde{A}_t \frac{g}{2\sqrt{\pi G}}$, $Q = \tilde{Q} \frac{2\sqrt{\pi G}}{g}$, $\mu = \tilde{\mu} \frac{g}{2\sqrt{\pi G}}$; and to those of [157] by the identification $1/g^2 = \ell^2/G_N$ where ℓ is an extra length scale introduced there to distinguish the coupling of the Maxwell field.

The charge is naturally defined in terms of Gauss' law, *i.e.*,

$$Q = \oint *F = \frac{q \Omega_{k,d-1} \sqrt{(d-1)(d-2)}}{2g\sqrt{2\pi G_N}} \quad (4.96)$$

where the $(d-1)$ -form $*F$ is the Hodge dual of the field strength $F_{ab} = \partial_a A_b - \partial_b A_a$. Of course, the Maxwell field in the bulk is dual to a global symmetry current in the boundary theory.²⁰ In this holographic context, the charge (4.96) also corresponds to the integral of the zeroth component of the boundary current over a constant τ slice. The chemical potential can be determined using the thermodynamic relation $dM = TdS + \mu dQ$,

$$\mu = \frac{g}{2\sqrt{2\pi G_N}} \frac{L}{R} \sqrt{\frac{d-1}{d-2}} \frac{q}{r_+^{d-2}}. \quad (4.97)$$

Comparing to eq. (4.93), this also corresponds to the ‘non-normalizable’ mode of the gauge potential, *i.e.*, $\mu = \lim_{r \rightarrow \infty} A_\tau$.

We note that the action (4.91) provides a well defined variational principle where we keep the gauge potential fixed at the boundary. Hence if we were examining the thermodynamics of these black holes, *e.g.*, with the corresponding Euclidean action, then we would be working with the grand canonical ensemble where the chemical potential μ is fixed. That is, implicitly, our control parameters are the temperature T and the chemical potential μ [156, 157]. Hence the full geometry of the eternal charged black hole is dual to the charged thermofield double state, given in eq. (4.94). Alternatively, we could consider a fixed charge ensemble, but this would require adding a boundary term of the form $1/g^2 \int_{\partial\mathcal{M}} d^d x \sqrt{\gamma} n^a F_{ab} A^b$ to the action. We comment further on the features of adding this surface term in chapter 7 (see also [70, 89]).

It would be interesting to pursue this possibility in the context of the complexity=action proposal, where it seems that we would need to include this boundary term on all of the boundaries of the WDW patch.

In order to express our results for the complexity in terms of boundary quantities, it will be useful to also have holographic expressions for the central charges associated with the two-point functions of the boundary stress tensor (*e.g.*, [142, 158, 159]) and currents (*e.g.*, [160, 161]). That is, for a d -dimensional CFT, the leading singularities in the vacuum correlators take the form:

$$\langle T_{\mu\nu}(x) T_{\rho\sigma}(0) \rangle = \frac{C_T}{x^{2d}} \mathcal{I}_{ab,cd}, \quad \langle J_\mu(x) J_\nu(0) \rangle = \frac{C_J}{x^{2(d-1)}} I_{\mu\nu}(x) \quad (4.98)$$

²⁰The current can be defined by varying the boundary action with respect to the gauge field, *e.g.*, [157].

where

$$\mathcal{I}_{ab,cd} \equiv \frac{1}{2} (I_{\mu\nu}(x)I_{\rho\sigma}(x) + I_{\mu\sigma}(x)I_{\nu\rho}(x)) - \frac{1}{d}\eta_{\mu\nu}\eta_{\rho\sigma}, \quad I_{\mu\nu} \equiv \eta_{\mu\nu} - 2\frac{x_\mu x_\nu}{x^2}. \quad (4.99)$$

For our holographic framework, the two central charges can then be expressed in terms of bulk parameters as

$$C_T = \frac{d+1}{d-1} \frac{\Gamma(d+1)}{8\pi^{(d+2)/2} \Gamma(d/2)} \frac{L^{d-1}}{G_N}, \quad C_J = \frac{(d-2)\Gamma(d)}{2\pi^{d/2}\Gamma(d/2)} \frac{L^{d-3}}{g^2}. \quad (4.100)$$

It will be convenient to work in terms of the following dimensionless quantities:

$$x \equiv \frac{r}{r_+}, \quad y \equiv \frac{r_-}{r_+}, \quad z \equiv \frac{L}{r_+}. \quad (4.101)$$

Here, x is a dimensionless radial coordinate, while y and z can be expressed in terms of dimensionless boundary quantities. In particular, combining the expressions above yields

$$\nu \equiv \sqrt{\frac{C_J}{C_T}} \frac{\mu}{T} = h(y, z), \quad RT = \tilde{h}(y, z). \quad (4.102)$$

Of course, these equations can be inverted and so one can think directly of y and z as boundary quantities. As we will see, all our results can be expressed as functions of ν and RT , or alternatively of y and z . Explicit expressions for $h(y, z)$ and $\tilde{h}(y, z)$ for the different dimensions and geometries read

$$h(y, z) = \frac{2\sqrt{2}\pi(d-1) \left(y^{\frac{d}{2}-1} \sqrt{1-y^{d-2}} \sqrt{(kz^2+1) - y^{d-2}(kz^2+y^2)} \right)}{\sqrt{d(d+1)} \left((d-2)kz^2 + d - 2y^{d-2} \left((d-2)kz^2 + d - 1 \right) + (d-2)y^{2(d-2)}(kz^2+y^2) \right)},$$

$$\tilde{h}(y, z) = \frac{(d-2)kz^2 + d - 2y^{d-2} \left((d-2)kz^2 + d - 1 \right) + (d-2)y^{2(d-2)}(kz^2+y^2)}{4\pi z (1 - y^{d-2})}. \quad (4.103)$$

It is instructive to expand these functions in the small charge limit (*i.e.*, small y) where one obtains

$$h(y, z) = \frac{2\sqrt{2}\pi(d-1)\sqrt{1+kz^2}}{\sqrt{d(d+1)}(d+(d-2)kz^2)} y^{\frac{d}{2}-1} \times$$

$$\times \left[1 + \left(1 + \frac{1}{2} \frac{1}{(1+kz^2)} - \frac{2}{d+(d-2)kz^2} \right) y^{d-2} + \mathcal{O}(y^d) \right] \quad (4.104)$$

$$\tilde{h}(y, z) = \frac{d+(d-2)kz^2}{4\pi z} - \frac{(1+kz^2)}{4\pi z} (d-2)y^{d-2} + \mathcal{O}(y^{2(d-2)}).$$

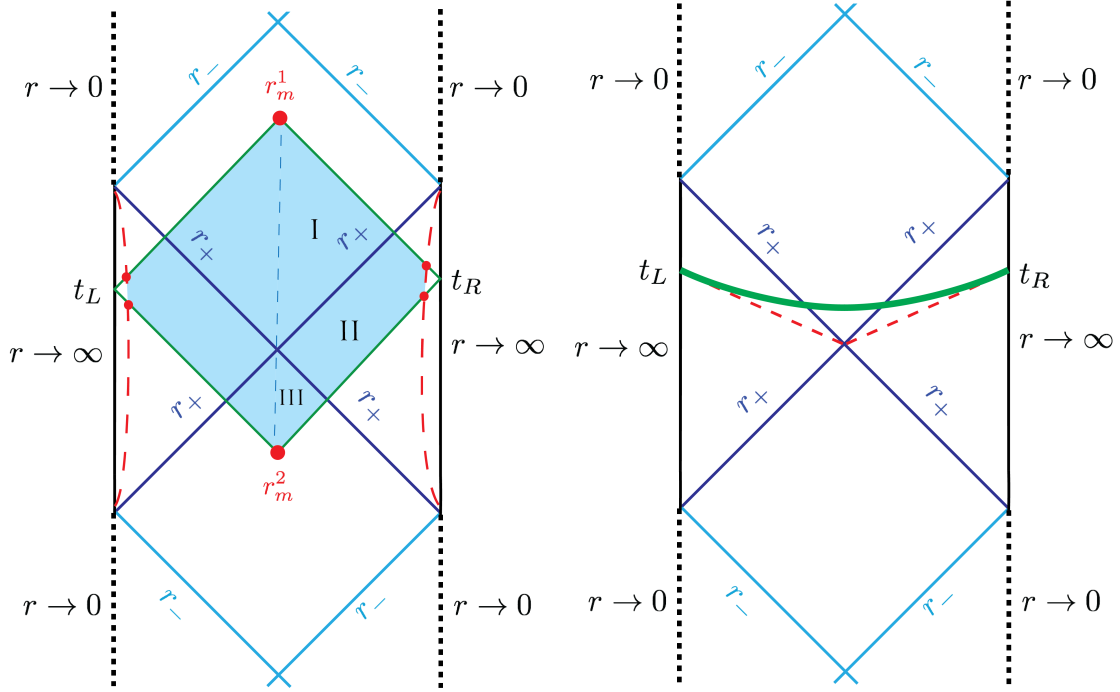


Figure 4.8: Penrose diagrams for a charged black hole. On the left figure we breakdown the action calculation for the Wheeler-DeWitt patch. The future (past) corner approaches the inner (outer) horizon in the late time limit. On the right, we identify the maximal volume that is evaluated in the CV proposal. As in section 4.1 we have for the case of a general boundary size $t = \frac{L}{R}\tau$.

As expected, the dimensionless quantity ν goes to zero and TR to the uncharged limit as in eq. (4.39). From the expansions in eq. (4.104), we can also conclude that the chemical potential, $\sqrt{\frac{C_I}{C_T}}\mu R = \tilde{h}(y, z)h(y, z)$ scales as $\propto y^{\frac{d-2}{2}}$ for small charges. Similarly, the blackening factor can be expressed as $f(x, y, z)$ where x was defined in eq. (4.101).

Complexity of Formation: The complexity of formation for uncharged black holes was examined in detail in chapter 3. Hence for completeness, we also examine the ‘complexity of formation’ of charged black holes here and the corresponding calculations are described in detail in appendix B.3. The question of interest is what is the additional complexity

involved in preparing the two copies of the boundary CFT in the charged entangled thermofield double state (4.94) compared to preparing each of the CFTs separately in their vacuum state. Using the CA proposal,²¹ the bulk calculation consists of evaluating the gravitational action for the WDW patch (anchored at $t_L = t_R = 0$) in the charged AdS black hole background and subtracting twice the action for the WDW patch in empty AdS space (*i.e.*, $\omega = q = 0$). A key feature of this subtraction is that all of the UV (large r) divergences cancel leaving a UV-finite result.

We discuss here the charged complexity of formation using the CA conjecture for the planar case, *i.e.*, $k = 0$, for $d = 4$. For small chemical potential, the charged complexity of formation can be written as a series expansion for small y ,

$$\Delta\mathcal{C}_A = \frac{S}{2\pi} \left(1 + \left(\frac{20}{3\pi} + \frac{4}{\pi} \log \left[\frac{yz \alpha R}{2 L} \right] \right) y^3 + \dots \right), \quad (4.105)$$

where S is the thermal entropy. Of course, we recover the $d = 4$ planar result found in chapter 3 in the limit of vanishing chemical potential, *i.e.*, $y \rightarrow 0$. We can rewrite the above expression without the explicit zR dependence, using the $k = 0$ and $d = 4$ instances of eq. (4.103), which reads

$$\nu = \frac{3\pi}{\sqrt{10}} \frac{y\sqrt{1+y^2}}{(2-y^2-y^4)}, \quad TR = \frac{(1-y^2)(2+y^2)}{2\pi z}. \quad (4.106)$$

The expansion of the complexity of formation then becomes

$$\Delta\mathcal{C}_A = \frac{S}{2\pi} \left(1 + \frac{10^{3/2}}{(3\pi)^4} \left(20 + 12 \log \left[\frac{10^{1/2} \alpha \nu}{3\pi^2 LT} \right] \right) \nu^3 + \dots \right). \quad (4.107)$$

As in section 4.1, we might simplify the above expression by choosing the normalization of the null normals at infinity to be $\alpha = L/R$, where R is to be interpreted not as the curvature scale, but instead as an arbitrary reference length scale in the boundary theory (for $k = 0$).

We also use the boundary quantities from eq. (4.106) to evaluate numerically the complexity of formation fixing the chemical potential and varying the temperature in figure 4.9. There is an unexpected behaviour when the temperature is very small, as the complexity of formation grows unbounded. The fact that the complexity of formation for extremal black holes of finite chemical potential is divergent suggests that the proposed ground state

²¹Of course, an analogous calculation can also be performed using the CV proposal, see appendix D of our work [66].

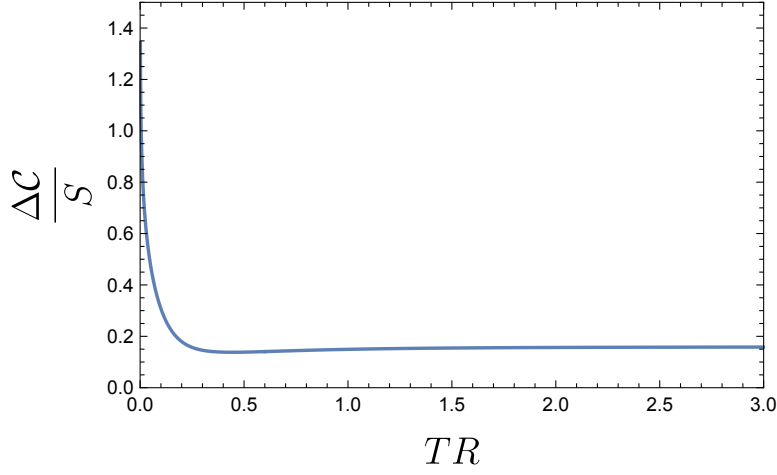


Figure 4.9: Complexity of formation divided by the entropy for the planar charged black hole in $d = 4$. Here we are subtracting the complexity of two copies of the vacuum spacetime (*i.e.*, the zero mass and zero charge limit of the planar black hole). In this plot, we keep the chemical potential fixed as $\sqrt{\frac{C_I}{C_T}}\mu R = \frac{1}{2}$. For a fixed chemical potential in the limit of zero temperature (dual to extremal black hole) the complexity of formation is divergent.

for large charged black holes in [34] should be revisited. It is also interesting to notice that in this limit of zero temperature with a fixed chemical potential, $d\mathcal{C}_A/d\tau$ goes to zero [34], as we will show in the following subsection. We will explore further some features of the charged complexity of formation in appendix B.3.

4.4.1 Complexity=Action

Next, we examine the time evolution of holographic complexity using the CA proposal for the eternal charged AdS black holes. The integrand of the bulk action is given by²²

$$I(r) \equiv \frac{1}{16\pi G_N} (\mathcal{R} - 2\Lambda) - \frac{1}{4g^2} F_{ab}F^{ab} = \frac{1}{16\pi G_N} \left(-\frac{2d}{L^2} + \frac{2(d-2)q^2}{r^{2(d-1)}} \right). \quad (4.108)$$

²²To simplify this expression, we have used the trace of Einstein equations, which yields $\mathcal{R} = -\frac{d(d+1)}{L^2} + \frac{d-3}{d-1} \frac{4\pi G_N}{g^2} F_{ab}F^{ab}$.

We then write the bulk action as

$$I_{\text{bulk}} = \frac{L}{R} \Omega_{k,d-1} \int dr r^{d-1} I(r) \int d\tau \quad (4.109)$$

where we still have to specify the limits of integration. In particular, we need to find the future (r_m^1) and past (r_m^2) meeting points of the null sheets bounding the WDW patch — see figure 4.8. These satisfy the following relations

$$\frac{L}{R} \frac{\tau}{2} + r_\infty^* - r^*(r_m^1) = 0, \quad \frac{L}{R} \frac{\tau}{2} - r_\infty^* + r^*(r_m^2) = 0. \quad (4.110)$$

Note that taking the time derivative of these relations yields:

$$\frac{R}{L} \frac{dr_m^1}{d\tau} = \frac{f(r_m^1)}{2}, \quad \frac{R}{L} \frac{dr_m^2}{d\tau} = -\frac{f(r_m^2)}{2}. \quad (4.111)$$

We again divide the bulk contribution into three separate regions

$$\begin{aligned} I_{\text{bulk}}^{\text{I}} &= 2\Omega_{k,d-1} \int_{r_m^1}^{r_+} I(r) r^{d-1} \left(\frac{\tau}{2} + \frac{R}{L} (r_\infty^* - r^*(r)) \right) dr \\ I_{\text{bulk}}^{\text{II}} &= 4\Omega_{k,d-1} \int_{r_+}^{r_m^{\text{max}}} I(r) r^{d-1} \frac{R}{L} (r_\infty^* - r^*(r)) dr \\ I_{\text{bulk}}^{\text{III}} &= 2\Omega_{k,d-1} \int_{r_m^2}^{r_+} I(r) r^{d-1} \left(-\frac{\tau}{2} + \frac{R}{L} (r_\infty^* - r^*(r)) \right) dr. \end{aligned} \quad (4.112)$$

Differentiating with respect to τ we see once again (as in the neutral case) that the contributions due to differentiating the limits of integration vanish using eq. (4.110). The contribution outside the black hole (region II) is independent of time.²³ Hence the only nonvanishing contribution comes from differentiating inside the integrals and we obtain

$$\frac{dI_{\text{bulk}}}{d\tau} = \frac{L}{R} \Omega_{k,d-1} \int_{r_m^1}^{r_m^2} r^{d-1} I(r) dr = \frac{L}{R} \frac{\Omega_{k,d-1}}{8\pi G_N} \left[\frac{r^d}{L^2} + \frac{q^2}{r^{d-2}} \right] \Bigg|_{r_m^2}^{r_m^1}. \quad (4.113)$$

There are no contributions to $d\mathcal{C}_A/d\tau$ from the surface terms or from the asymptotic boundaries here, but we do expect the two joints (at $r = r_m^1$ and r_m^2) to contribute:

$$I_{\text{corner}} = -\frac{\Omega_{k,d-1}}{8\pi G_N} \left[(r_m^1)^{d-1} \log \left[\frac{L^2 |f(r_m^1)|}{R^2 \alpha^2} \right] + (r_m^2)^{d-1} \log \left[\frac{L^2 |f(r_m^2)|}{R^2 \alpha^2} \right] \right]. \quad (4.114)$$

²³This results from the boost invariance of the exterior geometry, as noted in [33, 34].

Differentiating the corner contribution with respect to τ then gives

$$\frac{dI_{\text{corner}}}{d\tau} = -\frac{L}{R} \frac{\Omega_{k,d-1}}{16\pi G_N} \left[(d-1)r^{d-2}f(r) \log \frac{L^2|f(r)|}{R^2\alpha^2} + r^{d-1}\partial_r f(r) \right] \Bigg|_{r_m^2}^{r_m^1}, \quad (4.115)$$

where we used eq. (4.110). Combining the nonvanishing contributions together leads to

$$\frac{d\mathcal{C}_A}{d\tau} = \frac{L}{R} \frac{\Omega_{k,d-1}(d-1)}{8\pi^2 G_N} \frac{q^2}{r^{d-2}} \Bigg|_{r_m^2}^{r_m^1} - \frac{L}{R} \frac{\Omega_{k,d-1}(d-1)}{16\pi^2 G_N} r^{d-2} f(r) \log \frac{L^2|f(r)|}{R^2\alpha^2} \Bigg|_{r_m^2}^{r_m^1}. \quad (4.116)$$

As a consistency check, we note that in the late time limit, we recover eq. (3.39) of [63]:

$$\lim_{\tau \rightarrow \infty} \frac{d\mathcal{C}_A}{d\tau} = \frac{\Omega_{k,d-1}(d-1)q^2}{8\pi^2 G_N} \frac{L}{R} \frac{1}{r^{d-2}} \Bigg|_{r_+}^{r_-}, \quad (4.117)$$

where we have used that $r_m^1 \rightarrow r_-$ and $r_m^2 \rightarrow r_+$ in this limit. It is also possible to express this late time rate of change using the black hole mass and the dimensionless quantities from eq. (4.101) as

$$\lim_{\tau \rightarrow \infty} \frac{d\mathcal{C}_A}{d\tau} = \frac{2M}{\pi} \left(\frac{(1-y^{d-2})((1-y^d) + kz^2(1-y^{d-2}))}{(1-y^{2(d-1)}) + kz^2(1-y^{2(d-2)})} \right). \quad (4.118)$$

In these variables, the late time limit of the uncharged case is easily obtained with $y \rightarrow 0$.

Now it is straightforward to solve for the two meeting points numerically using eq. (4.110) and then to evaluate the rate of change in complexity (4.116). To illustrate these results, we show $d\mathcal{C}_A/d\tau$ for $d = 4$ in figures 4.10 and 4.11.²⁴ For these black holes, the boundary quantities ν and RT in eq. (4.102) can be obtained from the ratios y and z as

$$\nu = \sqrt{\frac{C_J}{C_T}} \frac{\mu}{T} = \frac{3\pi}{\sqrt{10}} \frac{y\sqrt{1+y^2+kz^2}}{(1-y^2)(2+y^2+kz^2)}, \quad RT = \frac{1}{2\pi} \frac{(1-y^2)(2+y^2+kz^2)}{z}. \quad (4.119)$$

In the figures, the rate of change in complexity is presented for fixed values of these boundary quantities.

²⁴As before, we set $\alpha = L/R$ for simplicity.

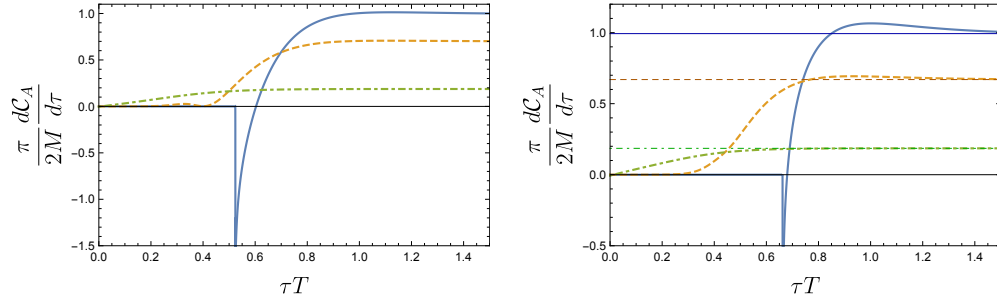


Figure 4.10: The time derivative of complexity with $d = 4$, $k = 1$ and non-zero chemical potential, obtained by fixing the parameters in eq. (4.119). The various curves correspond to: $\nu = 0.1$ in blue (solid) , $\nu = 1$ in orange (dashed) and $\nu = 5$ in green (dot-dashed) for $TR = 1$ (Left) and $TR = \frac{1}{2}$ (Right). In order to illustrate the violation of the bound, we explicitly show the late time limit from eq. (4.118) in the right figure.

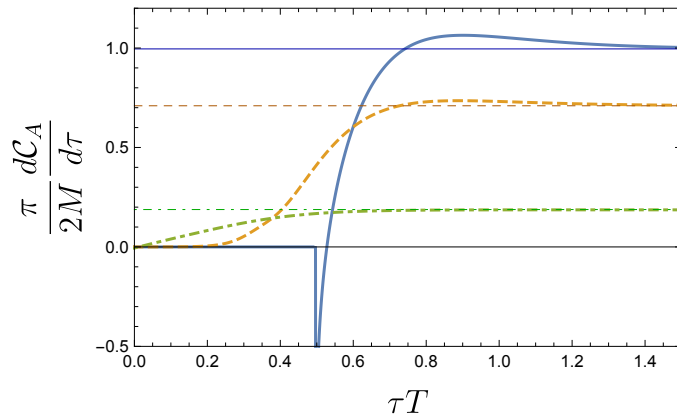


Figure 4.11: The time derivative of complexity with $d = 4$, $k = 0$ and non-zero chemical potential, obtained by fixing the parameters in eq. (4.119). The various curves correspond to: $\nu = 0.1$ in blue (solid) , $\nu = 1$ in orange (dashed) and $\nu = 5$ in green (dot-dashed). We varied the chemical potential while fixing the temperature as $TR = \frac{1}{2}$, where as before the scale R in the planar geometry is related to an arbitrary scale in the boundary theory.

Comments

Let us make a number of observations about these results for the charged black holes. First, we note that in both figures, for very small charge (or small chemical potential), the rate of change in complexity develops a minimum at some finite time. This minimum becomes deeper and sharper for smaller charges, and so the behaviour smoothly approaches that of the neutral black holes ($\nu = 0$), shown in figure 4.4. In particular, the pronounced minimum in $d\mathcal{C}_A/d\tau$ is centered around the neutral τ_c , and its shape resembles closely the negative divergent rate of change observed right after τ_c in the neutral case, and as noted above, the late time limit approaches $2M/\pi$, as expected for neutral AdS black holes.²⁵

Next, we might consider the extremal limit of the charged black holes where $T \rightarrow 0$. It is straightforward to show $d\mathcal{C}_A/d\tau \simeq 0$ in this limit. For example, from eq. (4.119), we see that this limit corresponds to $y \rightarrow 1$ and this certainly produces a vanishing rate of change for the late time limit in eq. (4.118). More generally, this limit corresponds to $r_- \rightarrow r_+$ and we find $r_m^1 \sim r_m^2$. The latter then produces a cancellation and vanishing $d\mathcal{C}_A/d\tau \simeq 0$ in eq. (4.116).

Late time expansion: In a very similar manner to the analysis of the late time limit in section 4.2, we can obtain the late time limit of the growth rate of the holographic complexity for charged black holes. First, we decompose the inverse blackening factor as

$$\frac{1}{f(r)} = \frac{1}{r_+ - r_-} \left(\frac{r_+}{F(r_+)r(r - r_+)} - \frac{r_-}{F(r_-)r(r - r_-)} + H(r) \right) \quad (4.120)$$

where we have defined:

$$f(r) \equiv F(r)(r - r_+)(r - r_-) \quad (4.121)$$

and $F(r)$ is a strictly positive function. Further, we have defined

$$H(r) = \frac{F(r_+)r - F(r)r_+}{F(r_+)F(r)r(r - r_+)} - \frac{F(r_-)r - F(r)r_-}{F(r_-)F(r)r(r - r_-)}, \quad (4.122)$$

which is regular both at r_+ and at r_- and decays at least as fast as $1/r^2$ when r approaches infinity. This leads to the tortoise coordinate:

$$r^*(r) = \frac{\log(|r - r_+|/r)}{F(r_+)(r_+ - r_-)} - \frac{\log(|r - r_-|/r)}{F(r_-)(r_+ - r_-)} + \frac{1}{r_+ - r_-} \int^r H(\tilde{r})d\tilde{r}. \quad (4.123)$$

²⁵In fact, one can easily show that eq. (4.41) is recovered in the zero charge limit analytically. The key observation is that r_- vanishes as $r_-^{d-2} = q^2/\omega^{d-2}$ in this limit. Along with $r_m^1 \sim r_-$ and $r_m^2 \simeq r_m^{(neutral)}$, eq. (4.116) reduces to the neutral growth rate (4.41) for $\tau > \tau_c$. We consider the early time behaviour in the zero charge limit below.

We have left the lower limit in the last integral implicit, as this choice does not influence the subtractions involved in the equations determining the meeting points. Solving for the first subleading order in the late time limit of eq. (4.110), we obtain

$$r_m^1 = r_- \left(1 + c_- e^{-\frac{F(r_-)(r_+ - r_-)}{2} \frac{L}{R} \tau} \right), \quad r_m^2 = r_+ \left(1 - c_+ e^{-\frac{F(r_+)(r_+ - r_-)}{2} \frac{L}{R} \tau} \right) \quad (4.124)$$

where c_+ and c_- are positive constants given by

$$c_- = \left(\frac{r_+ - r_-}{r_-} \right)^{\frac{F(r_-)}{F(r_+)}} e^{-F(r_-) \int_{r_-}^{\infty} H(\tilde{r}) d\tilde{r}}, \quad c_+ = \left(\frac{r_+ - r_-}{r_+} \right)^{\frac{F(r_+)}{F(r_-)}} e^{F(r_+) \int_{r_+}^{\infty} H(\tilde{r}) d\tilde{r}}. \quad (4.125)$$

From eq. (4.116), we can now demonstrate that

$$\begin{aligned} \frac{d\mathcal{C}_A}{d\tau} &= \lim_{\tau \rightarrow \infty} \frac{d\mathcal{C}_A}{d\tau} + \frac{(r_+ - r_-)^2 L^2 \Omega_{d-1} (d-1)}{2 R^2 16\pi^2 G_N} \tau \\ &\quad \times \left(c_+ r_+^{d-1} F(r_+)^2 e^{-\frac{F(r_+)(r_+ - r_-)}{2} \frac{L}{R} \tau} - c_- r_-^{d-1} F(r_-)^2 e^{-\frac{F(r_-)(r_+ - r_-)}{2} \frac{L}{R} \tau} \right) \end{aligned} \quad (4.126)$$

where we have neglected terms that decay exponentially compared to those that decay as τ times an exponential above. At very late times the exponent with smaller coefficient will dominate and will determine whether the limit is reached from above or from below. We have checked the ratio $F(r_+)/F(r_-) = -f'(r_+)/f'(r_-)$ for a variety of dimensions and geometries and found that it is in general positive and smaller than one. As a consequence, $d\mathcal{C}_A/d\tau$ generally approaches the late time limit from above.

Early time behaviour: We note that for the charged black holes, there is not a critical time before which the time derivative of the complexity is equal to zero. In the charged black hole, the past and future oriented joint terms (see the left panel in figure 4.8) start moving right away. However, we will show that for a small chemical potential, the time derivative of the complexity is exponentially suppressed at early times. In order to investigate this behaviour, we investigate the early time regime of the rate of change of complexity in an analytic expansion for small charges. To complete the picture, we also consider in this section the early time behaviour of the rate of change of complexity for near extremal black holes.

As we have already mentioned at the beginning of this subsection, in the limit in which the charge is small, the action does not change much for a certain period of time after $\tau = 0$. In this situation, the future and past corner points (*i.e.*, r_m^1 and r_m^2 respectively, or x_m^1 and x_m^2 in terms of the dimensionless coordinate $x = r/r_+$) are exponentially close

to the inner horizon r_- at early times. For instance in $d = 4$, we can derive the following expressions in a small charge expansion, *i.e.*, $y \rightarrow 0$,

$$\begin{aligned} x_m^1 &= y \left(1 + \exp \left[- \left(\frac{\pi(1 + kz^2)}{2 + kz^2} \frac{2\tau T + \sqrt{1 + kz^2}}{y^3} \right) + \mathcal{O} \left(\frac{1}{y} \right) \right] \right), \\ x_m^2 &= y \left(1 + \exp \left[- \left(\frac{\pi(1 + kz^2)}{2 + kz^2} \frac{-2\tau T + \sqrt{1 + kz^2}}{y^3} \right) + \mathcal{O} \left(\frac{1}{y} \right) \right] \right). \end{aligned} \quad (4.127)$$

This expansion demonstrates that the two corners remain exponentially close to r_- at early times. Given the above expression, it is clear that r_m^1 never leaves this regime and keeps approaching r_- . However, in the second expression for r_m^2 , the leading term in the exponent flips its sign at some $\tau = \tau_c = \frac{1}{2T} \sqrt{1 + kz^2}$, which is precisely the uncharged critical time given in eq. (4.58). Hence the rate of change of complexity given by eq. (4.116) is exponentially suppressed as long as $\tau \lesssim \tau_c$.

Another case for which the early time behaviour can be studied in an analytic expansion is the near-extremal black holes. In this case, the inner and outer horizons are very close to each other as $y \rightarrow 1$. If we define $y = 1 - \epsilon$ where $\epsilon \ll 1$, eq. (4.110) yields at early times

$$\begin{aligned} x_m^1 &= 1 - \frac{\epsilon}{2} (1 + \pi\tau T) + \mathcal{O}(\epsilon\tau^3 T^3, \epsilon^2\tau T, \epsilon^2 \log \epsilon), \\ x_m^2 &= 1 - \frac{\epsilon}{2} (1 - \pi\tau T) + \mathcal{O}(\epsilon\tau^3 T^3, \epsilon^2\tau T, \epsilon^2 \log \epsilon). \end{aligned} \quad (4.128)$$

In general, the geometry and hence, the complexity are symmetric under $\tau \rightarrow -\tau$. Therefore only even derivatives of \mathcal{C}_A are nonvanishing at $\tau = 0$, *e.g.*, $d\mathcal{C}_A/d\tau|_{\tau=0} = 0$. We can evaluate the second derivative of \mathcal{C}_A at $\tau = 0$ using eqs. (4.116) and (4.111), and the expansion for $x_m \equiv x_m^1 = x_m^2$ at $\tau = 0$ which reads

$$\begin{aligned} x_m &= 1 - \frac{\epsilon}{2} + \frac{(3kz^2 + 7) \epsilon^2 \log(\epsilon)}{4(kz^2 + 3)} - \frac{\epsilon^2}{8(kz^2 + 3)} \times \left(16\pi \sqrt{\frac{1}{kz^2 + 2}} + 3 + 28 \log(2) \right. \\ &\quad \left. + kz^2 \left(4\pi (kz^2 + 4) \sqrt{\frac{1}{kz^2 + 2}} + 1 + 6 \log(4) \right) - 8 (kz^2 + 2)^{3/2} \cot^{-1} \left(\sqrt{kz^2 + 2} \right) \right). \end{aligned} \quad (4.129)$$

Hence using the above results, the first nonvanishing derivative becomes

$$\left. \frac{d^2 \mathcal{C}_A}{d\tau^2} \right|_{\tau=0} = \frac{4(kz^2 + 2)}{2kz^2 + 3} \epsilon MT + \mathcal{O}(\epsilon^3). \quad (4.130)$$

Note that the temperature here is of order ϵ and as a consequence the leading term in an ϵ expansion is in fact of order ϵ^2 . Despite being suppressed by the parameter ϵ , the complexity grows quadratically (and the rate of change grows linearly) with τ at early times.

Lloyd’s bound: A generalization of Lloyd’s bound for the case of charged black holes has been proposed in [34] (see also [162]). According to this suggestion, the natural bound for states at a finite chemical potential becomes

$$\frac{d\mathcal{C}_A}{dt} \leq \frac{2}{\pi} \left[(M - \mu Q) - (M - \mu Q)|_{gs} \right]. \quad (4.131)$$

This bound was inspired by the late time growth rate of holographic complexity for the charged black holes. One important element of this proposed bound is that it involves the subtraction of certain thermodynamic quantities associated with the ground state (gs) of the system in question, which according to the proposal of [34] is the state minimizing $(M - \mu Q)$ for a given value of the chemical potential. For instance, for spherical black holes with $\mu < \frac{gL}{2R\sqrt{2\pi G}} \sqrt{\frac{d-1}{d-2}}$, the ground state is simply the vacuum solution ($M = Q = 0$) with a constant gauge field, while for larger chemical potentials, the ground state is the extremal black hole with same chemical potential μ as the state of interest. However, it was also found in [34] that the proposed bound (4.131) is violated for black holes which are intermediate or large compared to the AdS radius ($r_+ \gtrsim L$), while for small black holes the bound is exactly saturated. On the other hand, we showed earlier that the complexity calculated from the action always approaches its late time limit from above, and as a consequence we conclude that the bound in eq. (4.131) is always violated.

4.4.2 Complexity=Volume

We can also extend the analysis of section 4.3 to evaluate the rate of change of complexity for the charged case using the CV proposal (3.42). A maximal volume connecting the two boundaries anchored at t_L and t_R is depicted on the right side of figure 4.8. The analysis and the results are very similar to the uncharged case. For example, one still calculates the rate of change by computing r_{min} (or the associated E) in eq. (4.66), but now with the blackening factor for charged solutions in eq. (4.92). The growth rate can be evaluated as detailed in section 4.3.2.

We present some of the results in figures 4.12 and 4.13. The growth rate depends on the charge parameter as expected, and it also approaches zero near the extremal limit,

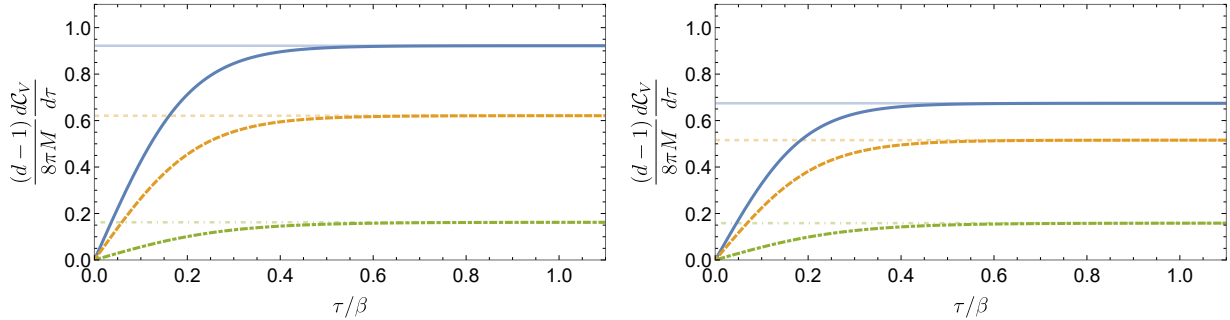


Figure 4.12: The time derivative of complexity with $d = 4$, $k = 1$ with non-zero chemical potential, by fixing the parameters in eq. (4.119). The various curves correspond to: $\nu = 0.1$ in blue (solid), $\nu = 1$ in orange (dashed) and $\nu = 5$ in green (dot-dashed) for $TR = 1$ (left) and $TR = \frac{1}{2}$ (right). Late time limits are obtained from eqs. (4.75), (4.77) and are indicated by horizontal lines of the appropriate colour.

analogous to the previous results from CA. It smoothly approaches the neutral behaviour (*e.g.*, shown in figure 4.7) in the limit $q \rightarrow 0$.

4.5 Discussion

In this chapter, we computed the general time dependence of holographic complexity in various AdS black hole geometries. Further we examined the time dependence using both the complexity=action (CA) and the complexity=volume (CV) conjectures. Using the CV conjecture, the rate of change of complexity is a positive monotonically increasing function of time, and it saturates to a positive constant as $t \rightarrow \infty$. In particular, for planar black holes, the limiting rate is given by eq. (4.80),

$$\lim_{\tau \rightarrow \infty} \frac{d\mathcal{C}_V}{d\tau} = \frac{8\pi M}{d-1}, \quad (4.80)$$

as was first found in [32]. When the boundary geometry is curved, this result is modified by various curvature corrections which become important when the temperature is of the same order as the curvature scale, *i.e.*, $RT \lesssim 1$.

Using the CA conjecture, the rate of change of the complexity shows some curious features. Of course, there is a universal late time rate of growth

$$\lim_{\tau \rightarrow \infty} \frac{d\mathcal{C}_A}{d\tau} = \frac{2M}{\pi}, \quad (4.132)$$

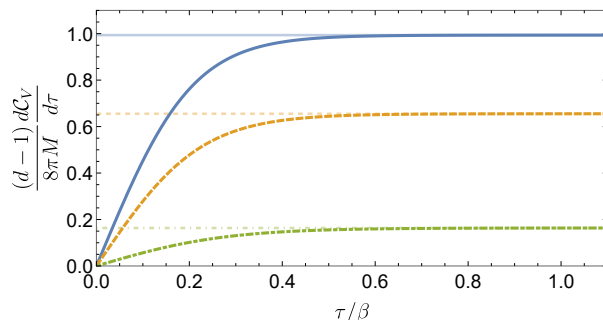


Figure 4.13: The time derivative of complexity with $d = 4$, $k = 0$ with non-zero chemical potential, by fixing the parameters in eq. (4.119). The various curves correspond to: $\nu = 0.1$ in blue (solid), $\nu = 1$ in orange (dashed) and $\nu = 5$ in green (dot-dashed). Curves are independent of TR in eq. (4.102) as expected for the planar geometry. Late time limits are obtained from eqs. (4.75), (4.77) and are indicated by horizontal lines of the appropriate colour.

as shown in eq. (4.33). This universal rate, discovered in [33, 34], holds in any number of dimensions and is not affected by the boundary curvature. However, as also shown in eq. (4.33), $d\mathcal{C}_A/d\tau$ overshoots this late time limit at early times and approaches the final limit from above. Further $d\mathcal{C}_A/d\tau$ is initially zero and the complexity only begins to change after some critical time τ_c (for $d \geq 3$). This initial phase of constant complexity was also observed in [33, 34]. In the bulk, the vanishing of $d\mathcal{C}_A/d\tau$ results because of the ‘boost’ symmetry of the eternal black hole geometry and the fact that in this initial period of time the WDW patch touches both the past and future singularities, *e.g.*, see the left panel in figure 4.1. A third curious feature that we found is that immediately after $\tau = \tau_c$, $d\mathcal{C}_A/d\tau$ is divergent and negative, as shown in eq. (4.34)²⁶ — see also figure 4.4.

We reiterate that the three features above only appear for the time rate of change evaluated with the CA proposal. None of these features appeared in the results found using the CV proposal in section 4.3. Further, when a chemical potential was introduced in section 4.4, this washed out the unusual behaviour at early times, at least when the chemical potential was comparable to the temperature, as shown in figures 4.10 and 4.11. Of course, as we discussed, the limit $q \rightarrow 0$ was a smooth one and the curious behaviour found for the neutral black holes was recovered. So when the chemical potential was small but nonvanishing, $d\mathcal{C}_A/d\tau$ varied very little for an initial period and then quickly dipped

²⁶This negative spike (as well as the overshoot of the late time limit) in $d\mathcal{C}_A/d\tau$ also appears in different holographic settings, such as the holographic dual of non-commutative SYM theories [163]. We thank Josiah Couch for discussing his work with us.

to negative values before rising again. We can also add that with a chemical potential, $d\mathcal{C}_A/d\tau$ would still overshoot the late time limit but that the amount by which the limit was exceeded was much less pronounced when the chemical potential became large.

At this point, let us add that the curious behaviour found with the CA proposal also seems to be particular to the eternal black hole, *i.e.*, to the thermofield double state (1.21). Analogous computations of the action for a one-sided black hole yield results more similar to those found here with the CV proposal, as we will evaluate in chapter 5. That is, in this context, $d\mathcal{C}_A/d\tau$ is a positive monotonically increasing function of time, which saturates to some positive constant in the late time limit. For both proposals, the late time limit is reached exponentially fast, with a characteristic time which is of the order of the inverse temperature. This can be seen explicitly in eq. (4.33) for the CA calculation, and in appendix C of [66] for the CV calculation.

In the above discussion, we commented that for higher dimensions (*i.e.*, $d \geq 3$), the action (for neutral black holes) does not change at all for some period $-\tau_c \leq \tau \leq \tau_c$ and then changes very rapidly just after $\tau = \tau_c$. We observe that the time scale τ_c is of the order of the thermal time scale $\beta = 1/T$, *e.g.*, see eq. (4.58) for $d = 4$. In particular, the latter equation demonstrates that the critical time is a physical quantity independent of the ambiguity introduced by the normalization constant α of null normals. In contrast, the period of time over which $d\mathcal{C}_A/d\tau$ is negative, depends both on β and on α . For very small black holes, it is possible to obtain an estimate of this period by equating the RHS of eq. (4.34) with the constant term in the complexity $2M/\pi$ and we see that this period depends explicitly on the reference scale ℓ (as in $\alpha = L/\ell$) (*i.e.*, the spike lasts for $\delta t_0 \sim \beta (\ell/\beta)^{2(d-1)/(d-2)}$). However, we might add that this negative spike can grow arbitrarily wide²⁷ for extremely large values of ℓ , or alternatively, for extremely small values of the parameter α . While the latter remains a logical possibility, it also seems very unnatural for our complexity calculations, *e.g.*, see [38, 65].

However, one might argue that the holographic definition of circuit complexity is not robust enough to consider time scales smaller than β in the context of the eternal black hole.²⁸ That is, we might only want to consider the behaviour of complexity over time scales which are longer than the thermal time scale. Therefore we defined an averaged version of $d\mathcal{C}_A/d\tau$ in eq. (4.35), which is essentially a symmetric discrete time derivative with a time step $\Delta t = \gamma/T$. With a large enough γ , the complexity begins changing right away and the sharp negative spike in $d\mathcal{C}_A/d\tau$ is washed out by the averaging procedure.²⁹ However, we

²⁷The growth rate is exceptionally slow with $\delta t_0 \sim \beta \log[\log(\ell/\beta)]$ for very large values of ℓ .

²⁸We thank Lenny Susskind, Dan Roberts and Brian Swingle for correspondence on this point.

²⁹This simply requires that $d\mathcal{C}_A/d\tau > 0$ at $\tau = \gamma\beta/2$.

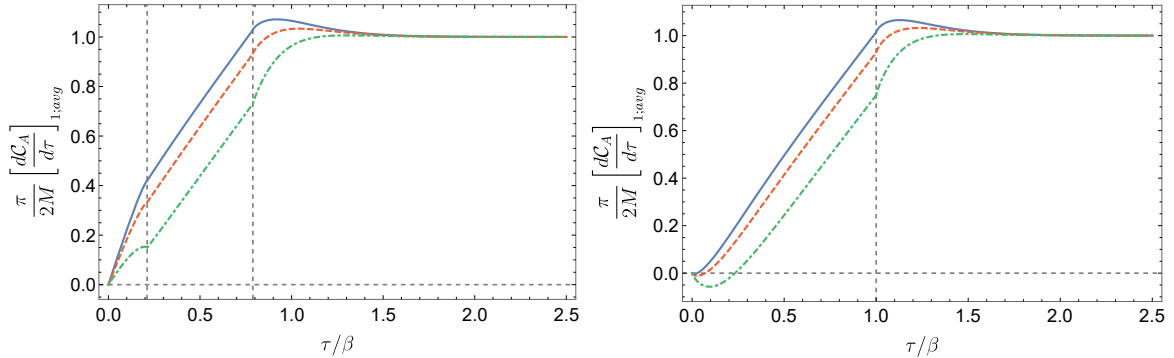


Figure 4.14: The averaged rate of growth of complexity from eq. (4.35) (with $\gamma = 1$) as a function of time for the $d = 3$ planar black hole (left) and $d = 4$ planar (right). Results are shown for several values of the horizon radius — $r_h/L = 1$ (blue), $r_h/L = 1.5$ (dashed red) and $r_h/L = 3.5$ (dot-dashed green). Note that, as in figures 4.2 and 4.4, smaller black holes violate the Lloyd bound more strongly. Note also, that the averaged derivative is discontinuous at $|\tau/\beta \pm \frac{1}{2}| = \tau_c/\beta$, where for $d = 3$, $\tau_c/\beta = \frac{1}{2\sqrt{3}}$ and for $d = 4$, $\tau_c/\beta = \frac{1}{2}$.

note that this averaging does not remove the behaviour where the rate of change overshoots its late time limit. This feature should not be associated with short times since in fact, the late time limit is being approached from above, as shown in eq. (4.33). Some examples of these averaged growth rates are shown in figure 4.14.

Recall that [33, 34] suggested that the late time limit of $d\mathcal{C}_A/d\tau$ may be related to Lloyd’s bound $2M/\pi$ for the rate of computation for a system of energy M [116]. These authors also proposed a generalization of Lloyd’s bound that should apply for charged black holes — see eq. (4.131). However, they also pointed out apparent violations of the latter bound for intermediate or large charge black holes (*i.e.*, $r_+ \gtrsim L$). However, our calculations of the rate of change of holographic complexity for general times showed that $d\mathcal{C}_A/d\tau$ always overshoots the late time limit. As a consequence, for every situation that we examined in sections 4.2 and 4.4.1, the corresponding bound on $d\mathcal{C}_A/d\tau$ was violated. This certainly calls into question these proposals or at least their interpretation (as we describe next).

Let us comment that similar violations are observed for the proposed bounds for the maximal rate of entanglement growth in relativistic systems [164, 165].³⁰ In this case, the proposal is that following a quantum quench, the rate of growth of the entanglement

³⁰We thank Mark Mezei for explaining this point to us.

entropy for a large region will be bounded by

$$\frac{1}{s_{eq} A} \frac{dS_{EE}}{dt} \leq v_E \tag{4.133}$$

where s_{eq} is the equilibrium entropy density, A is the area of the entangling surface, and $v_E (\leq 1)$ is a universal velocity that depends on the dimension of the spacetime. In certain contexts, this bound can be proven but it requires considering a certain scaling regime where $\beta \ll t, R$ where R is the characteristic size of the entangling region [166]. In contrast, in numerical studies, one may find that the rate of growth actually overshoots the expected bound, *e.g.*, [165, 167]. By analogy, it may be that one should only interpret the bounds on the growth of complexity in a particular scaling regime. For example, if we demand that $\beta \ll t$, then the corrections in eq. (4.33) to the late time limit would be vanishingly small. We might also point out that one needs to test carefully the validity of the assumptions entering in the derivation of Lloyd’s bound in a holographic setup, in particular the use of orthogonalizing gates [82].

We must also comment that the precise details of the manner in which $d\mathcal{C}_A/d\tau$ overshoots the late time limit depend on the normalization constant α , which fixes the normal vectors on the null boundaries of the WDW patch. In our various plots, *e.g.*, figures 4.2 and 4.4, we chose $\alpha = L/R$ for simplicity and as a result, the late time limit was only exceeded by a relatively small amount. However, by choosing α to be very large, the amount by which $d\mathcal{C}_A/d\tau$ overshoots this limit can be made very large. This is easily demonstrated by examining eq. (4.41) evaluated for two different values of the normalization constant, *i.e.*, α_1 and α_2 , but for the same time τ where $d\mathcal{C}_A/d\tau$ exceeds the late time limit for α_1 . Now we see in eq. (4.41) shows that with α_2 , $d\mathcal{C}_A/d\tau$ is the previous value plus a positive quantity multiplying $\log(\alpha_2/\alpha_1)$ and so by choosing α_2 large enough, we can make the excess as large as we want. An analogous result follows if we include the counterterm in eq. (2.11).

We can also study the maximal rate of complexity growth analytically when α is very large. The simplest case to consider here is $d = 2$ for which the maximum was calculated in appendix B.1. For example, if we choose $\alpha = L/\delta$, then eq. (B.23) yields

$$\left. \frac{d\mathcal{C}_A}{d\tau} \right|_{max} = \frac{2M}{\pi} \left(1 + \log \left[\frac{1}{2\pi\delta T} \right] \right) . \tag{4.134}$$

However, we should also remark that in this instance, the violation is an early time feature, *i.e.*, $d\mathcal{C}_A/d\tau$ peaks at precisely $\tau = 0$ and the width of the peak is of order β . Hence the averaging discussed above will reduce the excess but it will still remain significant with

this extreme choice of α . A similar result holds in higher dimensions. For instance, if we consider the planar uncharged black holes in section 4.1 with $\alpha = L/\delta$, then the limit $\delta \rightarrow 0$ yields

$$\left. \frac{d\mathcal{C}_A}{d\tau} \right|_{max} = \frac{2M}{\pi} \log \left(\frac{d}{4\pi\delta T} \right) + \mathcal{O} \left(\log \left(\log \frac{1}{\delta T} \right) \right), \quad (4.135)$$

for the leading behaviour of the peak of the growth rate. Note that this result reproduces the leading behaviour in eq. (4.134) with $d = 2$.

Having noted that the amount by which $d\mathcal{C}_A/d\tau$ exceeds that late time limit is controlled by α , we might add that this produces a finite shift in the complexity. That is comparing the complexity at late times for different choices of α has a rather simple expression

$$\Delta\mathcal{C}_A(\alpha_1) - \Delta\mathcal{C}_A(\alpha_2) = \frac{S}{2\pi^2} \log(\alpha_1^2/\alpha_2^2). \quad (4.136)$$

That is, the total shift in the complexity caused by the overshoot scales with S , the entanglement entropy between the two CFTs in the thermofield double state (1.21). The Δ for the complexities in this difference indicates that we are subtracting two copies of the vacuum complexity. This subtraction removes the α dependence of the UV divergent contributions, which is not captured in the time derivative $d\mathcal{C}_A/d\tau$.³¹ Of course, we should also recall that the total holographic complexity diverges in this late time limit, since it is growing linearly with time.

As we first noted in eq. (4.46), we should choose $\alpha = L/\ell$ in order that our general results for $d\mathcal{C}_A/d\tau$ can be fully expressed in terms of boundary quantities. That is, the argument of the logarithm in eq. (4.46) contains an errant factor of the AdS scale, which is not a quantity that the boundary CFT should know about, but this can be eliminated using our freedom in choosing α . However, this choice for α also introduces some new scale ℓ in the boundary theory. It is reassuring that precisely the same situation arises in the UV divergences of holographic complexity [65]. That is, the contributions to the gravitational action coming from the joints where the null boundaries intersect the asymptotic cutoff surface also introduce logarithms where the argument contains the combination L/α , as in eq. (4.46). Of course, choosing $\alpha = L/\ell$ leaves us with the question of what the most appropriate choice for ℓ would be. While the ambiguity left in choosing ℓ may have originally seemed problematic, it was recently found that precisely the same ambiguity appears in complexity models for quantum field theory [38, 39] where the complexity of ground states of free

³¹From [65], the leading UV behaviour is $[\mathcal{C}_A]_{UV}(\alpha_1) - [\mathcal{C}_A]_{UV}(\alpha_2) \simeq -\frac{L^{d-1}}{4\pi^2 G_N} \frac{V}{\delta^{d-1}} \log(\alpha_1^2/\alpha_2^2)$.

scalar field theories were examined.³² Further let us add that setting $\ell = e^\sigma \delta$, where σ is some numerical factor and δ is the short-distance cutoff in the boundary theory, was a convenient choice because it removed an extra logarithmic factor in the leading UV divergence. However, our results show that with this choice, $d\mathcal{C}_A/d\tau$ would depend on the short-distance cutoff, *i.e.*, an apparently IR contribution to the complexity would now depend on the UV cutoff.

To close our discussion, we would like to return to our calculations of the complexity of charged AdS black holes. In particular, in section 4.4 (and appendix B.3), we found that the complexity of formation diverged for extremal charged black holes. Both these results appeared using either the CA or CV conjectures. We stress that in the complexity of formation, there was still a cancellation of the UV divergences associated with the asymptotic boundary. Instead this divergence was a new IR divergence, associated with the infinitely long throat of the extremal black holes. Further, the results in section 4.4 indicate that the rate of change of the complexity vanishes for extremal black holes. If one considers the CA predictions, we find that extremal black holes with finite chemical potential has these IR divergences, while systems with zero chemical potential and zero temperature (*i.e.*, extremal hyperbolic black holes without any charge) have finite contributions to the complexity from the IR.³³ In order to illustrate these results, figure 4.15 shows a schematic phase diagram for the hyperbolic black holes for $d = 4$, in terms of the y and z variables introduced in eq. (4.101). There is a line of states at $y = 1$ with finite chemical potential and zero temperature with infinite complexity, while the states with zero chemical potential ends in a point $y = 1, z = \sqrt{2}$ with finite complexity.

Combining these results suggests a ‘Third Law of Complexity’.³⁴ That is, the corresponding ‘extremal’ thermofield double states (4.94) at zero temperature and finite chemical potential are infinitely complex compared to the finite temperature states. Hence no physical process should be able to produce the extremal states in a finite amount of time. It would be interesting to further test this idea by examining the complexity of extremal spinning black holes [168, 169].

³²The complexity for a free scalar quantum field theory in the time-dependent thermofield double state, and the similarities and differences with the holographic results presented in this chapter, is discussed in [49]. We will briefly comment some of these results in section 7.1 of chapter 7.

³³We might add that using the CV proposal actually yields a similar IR divergence for these black holes as discussed in chapter 3.

³⁴We thank Henry Maxfield and Robie Hennigar for independently suggesting this connection.

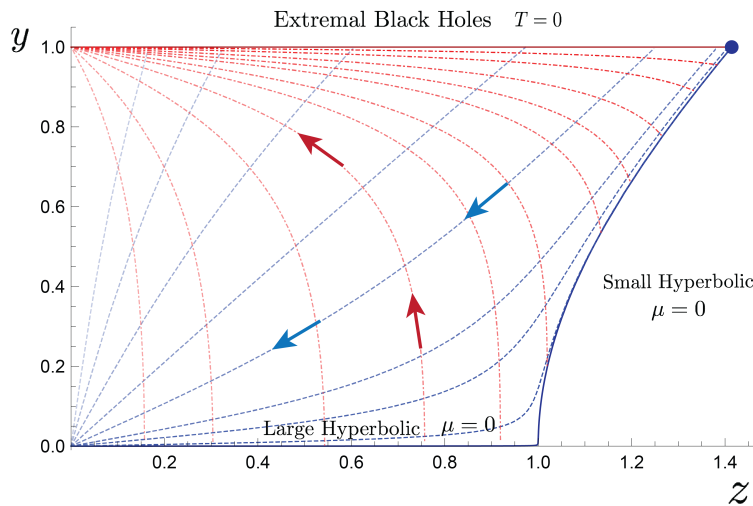


Figure 4.15: Lines of constant μR (dashed blue) and constant TR (dot-dashed red) for the hyperbolic black hole in $d = 4$, with $y = \frac{r_-}{r_+}$ and $z = \frac{L}{r_+}$. The temperature and chemical potential increase as one moves towards the left, as indicated by the arrows. The line of extremal black holes at $y = 1$ with finite chemical potential has states with infinite complexity. However, the extremal black hole represented by the blue dot with coordinates $y = 1, z = \sqrt{2}$ is the small uncharged extremal hyperbolic black hole, with zero chemical potential and finite complexity (using the CA proposal).

Chapter 5

Holographic Complexity in Vaidya Spacetimes: One-sided black holes

In this chapter we study the time evolution of holographic complexity in Vaidya shock wave spacetimes [170–172], with a collapsing shell of null matter in asymptotic AdS spacetimes. In fact, holographic complexity has already been studied for these geometries both for one-sided black holes, *e.g.*, [87, 173], where the shell is injected into empty AdS space, and for two-sided black holes, *e.g.*, [32–34, 174], where the shell falls into an existing eternal black hole. In the present chapter, we focus on the case of black hole formation, *i.e.*, one-sided black holes, and we will also consider shock waves falling into an eternal black hole in the next chapter. First, we demonstrate that the null fluid action vanishes on-shell, and hence does not contribute to the WDW action. The standard prescription to evaluate the WDW action chooses the generators of the null boundaries to be affinely parametrized [63]. However, we demonstrate that this prescription yields unsatisfactory results, *e.g.*, the complexity actually decreases in the case of a two-dimensional boundary CFT. This situation can be corrected by supplementing the gravitational action with an additional counterterm on the null boundaries. This counterterm was introduced in [63] to establish the invariance of I_{WDW} under reparametrizations of the null boundaries. For stationary spacetimes, the addition of this counterterm does not significantly change the properties of the holographic complexity discussed in the previous chapters. However, it appears to be an essential ingredient of the CA proposal (1.24) if the WDW action is to properly describe the holographic complexity of dynamical spacetimes, such as the Vaidya geometries. We also evaluate the holographic complexity for these spacetimes using the CV proposal (1.23) and compare the behaviour of the complexity for these two approaches. Our results are stated for general spacetime dimensions, as well as for both planar and spherical horizons.

The remainder of the chapter is organized as follows: In section 5.1, we begin by constructing an action for a null fluid and we demonstrate that the on-shell fluid action vanishes. While this simplifies the evaluation of the WDW action, in section 5.1.2, we carefully examine the contribution of the region containing a narrow shell of null fluid and show that it vanishes as the width of the shell shrinks to zero. Hence with an infinitely thin shell, the WDW action can be evaluated as the sum of the actions for two separate regions, the first inside the shell and the second outside the shell. In section 5.1.3, we consider the counterterm for null boundaries and consider its contribution in presence of a collapsing shell of null fluid. In section 5.2, we study the evolution of the holographic complexity, using both the CA and CV conjectures, in the formation of a black hole modelled by the Vaidya geometry for a null shell collapsing into the AdS vacuum spacetime. In section 5.3, we briefly discuss our results and indicate some possible future directions.

This chapter is adapted from [67].

5.1 Null Fluid and the Vaidya Geometry

We start by introducing the background spacetime for our present studies of holographic complexity, namely the AdS-Vaidya spacetime. Vaidya geometries are a special class of metrics which among other things provide an analytic description of the formation of black holes by a gravitational collapse [170, 171]. The collapse that can be studied here is generated by sending in a homogeneous shell composed of null fluid (or null dust), and the construction is easily extended to the case of asymptotically AdS boundary conditions, *e.g.*, [172]. In the latter holographic setting, the limit of sending in an infinitely thin, spherically symmetric shell of matter with finite energy has been studied extensively — *e.g.*, see [175–184].

We will be studying holographic complexity for a d -dimensional boundary CFT dual to an asymptotically AdS $_{d+1}$ Vaidya spacetime with a metric given by

$$ds^2 = -F(r, v) dv^2 + 2 dr dv + r^2 d\Sigma_{k, d-1}^2$$

$$\text{with } F(r, v) = \frac{r^2}{L^2} + k - \frac{f_p(v)}{r^{d-2}}. \quad (5.1)$$

If we fix the profile $f_p(v) = \omega^{d-2}$ to be a fixed constant, these metrics would correspond precisely to the black hole geometries in $d \geq 3$ for which the holographic complexity was studied in the previous chapters.¹ In particular, they are written in terms of the

¹It is straightforward to extend these metrics to the special case of $d = 2$, and we treat the corresponding process of BTZ black hole formation separately in section 5.2.

Eddington-Finkelstein coordinate v , parameterizing ingoing null rays. Further, L denotes the AdS curvature scale while k indicates the curvature of the horizon² situated at $r = r_h$ as given by eq. (6.11). However, the profile $f_p(v)$ may be taken from a large class of functions and then the metric (5.1) describes the collapse of a shell of null fluid. Generally, one would require that the profile is positive to ensure that the total mass is positive at all times,³ and monotonically increasing so that the energy density of the shell is everywhere positive — see below. As an example, consider the profile

$$f_p(v) = \omega_1^{d-2} (1 - \mathcal{H}(v - v_s)) + \omega_2^{d-2} \mathcal{H}(v - v_s), \quad (5.2)$$

where $\mathcal{H}(v)$ is the Heaviside step function. This profile describes an infinitely thin shell collapsing along the null surface $v = v_s$, and it generates a sharp transition connecting one black hole geometry with mass proportional to ω_1^{d-2} to another black hole with mass proportional to ω_2^{d-2} . In section 5.2, we will choose $\omega_1 = 0$ in which case this profile (5.2) corresponds to a shell collapsing into the AdS vacuum and forming a (one-sided) black hole.

5.1.1 Action for a Null Fluid

To evaluate the holographic complexity using the CA conjecture, we need to take into account the action of the matter fields in the collapsing shell. Hence, we present here a construction of the action principle for a null fluid, which is inspired in part by the fluid actions given in [185, 186].⁴ Let us also note that, a null fluid action was also constructed in [189] using a complementary set of variables.⁵ Further, in a particular limit, it is also possible to use a massless scalar field as the source in the Vaidya metric [175].⁶

²As usual, k takes three different values, $\{+1, 0, -1\}$, which correspond to spherical, planar, and hyperbolic horizon geometries, respectively. Following the notation of the previous chapters, we will use $\Omega_{k,d-1}$ to denote the dimensionless volume of the corresponding spatial geometry in the expressions below. For $k = +1$, this is just the volume of a $(d-1)$ -dimensional unit sphere, *i.e.*, $\Omega_{1,d-1} = 2\pi^{d/2}/\Gamma(d/2)$, while for hyperbolic and planar geometries, we must introduce an infrared regulator to produce a finite volume.

³In fact, the stress-tensor depends on the derivative of the profile function with respect to v (see eq. (5.9) below), so that one should choose the profile to increase monotonically to ensure the energy density is everywhere positive. Note that for $k = -1$, the mass can take negative values in a restricted range.

⁴There is an enormous literature on the subject of the action principle for relativistic fluids, *e.g.*, see [187, 188] for further discussion of perfect fluids.

⁵We note that the on-shell action also vanishes using this alternative approach.

⁶However, this description breaks down near the singularity, *i.e.*, the solution is not well approximated by the Vaidya metric there. Therefore we did not adopt this approach since in general, the near-singularity region makes a finite contribution to the holographic complexity in CA calculations.

The stress tensor of a null fluid takes the following simple form

$$T_{\mu\nu} = \varepsilon(x^\mu) \ell_\mu \ell_\nu, \quad (5.3)$$

where ℓ^μ is a null vector, *i.e.*, $\ell^\mu \ell_\mu = 0$. We can compare the above expression to the stress tensor for a conventional relativistic fluid: $T_{\mu\nu} = (\varepsilon + p)u_\mu u_\nu + p g_{\mu\nu}$ where ε and p are the local energy density and pressure, respectively. Further, u^μ is the local four-velocity of the fluid elements, with $u^\mu u_\mu = -1$. Hence eq. (5.3) can be thought of as the limit where the fluid velocity becomes null and the pressure vanishes, *i.e.*, $u^\mu \rightarrow \ell^\mu$ and $p = 0$. Now one can show that the on-shell action for a conventional fluid is simply an integral of the local pressure [185] and hence this result suggests that the on-shell action for a null fluid should vanish. We demonstrate below this intuitive result is in fact correct. We follow in part the construction in [186], but adapt it to describe the null fluid stress tensor (5.3).

We take the following ansatz for the fluid action

$$I_{\text{fluid}} = \int d^{d+1}x \sqrt{-g} \mathcal{L}_{\text{fluid}} \quad \text{where} \quad \mathcal{L}_{\text{fluid}}(\lambda, \phi, s, \ell^\mu, g_{\mu\nu}) = \lambda g_{\mu\nu} \ell^\mu \ell^\nu + s \ell^\mu \partial_\mu \phi. \quad (5.4)$$

This action involves a number of auxiliary fields, beginning with λ which is a Lagrange multiplier imposing the constraint that ℓ^μ is null on shell. With only the first term in the Lagrangian, we would obtain equations of motion which set $\ell^\mu = 0$ (or $\lambda = 0$) everywhere, and hence the corresponding stress tensor would also vanish. Therefore, the second term, involving a contraction of ℓ^μ with the derivative of a new scalar ϕ , is added in eq. (5.4). The field s can in principle be reabsorbed with a redefinition of ℓ^μ (and in this sense it represents a redundancy in the description) but we will keep it to allow for an arbitrary rescaling of ℓ^μ . The equations of motion for the full action (5.4) are:

$$\frac{1}{\sqrt{-g}} \frac{\delta I_{\text{fluid}}}{\delta \lambda} = \ell_\mu \ell^\mu = 0, \quad (5.5a)$$

$$\frac{1}{\sqrt{-g}} \frac{\delta I_{\text{fluid}}}{\delta \ell^\mu} = 2\lambda \ell_\mu + s \partial_\mu \phi = 0, \quad (5.5b)$$

$$\frac{1}{\sqrt{-g}} \frac{\delta I_{\text{fluid}}}{\delta \phi} = -\nabla_\mu (s \ell^\mu) = 0, \quad (5.5c)$$

$$\frac{1}{\sqrt{-g}} \frac{\delta I_{\text{fluid}}}{\delta s} = \ell^\mu \partial_\mu \phi = 0. \quad (5.5d)$$

These equations of motion provide us with an interpretation of the various fields. Of course, eq. (5.5a) enforces that ℓ^μ is null on-shell. Eq. (5.5b) indicates that the null ‘fluid velocity’ ℓ^μ and the gradient of ϕ point in the same direction and fixes the prefactor in

the proportionality relation between them in terms of the fields s and λ . In this sense, ϕ plays a role analogous to the velocity potential in potential flows [186]. Eq. (5.5c) implies that s has an interpretation of a conserved charge density. Since all fields are real (*i.e.*, the fluid is neutral) s can be understood as the entropy density [186]. Eq. (5.5d) follows automatically by contracting eq. (5.5b) with ℓ^μ . Varying the action with respect to the metric yields the stress tensor

$$T_{\mu\nu} \equiv -\frac{2}{\sqrt{-g}} \frac{\delta I_{\text{fluid}}}{\delta g^{\mu\nu}} = -s(\ell_\mu \partial_\nu \phi + \ell_\nu \partial_\mu \phi) - 2\lambda \ell_\mu \ell_\nu + g_{\mu\nu}(s \ell^\sigma \partial_\sigma \phi + \lambda \ell^\sigma \ell_\sigma). \quad (5.6)$$

On-shell, this expression reduces to the desired form

$$T_{\mu\nu} = 2\lambda \ell_\mu \ell_\nu, \quad (5.7)$$

and comparing to eq. (5.3), we see that λ is proportional to the energy density *i.e.*, $\varepsilon = 2\lambda$. Further, we note that imposing the equations of motion (5.5) yields a vanishing action (5.4), *i.e.*,

$$[I_{\text{fluid}}]_{\text{on-shell}} = 0. \quad (5.8)$$

Therefore, in evaluating the holographic complexity using the CA conjecture, our calculations reduce to evaluating the geometrical quantities in the gravitational action (2.10) with the Vaidya metric (5.1) and there will be no explicit contribution from the matter fields.

Upon substituting the metric (5.1) into the Einstein equations, only the vv component is nontrivial with

$$E_{vv} = \frac{(d-1)}{2r^{d-1}} f'_p(v) = 8\pi G_N T_{vv}. \quad (5.9)$$

We see from eq. (5.7) that this forces ℓ_μ to point in the v direction, *i.e.*, $\ell_\mu dx^\mu \propto dv$. Recall that retaining the parameter s in eq. (5.4) meant that we could rescale ℓ_μ at will, and we use this freedom to pick an affine parametrization of the form $\ell_\mu dx^\mu = dv$. In this case, combining eqs. (5.7) and (5.9) yields

$$\lambda = \frac{(d-1)}{32\pi G_N} \frac{f'_p(v)}{r^{d-1}}. \quad (5.10)$$

Since we identified $\lambda = 2\varepsilon$, we see here that the energy density is proportional to the derivative of the profile $f_p(v)$. Next, eq. (5.5c) yields

$$\partial_r(r^{d-1}s) = 0 \quad (5.11)$$

and as a result, the entropy density is given by

$$s = \frac{s_0}{r^{d-1}}. \quad (5.12)$$

In eq. (5.5b), we see that we must have $\phi = \phi(v)$ and the full equation becomes

$$s_0 \partial_v \phi + \frac{d-1}{16\pi G_N} f_p'(v) = 0. \quad (5.13)$$

Integrating this equation then produces

$$\phi = \phi_0 - \frac{(d-1)}{16\pi G_N s_0} f_p(v). \quad (5.14)$$

The integration constants, s_0 and ϕ_0 , will be fixed by the asymptotic boundary conditions for the matter.

5.1.2 Null Fluids & Complexity=Action

Having constructed a consistent null fluid action, which we showed vanishes on-shell, and found the corresponding source for the AdS-Vaidya geometry (5.1), we can begin to study the holographic complexity in these dynamical spacetimes. In particular, to study the complexity=action proposal (1.24), we showed that the null fluid action vanishes and so we need only to consider the gravitational action in the Vaidya spacetimes sourced by a collapsing shell of null fluid. Further, in section 5.2 and in chapter 6, we focus on the case where the shell is very thin, *i.e.*, the profile takes the form given in eq. (5.2). Using the additivity of the gravitational action [63], the problem essentially then factorizes into evaluating the action for two stationary spacetime regions: one before the collapse, characterized by the mass parameter ω_1 , and one after, characterized by ω_2 . However, in this section, we wish to verify that the null shell does not contribute to the Wheeler-DeWitt (WDW) action by first considering a thin but finite-width shell — see figure 5.1. That is, we split the spacetime into three regions: the stationary region before the collapse, the shell of finite width, and the stationary region after the collapse. In this section, we will only focus on the contribution of the null shell to the WDW action and we will confirm that in the limit that the width of the shell shrinks to zero this contribution vanishes, as expected. However, this analysis will also reveal a new boundary condition on the null normal to the past boundary of the WDW patch as it crosses the collapsing shell.

Recall that the CA conjecture (1.24) proposes that the complexity of the CFT state on some time slice Σ in the boundary is given by the bulk action evaluated on the corresponding WDW patch. For the Vaidya geometries with a null fluid, the bulk action becomes the sum of I_{fluid} given in eq. (5.4) and I_{grav} given by eq. (2.10). Recall that, as we showed in eq. (5.8), the fluid action I_{fluid} vanishes when evaluated for a solution of the fluid equations

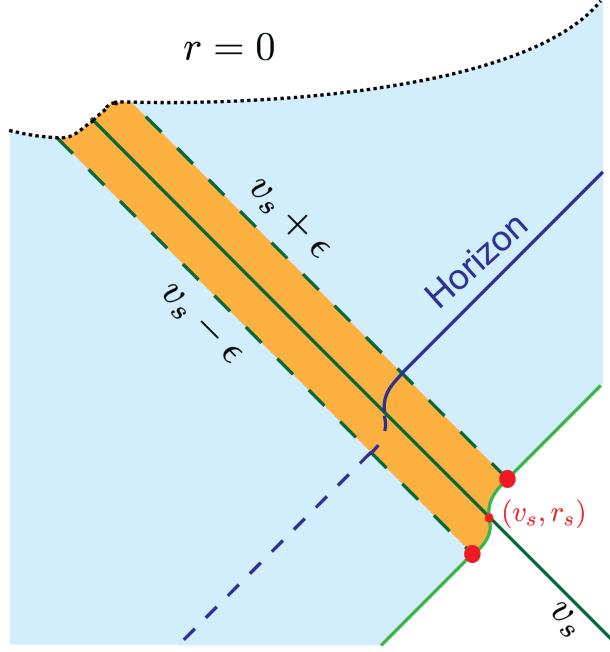


Figure 5.1: The null shell has a finite thickness 2ε around the null ray $v = v_s$. The portion enclosed by the WDW patch is shaded in orange. The contribution of the two joints indicated by red dots exactly cancels the surface term for the portion of the null boundary connecting the joints, where we have a time dependent $\kappa(v)$.

of motion (5.5a)-(5.5d). Of course, this does not imply that there is no consequence of the shock wave, but rather that its effect only appears through the backreaction of the geometry, namely, in forming the collapsing geometry (5.1).

As discussed above, we want to consider an AdS-Vaidya spacetime (5.1) where the shell of null fluid is narrow but still has a finite width. In particular, the shell will extend from $v_{\min} = v_s - \varepsilon$ to $v_{\max} = v_s + \varepsilon$, as shown in figure 5.1. Further, the shell will separate two stationary⁷ spacetime regions characterized by the mass parameter ω_1^{d-2} inside the shell and by ω_2^{d-2} outside the shell. The details of the profile $f_p(v)$ in the metric will not be important but we assume that it is continuous (and smoothly increasing). Of course, from integrating eq. (5.9) across the shell, the profile must also satisfy

$$f_p(v_s + \varepsilon) - f_p(v_s - \varepsilon) = \int_{\text{shell}} dv f'_p(v) = \omega_2^{d-2} - \omega_1^{d-2}. \quad (5.15)$$

⁷That is, ∂_t satisfies the usual Killing equations in either region.

With these choices, in the limit $\varepsilon \rightarrow 0$, the profile reduces to that given in eq. (5.2).⁸

Now we will evaluate the contribution of the null shell to the WDW action, but we will be particularly interested in the limit where the shell becomes infinitely thin, *i.e.*, $\varepsilon \rightarrow 0$. Let us examine the various terms in eq. (2.10). First, of course, the fluid action I_{fluid} vanishes on-shell, as we showed in the previous section. The bulk term in I_{grav} is (approximately) proportional to the volume of the shell and so vanishes in the limit that $\varepsilon \rightarrow 0$. Similarly evaluating the GHY term at the $r = 0$ singularity (following the prescription in chapter 3) yields a result which vanishes as $\varepsilon \rightarrow 0$. The Hayward joint terms are not relevant for this particular region and hence we turn to the null surface and null joint terms.

First, we must introduce (outward-directed) normals for the upper and lower null boundaries,⁹

$$\begin{aligned} v = v_s + \varepsilon & : & k_\mu^{s+} dx^\mu &= \beta dv , \\ v = v_s - \varepsilon & : & k_\mu^{s-} dx^\mu &= -\beta dv . \end{aligned} \tag{5.16}$$

With this choice, these null normals are affinely parameterized and therefore the null surface term vanishes, *i.e.*, $\kappa = 0$, for these two boundaries. We might add that the null joint terms vanish where these boundaries meet the singularity at $r = 0$ because there the transverse volume vanishes for these two joints.

The final boundary for the shell region is a portion of the past null boundary of the WDW patch. From the metric (5.1), we can see that the normal to this boundary can be written as

$$k^\mu \partial_\mu = H(r, v) \left(\frac{2}{F(r, v)} \partial_v + \partial_r \right) , \tag{5.17}$$

where $F(r, v)$ is the usual metric function — see eq. (5.1). Note that with eq. (5.17), we are describing the null normal for the entire past null boundary $\mathcal{B}_{\text{past}}$. Hence in the regions beyond the shell, the metric function F simplifies to

$$F(r, v) = f_i(r) = \frac{r^2}{L^2} + k - \frac{\omega_i^{d-2}}{r^{d-2}} , \tag{5.18}$$

⁸Our calculations here are general enough to accommodate both black hole formation which we examine in section 5.2, and null shocks in an eternal black hole background which we will study in chapter 6

⁹We have chosen the same normalization constant β for the two normals to simplify the final result, *i.e.*, this choice ensures that the null joint terms exactly cancel with the surface term below. Of course, another choice would yield the same result for the total action of the WDW patch after summing with the relevant boundaries and joints for the portions of the WDW patch above/below the null shell, since these are all inner boundaries of the WDW patch that we have introduced. However, we note that if the two normals in eq. (5.16) were not normalized with the same constant, the null shell would make a nonvanishing contribution to the total action.

with $i = 1$ and 2 denoting the region inside ($v < v_{\min}$) and outside ($v > v_{\max}$) of the shell, respectively. Of course, across the shell, F depends on both r and v as shown in eq. (5.1). Further, we have introduced an overall factor $H(r, v)$ in eq. (5.17) to allow for the possibility that the normalization of the null normal changes when the past boundary crosses the shell of null fluid. For $v > v_{\max}$, we will set H to be a fixed constant, *i.e.*, $H(r, v) = \alpha$ to match the asymptotic boundary condition $k \cdot \hat{t} = -\alpha$ (see discussion above). As we will see below, this simple choice also ensures that $\kappa = 0$ on this outer portion of the past boundary. Similarly for $v < v_{\min}$, we set $H(r, v) = \tilde{\alpha}$ which is again a positive constant in order for the null generators to be affinely parametrized on the inner portion of the null boundary. However, we have taken the liberty to choose an independent constant $\tilde{\alpha}$ since this portion of the boundary never reaches asymptotic infinity. Expressing this normal (5.17) as a form, we have

$$k_\mu dx^\mu = H(r, v) \left(-dv + \frac{2}{F(r, v)} dr \right). \quad (5.19)$$

Then in the region above the shell where $F(r, v) = f_2(r)$, eq. (5.19) takes the expected form $k_\mu dx^\mu = -\alpha du \equiv -\alpha (dv - 2dr/f_2(r))$. That is, in the region above the null shell, the past null boundary $\mathcal{B}_{\text{past}}$ is a surface where the outgoing Eddington-Finkelstein coordinate is constant (see eqs. (5.37) and (5.39) below) and fixing H to be a constant ensures that κ vanishes there. Similarly in the region below the null shell, we find $k_\mu dx^\mu = -\tilde{\alpha} du$ and again $\kappa = 0$ on this portion of the past boundary.

On the other hand, because of the r and v dependence of $F(r, v)$ and $H(r, v)$ within the shell of null fluid, the null normal (5.17) will only be affinely parametrized on this portion of $\mathcal{B}_{\text{past}}$ with a special choice of H . We will return to this special choice below, but for now we consider more general possibilities for which $\kappa \neq 0$. In particular, using $k^\rho \nabla_\rho k_\mu = \kappa k_\mu$, we find

$$\begin{aligned} \kappa &= \left(\frac{2}{F} \partial_v + \partial_r \right) H(r, v) - \frac{2H}{F^2} \partial_v F(r, v) \\ &= k^\mu \partial_\mu \log H(r, v) - k^\mu \partial_\mu \log F(r, v) + H \partial_r \log F(r, v) \\ &= \frac{d}{d\lambda} \log \frac{H(r, v)}{F(r, v)} + \frac{H}{F} \partial_r F(r, v), \end{aligned} \quad (5.20)$$

where in the second line, we have used eq. (5.17) to express κ in terms of derivatives along the null boundary. In the final line, we have introduced λ , which parametrizes the null rays in the boundary such that $k^\mu = \partial x^\mu / \partial \lambda$. Note that in the extra term in the last line, there is a partial derivative with respect to r , but to evaluate κ , we must calculate this quantity on the null boundary.

The resulting surface term in the gravitational action is then¹⁰

$$\begin{aligned} I_\kappa &= \frac{1}{8\pi G_N} \int_{\mathcal{B}_{\text{past}}} d\lambda d^{d-1}\theta \sqrt{\gamma} \kappa \\ &= \frac{\Omega_{k,d-1}}{8\pi G_N} \int_{\mathcal{B}_{\text{past}} \cap \text{shell}} d\lambda r^{d-1} \left[\frac{d}{d\lambda} \log \frac{H(r,v)}{F(r,v)} + \frac{H}{F} \partial_r F(r,v) \right]. \end{aligned} \quad (5.21)$$

Now at the center of the shock (*i.e.*, $v = v_s$), the radial coordinate takes some value¹¹ $r = r_s$ and throughout the shell $r = r_s + \mathcal{O}(\varepsilon)$. Hence to leading order in ε/r_s , we can fix $r = r_s$ in the above integral, in which case the first term reduces to

$$\begin{aligned} I_{\kappa,1} &= \frac{\Omega_{k,d-1}}{8\pi G_N} r_s^{d-1} \int_{\lambda_{\min}}^{\lambda_{\max}} d\lambda \frac{d}{d\lambda} \log \frac{H(r,v)}{F(r,v)} + \mathcal{O}(\varepsilon/r_s) \\ &= \frac{\Omega_{k,d-1}}{8\pi G_N} r_s^{d-1} \log \frac{F(r_s, v_{\min}) H(r_s, v_{\max})}{F(r_s, v_{\max}) H(r_s, v_{\min})} + \mathcal{O}(\varepsilon/r_s). \end{aligned} \quad (5.22)$$

Now we must still evaluate the integral over the second term in eq. (5.21). Here it is convenient to convert this to an integration over v along the boundary using $dv/d\lambda = 2H/F$ from eq. (5.17). Then this contribution to the boundary term becomes

$$I_{\kappa,2} = \frac{\Omega_{k,d-1}}{16\pi G_N} \int_{v_{\min}}^{v_{\max}} dv \left[r^{d-1} \partial_r F(r,v) \right]_{r=h(v)}, \quad (5.23)$$

where we have expressed the null boundary as a constraint equation $r = h(v)$. Of course, for the present thin shell, we have $r \simeq r_s + \varepsilon \tilde{h}(v/r_s)$ where $\tilde{h}(v/r_s)$ is a smooth dimensionless function. Similarly, $\partial_r F$ remains finite across the shell,¹² and so we have $I_{\kappa,2} = \mathcal{O}(\varepsilon)$ since the range of integration is $\delta v = v_{\max} - v_{\min} = 2\varepsilon$. Therefore, in the limit $\varepsilon \rightarrow 0$, the surface term reduces to

$$I_\kappa = \frac{\Omega_{k,d-1}}{8\pi G_N} r_s^{d-1} \log \frac{2\beta \alpha}{f_2(r_s)} - \frac{\Omega_{k,d-1}}{8\pi G_N} r_s^{d-1} \log \frac{2\beta \tilde{\alpha}}{f_1(r_s)}, \quad (5.24)$$

¹⁰We would like to point out a crucial typo in [63] and [65]. In [63], there is a typo in the conventions established in appendix C (but not in the main text). In particular, in eq. (C1), the overall sign of the surface term for null boundaries should be flipped. Similarly, there should be an overall flip of the sign of this surface term in appendix A of [65], *i.e.*, the sign in front of the null boundary term in eq. (A.1) should be a plus.

¹¹Of course, this position matches that described in the main text for an infinitely thin shell to within $\mathcal{O}(\varepsilon)$.

¹²That is, $\partial_r F$ does acquire any terms proportional to a delta-function $\delta(v)$ in the limit $\varepsilon \rightarrow 0$.

where we have written the final result as a sum of two terms, in a suggestive manner.¹³ Note that in converting the expression in eq. (5.22) to the above result, we have used the fact that at either edge of the shell, $F(r, v)$ precisely matches the metric function $f_i(r)$ in the corresponding region beyond the shell, *e.g.*, $F(r, v_{\max}) = f_2(r)$. A similar matching applies for the normalization function, as we described above, *i.e.*, $H(r_s, v_{\max}) = \alpha$ and $H(r_s, v_{\min}) = \tilde{\alpha}$.

Now the final contribution to the action of the null shell comes from the null joints where the two edges (*i.e.*, $v = v_s \pm \varepsilon$) intersect the past boundary of the WDW patch (indicated by red dots in figure 5.1). Given the null normals in eqs. (5.16) and (5.17), it is straightforward to evaluate these contributions using the prescription given in [65] with the result

$$\begin{aligned} I_{\text{joint}} &= - \left[\frac{\Omega_{k,d-1}}{8\pi G_N} r^{d-1} \log \frac{\beta \alpha}{f_2(r)} \right]_{r=h(v_{\max})} + \left[\frac{\Omega_{k,d-1}}{8\pi G_N} r^{d-1} \log \frac{\beta \tilde{\alpha}}{f_1(r)} \right]_{r=h(v_{\min})} \\ &\stackrel{\varepsilon \rightarrow 0}{=} - \frac{\Omega_{k,d-1}}{8\pi G_N} r_s^{d-1} \log \frac{\beta \alpha}{f_2(r_s)} + \frac{\Omega_{k,d-1}}{8\pi G_N} r_s^{d-1} \log \frac{\beta \tilde{\alpha}}{f_1(r_s)} \end{aligned} \quad (5.25)$$

where $r = h(v)$ again denotes the position of $\mathcal{B}_{\text{past}}$. In the second line, we have used that within our narrow shell, the radial position of this boundary is fixed up to order ε corrections, *i.e.*, $r = h(v) \simeq r_s + \varepsilon \tilde{h}(v/r_s)$. Now we see that the two nonvanishing contributions to the action evaluated on the thin null shell precisely cancel! That is, combining eqs. (5.24) and (5.25), we have

$$I_{\text{shell}} \stackrel{\varepsilon \rightarrow 0}{=} I_{\kappa} + I_{\text{joint}} = 0. \quad (5.26)$$

Therefore we have shown that in the limit of an infinitely thin shell, evaluating the WDW action in the Vaidya spacetime (5.1) reduces to two separate calculations: one for evaluating the action I_2 of the region outside of the shell ($v > v_s$) and another for evaluating the action I_1 of the inside region ($v < v_s$).

Notice that our result (5.26) for the vanishing of the shell action did not require that we specify the value of $\tilde{\alpha}$, the normalization constant for the null normal on the portion of the past boundary $\mathcal{B}_{\text{past}}$ before the collapse. Hence we are left with an ambiguity in evaluating I_1 , the part of the WDW action coming from the region inside the null shell. This ambiguity is, of course, related to the ambiguities discussed in [63] and it arises here because our calculations left κ unspecified on the portion of the past boundary inside the

¹³Recall that β is the normalization constant for the normals to the surfaces $v = v_s \pm \varepsilon$ (see eq. (5.16)), but note that the $\log \beta$ terms cancel in the difference between the two terms in eq. (5.24).

shell — see eq. (5.20). As discussed above, the most natural way to fix this ambiguity is to simply set $\kappa = 0$. In fact, we already made this choice for all of the other null boundaries above and it is certainly possible to fix $\kappa = 0$ on $\mathcal{B}_{\text{past}}$ inside the shell as well. One would simply treat eq. (5.20) with $\kappa = 0$ as a (first order) differential equation for $H(r, v)$, or rather $H(\lambda)$ since we are only interested in the value of H on the null boundary. The integration constant in this equation is fixed by setting $H = \alpha$ at the upper edge of the shell, *i.e.*, at $v = v_{\text{max}}$. Solving the differential equation will then determine the value of $\tilde{\alpha}$ as the value that H reaches at the lower edge of the shell, *i.e.*, $v = v_{\text{min}}$. However, we can easily determine this value (at least in the limit $\varepsilon \rightarrow 0$) by examining the result for I_κ in eq. (5.24). If $\kappa = 0$ everywhere along the boundary, this contribution must vanish and so we must have

$$\tilde{\alpha} = \alpha \frac{f_1(r_s)}{f_2(r_s)}. \quad (5.27)$$

We might also observe that the sum of the null joint terms in eq. (5.25) also vanishes with this particular choice for $\tilde{\alpha}$. In any event, as expected, we see that fixing $\kappa = 0$ everywhere removes the ambiguity in evaluating I_1 by fixing the value of $\tilde{\alpha}$ along the corresponding portion of the past null boundary.

5.1.3 Counterterm for Null Boundaries

As we discussed above, various ambiguities arise in calculating the WDW action coming from contributions associated with the null boundaries [63]. We followed a standard approach suggested in [63] to fix the corresponding null normals, however, an alternate approach which was also suggested there was to add to the counterterm action in eq. (2.11). Including this surface term does not effect certain key results for the CA proposal, *e.g.*, the complexity of formation in chapter 3 or the late-time rate of growth for an eternal black hole in chapter 4. On the other hand, it was found to modify the structure of the UV divergences in an interesting way [190] and it also modifies the details of the transient behaviour in the time evolution for an eternal black hole discussed in chapter 4.¹⁴ We note that these previous studies involved stationary spacetimes, and we will see below and in chapter 6 that the inclusion of the counterterm is essential in dynamical spacetimes, such as the Vaidya geometries (5.1), in order to reproduce some key properties of complexity.

We will explore the effect of the counterterm (2.11) in detail in the next section, but here we will extend some of the previous calculations to include the contributions of this surface term. In particular, let us consider including this term on the past null boundary

¹⁴In particular, see appendices B.1 and B.4.

$\mathcal{B}_{\text{past}}$. In evaluating this contribution, the essential behaviour will be determined by the normalization function $H(r, v)$ appearing in the null normal (5.17). Hence, considering the limit $\varepsilon \rightarrow 0$,¹⁵ we have $H(r, v) = \alpha$ above the shell (*i.e.*, for $v > v_s$) and $H(r, v) = \tilde{\alpha}$ below the shell (*i.e.*, for $v < v_s$). Recall that $H(r, v)$ is only defined along the null boundary, and so in the following, it will be helpful to treat H as a function of the radial coordinate (along $\mathcal{B}_{\text{past}}$), *i.e.*,

$$H(r, v) = \alpha \mathcal{H}(r - r_s) + \tilde{\alpha} (1 - \mathcal{H}(r - r_s)) , \quad (5.28)$$

where \mathcal{H} stands for the Heaviside function. Further, the inner normalization constant $\tilde{\alpha}$ is determined by eq. (5.27). Further, from eq. (5.17), we have $dr/d\lambda = H(r, v)$. Hence we evaluate the null expansion (2.12) as

$$\Theta = \frac{H(r, v)}{r^{d-1}} \frac{d}{dr} (r^{d-1}) = \frac{(d-1)H(r, v)}{r} . \quad (5.29)$$

Now the counterterm contribution (2.11) becomes

$$I_{\text{ct}} = \frac{\Omega_{k,d-1}(d-1)}{8\pi G_N} \int_{r_{\text{min}}}^{r_{\text{max}}} dr r^{d-2} \log \left(\frac{(d-1)t_L H(r, v)}{r} \right) , \quad (5.30)$$

where we replaced $d\lambda = dr/H(r, v)$. The upper limit of the radial integral will be $r_{\text{max}} = L^2/\delta$, where δ is the short-distance cutoff in the boundary CFT. The lower limit r_{min} will depend on the details of the situation for which we are evaluating the holographic complexity. Using eq. (C.4), we may evaluate the integral in eq. (6.49) to find

$$\begin{aligned} I_{\text{ct}} = & \frac{\Omega_{k,d-1}}{8\pi G_N} r_{\text{max}}^{d-1} \left[\log \left(\frac{(d-1)t_L \alpha}{r_{\text{max}}} \right) + \frac{1}{d-1} \right] \\ & - \frac{\Omega_{k,d-1}}{8\pi G_N} r_{\text{min}}^{d-1} \left[\log \left(\frac{(d-1)t_L \tilde{\alpha}}{r_{\text{min}}} \right) + \frac{1}{d-1} \right] + \frac{\Omega_{k,d-1}}{8\pi G_N} r_s^{d-1} \log \left(\frac{\tilde{\alpha}}{\alpha} \right) \end{aligned} \quad (5.31)$$

and hence upon substituting for $\tilde{\alpha}$ using eq. (5.27), we find

$$I_{\text{ct}} = \dots + \frac{\Omega_{k,d-1}}{8\pi G_N} r_s^{d-1} \log \left(\frac{f_1(r_s)}{f_2(r_s)} \right) . \quad (5.32)$$

In this expression, we have focused on the contribution that appears where the past boundary crosses the null shell (*i.e.*, $r = r_s$). Note that this term appears similar to the expressions appearing in eq. (5.24) or (5.25) if we substituted $\tilde{\alpha} = \alpha$ in the latter. It will turn out that this particular surface contribution will play an essential role in determining the (proper) behaviour of the holographic complexity.

¹⁵The following results would remain unchanged if we first evaluate the counterterm contribution with a small but finite width and only take the limit $\varepsilon \rightarrow 0$ afterwards.

5.2 Complexity in Black Hole Formation

In this section, we study the case of a thin shell of null fluid collapsing in empty AdS to form a black hole. In these geometries describing a one-sided black hole, we evaluate the holographic complexity, using the Complexity=Action proposal in section 5.2.1, and the Complexity=Volume proposal in section 5.2.2. From the perspective of the boundary CFT, this geometry describes a quantum quench, *e.g.*, see [176–179, 191–193]. The CFT begins in the vacuum state and then, say, at $t = 0$, we act with a (homogeneous) operator which injects energy into the system creating an excited state.

The bulk geometry is described by eq. (5.1) with the profile

$$f_p(v) = \omega^{d-2} \mathcal{H}(v), \quad (5.33)$$

where $\mathcal{H}(v)$ is the Heaviside step function. This is a simplified version of the profile in eq. (5.2) where we set $\omega_1 = 0$ and $v_s = 0$, as well as $\omega_2 = \omega$. Here we focus on dimensions $d \geq 3$, and the special case of BTZ black holes (*i.e.*, $d = 2$) will be treated separately below. Hence the metric function F becomes

$$v < 0 : \quad F(r, v) = f_{\text{vac}}(r) = \frac{r^2}{L^2} + k, \quad (5.34)$$

$$v > 0 : \quad F(r, v) = f_{\text{BH}}(r) = \frac{r^2}{L^2} + k - \frac{\omega^{d-2}}{r^{d-2}}. \quad (5.35)$$

We consider these collapses for planar and spherical shells (and horizons), *i.e.*, $k = 0$ and $k = +1$.¹⁶ As noted above, these AdS-Vaidya geometries can be interpreted as the holographic dual of the quantum quenches described above for the boundary CFT in the d -dimensional geometry.¹⁷

$$ds_{\text{bdry}}^2 = -dt^2 + L^2 d\Sigma_{k,d-1}^2. \quad (5.36)$$

Here we have simply defined the boundary time $t = v$ at $r \rightarrow \infty$. In the regime $t > 0$ in the boundary CFT (*i.e.*, $v > 0$), the energy is determined as usual by the black hole mass from $f_{\text{BH}}(r)$ in eq. (5.35), *i.e.*, given by eq. (2.7). In this part of the geometry, we determine the horizon radius with $f_{\text{BH}}(r = r_h) = 0$ which corresponds to eq. (2.4). Then, using the

¹⁶The case $k = -1$ with hyperbolic spatial sections is somewhat different since a time slice only covers half of a constant time surface in the global AdS boundary, *e.g.*, see chapter 3. The present discussion could be extended to cover this case if shells of null fluid were injected symmetrically from both halves of a global boundary time slice.

¹⁷As is conventional, the AdS curvature scale L also appears here as the curvature scale of the boundary. However, a simple Weyl scaling in the boundary theory can be used to separate these two scales, see the conventions in chapter 4.

usual gravitational expressions, we can assign an effective temperature and entropy to the corresponding excited state as given by eqs. (2.6) and (2.8).

In the following, it will also be useful to construct the radial tortoise coordinates on each side of the shock wave as:

$$\begin{aligned}
v > 0 : \quad r_{\text{BH}}^*(r) &= - \int_r^\infty \frac{d\tilde{r}}{f_{\text{BH}}(\tilde{r})}, \\
v < 0 : \quad r_{\text{vac}}^*(r) &= - \int_r^\infty \frac{d\tilde{r}}{f_{\text{vac}}(\tilde{r})} = \begin{cases} -L^2/r & \text{for } k = 0 \\ L \left(\tan^{-1}(r/L) - \frac{\pi}{2} \right) & \text{for } k = +1 \end{cases},
\end{aligned} \tag{5.37}$$

where $f_{\text{BH}}(r)$ and $f_{\text{vac}}(r)$ are given in eqs. (5.35) and (5.34), respectively. Note that the sign is chosen in eq. (5.37) to ensure that $dr^* = dr/f$ and the range of integration ensures that the tortoise coordinates vanish at infinity, *i.e.*,

$$\lim_{r \rightarrow \infty} r_{\text{vac, BH}}^*(r) \rightarrow 0. \tag{5.38}$$

Now we can define an outgoing null coordinate u and an auxiliary time coordinate t as

$$u \equiv v - 2r^*(r), \quad t \equiv v - r^*(r). \tag{5.39}$$

Notice that these coordinates are discontinuous across the shell because $f(r)$ changes from the vacuum to a black hole spacetime, as in eqs. (5.34) and (5.35). Of course, r and the ingoing coordinate v are globally defined, but it is still useful to consider t and u if one properly matches these coordinates across the collapsing shell. In particular, we will represent the collapsing-shell geometries with Penrose diagrams, or rather ‘Penrose-like’ diagrams, as shown in figure 5.2. These diagrams can be smoothly ruled with lines of constant u and v . Since u is discontinuous, this introduces a(n unphysical) jump as the outgoing null rays cross the shell. The spacetime is, of course, continuous along this surface and the outgoing null rays are smooth, as can be seen by regulating the thin shell to have a small but finite thickness, as was discussed in section 5.1. Further, these jumps in the outgoing null rays can be removed by deforming the Penrose diagrams to the future or the past of the shell, but the undeformed figures are simpler to construct and we found that they provide a useful intuitive picture of the geometry.

In order to translate the bulk results into boundary quantities, it is useful to work in terms of the dimensionless variables (following chapter 4) defined as

$$x \equiv \frac{r}{r_h}, \quad z \equiv \frac{L}{r_h}. \tag{5.40}$$

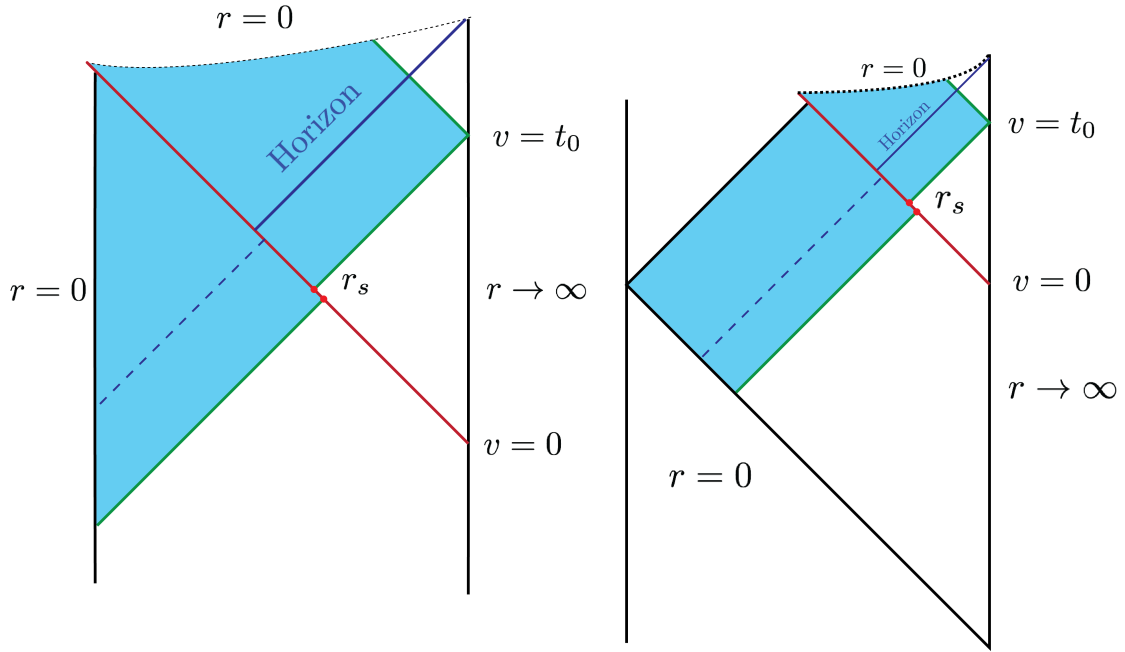


Figure 5.2: Penrose-like diagrams for the thin shell collapsing geometries, we represent spherical horizon collapse from global AdS (left) and planar horizon from Poincaré patch (right). In order to not distort the diagrams, we represent the discontinuity in the outgoing coordinate u by a jump while crossing the collapsing shell, *e.g.*, the dashed blue line indicates the extension of the event horizon into the region before the collapsing shell. We use r_s to denote the radial position where the null boundary of the WDW patch crosses the shock wave.

The temperature in eqs. (2.6) and (2.8) can be recast in terms of z as

$$LT = \frac{1}{4\pi z} (d + k(d-2)z^2), \quad (5.41)$$

or alternatively, this expression can be inverted in order to express z as a function of LT ,

$$z = \frac{d}{\sqrt{4\pi^2(LT)^2 - (d-2)dk + 2\pi LT}}. \quad (5.42)$$

Note that for the planar case (*i.e.*, $k = 0$), this expression simplifies $z = d/(4\pi LT)$. Now any result that depends on z can be regarded as a boundary quantity defined in terms of LT with eq. (6.20).

Further, following the notation in chapter 4, it is useful to define a dimensionless tortoise coordinate. We write

$$x^*(x, z) \equiv \frac{r_h}{L^2} r^*(r) = - \int_x^\infty \frac{dx}{\tilde{f}(x, z)}, \quad (5.43)$$

$$\text{where} \quad \tilde{f}(x, z) = z^2 f(r, r_h),$$

where $\tilde{f}(x, z)$ is the blackening factor written in terms of the dimensionless coordinates x and z and rescaled by z^2 . That is, combining eqs. (5.34), (5.35), (2.4) and (5.40), we find

$$\begin{aligned} v < 0 : \quad & \tilde{f}_{\text{vac}}(x, z) = x^2 + k z^2, \\ v > 0 : \quad & \tilde{f}_{\text{BH}}(x, z) = x^2 + k z^2 - \frac{1 + k z^2}{x^{d-2}}. \end{aligned} \quad (5.44)$$

We note that for the planar case (*i.e.*, $k = 0$), $\tilde{f}(x, z)$ is actually independent of z .

5.2.1 Complexity=Action

The CA proposal (1.24) suggests that we can calculate the complexity of the CFT state on some time slice Σ in the boundary by evaluating the action of the dual gravitational configuration on the corresponding WDW patch in the bulk. We have already introduced the null fluid and gravitational actions in section 5.1 — see eqs. (5.8) and (2.10). Further in section 5.1.2, we showed that in the limit of a thin collapsing shell of null fluid, the WDW action is given by the sum of the actions separately evaluated on the portion of the WDW patch outside of the shell and on the portion inside the shell. As we will see below,

this greatly simplifies the calculation since the spacetime geometry is stationary in each of these regions.

Let us begin by examining in more detail the structure of the WDW patch, as shown in the Penrose-like diagrams of the collapsing geometries in figure 5.2. We anchor the WDW patch to a constant time slice in the boundary, with some $t = t_0 \geq 0$ — recall that the collapsing shell starts at the asymptotic boundary at $t = 0$. The future null boundary of the WDW patch is then defined by the surface $v = t_0$ — see eqs. (5.38) and (5.39) — and this boundary segment terminates at the curvature singularity at $r = 0$. The past null boundary of the WDW patch is defined by $u = t_0 = v - 2r_{\text{BH}}^*(r)$, where the outgoing null coordinate is defined in eq. (5.39). However, at this point, we must recall from eq. (5.37) that the definition of the radial tortoise coordinate $r^*(r)$, and hence the null coordinate u , depends on whether we are to the future or the past of the collapsing shell. The null boundary of the WDW patch meets the collapsing shell at $r = r_s$ which is given by

$$2r_{\text{BH}}^*(r_s) + t_0 = 0, \quad (5.45)$$

where we are using the tortoise coordinate defined for $v \geq 0$, and it will be useful in the following to note that

$$\frac{dr_s}{dt_0} = -\frac{1}{2} f_{\text{BH}}(r_s). \quad (5.46)$$

Now v and r are continuous as we cross the collapsing shell, but since the form of the tortoise coordinate changes here, there is a jump in u (and in our Penrose diagrams). Hence to the past of the shell, the past boundary of the WDW patch is described by $u = -2r_{\text{vac}}^*(r_s) = v - 2r_{\text{vac}}^*(r)$, which then reaches $r = 0$ at $v = 2r_{\text{vac}}^*(0) - 2r_{\text{vac}}^*(r_s)$. In this description of the WDW patch, we have overlooked various cut-off surfaces, *e.g.*, at the UV boundary or at the curvature singularity, but these details will be the same as in chapter 3.

In our Vaidya geometry with an infinitely thin shell, the surface $v = 0$ naturally divides the WDW patch into two regions: 1) for $v < 0$, the geometry is simply the AdS vacuum, and 2) for $v > 0$, the geometry matches that of a static AdS black hole. In section 5.1.2, we smoothed out the geometry by giving the shell a (small) finite width and we were able to rigorously show that the action of the shell (within the WDW patch) vanishes when the width shrinks to zero. Hence in evaluating I_{WDW} , we can simply calculate the action on regions 1 and 2 separately, and then simply add the results together.

Action Calculation

The evaluation of the action (2.10) on the WDW patch was carefully analyzed in [63], and in calculating the various contributions below. The bulk integral can be written in the r, v coordinates as

$$I_{\text{bulk}} = -\frac{d\Omega_{k,d-1}}{8\pi L^2 G_N} \int_{\text{WDW}} r^{d-1} dr dv, \quad (5.47)$$

with the WDW patch as described above — see also figure 5.2. Integrating over v first, yields

$$I_{\text{bulk}} = -\frac{d\Omega_{k,d-1}}{8\pi L^2 G_N} \left[\int_0^{r_s} r^{d-1} (2r_{\text{vac}}^*(r_s) - 2r_{\text{vac}}^*(r) + t_0) dr - 2 \int_{r_s}^{\infty} r^{d-1} r_{\text{BH}}^*(r) dr \right]. \quad (5.48)$$

Using eq. (5.46) for dr_s/dt_0 , it is possible to show that the time derivative of this integral becomes

$$\frac{dI_{\text{bulk}}}{dt_0} = -\frac{\Omega_{k,d-1}}{8\pi L^2 G_N} r_s^d \left(1 - \frac{f_{\text{BH}}(r_s)}{f_{\text{vac}}(r_s)} \right). \quad (5.49)$$

We can write the above expression in terms of the black hole mass using eq. (2.7) and $d > 2$, which then leads to

$$\frac{dI_{\text{bulk}}}{dt_0} = -\frac{2M}{(d-1)} \frac{x_s^2}{(kz^2 + x_s^2)}, \quad (5.50)$$

where we have used the dimensionless coordinate $x_s \equiv r_s/r_h$.

We evaluate the GHY boundary term at the future singularity with the prescription discussed in chapter 3, but with total time lapse equal to t_0 . Therefore,

$$\begin{aligned} I_{\text{GHY}} &= -\lim_{r \rightarrow 0} \frac{\Omega_{k,d-1}}{16\pi G_N} r^{d-1} \left(\partial_r f_{\text{BH}}(r) + \frac{2(d-1)}{r} f_{\text{BH}}(r) \right) t_0 \\ \frac{dI_{\text{GHY}}}{dt_0} &= \frac{d\Omega_{k,d-1}}{16\pi G_N} \omega^{d-2} = \frac{dM}{(d-1)}. \end{aligned} \quad (5.51)$$

As usual, we demand that the null boundaries are affinely parametrized, which yields $\kappa = 0$. Hence the null surface terms do not contribute to the WDW action or its time derivative.

The only nonvanishing joint contributions to the time derivative of the holographic complexity arise where the past null boundary intersects with the collapsing shell, as indicated by the two big red dots in figure 5.2. These joints are codimension-two surfaces at the intersection of two null hypersurfaces, and so we need to define the appropriate null

normals. The null normal for the past boundary of the WDW patch was defined quite generally in eq. (5.19). For the present geometry described by eqs. (5.34) and (5.35), this expression becomes

$$k_\mu dx^\mu = \begin{cases} \alpha \left(-dv + \frac{2}{f_{\text{BH}}(r)} dr \right) & \text{for } r > r_s, \\ \tilde{\alpha} \left(-dv + \frac{2}{f_{\text{vac}}(r)} dr \right) & \text{for } r < r_s. \end{cases} \quad (5.52)$$

As we are dividing the WDW patch into two regions along the collapsing shell, we also need to introduce two (outward-directed) null normals which we denote

$$\begin{aligned} v > 0 & : & k_\mu^2 dx^\mu &= -\beta dv, \\ v < 0 & : & k_\mu^1 dx^\mu &= \beta dv, \end{aligned} \quad (5.53)$$

where β is some arbitrary normalization constant.¹⁸ Combining the two joint contributions of interest then yields

$$\begin{aligned} I_{\text{joint}} &= \frac{\Omega_{k,d-1}}{8\pi G_N} r_s^{d-1} \log \frac{2\beta\alpha}{f_{\text{BH}}(r_s)} - \frac{\Omega_{k,d-1}}{8\pi G_N} r_s^{d-1} \log \frac{2\beta\tilde{\alpha}}{f_{\text{vac}}(r_s)} \\ &= \frac{\Omega_{k,d-1} r_s^{d-1}}{8\pi G_N} \log \left[\frac{\alpha f_{\text{vac}}(r_s)}{\tilde{\alpha} f_{\text{BH}}(r_s)} \right]. \end{aligned} \quad (5.54)$$

However, at this point we recall that if we demand that $\kappa = 0$ all along this past boundary, then the normalization constant $\tilde{\alpha}$ must be fixed as in eq. (5.27), which yields

$$\tilde{\alpha} = \alpha \frac{f_{\text{vac}}(r_s)}{f_{\text{BH}}(r_s)}, \quad (5.55)$$

for the present situation. However, we easily see that substituting this result into eq. (5.54) yields $I_{\text{joint}} = 0!$ Of course, this result might have been anticipated by realizing that the past null boundary is perfectly smooth and so without our division of the WDW patch into various regions the only way in which this boundary could contribute to I_{WDW} would be through the κ surface term. However, if we demand that $\kappa = 0$ everywhere along this boundary, then all of the contributions coming from this surface must vanish. Of course, since I_{joint} vanishes, it will not contribute to the time derivative of the WDW action.

Time Dependence of Complexity, Version 1

Hence combining all of the terms in eq. (2.10), we found that there are only two nonvanishing contributions to the time derivative of the WDW action. These come from the

¹⁸We can compare these normals to those in eq. (5.16) for the edges of the finite-width shell.

bulk integral in eq. (5.49), and GHY surface term on the spacelike boundary at the future singularity in eq. (5.51). Combining these two expressions, we find (for $d > 2$)

$$\frac{d\mathcal{C}_A}{dt_0} = \frac{d-2}{d-1} \frac{M}{\pi} \left(1 + \frac{2}{d-2} \frac{kz^2}{kz^2 + x_s^2} \right). \quad (5.56)$$

For $k = 0$, this expression simplifies and the rate of growth of the complexity is simply a constant,

$$\left. \frac{d\mathcal{C}_A}{dt_0} \right|_{k=0} = \frac{d-2}{d-1} \frac{M}{\pi}. \quad (5.57)$$

However, we observe that this growth rate is much lower than the late time limit found in an eternal black hole background [33, 34] *i.e.*, $d\mathcal{C}_A/dt_0|_{\text{eternal}} = 2M/\pi$ as $t_0 \rightarrow \infty$.

For $k = +1$, the rate acquires a time dependence through the coordinate x_s . At early times, x_s is close to the boundary, *i.e.*, $x_s \rightarrow \infty$ as $t_0 \rightarrow 0$, and hence the rate of change in eq. (5.56) starts at the same value of the planar geometry (5.57). On the other hand, at very late times, the meeting point approaches the horizon, *i.e.*, $x_s \rightarrow 1$ as $t_0 \rightarrow \infty$ and hence the growth rate approaches

$$\left. \frac{d\mathcal{C}_A}{dt_0} \right|_{\text{late time}} = \frac{d-2}{d-1} \frac{M}{\pi} \left(1 + \frac{2}{d-2} \frac{kz^2}{kz^2 + 1} \right). \quad (5.58)$$

Hence for spherical black holes (*i.e.*, $k = +1$), the late time limit yields a slightly larger growth rate than in the planar case. For very high temperatures, the increase is very small since in this regime the horizon radius is much larger than the AdS curvature scale and hence $z = L/r_h \ll 1$. The correction is largest at the Hawking-Page transition, for which $z = 1$ and we find $d\mathcal{C}_A/dt_0 = M/\pi$ at late times. Hence the late time limit in eq. (5.58) is always smaller than the corresponding result [33, 34] for the eternal black hole geometry with any d and for both $k = 0$ and $+1$. This mismatch may seem somewhat surprising since at late times, the WDW patch in figure 5.2 is almost entirely in region 2, where the geometry matches that of a static black hole, as given in eq. (5.35). Further, the above expressions suggest that the rate vanishes for $d = 2$. Strictly speaking the previous calculations must be redone for the case of BTZ black holes, but the new calculations reproduce $d\mathcal{C}_A/dt_0 = 0$ for $d = 2$ — see below.

We will see in a moment that adding the boundary counterterm (2.11) to the gravitational action restores the expected late time limit, however, we first examine the late and early time limits in more detail. In eq. (5.56), we have written the rate of complexity growth in terms of dimensionless boundary quantities. Hence, it is useful to write eq. (5.45)

as an equation determining x_s as a function of the time (normalized by the temperature),

$$2x_{\text{BH}}^*(x_s, z) + \frac{4\pi T t_0}{d + k z^2 (d - 2)} = 0, \quad (5.59)$$

where x_{BH}^* is given by eq. (5.43) with $\tilde{f}_{\text{BH}}(x, z)$ in eq. (5.44). Again, the dynamical variable in the problem is the (dimensionless) distance x_s , that ranges from infinity (*i.e.*, close to the asymptotic boundary) at early times, to one (*i.e.*, close to the event horizon) at late times.

Early times: We begin by examining the early time behaviour of the meeting point x_s , *i.e.*, immediately after the shell appears with $T t_0 \ll 1$. Again, we restrict the analysis to $d \geq 3$ and consider $d = 2$ separately below. From eq. (5.59), we can expand x_s for early times to find¹⁹

$$x_s = \frac{d + (d - 2)kz^2}{2\pi} \frac{1}{T t_0} - \frac{2\pi}{3} \frac{kz^2}{d + (d - 2)kz^2} T t_0 + \mathcal{O}(T^3 t_0^3). \quad (5.60)$$

Substituting the above expression into eq. (5.56) then yields

$$\left. \frac{dC_A}{dt_0} \right|_{\text{early time}} = \frac{d - 2}{d - 1} \frac{M}{\pi} + \frac{8\pi M}{d - 1} \left(\frac{kz^2}{d + (d - 2)kz^2} \right) T^2 t_0^2 + \mathcal{O}(T^4 t_0^4). \quad (5.61)$$

Hence to leading order, we recover the limit given by eq. (5.57) and above, we see that the rate begins to grow at order $(T t_0)^2$.

Late times: To examine the late time behaviour, we follow the arguments in chapter 4. Suppose that we rewrite the rescaled blackening factor by factoring out the root corresponding to the horizon. In this way, we find

$$\tilde{f}(x) = \tilde{F}(x)(x - 1), \quad \text{where} \quad \tilde{F}(x = 1) = d + k(d - 2)z^2. \quad (5.62)$$

In the second expression, we have used eq. (5.41) to evaluate the function $\tilde{F}(x = 1)$ at the horizon. At late times x_s approaches 1, and we can solve the meeting condition in eq. (5.59) in this limit by using the decomposition

$$\frac{1}{\tilde{f}(x, z)} = \frac{1}{\tilde{F}(1)(x - 1)} + \frac{\tilde{F}(1) - \tilde{F}(x)}{\tilde{F}(1)\tilde{F}(x)(x - 1)}. \quad (5.63)$$

¹⁹The corrections in eqs. (5.60) and (5.75) are slightly different for $d = 3$. In particular, we find $x_s(d = 3) = \frac{3+kz^2}{2\pi} \frac{1}{T t_0} - \frac{2\pi kz^2}{3(3+kz^2)} T t_0 + \frac{\pi^2(1+kz^2)}{(3+kz^2)^2} (T t_0)^2 + \mathcal{O}(t_0^3 T^3)$, and $\left. \frac{dC_A}{dt_0} \right|_{d=3} = \frac{2M}{\pi} \left(\frac{1}{2} + \frac{2\pi^3(1+kz^2+1)}{(3+kz^2)^3} \right) T^3 t_0^3 + \mathcal{O}(t_0^6 T^6)$. Note the additional $\mathcal{O}(T^2 t_0^2)$ term in the first expression while the $\mathcal{O}(T^5 t_0^5)$ correction vanishes in the second expression.

Then we can write the tortoise coordinate as

$$x^*(x) = \frac{1}{\tilde{F}(1)} \log \frac{|x-1|}{\tilde{\ell}} + \int^x d\tilde{x} \frac{\tilde{F}(1) - \tilde{F}(\tilde{x})}{\tilde{F}(1)\tilde{F}(\tilde{x})(\tilde{x}-1)}, \quad (5.64)$$

and $\tilde{\ell}$ is some integration constant. With this decomposition, we can solve eq. (5.59) for late times

$$x_s = 1 + c_1 e^{-2\pi T t_0} + \dots, \quad (5.65)$$

and the constant c_1 is given by

$$c_1 = \lim_{x_{max} \rightarrow \infty} (x_{max} - 1) e^{\int_1^{x_{max}} d\tilde{x} \frac{\tilde{F}(1) - \tilde{F}(\tilde{x})}{\tilde{x}(\tilde{x}-1)}}, \quad (5.66)$$

which is a (finite) positive constant.

Substituting eq. (5.65) into the growth rate (5.56), the late time limit becomes

$$\left. \frac{d\mathcal{C}_A}{dt_0} \right|_{\text{late time}} = \frac{M(d-2+dkz^2)}{\pi(d-1)(kz^2+1)} - \frac{4c_1 M kz^2}{\pi(d-1)(kz^2+1)^2} e^{-2\pi t_0 T} + \mathcal{O}(e^{-4\pi T t_0}). \quad (5.67)$$

The first term matches our previous expression (5.58) for the late time limit. The second term shows that the limiting growth rate is approached from below, and that this behaviour corresponds to an exponential decay controlled by the thermal length scale, *i.e.*, $1/T$.

In fact, given the expression in eq. (5.56), it is not hard to show that the growth rate (for $k = +1$) begins at $t_0 = 0$ with value given in eq. (5.57) and then rises monotonically to reach the late time rate (5.58) in a time of order $t_0 \sim 1/T$. Further, it is straightforward to explicitly evaluate eq. (5.56) and plot $d\mathcal{C}_A/dt_0$ as a function of time in various examples. Below in figures 5.3 and 5.4, we show the growth rates (both without and with the counterterm) for various temperatures with $d = 2$, and with $d = 3$ and 4, respectively.

Time Dependence of Complexity, Version 2

Next, we wish to examine the effect of adding the counterterm (2.11) for null boundaries to the gravitational action. Recall that for an eternal black hole background, adding this counterterm did not affect the late-time rate of growth of the holographic complexity but it did change the details of the transient behaviour in the time evolution, as discussed in chapter 4.

In principle, this term should be evaluated on both the future and past null boundaries of the WDW patch — see figure 5.2. However, the future boundary is entirely in region

2, where the geometry is identical to that of the eternal black hole. In particular, in this region, the time t is a Killing coordinate and so the contribution of the counterterm on the future boundary is unchanged under time translations. That is, on this boundary, the counterterm does not contribute to the complexity growth rate.

Therefore we only evaluate the counterterm on the past null boundary $\mathcal{B}_{\text{past}}$. This calculation was discussed in section 5.1.3 and the required integral is given by eqs. (C.4) and (6.49). For the present case, the limits of integration are $r_{\text{max}} = L^2/\delta$ and $r_{\text{min}} = 0$. Hence the result in eq. (6.50) becomes

$$I_{\text{ct}} = \frac{\Omega_{k,d-1}}{8\pi G_N} \frac{L^{2(d-1)}}{\delta^{d-1}} \left[\log\left(\frac{(d-1)t_L \delta \alpha}{L^2}\right) + \frac{1}{d-1} \right] + \frac{\Omega_{k,d-1}}{8\pi G_N} r_s^{d-1} \log\left(\frac{f_{\text{vac}}(r_s)}{f_{\text{BH}}(r_s)}\right), \quad (5.68)$$

where implicitly we have assumed that $\kappa = 0$ and so the normalization constant $\tilde{\alpha}$ is fixed by eq. (5.27). The first term above contributes to the UV divergences in the complexity [65, 190] and is independent of t_0 . Hence only the second term contributes to the growth rate through the variation of r_s , the radius where the past boundary meets the null shell. In particular, we recall from eq. (5.46) that

$$\frac{dr_s}{dt_0} = -\frac{1}{2} f_{\text{BH}}(r_s). \quad (5.69)$$

As a result, the time derivative of eq. (5.68) becomes

$$\begin{aligned} \frac{dI_{\text{ct}}}{dt_0} = & -\frac{\Omega_{k,d-1}(d-1)}{16\pi G_N} r_s^{d-2} f_{\text{BH}}(r_s) \log\left(\frac{f_{\text{vac}}(r_s)}{f_{\text{BH}}(r_s)}\right) \\ & -\frac{\Omega_{k,d-1}}{16\pi G_N} r_s^{d-1} f_{\text{BH}}(r_s) \left[\frac{f'_{\text{vac}}(r_s)}{f_{\text{vac}}(r_s)} - \frac{f'_{\text{BH}}(r_s)}{f_{\text{BH}}(r_s)} \right]. \end{aligned} \quad (5.70)$$

Expressing this result in terms of the dimensionless quantities (5.40) then yields

$$\frac{dI_{\text{ct}}}{dt_0} = \frac{dM}{d-1} \left(1 - \frac{2kz^2}{x_s^2 + kz^2} \right) + \frac{M x_s^{d-2} \tilde{f}_{\text{BH}}(x_s, z)}{\pi(1+kz^2)} \log\left(\frac{\tilde{f}_{\text{BH}}(x_s, z)}{\tilde{f}_{\text{vac}}(x_s, z)}\right), \quad (5.71)$$

using eq. (2.4) for the mass, and the expression for $\tilde{f}(x, z)$ in eq. (5.44).

Hence when the action (2.10) is supplemented by the counterterm (2.11), the total time derivative of the holographic complexity is given by combining the expressions in eqs. (5.49), (5.51) and (5.70). Alternatively, we can simply add eq. (5.71) to the previous result in eq. (5.56), which yields

$$\frac{d\mathcal{C}'_{\Lambda}}{dt_0} = \frac{2M}{\pi} + \frac{M x_s^{d-2} \tilde{f}_{\text{BH}}(x_s, z)}{\pi(1+kz^2)} \log\left(\frac{\tilde{f}_{\text{BH}}(x_s, z)}{\tilde{f}_{\text{vac}}(x_s, z)}\right) \quad (5.72)$$

for $t_0 \geq 0$. The most striking feature of the new result is that at late times, the new rate approaches the expected limit, *i.e.*, $d\mathcal{C}'_{\Lambda}/dt_0|_{t_0 \rightarrow \infty} = 2M/\pi$ [33, 34]. In particular, as $t_0 \rightarrow \infty$, r_s approach the horizon sending the blackening factor $f_{\text{BH}}(r_s)$ to zero (*i.e.*, at late times, $x_s \rightarrow 1$ and $\tilde{f}_{\text{BH}}(x_s \rightarrow 1, z) \rightarrow 0$) and hence the second term in the above expression vanishes.

Further we note that at $t_0 = 0$, r_s begins at asymptotic infinity. As t_0 increases from zero, r_s decreases monotonically — see eq. (5.69) — and at late times, $r_s \rightarrow r_h$. Using the explicit form of the blackening factors in eqs. (5.34) and (5.35), it is also straightforward to show that the second term in eq. (5.72) is always negative and that $d^2\mathcal{C}'_{\Lambda}/dt_0^2 \geq 0$.²⁰ Therefore $d\mathcal{C}'_{\Lambda}/dt_0$ is monotonically increasing and approaches the late time limit from below. These features contrast with the corresponding results for the eternal black hole in chapter 4, and as previously noted in [173], for the process of black hole formation, $d\mathcal{C}'_{\Lambda}/dt_0$ respects the proposed bound on the rate of complexity growth suggested in [33, 34], *i.e.*, $d\mathcal{C}'_{\Lambda}/dt_0 \leq 2M/\pi$.

We observe that for $k = 0$, eq. (5.72) simplifies somewhat yielding

$$\frac{d\mathcal{C}'_{\Lambda}}{dt_0} = \frac{2M}{\pi} - \frac{M}{\pi} (x_s^d - 1) \log \left[\frac{x_s^d}{x_s^d - 1} \right], \quad (5.73)$$

where x_s is given by

$$\left(\frac{1}{x_s^d - 1} \right)^{1/d} {}_2F_1 \left(\frac{1}{d}, \frac{1}{d}; 1 + \frac{1}{d}; -\frac{1}{x_s^d - 1} \right) = \frac{2\pi T t_0}{d}. \quad (5.74)$$

Next let us apply the previous analysis for early and late times to evaluate the behaviour of the complexity evaluated with the modified action. In both cases, we focus on $d \geq 3$ and consider the special case $d = 2$ in detail afterwards.

Early times: Here, we apply eq. (5.60) to evaluate the complexity growth rate in eq. (5.72) for $T t_0 \ll 1$,

$$\left. \frac{d\mathcal{C}'_{\Lambda}}{dt_0} \right|_{\text{early time}} = \frac{2M}{\pi} \left(\frac{1}{2} + \frac{(2\pi)^d}{4} \frac{1 + kz^2}{(d + (d-2)kz^2)} T^d t_0^d + \mathcal{O}(T^{d+2} t_0^{d+2}) \right). \quad (5.75)$$

Therefore, we see that for $d \geq 3$, the early time behavior is given by M/π , for both spherical and planar black holes, *i.e.*,

$$\left. \frac{d\mathcal{C}'_{\Lambda}}{dt_0} \right|_{t_0 \rightarrow 0^+} = \frac{M}{\pi}. \quad (5.76)$$

²⁰Recall that we are focusing on $k = 0$ and $+1$ in this discussion.

That is, the rate of growth of the holographic complexity begins at precisely one-half the late time limit. Recall that in chapter 4, it was found that for the eternal black hole, $d\mathcal{C}_A/dt_0$ remained zero up to a critical time, at which point it became negatively divergent. The rate then quickly rose to positive values but this transient behaviour depended on the choice of the normalization constant α . In the bulk, this transition corresponds to the moment when the past boundary of the WDW patch lifts off from the white hole singularity and the past null boundaries begin to meet at a joint above the past singularity.

Late time expansion: Next we apply eq. (5.65) to evaluate the late time expansion of the growth rate in eq. (5.72),

$$\left. \frac{d\mathcal{C}'_A}{dt_0} \right|_{\text{late time}} = \frac{2M}{\pi} - 2M \frac{d + (d-2)kz^2}{(1+kz^2)} c_1 e^{-2\pi T t_0} T t_0 + \dots \quad (5.77)$$

As argued above, we see that the late time limit is approached from below. Further, this behaviour is an exponential decay controlled by the thermal length scale, *i.e.*, $1/(2\pi T)$. A similar exponential decay is found in the eternal black hole geometry but there the late time limit is approached from above, as shown in the previous chapter.

Examples:

We turn our attention to numerically evaluating eq. (5.72) in $d = 3$ and $d = 4$ with $k = +1$, as well as investigating the special case of $d = 2$ where the collapse forms a BTZ black hole. We start with the latter, for which the coordinate x_s can be determined analytically as a function of time.

$d = 2$: For $d = 2$, the collapsing shell produces a BTZ black hole with [124, 125]

$$f_{\text{BH}}(r) = (r^2 - r_h^2)/L^2. \quad (5.78)$$

Hence the corresponding dimensionless blackening factor (5.44) simplifies to $\tilde{f}_{\text{BH}}(x) = x^2 - 1$ for $v > 0$. The physical parameters describing the BTZ geometry are

$$M = \frac{\Omega_{k,1} r_h^2}{16\pi G_N L^2}, \quad T = \frac{r_h}{2\pi L^2}, \quad S = \frac{\Omega_{k,1} r_h}{4G_N} = \frac{\pi}{6} c \Omega_{k,1} L T, \quad (5.79)$$

where $c = 3L/(2G_N)$ is the central charge of the boundary CFT. The choices $k = 0$ and 1 correspond to the Ramond and Neveu-Schwarz vacuum, respectively, of the boundary theory [144]. While in principle, the results for the Ramond vacuum are already described

by eqs. (5.73) and (5.74) above, we consider both possibilities in the following.²¹ Eq. (5.59) simplifies with $d = 2$, and we can solve for x_s analytically,

$$x_s = \coth(\pi T t_0). \quad (5.80)$$

First, we analyze the rate of change of complexity for BTZ black holes without the inclusion of the counterterm. The rate of change is then given by summing eqs. (5.49) and (5.51),

$$\frac{d\mathcal{C}_A}{dt_0} = -\frac{M}{\pi} \frac{2kz^2(x_s^2 - 1)}{x_s^2 + kz^2}. \quad (5.81)$$

There are differences in the rate of change of BTZ in comparison to the higher dimensional cases ($d > 2$) in eq. (5.56). First, for a collapse of the Ramond vacuum ($k = 0$), the rate of change is exactly zero!

Further, for the collapse from the Neveu-Schwarz vacuum ($k = +1$), the rate of change begins with negative values,

$$\left. \frac{d\mathcal{C}_A}{dt_0} \right|_{\text{early time}} = -\frac{2Mkz^2}{\pi} + 2Mkz^2\pi(1 + kz^2)T^2t_0^2 + \mathcal{O}(T^4t_0^4). \quad (5.82)$$

In fact, the time derivative never becomes positive and instead approaches the late time limit (*i.e.*, 0) from below,

$$\left. \frac{d\mathcal{C}_A}{dt_0} \right|_{\text{late time}} = -\frac{8kz^2M}{\pi(1 + kz^2)} e^{-2\pi T t_0} + \mathcal{O}(e^{-4\pi T t_0}). \quad (5.83)$$

We show the full profile of the rate of change of complexity for various temperatures in the left panel of figure 5.3.

Next, we evaluate the rate of change of complexity including the contribution of the boundary counterterm. Continuing with either $k = 0$ or 1, we have $\tilde{f}_{\text{vac}}(x) = x^2 + kz^2$ from eq. (5.44). The time derivative of complexity then reads

$$\frac{d\mathcal{C}'_A}{dt_0} = \frac{2M}{\pi} - \frac{M}{\pi} (x_s^2 - 1) \log\left(\frac{x_s^2 + kz^2}{x_s^2 - 1}\right). \quad (5.84)$$

Using eq. (5.80) for the early time limit (in which case, $x_s \rightarrow \infty$), eq. (5.84) yields

$$\left. \frac{d\mathcal{C}'_A}{dt_0} \right|_{t_0 \rightarrow 0^+} = \frac{M}{\pi} \left(1 - \frac{k}{4\pi^2 L^2 T^2}\right), \quad (5.85)$$

²¹Recall that the ground state energy vanishes for the Ramond vacuum, but for the Neveu-Schwarz vacuum, it is negative: $E_{\text{R},0} = -1/(8\pi G_N) = -c/(12\pi L)$.

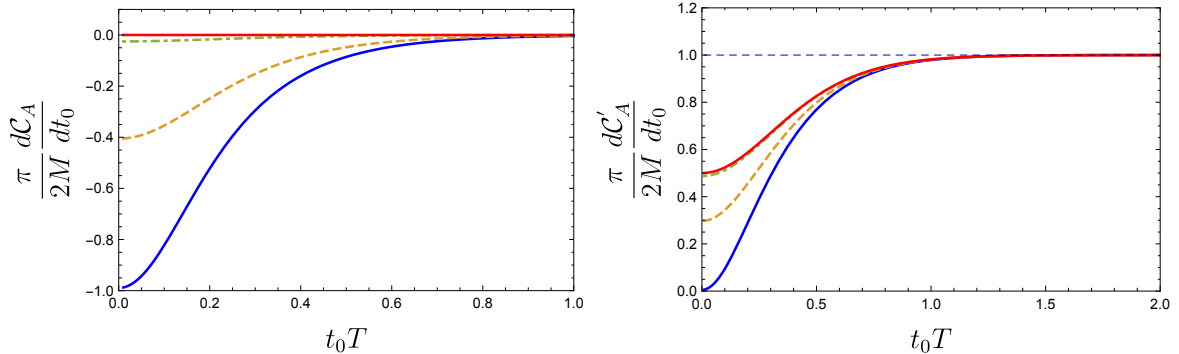


Figure 5.3: The growth rate for the complexity, evaluated without (left) and with (right) the boundary counterterm in $d = 2$. In both plots we have the collapse from Neveu-Schwarz vacuum (*i.e.*, $k = +1$) with temperatures $LT = 0.16$ (blue, solid), $LT = 0.25$ (orange dashed) and $LT = 1.0$ (green dot-dashed). The collapse from Ramond vacuum (*i.e.*, $k = 0$) is shown in red. For the NS vacuum, the growth rate always starts at different values for different temperatures, as given by eq. (5.82) (left) and eq. (5.85) (right). In both cases, the high temperature limit of the NS collapse approaches the Ramond collapse. At late times, independent of the temperature, the rate of change approaches zero on the left, and $2M/\pi$ on the right.

where we substituted $z = 1/(2\pi LT)$, from eq. (5.41) with $d = 2$. Recall that for higher dimensional black holes (*i.e.*, with $d \geq 3$), this limit was always M/π , as shown in eq. (5.76). The above result matches this previous limit for the Ramond vacuum (with $k = 0$), but for the Neveu-Schwarz vacuum (with $k = 1$), the initial rate is reduced by a factor depending on the temperature. Notice that the correction factor (*i.e.*, the factor in brackets) in eq. (5.85) is positive above the Hawking-Page transition (*i.e.*, for $2\pi LT > 1$), and it vanishes at precisely $2\pi LT = 1$.

In the late time limit, combining eqs. (5.80) and (5.84) yields

$$\frac{d\mathcal{C}'_A}{dt_0} = \frac{2M}{\pi} (1 - 4\pi T t_0 e^{-2\pi T t_0} + \dots) . \quad (5.86)$$

Hence the growth rate approaches its late time value from below in more or less the same way as in eq. (5.77) for higher dimensions.

We show the full time evolution of $d\mathcal{C}'_A/dt_0$ for a range of temperatures beginning with the Neveu-Schwarz vacuum (*i.e.*, $k = +1$) in figure 5.3. For small temperatures, it starts at a different rate from the higher dimensional examples, as shown in eq. (5.85), but the

rate starts at approximately M/π for higher temperatures. In addition, the rate of growth increases monotonically from the initial rate and the late time limit is approached from below as well. Further, the $d\mathcal{C}'_A/dt_0$ essentially reaches $2M/\pi$ at a time $t_0 \sim 1/T$

$d = 3$: Next, we turn our attention to evaluating numerically the growth rate of complexity with a spherical collapsing shell in $d = 3$. The dimensionless tortoise coordinate given by eq. (5.43) reads

$$x_{BH}^*(x, z) = \frac{\sqrt{4kz^2 + 3} \left(2 \log \left(\frac{|x-1|}{\sqrt{kz^2 + x^2 + x + 1}} \right) \right) + (4kz^2 + 6) \tan^{-1} \left(\frac{2x+1}{\sqrt{4kz^2 + 3}} \right)}{2(kz^2 + 3)\sqrt{4kz^2 + 3}}. \quad (5.87)$$

We can then solve numerically the transcendental equation (5.59) for x_s , and evaluate eq. (5.72).

We show the time dependence of both $d\mathcal{C}_A/dt_0$ and $d\mathcal{C}'_A/dt_0$ for the spherical boundary geometry (*i.e.*, $k = +1$) in the left panel of figure 5.4 for several temperatures. Recall that z is determined in terms of LT by eq. (6.20). As discussed above, $d\mathcal{C}'_A/dt_0$ (with the counterterm) approaches $2M/\pi$ from below at late times and starts with M/π immediately after the shell is injected from the boundary. For $d\mathcal{C}_A/dt_0$ (without the counterterm), the late time limit is much lower (*i.e.*, it does not match that found with eternal black holes) and depends on the value of the temperature, as in eq. (5.58).

$d = 4$: For $d = 4$, the relevant dimensionless tortoise coordinate in eq. (5.43) reads

$$x_{BH}^*(x, z) = -\frac{1}{2kz^2 + 4} \left[\sqrt{kz^2 + 1} \left(\pi - 2 \tan^{-1} \left(\frac{x}{\sqrt{kz^2 + 1}} \right) \right) - \log \left(\frac{x-1}{x+1} \right) \right]. \quad (5.88)$$

Therefore, we can solve numerically eq. (5.59) for the meeting point x_s , which then allows us to evaluate the complexity growth rates with and without the inclusion of the boundary counterterm (2.11) in eqs. (5.72) and (5.56), respectively. Recall that z is determined in terms of LT by eq. (6.20). We show $d\mathcal{C}_A/dt_0$ and $d\mathcal{C}'_A/dt_0$ for several temperatures (and the spherical geometry with $k = +1$) in the right panel of figure 5.4. Again, as discussed above, we see that when the counterterm is included, $d\mathcal{C}'_A/dt_0$ starts with M/π at $t_0 = 0$ and rises monotonically to $2M/\pi$ at late times. Without the counterterm, the late time growth rate does not match the eternal black hole geometry, and it depends on the temperature, as given by eq. (5.58).

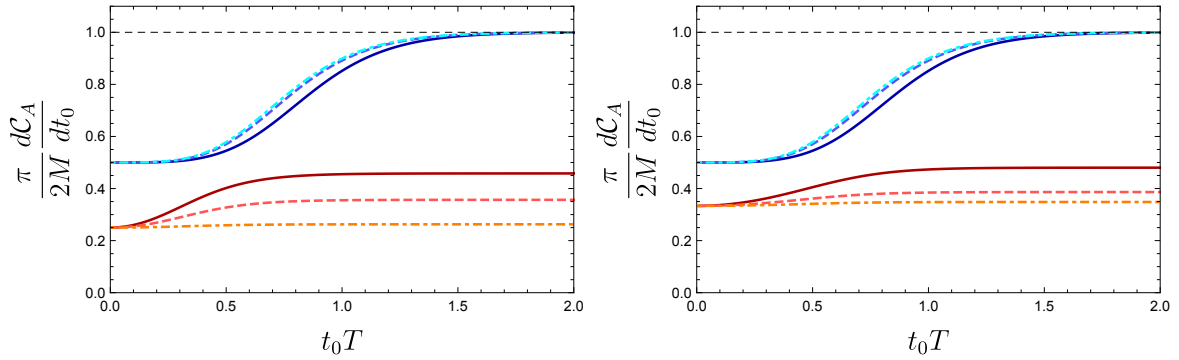


Figure 5.4: The growth rate for the complexity in $d = 3$ (left) and $d = 4$ (right) and spherical geometry ($k = +1$), evaluated without (red and orange curves) and with (blue and cyan curves) the boundary counterterm (2.11). In both case, we evaluate the growth rate for temperatures $TL = 0.35$ (solid), $TL = 0.5$ (dashed) and $TL = 2.0$ (dot-dashed) in the left and $TL = 0.5$ (solid), $TL = 0.8$ (dashed) and $TL = 1.5$ (dot-dashed) in the right figure. In both dimensions, $d\mathcal{C}_A/dt_0$ (without the counterterm) starts at the value of the planar rate of change given by eq. (5.61) and approaches the late time limit from below in eq. (5.58). The late time growth rate in this case is smaller than the one for the eternal black hole, and it depends on the temperature. With the inclusion of the counterterm, $d\mathcal{C}'_A/dt_0$ starts at half of its late time limit, then it grows at times of the order of the thermal length, and approaches the eternal black hole bound from below.

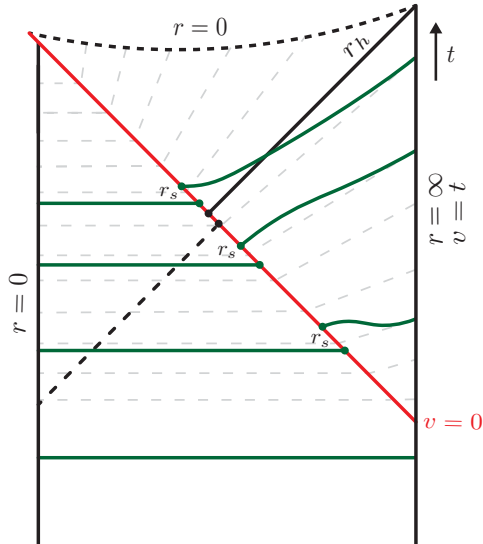


Figure 5.5: Penrose-like diagram of maximal volume surfaces at different times embedded in the Vaidya AdS spacetime. Constant time slices are indicated by thin dashed gray lines and the maximal volume surfaces asymptote them near the boundary. The event horizon extends past the shell, as we have indicated by a thick dashed gray line. Since the momentum (5.90) of the surfaces is positive, they evolve towards decreasing time outside the horizon. Surfaces lie on constant time slices in the vacuum part of spacetime to avoid a conical singularity at $r = 0$.

5.2.2 Complexity=Volume

In this section, we evaluate the holographic complexity following the CV conjecture (1.23) for the same Vaidya spacetime describing the formation of a black hole with the collapse of a(n infinitely) thin shell of null fluid. Our calculations closely follow those in the section 4.3 of the previous chapter. The maximal volume surfaces take the form illustrated in figure 5.5.

We are again working with the Vaidya metric in eq. (5.1) with $f_P(v) = \omega^{d-2} \mathcal{H}(v)$, as in eq. (5.33). To find the maximal volume slices anchored to the boundary time slice at $v = t_0$, we must extremize the following

$$\mathcal{V} = \Omega_{k,d-1} \int \mathcal{L} d\lambda = \Omega_{k,d-1} \int d\lambda r^{d-1} \sqrt{-F\dot{v}^2 + 2\dot{v}\dot{r}}, \quad (5.89)$$

where we have taken advantage of the “rotational” symmetry to integrate out spatial boundary directions. The remaining radial direction on the (codimension-one) bulk sur-

faces is parameterized by λ above and the surface is defined by its trajectory in the rv -plane, $(r(\lambda), v(\lambda))$.

Our metric is independent of the coordinate v in each part of the spacetime, *i.e.*, $v > 0$ and $v < 0$, separately. Hence, in each of these regions, we have the conserved “momentum,”

$$P = \frac{\partial \mathcal{L}}{\partial \dot{v}} = \frac{r^{d-1}(\dot{r} - F\dot{v})}{\sqrt{-F\dot{v}^2 + 2\dot{v}\dot{r}}} . \quad (5.90)$$

Now the expression in eq. (5.89) is invariant under reparametrizations of λ and we make the following convenient gauge choice:

$$\sqrt{-F\dot{v}^2 + 2\dot{v}\dot{r}} = r^{d-1} . \quad (5.91)$$

We can use this condition to simplify the v -momentum (5.90) as follows

$$P = \dot{r} - F\dot{v} . \quad (5.92)$$

We can then use eqs. (5.91) and (5.92) to express \dot{r} and \dot{v} in terms of r and P

$$\begin{aligned} \dot{r} &= \pm \sqrt{F(r)r^{2(d-1)} + P^2} , \\ \dot{v} &= \frac{\dot{r} - P}{F(r)} = \frac{1}{F(r)} \left(-P \pm \sqrt{F(r)r^{2(d-1)} + P^2} \right) , \end{aligned} \quad (5.93)$$

where in principle, either sign may play a role since r may be increasing or decreasing as we move along the surface. However, we will see that \dot{r} (as well as \dot{v}) will be positive in general for the solutions of interest, and P will be positive. Since P is not conserved in the full spacetime (due to the $\mathcal{H}(v)$ in the profile (5.33)), it is convenient to have the full equations of motion:

$$\begin{aligned} \ddot{v} &= (d-1)r^{2d-3} - \frac{\dot{v}^2}{2} \partial_r F , \\ \ddot{r} &= \frac{\dot{v}^2}{2} \partial_v F + \frac{1}{2} \partial_r (r^{2d-2} F) , \end{aligned} \quad (5.94)$$

where we simplified these expressions using eq. (5.91). Here we see that $\partial_v F$ only enters on the right-hand side of the equation for \ddot{r} . Hence integrating eq. (5.94) over an infinitesimal interval around the shell at $v = 0$, we conclude that \dot{v} is continuous across the shell while \dot{r} jumps discontinuously with

$$\dot{r}_{\text{BH}}(r_s) = \dot{r}_{\text{vac}}(r_s) + \frac{\dot{v}(r_s)}{2} (f_{\text{BH}}(r_s) - f_{\text{vac}}(r_s)) , \quad (5.95)$$

where r_s denotes the value of the radial coordinate at which our extremal volume surface meets the collapsing shell. It is also useful to recast the \dot{r} equation as follows:

$$\dot{r}^2 - F(r) r^{2(d-1)} = P^2. \quad (5.96)$$

This equation takes the form of a classical Hamiltonian constraint for a particle of mass $m = 2$ and with energy $E = P^2$ moving in a potential $U(r) = -F(r)r^{2(d-1)}$. This gives us an intuitive picture to understand the evolution of the surface on either side of the collapsing shell.²² The effective potential is depicted in figure 5.6 for the black hole geometry. We see that depending on the value of P_{BH}^2 certain values of r may not be accessed. It will be useful in what follows to keep in mind the maximal value of the black hole potential $U_{\text{BH,max}} \equiv P_m^2$ and the value $r = r_m$ for which it is obtained. They are obtained by solving the following equations:

$$\partial_r [f_{\text{BH}}(r_m) r_m^{2(d-1)}] = 0, \quad P_m^2 = -f_{\text{BH}}(r_m) r_m^{2(d-1)}. \quad (5.97)$$

The boundary conditions for our surface are determined as follows: In order for the extremal surfaces to avoid a conical singularity at $r = 0$, we require that $\dot{t} = \dot{v} - \dot{r}/f = 0$ there.²³ Eq. (5.92) then fixes $P_{\text{vac}} = 0$, the conserved momentum in the vacuum part of the spacetime ($v < 0$). When the surface crosses the collapsing shell at $r = r_s$, eq. (5.93) then determines

$$\dot{r}_{\text{vac}}(r_s) = r_s^{d-1} \sqrt{f_{\text{vac}}(r_s)}, \quad \dot{v}(r_s) = \frac{r_s^{d-1}}{\sqrt{f_{\text{vac}}(r_s)}}. \quad (5.98)$$

Hence the value of the v -momentum and \dot{r} on the black hole side of the shell can be read from eqs. (5.92) and (5.95),

$$P_{\text{BH}} = r_s^{d-1} \frac{f_{\text{vac}}(r_s) - f_{\text{BH}}(r_s)}{2\sqrt{f_{\text{vac}}(r_s)}} = \frac{r_s \omega^{d-2}}{2\sqrt{f_{\text{vac}}(r_s)}}, \quad \dot{r}_{\text{BH}}(r_s) = r_s^{d-1} \frac{f_{\text{BH}}(r_s) + f_{\text{vac}}(r_s)}{2\sqrt{f_{\text{vac}}(r_s)}}. \quad (5.99)$$

The last boundary condition is that we are anchoring the extremal surface to the boundary time slice at $v = t_0 > 0$. Hence using eq. (5.93), we integrate from the shell to the

²²Note that this picture also agrees with eq. (5.94), which *away* from the shell can be cast in the form: $m \ddot{r} = \partial_r U(r)$. Of course, we must keep in mind that both $U(r)$ and E will jump discontinuously at $r = r_s$ where the extremal surface crosses the shell.

²³We observe that this boundary condition yields $\dot{t} = 0$ throughout the vacuum region. Further, we note that while this boundary condition is obvious for $k = +1$, it is more subtle in the planar geometry with $k = 0$. In the latter case, we need to introduce a timelike regulator surface at some $r = \epsilon_0$ and consider the limit $\epsilon_0 \rightarrow 0$, as in chapter 3.

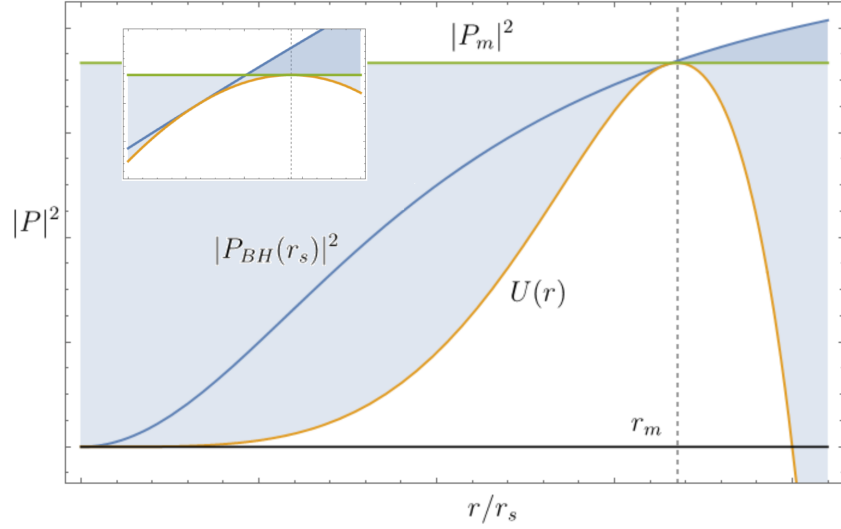


Figure 5.6: Generic form of the potential $U(r) = -f_{\text{BH}}(r)r^{2(d-1)}$ (yellow curve) as a function of r for black holes with $k = 1$ and $d \geq 3$, or for BTZ black holes in $d = 2$. The peak of the potential corresponds to r_m (dashed gray line) and the corresponding energy P_m^2 (green line) is defined in eq. (5.97). The blue curve corresponds to the energy in the black hole side as a function of r_s where the shell is crossed, for $k = 1$ and $d \geq 3$ or for BTZ black holes in $d = 2$ with the Neveu-Schwarz vacuum. The point where the yellow and blue curves meet indicates a change in the direction of the velocity $\dot{r}_{\text{BH}}(r_s)$. To reach the asymptotic boundary we require $P_{\text{BH}}^2 \geq P_m^2$. That is, r_s should be larger than the value at the intersection of the blue and green curves — see inset.

asymptotic boundary

$$t_0 = \int_0^{t_0} dv = \int_{r_s}^{\infty} \frac{\dot{v}}{\dot{r}} dr = \int_{r_s}^{\infty} \left(1 - \frac{P_{\text{BH}}}{\sqrt{f_{\text{BH}}(r)r^{2(d-1)} + P_{\text{BH}}^2}} \right) \frac{dr}{f_{\text{BH}}(r)}. \quad (5.100)$$

Now eqs. (5.99) and (5.100) relate the boundary time t_0 , the momentum P_{BH} in the black hole part of spacetime ($v > 0$), and the radius r_s at which our extremal surface crosses the shell.

We can use these equations to prove that the momentum P_{BH} on the black hole side is always positive. As a consequence the surfaces outside the black hole cross decreasing time slices. It is also easy to show that $P_{\text{BH}}^2 - U(r)$ is in general positive, so that the Hamiltonian constraint (5.96) is consistent with $\dot{r}_{\text{BH}}^2 > 0$ and so we have shown that the extremal surface is always able to cross the shell. Figure 5.6 depicts the effective potential $U(r) = -f_{\text{BH}}(r)r^{2(d-1)}$ (yellow line) and also the effective energy P_{BH}^2 as a function of the crossing radius r_s (blue line), using eq. (5.99). We note that if the latter energy is below the peak of the potential, *i.e.*, $P_{\text{BH}}^2 < P_m^2$ from eq. (5.97), then the trajectory cannot escape the potential barrier and terminates on the singularity at $r = 0$. A special point in the figure is where the yellow and blue curves meet — see inset. At that point $\dot{r}_{\text{BH}}(r_s)$ vanishes and in fact, this is the point where the direction of \dot{r} is flipped. That is, $\dot{r}_{\text{BH}}(r_s)$ is positive for larger values of r_s , while it is negative for smaller values of r_s and the extremal surface is headed towards the singularity at $r = 0$ right after the crossing. In any event, we are only interested in extremal surfaces which reach the asymptotic boundary and so we require $P_{\text{BH}}^2 \geq P_m^2$.

We can see from eq. (5.100) that as the latter inequality is saturated the boundary time diverges, *i.e.*, $t_0 \rightarrow \infty$ when $P_{\text{BH}}^2 \rightarrow P_m^2$. This does not happen exactly at $r_s = r_m$ but rather at a slightly lower value of r_s — see the inset in figure 5.6 where the energy $P_{\text{BH}}(r_s)^2$ (blue line) crosses P_m^2 (green line). To prove that the point for which the momentum is equal to P_m occurs with $r_s < r_m$ we can use the following general argument: First we note from general consideration that \dot{r}_{BH} is a monotonic function of r_s . In addition, we can check that $\dot{r}_{\text{BH}}(r_s = r_m)$ is positive. To do that we use eq. (5.97) for r_m

$$\frac{2r_m^2}{L^2} + 2k - \frac{\omega^{d-2}}{r_m^{d-2}} = \frac{2k}{d}, \quad (5.101)$$

as well as eq. (5.99) for the velocity \dot{r}_{BH} after the crossing

$$\dot{r}_{\text{BH}}(r_s = r_m) = \frac{r_m^{d-2}}{2\sqrt{r_m^2/L^2 + 1}} \left(\frac{2r_m^2}{L^2} + 2k - \frac{\omega^{d-2}}{r_m^{d-2}} \right) = \frac{r_m^{d-2}k}{d\sqrt{r_m^2/L^2 + 1}}. \quad (5.102)$$

The latter is strictly positive when $k = 1$ (and is exactly zero for $k = 0$). In fact, the blue curve for $k = 0$ becomes a line of constant energy $P^2 = P_m^2$.

With the gauge choice in eq. (5.91), the maximal volume (5.89) becomes $\mathcal{V} = \Omega_{k,d-1} \int d\lambda r^{2d-2}$. We evaluate the latter as

$$\begin{aligned} \mathcal{V} &= \Omega_{k,d-1} \left[\int_0^{r_s} \frac{dr}{\dot{r}} r^{2d-2} + \int_{r_s}^{\infty} \frac{dr}{\dot{r}} r^{2d-2} \right] \\ &= \Omega_{k,d-1} \int_0^{r_s} \frac{dr r^{d-1}}{\sqrt{f_{\text{vac}}(r)}} + \Omega_{k,d-1} \int_{r_s}^{r_{\text{max}}} \frac{dr r^{2(d-1)}}{\sqrt{f_{\text{BH}}(r)r^{2(d-1)} + P_{\text{BH}}^2}} \end{aligned} \quad (5.103)$$

and we have introduced the UV cutoff r_{max} to produce a finite volume. It is convenient to use eq. (5.100) to re-express the second integral as follows

$$\mathcal{V} = \Omega_{k,d-1} \left[\int_0^{r_s} \frac{dr r^{d-1}}{\sqrt{f_{\text{vac}}(r)}} + \int_{r_s}^{r_{\text{max}}} dr \left[\frac{\sqrt{f_{\text{BH}}(r)r^{2(d-1)} + P_{\text{BH}}^2}}{f_{\text{BH}}(r)} - \frac{P_{\text{BH}}}{f_{\text{BH}}(r)} \right] + P_{\text{BH}} t_0 \right]. \quad (5.104)$$

We note that our expressions for the time and volume match those found in appendix A of [87] for the case of $d = 2$ and $r_h = L$.

With all this technology in hand, we are ready to compute the time derivative of the holographic complexity using eq. (1.23). It is straightforward to check that the continuity of \dot{v} across the shell implies that the contributions from differentiating the limits of integration vanish. Using again eq. (5.100), a second cancellation arises from the derivative of the momentum inside the second integral and in the last term of (5.104). We are finally left with

$$\frac{d\mathcal{C}_V}{dt_0} = \frac{1}{G_N L} \frac{d\mathcal{V}}{dt_0} = \frac{\Omega_{k,d-1}}{G_N L} P_{\text{BH}}. \quad (5.105)$$

This surprisingly simple result bears some similarity to the expression for the rate of change of the volume complexity in the eternal black hole discussed in chapter 4. However, we note that the expression (5.99) relating the P_{BH} and r_s is different here than that relating the momentum and r_{min} there.

The above result (5.105) is implicit because in general it still requires solving eqs. (5.100) and (5.99) for P_{BH} (or equivalently r_s) given the boundary time t_0 . However, these equations are simply solved for the planar geometry with $k = 0$ and one obtains

$$P_{\text{BH}} = \frac{r_h^d}{2L}, \quad \frac{d\mathcal{C}_V}{dt_0} = \frac{8\pi M}{d-1}. \quad (5.106)$$

Hence for the planar geometry, holographic complexity begins growing as soon as $t_0 > 0$ and the rate of growth is a fixed constant for all times. Further, this constant rate matches the

late time rate of growth found for the eternal black hole in [32] and chapter 4. Our results for the spherical geometry confirm that the interpretation presented in appendix A of [87] for BTZ black holes also holds in higher dimensions. Namely that the main contribution in the late time limit comes from the extremal surface wrapping around a surface of constant $r = r_m$ while the contributions coming from the smaller value of r reached by our surface, as well as the portions reaching to the boundary, are approximately constant and do not influence the time derivative of the holographic complexity.

Early Time Behaviour

We can evaluate analytically the early time limit $t_0 \rightarrow 0$. For early times we know that $r_s \rightarrow \infty$ and using eq. (5.99), we see that for black holes in $d > 2$:

$$\lim_{t_0 \rightarrow 0} P_{\text{BH}} = \frac{L \omega^{d-2}}{2}, \quad (5.107)$$

where as given in eq. (2.4), $\omega^{d-2} = r_h^{d-2}(r_h^2/L^2 + k)$. Now using eq. (5.105), this leads to

$$\lim_{t_0 \rightarrow 0} \frac{d\mathcal{C}_V}{dt_0} = \frac{8\pi M}{d-1}. \quad (5.108)$$

That is, as noted above for the planar geometry, the rate of growth of the holographic complexity immediately jumps to a nonvanishing (positive) value for $t > t_0$. We also observe that the early time rate in eq. (5.108), which holds for both $k = 0$ and $+1$, matches the $k = 0$ result in eq. (5.106), which holds for all times.

Late Time Behaviour

Another limit that we consider is the late time limit $t_0 \rightarrow \infty$: In the late time limit, we have already explained that the value of the momentum reaches P_m defined in eq. (5.97). In this case, our surface wraps around the surface of constant $r = r_m$, but the volume required to reach the minimal value of r_s below r_m and to reach the boundary above r_m remains (approximately) constant. The contribution to the increasing growth of complexity at late times comes from the part of the surface which wraps around the $r = r_m$ surface. This will give us the value of P_{BH} in the late time limit for our numerical solutions below. One then finds that the rate of growth of the holographic complexity (for $d > 2$) at late times satisfies

$$\lim_{t_0 \rightarrow \infty} \frac{(d-1)}{8\pi M} \frac{d\mathcal{C}_V}{dt_0} = \frac{2P_m}{\omega^{d-2}L}. \quad (5.109)$$

In general, eq. (5.97) cannot be solved analytically. However we can solve it in a large temperature expansion (or equivalently for small $z = L/r_h$ — see eq. (5.40))

$$r_m = \frac{r_h}{2^{\frac{1}{d}}} \left[1 - \frac{(2^{2/d}(d-1) - d)}{d^2} k z^2 + \frac{(d-1) \left(-d^2 + 2^{\frac{2}{d}+1} d + 2^{4/d}(d-3)(d-1) \right)}{2 d^4} k^2 z^4 + \mathcal{O}(z^4) \right]. \quad (5.110)$$

It is then possible to extract P_m using eq. (5.97) and to use eq. (5.109) to determine the late time rate of change of the holographic complexity. Finally relating z to the temperature with eq. (5.41), we conclude

$$\lim_{t_0 \rightarrow \infty} \frac{(d-1)}{8\pi M} \frac{d\mathcal{C}_V}{dt_0} = 1 - \frac{2^{\frac{2}{d}-1} d^2 k}{(4\pi)^2 (LT)^2} + \frac{2^{\frac{2}{d}} (\gamma - d(d-3)) d^2 k^2}{(4\pi)^4 (LT)^4} + \mathcal{O}\left(\frac{1}{L^6 T^6}\right), \quad (5.111)$$

where we have introduced the parameter $\gamma \equiv 2^{\frac{2}{d}-3}(3d-2)(d-2)$. Hence with a spherical spatial geometry (*i.e.*, $k = +1$), there are curvature corrections which reduce the late time growth rate of the holographic complexity. That is, $d\mathcal{C}_V/dt_0$ begins with the value $8\pi M/(d-1)$ shown in eq. (5.108), but then it decreases to a smaller growth rate at late times — see also figure 5.8. However, for the planar geometry (*i.e.*, $k = 0$), the growth rate remains a fixed constant, as shown in eq. (5.106).

Two Boundary Dimensions ($d = 2$)

The collapse with $d = 2$ forms a BTZ black hole with $f_{\text{BH}}(r) = (r^2 - r_h^2)/L^2$ [124, 125]. Recall that the mass, temperature and entropy are given in eq. (6.73) and the choices $k = 0$ or 1 in $f_{\text{vac}}(r)$ correspond to the Ramond and Neveu-Schwarz vacuum, respectively, in the boundary theory.

The analysis follows identically to the previous case, with the obvious replacement of the blackening factors. For the early time limit we may use eq. (5.99) with $r_s \rightarrow \infty$ to obtain

$$\lim_{t_0 \rightarrow 0} P_{\text{BH}} = \frac{L}{2} \left(\frac{r_h^2}{L^2} + k \right). \quad (5.112)$$

Next, using eq. (5.105) for the rate of change of the holographic complexity, we obtain:

$$\lim_{t_0 \rightarrow 0} \frac{d\mathcal{C}_V}{dt_0} = 8\pi M \left(1 + k \frac{L^2}{r_h^2} \right) = 8\pi M \left(1 + \frac{k}{(2\pi L T)^2} \right). \quad (5.113)$$

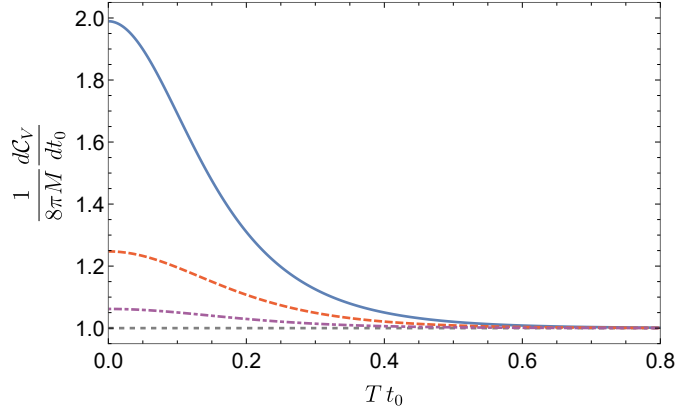


Figure 5.7: Rate of change of complexity evaluated from the complexity=volume conjecture in the Vaidya-AdS spacetime for the BTZ black hole with the Neveu-Schwarz vacuum for several values of the temperature, *i.e.*, for $TL = 0.16$ (blue), $TL = 0.32$ (red, dashed) and $TL = 0.64$ (purple, dot-dashed).

For the late time limit, we can solve eq. (5.97) analytically and obtain

$$r_m = \frac{r_h}{\sqrt{2}}, \quad P_m = \frac{r_h^2}{2L} \quad (5.114)$$

and hence we find

$$\lim_{t_0 \rightarrow \infty} \frac{d\mathcal{C}_V}{dt_0} = 8\pi M, \quad (5.115)$$

which is independent of the value of k . For the Ramond vacuum (*i.e.*, $k = 0$), $d\mathcal{C}_V/dt_0$ is a fixed constant for all times, as expected from eq. (5.106) for the planar geometry. However, we see that for the Neveu-Schwarz vacuum (*i.e.*, $k = 1$), the early rate of growth is higher than the late time rate of growth.²⁴ In figure 5.7, we numerically evaluate the rate of growth of the holographic complexity for intermediate times.

Numerical Results

We evaluated numerically the rate of growth of the holographic complexity for the spherical geometries with $d = 3$ and 4, shown in figure 5.8. We note a number of interesting features: First, of course, the early and late time rates match those discussed above. Second, in all

²⁴Our results for the BTZ black hole are the same as those in appendix A of [87]. There the authors have set $r_h = L$ and the early and late time limits in their eqs. (A.65) and (A.69) match with ours above.

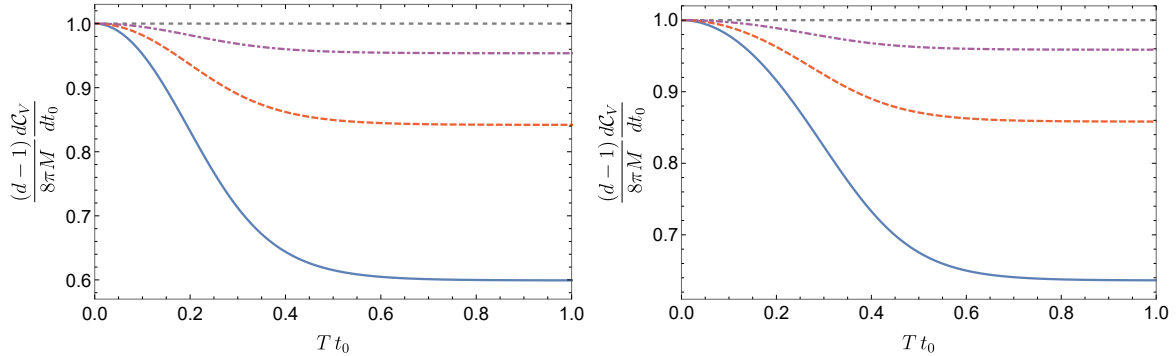


Figure 5.8: Rate of change of complexity evaluated from the complexity=volume conjecture in the spherical ($k = 1$) Vaidya-AdS spacetime in $d = 3$ (left) for $TL = 0.32$ (blue), $TL = 0.52$ (red, dashed) and $TL = 0.98$ (purple, dot-dashed) and $d = 4$ (right) for $TL = 0.48$ (blue), $TL = 0.72$ (red, dashed) and $TL = 1.32$ (purple, dot-dashed).

of the cases shown, the rate of growth decreases at early times and the late time limit is approached from above. Recall from eq. (5.113), that the rate of growth is highest at early times for the Neveu-Schwarz vacuum in $d = 2$ — see also figure 5.7.

5.3 Discussion

In section 5.2, we examined holographic complexity in the Vaidya geometry (5.1) for the case where a shell of null fluid is injected into empty AdS and collapses to form a black hole. Hence these geometries describe one-sided black holes, a situation which was previously considered in, *e.g.*, [87, 173] in the context of holographic complexity. Of course, using either the CA or CV approaches, we found that holographic complexity remains constant until the moment when the thin shell is injected. After that the complexity immediately begins to grow and the rate of growth monotonically approaches the corresponding late time limit.

In fact, using the CV conjecture, we found that for planar geometries in $d \geq 3$, the complexity grows at a constant rate which is equal to the late time rate of planar eternal black holes found in chapter 4, *i.e.*,

$$\frac{d\mathcal{C}_V}{dt} = \frac{8\pi M}{d-1}. \quad (5.116)$$

For spherical geometries, the growth rate at early times is the same as the above expression, but the rate then decreases monotonically, as shown in figure 5.8. Hence the (positive) curvature of the boundary geometry reduces the late time growth rate below that in eq. (5.116), but this reduction is smaller for high temperature black holes. In eq. (5.111) for large temperatures, we expressed the final rate in terms of an expansion in $1/(LT)^2$, *i.e.*, the curvature of the boundary geometry divided by the temperature, and we can see that the late time rate approaches eq. (5.116) for very high temperatures. Comparing eq. (5.111) to eq. (4.84), we can see that the curvature corrections for the present one-sided black holes precisely match those found for the analogous eternal black hole backgrounds. This agreement becomes obvious when we realize that eq. (5.97) which determines late time limit (5.109) is identical to the corresponding equation for the eternal black hole in chapter 4.

Similar results were found for the BTZ black hole. In particular, beginning with the Ramond vacuum (with $k = 0$), the growth rate is a fixed constant for all $t_0 > 0$ and matches the expression in eq. (5.116) with $d = 2$. Starting with the Neveu-Schwarz vacuum (with $k = +1$), the growth rate decreases, similar to what was observed above for $d \geq 3$. However, in this case, the initial rate is increased, as shown in eq. (5.113), and the final rate (5.115) matches eq. (5.116), corresponding to the final rate for the eternal black hole background — see also figure 5.7. The rate of change in complexity relaxes to its late time limit at times of the order of $t \sim 1/T$. All of these results are in accord with the expectations and calculations presented in [87]. In particular, the geometry of a one-sided black hole naturally includes regions behind the event horizon where time slices are growing to infinite volume (or as we discuss below, where the gravitational action grows without bound).

Above, we highlighted ways in which the CV results were the same for the one-sided and eternal (two-sided) black holes. However, we must also point out how the complexity for the Vaidya geometry differs from that for the eternal black holes discussed in chapter 4 (see also [194]). First, for planar black holes, the rate of growth of complexity in the eternal case had a transient period in which the rate of change in complexity gradually rose to its final value. As noted above for the collapsing shell, the growth rate jumps discontinuously at $t_0 = 0$ to a value in eq. (5.116) and remains constant. For spherical eternal black holes, the growth rate increased towards the final late time rate, while here we observed a decreasing rate which approaches the late time limit from above.

Turning to the CA proposal (1.24), we began in section 5.1 by constructing an action (5.4) for the null fluid, which sources the Vaidya metric (5.1).²⁵ With this construction, we confirmed that when evaluated on a solution of the equations of motion, the null fluid action

²⁵We remind the reader that a similar action was derived in [189] using complementary variables.

vanishes. As a result, in applying the CA conjecture (1.24) to evaluate the holographic complexity of the Vaidya metric in section 5.2, the only nonvanishing contributions come from the gravitational action (2.10). While this simplifies the task of evaluating the WDW action, we also carefully examined the contribution of the spacetime region containing a narrow shell of null fluid and we found that it vanishes as the width of the shell shrinks to zero. We note that this vanishing result required a precise cancellation of the κ surface term and joint terms on the past null boundary, as indicated in eq. (5.26). Hence with an infinitely thin shell, the WDW action can be evaluated as the sum of the actions for two separate regions, the first inside the shell and the second outside the shell. We might observe that a similar statement holds for the calculations with the CV proposal (1.23), where the extremal volume was found by evaluating separately the corresponding equations of motion inside and outside of the shell. Further in passing, we note that the vanishing of the gravitational action for the spacetime region containing the null fluid shell, was an implicit assumption in various previous studies of holographic complexity, *e.g.*, [77, 173, 195].

In evaluating the holographic complexity on the collapsing null shell geometry in section 5.2.1, one of our most striking results was that the late time growth rate did not match that found in an eternal black hole background. To be precise, the result in eq. (5.58) for $d \geq 3$ was evaluated using the gravitational action (2.10) and the standard prescription that the generators of the null boundaries are affinely parameterized (*i.e.*, $\kappa = 0$).²⁶ Perhaps even more striking is the result for $d = 2$. Combining eqs. (5.80) and (5.81), we have

$$\frac{d\mathcal{C}_A}{dt_0} = -\frac{2M}{\pi} \frac{k}{4\pi^2 L^2 T^2 + (4\pi^2 L^2 T^2 + k) \sinh^2(\pi T t_0)}, \quad (5.117)$$

where we have also substituted $z = 1/(2\pi LT)$ from eq. (6.20). Hence with $k = 0$, the growth rate simply vanishes in $d = 2$, while with $k = +1$, it is actually negative and only approaches zero at late times. That is, for $k = +1$ and $d = 2$, the standard CA prescription yields a holographic complexity that decreases in time!

Clearly, this is an unsatisfactory result, however, we also found that the situation was corrected by adding the boundary counterterm (2.11) on the null surfaces. In particular, with this slightly modified prescription, the late time rate of growth was identical to that found for eternal black holes. That is, eq. (5.72) yields $d\mathcal{C}'_A/dt_0|_{t_0 \rightarrow \infty} = 2M/\pi$ for both $k = 0, +1$ and any $d \geq 3$. Hence, both the CV and CA approaches yield a late time growth rate which matches the rate found for the analogous eternal black hole backgrounds, as

²⁶Recall that this prescription also fixes the relative normalization of the null normals on the two sides of the shell, see eq. (5.27).

long as the gravitational action includes the extra counterterm. Further, from eq. (5.84), we can see that for $d = 2$,

$$\frac{d\mathcal{C}'_A}{dt_0} = \frac{2M}{\pi} - \frac{M}{\pi \sinh^2(\pi T t_0)} \log \left[1 + \left(1 + \frac{k}{4\pi^2 L^2 T^2} \right) \sinh^2(\pi T t_0) \right]. \quad (5.118)$$

Hence for both $k = 0$ and $+1$, there is a transient behaviour at early times but the growth rate reaches the expected late time limit by $t_0 \sim 1/T$. We also note that eq. (5.118) yields $d\mathcal{C}'_A/dt_0$ which is positive for all times. Hence adding the boundary counterterm repairs the previous problematic result (5.117) for $d = 2$. Therefore, we conclude that it is essential in defining the CA proposal (1.24) to supplement the gravitational action (2.10) with the boundary counterterm (2.11). This conclusion will be reinforced by our analysis of shock waves in an eternal black hole background in chapter 6.

We also discuss this conclusion further below, but first let us examine the behaviour of the holographic complexity, using the modified prescription, for the collapsing null shell in more detail. Of course, as observed above, the modified prescription yields the same universal late time limit as found for the eternal black holes [33, 34]. But closer examination of eq. (5.72) shows that $d\mathcal{C}'_A/dt_0$ begins at precisely half this rate at $t_0 = 0$ for $d \geq 3$ (as well as $d = 2$ with $k = 0$) and that the growth rate increases monotonically towards the late time limit. As shown in eq. (5.77), $d\mathcal{C}'_A/dt_0$ relaxes to this limit with an exponential decay controlled by the thermal time scale $1/(2\pi T)$. Generally, as shown in figure 5.4, the growth rate has essentially reached this late time limit at $t \sim 1/T$.

We might recall that when the CA approach was applied to study the time evolution of the holographic complexity in the eternal black hole geometry in chapter 4 [194], a number of unusual features arose. First, the holographic complexity does not change at all until some $t_c \sim 1/T$ for $d \geq 3$. Second, at t_c , there is a sudden spike in $d\mathcal{C}_A/dt$ where it actually becomes (infinitely) negative. After this spike, $d\mathcal{C}_A/dt$ grows rapidly and overshoots the late time rate. Then the growth rate approaches the late time limit with an exponential decay from above. Further, we note that the details of this transient behaviour depend on α , the parameter appearing in the normalization of the null normals on the boundaries of the WDW patch. Of course, these calculations were found using the standard prescription which did not include the null boundary counterterm. However, including the counterterm contributions does not modify the above description in any essential way, *e.g.*, see appendices B.1 and B.4, except that the undetermined normalization constant α is replaced the undetermined scale t_L , appearing in eq. (2.11).²⁷ Hence it is

²⁷The counterterm (2.11) was introduced to ensure the reparameterization invariance of the action and hence when this term is included, the action is completely independent of α .

interesting to observe that these unusual features are absent in $d\mathcal{C}'_A/dt_0$ calculated for the formation of a black hole, rather than an eternal black hole. In particular, we emphasize the counterterm scale t_L does not come into play in the time evolution of the complexity for the collapsing shell.

Our conclusion above was that without the null surface counterterm (2.11), evaluating the gravitational action on the WDW patch did not yield an observable that could be associated with complexity in the boundary theory. For example, eq. (5.58) shows that the late time growth rate after the formation of a black hole does not match that found for an eternal black hole, *i.e.*, $2M/\pi$. This discrepancy is somewhat surprising since at late times, the largest portion of the WDW patch is above the shell, where the geometry is precisely that of a static black hole — see figure 5.2. However, recall that in evaluating $d\mathcal{C}_A/dt$ in the eternal black hole geometry, an essential contribution comes from the joint where the two past null boundaries meet behind the past event horizon as shown in chapter 4. Of course, there is no counterpart of this joint contribution in the Vaidya geometry describing black hole formation.²⁸ However, upon adding the counterterm, an extra boundary contribution appears where the past boundary of the WDW patch crosses the null shell (see eqs. (6.50) and (5.68)), and then its time derivative provides precisely the extra contribution needed to restore the late time growth rate for the holographic complexity (see eq. (5.71)).

Holographic complexity using the CA proposal has recently been applied in a number of situations involving null shells, *e.g.*, [77, 78, 173, 195, 196]. In particular, we should also compare our results with those of [173], which evaluates the holographic complexity using the CA proposal for precisely the same Vaidya geometries (with $k = 0$) that were studied here. In fact, we can see that the results for the growth rate are precisely the same by comparing eq. (5.73) with eq. (56) of [173]. The primary way in which the two calculations differ is that in [173], the author sets $\tilde{\alpha} = \alpha$ and so implicitly the null generators of the past boundary are not affinely parameterized as they cross the null shell. However, this choice does not affect the final answer. Imagine that we allow α and $\tilde{\alpha}$ to be arbitrary constants. Then the counterterm contribution at $r = r_s$ appears in eq. (5.31) while the corresponding joint contributions appear in eq. (5.54). It is straightforward to see that combining these two contributions yields

$$I_{\text{joint}} + I_{\text{ct}} = \frac{\Omega_{k,d-1} r_s^{d-1}}{8\pi G_N} \log \left[\frac{f_{\text{vac}}(r_s)}{f_{\text{BH}}(r_s)} \right], \quad (5.119)$$

which is completely independent of both α and $\tilde{\alpha}$. One might note that in fact the coun-

²⁸Geometrically, the closest analog of this joint would be where the past null boundary reaches $r = 0$ in the AdS vacuum region. However, this point does not contribute to the gravitational action, as discussed in chapter 3.

terterm contribution at r_s vanishes with the choice $\tilde{\alpha} = \alpha$, as in [173]. Hence although some of the intermediate steps may differ, the final results for the holographic complexity here and in [173] agree.

In some of the other recent studies of the CA proposal with null shells, the counterterm (2.11) was included [195, 196] but in other, it was not [77, 78]. In all of these cases, it was assumed that the contribution of the (infinitely thin) null shell was zero, as we explicitly demonstrated in section 5.1.2, and so the WDW action was determined by adding together the action evaluated separately on the regions above and below the shell, as in our calculation. It is particularly interesting to compare [77] and [195], which both studied holographic complexity in hyperscaling violating geometries, but the first did not include the counterterm while the second did. The same simple but ad hoc prescription for the normalization of the null boundary normals was chosen in [77] as in [173], *i.e.*, $\tilde{\alpha} = \alpha$. The observation above was that with this choice, the counterterm contribution generated at r_s vanishes and so it is not surprising the main results for the growth rate in [77] and [195] agree. However, we note that differences appear in the transient behaviour if this ad hoc prescription is applied for a null shell falling into an eternal black hole as we will discuss in chapter 6. Further, there is no obvious covariant principle which produces the choice $\tilde{\alpha} = \alpha$, *i.e.*, this parameterization appears to be an arbitrary coordinate-dependent choice. For example then, it is not clear what the corresponding prescription for a null shell of finite width should be.

Future Directions

One of our key results was that if the gravitational action evaluated on the WDW patch is to properly describe the complexity of the boundary state, then one must include the counterterm (2.11) on the null boundaries. This counterterm was originally constructed in [63] to ensure that the action did not depend on the parametrization of the null boundaries. In particular, this term does not play a role in producing a well-defined variational principle for the gravitational action. Previous studies of holographic complexity using the CA proposal focused on stationary spacetimes, *e.g.*, eternal black hole backgrounds, and it was found that this extra surface term does not modify the essential properties of the holographic complexity, *e.g.*, the complexity of formation or the late-time rate of growth. This points out the importance of testing various proposal for holographic complexity in dynamical spacetimes, such as the Vaidya geometries (5.1).

Additional topics to explore would include extending our results to collapsing charged shells, to shells of finite width, to shells of other kinds of matter, including higher curvature corrections as in [69] or to localized shocks as in [174].

As emphasized in [173], the growth rate for the collapsing null shell calculated using the (modified) CA proposal always obeys the bound $dC'_A/dt \leq 2M/\pi$. It was proposed in [33, 34] that this bound may be related to Lloyd’s bound for the maximum rate of computation for a system with a fixed energy [116]. However, as noted above, transient violations of the proposed bound were already identified in studying the time evolution of complexity in an eternal black hole background in chapter 4. Further, even stronger violations were found in the dual of a noncommutative gauge theory [163] and in hyperscaling violating geometries [77, 195].²⁹ Therefore, while the proposed bound cannot be universal, it remains an interesting question to understand the situations when it does apply and when not, and the underlying reasons for this.

Another interesting direction would be to study the evolution of complexity for quantum quenches in a field theory context. Some initial studies of this question appear in [54, 55], which examine the evolution of the complexity through a mass quench in a free scalar field theory (analogous to those studied in [191–193]). A remarkable feature of these quenches is that the scalar field remains in a Gaussian state throughout the entire process, and so methods developed in [38, 39, 47, 49] can still be applied to evaluate the complexity. The comparison of our holographic results with those in [54] is not straightforward since, *e.g.*, the initial and final masses are nonvanishing (*i.e.*, neither the initial nor final scalar theories are CFTs). However, we might note that the QFT calculations suggest that the complexity growth rate at early times increases as the energy injected by the quench increases. Hence this behaviour would be in rough agreement with our holographic results where the initial growth rate is proportional to the energy carried by the null shell, *i.e.*, see eqs. (5.75) and (5.85) for the CA proposal, and eq. (5.108) for the CV proposal. On the other hand, in [54], the authors found that in most instances, the complexity quickly saturated (at least approximately) while, of course, the holographic complexity continues to grow linearly at late times. Further, the complexity in the QFT quench showed a strong dependence on the mass scale M associated with the unentangled reference state. In [38, 39], it was suggested the dependence on M could be associated with dependence of the holographic complexity α , which seems to be traded for the dependence on scale t_L with the addition of the boundary counterterm as we discuss in chapter 6. However, the holographic growth rate, *e.g.*, in eq. (5.72) shows no dependence on t_L at all, and so this points to another mismatch between the holographic and QFT results. One possible way to improve the comparison of the holographic and QFT quenches would be to consider CFT-to-CFT quenches for a free scalar (in which the initial and final masses both vanish) using the protocol described in section 3.2 of [193]. Another simple extension of this chapter would be to study the

²⁹Violations of the analogous bound proposed for systems with a chemical potential were also found in certain instances [34, 145, 155].

complexity for a mass quench of a free fermion, using the techniques of [\[47\]](#).

Chapter 6

Holographic Complexity in Vaidya Spacetimes: Two-sided black holes

We continue to examine the holographic complexity for Vaidya geometries in which a thin null shell collapses into an eternal black hole in this chapter — see figure 6.1. Such shock wave geometries have already been extensively studied in the context of holographic complexity, *e.g.*, [32, 34, 87, 174], however, these studies focused on the case where the energy in the shock was small. Using the formalism developed in chapter 5, we will not need to restrict our attention to this regime of light shocks here. Further, we will investigate the full time evolution of the holographic complexity, *i.e.*, including the transient regime, and this will allow us to identify several critical times that arise as the WDW patch (or the maximal volume surface) evolves forward in the background geometry. As well as the time evolution, we will investigate the complexity of formation in these shock wave geometries. As we found in chapter 5, we will argue that the inclusion of the null surface counterterm is crucial in these dynamical spacetimes in order for the CA proposal (1.24) to properly produce the expected properties of complexity, such as the ‘switchback’ effect [32, 87, 184]. We summarize the main results in some detail at the beginning of section 6.3.

The rest of the chapter is organized as follows: In section 6.1, we review the Vaidya background geometries in the context of two-sided black holes. We restrict our attention to thin shells of null fluid for which the action vanishes when the thickness shrinks to zero, as we showed in chapter 5. Next, we investigate the holographic complexity in these background geometries using the CA proposal in 6.2. We evaluate the time evolution and complexity of formation in the presence of light and heavy shock waves, and also examine the consequences of not including the null surface counterterm. We review our main results and discuss their physical implications in section 6.3, where we also present

some future directions. We leave some technical details to the appendices: In appendix C.1, we evaluate the counterterm contributions to the WDW patch and review its implications for the UV structure of complexity. In appendix C.2, we present some numerical results for the holographic complexity in higher dimensions using the CA conjecture.

This chapter is an adaptation of [68].

6.1 Background Geometry

Recall that the (unperturbed) eternal black hole geometry is dual to a thermofield double (TFD) state [30], which is a pure state in which the degrees of freedom of two identical copies of the boundary CFT are entangled,

$$|TFD\rangle \equiv Z^{-1/2} \sum_{n=0}^{\infty} e^{-\frac{1}{2}\beta E_n} |E_n\rangle_L |E_n\rangle_R, \quad (6.1)$$

where the two copies are denoted as left (L) and right (R), in analogy to the left and right boundaries of the eternal geometry. Tracing out either the left or right CFT leaves a thermal density matrix with inverse temperature β . While this density matrix is invariant under time translations, we can time evolve the two sets of degrees of freedom in the TFD state independently to produce

$$\begin{aligned} |TFD(t_L, t_R)\rangle &= U_L(t_L) U_R(t_R) |TFD\rangle, \\ &= Z^{-1/2} \sum_{n=0}^{\infty} e^{-\frac{1}{2}\beta E_n - iE_n(t_L + t_R)} |E_n\rangle_L |E_n\rangle_R, \end{aligned} \quad (6.2)$$

where $U_{L,R}$ are the usual time evolution operators for the corresponding CFTs, *i.e.*, $U_L(t_L) = e^{-iH_L t_L}$ and $U_R(t_R) = e^{-iH_R t_R}$. One immediate observation is that the state is invariant when we shift

$$t_L \rightarrow t_L + \Delta t, \quad t_R \rightarrow t_R - \Delta t, \quad (6.3)$$

i.e., the TFD state (6.1) is invariant if we time evolve with the combined Hamiltonian $H_L - H_R$. Of course, this invariance is reflected in the ‘boost symmetry’ of the dual black hole geometry. As a result, the holographic complexity remains unchanged by the above shifts (6.3), *i.e.*, it only depends on the combination $t_L + t_R$ (*e.g.*, see [32, 34] and chapter 4).

In the following, we study Vaidya geometries describing a thin shell of null fluid (or shock wave) injected into an eternal black hole background. Following [183, 184], these Vaidya geometries describe¹ a perturbation of the TFD state (6.1),

$$|TFD\rangle_{pert} = \mathcal{O}_R(-t_w) |TFD\rangle = U_R(t_w) \mathcal{O}_R U_R^\dagger(t_w) |TFD\rangle, \quad (6.4)$$

where $\mathcal{O}_R(-t_w)$ is operator inserted in the right CFT at a time $-t_w$ (see also figure 1.5).² In the second expression, we are describing this precursor as $\mathcal{O}_R(-t_w) = U_R(t_w) \mathcal{O}_R U_R^\dagger(t_w)$, *i.e.*, $U_R^\dagger(t_w)$ evolves the right degrees of freedom backwards by a time t_w , \mathcal{O}_R is inserted and then the right CFT is evolved forward by t_w . In the following, we will use the complexity of formation (in the Vaidya geometry) to evaluate the complexity of the precursor, *i.e.*, to compare the complexities of $|TFD\rangle_{pert}$ and $|TFD\rangle$. The nontrivial cancellations in the complexity of the precursor are connected to the switchback effect [32, 87, 184].

We will also examine the complexity of the time evolved state

$$\begin{aligned} |TFD(t_L, t_R)\rangle_{pert} &= U_L(t_L) U_R(t_R) |TFD\rangle_{pert} \\ &= U_L(t_L) U_R(t_R + t_w) \mathcal{O}_R U_R^\dagger(t_w) |TFD\rangle \\ &= U_R(t_R + t_w) \mathcal{O}_R U_R(t_L - t_w) |TFD\rangle, \end{aligned} \quad (6.5)$$

where in the last line, we use the boost symmetry of the TFD state, *i.e.*, $U_L(t_L) |TFD\rangle = U_R(t_R) |TFD\rangle$, and that U_L commutes with all operators in the right CFT [32]. In this case, inserting \mathcal{O}_R at a fixed time $-t_w$ breaks the shift symmetry (6.3). However, from the above expression, it is clear that if we combine the previous translations of the left and right times with a shift the insertion time,

$$t_w \rightarrow t_w + \Delta t, \quad (6.6)$$

then the time-evolved state in eq. (6.5) is invariant. We will refer to the combination of eqs. (6.3) and (6.6) together as the *time-shift symmetry* of the problem. Of course, this will also produce a symmetry for the holographic complexity and as a result, we will find

¹Our geometries are more properly interpreted in terms of a thermal quench, *e.g.*, [191, 192], where some boundary coupling is rapidly varied at $t_R = -t_w$. Instead, eq. (6.4) corresponds to an excited state in which the excitation becomes coherent at $t_R = -t_w$ (but with no variations of the couplings). The corresponding bulk geometry involves a null shell which emerges from the white hole singularity and reflects off of the right asymptotic boundary at $t_R = -t_w$ to become a collapsing shell, *e.g.*, see [32, 183, 184]. Since our evaluations of the holographic complexity always involve $t_R > -t_w$, our results would be the same for either geometry.

²The details of the operator will not be important for our analysis, however, for the special case of $d = 2$, [197] provides a detailed description of the dual of the Vaidya-AdS₃ geometry.

that the holographic complexity only depends on two combinations of the boundary times, $t_R + t_w$ and $t_L - t_w$, which appear in eq. (6.5).

Let us now turn to the dual geometry in the bulk. As noted above, we consider the AdS-Vaidya spacetimes constructed in chapter 5, sourced by the collapse of a spherically symmetric shell of null fluid. In particular, we consider the profile $f_p(v)$ in eq. (5.2) that describes the collapse of an infinitely thin shell of null fluid, which raises the mass of the black hole from M_1 to M_2 where

$$M_i = \frac{(d-1)\Omega_{k,d-1}}{16\pi G_N} \omega_i^{d-2}. \quad (6.7)$$

Further, in eq. (5.2), we implicitly consider the shock wave as coming from the right boundary at some early time $v_s = -t_w$ (with $t_w > 0$), in accord with our description of the boundary state (6.4). Hence we have

$$v_R < -t_w : \quad F(r, v) = f_1(r) = \frac{r^2}{L^2} + k - \frac{\omega_1^{d-2}}{r^{d-2}}, \quad (6.8)$$

$$v_R > -t_w : \quad F(r, v) = f_2(r) = \frac{r^2}{L^2} + k - \frac{\omega_2^{d-2}}{r^{d-2}}. \quad (6.9)$$

where the coordinates r and v_R cover the right exterior region and the future black hole interior, labeled I and II in figure 6.1. There is a corresponding set of coordinates r and v_L covering the left exterior region and the past white hole interior, labeled III and IV in the figure. The shock wave does not enter either of the latter regions and so we have

$$\text{for all } v_L : \quad F(r, v) = f_1(r) = \frac{r^2}{L^2} + k - \frac{\omega_1^{d-2}}{r^{d-2}}. \quad (6.10)$$

On either side of the shock wave, the geometry (5.1) corresponds to that of a (static) AdS black hole, whose horizon radius $r_{h,i}$ determined by³

$$\omega_i^{d-2} = r_{h,i}^{d-2} \left(\frac{r_{h,i}^2}{L^2} + k \right). \quad (6.11)$$

As noted above, in each of these regions, the mass is given by eq. (6.7) and further, the temperature and entropy become

$$T_i = \frac{1}{4\pi} \left. \frac{\partial f}{\partial r} \right|_{r=r_{h,i}} = \frac{1}{4\pi r_{h,i}} \left(d \frac{r_{h,i}^2}{L^2} + (d-2)k \right), \quad S_i = \frac{\Omega_{k,d-1}}{4G_N} r_{h,i}^{d-1}. \quad (6.12)$$

³Let us note here that for $k = -1$, we will only consider ‘large’ hyperbolic black holes with $r_h > L$, which have the casual structure illustrated in figure 6.1.

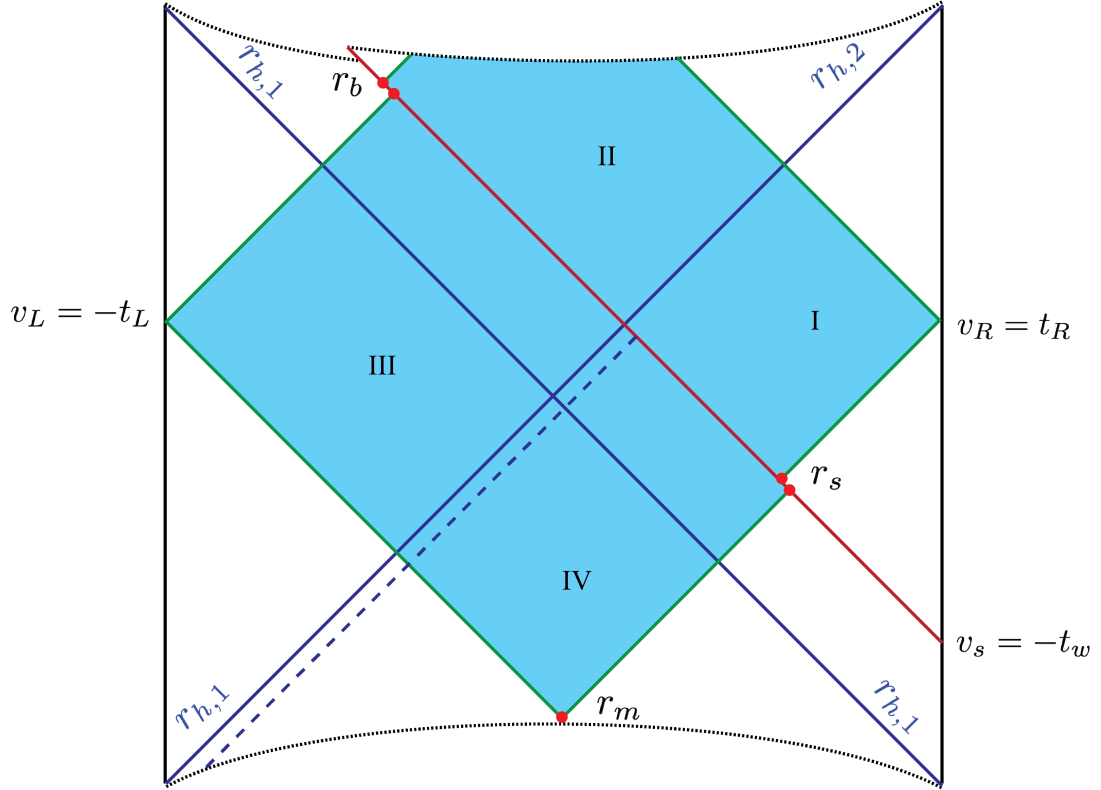


Figure 6.1: Penrose-like diagram for one shock wave on an eternal black hole geometry. At $v_s = -t_w$ a thin shock is injected at the right boundary which raises the mass of the black hole from M_1 to M_2 . We identify three points in the geometry that depend on time, r_m , where the boundaries of the WDW patch cross behind the past horizon, r_s , where the boundary of the WDW patch crosses the collapsing shell in the right exterior, and r_b where the boundary of the WDW patch crosses the shock wave inside the future black hole.

We define the tortoise coordinates with respect to eqs. (6.8)–(6.10) as

$$\text{for all } v_L \text{ \& for } v_R < -t_w : \quad r_1^*(r) = - \int_r^\infty \frac{dr}{f_1(r)}, \quad (6.13)$$

$$v_R > -t_w : \quad r_2^*(r) = - \int_r^\infty \frac{dr}{f_2(r)}, \quad (6.14)$$

where again we chose the range of integration such that both expressions satisfy $\lim_{r \rightarrow \infty} r_{1,2}^*(r) \rightarrow 0$. Using the tortoise coordinates, we can define an outgoing null coordinate u and an auxiliary time coordinate t as

$$u_{1,2} \equiv v - 2r_{1,2}^*(r), \quad t_{1,2} \equiv v - r_{1,2}^*(r). \quad (6.15)$$

Again these coordinates are discontinuous across the shell because $f(r)$ jumps from eq. (6.8) to eq. (6.9) at $v_R = -t_w$. In analogy to the diagrams in chapter 5, we represent the shock wave geometries with Penrose-like diagrams (*e.g.*, see figure 6.1), which can be smoothly ruled with lines of constant u and v . As before, since the coordinate u is discontinuous, this introduces a(n unphysical) jump as the outgoing null rays cross the shock wave. Of course, the spacetime is continuous along this surface and the outgoing null rays are smooth, as can be seen by regulating the thin shell to have a finite thickness — see section 5.1.

Before we proceed further, let us comment on synchronizing the times between the left and right boundaries. In principle, the left boundary time t_L is completely independent of the right boundary time t_R in the eternal black hole geometry. However, implicitly, they are synchronized by considering a geometric construction, *e.g.*, where an extremal codimension-one surface that runs from one boundary to the other through the bifurcation surface. This surface connects the time slice t_L on the left boundary to the time slice $t_R = -t_L$ on the right boundary. The minus sign arises here because of our convention that the boundary times increase upwards on both boundaries in figure 6.1. Hence one might worry that the two boundary times cannot be synchronized in a natural way. However, we observe that the above geometric construction is unaffected for times $t_L > t_w$, for which the extremal surface will reach the right boundary at times $t_R < -t_w$. That is, for late (early) times on the left (right) boundary, the desired extremal surfaces do not meet the shock wave and remain entirely within the portion of the spacetime where $F(v, r) = f_1(r)$. Once the boundary times are synchronized in these regions, this synchronization is straightforwardly extended to the entire boundaries. Implicitly, this is how we match the left and right boundary times in the following.

It will be useful to define some dimensionless quantities in order to express the evolution

of complexity, as well as the complexity of formation, in the following. We define,⁴

$$w \equiv \frac{r_{h,2}}{r_{h,1}}, \quad z \equiv \frac{L}{r_{h,2}}, \quad x \equiv \frac{r}{r_{h,2}}, \quad (6.16)$$

which for positive-energy shock waves, yields $w > 1$. Also note that for planar (and BTZ) black holes, w is proportional to the ratio of temperatures, *i.e.*, $w = T_2/T_1$, for $k = 0$ (or $d = 2$) which can be seen by using eq. (6.12). The ratio between the masses and the entropies reads

$$\frac{M_2}{M_1} = w^d \frac{(1 + kz^2)}{(1 + kz^2w^2)} \quad \text{and} \quad \frac{S_2}{S_1} = w^{d-1}. \quad (6.17)$$

It is also useful to rescale the blackening factor such that

$$f_2(r, L) = \frac{1}{z^2} \tilde{f}(x, z), \quad f_1(r, L) = \frac{1}{w^2 z^2} \tilde{f}(wx, wz), \quad (6.18)$$

where

$$\tilde{f}(x, z) \equiv x^2 + kz^2 - \frac{1}{x^{d-2}} (1 + kz^2). \quad (6.19)$$

Note that $\tilde{f}(x, z)$ is not a function of z for planar holes (*i.e.*, $k = 0$). Finally, if a physical quantity depends on z , we can use eq. (6.12) to express z as a function of LT_2 ,

$$z = \frac{d}{\sqrt{4\pi^2(LT_2)^2 - (d-2)dk + 2\pi LT_2}}. \quad (6.20)$$

6.2 Complexity = Action

In order to evaluate the holographic complexity using the complexity=action proposal (1.24), we begin by writing the total action as

$$I = I_{\text{grav}} + I_{\text{ct}} + I_{\text{fluid}}, \quad (6.21)$$

where I_{fluid} is the null fluid action, as constructed in section 5.1. There we showed that I_{fluid} vanishes on shell, and so the imprint of the shock wave in the CA calculations comes only from its backreaction on the metric. Further, we showed that as the width of the null shell shrinks to zero, the action of the spacetime region occupied by the shell itself vanishes.

⁴Note that here, z and x are defined as the ratio of the AdS scale L or the radius r with the final horizon size $r_{h,2}$. Using the ratio w one can easily construct quantities normalized by $r_{h,1}$ instead.

Hence for an infinitely thin shell, as introduced in eq. (5.2), the action can be evaluated by separately evaluating the action on the portion of the WDW patch above the shell and that below the shell.

The gravitational action I_{grav} is given by eq. (2.10) and we have also included the additional surface term for the null boundaries given by eq. (2.11). This counterterm is not needed to produce a well defined variational principle for the gravitational action, *i.e.*, I_{ct} only depends on intrinsic boundary data. Instead it was introduced in [63] to ensure that the action is reparametrization invariant. In chapter 5, we found that including the counterterm was essential if the WDW action was to reproduce certain properties expected of the complexity in dynamical spacetimes and hence it is included in (most of) our CA calculations here.

However, we will also expand our arguments indicating that the counterterm (2.11) is an essential part of the gravitational action by considering our results after we remove the counterterm contributions. In this case, we must come to grips with the various ambiguities arising from the surface and joint terms associated with the null boundaries, *e.g.*, see discussion in [63]. We follow the prescription in [63] where we set $\kappa = 0$ by choosing an affine parametrization for the null normals. Further, we fix the overall normalization of these null vectors by their inner product with the asymptotic timelike Killing vector at the boundary, $\hat{t} = \partial_t$, *i.e.*, we set $\hat{t} \cdot k = \pm\alpha$.

In section 6.2.1, we evaluate the time evolution (including the null counterterm) for the Vaidya spacetimes described in section 6.1, and then we examine their complexity of formation in section 6.2.2. In section 6.2.3, we (mostly) focus on the BTZ black hole (*i.e.*, $d = 2$) and demonstrate that the CA calculations without the inclusion of the counterterm fail to produce the expected behaviour of holographic complexity. In appendix C.1, we discuss some further details on the influence of the null counterterm in Vaidya spacetimes. In appendix C.2 we discuss the complexity evolution for higher ($d > 2$) dimensional black holes, focusing mostly on $d = 4$.

6.2.1 Time Evolution

Consider the shock wave spacetime represented in figure 6.1, with the Penrose-like diagram describing the geometry in eqs. (6.8–6.10). The null shell is injected at the right boundary at $v_s = -t_w$ (with $t_w > 0$), raising the mass of the black hole from M_1 to M_2 . We can study the time evolution of the holographic complexity in many different ways. However, for simplicity, we will focus on a symmetric time evolution with $t_L = t/2 = t_R$ starting at $t_L = t_R = 0$, in analogy to the analysis in chapter 4.

We identify the three positions which are important in defining the WDW patch, depending on the time: r_b is where the boundary of the WDW patch originating from the left boundary meets the shock wave inside the future black hole; r_s is the surface where the WDW boundary in the right exterior meets the shock wave; and r_m is where the past null boundary segments of the WDW patch meet inside the white hole region — see figure 6.1. Of course, depending on the parameters of the problem, r_b and r_m could be behind the singularities. In particular, if $r_m < 0$, the WDW patch has a spacelike boundary segment running along the past singularity. In this section, we carefully evaluate all these possibilities in the shock wave black hole geometry, and show how the critical times where r_b and r_m cross $r = 0$ produce transitions between different behaviours of the holographic complexity.

We calculate the bulk action given by eq. (2.10) by using the same prescription discussed in chapter 5, *i.e.*, implicitly we evaluate the total gravitational action as the sum of the action evaluated on the regions comprising the WDW patch to the future and the past of the shock wave. We start here by identifying the three positions introduced above (*i.e.*, r_b , r_s and r_m) as functions of the times⁵ $v_L = -t_L$ and $v_R = t_R$ at which the WDW patch is anchored on the left and right boundaries,

$$\begin{aligned} t_L - t_w &= 2r_1^*(r_b), \\ t_R + t_w &= -2r_2^*(r_s), \\ t_L - t_w &= 2r_1^*(r_s) - 2r_1^*(r_m). \end{aligned} \tag{6.22}$$

Recall that t_w is defined to be positive. Given eqs. (6.13) and (6.14), the time evolution of these positions is relatively simple. For example, if t_L is held fixed, eq. (6.22) implies that

$$\frac{dr_b}{dt_R} = 0, \quad \frac{dr_s}{dt_R} = -\frac{f_2(r_s)}{2}, \quad \frac{dr_m}{dt_R} = -\frac{f_1(r_m)}{2} \frac{f_2(r_s)}{f_1(r_s)}. \tag{6.23}$$

Similarly, when t_R is held constant, the evolution with the left boundary time becomes

$$\frac{dr_b}{dt_L} = \frac{f_1(r_b)}{2}, \quad \frac{dr_s}{dt_L} = 0, \quad \frac{dr_m}{dt_L} = -\frac{f_1(r_m)}{2}. \tag{6.24}$$

Recall that we will be interested in $t_L = t/2 = t_R$ in the following, and so when required we can combine the above results in the appropriate linear combination.

⁵The minus sign arises for t_L because our convention is that the left boundary time increases as we run upwards in figure 6.1, while v_L increases as we move down diagonally towards the bottom left corner.

Bulk contribution

We start by evaluating the bulk action for the WDW patch represented in figure 6.1. As before, the Einstein-Hilbert contribution to the action is $\mathcal{R} - 2\Lambda = -\frac{2d}{L^2}$ in $d + 1$ bulk dimensions. The total bulk action reads

$$\begin{aligned}
I_{\text{bulk}} = & \left(\frac{\Omega_{k,d-1}}{16\pi G_N} \right) \left(-\frac{2d}{L^2} \right) \left[\int_{r_s}^{r_{\text{max}}} dr r^{d-1} (-2r_2^*(r)) + \int_{r_b}^{r_s} dr r^{d-1} (t_R + t_w) \right. \\
& \int_{r_{h,1}}^{r_s} dr r^{d-1} (2r_1^*(r_s) - 2r_1^*(r)) + \int_{r_m}^{r_{h,1}} dr r^{d-1} (-t_L + t_w - 2r_1^*(r) + 2r_1^*(r_s)) + \\
& + \int_{r_{h,1}}^{r_{\text{max}}} dr r^{d-1} (-2r_1^*(r)) + \int_{r_b}^{r_{h,1}} dr r^{d-1} (-t_w + t_L - 2r_1^*(r)) + \\
& \left. + \int_0^{r_b} dr r^{d-1} (t_R + t_w - 2r_2^*(r) + 2r_2^*(r_b)) \right]. \tag{6.25}
\end{aligned}$$

Now, we fix the left boundary time t_L and vary t_R in the right boundary, as in eq. (6.23). The time derivative of the bulk action with respect to the right boundary reads

$$\frac{dI_{\text{bulk}}}{dt_R} = -\frac{\Omega_{k,d-1}}{8\pi G_N L^2} \left[r_s^d \left(1 - \frac{f_2(r_s)}{f_1(r_s)} \right) + r_m^d \frac{f_2(r_s)}{f_1(r_s)} \right]. \tag{6.26}$$

In addition, we can write the time derivative with respect to the left boundary evolution t_L in eq. (6.24),

$$\frac{dI_{\text{bulk}}}{dt_L} = -\frac{\Omega_{k,d-1}}{8\pi G_N L^2} \left[r_m^d - r_b^d \left(1 - \frac{f_1(r_b)}{f_2(r_b)} \right) \right]. \tag{6.27}$$

With respect to a symmetric time evolution $t_L = t_R = t/2$, we sum the linear combination of eqs. (6.26) and (6.27),

$$\frac{dI_{\text{bulk}}}{dt} = -\frac{\Omega_{k,d-1}}{16\pi G_N L^2} \left[r_m^d \left(1 + \frac{f_2(r_s)}{f_1(r_s)} \right) - r_b^d \left(1 - \frac{f_1(r_b)}{f_2(r_b)} \right) + r_s^d \left(1 - \frac{f_2(r_s)}{f_1(r_s)} \right) \right]. \tag{6.28}$$

Boundary surface contributions

We now turn our attention to the boundary surface contributions in the action in eq. (2.10). As suggested in [63], we choose the normals to the null boundaries to be affinely parametrized (before and after the shock wave — see discussion in chapter 5). Therefore the parameter κ and the corresponding boundary term vanishes for all of these null boundary segments.

There are, however, two possible boundary contributions to the action, namely, evaluating the Gibbons-Hawking-York (GHY) term on a spacelike (regulator) surface right before the future singularity, and also in the regime that r_m is behind the singularity, a similar contribution arises from the past singularity.⁶

We will denote the critical times at which r_m leaves the past singularity (*i.e.*, r_m becomes positive) as $t_{L,c1}$ and $t_{R,c1}$. From eq. (6.22), we have

$$t_{R,c1} = -t_w - 2r_2^*(r_s), \quad t_{L,c1} = t_w + 2r_1^*(r_s) - 2r_1^*(0). \quad (6.29)$$

We can apply this result as follows: If we choose a value for $t_{R,c1}$, then the first equation determines a particular value of r_s and the second equation determines the value $t_{L,c1}$ at which the WDW patch lifts off the past singularity. Similarly, if instead we choose a value for $t_{L,c1}$, we can apply the equations in the opposite order to determine the value of $t_{R,c1}$ at which the WDW patch lifts off the past singularity. There is also a second critical time for the left boundary, which we will denote $t_{L,c2}$ and it is the time at which the crossing point r_b touches the singularity, *i.e.*,

$$t_{L,c2} = t_w + 2r_1^*(0). \quad (6.30)$$

Of course, whether there are critical times in the range of time evolution that we are studying depends on how early and how energetic the shock wave was. However, once the latter parameters are chosen, one can determine with eqs. (6.29) and (6.30) whether there are critical times and find their respective values.

Now, we first investigate the GHY term at the future singularity. As usual *e.g.*, [34] and chapter 3, we introduce a regulator surface at $r = \varepsilon$ and after evaluating the GHY term on this surface, we take the limit $\varepsilon \rightarrow 0$. Since $t_L > 0$ and $v_s = -t_w < 0$, there are two possibilities: $t_L < t_{L,c2}$ for which the crossing point r_b arises in the black hole interior region; and $t_L > t_{L,c2}$ for which the future null boundary of WDW patch from the left boundary reaches the singularity without crossing the shock wave. For $t_L < t_{L,c2}$, we have

$$I_{GHY}^{(f)} = -\frac{\Omega_{k,d-1}}{8\pi G_N} \left(\frac{-d\omega_2^{d-2}}{2} \right) (t_R + t_w + 2r_2^*(r_b) - 2r_2^*(0)), \quad (6.31)$$

which leads to

$$\frac{dI_{GHY}^{(f)}}{dt_R} = \frac{\Omega_{k,d-1}}{8\pi G_N} \frac{d\omega_2^{d-2}}{2} \quad \text{and} \quad \frac{dI_{GHY}^{(f)}}{dt_L} = \frac{\Omega_{k,d-1}}{8\pi G_N} \frac{d\omega_2^{d-2}}{2} \frac{f_1(r_b)}{f_2(r_b)}. \quad (6.32)$$

⁶We do not consider possible surface terms at the UV regulator surfaces because these contributions will be independent of time, *e.g.*, see [65] and chapter 4.

In contrast, for $t_L > t_{L,c2}$, we have

$$I_{GHY}^{(f)} = -\frac{\Omega_{k,d-1}}{8\pi G_N} \left(\frac{-d\omega_2^{d-2}}{2} \right) (t_R + t_w) - \frac{\Omega_{k,d-1}}{8\pi G_N} \left(\frac{-d\omega_1^{d-2}}{2} \right) (-t_w + t_L - 2r_1^*(0)) , \quad (6.33)$$

which results in

$$\frac{dI_{GHY}^{(f)}}{dt_R} = \frac{\Omega_{k,d-1}}{8\pi G_N} \frac{d\omega_2^{d-2}}{2} \quad \text{and} \quad \frac{dI_{GHY}^{(f)}}{dt_L} = \frac{\Omega_{k,d-1}}{8\pi G_N} \frac{d\omega_1^{d-2}}{2} . \quad (6.34)$$

Now, the GHY contribution from the past singularity follows a similar analysis. Whenever $t_R < t_{R,c1}$ or $t_L < t_{L,c1}$, the WDW patch intersects the past singularity and one finds the following GHY contribution

$$I_{GHY}^{(p)} = \frac{\Omega_{k,d-1}}{8\pi G_N} \left(\frac{d\omega_1^{d-2}}{2} \right) (-t_L + t_w + 2r_1^*(r_s) - 2r_1^*(0)) . \quad (6.35)$$

The time derivatives of this result then become

$$\frac{dI_{GHY}^{(p)}}{dt_R} = -\frac{\Omega_{k,d-1}}{8\pi G_N} \frac{d\omega_1^{d-2}}{2} \frac{f_2(r_s)}{f_1(r_s)} \quad \text{and} \quad \frac{dI_{GHY}^{(p)}}{dt_L} = -\frac{\Omega_{k,d-1}}{8\pi G_N} \frac{d\omega_1^{d-2}}{2} . \quad (6.36)$$

Joint contributions

We now focus on the joint contributions to the action (2.10) evaluated on the WDW patch. In principle, such contributions arise where the null boundaries intersect the UV regulator surfaces near the asymptotic boundary. However, these contributions are time independent and so we ignore them in the following. Similarly, there are joint contributions where the null boundaries intersect the regulator surfaces $r = \varepsilon$ near the singularities but these vanish in the limit $\varepsilon \rightarrow 0$. This leaves three possible different contributions coming from joints at $r = r_b$, r_s and r_m , as shown in figure 6.1.⁷ The joint contributions at r_s and r_b are analogous to the ones discussed in the one sided geometry in chapter 5, while the contribution from r_m is similar to the joint action found in unperturbed eternal black holes in chapter 4.

We start by evaluating the sum of joint contributions where the past null boundary of the WDW patch crosses the shock wave, *i.e.*, at $r = r_s$. The relevant null normals on the

⁷In the case where $r_b < 0$, there would be additional joints where the shock wave hits the future singularity, *i.e.*, on the regulator surface $r = \varepsilon$ at $v = -t_w$. However, these again yield a vanishing contribution in the limit $\varepsilon \rightarrow 0$.

past boundary are

$$k_\mu^p dx^\mu = \begin{cases} \alpha \left(-dv + \frac{2}{f_2(r)} dr \right) & \text{for } r > r_s, \\ \tilde{\alpha} \left(-dv + \frac{2}{f_1(r)} dr \right) & \text{for } r < r_s. \end{cases} \quad (6.37)$$

Further we introduce the two normals along the collapsing shock wave,

$$\begin{aligned} v > -t_w & : & k_\mu^{s+} dx^\mu &= -\beta dv, \\ v < -t_w & : & k_\mu^{s-} dx^\mu &= \beta dv. \end{aligned} \quad (6.38)$$

The sum of the two joint contributions then reads

$$I_{\text{joint}}^{(I)} = \frac{\Omega_{k,d-1} r_s^{d-1}}{8\pi G_N} \log \left(\frac{\alpha f_1(r_s)}{\tilde{\alpha} f_2(r_s)} \right). \quad (6.39)$$

We note that in eq. (6.37), the normalization constant α was fixed with the usual asymptotic condition $k^p \cdot \hat{t} = -\alpha$ [63]. However, to fix the normalization constant $\tilde{\alpha}$ below the shell, we demand that the null boundary is affinely parametrized across the shock wave, *i.e.*, $\kappa = 0$, following the discussion in chapter 5. The latter constraint imposes

$$\frac{\tilde{\alpha}}{\alpha} = \frac{f_1(r_s)}{f_2(r_s)}. \quad (6.40)$$

As a consequence, the corner contributions at r_s vanish, as was discussed for the one-sided collapse in previous chapter, *i.e.*,

$$I_{\text{joint}}^{(I)} = 0. \quad (6.41)$$

Next, we evaluate the sum of joint terms where the future null boundary of the WDW patch crosses the shock wave, *i.e.*, at $r = r_b$. The (outward-directed) null normal to this future boundary is

$$k_\mu^f dx^\mu = \begin{cases} \alpha \left(-dv + \frac{2}{f_1(r)} dr \right) & \text{for } r > r_b, \\ \hat{\alpha} \left(-dv + \frac{2}{f_2(r)} dr \right) & \text{for } r < r_b. \end{cases} \quad (6.42)$$

Using the null normals along the shock wave in eq. (6.38), the total contribution to the action is

$$I_{\text{joint}}^{(II)} = \frac{\Omega_{k,d-1} r_b^{d-1}}{8\pi G_N} \log \left(\frac{\alpha f_2(r_b)}{\hat{\alpha} f_1(r_b)} \right). \quad (6.43)$$

Once again, the condition of affine parametrization across the shock wave fixes the ratio between the normalization constants in eq. (6.42) with

$$\frac{\hat{\alpha}}{\alpha} = \frac{f_2(r_b)}{f_1(r_b)}. \quad (6.44)$$

Therefore, the joint contributions at r_b also vanishes ,

$$I_{\text{joint}}^{(\text{II})} = 0. \quad (6.45)$$

Finally, we turn to the possible contribution from the joint where the two past null boundaries of the WDW patch meet inside the white hole region, *i.e.*, at r_m . This joint contribution is evaluated with k^p in eq. (6.37) on the right boundary (with $r < r_s$), and

$$k_\mu^L dx^\mu = \alpha dv \quad (6.46)$$

for the normal to the left null boundary.⁸ The resulting joint contribution then reads, with the affine parametrization condition (6.40),

$$I_{\text{joint}}^{(\text{III})} = -\frac{\Omega_{k,d-1} r_m^{d-1}}{8\pi G_N} \log \left(\frac{|f_1(r_m)|}{\alpha \tilde{\alpha}} \right) = -\frac{\Omega_{k,d-1} r_m^{d-1}}{8\pi G_N} \log \left(\frac{|f_1(r_m)| f_2(r_s)}{\alpha^2 f_1(r_s)} \right). \quad (6.47)$$

The time derivatives of this joint contribution then become

$$\begin{aligned} \frac{dI_{\text{joint}}^{(\text{III})}}{dt_R} &= \frac{(d-1)\Omega_{k,d-1}}{16\pi G_N} r_m^{d-2} f_1(r_m) \frac{f_2(r_s)}{f_1(r_s)} \log \left[\frac{|f_1(r_m)| f_2(r_s)}{\alpha^2 f_1(r_s)} \right] \\ &\quad + \frac{\Omega_{k,d-1}}{16\pi G_N} \frac{f_2(r_s)}{f_1(r_s)} \left[\frac{2r_m^d}{L^2} + (d-2)\omega_1^{d-2} \right] + \frac{\Omega_{k,d-1} r_m^{d-1}}{16\pi G_N} \left[f_2'(r_s) - f_1'(r_s) \frac{f_2(r_s)}{f_1(r_s)} \right], \\ \frac{dI_{\text{joint}}^{(\text{III})}}{dt_L} &= \frac{(d-1)\Omega_{k,d-1}}{16\pi G_N} r_m^{d-2} f_1(r_m) \log \left[\frac{|f_1(r_m)| f_2(r_s)}{\alpha^2 f_1(r_s)} \right] \\ &\quad + \frac{\Omega_{k,d-1}}{16\pi G_N} \left[\frac{2r_m^d}{L^2} + (d-2)\omega_1^{d-2} \right]. \end{aligned} \quad (6.48)$$

⁸Without loss of generality, we are assuming here that the null normals are normalized at both the left and right boundaries with the same constant. In fact, when we add the counterterm (2.11) which ensures reparametrization invariance to the null boundaries, the total action will be independent of α .

Counterterm contributions

Next we examine the contributions of the counterterm (2.11) to the time derivative of the holographic complexity. The counterterm is evaluated on each of the four null boundaries of the WDW patch in appendix C.1, but only three of these contribute to the growth rate. First, for the right past boundary, we have

$$I_{\text{ct}}^{(\text{I})} = \text{“UV terms”} - \frac{\Omega_{k,d-1}}{8\pi G_N} r_m^{d-1} \left[\log\left(\frac{(d-1)\alpha\ell_{\text{ct}}}{r_m}\right) + \frac{1}{d-1} \right] + \frac{\Omega_{k,d-1}}{8\pi G_N} (r_s^{d-1} - r_m^{d-1}) \log\left(\frac{f_1(r_s)}{f_2(r_s)}\right). \quad (6.49)$$

The above expression corresponds to eq. (C.7) after we have substituted the affine parametrization condition (6.40). We have also left implicit the terms coming from the UV regulator surface at $r = r_{\text{max}}$, since they are time independent and so do not contribute to the growth rate. Of course, if we are considering early times (*i.e.*, $t_{\text{R}} < t_{\text{R},\text{c1}}$ or $t_{\text{L}} < t_{\text{L},\text{c1}}$) when this boundary ends on the past singularity, we simply set $r_m = 0$ in the above expression leaving only the contribution for the crossing point $r = r_s$.

For the left future boundary, we find

$$I_{\text{ct}}^{(\text{II})} = \text{“UV terms”} + \frac{\Omega_{k,d-1}}{8\pi G_N} r_b^{d-1} \log\left(\frac{f_2(r_b)}{f_1(r_b)}\right), \quad (6.50)$$

by substituting eq. (6.44) for \hat{a} into eq. (C.8). Here we are implicitly assuming that this boundary always terminates on the future singularity and for late times (*i.e.*, $t_{\text{L}} > t_{\text{L},\text{c2}}$) when this boundary does not cross the shock wave, we simply set $r_b = 0$ above. We also consider the left past boundary, for which eq. (C.9) yields

$$I_{\text{ct}}^{(\text{III})} = \text{“UV terms”} - \frac{\Omega_{k,d-1}}{8\pi G_N} r_m^{d-1} \left[\log\left(\frac{(d-1)\alpha\ell_{\text{ct}}}{r_m}\right) + \frac{1}{d-1} \right]. \quad (6.51)$$

We might note that this contribution is identical to the first line in eq. (6.49). Again, we set $r_m = 0$ above for early times (*i.e.*, $t_{\text{R}} < t_{\text{R},\text{c1}}$ or $t_{\text{L}} < t_{\text{L},\text{c1}}$) when this boundary ends on the past singularity. Finally, we also have the counterterm contribution for the right future boundary in eq. (C.10) but as noted above, it will not contribute to the complexity growth rate, since we only consider the regime when this surface terminates at the future singularity at $r = 0$.

We now evaluate the time derivative of these three contributions in turn by using eqs. (6.23) and (6.24) to evaluate the time derivatives of r_s , r_b and r_m . Let us begin with

eq. (6.50) and consider the regime $t_L < t_{L,c2}$, which yields

$$\begin{aligned} \frac{dI_{\text{ct}}^{(\text{II})}}{dt_{\text{R}}} &= 0, \\ \frac{dI_{\text{ct}}^{(\text{II})}}{dt_{\text{L}}} &= -\frac{\Omega_{k,d-1}}{16\pi G_N} \left[\frac{2r_b^d}{L^2} \left(1 - \frac{f_1(r_b)}{f_2(r_b)} \right) + (d-2) \left(\omega_1^{d-2} - \omega_2^{d-2} \frac{f_1(r_b)}{f_2(r_b)} \right) \right] \\ &\quad + \frac{(d-1)\Omega_{k,d-1}}{16\pi G_N} r_b^{d-2} f_1(r_b) \log \left(\frac{f_2(r_b)}{f_1(r_b)} \right). \end{aligned} \quad (6.52)$$

Of course, for later times $t_L > t_{L,c2}$, both of these time derivatives vanish since $r_b = 0$.

Given the similarities between eqs. (6.49) and (6.51), we combine $I_{\text{ct}}^{(\text{I})}$ and $I_{\text{ct}}^{(\text{III})}$ in evaluating the time derivatives. For early times (*i.e.*, $t_{\text{R}} < t_{\text{R},c1}$ or $t_L < t_{L,c1}$), we set $r_m = 0$, and the time derivatives only act on r_s producing

$$\begin{aligned} \frac{d}{dt_{\text{R}}} (I_{\text{ct}}^{(\text{I})} + I_{\text{ct}}^{(\text{III})}) \Big|_{r_m=0} &= \frac{\Omega_{k,d-1}}{16\pi G_N} \left[\frac{2r_s^d}{L^2} \left(1 - \frac{f_2(r_s)}{f_1(r_s)} \right) + (d-2) \left(\omega_2^{d-2} - \omega_1^{d-2} \frac{f_2(r_s)}{f_1(r_s)} \right) \right] \\ &\quad - \frac{(d-1)\Omega_{k,d-1}}{16\pi G_N} r_s^{d-2} f_2(r_s) \log \left[\frac{f_1(r_s)}{f_2(r_s)} \right], \end{aligned} \quad (6.53)$$

$$\frac{d}{dt_{\text{R}}} (I_{\text{ct}}^{(\text{I})} + I_{\text{ct}}^{(\text{III})}) \Big|_{r_m=0} = 0.$$

At later times (*i.e.*, $t_{\text{R}} < t_{\text{R},c1}$ or $t_L < t_{L,c1}$), r_m becomes a dynamical variable and so there are additional contributions to the above time derivatives

$$\begin{aligned} \frac{d}{dt_{\text{R}}} (I_{\text{ct}}^{(\text{I})} + I_{\text{ct}}^{(\text{III})}) &= \frac{d}{dt_{\text{R}}} (I_{\text{ct}}^{(\text{I})} + I_{\text{ct}}^{(\text{III})}) \Big|_{r_m=0} - \frac{\Omega_{k,d-1}(d-1)}{16\pi G_N} r_m^{d-2} \left[f_2'(r_s) - \frac{f_2(r_s)}{f_1(r_2)} f_1'(r_s) \right] \\ &\quad + \frac{\Omega_{k,d-1}(d-1)}{8\pi G_N} r_m^{d-2} f_1(r_m) \frac{f_2(r_s)}{f_1(r_s)} \log \left[\frac{(d-1) f_1(r_s)}{r_m f_2(r_s)} \ell_{\text{ct}} \alpha \right] \\ \frac{d}{dt_{\text{L}}} (I_{\text{ct}}^{(\text{I})} + I_{\text{ct}}^{(\text{III})}) &= \frac{\Omega_{k,d-1}(d-1)}{8\pi G_N} r_m^{d-2} f_1(r_m) \log \left[\frac{(d-1) f_1(r_s)}{r_m f_2(r_s)} \ell_{\text{ct}} \alpha \right]. \end{aligned} \quad (6.54)$$

Of course, we will see below that when these counterterm contributions are combined with those from the rest of the gravitational action, the dependence on the normalization constant α is completely eliminated — see also eq. (C.12).

Time Dependence of Complexity

We can now evaluate the time dependence of the holographic complexity by summing the various expressions above. However, we can consider many different forms for the time

evolution, *e.g.*, varying t_L alone or t_R alone. For simplicity, we will focus on the symmetric case where we vary $t = t_L + t_R$ while fixing $t_L - t_R = 0$. This approach is closely related to the time evolution studied in chapter 4 for an unperturbed eternal black hole (without any shock waves). In principle though, the results above would easily allow one to study the evolution of the holographic complexity according to any other linear combination $t' = a t_L + b t_R$.

Further, in analogy with chapter 4, we will focus on the evolution for $t > 0$.⁹ However, there remains two important factors in determining how the holographic complexity grows, namely, the time at which the shock wave is sent in from the right boundary and its mass, *i.e.*, the values of t_w and $M_2 - M_1$. In particular, these will determine the geometry of the WDW patch as discussed around eqs. (6.29) and (6.30). That is, as seen in studying the CA conjecture in the unperturbed eternal black hole, *e.g.*, [34] and chapter 4, we are generally in a regime where $r_m < 0$ at $t = 0$ and the WDW patch touches some interval on the past singularity. Hence in the present situation, the shock wave parameters affect the critical time t_{c1} when r_m becomes positive and the WDW patch terminates above the past singularity. This critical time is determined by setting $t_{L,c1} = t_{c1}/2 = t_{R,c1}$ in eq. (6.29), which then yields

$$t_{c1} = 2t_w - 4r_1^*(0) + 4r_1^*(r_s), \quad r_1^*(r_s) + r_2^*(r_s) = r_1^*(0) - t_w. \quad (6.55)$$

Here the second equation determines the value of r_s which should be substituted into the first to determine t_{c1} . Generally, increasing t_w or the mass of the shock, *i.e.*, increasing $M_2 - M_1$, increases the value of t_{c1} .¹⁰

Now similarly, we are generally in a regime at $t = 0$ where the WDW patch touches some interval on the future singularity. If we evolve forward in time, this interval simply expands but there is another critical time t_{c2} where the interval includes the point where

⁹Although we also consider some times slightly before $t = 0$.

¹⁰These statements can be confirmed as follows: For a fixed ratio $w = r_{h,2}/r_{h,1}$, the following identity holds

$$\frac{dt_{c1}}{dt_w} = \frac{2(\omega_2^{d-2} - \omega_1^{d-2})}{r_s^{d-2}(f_1(r_s) + f_2(r_s))}. \quad (6.56)$$

Assuming $M_2 > M_1$, the above derivative is positive and so the effect of increasing t_w here is to increase the value of t_{c1} . Similarly, we have

$$\frac{dt_{c1}}{dw} = -\frac{4f_2(r_2)}{f_2(r_2) + f_1(r_2)} \frac{dr_2^*}{dw} \Big|_{r_s}, \quad (6.57)$$

and increasing M_2 for a fixed r_s decreases $r_2^*(r_s)$. Hence increasing the mass of the second black hole also increases t_{c1} .

the shock wave hits the singularity. That is, t_{c2} is the time when r_b vanishes (and then becomes negative for larger values of t). Substituting $t_{L,c2} = t_{c2}/2$ into eq. (6.22), we find this critical time to be

$$t_{c2} = 2t_w + 4r_1^*(0). \quad (6.58)$$

Here again, the effect of increasing t_w is to increase t_{c2} , while varying $M_2 - M_1$ has no effect on the value of t_{c2} (if we assume that M_1 is fixed).

We would like to add one more critical time to this list, in analogy with the evolution of the holographic complexity for the unperturbed eternal black hole in chapter 4. In that instance, there was actually an interval $-t_{c1} \leq t \leq t_{c1}$ in which the complexity did not change. We will find a similar plateau in the case of the shock wave geometries where the rate of change is small but since shock wave breaks the time-shift symmetry, we introduce a new critical time t_{c0} to denote the beginning of this period, $-t_{c0} \leq t \leq t_{c1}$. Geometrically, this time is the time at which the WDW patch lifts off of the future singularity if we push t to sufficiently negative values. This critical time can be determined in a similar way to finding t_{c1} and the result is

$$t_{c0} = 2t_w - 4r_2^*(0) + 4r_2^*(r_b), \quad r_1^*(r_b) + r_2^*(r_b) = r_2^*(0) - t_w. \quad (6.59)$$

Here again, we determine r_b from the second equation and then substitute this value into the first equation to determine t_{c0} . We may note that $r_b < r_{h,1}$, *i.e.*, the (future) null boundary of the WDW (on the left) crosses the shock wave behind the black hole horizon, and so one can easily show that $t_{c0} < 2t_w$. In some sense, $t = -2t_w$ is the next critical time since at this point the right boundary time slice coincides with the point on the boundary surface where the shock wave originates.

Comparing eqs. (6.55) and (6.58), we find

$$t_{c2} - t_{c1} = 8r_1^*(0) - 4r_1^*(r_s(t_{c1})). \quad (6.60)$$

Now with our conventions $r_1^*(0)$ and $r_1^*(r_s)$ will be negative quantities — see eq. (6.13) — and so there is a competition to determine the sign of this difference.¹¹ However, at least if t_w and/or $(M_2 - M_1)$ are sufficiently large, we expect that $t_{c2} - t_{c1} > 0$. In this scenario, there are three regimes of the WDW patch geometry to be considered,

$$\begin{aligned} \text{I} & : -t_{c0} < t < t_{c1} & r_b, r_s \text{ exist; } r_m < 0 \\ \text{II} & : t_{c1} < t < t_{c2} & r_b, r_s, r_m, \text{ exist} \\ \text{III} & : t > t_{c2} & r_s, r_m \text{ exist; } r_b < 0. \end{aligned} \quad (6.61)$$

¹¹Again, $d = 2$ is a special case with $r_1^*(0) = 0$ — see eq. (6.74) below.

For the regime I in eq. (6.61), the total rate of change of complexity consists of the bulk contribution in eq. (6.28) (with $r_m = 0$), eqs. (6.32) and (6.36) for the GHY contributions from the past and future singularities, respectively, and the two counterterm contributions from eqs. (6.53) and (6.52). The final result then becomes

$$\begin{aligned} \frac{d\mathcal{C}_A^{(I)}}{dt} &= \frac{M_2}{\pi} \left(1 + \frac{f_1(r_b)}{f_2(r_b)} \right) - \frac{M_1}{\pi} \left(1 + \frac{f_2(r_s)}{f_1(r_s)} \right) \\ &\quad + \frac{M_1}{2\pi} \frac{r_b^{d-2}}{\omega_1^{d-2}} f_1(r_b) \log \frac{f_2(r_b)}{f_1(r_b)} - \frac{M_2}{2\pi} \frac{r_s^{d-2}}{\omega_2^{d-2}} f_2(r_s) \log \frac{f_1(r_s)}{f_2(r_s)}. \end{aligned} \quad (6.62)$$

In regime II, we only need the GHY contribution in eq. (6.32) from the future singularity, the counterterm in the left future boundary of the WDW patch in eq. (6.52) and the sum of the joint contribution at r_m in eq. (6.48) with the two past counterterm contributions, given by eq. (6.54). In this case, the total reads

$$\begin{aligned} \frac{d\mathcal{C}_A^{(II)}}{dt} &= \frac{M_2}{\pi} \left(1 + \frac{f_1(r_b)}{f_2(r_b)} \right) + \frac{M_1}{2\pi} \frac{r_m^{d-2}}{\omega_1^{d-2}} f_1(r_m) \left(1 + \frac{f_2(r_s)}{f_1(r_s)} \right) \log \left(\frac{|f_1(r_m)|(d-1)^2 \ell_{\text{ct}}^2}{r_m^2} \right) \\ &\quad + \frac{M_1}{2\pi} \frac{r_b^{d-2}}{\omega_1^{d-2}} f_1(r_b) \log \frac{f_2(r_b)}{f_1(r_b)} - \frac{M_2}{2\pi} \frac{r_s^{d-2}}{\omega_2^{d-2}} f_2(r_s) \log \frac{f_1(r_s)}{f_2(r_s)}. \end{aligned} \quad (6.63)$$

In the last regime, the GHY contribution from the future singularity is given by eq. (6.34) and the sum of the joint at r_m in eq. (6.48) with the counterterm contributions from the past boundaries in eq. (6.54). Hence the rate of growth in this regime is

$$\begin{aligned} \frac{d\mathcal{C}_A^{(III)}}{dt} &= \frac{M_1 + M_2}{\pi} + \frac{M_1}{2\pi} \frac{r_m^{d-2}}{\omega_1^{d-2}} f_1(r_m) \left(1 + \frac{f_2(r_s)}{f_1(r_s)} \right) \log \left(\frac{|f_1(r_m)|(d-1)^2 \ell_{\text{ct}}^2}{r_m^2} \right) \\ &\quad - \frac{M_2}{2\pi} \frac{r_s^{d-2}}{\omega_2^{d-2}} f_2(r_s) \log \frac{f_1(r_s)}{f_2(r_s)}. \end{aligned} \quad (6.64)$$

Dimensionless variables

In addition to the dimensionless variables in eq. (6.16), it is also useful to define dimensionless coordinates corresponding to the three positions r_b , r_s and r_m ,

$$x_s \equiv \frac{r_s}{r_{h,2}}, \quad x_m \equiv \frac{r_m}{r_{h,1}}, \quad x_b \equiv \frac{r_b}{r_{h,1}}. \quad (6.65)$$

Note that these definitions are not completely harmonious with the definition $x = r/r_{h,2}$ in eq. (6.16). In the definition above, we have chosen to normalize r_s with $r_{h,2}$ such that the minimum value of x_s is one, but r_b and r_m are normalized with $r_{h,1}$ such that the maximum value of x_b and x_m is 1 as well. The addition of the counterterm (2.11) introduces one more length scale ℓ_{ct} and so it will be useful to define the dimensionless quantity

$$\tilde{\ell}_{ct} \equiv \frac{\ell_{ct}}{L}. \quad (6.66)$$

Using the rescaled blackening factors in eq. (6.18), we can rewrite the rates of change of complexity in eqs. (6.62), (6.63), (6.64) and (6.66) as

$$\begin{aligned} \frac{d\mathcal{C}_A^{(I)}}{dt} &= \frac{M_2}{\pi} \left(1 + \frac{\tilde{f}(x_b, wz)}{w^2 \tilde{f}(x_b/w, z)} \right) - \frac{M_1}{\pi} \left(1 + \frac{w^2 \tilde{f}(x_s, z)}{\tilde{f}(wx_s, wz)} \right) \\ &+ \frac{M_1}{2\pi} \frac{x_b^{d-2}}{1 + kz^2 w^2} \tilde{f}(x_b, wz) \log \frac{w^2 \tilde{f}(x_b/w, z)}{\tilde{f}(x_b, wz)} - \frac{M_2}{2\pi} \frac{x_s^{d-2}}{1 + kz^2} \tilde{f}(x_s, z) \log \frac{\tilde{f}(wx_s, wz)}{w^2 \tilde{f}(x_s, z)}, \end{aligned} \quad (6.67)$$

$$\begin{aligned} \frac{d\mathcal{C}_A^{(II)}}{dt} &= \frac{M_2}{\pi} \left(1 + \frac{\tilde{f}(x_b, wz)}{w^2 \tilde{f}(x_b/w, z)} \right) \\ &+ \frac{M_1}{2\pi} \frac{x_m^{d-2}}{1 + kz^2 w^2} \left(1 + \frac{w^2 \tilde{f}(x_s, z)}{\tilde{f}(wx_s, wz)} \right) \tilde{f}(x_m, wz) \log \frac{|\tilde{f}(x_m, wz)|(d-1)^2 \tilde{\ell}_{ct}^2}{x_m^2} \\ &+ \frac{M_1}{2\pi} \frac{x_b^{d-2}}{1 + kz^2 w^2} \tilde{f}(x_b, wz) \log \frac{w^2 \tilde{f}(x_b/w, z)}{\tilde{f}(x_b, wz)} - \frac{M_2}{2\pi} \frac{x_s^{d-2}}{1 + kz^2} \tilde{f}(x_s, z) \log \frac{\tilde{f}(wx_s, wz)}{w^2 \tilde{f}(x_s, z)}, \end{aligned} \quad (6.68)$$

$$\begin{aligned} \frac{d\mathcal{C}_A^{(III)}}{dt} &= \frac{M_1 + M_2}{\pi} - \frac{M_2}{2\pi} \frac{x_s^{d-2}}{1 + kz^2} \tilde{f}(x_s, z) \log \frac{\tilde{f}(wx_s, wz)}{w^2 \tilde{f}(x_s, z)} \\ &+ \frac{M_1}{2\pi} \frac{x_m^{d-2}}{1 + kz^2 w^2} \left(1 + \frac{w^2 \tilde{f}(x_s, z)}{\tilde{f}(wx_s, wz)} \right) \tilde{f}(x_m, wz) \log \frac{|\tilde{f}(x_m, wz)|(d-1)^2 \tilde{\ell}_{ct}^2}{x_m^2}. \end{aligned} \quad (6.69)$$

Early and late time behaviours

We now turn our attention to two simple limits for the rate of change of complexity. First, let us consider early times which means that we should consider the growth rate given in eq. (6.62). Now, if t_w is sufficiently large, then r_s approaches $r_{h,2}$ and r_b approaches $r_{h,1}$, *i.e.*, $f_2(r_s), f_1(r_b) \rightarrow 0$. In this limit, the growth rate in eq. (6.67) simplifies to

$$\left. \frac{d\mathcal{C}_A^{(I)}}{dt} \right|_{t_w \rightarrow \infty} = \frac{M_2 - M_1}{\pi} + \mathcal{O}(T_1(2t_w - t)e^{-\pi T_1(2t_w - t)}), \quad (6.70)$$

i.e., it is simply proportional to the difference of masses.

Another simple limit occurs at late times, when the growth rate is given by eq. (6.69). In this case, irrespective of the value of t_w , r_m and r_s approach $r_{h,1}$ and $r_{h,2}$, respectively, *i.e.*, $f_1(r_m)$, $f_2(r_s) \rightarrow 0$. In this case, the growth rate of the holographic complexity is given by the sum of the black hole masses, *i.e.*,

$$\left. \frac{d\mathcal{C}_A^{(\text{III})}}{dt} \right|_{t \rightarrow \infty} = \frac{M_1 + M_2}{\pi} + \frac{M_1}{2} \left(\frac{d + (d-2)kz^2}{1 + kz^2} \right) T_1 t e^{-\pi T_1 (t - 2t_w - 4r_1^*(r_{h,2}))} + \mathcal{O}(e^{-\pi T_1 t}), \quad (6.71)$$

as was previously argued in [34]. Further, we note that the second term in eq. (6.71) is always positive, and therefore $d\mathcal{C}_A/dt$ approaches the previous late time limit from above. Similar behaviour was found for the unperturbed eternal black holes in chapter 4. In analogy to these earlier results, we also note that the next correction term, of order $e^{-\pi T_1 t}$, depends on the normalization factor $\tilde{\ell}_{\text{ct}}$. We add that more generally, the dependence on $\tilde{\ell}_{\text{ct}}$ is more pronounced at early times.

A case study: BTZ black holes

It is instructive to analyze the particular case of BTZ black holes (*i.e.*, $d = 2$), since the positions r_s , r_m and r_b can be determined analytically. First, the two blackening factors are given by

$$f_1(r) = \frac{r^2 - r_{h,1}^2}{L^2} \quad \text{and} \quad f_2(r) = \frac{r^2 - r_{h,2}^2}{L^2}. \quad (6.72)$$

For each black hole (so r_h can be either $r_{h,1}$ and $r_{h,2}$), the physical quantities characterizing the black hole solutions are

$$M = \frac{\Omega_{k,1} r_h^2}{16\pi G_N L^2}, \quad T = \frac{r_h}{2\pi L^2}, \quad S = \frac{\Omega_{k,1} r_h}{4G_N} = \frac{\pi}{6} c \Omega_{k,1} L T, \quad (6.73)$$

and $c = 3L/(2G_N)$ is the central charge of the boundary CFT. In the above formulas, $k = 0$ and 1 correspond to the Ramond and Neveu-Schwarz vacuum, respectively, of the boundary theory [144].

With the blackening factors in eq. (6.72), we can evaluate the tortoise coordinates in eqs. (6.13) and (6.14) as

$$r_1^*(r) = \frac{L^2}{2r_{h,1}} \log \left(\frac{|r - r_{h,1}|}{r + r_{h,1}} \right), \quad r_2^*(r) = \frac{L^2}{2r_{h,2}} \log \left(\frac{|r - r_{h,2}|}{r + r_{h,2}} \right). \quad (6.74)$$

We choose to normalize the time coordinates by the temperature of the final (more massive) black hole, which reads

$$T_2 = \frac{r_{h,2}}{2\pi L^2}. \quad (6.75)$$

For the BTZ geometry, w which is the ratio of the horizon sizes in eq. (6.16) is just the ratio of the temperatures,

$$w = T_2/T_1. \quad (6.76)$$

Further, we note that $M_2/M_1 = w^2$ and $S_2/S_1 = w$.

Now combining eqs. (6.22), (6.65) and (6.74), as well as the above ratio (6.76), yields the following:

$$\begin{aligned} x_s &= \frac{1 + e^{-2\pi T_2(t_R+t_w)}}{1 - e^{-2\pi T_2(t_R+t_w)}}, & x_b &= \frac{e^{-2\pi T_1(t_L-t_w)} - 1}{e^{-2\pi T_1(t_L-t_w)} + 1}, \\ x_m &= \frac{wx_s + 1 - (wx_s - 1)e^{-2\pi T_1(t_L-t_w)}}{wx_s + 1 + (wx_s - 1)e^{-2\pi T_1(t_L-t_w)}}. \end{aligned} \quad (6.77)$$

With these three expressions, the growth rates in eqs. (6.67–6.69) are implicitly expressed entirely in terms of boundary quantities. Further, from eq. (6.72), we see that $r_1^*(0) = 0$ and hence the critical times in eqs. (6.55–6.59) simplify to

$$t_{c2} = 2t_w, \quad t_{c1} = 2t_w - 4|r_1^*(r_s)| \quad \text{and} \quad t_{c0} = 2t_w - 4|r_2^*(r_b)|. \quad (6.78)$$

While we do not have an analytic expression for r_s , it is easily determined numerically by combining the expressions in eqs. (6.55) and (6.72), and similarly for r_b . We return to examine the critical times t_{c1} and t_{c0} in more detail in a moment. In any event, we see that we are in the situation with $t_{c1} < t_{c2}$ and so the evolution of the holographic complexity is described by the scenario in eq. (6.61) and so let us explicitly examine $d\mathcal{C}_A/dt$ in a few examples.

In figure 6.2, we show $d\mathcal{C}_A/dt$ for a very light shock wave where $w = 1 + 10^{-5}$. In the left panel, we show the results for $T_2 t_w = 2$, and in the right, for $T_2 t_w = 6$. For both cases, the growth rate is essentially zero over the period $-t_{c0} \lesssim t \lesssim t_{c1}$, however, this is a longer time period for a larger value of t_w . Immediately after t_{c1} , there is a negative spike in the rate of growth, which is similar to the one found for the eternal BTZ black hole with the inclusion of the counterterm in appendix B.1. Note that this very small initial growth rate is consistent with eq. (6.70) since the difference $(M_2 - M_1) = (w^2 - 1)M_1$. Further, the separation $t_{c2} - t_{c1}$ (as well as $2t_w - t_{c0}$) appears to be independent of t_w . We will examine these observations further in the following.

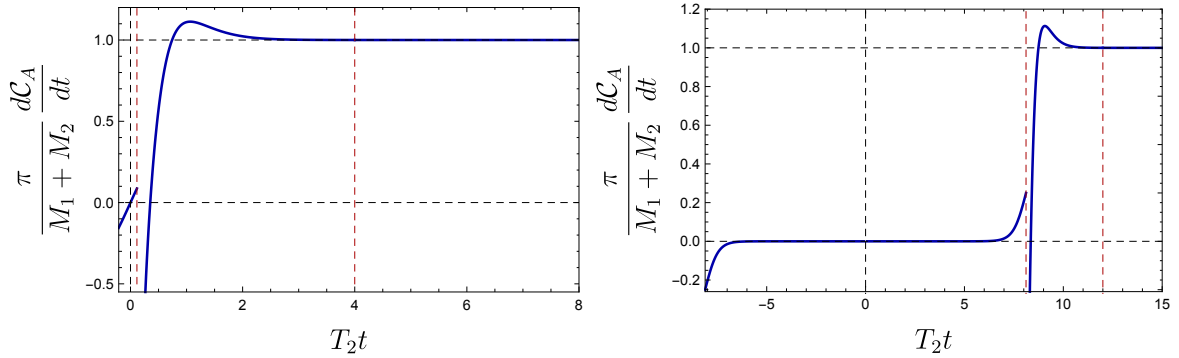


Figure 6.2: Time derivative of complexity, evolving both boundaries as $t_L = t_R = \frac{t}{2}$ with $T_2 t_w = 2$ (left) and $T_2 t_w = 6$ (right). We have set $w = 1 + 10^{-5}$ and $\tilde{\ell}_{ct} = 1$. The condition on z implies that the smaller black hole is at the Hawking-Page transition, for both cases. The lower horizontal dashed line (near zero) corresponds to $(M_2 - M_1)/(M_2 + M_1)$, and by construction, the late time limit approaches 1 at the higher horizontal line. The horizontal axis in both figures starts from the respective t_{c0} in eq. (6.78). The first vertical black dashed line appears at $t = 0$, while the vertical red dashed lines appear at t_{c1} (left) and $t_{c2} = 2t_w$ (right), see also eq. (6.78). There is a negative spike right after t_{c1} , where x_m is close to the past singularity. For the earlier shock wave in the right figure, there is a long regime where the rate of change is close to zero. In both cases, the late time limit is approached from above.

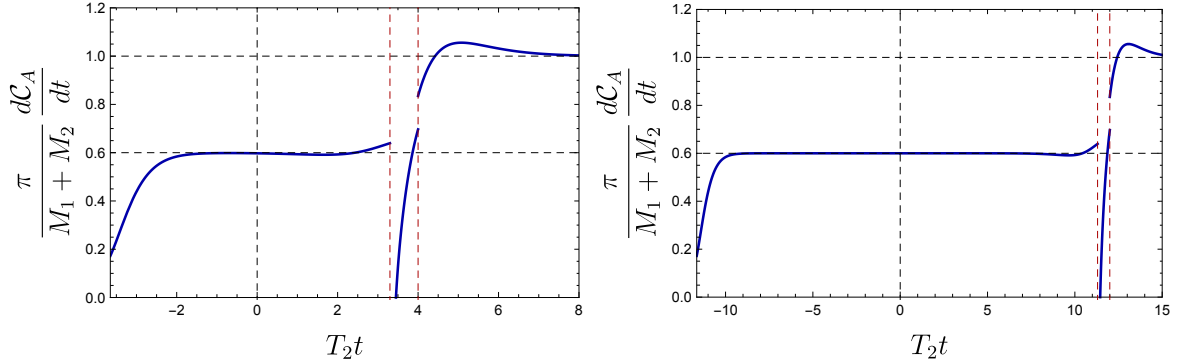


Figure 6.3: Time derivative of complexity, evolving both boundaries as $t_L = t_R = \frac{t}{2}$, with $T_2 t_w = 2$ (left) and $T_2 t_w = 6$ (right). In both cases, we have set $w = 2$ and $\tilde{\ell}_{ct} = 1$. The lower horizontal black dashed line corresponds to the time derivative at early times, *i.e.*, $(M_2 - M_1)/\pi$ in eq. (6.70), and the higher line to the late time limit, *i.e.*, $(M_2 + M_1)/\pi$ in eq. (6.71). The horizontal axis starts at t_{c0} , and the critical times t_{c1} and t_{c2} are shown by the left and right vertical dashed red lines, respectively. There is a negative spike right after t_{c1} , where x_m is close to the past singularity. Pushing the shock wave to the past increases the plateau where the time derivative is given roughly by the difference of the masses.

In figure 6.3, we show $d\mathcal{C}_A/dt$ for a heavier shock wave where $w = 2$ (*i.e.*, the temperature doubles or the black hole mass increases by a factor of four) and $z = 1/w$, such that the smaller black hole is at the Hawking-Page transition. In the left panel, we show the results for $T_2 t_w = 2$, and in the right, for $T_2 t_w = 6$. For both cases, the growth rate is significantly lower (than the final rate) in the period $-t_{c0} \lesssim t \lesssim t_{c1}$. This plateau is more evident in the case with a larger value of t_w . Rather than vanishing in this period, $d\mathcal{C}_A/dt$ is given by the difference $M_2 - M_1$, as in eq. (6.70). Note that the separation $t_{c2} - t_{c1}$ (as well as $2t_w - t_{c0}$) again appears to be independent of t_w , but is a smaller interval (when normalized by T_2) than with a very light shock wave, as in figure 6.2.

Critical times in BTZ

Here, we examine the critical times for the special case $d = 2$ in more detail. Recall that in this case, eq. (6.72) yields $r_1^*(0) = 0$ and hence the critical times in eqs. (6.55)-(6.59) simplify to the expressions given in (6.78). Hence the critical time where the endpoint of the shock wave on the future singularity enters the WDW patch is simply given by

$t_{c2} = 2t_w$.¹² However, the critical times t_{c1} and $-t_{c0}$ where the WDW patch lifts off of the past singularity and first impinges on the future singularity, respectively, have a more interesting structure. From eq. (6.70), we found that during the period $-t_{c0} \lesssim t \lesssim t_{c1}$,¹³ the growth rate of the holographic complexity is roughly proportional to the difference of the masses, at least when t_w is sufficiently large. This plateau with $d\mathcal{C}_A/dt \simeq (M_2 - M_1)/\pi$ is clearly shown in figures 6.2 and 6.3.¹⁴

From eq. (6.78), we have $t_{c1} = 2t_w - 4|r_1^*(r_s)|$ for the $d = 2$ shock wave geometries. We would like to understand this result in terms of boundary quantities and this is most simply done by considering various limits. First, suppose that the shock wave is very heavy, *i.e.*, w in eq. (6.76) is a large parameter. Recalling that t_{c1} is the critical time when x_m becomes positive, we may use eq. (6.77) to find

$$t_{c1} = 2t_w - \frac{2}{\pi T_2} + \mathcal{O}\left(\frac{1}{w^2 T_2}\right), \quad (6.79)$$

for large w . For very high temperatures, the above expression implies that this critical time approaches t_{c2} , *i.e.*, $t_{c1} \rightarrow 2t_w = t_{c2}$.

We also consider the case of a very light shock for which w can be parametrized as $w = 1 + \epsilon$. Using eqs. (6.73) and (6.76), the ratio of the masses is given by

$$\frac{M_2}{M_1} = w^2 = 1 + 2\epsilon + \epsilon^2, \quad (6.80)$$

and hence the energy of the shock E is given by

$$\frac{E}{M_1} = 2\epsilon + \epsilon^2 \simeq 2\epsilon. \quad (6.81)$$

Now again using eq. (6.77), we have in the limit $e^{-2\pi T_2 t_w} \ll \epsilon \ll 1$

$$t_{c1} = 2t_w + \frac{1}{\pi T_1} \log \frac{\epsilon}{2} - \frac{\epsilon}{2\pi T_1} + \mathcal{O}\left(\frac{\epsilon^2}{T_1}\right). \quad (6.82)$$

¹²Note that this corresponds to $t_L = t_w$ and this simple result arises from the special property that the singularity is a straight horizontal line in a Penrose diagram describing the BTZ black hole [198].

¹³This was regime I in eq. (6.61).

¹⁴In these figures, we can see that there are significant tails on the plateau in the interval $-t_{c0} \leq t \leq t_{c1}$. A better estimate of the length of the plateau can be determined from the analytic expressions of x_b and x_s in eq. (6.77), as follows: The plateau is in the regime where both x_s and x_b are close to 1. Let us define the ‘‘boundaries’’ of the plateau with the conditions that $x_s \approx 1 + 2e^{-\gamma\pi} + \mathcal{O}(e^{-2\gamma\pi})$ and $x_b \approx 1 - 2e^{-\gamma\pi} + \mathcal{O}(e^{-2\gamma\pi})$, where γ is a number of order 1. It then follows that the length of the plateau is approximately $T_2 \Delta t_{\text{pl}} \approx 4T_2 t_w - \gamma(w + 1)$.

Following [183], we can relate the first correction to the scrambling time [111]. If one considers E to be of the order of the energy of a few thermal quanta of energy, then we may use eqs. (6.73) and (6.81) to write¹⁵

$$\frac{2}{\epsilon} \simeq \frac{4M_1}{E} \simeq \frac{4M_1}{2T_1} \simeq S_1. \quad (6.83)$$

Hence eq. (6.82) becomes

$$t_{c1} = 2(t_w - t_{scr}^*) + \mathcal{O}(\epsilon) \quad (6.84)$$

where

$$t_{scr}^* \equiv \frac{1}{2\pi T_1} \log \frac{2}{\epsilon} = \frac{1}{2\pi T_1} \log S_1. \quad (6.85)$$

Having evaluated the behaviour of the critical time t_{c1} for heavy and light shocks in eqs. (6.79) and (6.82), respectively, we plot the numerical solution from eq. (6.78) in figure 6.4. In the left panel, we show the behaviour of t_{c1} as a function of $\log(\epsilon/2)$ for early shock waves, *i.e.*, for which $x_s - 1 \simeq 2e^{-2\pi T_2 t_w} \ll 1$. In the figure, we clearly see the transition between the light shock behaviour (where $2t_w - t_{c1}$ depends linearly on $\log(\epsilon/2)$) and the heavy shock behaviour (where $2t_w - t_{c1}$ is constant) and that the value of w where the transition occurs is independent of t_w . Recall that an essential assumption in deriving eq. (6.82) was that the order of limits $e^{-2\pi T_2 t_w} \ll \epsilon \ll 1$ held. The geometrical interpretation of this limit is that x_s is exponentially close to 1, and therefore corrections of order $e^{-2\pi T_2 t_w}$ are much smaller than corrections to the energy from the shock wave, which are of order ϵ . Therefore in figure 6.4 where the value of t_w is fixed for each curve, we see there is a regime of very small ϵ where $\epsilon \lesssim e^{-2\pi T_2 t_w}$ where the difference $2t_w - t_{c1}$ again saturates at some constant value. In the right panel of figure 6.4, we show the behaviour when the shock waves are not sent very early. In this regime, t_{c1} just transitions between two different constant regimes without much of a linear regime in between. Further, increasing the mass ratio decreases the critical time. For large w , notice that most curves (with big enough t_w) saturate to 1, which is consistent with the large w expansion in eq. (6.79). Note that the plots produced here in figure 6.4 also represent the difference $t_{c2} - t_{c1}$, since for $d = 2$ from eq. (6.78) we have $t_{c2} = 2t_w$. Hence in the early shock regime, the right panel shows that the separation between these two critical times is independent of t_w (except for very small ϵ), as observed in figures 6.2 and 6.3.

Next, we turn our attention to $t_{c0} = 2t_w - 4|r_2^*(r_b)|$ from eq. (6.78), which for early shock waves (*i.e.*, t_w large) represents the beginning (*i.e.*, at $t = -t_{c0}$) of the plateau where the rate of growth is approximately $(M_2 - M_1)/\pi$. We begin by considering light shock

¹⁵Note that we chose $E \simeq 2T_1$ to simplify the subsequent expressions.

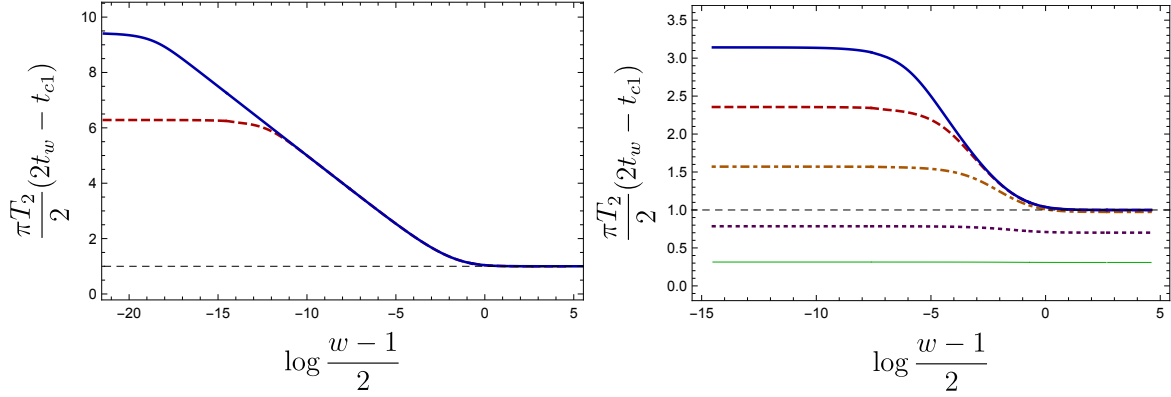


Figure 6.4: Dependence of the critical time t_{c1} on $\log \frac{w-1}{2} = \log(\epsilon/2)$, which parametrizes the energy in the shock wave. In the left panel, we show the behaviour of t_{c1} for early shock waves: $T_2 t_w = 3$ in solid blue, and $T_2 t_w = 2$ in dashed red. In this case, we see the transition between the light shock behaviour (6.82) and the heavy shock behavior (6.79). In the right panel, we show the behaviour of t_{c1} when the shock wave is not sent very early, *i.e.*, with $T_2 t_w = 0.1, 0.25, 0.5, 0.75, 1$ from bottom to top. For these parameters, the range of w that has approximately a log dependence starts appearing as the shock wave is sent earlier (larger t_w). The horizontal thin dashed black line is just 1 (for both panels).

waves in the limit with $e^{-2\pi T_1 t_w} \ll \epsilon \ll 1$. In this scenario, $r_b \rightarrow r_{h,1}$ as the ratio of temperatures approaches one (*i.e.*, $w \rightarrow 1$), and $r_b \rightarrow 0$ as w increases. Therefore, we can expand eq. (6.59) for $w = 1 + \epsilon$ with ϵ small,¹⁶

$$t_{c0} = 2(t_w - t_{\text{scr}}^*) + \frac{\epsilon}{\pi T_1} \left(\log \frac{2}{\epsilon} - \frac{1}{2} \right) + \mathcal{O}(\epsilon^2 \log \epsilon). \quad (6.86)$$

For heavy shock waves (*i.e.*, large w), t_{c0} scales as

$$t_{c0} = t_w \left(2 - \frac{4}{w^2} + \mathcal{O}(w^{-4}) \right). \quad (6.87)$$

In figure 6.5, we show the numerical solution of eq. (6.59) for $T_2 t_w = 2$ in the left panel, and $T_2 t_w = 0.25$ in the right panel. For the early shock wave and small ϵ , we see that t_{c0} depends linearly on $\log \epsilon$. As a result, the plateau (where the derivative is close to zero) will extend far into the past. If the shock wave is not sent early enough the range with this log dependence is much shorter, similar to the behaviour found for t_{c1} .

¹⁶Note that in this case, the expression would be simpler if we had defined the scrambling time with T_2 . That is, using $t_{\text{scr}}^* = \frac{1}{\pi T_2} \log(2/\epsilon)$, rather than the definition in eq. (6.85), would remove the $\epsilon \log \epsilon$ correction in eq. (6.86).

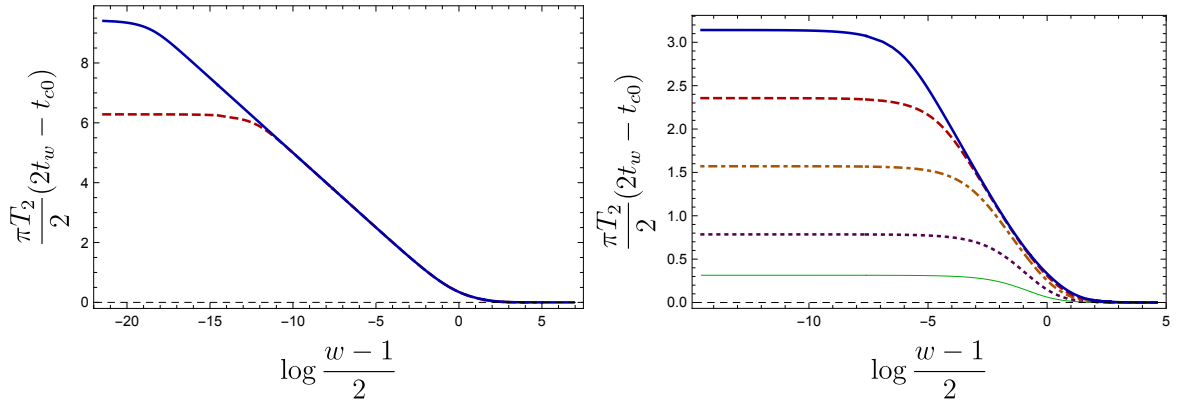


Figure 6.5: Dependence of the critical time t_{c0} on the energy of the shock wave, parametrized by the temperature ratio w for BTZ. In the left, we show the behaviour of t_{c0} with respect to early shock waves with $T_2 t_w = 3$ in solid blue, $T_2 t_w = 2$ in dashed red. Similarly to t_{c1} in figure 6.4, as w approaches one, there is a stretched range of w such that t_{c1} grows as a logarithm, and the earlier the shock wave the longer this log regime. Also, we see that it approaches $2t_w$ in the large w regime. In the right, we show the behaviour of t_{c0} when the shock wave is not sent early enough, with $T_2 t_w = 0.1, 0.25, 0.5, 0.75, 1$ from bottom to top. As the shock wave is sent earlier, the region with log dependence becomes more pronounced.

We focused our analysis of the critical times here on the special case of $d = 2$ because many features, such as the dependence of x_s and x_b on t_w , were analytic. In addition, since eq. (6.74) yields $r^*(0) = 0$ for $d = 2$, $t_{c2} - t_{c1}$ was always positive and t_{c2} was simply given by $2t_w$. We investigate higher dimensions (in particular $d = 4$) in appendix C.2. There, the fact that $r^*(0) \neq 0$ leads to some modifications for shock waves not inserted early enough, *i.e.*, for small t_w , we may find that $t_{c2} - t_{c1}$ is negative. On the other hand, if the shock wave is sent early enough, it is also true that in higher dimensions, there is a plateau of rate of change $(M_2 - M_1)/\pi$ that extends for a length of time of approximately $4t_w$.

6.2.2 Complexity of Formation

In this section, we consider the complexity of formation, as previously discussed in chapter 3. There, we compared the complexity of preparing two copies of the boundary CFT in the thermofield double state (TFD) at $t_L = t_R = 0$ to the complexity of preparing each of the CFT's in its vacuum state,

$$\Delta\mathcal{C} = \mathcal{C}(|TFD\rangle) - \mathcal{C}(|0\rangle \otimes |0\rangle). \quad (6.88)$$

Using the CA conjecture (1.24), the holographic calculation was to evaluate the WDW action for $t_L = t_R = 0$ in an eternal black hole background and subtract that for two copies of the AdS vacuum geometry. This difference removed the UV divergences leaving a finite quantity. For neutral black holes, we found that at high temperatures generally $\Delta\mathcal{C}$ was proportional to the entropy of the black hole or alternatively, the entanglement entropy in the TFD state, plus small curvature corrections. However, $d = 2$ was a special case where for the BTZ black hole, $\Delta\mathcal{C}$ was a constant proportional to the central charge.

In the following, we aim to evaluate the complexity of formation for the perturbed state dual to the shock wave geometry, again at $t_L = t_R = 0$.¹⁷ The resulting $\Delta\mathcal{C}_A$ can be studied as a function of t_w and $M_2 - M_1$. We illustrate this setup with the Penrose diagram of figure 6.6. The calculation follows straightforwardly from the considerations of the previous subsection. For instance, the bulk integral is obtained with $r_m = 0$ and also by setting $t_L = t_R = 0$ in eq. (6.25). Also, we have to subtract two copies of the vacuum,

¹⁷The boundary times are synchronized according to the procedure outlined at the beginning of this section — see the discussion above eq. (6.16).

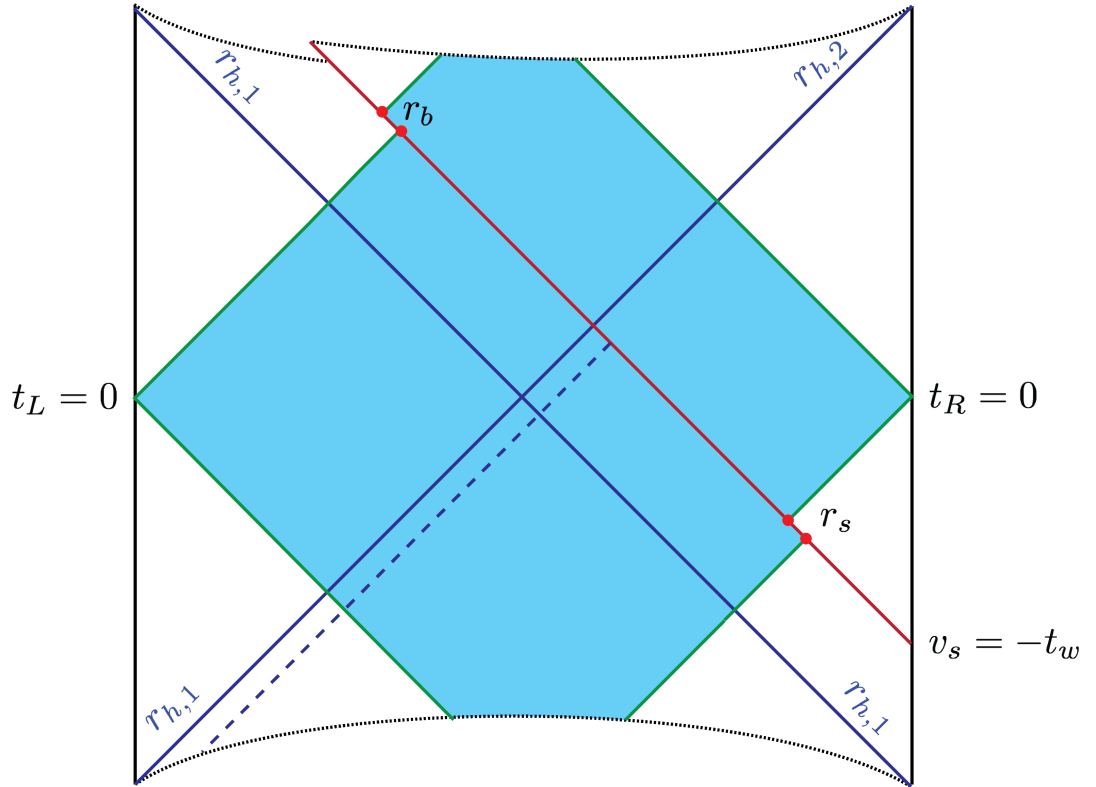


Figure 6.6: Penrose-like diagram for one shock wave sent from the right boundary at $v_s = -t_w$ on an eternal black hole geometry, with the Wheeler-DeWitt patch anchored at $t_L = t_R = 0$, which we will call the complexity of formation, in analogy to the case studied in chapter 3 of the unperturbed eternal black hole geometry. There are two coordinates r_b and r_s that are usually given by a transcendental equation as functions of w and t_w , as shown in eq. (6.22). The effect of crossing the collapsing shell from the right boundary is to increase the surface of the WDW patch above the past singularity.

which was discussed in detail in chapter 3. We have then

$$\begin{aligned} \Delta I_{\text{bulk}} &= \left(\frac{\Omega_{k,d-1}}{16\pi G_N} \right) \left(-\frac{2d}{L^2} \right) \left[\int_{r_s}^{r_{\text{max}}} dr r^{d-1} (-2r_2^*(r)) + \int_{r_b}^{r_{\text{max}}} dr r^{d-1} (-2r_1^*(r)) \right. \\ &\quad \left. + \int_0^{r_s} dr r^{d-1} (t_w + 2r_1^*(r_s) - 2r_1^*(r)) + \int_0^{r_b} dr r^{d-1} (t_w + 2r_2^*(r_b) - 2r_2^*(r)) \right] - 2I_{\text{bulk,vac}}, \end{aligned} \quad (6.89)$$

where r_b and r_s are given by eq. (6.22) with $v_L = v_R = 0$, and $I_{\text{bulk,vac}}$ is the appropriate vacuum bulk integral given by

$$2I_{\text{bulk,vac}} = \left(\frac{\Omega_{k,d-1}}{16\pi G_N} \right) \left(-\frac{2d}{L^2} \right) \int_0^{r_{\text{max}}} dr r^{d-1} (-4r_{\text{vac}}^*(r)), \quad (6.90)$$

with

$$r_{\text{vac}}^*(r) = - \int_r^\infty \frac{dr}{k + r^2/L^2}, \quad \lim_{r \rightarrow \infty} r_{\text{vac}}^*(r) = 0. \quad (6.91)$$

The only nonvanishing contributions from the boundary surfaces are the two GHY contributions at the past and future singularities, given by eqs. (6.31) and (6.35) with $v_L = v_R = 0$, which results in

$$\Delta I_{GHY} = \frac{d\Omega_{k,d-1}}{16\pi G_N} [\omega_1^{d-2} (t_w + 2r_1^*(r_s) - 2r_1^*(0)) + \omega_2^{d-2} (t_w + 2r_2^*(r_b) - 2r_2^*(0))] . \quad (6.92)$$

Finally, we need to add the contribution of the two counterterms in eqs. (6.49) and (6.50) with $r_m = 0$. The UV contributions cancel when subtracting the vacuum, so as a result we have

$$\Delta I_{\text{ct}} = \frac{\Omega_{k,d-1}}{8\pi G_N} \left[r_s^{d-1} \log \left(\frac{f_1(r_s)}{f_2(r_s)} \right) + r_b^{d-1} \log \left(\frac{f_2(r_b)}{f_1(r_b)} \right) \right]. \quad (6.93)$$

As argued in chapter 3, the joint contributions at the UV regulator surface precisely cancel the same contributions from the vacuum geometries.

Combining all of these contributions then yields the desired complexity of formation,

$$\Delta \mathcal{C}_A = \frac{\Delta I_{\text{bulk}} + \Delta I_{GHY} + \Delta I_{\text{ct}}}{\pi}. \quad (6.94)$$

This result is more complicated than the complexity of formation for the unperturbed BH geometry, since the points r_s and r_b are determined by inverting a transcendental equation (for higher dimensional black holes). However, it can be studied analytically for $d = 2$ and we consider this special case in the following. We will also consider $\Delta \mathcal{C}_A$ for planar AdS₅ black holes in appendix C.2.

It is straightforward to evaluate eq. (6.94) for $d = 2$, and it is instructive to compare the result to the complexity of formation for the unperturbed BTZ black hole. The latter was evaluated in chapter 3, where we found $\Delta\mathcal{C}_{\text{NS}} = -c/3$ when subtracting the complexity of the Neveu-Schwarz vacuum (*i.e.*, $k = +1$).¹⁸ Comparing the result for the perturbed state to $\Delta\mathcal{C}_{\text{NS}}$ then yields

$$\begin{aligned} \frac{\Delta\mathcal{C}_A - \Delta\mathcal{C}_{\text{NS}}}{|\Delta\mathcal{C}_{\text{NS}}|} = LT_1 & \left[\frac{w^2 - 1}{w} \log\left(\frac{x_s - 1}{x_s + 1}\right) + wx_s \log\left(\frac{w^2 x_s^2 - 1}{w^2 (x_s^2 - 1)}\right) \right. \\ & + (w^2 - x_b^2) \log\left(\frac{1 + x_b}{1 - x_b}\right) - \frac{w^2 - x_b^2}{w} \log\left(\frac{w + x_b}{w - x_b}\right) \\ & \left. + x_b \log\left(\frac{w^2 - x_b^2}{1 - x_b^2}\right) \right]. \end{aligned} \quad (6.95)$$

Here the coordinates x_s and x_b are given by eq. (6.77) with $t_L = t_R = 0$,

$$x_s = \frac{1 + e^{-2\pi T_2 t_w}}{1 - e^{-2\pi T_2 t_w}}, \quad x_b = \frac{1 - e^{-2\pi T_1 t_w}}{1 + e^{-2\pi T_1 t_w}}. \quad (6.96)$$

In the left panel of figure 6.7, we show the effect of a light shock wave on the complexity of formation as a function of t_w . Initially there is a period where $\Delta\mathcal{C}_A = \Delta\mathcal{C}_{\text{NS}}$ after which $\Delta\mathcal{C}_A$ begins to grow linearly. As the shock is made lighter (*i.e.*, as w is brought closer to one), this period over which the complexity of formation is essentially unchanged grows longer. In the period of linear growth, the slope seems more or less the same independent of w . In the right panel, we show the effect of heavier shock waves. In this regime, the complexity of formation starts changing immediately, even for small t_w , and $\Delta\mathcal{C}_A$ rapidly enters a regime of linear growth with increasing t_w . In appendix C.2, similar features are found with shock wave geometries which are inserted into a planar AdS₅ black hole spacetime.

We want to investigate the behaviour of figure 6.7 analytically in the case of a very light shock wave with $w = 1 + \epsilon$. We start by analyzing eq. (6.95) in the limit where the shock wave enters at a very early time, *i.e.*, $T_2 t_w \gg 1$. In eq. (6.96), the coordinates x_s and x_b become

$$x_s = 1 + 2e^{-2\pi T_1 t_w} + \mathcal{O}(\epsilon e^{-2\pi T_1 t_w}, e^{-4\pi T_1 t_w}), \quad x_b = 1 - 2e^{-2\pi T_1 t_w} + \mathcal{O}(e^{-4\pi T_1 t_w}). \quad (6.97)$$

In this limit, the leading order behaviour of eq. (6.95) reduces to

$$\frac{\Delta\mathcal{C}_A - \Delta\mathcal{C}_{\text{NS}}}{|\Delta\mathcal{C}_{\text{NS}}|} = LT_1 \log\left(\frac{(wx_s - 1)(w - x_b)}{(x_s - 1)(1 - x_b)}\right) + \mathcal{O}(\epsilon, e^{-2\pi T_2 t_w}). \quad (6.98)$$

¹⁸With c being the central charge of the boundary CFT, which is given by $c = 3L/(2G_N)$.

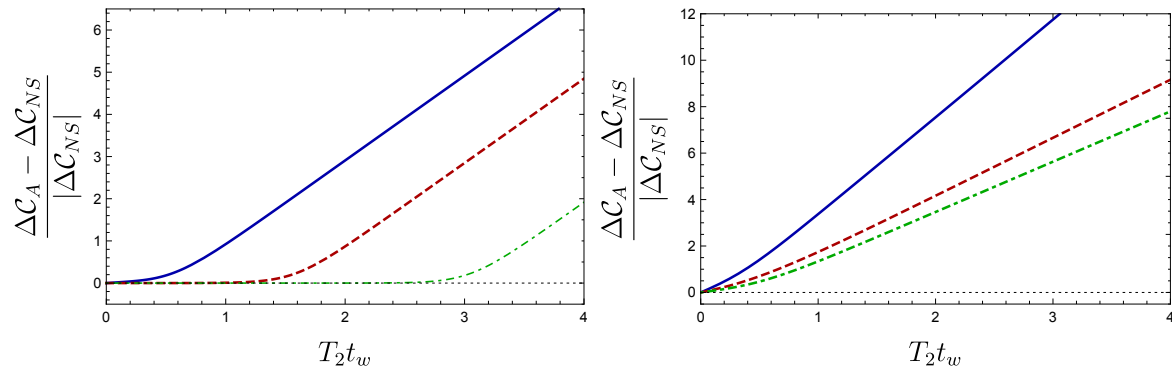


Figure 6.7: The complexity of formation for BTZ black holes for $z = 1/w$, such that the smaller black hole is at the Hawking-Page transition, or alternatively we could normalize the complexity of formation by the entropy, which would remove the overall multiplicative factor of z , cf. eq. (6.95). In the left panel, we evaluate the complexity of formation for light shock waves as a function of $T_2 t_w$. The energies of the shock waves are parametrized by the temperature ratio w , with $w = 1 + 10^{-1}$ (solid blue), $w = 1 + 10^{-4}$ (dashed red) and $w = 1 + 10^{-8}$ (dot-dashed green). For a period of time of the order of the scrambling time (6.85), the complexity of formation is approximately the same as the unperturbed state. For early shocks (*i.e.*, larger t_w), the complexity of formation grows linearly with t_w . In the right panel, we show the complexity of formation for heavier shocks, $w = 4$ (solid blue), $w = 2.5$ (dashed red) and $w = 1.5$ (dot-dashed green). For these parameters, we see that the complexity of formation starts changing immediately and rapidly approaches a regime of linear growth with increasing t_w .

Now there are two interesting regimes to consider: $\epsilon \ll 2e^{-2\pi T_2 t_w}$ and $\epsilon \gg 2e^{-2\pi T_2 t_w}$. Of course, the transition between these two regimes occurs when $\epsilon \approx 2e^{-2\pi T_1 t_w}$, *i.e.*, when $t_w \approx \frac{1}{2\pi T_1} \log(2/\epsilon) = t_{\text{scr}}^*$ using eq. (6.85). That is, the transition occurs when the perturbation of the thermofield double state is made approximately one scrambling time before the complexity of formation is evaluated!

In the first regime, we can simply approximate $w \approx 1$ in the argument of the log in eq. (6.98), and as a consequence, the latter becomes

$$\frac{\Delta\mathcal{C}_A - \Delta\mathcal{C}_{\text{NS}}}{|\Delta\mathcal{C}_{\text{NS}}|} = \mathcal{O}(e^{-2\pi T_2 t_w}) \quad (6.99)$$

where we have omitted order ϵ corrections because by assumption they were smaller than the exponential. This is the regime where the complexity of formation is essentially the same as the unperturbed geometry in figure 6.7.

In the second regime with $\epsilon \gg e^{-2\pi T_2 t_w}$, the denominator of the log in eq. (6.98) becomes the dominant part, with

$$\frac{\Delta\mathcal{C}_A - \Delta\mathcal{C}_{\text{NS}}}{|\Delta\mathcal{C}_{\text{NS}}|} = 2LT_1 \left[2\pi T_1 t_w + \log\left(\frac{\epsilon}{2}\right) \right] + \mathcal{O}(\epsilon). \quad (6.100)$$

Hence this second regime is where $\Delta\mathcal{C}_A$ grows linearly with t_w in figure 6.7. Using the expressions in eq. (6.73) (with $\Omega_{1,1} = 2\pi$ and $2M_1 = S_1 T_1$) and the scrambling time in eq. (6.85), as well as $|\Delta\mathcal{C}_{\text{NS}}| = c/3$, we can rewrite the last result as

$$\Delta\mathcal{C}_A = \Delta\mathcal{C}_{\text{NS}} + \frac{4M_1}{\pi} (t_w - t_{\text{scr}}^*) + \mathcal{O}(\epsilon). \quad (6.101)$$

Hence we can approximate the complexity of formation in both regimes with the following simple expression:

$$\Delta\mathcal{C}_A \simeq \Delta\mathcal{C}_{\text{NS}} + \Theta(t_w - t_{\text{scr}}^*) \frac{4M_1}{\pi} (t_w - t_{\text{scr}}^*). \quad (6.102)$$

For the heavy shock waves, *i.e.*, (relatively) large w , we see from the right panel of figure 6.7 that $\Delta\mathcal{C}_A$ begins increasing immediately as t_w increases from zero. From eq. (6.95), we can evaluate the slope of this increase,

$$\left. \frac{d\Delta\mathcal{C}_A}{dt_w} \right|_{t_w \rightarrow 0^+} = \frac{1}{\pi} \left(M_2 - M_1 + M_1 \log \left[\frac{M_2}{M_1} \right] \right) \equiv \gamma_0. \quad (6.103)$$

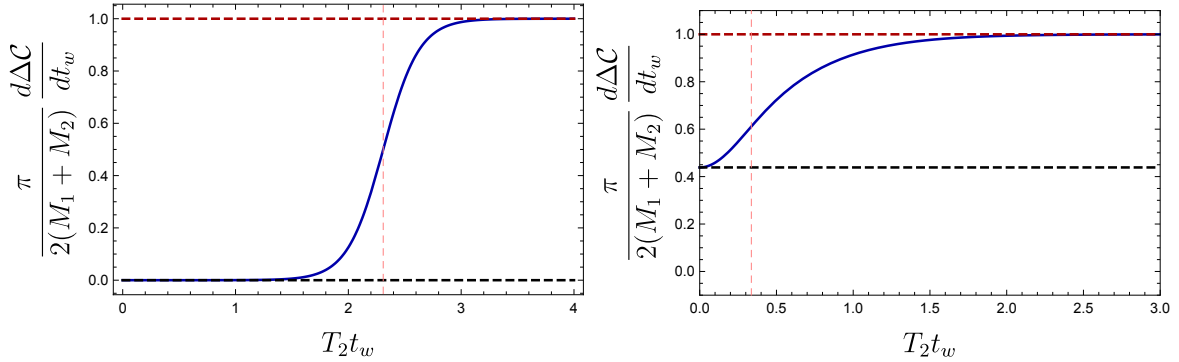


Figure 6.8: The derivative of the complexity of formation with respect to t_w . The black dashed line is the expected slope at $t_w = 0$, and the dashed red line is the slope at large t_w (normalized in the plot to approach 1). For both panels, we adopt $z = 1/w$. The left panel illustrates the behaviour for a light shock wave, with $w = 1 + 10^{-6}$. In this regime, described by eq. (6.102), the slope is approximately zero until $t \simeq t_{\text{scr}}^*$ (vertical dashed line), at which point it rapidly rises to the final constant value, $4M_1/\pi$. The right panel illustrates the behaviour for a heavy shock wave, with $w = 2$. In this regime, the slope starts at γ_0 in eq. (6.103) and rapidly rises to the final constant value $2(M_1 + M_2)/\pi$. In this case, the vertical dashed line indicates $t_w = t_{\text{del}}$ from eq. (6.105).

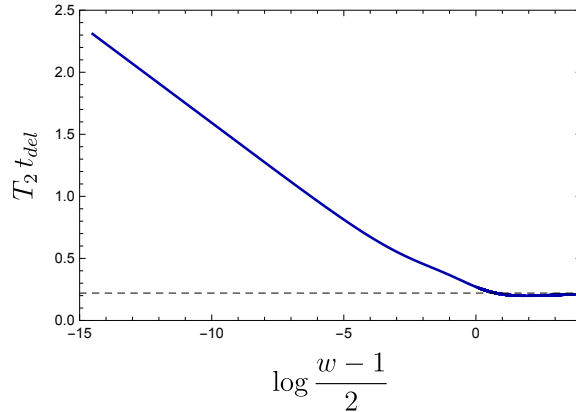


Figure 6.9: The ‘delay’ time (6.105) as a function of the energy in the shock wave. For $w \sim 1$, we have a line of slope -1 , which is characteristic of the scrambling time in eq. (6.85), as expected from eq. (6.106). For heavy shock waves, t_{del} approaches a constant proportional to $1/T_2$, as shown in eq. (6.107).

Of course, this result vanishes for light shock waves, with $M_2 \approx M_1$, and we recover the result in eq. (6.102). We can also use eq. (6.95) to determine the linear growth for larger values of t_w ,

$$\Delta\mathcal{C}_A \simeq \Delta\mathcal{C}_{\text{NS}} + \frac{2}{\pi}(M_2 + M_1)(t_w - t_{\text{del}}) + \mathcal{O}(t_w e^{-t_w}) \quad (6.104)$$

where the generalized ‘delay’ time can be written as

$$t_{\text{del}} = \frac{w+1}{2\pi T_2(w^2+1)} \left[(2w-1) \log\left(\frac{2}{w-1}\right) + \frac{2w^2}{w+1} \log w + \log\left(\frac{2}{w+1}\right) \right]. \quad (6.105)$$

It is straightforward to see that this expression reduces to the scrambling time (6.85) when $w \rightarrow 1$. More precisely, with $w = 1 + \epsilon$ and $\epsilon \ll 1$,

$$t_{\text{del}} = t_{\text{scr}}^* + \frac{1}{4\pi T_1} \left(1 + 5 \log \frac{2}{\epsilon} \right) \epsilon + \mathcal{O}(\epsilon^2 \log \epsilon). \quad (6.106)$$

Eq. (6.104) provides an extension to general values of w of eq. (6.101), which applies only for light shock waves (*i.e.*, $w \simeq 1$), and in this sense, t_{del} replaces t_{scr}^* for general shocks. Roughly, we can think of this time as characterizing when there is a transition between the early time behaviour given in eq. (6.103) and the late time behaviour given in eq. (6.104). As shown in figure 6.7, this is a sharp transition between two distinct regimes for light shock waves, but not for the heavy shock waves. In the latter case, there is not an extended period of time where eq. (6.103) applies. In any event, considering t_{del} for large values of w , we find to leading order

$$t_{\text{del}} = \frac{1}{\pi T_2} \left[\log 2 - \frac{1}{w} \log w + \frac{1 + \log 2}{w} + \mathcal{O}(w^{-2}) \right], \quad (6.107)$$

that is, the delay time is simply a constant proportional to the inverse temperature of the final black hole, which is then a small time in the limit of large w .

Figure 6.8 shows the variation of $d\Delta\mathcal{C}_A/dt_w$ for a light and a heavy shock wave. We see that for the light shock wave, the slope vanishes initially but then rapidly rises to the final constant value at $t \simeq t_{\text{scr}}^*$, corresponding to the two regimes shown in the left panel of figure 6.7 — see also eq. (6.102). Instead, for the heavy shock wave, the slope is initially nonvanishing and proportional to γ_0 in equation (6.103) and rises quickly to the final constant value, again in agreement with the results shown in the right panel of figure 6.7. Figure 6.9 shows t_{del} as a function of $\log\left(\frac{w-1}{2}\right)$. For $w \sim 1$, a line of slope -1 appears since $t_{\text{del}} \simeq t_{\text{scr}}^*$, as shown in eq. (6.106). For heavy shock waves, t_{del} approaches a constant proportional to $1/T_2$, as shown in eq. (6.107).

6.2.3 ‘Complexity’ without the Counterterm

In this section, we turn our attention to the effects of dropping the counterterm (2.11) from the bulk action (6.21). For stationary spacetimes, the WDW action does not seem to be effected in an important way if this surface term is not included. However, in studying holographic complexity for the formation of a black hole in chapter 5, we found that the counterterm is an essential ingredient for the CA proposal. The most dramatic effect of dropping the counterterm was found for $d = 2$ (and $k = +1$) where, without the counterterm, the holographic complexity actually decreased throughout the black hole formation process and the rate of change only approached zero for asymptotically late times. In the following, we show that without the counterterm, the holographic calculations fail to reproduce the expected late time growth rate and that the complexity of formation in $d = 2$ does not exhibit the behaviour that is characteristic of the switchback effect.

Note that without the counterterm (2.11), we must deal with the ambiguities associated with the surface and joint terms on the null boundaries of the WDW patch. We follow the standard prescription proposed in [63] where we set $\kappa = 0$ by choosing affine parametrization for the null normals. Further, we fix the overall normalization of these null vectors with $\hat{t} \cdot k = \pm\alpha$ (where \hat{t} is the asymptotic Killing vector producing time flow in the boundary). Of course, we have already adopted these conventions in the previous sections and so it is straightforward to simply drop the counterterm contributions in eqs. (6.49)-(6.51) (and implicitly, also eq. (C.10)) from the previous analysis. We tentatively denote the resulting quantity as ‘complexity’ *i.e.*,

$$\tilde{\mathcal{C}}_A = \frac{I_{\text{WDW}} - I_{\text{ct}}}{\pi}, \quad (6.108)$$

but as in chapter 5, we will find that this gravitational observable fails to behave in the manner expected of complexity.

Time Evolution

Here, we evaluate the growth rate of $\tilde{\mathcal{C}}_A$ for the three different regimes described in eq. (6.61). First, in regime I (*i.e.*, $-t_{c0} < t < t_{c1}$), the total rate of change of complexity only receives contributions from the bulk term in eq. (6.28) (with $r_m = 0$), and from the GHY surface terms in eqs. (6.32) and (6.36) at the past and future singularities,

respectively. The growth rate then becomes

$$\begin{aligned} \frac{d\tilde{\mathcal{C}}_A^{(I)}}{dt} = & -\frac{M_2}{(d-1)\pi} \frac{r_s^d}{\omega_2^{d-2}L^2} \left(1 - \frac{f_2(r_s)}{f_1(r_s)}\right) + \frac{M_1}{(d-1)\pi} \frac{r_b^d}{\omega_1^{d-2}L^2} \left(1 - \frac{f_1(r_b)}{f_2(r_b)}\right) \\ & + \frac{dM_2}{2(d-1)\pi} \left(1 + \frac{f_1(r_b)}{f_2(r_b)}\right) - \frac{dM_1}{2(d-1)\pi} \left(1 + \frac{f_2(r_s)}{f_1(r_s)}\right). \end{aligned} \quad (6.109)$$

In regime II (*i.e.*, $t_{c1} < t < t_{c2}$), the WDW patch has lifted off of the past singularity and so in addition to the bulk contribution (6.28) and the GHY contribution (6.32) from the future singularity, we also have the joint contribution at r_m in eq. (6.48). Combining these then yields

$$\begin{aligned} \frac{d\tilde{\mathcal{C}}_A^{(II)}}{dt} = & -\frac{M_2}{(d-1)\pi} \frac{r_s^d}{\omega_2^{d-2}L^2} \left(1 - \frac{f_2(r_s)}{f_1(r_s)}\right) + \frac{M_1}{(d-1)\pi} \frac{r_b^d}{\omega_1^{d-2}L^2} \left(1 - \frac{f_1(r_b)}{f_2(r_b)}\right) \\ & + \frac{dM_2}{2(d-1)\pi} \left(1 + \frac{f_1(r_b)}{f_2(r_b)}\right) + \frac{(d-2)M_1}{2(d-1)\pi} \left(1 + \frac{f_2(r_s)}{f_1(r_s)}\right) \\ & + \frac{M_1}{\pi(d-1)} \frac{r_m^{d-1}r_s}{\omega_1^{d-2}L^2} \left[\left(1 - \frac{f_2(r_s)}{f_1(r_s)}\right) + \frac{(d-1)L^2}{2r_s^d} \left(\omega_2^{d-2} - \omega_1^{d-2} \frac{f_2(r_s)}{f_1(r_s)}\right) \right] \\ & + \frac{M_1}{2\pi} \frac{r_m^{d-2}}{\omega_1^{d-2}} f_1(r_m) \left(1 + \frac{f_2(r_s)}{f_1(r_s)}\right) \log \left[\frac{|f_1(r_m)|}{\alpha^2} \frac{f_2(r_s)}{f_1(r_s)} \right]. \end{aligned} \quad (6.110)$$

In the final regime III (*i.e.*, $t > t_{c2}$), the relevant contributions are: the bulk term given by eq. (6.28) (with $r_b = 0$), the GHY contribution from the future singularity given by eq. (6.34) and the joint term at r_m given by eq. (6.48). The rate of change of the complexity in this regime is

$$\begin{aligned} \frac{d\tilde{\mathcal{C}}_A^{(III)}}{dt} = & -\frac{M_2}{(d-1)\pi} \frac{r_s^d}{\omega_2^{d-2}L^2} \left(1 - \frac{f_2(r_s)}{f_1(r_s)}\right) + \frac{d(M_2 + M_1)}{2(d-1)\pi} + \frac{(d-2)M_1}{2(d-1)\pi} \left(1 + \frac{f_2(r_s)}{f_1(r_s)}\right) \\ & + \frac{M_1}{\pi(d-1)} \frac{r_m^{d-1}r_s}{\omega_1^{d-2}L^2} \left[\left(1 - \frac{f_2(r_s)}{f_1(r_s)}\right) + \frac{(d-1)L^2}{2r_s^d} \left(\omega_2^{d-2} - \omega_1^{d-2} \frac{f_2(r_s)}{f_1(r_s)}\right) \right] \\ & + \frac{M_1}{2\pi} \frac{r_m^{d-2}}{\omega_1^{d-2}} f_1(r_m) \left(1 + \frac{f_2(r_s)}{f_1(r_s)}\right) \log \left[\frac{|f_1(r_m)|}{\alpha^2} \frac{f_2(r_s)}{f_1(r_s)} \right]. \end{aligned} \quad (6.111)$$

Early and late time behaviours

Of course, the critical times in the time evolution depend only on the background geometry and so these basic features in the time evolution remain unchanged if we choose to

study $\tilde{\mathcal{C}}_A$, without the counterterm contributions. However, if the shock wave was injected early enough, there were two clear plateaus in $d\tilde{\mathcal{C}}_A/dt$ (which included the counterterm contributions), given by eqs. (6.70) and (6.71). So we examine to see to what extent these plateaus arise for $d\tilde{\mathcal{C}}_A/dt$.

The first plateau is found in the regime of large t_w , such that r_s is very close to $r_{h,2}$ and r_b to $r_{h,1}$. In this limit, the growth rate in eq. (6.109) becomes

$$\left. \frac{d\tilde{\mathcal{C}}_A^{(1)}}{dt} \right|_{t_w \rightarrow \infty} = \frac{d-2}{2(d-1)\pi} (M_2 - M_1) + \frac{kz^2}{(d-1)\pi} \left(\frac{M_2}{1+kz^2} - \frac{w^2 M_1}{1+kw^2z^2} \right) + \mathcal{O}(e^{-\pi T_1(2t_w-t)}) . \quad (6.112)$$

Comparing to eq. (6.70), we see that here we also have a similar plateau with the rate being proportional to $(M_2 - M_1)$, at least for $k = 0$, but in general there are curvature corrections to this result. Further note that for the BTZ black hole (*i.e.*, $d = 2$), the time derivative is always zero, irrespective of the shock wave energy

$$\left. \frac{d\tilde{\mathcal{C}}_A^{(1)}}{dt} \right|_{d=2} = 0 , \quad (6.113)$$

because k does not play a role in the BTZ geometries.

The late time limit, analogously to that in eq. (6.71), is approached as r_s is close to $r_{h,2}$ and r_m close to $r_{h,1}$. However, without the inclusion of the counterterm, there are further considerations if the shock wave is light. If we denote the ratio of horizons as $w = 1 + \epsilon$, with ϵ small, there are two regimes to consider, that depend on a time scale related to the scrambling time in eq. (6.85), defined as

$$\hat{t}^* = \frac{1}{\pi T_1} \log \frac{2}{\epsilon} - 2t_w = 2t_{\text{scr}}^* - 2t_w . \quad (6.114)$$

If the late time regime is such that $t > \hat{t}^*$, then we can evaluate eq. (6.111) for x_m and x_s approaching 1, which yields

$$\begin{aligned} \left. \frac{d\tilde{\mathcal{C}}_A^{(\text{III})}}{dt} \right|_{t \rightarrow \infty, t > \hat{t}^*} &= \frac{M_1}{\pi} \left(1 + \frac{w(d+1)}{2(d-1)} \right) + \frac{d-2}{2(d-1)} \frac{M_2}{\pi} + \frac{kz^2}{(d-1)(1+kz^2)} \frac{M_2}{\pi} \\ &\quad - \frac{kz^2 w}{2} \frac{(d+1)w^2 - (d-1)}{(d-1)(1+kw^2z^2)} \frac{M_1}{\pi} + \mathcal{O}(T_2 t e^{-\pi T_1(t-2t_w)}) . \end{aligned} \quad (6.115)$$

In contrast to eq. (6.71), the late time rate here is not proportional to the expected sum of the masses, even for the planar horizons ($k = 0$) or in the limit of light but still non-zero

shocks ($w \sim 1$). For simplicity, let's rewrite eq. (6.115) for planar black holes ($k = 0$) and light shocks, such that $M_2 \approx M_1$. The late time limit then reads

$$\left. \frac{d\tilde{\mathcal{C}}_A^{(\text{III})}}{dt} \right|_{t \rightarrow \infty, t > \hat{t}^*} = \frac{2M_1}{\pi} \left(1 + \frac{1}{4(d-1)} \right) + \mathcal{O} \left(\frac{T_2 t}{w-1} e^{-\pi T_1 (t-2t_w)} \right). \quad (6.116)$$

If one wants to consider a shock wave with exactly zero energy, such that $w = 1$, then \hat{t}^* given by eq. (6.114) goes to infinity, which is equivalent to a regime where $t < \hat{t}^*$. This is equivalent to setting $w = 1$ in eq. (6.111), which simplifies to

$$\left. \frac{d\tilde{\mathcal{C}}_A^{(\text{III})}}{dt} \right|_{w=1} = \frac{2M_1}{\pi} + \frac{M_1}{2\pi} \frac{r_m^{d-2}}{\omega_1^{d-2}} f_1(r_m) \log \left[\frac{|f_1(r_m)|}{\alpha^2} \right], \quad (6.117)$$

and is simply the rate of change of the eternal black hole discussed in chapter 4. This demonstrates that the order of limits does not commute.

In addition, the heavy shock wave regime of the rate of change given by eq. (6.115) can be calculated by considering the limit $w \rightarrow \infty$. The rate of change becomes then, for $k = 0$ for simplicity,

$$\left. \frac{d\tilde{\mathcal{C}}_A^{(\text{III})}}{dt} \right|_{w \rightarrow \infty, t \rightarrow \infty} = \frac{M_2}{2\pi} \left(\frac{(d-2)}{(d-1)} + \mathcal{O} \left(\frac{T_2 t}{w^{d-1}} e^{-\pi T_1 (t-2t_w)} \right) \right), \quad (6.118)$$

which as expected is half of the one sided collapse value without the inclusion of the counterterm in eq. (5.58), and it is vanishing for BTZ ($d=2$).

Consider as an example the BTZ black hole, with $k = 0$ and $d = 2$. The late time regime for $t > \hat{t}^*$ reads

$$\left. \frac{d\tilde{\mathcal{C}}_A^{(\text{III})}}{dt} \right|_{d=2, t \rightarrow \infty} = \frac{1}{\pi} \left(M_1 + \frac{3}{2} \sqrt{M_2 M_1} \right) + \mathcal{O} \left(\frac{T_2 t}{w-1} e^{-\pi T_1 (t-2t_w)} \right), \quad (6.119)$$

where again we substituted $w^2 = M_2/M_1$ for $d = 2$. This expression again fails to produce the expected late time limit but we also see an unusual nonlinear dependence on the masses, *i.e.*, $\sqrt{M_2 M_1}$.

In figure 6.10, we investigate these limits for a very light but non-zero shock wave. We show the growth rate for BTZ black holes without the addition of the counterterm given by eq. (6.111), with $w = 1 + 10^{-33}$ (red) and $w = 1 + 10^{-37}$ (blue) and the vertical line representing \hat{t}^* as in eq. (6.114). For times which are large but smaller than \hat{t}^* , the

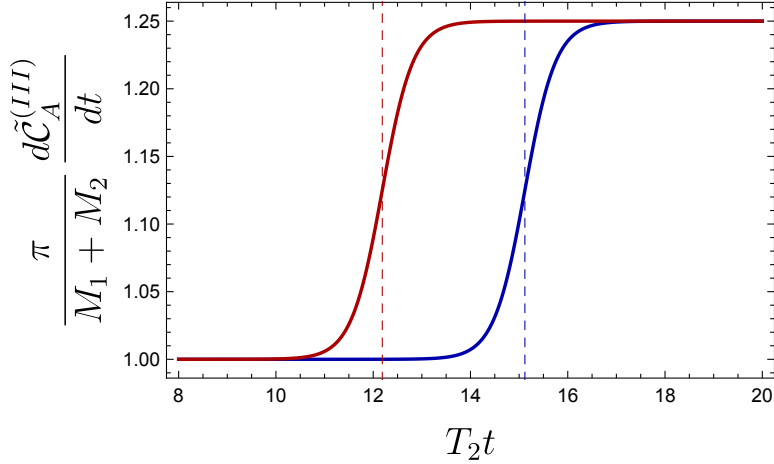


Figure 6.10: Rate of change of complexity for BTZ ($d = 2$) black hole without the addition of the counterterm, given by eq. (6.111). We study the transition between late time rates for very light shock waves, with $w = 1 + 10^{-33}$ (red) and $w = 1 + 10^{-37}$ (blue). The vertical lines represent the characteristic transition times \hat{t}^* , given by eq. (6.114). For light but non-zero shock waves, the late time limit is similar to the eternal black hole for $t < \hat{t}^*$, but for $t > \hat{t}^*$, it becomes the rate in eq. (6.119) (with $M_1 \approx M_2$).

effective late time limit is the same as the eternal black hole, but at $t \simeq \hat{t}^*$, there is a sharp transition to the late time limit of eq. (6.119) (with $M_1 \approx M_2$).

We compare the rate of change for BTZ with and without the inclusion of the counterterm in figure 6.11. We focus on heavy shock waves ($w = 2$), since for early times (before t_{c1}) there is a bigger discrepancy of rates, *i.e.*, vanishing without the counterterm or proportional to $M_2 - M_1$ with the counterterm. In addition, immediately after t_{c1} there is a large positive peak in the rate without counterterm, due to a factor of $f_2(r_s)$ in eq. (6.110), which approaches zero much faster than $f_1(r_m)$ for early shocks, since the exponent of r_s approaching $r_{h,2}$ at late times is proportional to $T_2(t + 2t_w)$, while r_m approaching $r_{h,1}$ is controlled by an exponent proportional to $T_1(t - 2t_w)$ for late times. Finally, the late time limit of the rate of change without the inclusion of the counterterm, as discussed previously, approaches the late time limit given by eq. (6.119), which does not reduce to the eternal black hole result for light shock waves.

Complexity of Formation

Turning now to the complexity of formation (6.88) but evaluated with eq. (6.108), *i.e.*, without the counterterm contribution (6.93). We consider the BTZ black hole (*i.e.*, $d = 2$) as a simple example. In this case, our previous result (6.95) is replaced with

$$\frac{\Delta\tilde{\mathcal{C}}_A - \Delta\mathcal{C}_{\text{NS}}}{|\Delta\mathcal{C}_{\text{NS}}|} = LT_1 \left[2 \coth^{-1}(wx_s) - \frac{2}{w} (w^2 - 1) \coth^{-1}(x_s) + (w^2 - x_b^2) \log\left(\frac{1 + x_b}{1 - x_b}\right) - w \log\left(\frac{w + x_b}{w - x_b}\right) + \frac{2x_b^2}{w} \tanh^{-1}\left(\frac{x_b}{w}\right) - \log\left(\frac{wx_s + 1}{wx_s - 1}\right) \right]. \quad (6.120)$$

We numerically evaluate eq. (6.120) and plot the complexity of formation as a function of the insertion time for light and heavy shock waves in figure 6.12. For both light and heavy shock waves, the complexity of formation just approaches a constant value for large t_w . Further, the latter value is less than the original $\Delta\mathcal{C}_{\text{NS}} = -c/3$ found with $t_w = 0$ (or alternatively, with no shock wave). Note that the transition to the final $\Delta\tilde{\mathcal{C}}_A$ essentially saturates after $T_1 t_w \sim 1$. We can evaluate the large t_w limit of eq. (6.120) analytically to find

$$\frac{\Delta\tilde{\mathcal{C}}_A - \Delta\mathcal{C}_{\text{NS}}}{|\Delta\mathcal{C}_{\text{NS}}|} \Big|_{t_w \rightarrow \infty} = -LT_1 \frac{w^2 - 1}{w} \log\left[\frac{w + 1}{w - 1}\right] + \mathcal{O}(T_2 t_w e^{-2\pi T_1 t_w}). \quad (6.121)$$

For light shock waves, the above difference vanishes as $w \rightarrow 1$, *i.e.*, $\Delta\tilde{\mathcal{C}}_A \rightarrow \Delta\mathcal{C}_{\text{NS}}$. On the other hand, for very heavy shocks (*i.e.*, $w \rightarrow \infty$), we find

$$\Delta\tilde{\mathcal{C}}_A \Big|_{w \rightarrow \infty} = \Delta\mathcal{C}_{\text{NS}} - S_1/\pi^2. \quad (6.122)$$

That is, for heavy shocks injected at early times, the complexity of formation decreases and it does so in a way that only depends on the initial black hole and not on the final black hole.

Of course, these results for $\Delta\tilde{\mathcal{C}}_A$ contrast with the previous results (including the counterterm) in figure 6.7, where the complexity of formation began to grow linearly for large t_w for both light and heavy shock waves. Therefore, if one studies the complexity of formation without the inclusion of the counterterm, there is no dependence on the scrambling time or on how early the shock wave was inserted. As we discuss in section 6.3, this means that $\tilde{\mathcal{C}}_A$ fails to exhibit the switchback effect for $d = 2$. Of course, this only strengthens the argument that this gravitational observable cannot be interpreted in term of complexity in the boundary theory.

6.3 Discussion

Using the framework established in chapter 5, we studied holographic complexity in Vaidya geometries (5.1) describing a shock wave propagating into an eternal black hole. Of course, this situation has already been well studied not only for a single shock wave but also for many shock waves as well, *e.g.*, [32–34, 174, 183, 184]. New directions investigated here were to study the full time dependence of the holographic complexity for both light and heavy shocks in section 6.2.1, and to evaluate the complexity of formation in section 6.2.2. In the following, we review our results in these calculations, and also consider their physical implications.

Complexity of Formation

The complexity of formation for the shock wave geometries was examined in section 6.2.2 using the CA approach. Recall that as originally studied in chapters 3 and 4, the complexity of formation was defined as the difference between the complexity of preparing two copies of the boundary CFT in the thermofield double state (TFD) at $t_L = t_R = 0$ and the complexity of preparing each of the CFT's in its vacuum state, as shown in eq. (6.88). A key feature of this quantity is that the difference of the complexities is UV finite.

In extending these calculations to the perturbed black holes, we first considered light shocks, *i.e.*, $w = r_{h,2}/r_{h,1} \simeq 1$, sent from the right boundary at some early time $t_R = -t_w$ — see left panel in figures 6.7 and C.3 for $d = 2$ and $d = 4$, respectively, with the CA approach. In this case, $\Delta\mathcal{C}$ was essentially unchanged for a wide range of t_w . But then beyond some critical t_w , *i.e.*, for earlier shock waves, $\Delta\mathcal{C}$ grew linearly as

$$\frac{d\Delta\mathcal{C}_A}{dt_w} = \frac{4M_1}{\pi}. \quad (6.123)$$

The critical injection time where this transition occurred was precisely given by the scrambling time, as defined in eqs. (6.85). Hence as a rough approximation, the complexity of formation can be described by two linear regimes, as shown in eq. (6.102) for $\Delta\mathcal{C}_A$. Of course, this is a manifestation of the switchback effect [32]. That is, we can think that we begin with the unperturbed TFD state at $t_L = 0 = t_R$. We then evolve the state backwards in time to $t_R = -t_w$, where we make the perturbation dual to the insertion of the shock wave, and then we evolve forward in time again to the initial time, *i.e.*, $t_R = 0$. The perturbation has a minor effect on the final state for $t_w < t_{\text{scr}}^*$, with the backward and forward time evolution essentially canceling out, and hence the complexity of formation remains

unchanged for these perturbations. However, the perturbation begins to have a dramatic effect in modifying the final state for $t_w > t_{\text{scr}}^*$ and hence we see that the complexity of formation begins to grow at this point — see further discussion below.

For higher energy shock waves on the other hand, the perturbation brings in an appreciable energy and accesses new degrees of freedom. Hence the state is modified even for small t_w and the regime in which the $\Delta\mathcal{C}$ is unchanged is absent. Instead, the complexity of formation as a function of t_w starts increasing right away with initial rate given by

$$\left. \frac{d\Delta\mathcal{C}_A}{dt_w} \right|_{t_w=0} = \frac{(M_2 - M_1)}{\pi}, \quad (6.124)$$

as in eq. (C.41).¹⁹ That is, this initial growth rate is driven by the energy in the shock wave, *i.e.*, it is proportional to the difference of the masses of the two black holes. As the injection time t_w continues to increase, $d\Delta\mathcal{C}/dt_w$ increases and soon saturates to a constant rate proportional to the sum of the masses

$$\frac{d\Delta\mathcal{C}_A}{dt_w} = \frac{2(M_1 + M_2)}{\pi}. \quad (6.125)$$

Of course, the latter matches eq. (6.123) in the limit where $M_2 \rightarrow M_1$.

Let us observe that we can connect these results to the time evolution of holographic complexity for one-sided black holes studied in chapter 5. The derivative of the complexity of formation with respect to t_w can be related via the time shift symmetry to the antisymmetric time evolution of the complexity, *i.e.*, using eqs. (6.3) and (6.6),

$$\frac{d\Delta\mathcal{C}}{dt_w} = \frac{d\mathcal{C}}{dt_R} - \frac{d\mathcal{C}}{dt_L}, \quad (6.126)$$

where we have used the fact that the complexity of preparing each CFT in its vacuum state is independent of the time and so we could replace $\Delta\mathcal{C}$ with \mathcal{C} on the right hand side. The limit of one-sided black holes is obtained by setting $M_1 = 0$, $M_2 = M$ and studying the dependence on the time $t_0 = t_R + t_w$, *i.e.*, the time after the perturbation is inserted. The second time interval $t_L - t_w$ appearing in our expressions will not play a role after setting $M_1 = 0$. Hence in eqs. (6.124) and (6.125), we set $M_1 = 0$ and $M_2 = M$ and trade the time evolution for an evolution in t_0 . Then taking the limit $t_w \rightarrow 0$ corresponds to the early time limit $t_0 \rightarrow 0$, for which eq. (6.124) yields $d\mathcal{C}_A/dt_0 = M/\pi$. Similarly taking $t_w \rightarrow \infty$

¹⁹Note that we have ignored the logarithmic term for $\Delta\mathcal{C}_A$ in eq. (6.103), which only appears for $d = 2$ but not higher boundary dimensions.

corresponds to the late time limit $t_0 \rightarrow \infty$, for which eq. (6.124) yields $d\mathcal{C}_A/dt_0 = 2M/\pi$. Indeed these limits precisely match eqs. (5.76) and (5.77). In particular, the relative factor of 2 between the early and late time limits of the CA results in eqs. (6.124) and (6.125) is the same ratio observed between the early and late time limits of one sided black holes, see *e.g.*, figure 5.4. Note that in taking this limit, the details of the left boundary time become unimportant and so one can also extract the same limit from the symmetric time evolution, as we explain below.

Time Evolution

We have also extended the previous studies of holographic complexity in shock wave geometries [32, 174] by studying the full time evolution of the holographic complexity for both light and finite energy shocks and using both the CA and the CV approaches. For simplicity, we focused on the symmetric time evolution $t_L = t_R = t/2$, which is readily compared with the time evolution in the unperturbed black hole backgrounds studied in chapter 4.

Let us begin by discussing the light shocks. Using both conjectures, we observed that if the shock was sent earlier than the scrambling time, the rate of change in complexity was approximately vanishing for a long period of time, centered around $t = 0$. At later times, the rate of growth of the complexity rapidly approaches the growth rate found in the unperturbed geometry. For the CA conjecture, we defined a number of critical times which characterized the transitions between the different regimes of the complexity growth. These were: $-t_{c,0}$, the time in the past where the WDW patch enters the future singularity; $t_{c,1}$, the time in which the point r_m leaves the past singularity; and $t_{c,2}$, the time in which the crossing point r_b enters the singularity, see figure 6.1. The plateau we have mentioned where the rate of computation vanishes appears for $-t_{c,0} \lesssim t \lesssim t_{c,1}$, see the right panel in figure 6.2. In the limit of early and light shocks in BTZ black holes, we were able to derive analytic expressions for the various critical times

$$t_{c,1} = t_{c,0} = 2t_w - \frac{1}{\pi T_1} \log \frac{2}{\epsilon} + O(\epsilon \log \epsilon), \quad (6.127)$$

and $t_{c,2} = 2t_w$ in the CA approach. Hence, we see the appearance of the scrambling time

$$t_{\text{scr}}^* = \frac{1}{2\pi T_1} \log \frac{2}{\epsilon} \quad (6.128)$$

in shortening of the plateau of constant complexity from $2t_w$. This is another manifestation of the switchback effect [32], as we explain below.

For heavier shocks, the regime of vanishing computation rate was replaced by a regime in which the rate of computation was approximately constant and proportional to the difference of the masses, *i.e.*, the energy carried by the shock wave,

$$\frac{d\mathcal{C}_A}{dt} = \frac{(M_2 - M_1)}{\pi}. \quad (6.129)$$

There is then a rapid transition where the rate of computation approaches the late-time limit, which is proportional to the sum of the masses,

$$\frac{d\mathcal{C}_A}{dt} = \frac{(M_1 + M_2)}{\pi}. \quad (6.130)$$

This late time limit was approached from above using the CA conjecture in all the cases analyzed.

As before, we can relate these results to analogous rates found for one-sided black holes in chapter 5. In particular, in eq. (6.130), we set $M_1 = 0$ and replace $t_R + t_w = t/2 + t_w = t_0$, $M_2 = M$, which yields $d\mathcal{C}_A/dt_0 = 2M/\pi$ and $d\mathcal{C}_V/dt_0 = \frac{8\pi M}{d-1}$. These then match the late time limits in eq. (5.77). In all these cases, we have assumed that the value of t_w was large and therefore they correspond to the $t_0 \rightarrow \infty$ limit of the one-sided black holes.

Null Surface Counterterm

Our calculations using the complexity=action proposal in section 6.2 included the counterterm (2.11) on the null boundaries of the WDW patch. Adding this surface term does not modify many key results for the CA proposal for eternal black holes, *e.g.*, the complexity of formation in chapter 3 or the late-time rate of growth discussed chapter 4. But it does modify the details of the transient behaviour in the time evolution. However, these comments are limited to the behaviour of holographic complexity in stationary spacetimes. In studying holographic complexity in Vaidya spacetimes in chapter 5, we found that the counterterm is an essential ingredient for the CA proposal. In particular, we showed that for geometries describing black hole formation, one does not recover the expected late time growth for general d . This effect was most dramatic for $d = 2$ (and $k = +1$) where the growth rate was actually negative throughout the process, *i.e.*, without the counterterm, the complexity appeared to decrease. In section 6.2.3, we also considered dropping the counterterm in our present calculations. There we found that without the counterterm, the holographic calculations again fail to reproduce the expected late time growth rate and that the complexity of formation does not exhibit the behaviour that is characteristic of

the switchback effect. Hence the gravitational observable associated with $I_{\text{wbdw}} - I_{\text{ct}}$ simply does not behave like complexity of the boundary state, and the results in section 6.2.3 reinforce our previous arguments that the counterterm should be regarded as an essential ingredient for the CA proposal.

One interesting aspect of the counterterm is that the structure of the UV divergences in the holographic complexity is modified, as was first noted in [190], and as is discussed in appendix C.1. Without the counterterm, the leading UV divergence takes the form (see eq. (C.14))

$$\tilde{\mathcal{C}}_{\text{A}}^{\text{UV}} \sim \frac{\mathcal{V}(\Sigma)}{\delta^{d-1}} \log\left(\frac{L}{\alpha \delta}\right), \quad (6.131)$$

where $\mathcal{V}(\Sigma)$ is the (total) volume of the time slice Σ on which the boundary state resides. To remove the AdS scale from $\tilde{\mathcal{C}}_{\text{A}}^{\text{UV}}$, [65] suggested that one should choose

$$\alpha = L/\ell, \quad (6.132)$$

where ℓ might be some other length scale associated with the microscopic rules used to define the complexity in the boundary theory. This choice then yields

$$\mathcal{C}^{\text{UV}} \sim \frac{\mathcal{V}(\Sigma)}{\delta^{d-1}} \log\left(\frac{\ell}{\delta}\right). \quad (6.133)$$

When the counterterm contributions are included, the α dependence in eq. (6.131) is eliminated and the leading UV divergence takes the form (see eq. (C.16))

$$\mathcal{C}_{\text{A}}^{\text{UV}} \sim \frac{\mathcal{V}(\Sigma)}{\delta^{d-1}} \log\left(\frac{(d-1)\ell_{\text{ct}}}{L}\right). \quad (6.134)$$

Of course, this expression suffers from the same deficiencies as eq. (6.131), *i.e.*, it contains the AdS scale which has no interpretation in the boundary theory, and it is ambiguous because the counterterm scale is undetermined. However, as before, we can use the latter ambiguity to eliminate the AdS scale. In particular, if we choose

$$\ell_{\text{ct}} = \frac{L}{d-1} \frac{\ell}{\delta}, \quad (6.135)$$

then the leading UV divergence takes the same form as in eq. (6.133). Of course, as before, one is left with the ambiguity of fixing the scale ℓ .

Now in comparing holographic complexity with calculations of complexity in a (free) scalar field theory [38, 39] (see also the discussion in chapter 7), it was noted that the

leading contribution to the complexity took precisely the form given in eq. (6.133).²⁰ In this case, the scale ℓ corresponds to the width of the unentangled Gaussian reference state appearing in the evaluation of the complexity. Hence it was suggested that the freedom of choosing this scale in the field theory calculations of complexity could be associated with the ambiguity of fixing α in the complexity=action proposal. Since we are now advocating that the latter proposal must include the null surface counterterm (2.11), we must instead associate this freedom with the ambiguity in fixing the counterterm scale, *e.g.*, as in eq. (6.135).

However, we would like to point out a difference in these two possibilities. This difference is highlighted by first choosing ℓ to be a UV scale. For example, with $\ell = e^\sigma \delta$, the logarithmic factor in eq. (6.133) simply provides a numerical factor²¹ and the leading UV divergence reduces to $\mathcal{C}^{\text{UV}} \sim \sigma \mathcal{V}(\Sigma)/\delta^{d-1}$. However, with this choice, eq. (6.132) yields $\alpha = e^{-\sigma} L/\delta$ while eq. (6.135) yields $\ell_{\text{ct}} = e^\sigma L/(d-1)$. Hence in previous discussions without the counterterm (*e.g.*, in chapter 4), the UV cutoff δ appears in the transient behaviour of $d\tilde{\mathcal{C}}_A/dt$, while $d\mathcal{C}_A/dt$ is completely independent of δ after the counterterm is included in the gravitational action. In contrast, if ℓ is chosen to be an IR scale, the leading UV divergence (6.133) is enhanced by the extra logarithmic factor $\log(\ell/\delta)$, and $d\tilde{\mathcal{C}}_A/dt$ is independent of δ while this UV cutoff explicitly appears in $d\mathcal{C}_A/dt$.

Of course, an interesting question is if either of these two behaviours is reflected in the QFT calculations of complexity. The effect of the reference scale on the complexity of the thermofield double state in a free scalar field theory was recently studied in [49] (see also 7.1). In this case, the transient behaviour in the time evolution does exhibit a nontrivial dependence on the reference scale. However, there is no potentially divergent behaviour found either in the case that $\ell \sim \delta$ or that ℓ remains an arbitrary IR scale. We might add however that this mismatch may not be very surprising. In particular, we note that the spectrum of the free scalar is not ‘chaotic’ enough to produce the linear growth found for holographic complexity.

Another interesting comparison that one might make is with the results of the covariant regulator used for the BTZ black hole in [34]. In this case, the boundary of the WDW patch is defined by two timelike geodesics that originate at the past joint and reach out to $r = r_{\text{max}}$ before falling back to the future singularity. While the leading UV divergent

²⁰We note that the logarithmic factor does not seem to arise for a free fermion [46, 47]. That is, the leading singularity takes the form $\mathcal{C}^{\text{UV}} \sim \mathcal{V}(\Sigma)/\delta^{d-1}$, which is similar to the holographic result found using the complexity=volume.

²¹In the QFT calculations [38, 39], this choice could be motivated by the fact that it renders the unitary connecting the (unentangled) reference state and the vacuum state continuous in momentum. That is, the unitary approaches the identity when the momentum approaches the cutoff.

term takes the form $\mathcal{V}(\Sigma)/\delta^{d-1}$, there is an explicit $\log \delta$ term appearing in the transient contributions to the rate of growth. Hence this regulator produces a result that is similar to the standard action calculations without the null surface term.

Integrated Complexity

We can also consider the behaviour of the integrated complexity, as shown for early and light shocks in BTZ black holes in figure 6.13. Comparing to the vacuum complexity, we start with the complexity of formation at $t = 0$ but with an early shock wave. This is much larger than the complexity of formation of the unperturbed black hole, *i.e.*, we are in the linearly rising regime in, *e.g.*, the left panel of figure 6.7. The complexity remains constant up to the critical time given by eq. (6.127). At (more or less) this time, the complexity matches that of the unperturbed black hole (of mass M_1) and it begins to grow such that the evolution is indistinguishable from the unperturbed evolution of an eternal black hole. That is, the effect of inserting these early (but light) shock waves is to lift the value of the initial complexity and then it remains fixed for a (long) initial period. For later times, the complexity not only grows in the same manner as, but is also essentially equal to, that of the unperturbed TFD. We note that this is a feature of the symmetric time evolution (*i.e.*, $t_L = t_R = t/2$), and we will discuss further how this is in accordance to quantum circuit models in the spirit of [32].

It is possible to interpret this behaviour in terms of summing two independent evolutions for the left and right boundary times.²² For early enough shocks, when evolving the right boundary time while holding the left time fixed, the complexity begins increasing immediately at the late time limit, *i.e.*, $d\mathcal{C}_A/dt_R \simeq 2M_2/\pi$. In contrast, when evolving t_L with t_R fixed, the complexity decreases until $t_L \sim t_w - t_{\text{scr}}^*$ and then makes a rapid transition to increasing with the same late-time growth rate. However, in both of these periods, the rate is governed by the mass of the past black hole, *i.e.*, $d\mathcal{C}_A/dt_L \simeq \pm 2M_1/\pi$. For a light shock wave with $M_2 \simeq M_1$, summing these two behaviours together produces the initial period where the complexity is constant in the symmetric time evolution. We show this behaviour for the CA proposal in the BTZ geometry in figure 6.14. In this example, we set $w = 1 + 10^{-5}$ and $t_w T_2 = 6$, and we also fix the boundary time which is not evolved at zero. We see in these examples that for times smaller than $2(t_w - t_{\text{scr}}^*)$, the left evolution is negative and opposite to the right evolution, such that it has vanishing rate in the symmetric case, as shown in figure 6.2. In addition, the behaviour for heavy shock waves follows from this discussion. For times smaller than $2t_w$, the left evolution contributes with

²²We thank Adam Brown for suggesting this explanation.

$\approx -2M_1/\pi$, while the right one with $\approx +2M_2/\pi$. Hence the rate is proportional to the difference of masses in this initial phase of the symmetric evolution, as in figure 6.3. We will discuss below a quantum circuit model that explains this behaviour.

To close this discussion, we recast various results from section 6.2 in order to develop some analytic understanding of the fact that the integrated holographic complexities match in the perturbed and unperturbed black holes (when working with light shocks and symmetric time evolution). We have already noted that for light shocks, the complexity of formation as a function of t_w remains constant until the critical injection time $t_{w,c}$ given by eqs. (6.85) for the CA approach. That is,

$$t_{w,c}^A = t_{scr}^* . \quad (6.136)$$

We therefore expect that for $t_w > t_{w,c}$ the complexity of formation will be increased compared to the unperturbed complexity of formation by

$$\Delta\mathcal{C}_A \simeq \Delta\mathcal{C}_{\text{unp}} + \frac{4M_1}{\pi} (t_w - t_{w,c}^A) . \quad (6.137)$$

Similarly, we can also approximate the time derivative of the complexity as a step function, which changes at the critical time t_{c1} (CA), from a rate proportional to the difference of the masses (*i.e.*, nearly vanishing for light shocks) to a rate proportional to the sum of the masses. Hence for times larger than this critical time, we have

$$\mathcal{C}_A(t) \simeq \Delta\mathcal{C}_A + \frac{2M_1}{\pi} (t - t_{c1}) . \quad (6.138)$$

Combining these two equations together yields

$$\mathcal{C}_A(t) \approx \Delta\mathcal{C}_{\text{unp}} + \frac{2M_1}{\pi} t , \quad (6.139)$$

again for times larger than the critical time. Note that this expression does not depend on t_w and as a consequence the time evolutions for different t_w all unify after a certain point. Further, the expression on the right hand side in both instances is approximately the time evolution of the unperturbed thermofield double. Hence the complexity of formation and the rate of growth are modified in such a way that at large times not only the rate of change of complexity matches the unperturbed result, but also the complexity itself.

A similar cancellation does *not* occur for heavier shocks (see figure 6.15), but one can use a similar reasoning to that above (neglecting the scrambling time) to show that the

relative shift between the holographic complexities at late times is approximately given by

$$\begin{aligned}\Delta\mathcal{C}_A(t) - \mathcal{C}_{A,NS} &\approx \frac{M_1 + M_2}{\pi} t + \gamma_3 \\ \gamma_3 &\equiv \frac{2(M_1 + M_2)}{\pi} (t_w - t_{\text{del}}) - 2\frac{M_1}{\pi} t_{c1},\end{aligned}\tag{6.140}$$

where t_{c1} and t_{del} are given by eqs. (6.55) and (6.105), respectively. For heavy and early shock waves, using eqs. (6.79) and (6.107) for the BTZ black hole, the shift simplifies to

$$\gamma_3 \approx \frac{2(M_2 - M_1)}{\pi} t_w + \frac{4M_1}{\pi^2 T_2} - \frac{2(M_1 + M_2) \log 2}{\pi^2 T_2} + \mathcal{O}\left(\frac{\log w}{w}\right).\tag{6.141}$$

In figure 6.15, we explicitly show that the integrated complexities line up very closely after shifting the curves by the term proportional to $(M_2 - M_1)t_w$.

Complexity=(Spacetime Volume)

Recently it was also suggested that the holographic description of boundary complexity might be simply given by the spacetime volume of the WDW patch, known as CV 2.0 [145]. Hence this CSV proposal defines

$$\mathcal{C}_{\text{STV}} = \frac{\nu}{16\pi G_N L^2} \int_{\text{WDW}} d^{d+1}x \sqrt{-g},\tag{6.142}$$

where ν is some numerical constant. It is straightforward to test the behaviour of this proposal in the present situation since the integrand is simply a constant in the bulk integral of the action, *i.e.*, $\mathcal{R} - 2\Lambda = -2d/L^2$. Therefore we can use our previous results for the bulk integrals to evaluate

$$\mathcal{C}_{\text{STV}} = -\frac{\nu}{2d} I_{\text{bulk}}.\tag{6.143}$$

For the symmetric time evolution, *i.e.*, $t_R = t_L = t/2$, we examine the growth rate for $t < t_{c1}$ in the case of early shock waves, which can be read from eqs. (6.28) and (6.143), with $r_m = 0$, $r_b \rightarrow r_{h,1}$ and $r_s \rightarrow r_{h,2}$,

$$\left. \frac{d\mathcal{C}_{\text{STV}}}{dt} \right|_{t_w \rightarrow \infty} = \frac{\nu}{2d(d-1)(1+kw^2z^2)} (M_2 - M_1),\tag{6.144}$$

which we can compare to the results for the CA and CV proposals in eq. (6.129). Further, for the late time limit, when r_m approaches $r_{h,1}$ and r_s approaches $r_{h,2}$, we find

$$\left. \frac{d\mathcal{C}_{\text{STV}}}{dt} \right|_{t \rightarrow \infty} = \frac{\nu}{2d(d-1)(1+kw^2z^2)} (M_2 + M_1) , \quad (6.145)$$

which we can compare to eq. (6.130).

It is straightforward to calculate the complexity of formation for planar black holes ($k = 0$) in higher dimensions, following the analysis at the end of appendix C.2. In this case, we simply consider the large t_w regime of eq. (6.89) rescaled as in eq. (6.143) and use the tortoise coordinates in eq. (C.54) which results in the following simple expression

$$\left. \frac{d\Delta\mathcal{C}_{\text{STV}}}{dt_w} \right|_{t_w \rightarrow \infty} = \frac{\nu}{d(d-1)} (M_2 + M_1) . \quad (6.146)$$

Next, we evaluate the dependence of the complexity of formation on t_w when the latter is close to zero, in which case r_s is close to the boundary. In this regime, we have from eq. (C.33)

$$\left. \frac{d\Delta\mathcal{C}_{\text{STV}}}{dt_w} \right|_{t_w \rightarrow 0} = \frac{\nu}{d(d-1)} (M_2 - M_1) . \quad (6.147)$$

In the limit where $M_2 \gg M_1$, both results can be related to the time evolution for the one-sided collapse, as discussed above for the CA and CV results, *i.e.*, these rates can be matched with eq.(5.50), rescaled by the factor in eq. (6.143).

Despite having a different overall multiplicative constant, the general properties of complexity seem to be satisfied by the CSV proposal (6.142). In particular, with this approach, the holographic complexity exhibits the switchback effect for any boundary dimension (including $d = 2$), and the late time rate of change has a smooth limit for light shock waves. Of course, given the simple relation of the spacetime volume to the bulk integral in the CA calculations, one can suggest another simple possibility. Namely, that the holographic complexity is described by the surface and joint terms in the gravitational action alone evaluated on the boundaries of the WDW patch. Our present calculations suggest that if we drop the bulk integral from eq. (2.10), the sum of the remaining surface and joint terms obey the expected properties of complexity, up to an overall normalization. Of course, to better understand this possibility and the CSV proposal more generally, it would be interesting to examine the results for background spacetimes in which matter fields deform the geometry in an interesting way. Of course, a simple example would be to compare the results of these new proposals to the results of the CA and CV proposals for charged black holes given in chapter 4.

Let us also add that [145] suggested a connection between the CSV proposal (6.142) and using the ‘thermodynamic volume’ to define the complexity,²³ which may further hint at connections to the black hole chemistry program, *e.g.*, see [200] for a review. Since the late time limit of geometries with two horizons, such as Reissner-Nordstrom black holes, reduces to a simple expression of differences of ‘internal energies’,²⁴ the authors of [145] suggested recasting complexity as a function of such extended thermodynamics variables. It would be an interesting future research direction to examine the physical consequences of these proposals for holographic complexity, in particular in the presence of shock waves.

Circuit Model

Next we would like to consider the connections of the behaviours observed in our holographic results to the switchback effect in more detail. Following the discussion of [32], we can interpret our results with some general considerations about quantum circuit models. As discussed in section 6.1, the boundary state of interest is the perturbed thermofield double state (6.4), in which the precursor

$$\mathcal{O}_R(-t_w) = U_R(t_w) \mathcal{O}_R U_R^\dagger(t_w) \quad (6.148)$$

is inserted in the right CFT (where $U_{L,R} = \exp[-iH_{L,R}t]$ are the usual time evolution operators). Of course, if \mathcal{O}_R was the identity operator, nothing would change in the state since the unitaries $U_R(t_w)$ and $U_R^\dagger(t_w)$ would simply cancel in eq. (6.148). On the other hand, if \mathcal{O}_R is a localized simple operator, $U_R(t_w)$ and $U_R^\dagger(t_w)$ would still approximately cancel until times of the order of the scrambling time t_{scr}^* , when the effect of the perturbation \mathcal{O}_R has propagated throughout the system. However, the behaviour will be somewhat different for ‘heavy’ operators which inject a finite amount of energy into the system and allow the circuit to access many new degrees of freedom. Therefore we begin with a discussion of the simple operators and return to consider the heavy operators afterwards.

As discussed in section 6.1, evolving the perturbed state independently in the left and right times yields the expression in eq. (6.5),

$$|TFD(t_L, t_R)\rangle_{\text{pert}} = U_R(t_R + t_w) \mathcal{O}_R U_R(t_L - t_w) |TFD\rangle . \quad (6.149)$$

²³However, we must add that this connection was recently called into question by [199]. In particular, the simple calculations of [145] were shown to not apply for black holes with scalar hair.

²⁴Strictly speaking the quantity associated to the inner Cauchy horizon does not have the usual thermodynamic interpretation, but nonetheless it is a useful identification to simplify the formulas. For example, see the early suggestions in [71, 201], and recent results in the context of Lovelock theories in [69].

One immediate observation is that there are two time scales appearing here: $t_{\text{R}} + t_w$ and $t_{\text{L}} - t_w$, precisely matching the holographic results in section 6.2. Of course, these are the invariant combinations that were naturally picked out by the time-shift symmetry described by eqs. (6.3) and (6.6). However, we would like to understand whether this perspective of the circuit models provides a deeper explanation of the behaviour of the holographic complexity.

The time evolution of the TFD state perturbed by a simple operator \mathcal{O}_{R} is schematically portrayed in figure 6.16. Along each leg of these sketches, we assume that new gates are being laid out at a fixed rate in the circuit preparing the desired state [32]. Further, as is evident from the holographic results or can be argued on more general grounds [31, 115], the rate is expected to be proportional to the energy of the system.²⁵ However, after the operator \mathcal{O}_{R} is inserted, the evolution ‘folds back’ in circuit space and the circuit complexity experiences the switchback effect, as illustrated in the figure. That is, most of the gates laid out in (the final stages of) the initial evolution are canceled out as the second stage of the evolution begins. This cancellation of gates is only effective for the scrambling time t_{scr}^* . Hence as illustrated in the figure, there are three regimes of interest which are distinguished by the value of $t_{\text{L}} - t_w$.

In figure 6.16 (a), if t_w is very large with respect to t_{L} , the initial (*i.e.*, furthest-to-the-right) operator evolves the state backwards by $|t_{\text{L}} - t_w|$, which we assume is bigger than the scrambling time. Then the second U_{R} carries the state forward again (assuming t_{R} is positive). The switchback effect comes into play and while the complexity grows on both legs of the evolution, the two time-evolution operators (at least partially) cancel out by an amount proportional to the scrambling time, as illustrated by the blue shaded region in the first panel of figure 6.16. That is, the complexity for the perturbation created by a simple operator grows as

$$\begin{aligned}
 t_{\text{L}} - t_w < -t_{\text{scr}}^* & : \quad \mathcal{C}_{\text{pert}} \approx 2M_1|t_{\text{L}} - t_w| + 2M_2(t_{\text{R}} + t_w) - 4M_1t_{\text{scr}}^* & (6.150) \\
 & \approx 4M_1(t_w - t_{\text{scr}}^*) + \Delta M(t + 2t_w - 2t_{\text{scr}}^*),
 \end{aligned}$$

where we substituted $t_{\text{L}} = t_{\text{R}} = t/2$ for the symmetric time evolution studied in section 6.2 in the second line. Here, we have also kept small corrections of order $\Delta M \equiv M_2 - M_1$. Hence we see that $d\mathcal{C}_{\text{pert}}/dt \sim \Delta M$ is proportional to the difference of masses, as found for the holographic complexity, *e.g.*, in eq. (6.70). However, since $M_2 \approx M_1$, this rate is very close to zero and the complexity effectively remains constant.

²⁵More precisely, one would argue that the rate is proportional to TS , the product of the temperature and the entropy. However, for a CFT as in the holographic framework, this product is proportional to the energy. In the following, we set this rate to be $2M$, twice the mass of the dual black hole.

The next regime corresponds to $-t_{\text{scr}}^* < t_L - t_w < 0$, as illustrated in part (b) of figure 6.16. In this range, $U_R(t_L - t_w)$ evolves the state backward and $U_R(t_R + t_w)$ evolves forward again. However, the switchback effect produces a cancellation for the duration of the first segment because it is less than the scrambling time. Hence the effective growth of the complexity is simply given by

$$\begin{aligned} -t_{\text{scr}}^* < t_L - t_w < 0 : \quad \mathcal{C}_{\text{pert}} &\approx 2M_2(t_R + t_w) - 2M_1|t_L - t_w|, \\ &\approx 2M_1 t + 2\Delta M t_w, \end{aligned} \quad (6.151)$$

where again we substituted $t_L = t_R = t/2$ and kept the corrections of order ΔM . Therefore in this second regime, the rate of growth already matches that in the unperturbed thermofield double state, *i.e.*, $d\mathcal{C}_{\text{pert}}/dt = d\mathcal{C}/dt$.

Of course, the final regime is when $t_L - t_w$ is positive, as sketched in part (c) of figure 6.16. In this case, both segments of the evolution move forward in time, and there is no opportunity for the switchback effect to modify the complexity and so the complexity simply grows as

$$\begin{aligned} 0 < t_L - t_w : \quad \mathcal{C}_{\text{pert}} &\approx 2M_2(t_R + t_w) + 2M_1(t_L - t_w) \\ &\approx 2M_1 t + \Delta M (t + 2t_w), \end{aligned} \quad (6.152)$$

where the second line corresponds to the symmetric time evolution. Again, in this third regime, the growth rate matches that of the unperturbed state.

Hence this simple model identifies two critical times for the symmetric time evolution after a simple perturbation, namely $t_{c1} = 2(t_w - t_{\text{scr}}^*)$ and $t_{c2} = 2t_w$. Comparing to eqs. (6.127)-(6.128), we see that these times are in good agreement with our holographic results for light shocks in BTZ. Looking at the growth rate suggested by the circuit model, we see that there are essentially two phases. Initially, the growth rate is almost zero and at $t = t_{c1}$, the complexity begins to grow with the same rate of the unperturbed state. Of course, this behaviour is in good agreement with the holographic results where we can see a rapid rise from zero to $2M_1$ after $t = t_{c1}$, as shown in the right panel of figures 6.2.

We can also compare the circuit model to the holographic results with a light shock for the complexity of formation by simply setting $t_L = t_R = 0 = t$. In this case, if we increase t_w from zero, we start in the (second) regime described by eq. (6.151). The switchback effect (almost) completely cancels the forward and backward evolution and hence the complexity and the complexity of formation are the same as in the unperturbed state. However, upon reaching $t_w \simeq t_{\text{scr}}^*$, we enter the (final) regime described by eq. (6.150). Hence the complexity of formation grows linearly with t_w for $t_w \gtrsim t_{\text{scr}}^*$. Again, this behaviour is in

agreement with our holographic results discussed above, and *e.g.*, as shown in eq. (6.102) for $\Delta\mathcal{C}_A$.

Our holographic calculations also considered heavy shock waves but in these cases, the perturbation is no longer dual to a simple operator. Rather the dual description would involve ‘heavy’ operators \mathcal{O}_R , which inject a finite amount of energy and allow the circuit to access new degrees of freedom. In this case, one does not expect a cancellation of the gates when the time evolution reverses. In particular, we can approximate the number of degrees of freedom before and after the perturbation as $S_1 \sim M_1/T_1$ and $S_2 \sim M_2/T_2$. Following [86, 87], we might analyze the circuit after the time reversal in terms of an epidemic model, however, the size of the initial infection is now of order $S_2 - S_1$. Hence if S_2 exceeds S_1 by some finite factor, we expect that the infection rapidly spreads through all of the degrees of freedom, *i.e.*, in a single time step — see further comments in the next subsection. In other words, the scrambling time in the above discussion is replaced by a much shorter delay time with

$$t_{\text{del}} \sim 1/T_2, \quad (6.153)$$

which matches our holographic results for heavy shocks, *e.g.*, as in eq. (6.79).

Hence for heavy operators, the transition between regimes essentially occurs when $t_L - t_w$ changes sign, *i.e.*, $t = 2t_w$. Following the above analysis of the circuit model, initially the complexity grows as

$$\begin{aligned} t_L < t_w : \quad \mathcal{C}_{\text{pert}} &\approx 2M_1|t_L - t_w| + 2M_2(t_R + t_w) \\ &\approx 2(M_2 + M_1)t_w + (M_2 - M_1)t, \end{aligned} \quad (6.154)$$

where the second line describes the symmetric time evolution, $t_L = t_R = t/2$. Similarly in the second regime, the growth is instead described by

$$\begin{aligned} t_L > t_w : \quad \mathcal{C}_{\text{pert}} &\approx 2M_1(t_L - t_w) + 2M_2(t_R + t_w) \\ &\approx 2(M_2 - M_1)t_w + (M_2 + M_1)t. \end{aligned} \quad (6.155)$$

Hence the rate of growth begins with $d\mathcal{C}_{\text{pert}}/dt \propto (M_2 - M_1)$, but then makes a transition to $d\mathcal{C}_{\text{pert}}/dt \propto (M_2 + M_1)$ for $t \gtrsim 2t_w$. Of course, this agrees with the behaviour of the holographic complexity with heavy shocks, *e.g.*, as shown in figures 6.3.

Setting $t = 0$, we can compare the complexity of formation in our holographic calculations for heavy shocks and in the simple circuit model. In particular, for very small injection times, *i.e.*, $t_w \lesssim t_{\text{del}}$, eq. (6.155) would apply, yielding $d\Delta\mathcal{C}/dt_w \propto M_2 - M_1$. However, the complexity rapidly transitions to the behaviour in eq. (6.154) where $d\Delta\mathcal{C}/dt_w \propto M_2 + M_1$. Of course, holography yields precisely this behaviour, as discussed in eqs. (6.124) and (6.125).

Simple Models

A simple model was proposed in [86, 87] for the evolution of the complexity in terms of an epidemic spreading of infected qubits when the system is evolved in time. The authors were considering the time evolution of a single qubit operator W given by the precursor $W(t) = U(t)WU(-t)$ and the suggestion was that the number of infected qubits $s(t)$ satisfies the following differential equation

$$\ell \frac{ds}{dt} = \frac{K - s}{K - 1} s \quad \longrightarrow \quad s(t) = \frac{K e^{t/\ell}}{K - 1 + e^{t/\ell}} \quad (6.156)$$

where K is the number of degrees of freedom and ℓ is a characteristic time step in the circuit. The boundary condition for the solution on the right was chosen as $s(t = 0) = 1$ since originally there was only a single infected qubit. Of course, this solution tends asymptotically to K . The complexity is then given by integrating over the infected qubits since these count the number of gates in the circuit which do not cancel out, and this leads to

$$\mathcal{C}_{\text{epidemic}}(t) = \frac{1}{\ell} \int_0^t dt s(t) = K \log(1 + e^{(t-t^*)/\ell}) \quad (6.157)$$

where $t^* = \ell \log K$ is the scrambling time. Comparing to the holographic results, one makes the natural identifications that $K \sim S$ and $\ell \sim \beta$.

It is not hard to generalize the above epidemic model to describe the complexity of the precursor $U_{\text{R}}(t_{\text{R}} + t_w) \mathcal{O}_{\text{R}} U_{\text{R}}(t_{\text{L}} - t_w)$ appearing in eq. (6.149), with two independent time evolutions from the left and right sides of the perturbation. One interesting feature of the epidemic toy model compared to the previous subsection is that it yields naturally the scrambling time. In addition as we will see, it gives rise to a regime of suppressed exponential growth which is characteristic of chaotic systems and which can be observed in our holographic results. The time evolution can again be pictured as sketched in figure 6.16. However, cases (a) and (b) will be treated together here as they both have $t_{\text{L}} - t_w < 0$, and we begin by describing the behaviour in this regime. Throughout the following, we will assume that $t_{\text{L}} + t_{\text{R}} > 0$, and of course, as in the holographic calculations, we assume $t_{\text{R}} + t_w > 0$.

The circuit relevant for $t_{\text{L}} - t_w < 0$ is depicted in figure 6.17 where the simple operator \mathcal{O}_{R} perturbing the circuit is indicated by the red dot and infected qubits are indicated by red stars. The two qubit gates that cancel out on the two sides of the unitary evolution are colored in green. In this case, we have to account for the cancellation of gates and this replaces the upper limit of integration in eq. (6.157) by $t_w - t_{\text{L}}$. Of course, we should then add a relevant count of the gates in the part of the circuit $U_{\text{R}}(t_{\text{R}} + t_w)$ that goes beyond

$t_w - t_L$, *i.e.*, in the final period of length $(t_R + t_w) - (t_w - t_L) = t_R + t_L$. This leads to the following result for the complexity in this simple epidemic model²⁶

$$\mathcal{C}_{\text{epidemic}}(t_L, t_R) = K \log \left(1 + e^{(t_w - t_L - t^*)/\ell} \right) + \frac{K}{2\ell} (t_L + t_R) . \quad (6.158)$$

If we further restrict to the symmetric time evolution, we obtain

$$\mathcal{C}_{\text{epidemic}}(t) = K \log \left(1 + e^{(t_w - \frac{t}{2} - t^*)/\ell} \right) + \frac{K}{2\ell} t . \quad (6.159)$$

Examining this result for a large insertion time t_w , we see two regimes. At early times $t \ll 2(t_w - t^*)$, we see that the complexity behaves as

$$\mathcal{C}_{\text{epidemic}}(t) \approx \frac{K}{\ell} (t_w - t^*) + K e^{-(t_w - t^*)/\ell} e^{\frac{t}{2\ell}} . \quad (6.160)$$

Hence there are two contributions, first the constant and second a term which grows exponentially. However the latter growth is suppressed by the exponentially small prefactor $e^{-(t_w - t^*)/\ell}$. Therefore we see that the complexity is approximately constant in this regime and, as we will see below, equal to the complexity of formation. (We will come back to the tiny exponential growth later). This regime (of early times and a simple operator) corresponds to the one in figure 6.16 (a) and indeed, the leading (constant) behaviour above in eq. (6.160) matches that in eq. (6.150) if we identify $K/\ell \approx 4M_1$. Of course, the present epidemic model does not account for the order ΔM contribution in eq. (6.150), while the previous simple circuit model does not account for the small exponential growth in eq. (6.160).

At later times $t \gg 2(t_w - t^*)$, we obtain

$$\mathcal{C}_{\text{epidemic}}(t) \approx \frac{K}{2\ell} t , \quad (6.161)$$

which restores the linear growth of the unperturbed evolution. This regime corresponds to the sketch in figure 6.16 (b). This result now matches that in eq. (6.151) with the previous identification, *i.e.*, now the prefactor becomes $K/(2\ell) \approx 2M_1$. Again, eq. (6.161) does not describe the order ΔM correction found in the circuit model discussion.

Of course, we can also consider the regime $t_L - t_w > 0$, which matches the sketch in figure 6.16 (c), in which case there are no cancellations (*i.e.*, no switchback) and so the

²⁶The factor of two in the second term is the same one mentioned in footnote 9 of [87] and is due to the fact that $K/2$ gates act in a unit time step.

count of necessary gates is simply given by

$$\mathcal{C}_{\text{epidemic}}(t_L, t_R) = \frac{K}{2\ell}(t_L - t_w) + \frac{K}{2\ell}(t_w + t_R) = \frac{K}{2\ell}(t_L + t_R). \quad (6.162)$$

Of course, restricting to symmetric time evolution with $t_L = t_R = t/2$, yields $\mathcal{C}_{\text{epidemic}}(t) = \frac{K}{2\ell}t$, as in eq. (6.161). This case matches the result in eq. (6.152) for the circuit model, up to the order ΔM correction.

Now we can also set $t = 0$ in eq. (6.159) to compare with the complexity of formation, which reads²⁷

$$\Delta\mathcal{C}_{\text{epidemic}}(t_w) = K \log(1 + e^{(t_w - t^*)/\ell}). \quad (6.163)$$

Of course, while our notation indicates the complexity of formation associated with the precursor, this quantity cannot predict (the part of) the complexity of formation associated with the state $|TFD\rangle$ appearing in the holographic calculations. In any event, initially with small t_w , *i.e.*, $t_w \ll t^*$, we obtain $\Delta\mathcal{C}_{\text{epidemic}}(t_w) \approx K e^{(t_w - t^*)/\ell}$, which indicates an exponential growth with t_w but again this term is suppressed by an exponential factor $e^{-t^*/\ell}$. In our discussion of the circuit model, this regime corresponds to the one in figure 6.16 (b) and the result matches that in eq. (6.151). In the second regime with $t_w \gg t^*$, eq. (6.163) yields $\Delta\mathcal{C}_{\text{epidemic}}(t_w) \approx K(t_w - t^*)/\ell$ which indicates a linear growth of the complexity of formation with respect to t_w after a delay of duration t^* . This regime corresponds to the one in figure 6.16 (a) and our result matches eq. (6.150).

We have seen that the epidemic model is in good agreement with the various different regimes of holographic complexity for light shocks. To obtain a more precise match, it is natural to choose $\ell = 1/\lambda_L$ where $\lambda_L = \frac{2\pi}{\beta}$ is the (quantum) Lyapunov exponent of gravitational systems that saturates the bound on chaos [202]. We demonstrate in figure 6.18 that an exponential growth with this particular exponent is indeed present in our holographic results for BTZ black holes. In addition, our previous identification $K/\ell \approx 4M_1$ now indicates that K is proportional to the entropy of the system. The scrambling time t^* then becomes approximately the fast scrambling time $t_{\text{scr}}^* \sim \frac{\beta}{2\pi} \log S$ of black holes [111, 183].

Let us add that all of the cases considered above correspond to $t_L + t_R > 0$. If instead we take $t_L + t_R < 0$, but keep $t_R + t_w > 0$ as in the holographic model, then the right side of the circuit in figure 6.17 is longer than the left part and the expression for the complexity becomes

$$\mathcal{C}_{\text{epidemic}}(t_L, t_R) = K \log(1 + e^{(t_R + t_w - t^*)/\ell}) + \frac{K}{2\ell} |t_L + t_R|. \quad (6.164)$$

²⁷This result matches eq. (6.157) with the replacement $t \rightarrow t_w$. Of course, this is no surprise since with $t_L = 0 = t_R$, the precursors in question match after this substitution and equating $W = \mathcal{O}_R$.

Further, let us mention that as discussed around eq. (6.153) when the energy of the insertion is large the infection will be as fast as a single time step in the system after the insertion which leads to $t_{\text{del}} \sim 1/T_2$. In the epidemic model this amounts to changing the boundary conditions to eq. (6.156) and starting with $K_2 - K_1$ infected qubits as the initial condition for the circuit after the insertion.

In addition, the authors of [32, 203] proposed that a good approximation for the complexity could be derived by looking at the lengths of geodesics stretching across the Einstein-Rosen bridge of a BTZ black hole²⁸

$$\mathcal{C}_{\text{simple}}(t_{\text{R}}, t_{\text{L}}) \equiv \tilde{K} \log \left[\cosh \frac{\pi(t_{\text{L}} + t_{\text{R}})}{\beta} + c \exp \left[\frac{\pi}{\beta} (2t_w - 2t_{\text{scr}}^* + t_{\text{R}} - t_{\text{L}}) \right] \right]. \quad (6.165)$$

Above, the normalization constant \tilde{K} should again reflect the number of degrees of freedom while c is some order one constant. Note that this expression is very similar to the previous one discussed in the context of the epidemic model. When $t_{\text{L}} + t_{\text{R}} \gg 0$ we may approximate $\cosh \frac{\pi(t_{\text{L}} + t_{\text{R}})}{\beta} \approx \frac{1}{2} \exp \left[\frac{\pi(t_{\text{L}} + t_{\text{R}})}{\beta} \right]$ which then yields the form (6.158) when identifying \tilde{K} and K . On the other hand, with $t_{\text{L}} + t_{\text{R}} \ll 0$, we may approximate $\cosh \frac{\pi(t_{\text{L}} + t_{\text{R}})}{\beta} \approx \frac{1}{2} \exp \left[-\frac{\pi(t_{\text{L}} + t_{\text{R}})}{\beta} \right]$ which then exactly takes the form (6.164). Hence, this expression (6.165) again produces the different behaviours described above.

First, let us consider the symmetric time evolution with $t_{\text{L}} = t_{\text{R}} = t/2$, this expression (6.165) reduces to

$$\mathcal{C}_{\text{simple}}(t) = \tilde{K} \log \left[\cosh(\pi t/\beta) + c \exp \frac{2\pi}{\beta} (t_w - t_{\text{scr}}^*) \right]. \quad (6.166)$$

For early shocks (*i.e.*, $t_w \gg t_{\text{scr}}^*$), the exponential term dominates the argument of the logarithm at early times. Therefore the holographic complexity is essentially constant until we reach the critical time $t \sim 2(t_w - t_{\text{scr}}^*)$, as described in figure 6.13. After this critical time, there is a transition to a linear growth at late times with $d\mathcal{C}_{\text{simple}}/dt \simeq \pi\tilde{K}/\beta$. The latter agrees quantitatively with our holographic results in eq. (6.130) with $\tilde{K}_{\text{A}} = 2S(d-1)/(d\pi^2)$ for the CA coefficient for planar black holes.

Alternatively, we may set $t_{\text{L}} = t_{\text{R}} = 0$ to examine the contribution of eq. (6.165) to the complexity of formation. In this case, the above expression simplifies to $\Delta\mathcal{C} \simeq K' \log \left[1 + c \exp \frac{2\pi}{\beta} (t_w - t_{\text{scr}}^*) \right]$. Here the exponential dominates the argument of the logarithm for $t_w > t_{\text{scr}}^*$ and in this regime of early shocks, the complexity of formation grows

²⁸An infinite (but state independent) constant was subtracted off in order to obtain a finite result [32].

linearly with $\Delta\mathcal{C} \sim 2\pi\tilde{K}(t_w - t_{\text{scr}}^*)/\beta$, which once again matches the expectation of the complexity of formation results if \tilde{K} assumes the values discussed above for CA and CV. We want to emphasize that it is surprising that the simple expression in eq. (6.165), based on geodesics in BTZ, captures so many properties of holographic complexity so well. It would be interesting to better understand this agreement in the future.

While we described the complexity of formation as being constant in the regime $t_w < t_{\text{scr}}^*$, the previous discussion indicates an exponential growth with t_w , as is characteristic of the epidemic model. Of course, we want to stress that this growth is highly suppressed since the prefactor for this exponential carries a factor of $\exp(-2\pi t_{\text{scr}}^*/\beta)$. In figure 6.18, we examine $\Delta\mathcal{C}$ in this initial regime carefully with a log plot, and we find that there is indeed an exponential growth, even though this is not at all evident in the original plots. Further, from the slope of the curves in figure 6.18, one can infer the correct Lyapunov exponent $\lambda_L = \frac{2\pi}{\beta}$ (to a good degree of accuracy).

Firewalls?

The strong sensitivity of the TFD state to small perturbations injected earlier than the scrambling time was already emphasized in [183], where it was pointed out that even a few thermal quanta of energy will be enough to completely distort the finely tuned correlations of the TFD state when sent early enough. In addition, as shown in the late time behaviour of the holographic complexity in figure 6.13, such deviations become indistinguishable at late times. In holography, this was explained by the fact that the energy of the shock wave is exponentially blueshifted as it falls to the event horizon [183]. Of course, the characteristic time scale for this to happen is the scrambling time, and is interpreted as the time it takes for these early perturbations to have been scrambled throughout the system. This blueshift also led the authors of [22, 204] to draw connections between such perturbations and firewalls. The point being that the infalling quanta can be viewed as a firewall by a (not-too late) infalling observer from the second boundary (*i.e.*, the left boundary in our calculations). This also suggests that the appearance of firewalls depends on the system with which the black hole is entangled (e.g., the measurements made on the radiation exiting the black hole). One intriguing possibility is that the growth of complexity can serve as a diagnostic of firewalls [31, 88, 203], in particular in the context of the shock wave geometries. We have already mentioned that the complexity will actually decrease when only t_L is pushed forward while holding $t_R = 0$ fixed²⁹ as long as $t_L < t_w - t^*$. The

²⁹To be more precise, according to [203], using holographic complexity as a diagnostic of firewalls at the left horizon also requires sending $t_R = \infty$ to avoid ambiguities.

suggested interpretation of [88, 203] is that the complexity is decreasing as a function of t_L as long as the shock wave is within a Planck distance from the horizon along the surface and this is precisely a manifestation of a firewall which will be encountered by an observer jumping in from the left side.

Future Directions

In chapter 5 by examining holographic complexity in one-sided Vaidya spacetimes, we found that the null surface counterterm (2.11) was an essential ingredient for the CA proposal (1.24). Our results here have reinforced this point. The most dramatic discrepancy was shown in section 6.2.3 where without the counterterm, the complexity of formation did not exhibit the switchback effect for $d = 2$. In section 6.2.3 and appendix C.2, we also found an unusual behaviour for the late time growth rate in the limit of very light shock waves. In particular without the counterterm, the growth rate approached the expected rate found for an eternal black hole, but at some characteristic time (6.114) related to the scrambling time, there was a transition to some more rapid growth, as illustrated in figure 6.10. The overall lesson here is the importance of testing various proposals for holographic complexity in dynamical spacetimes, such as the Vaidya geometries (5.1).

Other additional topics to explore include investigating localized shocks as in [174], as well as null fluid collapses of finite thickness. In addition, very little is known about higher curvature corrections to properties of complexity [69, 71] in shock wave backgrounds. As we discussed previously in this section, it would be interesting to further investigate the complexity=(spacetime volume) conjecture (6.142), and under which circumstances these proposals diverge from the CA and CV conjectures. Of course, it would also be interesting to better understand the connection between this proposal and the thermodynamic volume [145, 199].

In addition, it would be interesting to investigate to what extent the holographic results can be reproduced by complexity calculations in free field theories. For example, the switchback effect seems to be a very robust feature, which is naturally associated with the geodesic deviation of adjacent trajectories [86] in negatively curved geometries. Therefore, it would be interesting to investigate the complexity of precursors in a field theory context, *e.g.*, using [38, 39] where we have already seen that negatively curved spaces can arise. The Vaidya geometries studied here have an interpretation in terms of a thermal quench, *e.g.*, [191, 192], where some boundary coupling is rapidly varied at $t_R = -t_w$. Another interesting direction might be to combine the recent discussions of complexity in the thermofield double state [49, 194, 205] and in quantum quenches [54, 55] for Gaussian states to study the case of thermal quenches.

Further, it may be interesting to explore the implications of our results in the context of negative energy shock waves. In this case the negative rate of change of $M_2 - M_1$ before the scrambling time should be the main effect. Such negative energy shock waves play an important role in the construction of traversable wormholes [206, 207] and it would be interesting to check whether the profile of complexity can serve to diagnose them.

In addition, there has been recent progress on defining complexity for general CFT setups. In particular, it was proposed in [208] that the CV proposal can be related to the quantum information metric. This can be used to find the length of a circuit connecting two ground states whose respective Hamiltonians differ by an insertion of a primary operator. It would be interesting to understand in which cases the quantum information metric could also be used to study the relative complexity of states before and after a global quantum quench. Another proposal [42–45] ties the complexity to the minimization of a functional given in terms of a generalized Liouville action. It would be interesting to understand how to generalize this proposal to generic time dependent backgrounds and understand if it can be used to study the time dependence of a state after a quantum quench in order to compare with the holographic results here and in chapter 5.

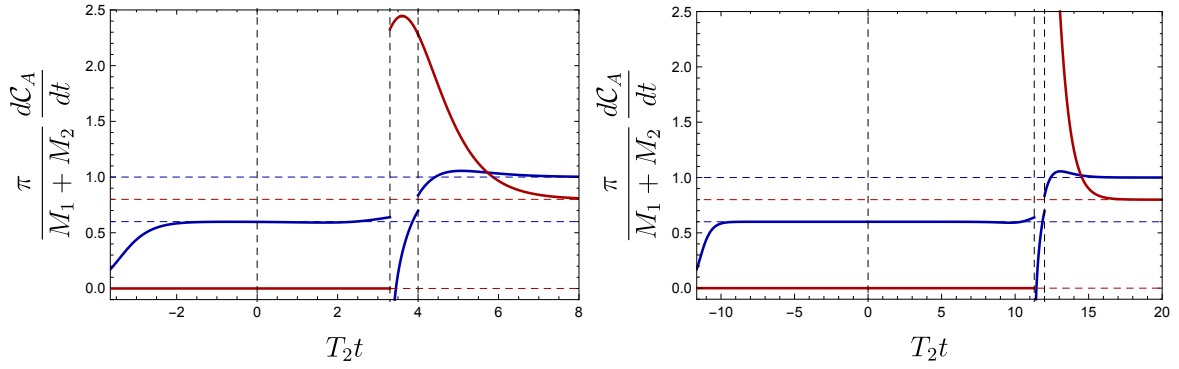


Figure 6.11: Rate of change of complexity evolving both boundaries as $t_L = t_R = \frac{t}{2}$, $w = 2$, $z = 1/w$, $\tilde{\ell}_{ct} = 1$ and $\alpha = 1$. In the left we evaluate $T_2 t_w = 2$ and in the right $T_2 t_w = 6$, and the blue curve is the rate of change with the inclusion of counterterm, while the red line is the rate of change without it. Despite being a shock wave that doubles the temperature, the rate of change is exactly zero without the inclusion of the counterterm for $t_{c0} < t < t_{c1}$, as opposed to being proportional to the difference of masses. In addition, there is a large positive peak after t_{c1} for the red curve, in contrast to the (short) negative spike of the blue curve. The peak in the red curve in the right figure is similar to the one in the left, but is sharper and reaches higher values the earlier the shock wave is sent. Finally, the late time limit is given by eq. (6.119), in contrast to $(M_1 + M_2)/\pi$, as discussed in section 6.2.1.

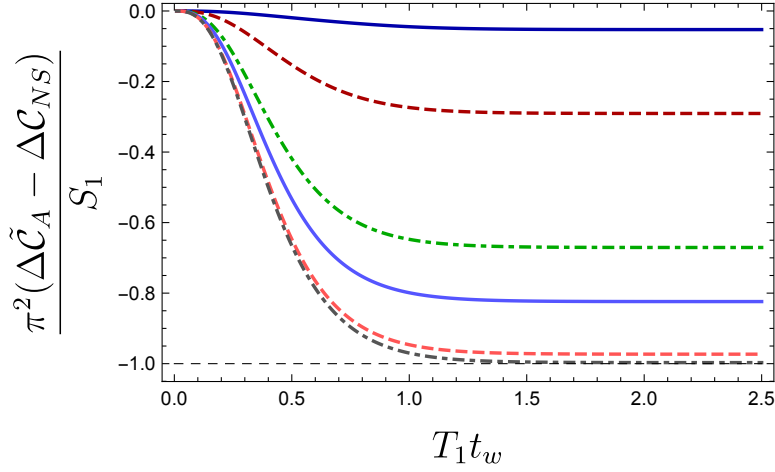


Figure 6.12: Complexity of Formation for BTZ black holes with no counterterm added to the null boundaries (and $\kappa = 0$). From top to bottom, we consider light to heavy shock waves, with $w = 1 + 10^{-2}$, $w = 1 + 10^{-1}$, $w = 1.5$, $w = 2$, $w = 5$ and $w = 15$. For $T_1 t_w$ of order 1, the complexity of formation with respect to the unperturbed one saturates to a constant, being close to zero for light shocks and $-S_1/\pi^2$ for heavy ones, represented by the horizontal black dashed line, as given by eq. (6.122).

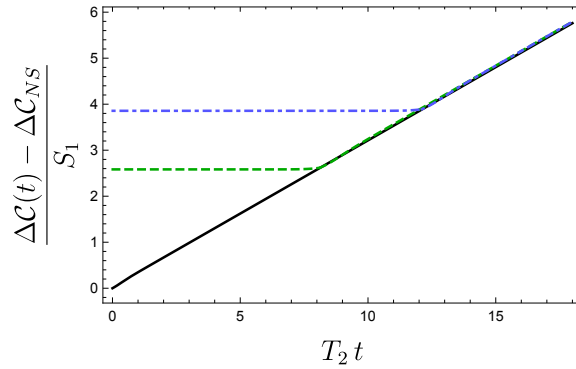


Figure 6.13: Complexity evolution in $d = 2$ for light shock waves. Using the CA proposal for $w = 1 + 10^{-5}$ and $\tilde{\ell}_{ct} = 1$. The unperturbed evolution is indicated by a solid blue line. We also plot the complexity evolution in the presence of shock waves – with $T_2 t_w = 6$ (dashed green) and 8 (dot-dashed light-blue). The initial values for those curves was fixed according to the complexity of formation. We see that the complexity does not change for a long period of time, and at late times, the complexity follows that of the unperturbed evolution.

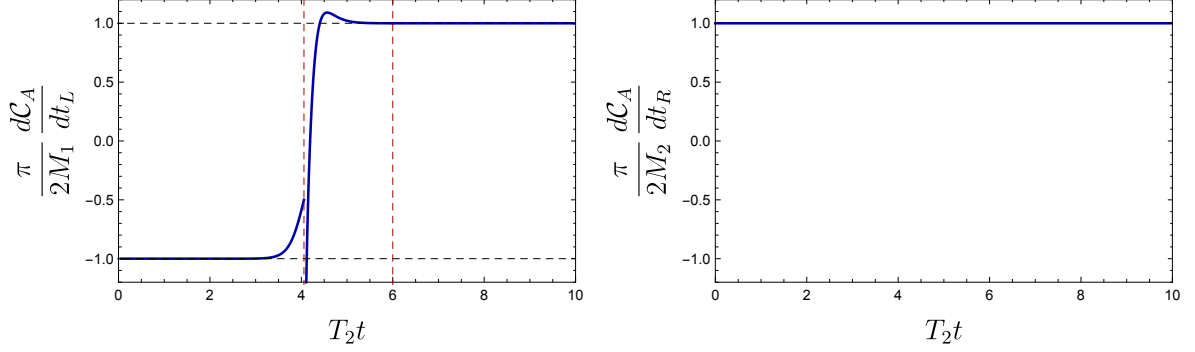


Figure 6.14: The time evolution of complexity using the CA proposal for $d = 2$. In the left panel, we fix $t_R = 0$ and evolve t_L , while in the right panel, we fix $t_L = 0$ and evolve t_R . In both cases, we have used $w = 1 + 10^{-5}$, $t_w T_2 = 6$ and in the left panel $\tilde{\ell}_{\text{ct}} = 1$. The vertical red lines in the left panel indicate the critical times at which r_m leaves the past singularity and later, when r_b enters the future one. For the right boundary time evolution, since the shock wave is sent early enough, r_s is already very close to $r_{h,2}$ and the flat profile is due to the fact that fixing $t_L = 0$ means that r_m stays behind the past singularity.

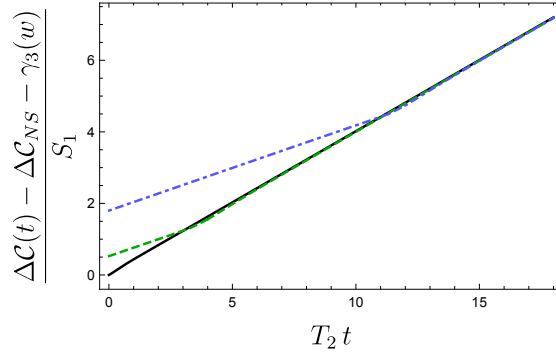


Figure 6.15: Complexity evolution in $d = 2$ for heavy shock waves. Using the CA proposal for $w = 2$ and $\tilde{\ell}_{\text{ct}} = 1$. We show the full complexity profile for two different times, $T_2 t_w = 2$ (dashed green), $T_2 t_w = 6$ (dot-dashed light blue). The shift between the curves is proportional to $(M_2 - M_1)t_w$ and matches the prediction of eq. (6.140).

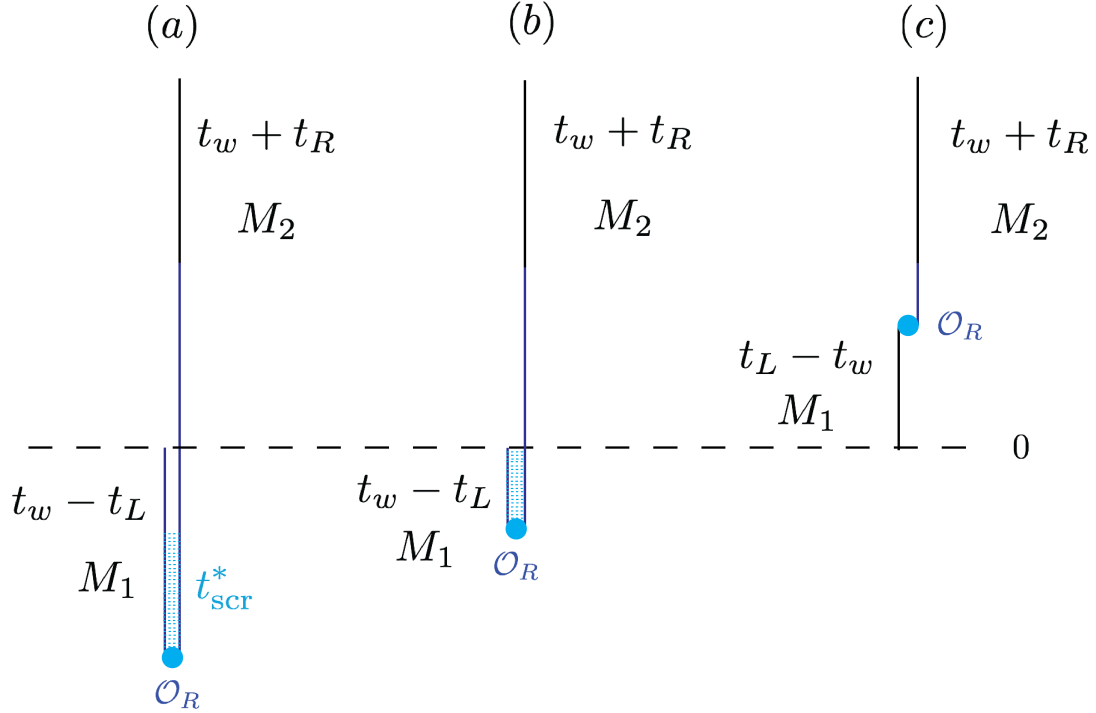


Figure 6.16: A representation of the insertion of a simple perturbation at an early time $-t_w$ for the thermofield double state as in (6.149), in analogy to the construction in figure 6 of [32]. (a) The regime where $t_L < (t_w - t_{\text{scr}}^*)$, which corresponds to rate of change under symmetric time evolution proportional to the difference of masses ($M_2 - M_1$). There is a cancellation in the time fold only during the scrambling time, which has to be accounted for in both sides of the evolution. (b) Transient regime that still represents a late time regime for light shock waves, such that $t_L > (t_w - t_{\text{scr}}^*)$ but $t_L < t_w$, so there is some folding to an earlier time. However, if such folding is smaller than the scrambling time, there is an effective cancellation of the gates, and because $M_2 \approx M_1$, the complexity matches that in regime (c). (c) The late time behaviour where $t_L > (t_w - t_{\text{scr}}^*)$ and $t_L > t_w$, so there is no folding backwards in the insertion of the operator.

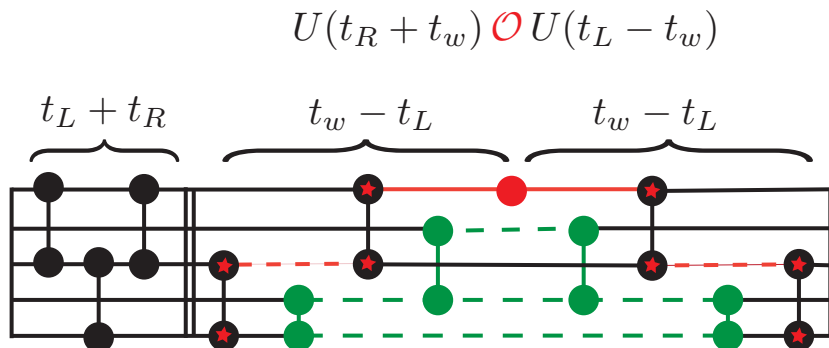


Figure 6.17: Illustration of the spread of infected qubits in the epidemic model when $t_L + t_R > 0$ and $t_w - t_L > 0$.

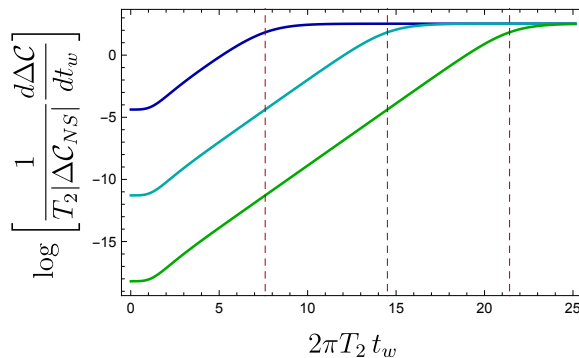


Figure 6.18: The derivative of the complexity of formation for BTZ black holes using the CA conjecture with respect to the insertion time t_w , for light shock waves characterized by $w = 1 + 10^{-3}$ (dark blue), $w = 1 + 10^{-6}$ (light blue) and $w = 1 + 10^{-9}$ (green). We observe a period of exponential growth until times of the order of the scrambling time, which then becomes a linear growth at late times where the plot saturates. We can read from this plot the correct Lyapunov exponent.

Chapter 7

Final remarks

The main goal of this thesis was to present a thorough analysis of the gravitational aspects of the holographic proposals for complexity, focusing on the complexity=action [33, 34] proposal. In particular, we paid careful attention to the contribution of boundary terms to the gravitational action [63]. In fact, such considerations enabled the evaluation of several properties of holographic complexity analyzed throughout this thesis.

In chapter 3, we evaluated the complexity of formation for holographic complexity, which measures the additional complexity required to build the thermofield double state in eq. (1.10) with respect to two copies of the vacuum. By carefully evaluating the contributions to the action, we were able to show that for AdS-Schwarzschild black holes, the complexity of formation was UV finite and did not depend on the ambiguities associated with the null boundaries. In addition, we also showed that for planar black holes (with $k = 0$), the complexity of formation was indeed positive and simply proportional to the entropy, as shown in eqs. (3.38) and (3.49).

In chapter 4, we investigated next the time dependence of the complexity as the thermofield double state was evolved forward in time, as in eq. (1.21). In AdS/CFT, this corresponds to a time evolution with both boundary times evolving upwards, as shown in the green slice of figure 1.2. We found that the late time rate of change of complexity is approached from above in the CA proposal, which implies that the originally proposed connection with Lloyd's bound is generically violated. We also found that the transient rate of change at early times depends on the ambiguities associated with the null boundaries of the WDW patch in the CA proposal. Imposing reparametrization invariance to the null normals did not significantly change any of the above conclusions, it only substituted one ambiguity in the overall normalization of the null vectors α in eq. (4.15) with another

in the form of the arbitrary length scale ℓ_{ct} in eq. (2.11). In addition, we investigated the complexity rate of change for charged AdS-Reissner-Nordstrom black holes and also found that the late time limit is approached from above. In contrast, we showed that the late time rate of change is approached from below in the CV proposal.

We turned our attention to Vaidya shock wave geometries in chapters 5 and 6. We found that the addition of the counterterm in eq. (2.11) is essential in order to reproduce properties of complexity. In chapter 5, we focused on one-sided geometries while in chapter 6, we focused on two-sided ones. We constructed a null fluid action in chapter 5, and we showed that it has a vanishing value on-shell. Therefore, the imprint of the null fluid only appears through the backreaction on the geometry. Next, we carefully investigated how the counterterm in eq. (2.11) is necessary in order to reproduce desired properties, such as a positive rate of change for quenches in $(1+1)$ CFTs. In addition, we also showed that for one-sided geometries, the late time rate of change of complexity is approached from below in the CA proposal, and from above in the CV, in contrast to the two-sided eternal results of chapter 4.

In chapter 6, we investigated the holographic complexity for two-sided shock wave geometries, perturbing one of the sides with an infalling shock wave carrying a finite positive energy. We show how the time evolution and the complexity of formation behave for both light and heavy shock waves, and we show how the complexity of formation in the shock wave geometry is intimately connected to the switchback effect. In addition, we show that in order to reproduce such effect, we also need to include the counterterm in eq. (2.11).

As final remarks, let us comment further on some important results that connect to the investigations in this thesis but were not included. We will briefly mention some results from the works of this author [39, 49, 69, 70], as well as some important results from [38, 65].

7.1 Lessons from quantum field theory models

A careful study on what implications complexity models using Nielsen’s geometric construction [108, 109] could have for the properties of quantum field theories was initiated in [38].¹ For concreteness, we focus on free scalar field theory, which can be realized by

¹In [39], we investigated a similar problem but with a different minimization procedure, based on the projective structure of Hilbert spaces of quantum theories, which results in a minimization procedure using a Fubini-Study (FS) metric. There are a few important differences with respect to Nielsen’s construction: it is not clear how to implement penalty factors in the FS approach, and in fact the space generated by

considering the continuum limit of harmonic oscillators in a lattice. Suppose we start with a “simple” reference state, in which the local degrees of freedom are all disentangled gaussians with width set by the reference scale μ . Notice that the reference scale μ and the momentum UV cutoff Λ are distinct quantities. This is equivalent to the ground state of the ultralocal Hamiltonian

$$H_R = \int_{\mathcal{B}} d^{d-1}x \left(\frac{1}{2} \pi(x)^2 + \frac{1}{2} \mu^2 \phi(x)^2 \right). \quad (7.1)$$

The target state under consideration could be, for instance, the ground state of the free scalar field theory, for which we write the Hamiltonian as

$$H = \int_{\mathcal{B}} d^{d-1}x \left(\frac{1}{2} \pi(x)^2 + \frac{1}{2} m^2 \phi(x)^2 + \frac{1}{2} (\partial_x \phi(x))^2 \right). \quad (7.2)$$

Of course, the set of possible gates we need to include depends on which task we want to investigate. Since we will mention some results relevant to the TFD state, we will consider the gates to be the quadratic combinations of ϕ 's and π 's. In order to calculate the complexity in the context of field theory, it is convenient to study a simpler problem first, concerning two harmonic oscillators. Essentially we can show that the problem of studying gaussian states factorizes, which leads us to extending the results to a lattice with N oscillators. Finally, we take the continuum limit and obtain the minimum circuits for the field theory, integrating up to a momentum UV cutoff Λ (see [38, 49] for more details in this procedure). For the problem of building the ground state of the free bosonic theory, it is enough to consider geodesics in the group manifold $GL(N, \mathbb{R})$. For the time evolution of the TFD, we need to consider the full symplectic group $SP(2N, \mathbb{R})$.

Let us comment first on the leading UV divergence in the complexity for building the vacuum of the Hamiltonian in eq. (7.2) from the unentangled state with ultralocal mass μ . For simplicity of presenting the results, let us assume that μ is of the order of the UV cutoff Λ , but always larger, such that $\mu > \Lambda$ holds. In addition, there are many possible cost functions to associate with the circuit paths, as indicated by eq. (1.17). In order to compare to holography, we find that a cost function associated to a L^1 norm (involving the sum of absolute values) is the choice that closely reproduces the holographic properties.²

the states is smaller than the space of possible unitaries, such that in general the geometries can be quite different. In addition, the FS approach does not depend on extra dimensionful parameters that could arise in order to make the elementary gates dimensionless, as ω_g in [48, 49]. One interesting property is that for the complexity of the vacuum of free scalar fields, the optimal paths, and as a consequence the complexities, agree with both the Nielsen and the FS approaches [38, 39].

²There is another choice of cost function that yields similar UV divergence structure to the holographic theories using the Schatten norm [47, 48] that is basis independent as well.

The QFT complexity of building the vacuum reads then [38, 39]

$$\mathcal{C}_1 \sim \text{vol } \Lambda^{d-1} \log \left[\frac{\mu}{\Lambda} \right] + \dots, \quad (7.3)$$

where vol corresponds to the spatial volume of the system. If we compare the leading UV divergence using the CA proposal with the inclusion of the null boundary counterterm, we would have a leading UV divergence that behaves like ([65, 190] and appendix C.1)

$$\mathcal{C}_A \sim c \frac{\text{vol}}{\delta^{d-1}} \log \left[\frac{\ell_{ct}}{L} \right] + \dots, \quad (7.4)$$

where c is the central charge and $\delta = \Lambda^{-1}$. The leading divergent term in eq. (7.4) is a surprising quantity from the point of view of the CFT, since the AdS radius of curvature L should not appear in CFT observables. Therefore, the ratio between ℓ_{ct} , associated with the null boundaries of the Wheeler-DeWitt patch, and L indicate an ambiguity in the CA proposal. Such ratio parallels the ambiguity found in the QFT calculation in the form of the argument μ/Λ of the logarithm in eq. (7.3). The similarities between eqs. (7.3) and (7.4) are not immediate consequences of the AdS/CFT duality, since they represent QFTs in the opposite side of the spectrum. The holographic results hold for theories with large number of degrees of freedom and strong coupling, while the free scalar field has central charge of order ~ 1 and no coupling. As we will discuss further, the fact that the QFTs are at very different ends of the spectrum seem to be crucial for the time evolution of the complexity of the TFD. In addition, the quantities analyzed in eqs. (7.3) and (7.4) are UV divergent terms that are not universal, so one should take the comparison as a more qualitative feature. It is promising nonetheless that such ambiguities map to each other in this analysis.

Next, we can evaluate the complexity of formation for the TFD state using a free scalar field. There are a few subtleties in the evaluation of this quantity; for instance, not only does the cost function influence the form of the final answer, but also the basis of the modes on which gates act, at least for cost functions associated with the L^1 norm. In [49], we evaluate the complexity in the diagonal basis, which is the basis in which the TFD state factorizes, and the left-right (LR) basis, which consists of generators that act on the physical left and right modes. The holographic complexity results seem to be more closely related to the construction in the LR basis, which is the one we present here. The ratio between the complexity of formation and the thermal entropy reads [49]

$$\left. \frac{\Delta \mathcal{C}_1^{(LR)}}{S_{th}} \right|_{\beta m=0} = \frac{2^d - 1}{d}. \quad (7.5)$$

Comparing to the holographic results of chapter 3 in eqs. (3.38) and (3.49), we see a striking resemblance. With these choices, the complexity of formation is independent of the UV cutoff scale, as well as the reference ultralocal mass μ . If we recall the results of chapter 3, for the uncharged black holes, the complexity of formation does not depend on the ambiguities associated with the null boundaries, given that we associate the same value of ℓ_{ct} to the black hole and vacuum spacetimes. In addition, under these choices, the UV divergences also cancel, leaving the expressions given by eqs. (3.38) and (3.49). In contrast, the dependence with the spacetime dimension grows faster for the free QFT example: while for large d , CA predicted an approximately linear dependence, the QFT results suggest an exponential enhancement. In addition, we found in chapter 3 that the complexity of formation vanished for $d = 2$, in contrast to the expression in eq. (7.5).

Finally, let us comment on the time evolution of the complexity of the TFD state. As such, let us focus on the example that had the most similarities with the holographic results for the UV divergences and the complexity of formation. That is, we will focus on the L^1 norm and left-right basis for the evaluation of the time dependence. It will be useful to define the dimensionless ratio between the temperature and the ultralocal reference mass as

$$\tilde{\gamma} \equiv \frac{1}{\beta \mu} = \frac{T}{\mu}. \quad (7.6)$$

We show the time dependence for different values of the reference scale in figure 7.1 (borrowed from [49]). The complexity for the time evolution of the TFD in bosonic free field theory saturates at times of the order of the inverse temperature, which is not the prediction for the holographic results of chapter 4. In this sense, large number of degrees of freedom and strongly interacting seem to be an essential ingredient for late time growth of complexity, as well as the chaotic/fast scrambler nature of the spectrum of holographic theories [111, 202].

In addition, the transient of the time derivative of complexity does depend on the reference scale μ , which is similar to the behaviour of the early time dependence on α or ℓ_{ct} for the CA proposal. We do however notice that the dependence on the reference scale is bounded in the QFT calculations, given that both the small and large limits of $\tilde{\gamma}$ saturate to the bottom curve in figure 7.1. We refer the reader to [49] for a broader discussion, where we also investigate an example where the transient rate of change varies more strongly with the reference scale μ .

There is still much to be understood about the role of complexity for characterizing quantum field theory properties. For instance, evaluating complexity for CFTs with simple holographic duals, which is the route taken by the works in [42–44] that associates complexity to an optimization of the Euclidean path integral. Another important step is to

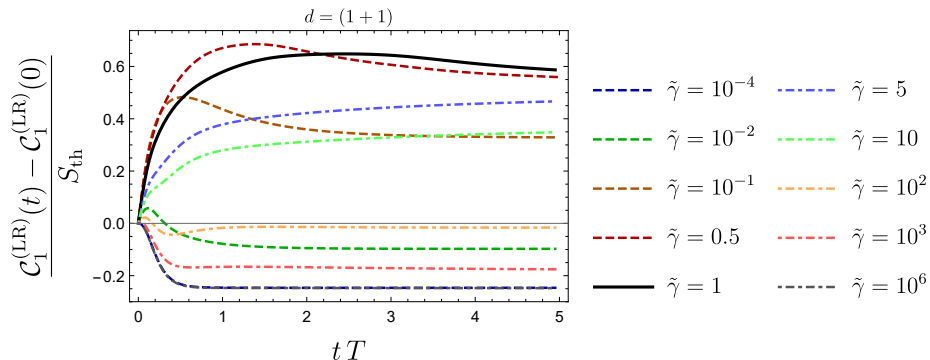


Figure 7.1: The time evolution of complexity with varying reference scale for the massless scalar in $d = 2$. The values of $\tilde{\gamma}$, see eq. (7.6), are $\tilde{\gamma} = 1$ (solid black), $\tilde{\gamma} < 1$ (dashed curves) and $\tilde{\gamma} > 1$ (dot-dashed curves). Both limits of large and small $\tilde{\gamma}$ are bounded, which can be seen by the overlapping curve at the bottom. By varying the reference scale, we obtain regimes where the complexity mostly increases with respect to the complexity of formation. For different values of $\tilde{\gamma}$, the complexity saturates to different constants at late times.

have a unified formalism in order to investigate interacting theories, which started being investigated in [50] (see also [209, 210]). In addition, a possibility of connecting the bulk symplectic form to the quantum overlap of boundary states was put forward in [51, 52]. The hope is that in the future the properties of quantum complexity in the boundary theory can provide a framework to sharpen our understanding of the holographic proposals of complexity. In addition, a solid understanding of quantum complexity for QFTs could give a new perspective on quantum many-body properties, analogous to the role of entanglement entropy in condensed matter systems.

The saturation of complexity at time scales of the inverse temperature for free field theories motivates the investigation of holographic complexity for theories away from the strongly coupled and large central charge limit. One simpler route to probe this regime is to consider higher curvature corrections to the Einstein-Hilbert gravitational action in eq. (1.2), which are inspired by low-energy regimes of certain string theory backgrounds. In [69], we investigated the correction to the growth rate of complexity using the CA proposal at late times for the Lovelock class of higher curvature gravity.

In general, there are quite a few subtleties that arise in the CA evaluation including higher curvature corrections. If the future boundary of the Wheeler-DeWitt patch approaches the curvature singularity, as in the AdS-Schwarzschild example in figure 1.7,

there are certain order of limit issues with how one regulates the boundary contribution at these regions of large curvature. However, at least in the case of charged Reissner-Nordstrom-like black holes, we can effectively provide a regulator mechanism with the addition of charge, as the future boundary of the WDW patch approaches at late times the inner horizon, instead of the black hole singularity, as shown in figure 4.8.

In the case of Lovelock gravity, the late growth rate of complexity in units of the inverse temperature is essentially given by the Jacobson-Myers entropy [211]

$$\frac{d\mathcal{C}_A^{\text{Lovelock}}}{d(Tt)} \sim S_{JM}, \quad (7.7)$$

which receives corrections for spherical and hyperbolic horizon geometries. It is also expected that for planar geometry, more generic forms of higher curvature corrections also modify the late time rate of change of complexity. Of course, there are quite a few subtleties with this observable in higher curvature theory, but at least the expression in eq. (7.7) suggests corrections to the rate of change when evaluated for CFTs dual to more complicated gravitational theories in the bulk. There is certainly still much to be understood for holographic complexity in this context.

7.2 Holographic complexity is equal to which action?

Let us conclude the discussion in this thesis by briefly commenting on our recent work [70] (see also [89]) that further explores one of the main results of chapters 5 and 6. It is true that one can add different surface terms which do not change the equations of motion, but in principle they do change the value of the action. For shock wave geometries in chapters 5 and 6, we found how a surface term that imposed reparametrization invariance was necessary in order to reproduce properties of complexity. In [70], we investigated dyonic black hole solutions, such that the geometry is fixed by the sum of the square of the electric and magnetic charges $q_T^2 = q_e^2 + q_m^2$, and we found the striking result that the rate of change of complexity in the CA proposal depends on the ratio between electric and magnetic charges. We show such dependence on the ratio of electric and magnetic charges in figure 7.2 (borrowed from [70]).

We can see in figure 7.2 that for purely magnetic black holes the late time rate of change of complexity vanishes. We also found that the switchback effect is absent by perturbing the purely magnetic solution with a shock wave [70].

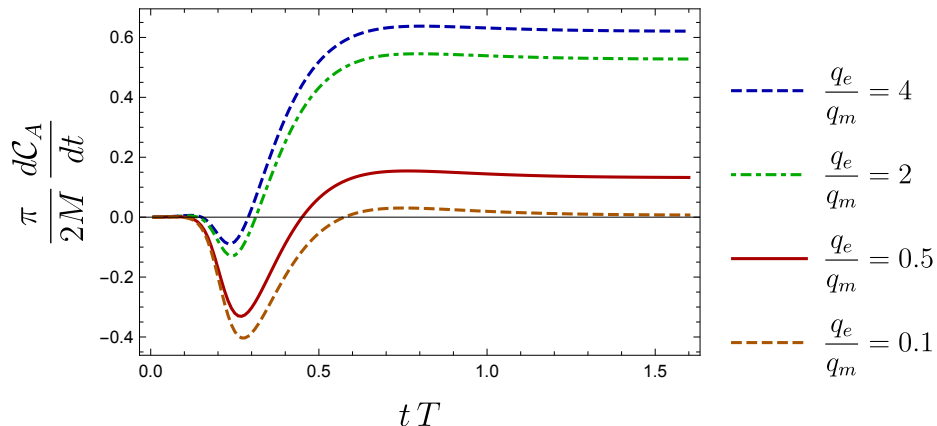


Figure 7.2: The rate of change of complexity for the dyonic black hole, with $r_- = 0.3 r_+$, $L = 0.5 r_+$ and $\ell_{\text{ct}} = L$. We fix the parameters that determine the geometry, but vary the ratio between electric and magnetic charges. When the charge is mostly magnetic, the growth rate of complexity approaches zero at late times. The limit $q_m \rightarrow 0$ essentially matches the top curve for $\frac{q_e}{q_m} = 10$. Similarly the $q_e \rightarrow 0$ and the $\frac{q_e}{q_m} = 0.1$ curves are indistinguishable on this scale.

One possible way to make the action of a purely magnetic black hole solution exhibit late time growth is by adding a surface term constructed with the gauge field [70]

$$I_{\mu Q} = \frac{\gamma}{g^2} \int_{\partial\mathcal{M}} d\Sigma_\mu F^{\mu\nu} A_\nu. \quad (7.8)$$

For $\gamma = 1$, this surface term has the interpretation of a Legendre transform in black hole thermodynamics. For instance, suppose we are evaluating an electrically charged solution, such that the Euclidean version of the action in eq. (4.91) and $\gamma = 0$ in eq. (7.8) yields the Gibbs free energy, which is associated with the grand canonical ensemble with fixed chemical potential μ and temperature. On the other hand, adding the surface term in eq. (7.8) with $\gamma = 1$ yields the Helmholtz free energy, associated with the temperature and total charge fixed. For the complexity=action proposal, the addition of eq. (7.8) can change the role of electric and magnetic solutions, such that for $\gamma = 1$, it is reversed: the purely electrically charged black hole would be the one with constant action at late times.

Our original motivation for revisiting the AdS-Reissner-Nordstrom black hole was to understand a surprising result in two bulk spacetime dimensions, that the usual action associated with the Jackiw-Teitelboim (JT) gravity did not exhibit properties of complexity, such as the late time growth, in the CA proposal. The JT model is the proposed grav-

itational holographic dual to a low-energy limit of the Sachdev-Ye-Kitaev (SYK) model [212–222], where the system acquires a reparametrization invariance. Since the SYK model exhibits maximal chaotic behaviour, we expect that both growth of complexity and the switchback effects to be present. The JT model can be derived from a dimensional reduction of higher dimensional magnetically charged near-extremal black holes. In fact, the JT model captures the near-horizon regimes of such near-extremal black holes, and as a consequence, the usual action for the JT model matches the predictions of the purely magnetic black hole solution in figure 7.2. Interestingly, the dimensional reduction of a surface term such as the one in eq. (7.8) would be related to the spacetime volume of the two-dimensional WDW patch. This reminds us of a slightly modified holographic proposal known as the complexity=volume 2.0 (CV2.0), where the holographic complexity is associated with the spacetime volume of the Wheeler-DeWitt patch. In addition, starting from the CA proposal for the higher dimensional black hole with the surface term in eq. (7.8) results in a combination of CA and CV2.0 for the JT gravity.

The previous discussion raises the important question that some actions simply do not have the right properties in order to be a good candidate for a holographic dual of complexity. There are a few possibilities to consider in this scenario, such as whether different actions are describing different circuit complexity models. For instance, one possible interpretation would be that modifying the action by surface terms may change the circuit complexity ingredients, such as the inclusion/exclusion of certain gates. Therefore, we could interpret that the gates relevant to construct the time evolution of the TFD state would be absent for certain circuit models, which could be an indication to why certain actions do not exhibit late time growth. In addition, different gravitational actions are associated to different thermodynamic ensembles. Another important question is to understand whether different thermodynamic ensembles play a role in studying the properties of complexity.

7.3 Future directions

In general, understanding the precise map of how holographic complexity proposals capture the richness of the circuit complexity models of QFTs is a very important task, and hopefully the works discussed in this thesis provide initial steps towards that direction. We hope that in the future we will have a clearer picture of the role of quantum circuit complexity for more complicated quantum field theories.

One striking fact about the properties of circuit complexity discussed throughout this thesis is that they yield relatively low values. Despite the complexity being large due to

the small distance correlations of field theories, once we employ a regularization scheme, we find quantities that are finite and simply of the order of the degrees of freedom of the system. For the holographic theories, the time evolution of the thermofield double only reaches exponential complexity at infinite time, such that the validity of the saddle point approximation of the gravitational action and the bulk geometry is called into question. For the field theory considerations, are we restricted to deal with low complexities due to the gaussianity of the states considered? Is there a general lesson to be extracted from this remark?

There are hints that complexity should have properties that are analogous to thermodynamic ones. The clearest connection is that with high probability the complexity should increase, which hints at a second law of complexity [41]. When quantum corrections are taken into account, the expectation is that the CA and CV proposals would get modified as well. Is it possible that these quantum corrections would imply a generalized second law, in analogy to the generalized second law of thermodynamics [91]? In addition, it was suggested recently [62] that there is also an analog of the first law for complexity, which should have interesting consequences for comparing predictions between bulk and boundary perspectives. Could these approaches suggest an explicit construction of the holographic dual of circuit complexity in the bulk geometry?

Quantum circuit complexity was the essential ingredient investigated in this thesis. Can we construct a more explicit connection to quantum information theory, and therefore extend the results discussed to algorithmic complexity [40]? As a more speculative point, are there properties of QFT that are (under reasonable assumptions) non-computable [223, 224]?

From the gravitational side of the AdS/CFT correspondence, there is still much to be understood about the properties of codimension-one surfaces. Entanglement entropy and codimension-two surfaces have been extensively explored [15, 96], and questions about the emergence of spacetime have illuminated many aspects of the holographic duality. Is there a similar role to be played by holographic complexity (or more generally, codimension-one surfaces)? Classically the wormhole keeps stretching forever, but can we explicitly show examples of quantum corrections in the bulk at late times such that the volume saturates? This problem is intimately tied to late time dynamics of chaotic systems [225], which also plays an important role in the description of the black hole interior.

The structure of entanglement entropy provided interesting toy models of the AdS/CFT correspondence, such as identifying the bulk physics with tensor networks. Is it possible to make a precise statement connecting geometry and tensor networks [226]? Is there a faithful representation of tensor networks with large number of degrees of freedom and

strongly coupled CFTs? Similarly, from the bulk perspective, can tensor network models of AdS/CFT be sensitive to sub-AdS scales?³

There has been considerable progress in understanding properties of quantum gravity in AdS spacetimes due to the AdS/CFT correspondence. Ultimately the goal is to translate the lessons to quantum gravity in different geometries, such as de Sitter spacetimes [228]. Interestingly, the difficulties associated to a precise description of the black hole interior are analogous to the ones in using the techniques of AdS/CFT for de Sitter. For instance, both problems do not contain the AdS boundary in order to provide well-defined boundary conditions for the quantum fields. Is it possible that by rephrasing the properties of quantum gravity in quantum information notions one can investigate quantum gravity in more complicated scenarios?

³See the recent work [227] for progress in this direction.

References

- [1] L. Susskind, “The World as a hologram,” *J. Math. Phys.* **36** (1995) 6377–6396, [arXiv:hep-th/9409089](#) [hep-th].
- [2] R. Bousso, “The Holographic principle,” *Rev. Mod. Phys.* **74** (2002) 825–874, [arXiv:hep-th/0203101](#) [hep-th].
- [3] J. M. Maldacena, “The Large N limit of superconformal field theories and supergravity,” *Int. J. Theor. Phys.* **38** (1999) 1113–1133, [arXiv:hep-th/9711200](#) [hep-th]. [Adv. Theor. Math. Phys.2,231(1998)].
- [4] E. Witten, “Anti-de Sitter space and holography,” *Adv. Theor. Math. Phys.* **2** (1998) 253–291, [arXiv:hep-th/9802150](#) [hep-th].
- [5] S. S. Gubser, I. R. Klebanov, and A. M. Polyakov, “Gauge theory correlators from noncritical string theory,” *Phys. Lett.* **B428** (1998) 105–114, [arXiv:hep-th/9802109](#) [hep-th].
- [6] O. Aharony, S. S. Gubser, J. M. Maldacena, H. Ooguri, and Y. Oz, “Large N field theories, string theory and gravity,” *Phys. Rept.* **323** (2000) 183–386, [arXiv:hep-th/9905111](#) [hep-th].
- [7] J. McGreevy, “Holographic duality with a view toward many-body physics,” *Adv. High Energy Phys.* **2010** (2010) 723105, [arXiv:0909.0518](#) [hep-th].
- [8] D. Harlow, “Jerusalem Lectures on Black Holes and Quantum Information,” *Rev. Mod. Phys.* **88** (2016) 015002, [arXiv:1409.1231](#) [hep-th].
- [9] M. Van Raamsdonk, “Lectures on Gravity and Entanglement,” in *Proceedings, Theoretical Advanced Study Institute in Elementary Particle Physics: New Frontiers in Fields and Strings (TASI 2015): Boulder, CO, USA, June 1-26, 2015*, pp. 297–351. 2017. [arXiv:1609.00026](#) [hep-th].

- [10] D. Harlow, “TASI Lectures on the Emergence of Bulk Physics in AdS/CFT,” *PoS TASI2017* (2018) 002, [arXiv:1802.01040 \[hep-th\]](#).
- [11] M. Ammon and J. Erdmenger, *Gauge/Gravity Duality: Foundations and Applications*. Cambridge University Press, 2015.
- [12] S. Ryu and T. Takayanagi, “Holographic derivation of entanglement entropy from AdS/CFT,” *Phys. Rev. Lett.* **96** (2006) 181602, [arXiv:hep-th/0603001 \[hep-th\]](#).
- [13] S. Ryu and T. Takayanagi, “Aspects of Holographic Entanglement Entropy,” *JHEP* **08** (2006) 045, [arXiv:hep-th/0605073 \[hep-th\]](#).
- [14] V. E. Hubeny, M. Rangamani, and T. Takayanagi, “A Covariant holographic entanglement entropy proposal,” *JHEP* **07** (2007) 062, [arXiv:0705.0016 \[hep-th\]](#).
- [15] M. Rangamani and T. Takayanagi, “Holographic entanglement entropy,” *Lect. Notes Phys.* **931** (2017) pp.1–246, [arXiv:1609.01287 \[hep-th\]](#).
- [16] B. Swingle, “Entanglement Renormalization and Holography,” *Phys. Rev.* **D86** (2012) 065007, [arXiv:0905.1317 \[cond-mat.str-el\]](#).
- [17] M. Headrick, “Entanglement Renyi entropies in holographic theories,” *Phys. Rev.* **D82** (2010) 126010, [arXiv:1006.0047 \[hep-th\]](#).
- [18] M. Van Raamsdonk, “Building up spacetime with quantum entanglement,” *Gen. Rel. Grav.* **42** (2010) 2323–2329, [arXiv:1005.3035 \[hep-th\]](#). [Int. J. Mod. Phys.D19,2429(2010)].
- [19] R. C. Myers and A. Sinha, “Holographic c-theorems in arbitrary dimensions,” *JHEP* **01** (2011) 125, [arXiv:1011.5819 \[hep-th\]](#).
- [20] A. Almheiri, D. Marolf, J. Polchinski, and J. Sully, “Black Holes: Complementarity or Firewalls?,” *JHEP* **02** (2013) 062, [arXiv:1207.3123 \[hep-th\]](#).
- [21] H. Casini, M. Huerta, and R. C. Myers, “Towards a derivation of holographic entanglement entropy,” *JHEP* **05** (2011) 036, [arXiv:1102.0440 \[hep-th\]](#).
- [22] J. Maldacena and L. Susskind, “Cool horizons for entangled black holes,” *Fortsch. Phys.* **61** (2013) 781–811, [arXiv:1306.0533 \[hep-th\]](#).

- [23] D. D. Blanco, H. Casini, L.-Y. Hung, and R. C. Myers, “Relative Entropy and Holography,” *JHEP* **08** (2013) 060, [arXiv:1305.3182 \[hep-th\]](#).
- [24] X. Dong, “Holographic Entanglement Entropy for General Higher Derivative Gravity,” *JHEP* **01** (2014) 044, [arXiv:1310.5713 \[hep-th\]](#).
- [25] J. Camps, “Generalized entropy and higher derivative Gravity,” *JHEP* **03** (2014) 070, [arXiv:1310.6659 \[hep-th\]](#).
- [26] T. Faulkner, M. Guica, T. Hartman, R. C. Myers, and M. Van Raamsdonk, “Gravitation from Entanglement in Holographic CFTs,” *JHEP* **03** (2014) 051, [arXiv:1312.7856 \[hep-th\]](#).
- [27] A. Lewkowycz and J. Maldacena, “Generalized gravitational entropy,” *JHEP* **08** (2013) 090, [arXiv:1304.4926 \[hep-th\]](#).
- [28] A. Almheiri, X. Dong, and D. Harlow, “Bulk Locality and Quantum Error Correction in AdS/CFT,” *JHEP* **04** (2015) 163, [arXiv:1411.7041 \[hep-th\]](#).
- [29] F. Pastawski, B. Yoshida, D. Harlow, and J. Preskill, “Holographic quantum error-correcting codes: Toy models for the bulk/boundary correspondence,” *JHEP* **06** (2015) 149, [arXiv:1503.06237 \[hep-th\]](#).
- [30] J. M. Maldacena, “Eternal black holes in anti-de Sitter,” *JHEP* **04** (2003) 021, [arXiv:hep-th/0106112 \[hep-th\]](#).
- [31] L. Susskind, “Computational Complexity and Black Hole Horizons,” *Fortsch. Phys.* **64** (2016) 44–48, [arXiv:1403.5695 \[hep-th\]](#). [*Fortsch. Phys.*64,24(2016)].
- [32] D. Stanford and L. Susskind, “Complexity and Shock Wave Geometries,” *Phys. Rev.* **D90** no. 12, (2014) 126007, [arXiv:1406.2678 \[hep-th\]](#).
- [33] A. R. Brown, D. A. Roberts, L. Susskind, B. Swingle, and Y. Zhao, “Holographic Complexity Equals Bulk Action?,” *Phys. Rev. Lett.* **116** no. 19, (2016) 191301, [arXiv:1509.07876 \[hep-th\]](#).
- [34] A. R. Brown, D. A. Roberts, L. Susskind, B. Swingle, and Y. Zhao, “Complexity, action, and black holes,” *Phys. Rev.* **D93** no. 8, (2016) 086006, [arXiv:1512.04993 \[hep-th\]](#).
- [35] J. Preskill, “Lecture notes on quantum information and computation,” <http://www.theory.caltech.edu/people/preskill/ph229/>.

- [36] S. Aaronson, “The Complexity of Quantum States and Transformations: From Quantum Money to Black Holes,” 2016. [arXiv:1607.05256 \[quant-ph\]](#).
- [37] J. Watrous, “Quantum computational complexity,” in *Encyclopedia of complexity and systems science*, pp. 7174–7201. Springer, 2009.
- [38] R. Jefferson and R. C. Myers, “Circuit complexity in quantum field theory,” *JHEP* **10** (2017) 107, [arXiv:1707.08570 \[hep-th\]](#).
- [39] S. Chapman, M. P. Heller, H. Marrochio, and F. Pastawski, “Towards Complexity for Quantum Field Theory States,” [arXiv:1707.08582 \[hep-th\]](#).
- [40] S. P. Jordan, K. S. M. Lee, and J. Preskill, “Quantum algorithms for quantum field theories,” *Science* **336** no. 6085, (2012) 1130–1133, <http://science.sciencemag.org/content/336/6085/1130.full.pdf>, <http://science.sciencemag.org/content/336/6085/1130>.
- [41] A. R. Brown and L. Susskind, “The Second Law of Quantum Complexity,” [arXiv:1701.01107 \[hep-th\]](#).
- [42] P. Caputa, N. Kundu, M. Miyaji, T. Takayanagi, and K. Watanabe, “Anti-de Sitter Space from Optimization of Path Integrals in Conformal Field Theories,” *Phys. Rev. Lett.* **119** no. 7, (2017) 071602, [arXiv:1703.00456 \[hep-th\]](#).
- [43] P. Caputa, N. Kundu, M. Miyaji, T. Takayanagi, and K. Watanabe, “Liouville Action as Path-Integral Complexity: From Continuous Tensor Networks to AdS/CFT,” *JHEP* **11** (2017) 097, [arXiv:1706.07056 \[hep-th\]](#).
- [44] P. Caputa and J. M. Magan, “Quantum computation as gravity,” [arXiv:1807.04422 \[hep-th\]](#).
- [45] A. Bhattacharyya, P. Caputa, S. R. Das, N. Kundu, M. Miyaji, and T. Takayanagi, “Path-Integral complexity for perturbed CFTs,” *JHEP* **07** (2018) 086, [arXiv:1804.01999 \[hep-th\]](#).
- [46] R. Khan, C. Krishnan, and S. Sharma, “Circuit Complexity in Fermionic Field Theory,” [arXiv:1801.07620 \[hep-th\]](#).
- [47] L. Hackl and R. C. Myers, “Circuit complexity for free fermions,” *JHEP* **07** (2018) 139, [arXiv:1803.10638 \[hep-th\]](#).

- [48] M. Guo, J. Hernandez, R. C. Myers, and S.-M. Ruan, “Circuit complexity for coherent states,” *JHEP* **10** (2018) 011, [arXiv:1807.07677 \[hep-th\]](#).
- [49] S. Chapman, J. Eisert, L. Hackl, M. P. Heller, R. Jefferson, H. Marrochio, and R. C. Myers, “Complexity and entanglement for thermofield double states,” *SciPost Phys.* **6** (2019) 034, [arXiv:1810.05151 \[hep-th\]](#).
- [50] A. Bhattacharyya, A. Shekar, and A. Sinha, “Circuit complexity in interacting QFTs and RG flows,” *JHEP* **10** (2018) 140, [arXiv:1808.03105 \[hep-th\]](#).
- [51] A. Belin, A. Lewkowycz, and G. Sárosi, “The boundary dual of the bulk symplectic form,” *Phys. Lett.* **B789** (2019) 71–75, [arXiv:1806.10144 \[hep-th\]](#).
- [52] A. Belin, A. Lewkowycz, and G. Sárosi, “Complexity and the bulk volume, a new York time story,” *JHEP* **03** (2019) 044, [arXiv:1811.03097 \[hep-th\]](#).
- [53] D. A. Roberts and B. Yoshida, “Chaos and complexity by design,” *JHEP* **04** (2017) 121, [arXiv:1610.04903 \[quant-ph\]](#).
- [54] D. W. F. Alves and G. Camilo, “Evolution of complexity following a quantum quench in free field theory,” *JHEP* **06** (2018) 029, [arXiv:1804.00107 \[hep-th\]](#).
- [55] H. A. Camargo, P. Caputa, D. Das, M. P. Heller, and R. Jefferson, “Complexity as a novel probe of quantum quenches: universal scalings and purifications,” *Phys. Rev. Lett.* **122** no. 8, (2019) 081601, [arXiv:1807.07075 \[hep-th\]](#).
- [56] T. Ali, A. Bhattacharyya, S. S. Haque, E. H. Kim, and N. Moynihan, “Time evolution of complexity: A critique of three methods,” [arXiv:1810.02734 \[hep-th\]](#).
- [57] T. Ali, A. Bhattacharyya, S. Shajidul Haque, E. H. Kim, and N. Moynihan, “Post-Quench Evolution of Distance and Uncertainty in a Topological System: Complexity, Entanglement and Revivals,” [arXiv:1811.05985 \[hep-th\]](#).
- [58] V. Balasubramanian, M. DeCross, A. Kar, and O. Parrikar, “Binding Complexity and Multiparty Entanglement,” *JHEP* **02** (2019) 069, [arXiv:1811.04085 \[hep-th\]](#).
- [59] K. Hashimoto, N. Iizuka, and S. Sugishita, “Time evolution of complexity in Abelian gauge theories,” *Phys. Rev. D* **96** (2017) 126001, [arXiv:1707.03840 \[hep-th\]](#).

- [60] B. Czech, “Einstein equations from varying complexity,” *Phys. Rev. Lett.* **120** (2018) 031601, [arXiv:1706.00965 \[hep-th\]](#).
- [61] F. Liu, R. Lundgren, P. Titum, J. R. Garrison, and A. V. Gorshkov, “Circuit Complexity across a Topological Phase Transition,” [arXiv:1902.10720 \[quant-ph\]](#).
- [62] A. Bernamonti, F. Galli, J. Hernandez, R. C. Myers, S.-M. Ruan, and J. Simón, “The First Law of Complexity,” [arXiv:1903.04511 \[hep-th\]](#).
- [63] L. Lehner, R. C. Myers, E. Poisson, and R. D. Sorkin, “Gravitational action with null boundaries,” *Phys. Rev.* **D94** no. 8, (2016) 084046, [arXiv:1609.00207 \[hep-th\]](#).
- [64] S. Chapman, H. Marrochio, and R. C. Myers, “Complexity of formation in holography,” *JHEP* **01** (2017) 062, [arXiv:1610.08063 \[hep-th\]](#).
- [65] D. Carmi, R. C. Myers, and P. Rath, “Comments on Holographic Complexity,” *JHEP* **03** (2017) 118, [arXiv:1612.00433 \[hep-th\]](#).
- [66] D. Carmi, S. Chapman, H. Marrochio, R. C. Myers, and S. Sugishita, “On the Time Dependence of Holographic Complexity,” *JHEP* **11** (2017) 188, [arXiv:1709.10184 \[hep-th\]](#).
- [67] S. Chapman, H. Marrochio, and R. C. Myers, “Holographic complexity in Vaidya spacetimes. Part I,” *JHEP* **06** (2018) 046, [arXiv:1804.07410 \[hep-th\]](#).
- [68] S. Chapman, H. Marrochio, and R. C. Myers, “Holographic complexity in Vaidya spacetimes. Part II,” *JHEP* **06** (2018) 114, [arXiv:1805.07262 \[hep-th\]](#).
- [69] P. A. Cano, R. A. Hennigar, and H. Marrochio, “Complexity growth rate in lovelock gravity,” *Phys. Rev. Lett.* **121** (2018) 121602, [arXiv:1803.02795 \[hep-th\]](#).
- [70] K. Goto, H. Marrochio, R. C. Myers, L. Queimada, and B. Yoshida, “Holographic Complexity Equals Which Action?,” *JHEP* **02** (2019) 160, [arXiv:1901.00014 \[hep-th\]](#).
- [71] R.-G. Cai, S.-M. Ruan, S.-J. Wang, R.-Q. Yang, and R.-H. Peng, “Action growth for AdS black holes,” *JHEP* **09** (2016) 161, [arXiv:1606.08307 \[gr-qc\]](#).
- [72] A. Reynolds and S. F. Ross, “Divergences in holographic complexity,” *Class. Quant. Grav.* **34** (2017) 105004, [arXiv:1612.05439 \[hep-th\]](#).

- [73] A. Reynolds and S. F. Ross, “Complexity in de Sitter space,” *Class. Quant. Grav.* **34** (2017) 175013, [arXiv:1706.03788 \[hep-th\]](#).
- [74] A. P. Reynolds and S. F. Ross, “Complexity of the AdS soliton,” *Class. Quant. Grav.* **35** (2018) 095006, [arXiv:1712.03732 \[hep-th\]](#).
- [75] M. Sinamuli and R. B. Mann, “Topological and time dependence of the action-complexity relation,” *Phys. Rev.* **D98** no. 2, (2018) 026005, [arXiv:1804.07333 \[hep-th\]](#).
- [76] J. L. F. Barbon and J. Martin-Garcia, “Holographic Complexity Of Cold Hyperbolic Black Holes,” *JHEP* **11** (2015) 181, [arXiv:1510.00349 \[hep-th\]](#).
- [77] B. Swingle and Y. Wang, “Holographic complexity of Einstein-Maxwell-Dilaton gravity,” *JHEP* **09** (2018) 106, [arXiv:1712.09826 \[hep-th\]](#).
- [78] C. A. Agón, M. Headrick, and B. Swingle, “Subsystem Complexity and Holography,” *JHEP* **02** (2019) 145, [arXiv:1804.01561 \[hep-th\]](#).
- [79] J. Couch, S. Eccles, T. Jacobson, and P. Nguyen, “Holographic Complexity and Volume,” *JHEP* **11** (2018) 044, [arXiv:1807.02186 \[hep-th\]](#).
- [80] R. Abt, J. Erdmenger, H. Hinrichsen, C. M. Melby-Thompson, R. Meyer, C. Northe, and I. A. Reyes, “Topological complexity in AdS₃/CFT₂,” *Fortsch. Phys.* **66** (2018) 1800034, [arXiv:1710.01327 \[hep-th\]](#).
- [81] R. Abt, J. Erdmenger, M. Gerbershagen, C. M. Melby-Thompson, and C. Northe, “Holographic Subregion Complexity from Kinematic Space,” *JHEP* **01** (2019) 012, [arXiv:1805.10298 \[hep-th\]](#).
- [82] W. Cottrell and M. Montero, “Complexity is simple!,” *JHEP* **02** (2018) 039, [arXiv:1710.01175 \[hep-th\]](#).
- [83] M. Flory and N. Miekley, “Complexity change under conformal transformations in AdS₃/CFT₂,” [arXiv:1806.08376 \[hep-th\]](#).
- [84] M. Flory, “A complexity/fidelity susceptibility g -theorem for AdS₃/BCFT₂,” *JHEP* **06** (2017) 131, [arXiv:1702.06386 \[hep-th\]](#).
- [85] L. Susskind, “Three Lectures on Complexity and Black Holes,” 2018. [arXiv:1810.11563 \[hep-th\]](#).

- [86] A. R. Brown, L. Susskind, and Y. Zhao, “Quantum complexity and negative curvature,” *Phys. Rev. D* **95** (2017) 045010, [arXiv:1608.02612 \[hep-th\]](#).
- [87] L. Susskind and Y. Zhao, “Switchbacks and the Bridge to Nowhere,” [arXiv:1408.2823 \[hep-th\]](#).
- [88] Y. Zhao, “Complexity and Boost Symmetry,” *Phys. Rev.* **D98** no. 8, (2018) 086011, [arXiv:1702.03957 \[hep-th\]](#).
- [89] A. R. Brown, H. Gharibyan, H. W. Lin, L. Susskind, L. Thorlacius, and Y. Zhao, “Complexity of Jackiw-Teitelboim gravity,” *Phys. Rev.* **D99** no. 4, (2019) 046016, [arXiv:1810.08741 \[hep-th\]](#).
- [90] T. Hartman, “Lecture notes: Quantum Gravity and Black Holes,” <http://www.hartmanhep.net/topics2015/gravity-lectures.pdf>.
- [91] J. D. Bekenstein, “Generalized second law of thermodynamics in black hole physics,” *Phys. Rev.* **D9** (1974) 3292–3300.
- [92] J. D. Bekenstein, “Black holes and entropy,” *Phys. Rev.* **D7** (1973) 2333–2346.
- [93] J. M. Bardeen, B. Carter, and S. W. Hawking, “The Four laws of black hole mechanics,” *Commun. Math. Phys.* **31** (1973) 161–170.
- [94] I. R. Klebanov and A. M. Polyakov, “AdS dual of the critical O(N) vector model,” *Phys. Lett.* **B550** (2002) 213–219, [arXiv:hep-th/0210114 \[hep-th\]](#).
- [95] G. ’t Hooft, “A Planar Diagram Theory for Strong Interactions,” *Nucl. Phys.* **B72** (1974) 461. [,337(1973)].
- [96] T. Nishioka, “Entanglement entropy: holography and renormalization group,” *Rev. Mod. Phys.* **90** no. 3, (2018) 035007, [arXiv:1801.10352 \[hep-th\]](#).
- [97] J. Eisert, M. Cramer, and M. B. Plenio, “Area laws for the entanglement entropy - a review,” *Rev. Mod. Phys.* **82** (2010) 277–306, [arXiv:0808.3773 \[quant-ph\]](#).
- [98] T. J. Osborne and M. A. Nielsen, “Entanglement in a simple quantum phase transition,” *Physical Review A* **66** (Sep, 2002) 032110, [arXiv:quant-ph/0202162 \[quant-ph\]](#).
- [99] I. R. Klebanov, D. Kutasov, and A. Murugan, “Entanglement as a probe of confinement,” *Nucl. Phys.* **B796** (2008) 274–293, [arXiv:0709.2140 \[hep-th\]](#).

- [100] P. Calabrese and J. L. Cardy, “Evolution of entanglement entropy in one-dimensional systems,” *J. Stat. Mech.* **0504** (2005) P04010, [arXiv:cond-mat/0503393](#) [cond-mat].
- [101] P. Calabrese and J. Cardy, “Entanglement entropy and conformal field theory,” *J. Phys.* **A42** (2009) 504005, [arXiv:0905.4013](#) [cond-mat.stat-mech].
- [102] H. Casini and M. Huerta, “A c-theorem for the entanglement entropy,” *J. Phys.* **A40** (2007) 7031–7036, [arXiv:cond-mat/0610375](#) [cond-mat].
- [103] H. Casini, M. Huerta, R. C. Myers, and A. Yale, “Mutual information and the F-theorem,” *JHEP* **10** (2015) 003, [arXiv:1506.06195](#) [hep-th].
- [104] H. Casini, E. Testé, and G. Torroba, “Markov Property of the Conformal Field Theory Vacuum and the a Theorem,” *Phys. Rev. Lett.* **118** no. 26, (2017) 261602, [arXiv:1704.01870](#) [hep-th].
- [105] Y. Takahashi and H. Umezawa, “Thermo field dynamics,” *Int. J. Mod. Phys.* **B10** (1996) 1755–1805.
- [106] W. Israel, “Thermo field dynamics of black holes,” *Phys. Lett.* **A57** (1976) 107–110.
- [107] J. B. Hartle and S. W. Hawking, “Path Integral Derivation of Black Hole Radiance,” *Phys. Rev.* **D13** (1976) 2188–2203.
- [108] M. A. Nielsen, M. R. Dowling, M. Gu, and A. M. Doherty, “Quantum computation as geometry,” *Science* **311** (2006) 1133–1135, [arXiv:quant-ph/0603161](#) [quant-ph].
- [109] M. A. Nielsen and M. R. Dowling, “The geometry of quantum computation,” [arXiv:quant-ph/0701004](#) [quant-ph].
- [110] D. N. Page, “Average entropy of a subsystem,” *Phys. Rev. Lett.* **71** (1993) 1291–1294, [arXiv:gr-qc/9305007](#) [gr-qc].
- [111] Y. Sekino and L. Susskind, “Fast Scramblers,” *JHEP* **10** (2008) 065, [arXiv:0808.2096](#) [hep-th].
- [112] N. Lashkari, D. Stanford, M. Hastings, T. Osborne, and P. Hayden, “Towards the Fast Scrambling Conjecture,” *JHEP* **04** (2013) 022, [arXiv:1111.6580](#) [hep-th].

- [113] P. Bocchieri and A. Loinger, “Quantum recurrence theorem,” *Phys. Rev.* **107** (Jul, 1957) 337–338. <https://link.aps.org/doi/10.1103/PhysRev.107.337>.
- [114] T. Hartman and J. Maldacena, “Time Evolution of Entanglement Entropy from Black Hole Interiors,” *JHEP* **05** (2013) 014, [arXiv:1303.1080](https://arxiv.org/abs/1303.1080) [[hep-th](#)].
- [115] L. Susskind, “Entanglement is not enough,” *Fortsch. Phys.* **64** (2016) 49–71, [arXiv:1411.0690](https://arxiv.org/abs/1411.0690) [[hep-th](#)].
- [116] S. Lloyd, “Ultimate physical limits to computation,” *Nature* **406** (Aug., 2000) , [quant-ph/9908043](https://arxiv.org/abs/quant-ph/9908043).
- [117] S. P. Jordan, “Fast quantum computation at arbitrarily low energy,” *Phys. Rev.* **A95** no. 3, (2017) 032305, [arXiv:1701.01175](https://arxiv.org/abs/1701.01175) [[quant-ph](#)].
- [118] J. W. York, Jr., “Role of conformal three geometry in the dynamics of gravitation,” *Phys. Rev. Lett.* **28** (1972) 1082–1085.
- [119] G. W. Gibbons and S. W. Hawking, “Action Integrals and Partition Functions in Quantum Gravity,” *Phys. Rev.* **D15** (1977) 2752–2756.
- [120] K. Parattu, S. Chakraborty, B. R. Majhi, and T. Padmanabhan, “A Boundary Term for the Gravitational Action with Null Boundaries,” *Gen. Rel. Grav.* **48** no. 7, (2016) 94, [arXiv:1501.01053](https://arxiv.org/abs/1501.01053) [[gr-qc](#)].
- [121] F. Hopfmüller and L. Freidel, “Gravity Degrees of Freedom on a Null Surface,” *Phys. Rev.* **D95** no. 10, (2017) 104006, [arXiv:1611.03096](https://arxiv.org/abs/1611.03096) [[gr-qc](#)].
- [122] I. Jubb, J. Samuel, R. Sorkin, and S. Surya, “Boundary and Corner Terms in the Action for General Relativity,” *Class. Quant. Grav.* **34** no. 6, (2017) 065006, [arXiv:1612.00149](https://arxiv.org/abs/1612.00149) [[gr-qc](#)].
- [123] I. S. Booth, “Metric based Hamiltonians, null boundaries, and isolated horizons,” *Class. Quant. Grav.* **18** (2001) 4239–4264, [arXiv:gr-qc/0105009](https://arxiv.org/abs/gr-qc/0105009) [[gr-qc](#)].
- [124] M. Banados, C. Teitelboim, and J. Zanelli, “The Black hole in three-dimensional space-time,” *Phys. Rev. Lett.* **69** (1992) 1849–1851, [arXiv:hep-th/9204099](https://arxiv.org/abs/hep-th/9204099) [[hep-th](#)].
- [125] M. Banados, M. Henneaux, C. Teitelboim, and J. Zanelli, “Geometry of the (2+1) black hole,” *Phys. Rev.* **D48** (1993) 1506–1525, [arXiv:gr-qc/9302012](https://arxiv.org/abs/gr-qc/9302012) [[gr-qc](#)]. [Erratum: *Phys. Rev.*D88,069902(2013)].

- [126] R. C. Myers, “Stress tensors and Casimir energies in the AdS / CFT correspondence,” *Phys. Rev.* **D60** (1999) 046002, [arXiv:hep-th/9903203 \[hep-th\]](#).
- [127] R. Emparan, C. V. Johnson, and R. C. Myers, “Surface terms as counterterms in the AdS / CFT correspondence,” *Phys. Rev.* **D60** (1999) 104001, [arXiv:hep-th/9903238 \[hep-th\]](#).
- [128] H. Casini, M. Huerta, and R. C. Myers, “Towards a derivation of holographic entanglement entropy,” *JHEP* **05** (2011) 036, [arXiv:1102.0440 \[hep-th\]](#).
- [129] R. B. Mann, “Black holes of negative mass,” *Class. Quant. Grav.* **14** (1997) 2927–2930, [arXiv:gr-qc/9705007 \[gr-qc\]](#).
- [130] R. Emparan, “AdS / CFT duals of topological black holes and the entropy of zero energy states,” *JHEP* **06** (1999) 036, [arXiv:hep-th/9906040 \[hep-th\]](#).
- [131] S. W. Hawking and D. N. Page, “Thermodynamics of black holes in anti-de sitter space,” *Comm. Math. Phys.* **87** no. 4, (1982) 577–588. <https://projecteuclid.org/443/euclid.cmp/1103922135>.
- [132] E. Witten, “Anti-de Sitter space, thermal phase transition, and confinement in gauge theories,” *Adv. Theor. Math. Phys.* **2** (1998) 505–532, [arXiv:hep-th/9803131 \[hep-th\]](#).
- [133] Y. M. Cho and I. P. Neupane, “Anti-de Sitter black holes, thermal phase transition and holography in higher curvature gravity,” *Phys. Rev.* **D66** (2002) 024044, [arXiv:hep-th/0202140 \[hep-th\]](#).
- [134] G. Hayward, “Gravitational action for space-times with nonsmooth boundaries,” *Phys. Rev.* **D47** (1993) 3275–3280.
- [135] D. Brill and G. Hayward, “Is the gravitational action additive?” *Phys. Rev. D* **50** (Oct, 1994) 4914–4919. <https://link.aps.org/doi/10.1103/PhysRevD.50.4914>.
- [136] S. de Haro, S. N. Solodukhin, and K. Skenderis, “Holographic reconstruction of space-time and renormalization in the AdS / CFT correspondence,” *Commun. Math. Phys.* **217** (2001) 595–622, [arXiv:hep-th/0002230 \[hep-th\]](#).
- [137] K. Skenderis, “Lecture notes on holographic renormalization,” *Class. Quant. Grav.* **19** (2002) 5849–5876, [arXiv:hep-th/0209067 \[hep-th\]](#).

- [138] R. B. Mann, “Misner string entropy,” *Phys. Rev.* **D60** (1999) 104047, [arXiv:hep-th/9903229 \[hep-th\]](#).
- [139] R. B. Mann, “Entropy of rotating Misner string space-times,” *Phys. Rev.* **D61** (2000) 084013, [arXiv:hep-th/9904148 \[hep-th\]](#).
- [140] C. Fefferman and C. R. Graham, “Conformal invariants,” in *Élie Cartan et les mathématiques d’aujourd’hui - Lyon, 25-29 juin 1984*, no. S131 in Astérisque, pp. 95–116. Société mathématique de France, 1985. http://www.numdam.org/item/AST_1985__S131__95_0.
- [141] C. Fefferman and C. R. Graham, “The ambient metric,” *arXiv e-prints* (Oct, 2007) arXiv:0710.0919, [arXiv:0710.0919 \[math.DG\]](#).
- [142] A. Buchel, J. Escobedo, R. C. Myers, M. F. Paulos, A. Sinha, and M. Smolkin, “Holographic GB gravity in arbitrary dimensions,” *JHEP* **03** (2010) 111, [arXiv:0911.4257 \[hep-th\]](#).
- [143] J. D. Brown and M. Henneaux, “Central charges in the canonical realization of asymptotic symmetries: an example from three-dimensional gravity,” *Comm. Math. Phys.* **104** no. 2, (1986) 207–226. <https://projecteuclid.org:443/euclid.cmp/1104114999>.
- [144] O. Coussaert and M. Henneaux, “Supersymmetry of the (2+1) black holes,” *Phys. Rev. Lett.* **72** (1994) 183–186, [arXiv:hep-th/9310194 \[hep-th\]](#).
- [145] J. Couch, W. Fischler, and P. H. Nguyen, “Noether charge, black hole volume, and complexity,” *JHEP* **03** (2017) 119, [arXiv:1610.02038 \[hep-th\]](#).
- [146] R.-Q. Yang, “Strong energy condition and complexity growth bound in holography,” *Phys. Rev.* **D95** no. 8, (2017) 086017, [arXiv:1610.05090 \[gr-qc\]](#).
- [147] G. Vidal, “Entanglement Renormalization,” *Phys. Rev. Lett.* **99** no. 22, (2007) 220405, [arXiv:cond-mat/0512165 \[cond-mat\]](#).
- [148] G. Vidal, “Class of quantum many-body states that can be efficiently simulated,” *Phys. Rev. Lett.* **101** (Sep, 2008) 110501. <https://link.aps.org/doi/10.1103/PhysRevLett.101.110501>.
- [149] G. Vidal, “Entanglement Renormalization: an introduction,” *arXiv e-prints* (Dec, 2009) arXiv:0912.1651, [arXiv:0912.1651 \[cond-mat.str-el\]](#).

- [150] G. Evenbly and G. Vidal, “Tensor Network Renormalization Yields the Multiscale Entanglement Renormalization Ansatz,” *Physical Review Letters* **115** (Nov, 2015) 200401, [arXiv:1502.05385 \[cond-mat.str-el\]](#).
- [151] B. Czech, L. Lamprou, S. McCandlish, and J. Sully, “Integral Geometry and Holography,” *JHEP* **10** (2015) 175, [arXiv:1505.05515 \[hep-th\]](#).
- [152] B. Czech, G. Evenbly, L. Lamprou, S. McCandlish, X.-L. Qi, J. Sully, and G. Vidal, “Tensor network quotient takes the vacuum to the thermal state,” *Phys. Rev.* **B94** no. 8, (2016) 085101, [arXiv:1510.07637 \[cond-mat.str-el\]](#).
- [153] B. Czech, L. Lamprou, S. McCandlish, and J. Sully, “Tensor Networks from Kinematic Space,” *JHEP* **07** (2016) 100, [arXiv:1512.01548 \[hep-th\]](#).
- [154] M. Miyaji, T. Numasawa, N. Shiba, T. Takayanagi, and K. Watanabe, “Distance between Quantum States and Gauge-Gravity Duality,” *Phys. Rev. Lett.* **115** no. 26, (2015) 261602, [arXiv:1507.07555 \[hep-th\]](#).
- [155] R.-G. Cai, M. Sasaki, and S.-J. Wang, “Action growth of charged black holes with a single horizon,” *Phys. Rev.* **D95** no. 12, (2017) 124002, [arXiv:1702.06766 \[gr-qc\]](#).
- [156] A. Chamblin, R. Emparan, C. V. Johnson, and R. C. Myers, “Charged AdS black holes and catastrophic holography,” *Phys. Rev.* **D60** (1999) 064018, [arXiv:hep-th/9902170 \[hep-th\]](#).
- [157] S. A. Hartnoll, “Lectures on holographic methods for condensed matter physics,” *Class. Quant. Grav.* **26** (2009) 224002, [arXiv:0903.3246 \[hep-th\]](#).
- [158] J. Erdmenger and H. Osborn, “Conserved currents and the energy momentum tensor in conformally invariant theories for general dimensions,” *Nucl. Phys.* **B483** (1997) 431–474, [arXiv:hep-th/9605009 \[hep-th\]](#).
- [159] H. Osborn and A. C. Petkou, “Implications of conformal invariance in field theories for general dimensions,” *Annals Phys.* **231** (1994) 311–362, [arXiv:hep-th/9307010 \[hep-th\]](#).
- [160] D. Z. Freedman, S. D. Mathur, A. Matusis, and L. Rastelli, “Correlation functions in the CFT(d) / AdS(d+1) correspondence,” *Nucl. Phys.* **B546** (1999) 96–118, [arXiv:hep-th/9804058 \[hep-th\]](#).

- [161] E. Barnes, E. Gorbatov, K. A. Intriligator, and J. Wright, “Current correlators and AdS/CFT geometry,” *Nucl. Phys.* **B732** (2006) 89–117, [arXiv:hep-th/0507146 \[hep-th\]](#).
- [162] R.-G. Cai, S.-M. Ruan, S.-J. Wang, R.-Q. Yang, and R.-H. Peng, “Action growth for AdS black holes,” *JHEP* **09** (2016) 161, [arXiv:1606.08307 \[gr-qc\]](#).
- [163] J. Couch, S. Eccles, W. Fischler, and M.-L. Xiao, “Holographic complexity and noncommutative gauge theory,” *JHEP* **03** (2018) 108, [arXiv:1710.07833 \[hep-th\]](#).
- [164] H. Liu and S. J. Suh, “Entanglement Tsunami: Universal Scaling in Holographic Thermalization,” *Phys. Rev. Lett.* **112** (2014) 011601, [arXiv:1305.7244 \[hep-th\]](#).
- [165] H. Liu and S. J. Suh, “Entanglement growth during thermalization in holographic systems,” *Phys. Rev.* **D89** no. 6, (2014) 066012, [arXiv:1311.1200 \[hep-th\]](#).
- [166] M. Mezei, “On entanglement spreading from holography,” *JHEP* **05** (2017) 064, [arXiv:1612.00082 \[hep-th\]](#).
- [167] J. S. Cotler, M. P. Hertzberg, M. Mezei, and M. T. Mueller, “Entanglement Growth after a Global Quench in Free Scalar Field Theory,” *JHEP* **11** (2016) 166, [arXiv:1609.00872 \[hep-th\]](#).
- [168] S. W. Hawking, C. J. Hunter, and M. Taylor, “Rotation and the AdS / CFT correspondence,” *Phys. Rev.* **D59** (1999) 064005, [arXiv:hep-th/9811056 \[hep-th\]](#).
- [169] G. W. Gibbons, H. Lu, D. N. Page, and C. N. Pope, “Rotating black holes in higher dimensions with a cosmological constant,” *Phys. Rev. Lett.* **93** (2004) 171102, [arXiv:hep-th/0409155 \[hep-th\]](#).
- [170] P. Chunilal Vaidya, “The external field of a radiating star in general relativity,” *Current Science* **12** (Mar., 1943) .
- [171] P. C. Vaidya, “The gravitational field of a radiating star,” *Proceedings of the Indian Academy of Sciences - Section A* **33** no. 5, (May, 1951) 264. <https://doi.org/10.1007/BF03173260>.
- [172] A. Wang and Y. Wu, “Generalized Vaidya solutions,” *Gen. Rel. Grav.* **31** (1999) 107, [arXiv:gr-qc/9803038 \[gr-qc\]](#).

- [173] M. Moosa, “Evolution of complexity following a global quench,” *JHEP* **03** (2018) 031, [arXiv:1711.02668 \[hep-th\]](#).
- [174] D. A. Roberts, D. Stanford, and L. Susskind, “Localized shocks,” *JHEP* **03** (2015) 051, [arXiv:1409.8180 \[hep-th\]](#).
- [175] S. Bhattacharyya and S. Minwalla, “Weak Field Black Hole Formation in Asymptotically AdS Spacetimes,” *JHEP* **09** (2009) 034, [arXiv:0904.0464 \[hep-th\]](#).
- [176] S. R. Das, T. Nishioka, and T. Takayanagi, “Probe Branes, Time-dependent Couplings and Thermalization in AdS/CFT,” *JHEP* **07** (2010) 071, [arXiv:1005.3348 \[hep-th\]](#).
- [177] J. Abajo-Arrastia, J. Aparicio, and E. Lopez, “Holographic Evolution of Entanglement Entropy,” *JHEP* **11** (2010) 149, [arXiv:1006.4090 \[hep-th\]](#).
- [178] V. Balasubramanian, A. Bernamonti, J. de Boer, N. Copland, B. Craps, E. Keski-Vakkuri, B. Muller, A. Schafer, M. Shigemori, and W. Staessens, “Thermalization of Strongly Coupled Field Theories,” *Phys. Rev. Lett.* **106** (2011) 191601, [arXiv:1012.4753 \[hep-th\]](#).
- [179] V. Balasubramanian, A. Bernamonti, J. de Boer, N. Copland, B. Craps, E. Keski-Vakkuri, B. Muller, A. Schafer, M. Shigemori, and W. Staessens, “Holographic Thermalization,” *Phys. Rev.* **D84** (2011) 026010, [arXiv:1103.2683 \[hep-th\]](#).
- [180] D. Garfinkle and L. A. Pando Zayas, “Rapid Thermalization in Field Theory from Gravitational Collapse,” *Phys. Rev.* **D84** (2011) 066006, [arXiv:1106.2339 \[hep-th\]](#).
- [181] V. E. Hubeny and H. Maxfield, “Holographic probes of collapsing black holes,” *JHEP* **03** (2014) 097, [arXiv:1312.6887 \[hep-th\]](#).
- [182] V. E. Hubeny, M. Rangamani, and E. Tonni, “Thermalization of Causal Holographic Information,” *JHEP* **05** (2013) 136, [arXiv:1302.0853 \[hep-th\]](#).
- [183] S. H. Shenker and D. Stanford, “Black holes and the butterfly effect,” *JHEP* **03** (2014) 067, [arXiv:1306.0622 \[hep-th\]](#).
- [184] S. H. Shenker and D. Stanford, “Multiple Shocks,” *JHEP* **12** (2014) 046, [arXiv:1312.3296 \[hep-th\]](#).

- [185] J. D. Brown, “Action functionals for relativistic perfect fluids,” *Class. Quant. Grav.* **10** (1993) 1579–1606, [arXiv:gr-qc/9304026 \[gr-qc\]](#).
- [186] S. A. Hartnoll and A. Tavanfar, “Electron stars for holographic metallic criticality,” *Phys. Rev.* **D83** (2011) 046003, [arXiv:1008.2828 \[hep-th\]](#).
- [187] B. F. Schutz, “Perfect fluids in general relativity: Velocity potentials and a variational principle,” *Phys. Rev. D* **2** (Dec, 1970) 2762–2773. <https://link.aps.org/doi/10.1103/PhysRevD.2.2762>.
- [188] S. Dubovsky, T. Gregoire, A. Nicolis, and R. Rattazzi, “Null energy condition and superluminal propagation,” *JHEP* **03** (2006) 025, [arXiv:hep-th/0512260 \[hep-th\]](#).
- [189] J. Bicak and K. V. Kuchar, “Null dust in canonical gravity,” *Phys. Rev. D* **56** (Oct, 1997) 4878–4895. <https://link.aps.org/doi/10.1103/PhysRevD.56.4878>.
- [190] A. Reynolds and S. F. Ross, “Divergences in Holographic Complexity,” *Class. Quant. Grav.* **34** no. 10, (2017) 105004, [arXiv:1612.05439 \[hep-th\]](#).
- [191] S. R. Das, D. A. Galante, and R. C. Myers, “Universal scaling in fast quantum quenches in conformal field theories,” *Phys. Rev. Lett.* **112** (2014) 171601, [arXiv:1401.0560 \[hep-th\]](#).
- [192] S. R. Das, D. A. Galante, and R. C. Myers, “Universality in fast quantum quenches,” *JHEP* **02** (2015) 167, [arXiv:1411.7710 \[hep-th\]](#).
- [193] S. R. Das, D. A. Galante, and R. C. Myers, “Quantum Quenches in Free Field Theory: Universal Scaling at Any Rate,” *JHEP* **05** (2016) 164, [arXiv:1602.08547 \[hep-th\]](#).
- [194] R.-Q. Yang, C. Niu, C.-Y. Zhang, and K.-Y. Kim, “Comparison of holographic and field theoretic complexities for time dependent thermofield double states,” *JHEP* **02** (2018) 082, [arXiv:1710.00600 \[hep-th\]](#).
- [195] M. Alishahiha, A. Faraji Astaneh, M. R. Mohammadi Mozaffar, and A. Mollabashi, “Complexity Growth with Lifshitz Scaling and Holographic Violation,” [arXiv:1802.06740 \[hep-th\]](#).
- [196] D. S. Ageev, I. Ya. Aref’eva, A. A. Bagrov, and M. I. Katsnelson, “Holographic local quench and effective complexity,” *JHEP* **08** (2018) 071, [arXiv:1803.11162 \[hep-th\]](#).

- [197] T. Anous, T. Hartman, A. Rovai, and J. Sonner, “Black Hole Collapse in the $1/c$ Expansion,” *JHEP* **07** (2016) 123, [arXiv:1603.04856 \[hep-th\]](#).
- [198] L. Fidkowski, V. Hubeny, M. Kleban, and S. Shenker, “The Black hole singularity in AdS / CFT,” *JHEP* **02** (2004) 014, [arXiv:hep-th/0306170 \[hep-th\]](#).
- [199] Z.-Y. Fan and M. Guo, “On the Noether charge and the gravity duals of quantum complexity,” *JHEP* **08** (2018) 031, [arXiv:1805.03796 \[hep-th\]](#).
- [200] D. Kubiznak, R. B. Mann, and M. Teo, “Black hole chemistry: thermodynamics with Lambda,” *Class. Quant. Grav.* **34** no. 6, (2017) 063001, [arXiv:1608.06147 \[hep-th\]](#).
- [201] H. Huang, X.-H. Feng, and H. Lu, “Holographic Complexity and Two Identities of Action Growth,” *Phys. Lett.* **B769** (2017) 357–361, [arXiv:1611.02321 \[hep-th\]](#).
- [202] J. Maldacena, S. H. Shenker, and D. Stanford, “A bound on chaos,” *JHEP* **08** (2016) 106, [arXiv:1503.01409 \[hep-th\]](#).
- [203] L. Susskind, “The Typical-State Paradox: Diagnosing Horizons with Complexity,” *Fortsch. Phys.* **64** (2016) 84–91, [arXiv:1507.02287 \[hep-th\]](#).
- [204] M. Van Raamsdonk, “Evaporating Firewalls,” *JHEP* **11** (2014) 038, [arXiv:1307.1796 \[hep-th\]](#).
- [205] R.-Q. Yang, “A Complexity for Quantum Field Theory States and Application in Thermofield Double States,” *Phys. Rev.* **D97** no. 6, (2018) 066004, [arXiv:1709.00921 \[hep-th\]](#).
- [206] J. Maldacena, D. Stanford, and Z. Yang, “Diving into traversable wormholes,” *Fortsch. Phys.* **65** no. 5, (2017) 1700034, [arXiv:1704.05333 \[hep-th\]](#).
- [207] Z. Fu, A. Maloney, D. Marolf, H. Maxfield, and Z. Wang, “Holographic complexity is nonlocal,” *JHEP* **02** (2018) 072, [arXiv:1801.01137 \[hep-th\]](#).
- [208] M. Miyaji, T. Numasawa, N. Shiba, T. Takayanagi, and K. Watanabe, “Distance between Quantum States and Gauge-Gravity Duality,” *Phys. Rev. Lett.* **115** no. 26, (2015) 261602, [arXiv:1507.07555 \[hep-th\]](#).
- [209] J. Cotler, M. R. Mohammadi Mozaffar, A. Mollabashi, and A. Naseh, “Renormalization group circuits for weakly interacting continuum field theories,” [arXiv:1806.02831 \[hep-th\]](#).

- [210] J. Cotler, M. R. Mohammadi Mozaffar, A. Mollabashi, and A. Naseh, “Entanglement renormalization for weakly interacting fields,” [arXiv:1806.02835 \[hep-th\]](#).
- [211] T. Jacobson and R. C. Myers, “Black hole entropy and higher curvature interactions,” *Phys. Rev. Lett.* **70** (1993) 3684–3687, [arXiv:hep-th/9305016 \[hep-th\]](#).
- [212] A. Almheiri and J. Polchinski, “Models of AdS₂ backreaction and holography,” *JHEP* **11** (2015) 014, [arXiv:1402.6334 \[hep-th\]](#).
- [213] S. Sachdev and J. Ye, “Gapless spin-fluid ground state in a random quantum Heisenberg magnet,” *Physical Review Letters* **70** (May, 1993) 3339–3342, [arXiv:cond-mat/9212030 \[cond-mat\]](#).
- [214] A. Kitaev, “Hidden correlations in the hawking radiation and thermal noise,” <http://online.kitp.ucsb.edu/online/joint98/kitaev/>.
- [215] A. Kitaev, “A simple model of quantum holography,” online.kitp.ucsb.edu/online/entangled15/kitaev/ and online.kitp.ucsb.edu/online/entangled15/kitaev2/.
- [216] J. Polchinski and V. Rosenhaus, “The Spectrum in the Sachdev-Ye-Kitaev Model,” *JHEP* **04** (2016) 001, [arXiv:1601.06768 \[hep-th\]](#).
- [217] J. Maldacena and D. Stanford, “Remarks on the Sachdev-Ye-Kitaev model,” *Phys. Rev.* **D94** no. 10, (2016) 106002, [arXiv:1604.07818 \[hep-th\]](#).
- [218] J. Maldacena, D. Stanford, and Z. Yang, “Conformal symmetry and its breaking in two dimensional Nearly Anti-de-Sitter space,” *PTEP* **2016** no. 12, (2016) 12C104, [arXiv:1606.01857 \[hep-th\]](#).
- [219] J. Engelsoy, T. G. Mertens, and H. Verlinde, “An investigation of AdS₂ backreaction and holography,” *JHEP* **07** (2016) 139, [arXiv:1606.03438 \[hep-th\]](#).
- [220] K. Jensen, “Chaos in AdS₂ Holography,” *Phys. Rev. Lett.* **117** no. 11, (2016) 111601, [arXiv:1605.06098 \[hep-th\]](#).
- [221] G. Sárosi, “AdS₂ holography and the SYK model,” *PoS Modave2017* (2018) 001, [arXiv:1711.08482 \[hep-th\]](#).

- [222] A. Kitaev and S. J. Suh, “The soft mode in the Sachdev-Ye-Kitaev model and its gravity dual,” *JHEP* **05** (2018) 183, [arXiv:1711.08467 \[hep-th\]](#).
- [223] T. Cubitt, D. Perez-Garcia, and M. M. Wolf, “Undecidability of the Spectral Gap (short version),” *Nature* **528** (2015) 207–211, [arXiv:1502.04135 \[quant-ph\]](#).
- [224] T. Cubitt, D. Perez-Garcia, and M. M. Wolf, “Undecidability of the Spectral Gap (full version),” [arXiv:1502.04573 \[quant-ph\]](#).
- [225] J. S. Cotler, G. Gur-Ari, M. Hanada, J. Polchinski, P. Saad, S. H. Shenker, D. Stanford, A. Streicher, and M. Tezuka, “Black Holes and Random Matrices,” *JHEP* **05** (2017) 118, [arXiv:1611.04650 \[hep-th\]](#). [Erratum: JHEP09,002(2018)].
- [226] A. Milsted and G. Vidal, “Geometric interpretation of the multi-scale entanglement renormalization ansatz,” [arXiv:1812.00529 \[hep-th\]](#).
- [227] N. Bao, G. Penington, J. Sorce, and A. C. Wall, “Holographic Tensor Networks in Full AdS/CFT,” [arXiv:1902.10157 \[hep-th\]](#).
- [228] D. Anninos, “De Sitter Musings,” *Int. J. Mod. Phys. A* **27** (2012) 1230013, [arXiv:1205.3855 \[hep-th\]](#).
- [229] R. Emparan, C. V. Johnson, and R. C. Myers, “Surface terms as counterterms in the AdS / CFT correspondence,” *Phys. Rev. D* **60** (1999) 104001, [arXiv:hep-th/9903238 \[hep-th\]](#).
- [230] A. Buchel, J. Escobedo, R. C. Myers, M. F. Paulos, A. Sinha, and M. Smolkin, “Holographic GB gravity in arbitrary dimensions,” *JHEP* **03** (2010) 111, [arXiv:0911.4257 \[hep-th\]](#).
- [231] P. A. Cano, “Lovelock action with nonsmooth boundaries,” *Phys. Rev. D* **97** no. 10, (2018) 104048, [arXiv:1803.00172 \[gr-qc\]](#).

APPENDICES

Appendix A

Appendices to chapter 3

A.1 Fefferman-Graham near Boundary Expansions

The action on the WDW patch is divergent since this region of the bulk spacetime extends all the way up to spatial infinity. In this appendix, we discuss how to regulate these divergences by introducing a UV cutoff surface at $r = r_{\max}$, following the standard approach in holographic calculations, see, *e.g.*, [127, 136, 137]. To make meaningful comparison between the two different spacetimes (*i.e.*, black hole and vacuum AdS) we need to be able to relate the cutoffs in the two geometries. We do this by choosing r_{\max} to correspond to the surface of $z = \delta$ in the asymptotic Fefferman Graham (FG) expansion for both cases.

A.1.1 Relating the Cutoffs

We begin by writing the metric (2.1) in the FG form:

$$ds^2 = \frac{dr^2}{f(r)} - f(r)dt^2 + r^2 d\Sigma_{k,d-1} = \frac{L^2}{z^2} (dz^2 + g_{ij}(z, x^i) dx^i dx^j) \quad (\text{A.1})$$

where

$$z = \frac{L^2}{r} + \frac{c_1}{r^2} + \dots + \frac{c_d}{r^{d+1}} + \frac{c_{d+1}}{r^{d+2}} + \dots \quad (\text{A.2})$$

goes to zero at the boundary and $g_{ij}(z \rightarrow 0, x^i)$ is the *finite* boundary metric (2.5). We fix the different coefficients c_i to obtain:

$$\frac{L}{z} dz = \frac{dr}{\sqrt{f(r)}}, \quad (\text{A.3})$$

where, as is implicit in eq. (A.2), we work in a series expansion for large r . We can invert the series (A.2) to obtain r_{\max} corresponding to the surface of constant $z = \delta$:

$$r_{\max} = \frac{L^2}{\delta} + \tilde{c}_1 + \dots + \tilde{c}_d \delta^{d-1} + \tilde{c}_{d+1} \delta^d + \dots \quad (\text{A.4})$$

The first coefficient to depend on r_h (and so, the first coefficient which differs from the FG expansion of vacuum AdS) is c_d (or equivalently \tilde{c}_d). This follows immediately from the form of the blackening factor in which the dependence on r_h starts at the d -th subleading order in the boundary expansion. In general, we can prove that

$$r_{\max}^{\text{BH}} - r_{\max}^{\text{vac}} = \frac{\omega^{d-2}}{2dL^{2(d-2)}} \delta^{d-1} + \mathcal{O}(\delta^{d+1}), \quad (\text{A.5})$$

as given in eq. (2.13). The proof goes as follows: Integrating eq. (A.3), we obtain

$$-L \log \frac{\delta}{L^2} = \int^{r_{\max}} \frac{dr}{\sqrt{f(r)}}. \quad (\text{A.6})$$

The integration constant was fixed here by assuming that to leading order $z = \frac{L^2}{r}$. Further we understand the left-hand side of eq. (A.6) to be defined by a large- r power series, *i.e.*,

$$\int^{r_{\max}} \frac{dr}{\sqrt{f(r)}} = \int^{r_{\max}} dr \left(\frac{L}{r} + \sum_{n=2}^{\infty} \frac{a_n}{r^n} \right) = L \log(r_{\max}) - \sum_{n=2}^{\infty} \frac{a_n}{(n-1)r_{\max}^{n-1}}. \quad (\text{A.7})$$

Now putting the UV cutoff surface at the $z = \delta$ surface in both the black hole and vacuum AdS backgrounds, we can subtract the corresponding equations to obtain

$$0 = \int^{r_{\max}^{\text{BH}}} \frac{dr}{\sqrt{f(r)}} - \int^{r_{\max}^{\text{vac}}} \frac{dr}{\sqrt{f_0(r)}}, \quad (\text{A.8})$$

where the upper limits are slightly different in the two integrals. If we substitute $r_{\max}^{\text{BH}} = r_{\max}^{\text{vac}} + \delta r_{\max}$ into the first integral, the leading order contribution in the shift δr_{\max} becomes

$$0 \simeq \frac{1}{\sqrt{f(r_{\max}^{\text{vac}})}} (r_{\max}^{\text{BH}} - r_{\max}^{\text{vac}}) + \int^{r_{\max}^{\text{vac}}} dr \left(\frac{1}{\sqrt{f(r)}} - \frac{1}{\sqrt{f_0(r)}} \right). \quad (\text{A.9})$$

This integral is convergent and we can expand this expression for large r ,

$$0 \simeq \frac{L}{r_{\max}^{\text{vac}}} (r_{\max}^{\text{BH}} - r_{\max}^{\text{vac}}) + \int^{r_{\max}^{\text{vac}}} dr \frac{\omega^{d-2} L^3}{2r^{d+1}}. \quad (\text{A.10})$$

Integrating the last expression and using the leading order result $r_{\max} = L^2/\delta$ (which applies for both geometries), we recover eq. (A.5).

Finally, we compute r_{\max} in the various vacuum AdS geometries by evaluating eq. (A.6) to obtain

$$z = \frac{2L^2}{r + \sqrt{kL^2 + r^2}} \quad (\text{A.11})$$

and

$$r_{\max}^{\text{vac}} = \frac{L^2}{\delta} - \frac{k\delta}{4}. \quad (\text{A.12})$$

As a consequence, eq. (A.5) yields

$$r_{\max}^{\text{BH}} = \frac{L^2}{\delta} - \frac{k\delta}{4} + \frac{\omega^{d-2}}{2dL^{2(d-2)}} \delta^{d-1} + \mathcal{O}(\delta^{d+1}). \quad (\text{A.13})$$

Finally for the BTZ case, eq. (A.6) can be evaluated explicitly using the blackening factor (2.38) which leads to:

$$r + \sqrt{r^2 - r_h^2} = \frac{2L^2}{z}, \quad r = \frac{L^2}{z} + \frac{zr_h^2}{4L^2}, \quad (\text{A.14})$$

and

$$r_{\max}^{\text{BTZ}} = \frac{L^2}{\delta} + \frac{\delta r_h^2}{4L^2}. \quad (\text{A.15})$$

A.1.2 Cutoff Independence of the Action

In this subsection we provide details for the various cancellations encountered in the main text when subtracting the vacuum AdS results from those of the black holes in the process of evaluating the action. It will be useful in our discussion to use the following relation

$$v_\infty - r^*(r_{\max}) = \delta + \dots + w(r_h)\delta^{d+1} + \mathcal{O}(\delta^{d+2}). \quad (\text{A.16})$$

where due to the form of the blackening factor (2.2) the r_h dependence first appears at order δ^{d+1} . Note that v_∞ cancels a possible integration constant and the expansion therefore starts at order δ . It is further possible to show¹

$$v_\infty - r^*(r_{\max}^{\text{BH}}) - (v'_\infty - r_0^*(r_{\max}^{\text{vac}})) = w(r_h) - w(0) = \frac{(d-1)}{2d(d+1)} \frac{\omega^{d-2}}{L^{2(d-1)}} \delta^{d+1} + \mathcal{O}(\delta^{d+2}). \quad (\text{A.17})$$

¹The notation v'_∞ and $r_0^*(r)$ refers to the vacuum AdS geometry — see appendix A.2.

The arguments are similar to those in the previous section and the leading contribution reads

$$\begin{aligned}
v_\infty - r^*(r_{\max}^{\text{BH}}) - (v'_\infty - r_0^*(r_{\max}^{\text{vac}})) &= \int_{r_{\max}^{\text{BH}}}^\infty \frac{dr}{f(r)} - \int_{r_{\max}^{\text{vac}}}^\infty \frac{dr}{f_0(r)} \\
&= \int_{r_{\max}^{\text{vac}}}^\infty \frac{f_0(r) - f(r)}{f_0(r)f(r)} - \frac{1}{f(r_{\max}^{\text{vac}})} (r_{\max}^{\text{BH}} - r_{\max}^{\text{vac}}) \\
&= \frac{(d-1)}{2d(d+1)} \frac{\omega^{d-2}}{L^{2(d-1)}} \delta^{d+1} + \mathcal{O}(\delta^{d+2}),
\end{aligned} \tag{A.18}$$

where we have used eq. (2.13).

With all this in hand, we are ready to prove some of the claims quoted in the main text regarding cancellations between vacuum and black hole contributions to the action of the WDW patch. The first claim is related to the bulk integrals. It explains why eq. (2.23) reduces to eq. (3.3) after subtracting the vacuum AdS contribution and why we can choose r_{\max} in eq. (3.3) to be either of the two cutoffs. We start with the difference of the bulk actions

$$\begin{aligned}
\Delta I_{\text{bulk}} &= -\frac{\Omega_{k,d-1} d}{2\pi G_N L^2} \int_0^{r_{\max}^{\text{BH}}} dr r^{d-1} (v_\infty - r^*(r)) \\
&\quad + \frac{\Omega_{k,d-1} d}{2\pi G_N L^2} \int_0^{r_{\max}^{\text{vac}}} dr r^{d-1} (v'_\infty - r_0^*(r)).
\end{aligned} \tag{A.19}$$

In particular, if we denote $r_{\max}^{\text{BH}} = r_{\max}^{\text{vac}} + X \delta^{d-1}$ where X was given in eq. (A.5) we recover eq. (3.3), with r_{\max} being the vacuum AdS cutoff, plus an addition

$$\delta I_{\text{bulk,BH}} = -\frac{\Omega_{k,d-1} d}{2\pi G_N L^2} X \delta^{d-1} \left[r^{d-1} (v_\infty - r^*(r)) \right]_{r=r_{\max}}. \tag{A.20}$$

Now to leading order, $r^{d-1} = r_{\max}^{d-1} = L^{2(d-1)}/\delta^{d-1}$ which is canceled by the factor δ^{d-1} in the pre-factor. But then $v'_\infty - r_0^*(L^2/\delta) \simeq \delta$ and so we find $\delta I_{\text{bulk,vac}} \propto \delta$.

The second claim we want to prove is that the surface contributions at the cutoff surfaces cancel between the black hole and vacuum AdS backgrounds. We find it convenient to define a function

$$g(r) = \partial_r f(r) + \frac{2(d-1)}{r} f(r), \tag{A.21}$$

and a function $g_0(r)$ defined by replacing $f(r)$ by the vacuum blackening factor $f_0(r)$ in the expression above. Using eq. (2.28) and subtracting the vacuum AdS result we obtain

$$\delta I_{\text{GHY}}(r = r_{\max}) = \delta_1 + \delta_2 + \delta_3 + \dots \tag{A.22}$$

where the ellipsis stands for higher orders in δ and we have defined the following expressions

$$\begin{aligned}\delta_1 &\equiv \frac{\Omega_{k,d-1} \delta r_{\max}^{d-1}}{4\pi G_N} g_0(r_{\max}^{\text{vac}}) \left(v'_\infty - r_0^*(r_{\max}^{\text{vac}}) \right), \\ \delta_2 &\equiv \frac{\Omega_{k,d-1} (r_{\max}^{\text{vac}})^{d-1}}{4\pi G_N} \delta g(r_{\max}) \left(v'_\infty - r_0^*(r_{\max}^{\text{vac}}) \right), \\ \delta_3 &\equiv \frac{\Omega_{k,d-1} (r_{\max}^{\text{vac}})^{d-1}}{4\pi G_N} g_0(r_{\max}^{\text{vac}}) [v_\infty - r^*(r_{\max}^{\text{BH}}) - (v'_\infty - r_0^*(r_{\max}^{\text{vac}}))],\end{aligned}\tag{A.23}$$

as well as

$$\delta r_{\max}^{d-1} \equiv (r_{\max}^{\text{BH}})^{d-1} - (r_{\max}^{\text{vac}})^{d-1} \simeq (d-1)(r_{\max}^{\text{vac}})^{d-2} (r_{\max}^{\text{BH}} - r_{\max}^{\text{vac}}) \simeq \frac{d-1}{2d} \omega^{d-2} \delta,\tag{A.24}$$

and

$$\begin{aligned}\delta g(r_{\max}) &\equiv g(r_{\max}^{\text{BH}}) - g_0(r_{\max}^{\text{vac}}) = g(r_{\max}^{\text{BH}}) - g(r_{\max}^{\text{vac}}) + g(r_{\max}^{\text{vac}}) - g_0(r_{\max}^{\text{vac}}) \\ &\simeq g'(r_{\max}^{\text{vac}}) (r_{\max}^{\text{BH}} - r_{\max}^{\text{vac}}) - d \frac{\omega^{d-2}}{(r_{\max}^{\text{vac}})^{d-1}} \simeq -(d-1) \frac{\omega^{d-2}}{L^{2(d-1)}} \delta^{d-1},\end{aligned}\tag{A.25}$$

and simplified the expressions using eq. (2.13). We can now show that all the contributions in eq. (A.23) are of order δ . For δ_1 we use eq. (A.24) together with

$$g_0(r_{\max}^{\text{vac}}) \simeq \frac{2dr_{\max}^{\text{vac}}}{L^2} \simeq \frac{2d}{\delta}\tag{A.26}$$

and eq. (A.16). For δ_2 we use again eq. (A.16) together with eq. (A.25) and $(r_{\max}^{\text{vac}})^{d-1} = L^{2(d-1)}/\delta^{d-1}$. For δ_3 we use in addition eq. (A.17). Therefore, we conclude that $\delta I_{\text{GHY}}(r = r_{\max}) \propto \delta$.

The last claim which we want to show is that the joint terms at the cutoff surfaces cancel between the black hole background and vacuum AdS. We use eq. (2.37) which we reiterate here for convenience:

$$I_{\text{jnt,cut}} = \frac{\Omega_{k,d-1}}{4\pi G_N} r_{\max}^{d-1} \log f(r_{\max}).\tag{2.37}$$

Dependence on r_h comes either from the cutoff, as in eq. (A.13), or from the explicit ω^{d-2} that appears in $f(r)$. Expanding the above expression for small δ we see that the dependence on the horizon radius is at most of order $\delta \log \delta$. Therefore, the joint terms near the boundary cancel between the black hole background and vacuum AdS when we take the $\delta \rightarrow 0$ limit.

A.2 Details for Vacuum AdS Actions

As explained in chapter 2, there are subtle differences for the vacuum geometries corresponding to $k = \{+1, 0, -1\}$. In particular, various caustics appear in the boundary of the WDW patch and there are also ‘mild’ orbifold singularities in the planar and hyperbolic geometries. The WDW patches for the vacuum AdS geometries are shown in figure 2.2. In the following, we carefully consider these new singularities in calculating the WDW action but our conclusion is that they do not affect the final result. That is, the only nonvanishing contributions for the vacuum actions are those already calculated in chapter 2, *i.e.*, the bulk action (2.23), as well as the GHY surface terms (2.28) and null joint terms (2.37) associated with the UV cutoff surface $r = r_{\max}$.

a) Spherical geometry: As noted before in chapter 2, the WDW patch terminates with a caustic at the past and future tips of the causal diamond shown in figure 2.2a for $k = +1$. These points are located at $(t, r) = (\pm v_\infty, 0)$. To determine the latter, we must first evaluate the tortoise coordinate (2.14) using $f_0(r)$, which yields

$$r_0^*(r) = L \tan^{-1}(r/L) , \quad (\text{A.27})$$

and eq. (2.18) then gives

$$v'_\infty = L \pi/2 . \quad (\text{A.28})$$

As mentioned in the previous section, boundary terms for such caustics were not considered in the recent discussion of [63] but we will argue that in fact, they do not contribute to the gravitational action as follows: Focusing on the future tip, we introduce a regulator surface at $t = v'_\infty - \epsilon_1$, which cuts off the future tip and produces a flat cap on the WDW patch — see figure A.1. The gravitational action can then be evaluated for this regulated geometry using the standard boundary terms, and the contribution of the caustic is recovered with the limit $\epsilon_1 \rightarrow 0$.

In evaluating the gravitational action with the new regulator surface, we must consider potential extra contributions of the GHY term (2.24) integrated over this cap and of the joint term (2.34) where this additional boundary intersects the null boundary $v = v'_\infty$. Hence, we introduce the (outward-pointing) unit normal to the regulator surface

$$\mathbf{t}' = t'_\mu dx^\mu = \sqrt{f_0(r)} dt . \quad (\text{A.29})$$

Now one can easily verify that on this surface, the trace of the extrinsic curvature vanishes and so the GHY term (2.24) makes no contribution. Next we can combine eq. (A.29)

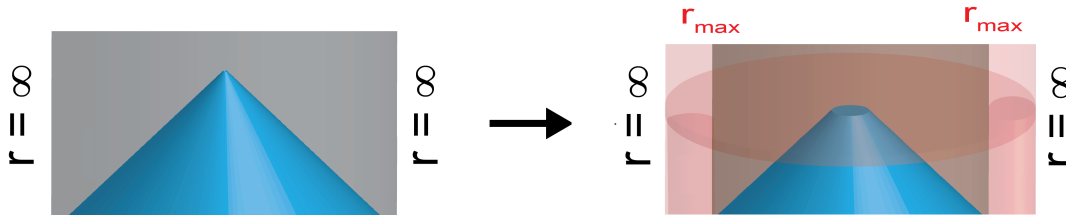


Figure A.1: The future caustic of the Wheeler-DeWitt patch in the vacuum global AdS geometry (left figure). The tip contribution can be effectively calculated by a regulator surface $t = v'_\infty - \epsilon_1$ (represented in the right figure) with well defined $\epsilon_1 \rightarrow 0$ limit.

with eq. (2.32) — after replacing $f(r)$ by $f_0(r)$ — to evaluate the corresponding joint term (2.34),

$$I_{\text{jnt,cap}} = \frac{\Omega_{1,d-1}}{16\pi G_N} \epsilon_1^{d-1} \log\left(1 + \frac{\epsilon_1^2}{L^2}\right). \quad (\text{A.30})$$

From this expression, we can easily see that the joint contribution vanishes in the limit $\epsilon_1 \rightarrow 0$. Hence our conclusion is that the caustic at the future tip of the WDW patch does not contribute to the gravitational action and, of course, the same is true for the past tip by symmetry. In the presence of the regulator surface, the bulk contribution is also modified but of course, this change vanishes in the limit $\epsilon_1 \rightarrow 0$.

b) Planar geometry: As described in chapter 2 with $k = 0$, a ‘conical’ or orbifold singularity appears in the vacuum geometry along the Poincaré horizon, due to the compactification of the spatial geometry. To carefully evaluate the corresponding gravitational action, we introduce a timelike regulator surface at $r = \epsilon_0$, as shown in figure 2.2b.²

We evaluate the contributions due to this regulator to the gravitational action and demonstrate that they vanish in the $\epsilon_0 \rightarrow 0$ limit. For the vacuum planar AdS space, we have $f_0(r) = r^2/L^2$ and the corresponding tortoise coordinate (2.14) is simply

$$r_0^*(r) = -L^2/r. \quad (\text{A.31})$$

In turn, using eq. (2.18), the future null boundary of the WDW patch is given by $v = v'_\infty = 0$.

²An alternative approach is to introduce spacelike regulator surfaces at $t = v'_\infty - r_0^*(\epsilon_1)$ and $t = v'_\infty + r_0^*(\epsilon_1)$. We have confirmed that one arrives at the same conclusion with this approach. That is, there are no additional contributions to the gravitational action coming from the orbifold singularity at $r = 0$.

In evaluating the gravitational action, the new surface term on the regulator surface takes the form in eq. (2.27), with the appropriate substitutions of $f_0(r)$, v'_∞ and $r_0^*(r)$, which yields

$$I_{\text{GHY}} = -\frac{d\Omega_{0,d-1}}{2\pi G_N} \epsilon_0^{d-1}. \quad (\text{A.32})$$

Similarly, the joint contribution where the null boundary intersects the regulator surface takes the form in the first line of eq. (2.36), with $f(r)$ replaced by $f_0(r)$, which yields

$$I_{\text{jnt,sing}} = -\frac{\Omega_{0,d-1}}{4\pi G_N} \epsilon_0^{d-1} \log(\epsilon_0^2/L^2). \quad (\text{A.33})$$

Of course, both of these expressions vanish in the limit $\epsilon_0 \rightarrow 0$. Further, the change in the bulk action produced by cutting off the radial integral at $r = \epsilon_0$ is proportional to ϵ_0^{d-1} , which again vanishes in the limit $\epsilon_0 \rightarrow 0$.

c) Hyperbolic geometry: Recall that the $k = -1$ vacuum actually describes an entangled state of two copies of the CFT on a hyperbolic geometry. With $f_0(r) = r^2/L^2 - 1$, there is a horizon at $r_h = L$ and even though locally the geometry corresponds to that of vacuum AdS space, the Penrose diagram looks essentially the same as for the black hole metric — see figure A.2. In particular, because we have compactified the hyperbolic geometry, there is an orbifold singularity at $r = 0$. The tortoise coordinate (2.14) becomes

$$r_0^*(r) = \frac{L}{2} \log \frac{|r - L|}{r + L}, \quad (\text{A.34})$$

and from eqs. (2.17) and (2.18), we see that the boundaries of the WDW patch are given by $v'_\infty = 0 = u'_\infty$. One can readily confirm that the null surfaces future boundaries on the left and right sides of the Penrose diagram meet at precisely $r = 0$.³ This joint is a particularly singular feature in the boundary of the WDW patch and so as before, we regulate the boundary geometry by cutting it off on the spacelike surface $r = \epsilon_0$, as shown in figure A.2. The gravitational action then receives extra contributions from the GHY term (2.24) integrated along this regulator surface and from the joint term (2.34) where this new boundary intersects the null boundary $v = v'_\infty = 0$. However, following calculations identical to those given previously, we find that both of these contributions vanish in the limit $\epsilon_1 \rightarrow 0$. Essentially the size of the relevant integration region shrinks to zero as ϵ_1^{d-1} and there is no compensating singularity in the other geometric factors — consider eqs. (2.27) and (2.36), with the appropriate substitutions of $f_0(r)$, v'_∞ and $r_0^*(r)$. As in

³As usual the tortoise coordinate (A.34) diverges at the horizon (*i.e.*, $r_0^*(r \rightarrow L) \rightarrow -\infty$), but then returns zero at $r = 0$. Hence the null-ray $v = 0$ hits the singularity $r = 0$ at precisely $t = 0$.

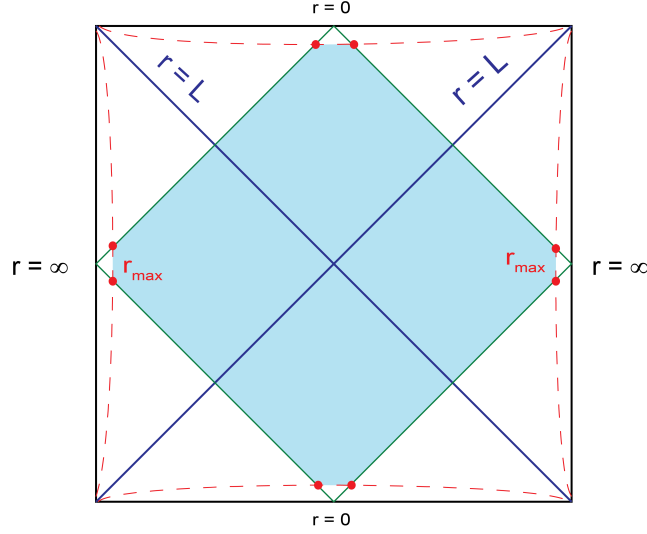


Figure A.2: Penrose diagram for the vacuum hyperbolic AdS space.

the previous cases, introducing the regulator surface changes the lower limit in the radial integration in the bulk contribution to produce a small modification, $\delta I_{\text{bulk}} \propto \epsilon_1^{d+1}$, which vanishes in the limit $\epsilon_1 \rightarrow 0$.

In addition, it is possible to write general expressions for the bulk contribution to the WDW action in general dimension. For d even we obtain:

$$2I_{\text{bulk}}^{\text{vac}} = -\frac{\Omega_{1,d-1} d}{2\pi G_N} \left(\frac{r_{\text{max}}^{d-1}}{(d-1)} + \sum_{n=1}^{\frac{d-2}{2}} (-k)^n \frac{L^{2n} r_{\text{max}}^{d-1-2n}}{(2n+1)(d-1-2n)} + \delta_{k,1} (-1)^{\frac{d}{2}} \frac{\pi L^{d-1}}{2d} \right), \quad (\text{A.35})$$

while for d odd:

$$2I_{\text{bulk}}^{\text{vac}} = -\frac{\Omega_{1,d-1} d}{2\pi G_N} \left(\frac{r_{\text{max}}^{d-1}}{(d-1)} + \sum_{n=1}^{\frac{d-3}{2}} (-k)^n \frac{L^{2n} r_{\text{max}}^{d-1-2n}}{(2n+1)(d-1-2n)} + (-k)^{\frac{d-1}{2}} \frac{L^{d-1}}{d^2} \left(1 + d \log \frac{r_{\text{max}}}{L} \right) \right). \quad (\text{A.36})$$

Note, that for odd dimensions, there is a logarithmic divergence while for even dimensions, there is an additional constant term for the spherical geometry. This is the origin of the $\delta_{k,1}$ term in the bulk action appearing in eq. (3.12).

A.3 Small Hyperbolic Black Holes

The ‘small’ hyperbolic black holes (*i.e.*, $k = -1$ and $r_h < L$) have a causal structure similar to that encountered for charged AdS black holes [156]. In this case, the blackening factor $f(r)$ in eq. (2.2) admits two positive real roots. This means that the black hole has two horizons, an inner one which we will denote by $r = r_-$ and an outer one with $r = r_h = r_+$. The relevant Penrose diagram is shown in figure A.3. One feature which can be noticed right away is that the null surfaces bounding the WDW patch do not fall into the singularity. Instead, they meet at some point between the two horizons which we will denote by $r = r_{\text{meet}}$ (of course $r_- < r_{\text{meet}} < r_+$). For this reason, instead of the surface term that we have encountered in the previous cases discussed in chapter 3 we will have two new joint contributions. The joint contributions can be computed according to the rules of [63].⁴ The total contribution from the two joints at $r = r_{\text{meet}}$ becomes

$$I_{\text{jnt}} = -\frac{\Omega_{-1,d-1}}{4\pi G_N} r_{\text{meet}}^{d-1} \log |f(r_{\text{meet}})|. \quad (\text{A.37})$$

The point in which the null rays meet $r = r_{\text{meet}}$ can be calculated from the following equation for the tortoise coordinate (2.14):

$$r^*(r_{\text{meet}}) = \frac{v_\infty - u_\infty}{2} = v_\infty. \quad (\text{A.38})$$

We will have to solve for r_{meet} numerically since this equation is usually transcendental. In addition, the bulk contribution for the small hyperbolic black holes is modified, since the volume integral only goes as low as r_{meet} now:

$$\Delta I_{\text{bulk}} = -\frac{\Omega_{-1,d-1} d}{2\pi G_N L^2} \left[\int_{r_{\text{meet}}}^{r_{\text{max}}} dr r^{d-1} [v_\infty - r^*(r)] - \int_0^{r_{\text{max}}} dr r^{d-1} [v'_\infty - r_0^*(r)] \right]. \quad (\text{A.39})$$

Combining these results, we obtain the complexity of formation for small hyperbolic black holes:

$$\Delta \mathcal{C} = \frac{1}{\pi} [\Delta I_{\text{bulk}} + I_{\text{jnt}}]. \quad (\text{3.4})$$

In the following, we study the cases of $d = 3$ and $d = 4$ in more detail. We also chose to include in this appendix the results for hyperbolic black holes in $d = 3$ with $L < r_h < \frac{2L}{\sqrt{3}}$ since these black holes have a blackening factor with three real roots, analogously to the case of small hyperbolic black holes, and so parts of the computation overlap. Note however that out of these three roots, only one is positive in this case, and so we have a single horizon and the same causal structure as the one for large hyperbolic black holes.

⁴In this case, we have a null-null joint for which the function a is given in eq. (A.59).

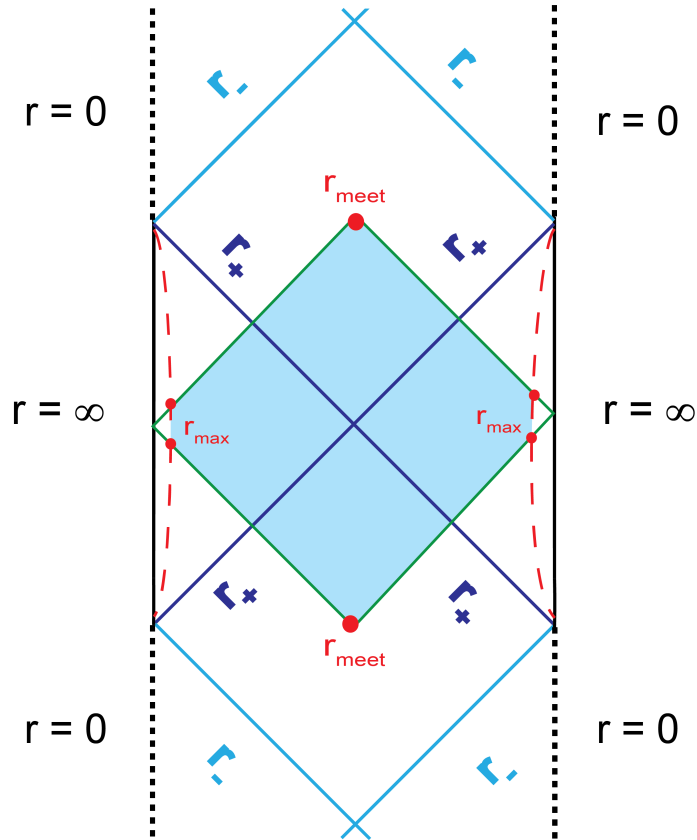


Figure A.3: Penrose diagram for small hyperbolic black holes with $r_h < L$. The outer horizon is drawn in dark blue and labeled r_+ and the inner horizon is drawn in lighter blue and labeled r_- . The two ingoing null rays meet in the region between the inner and outer horizon, and the joint term between them has a non vanishing contribution to the action.

A.3.1 $d = 4$

In $d = 4$, the blackening factor (2.2),

$$f(r) = \frac{r^2}{L^2} - 1 - \frac{r_h^2}{r^2} \left(\frac{r_h^2}{L^2} - 1 \right), \quad (\text{A.40})$$

has two positive real roots:

$$r_1 = r_h, \quad r_2 = \sqrt{L^2 - r_h^2}. \quad (\text{A.41})$$

For $r_h = L$ we should recover the results of hyperbolic vacuum AdS. The problem is completely symmetric under the redefinition $\tilde{r}_h = \sqrt{L^2 - r_h^2}$ and so no loss of generality is involved in assuming $r_h > r_2$. For the special case $r_h = L/\sqrt{2}$ the two horizons become degenerate which results in an extremal black hole. To obtain the tortoise coordinate one has to factorize the inverse blackening factor with respect to both roots. After integration we obtain:

$$r^*(r) = \frac{L^2}{2(r_h^2 - r_2^2)} \left(r_h \log \left[\frac{|r - r_h|}{r + r_h} \right] - r_2 \log \left[\frac{|r - r_2|}{r + r_2} \right] \right). \quad (\text{A.42})$$

The point where the ingoing null rays meet inside the black hole can be calculated numerically using eq. (A.42) and the meeting condition (A.38) which reads in this case

$$r^*(r_{\text{meet}}) = 0. \quad (\text{A.43})$$

Since the rays meet between the two horizons one has to choose the appropriate branches of the logs in eq. (A.42) when solving this equation. We show the result for r_{meet} in figure A.4.

For the bulk integral, we evaluate eq. (A.39) and obtain:

$$\begin{aligned} \Delta I_{\text{bulk}} = & \frac{\Omega_{-1,3}}{12\pi G_N (r_h^2 - r_2^2)} \left[3r_2 (r_{\text{meet}}^4 - r_2^4) \log \left[\frac{r_{\text{meet}} - r_2}{r_{\text{meet}} + r_2} \right] \right. \\ & \left. + 2r_{\text{meet}} (r_h^2 - r_2^2) (3L^2 + r_{\text{meet}}^2) + 3r_h (r_h^4 - r_{\text{meet}}^4) \log \left[\frac{r_h - r_{\text{meet}}}{r_h + r_{\text{meet}}} \right] \right], \end{aligned} \quad (\text{A.44})$$

and the joint contribution (A.37):

$$I_{\text{jnt}} = -\frac{\Omega_{-1,3}}{4\pi G_N} r_{\text{meet}}^3 \log |f(r_{\text{meet}})|. \quad (\text{A.45})$$

Substituting the numerical solution for r_{meet} , we obtain the result plotted in orange in figure 3.1.

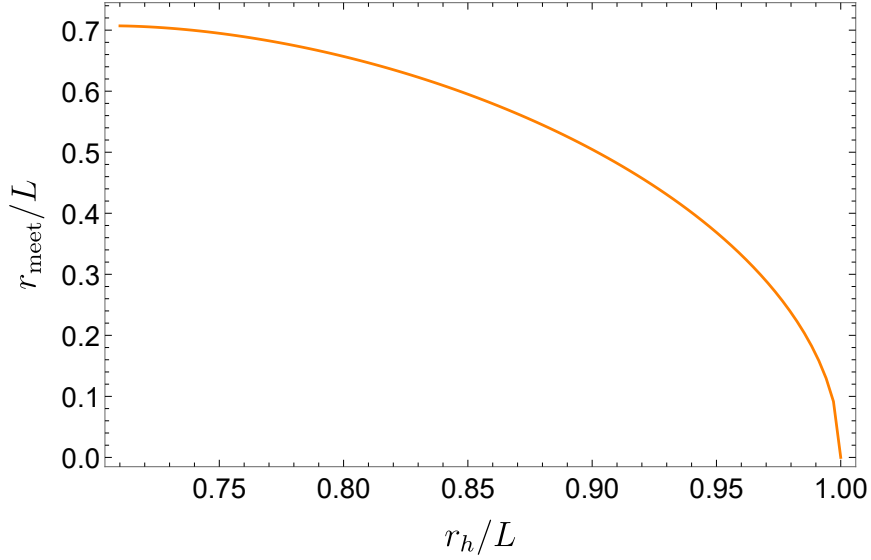


Figure A.4: The meeting point of the two ingoing null rays as a function of r_h . The meeting point is always between the inner and outer horizons. In particular, when the black hole becomes extremal the rays meet at $r_{\text{meet}} = r_h = L/\sqrt{2}$.

A.3.2 $d = 3$

In $d = 3$ when $r_h < \frac{2}{\sqrt{3}}L$ the blackening factor (2.2),

$$f(r) = \frac{r^2}{L^2} - 1 - \frac{r_h}{r} \left(\frac{r_h^2}{L^2} - 1 \right), \quad (\text{A.46})$$

has three real roots which we denote by

$$r_1 = r_h, \quad r_2 = \frac{1}{2} \left(\sqrt{4L^2 - 3r_h^2} - r_h \right), \quad r_3 = -\frac{1}{2} \left(\sqrt{4L^2 - 3r_h^2} + r_h \right). \quad (\text{A.47})$$

For small hyperbolic black holes ($r_h < L$), r_2 becomes positive and there are two event horizons (see figure A.3). The root r_3 is always negative and so does not indicate the presence of a third horizon. We study in this subsection both the case of $r_2 < 0$, $L < r_h < \frac{2}{\sqrt{3}}L$, *i.e.*, large hyperbolic black holes and the case of $r_2 > 0$, $r_h < L$, *i.e.*, small hyperbolic black holes. Once again for $r_h = L$, we recover vacuum AdS while for $r_h = L/\sqrt{3}$, our two horizons become degenerate. As before, we can assume without loss of generality that

$r_h > r_2$. The inverse blackening factor can be decomposed as follows:

$$\frac{1}{f(r)} = \frac{L^2}{(r_h - r_2)(r_h - r_3)(r_2 - r_3)} \left[\frac{r_h(r_2 - r_3)}{(r - r_h)} - \frac{r_2(r_h - r_3)}{(r - r_2)} + \frac{r_3(r_h - r_2)}{(r - r_3)} \right] \quad (\text{A.48})$$

leading to the following tortoise coordinate:

$$r^*(r) = \frac{L^2}{(r_h - r_2)(r_h - r_3)(r_2 - r_3)} \left[r_3 r_2 \log \frac{|r - r_2|}{|r - r_3|} + r_h r_2 \log \frac{|r - r_h|}{|r - r_2|} + r_3 r_h \log \frac{|r - r_3|}{|r - r_h|} \right] \quad (\text{A.49})$$

which implies $v_\infty = 0$.

$r_h < L$

For this range of parameters, we have that $r_2 > 0$ and the black hole has two horizons. The absolute values inside the logarithms differentiates the regions inside, outside, and between the inner and outer horizons. Evaluating eq. (A.39), we obtain:

$$\begin{aligned} \Delta I_{\text{bulk}} = & -\frac{\Omega_{-1,2}}{4\pi G_N (r_2 - r_3)(r_h - r_2)(r_h - r_3)} \left[-2r_2 (r_{\text{meet}}^3 - r_2^3) (r_h - r_3) \log \left(\frac{r_{\text{meet}} - r_2}{L} \right) \right. \\ & + 2r_3 (r_h - r_2) (r_{\text{meet}}^3 - r_3^3) \log \left(\frac{r_{\text{meet}} - r_3}{L} \right) - 2r_h (r_2 - r_3) (r_h^3 - r_{\text{meet}}^3) \log \left(\frac{r_h - r_{\text{meet}}}{L} \right) \left. \right] \\ & + \frac{\Omega_{-1,2} (2r_2 + 2r_3 + 2r_h + r_{\text{meet}}) r_{\text{meet}}}{4\pi G_N}, \end{aligned} \quad (\text{A.50})$$

where r_{meet} can again be computed numerically using eq. (A.49) and the condition (A.38) which reads in this case

$$r^*(r_{\text{meet}}) = 0. \quad (\text{A.51})$$

Since the null sheets meet between the two horizons one has to choose the appropriate branches of the logarithms in eq. (A.49) when solving this equation. We show the result for r_{meet} in figure A.5. The joint contribution (A.37) gives:

$$I_{\text{jnt}} = -\frac{\Omega_{-1,2}}{4\pi G_N} r_{\text{meet}}^2 \log |f(r_{\text{meet}})|. \quad (\text{A.52})$$

The total action is the sum of the bulk (A.50) and joint (A.52) terms. Substituting the numerical solution for r_{meet} we obtain the result plotted in orange in figure 3.2.

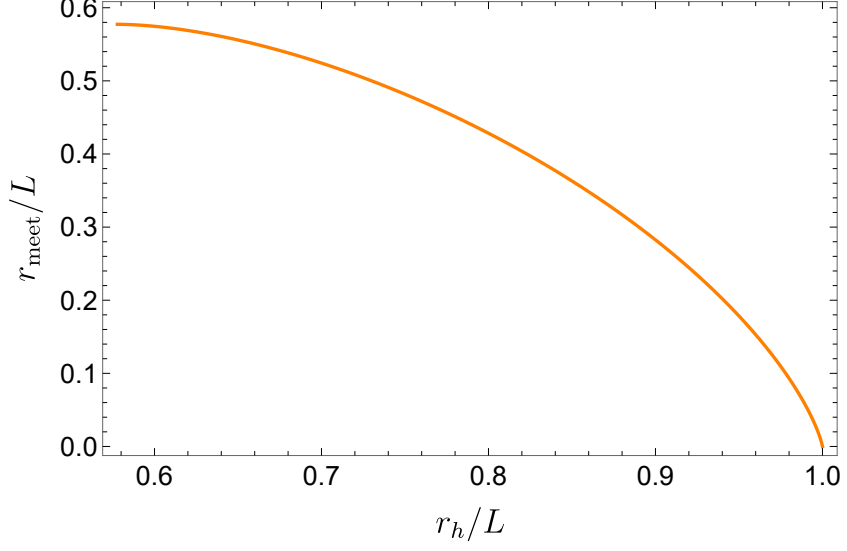


Figure A.5: Meeting point of the two ingoing null rays for hyperbolic black holes in AdS₄ as a function of the horizon radius. Orange plot (right) indicates the region in which $r_h > r_2$.

$$L < r_h < \frac{2L}{\sqrt{3}}$$

The black holes for this region of parameter space only have one positive root, since $r_2 < 0$. Therefore, we should use the tortoise coordinate (A.49) to evaluate the contributions to the action (3.2). We obtain:

$$\begin{aligned} \Delta I_{\text{bulk}} = & \frac{\Omega_{-1,2}}{2\pi G_N (r_2 - r_3)(r_h - r_2)(r_h - r_3)} \left[-r_2^4 (r_h - r_3) \log\left(-\frac{r_2}{L}\right) \right. \\ & \left. + r_3^4 (r_h - r_2) \log\left(-\frac{r_3}{L}\right) + r_h^4 (r_2 - r_3) \log\left(\frac{r_h}{L}\right) \right] \end{aligned} \quad (\text{A.53})$$

and

$$\begin{aligned} I_{\text{GHY}}^{\text{BH,sing}} = & -\frac{3r_h \Omega_{-1,2} (r_h^2 - L^2)}{4\pi G_N (r_2 - r_3)(r_h - r_2)(r_h - r_3)} \left[-r_2 (r_h - r_3) \log\left(-\frac{r_2}{L}\right) \right. \\ & \left. + r_3 (r_h - r_2) \log\left(-\frac{r_3}{L}\right) + r_h (r_2 - r_3) \log\left(\frac{r_h}{L}\right) \right]. \end{aligned} \quad (\text{A.54})$$

Combining these results, we recover the last missing part of figure 3.2.

A.3.3 Late-Time Growth of Complexity

This subsection is a small aside in which we extend the results of [63] for the rate of growth of complexity at late times to account for the possibility of small black holes with hyperbolic horizons. In this case the blackening factor (2.2) reads:

$$f(r) = \frac{r^2}{L^2} - 1 - \frac{r_h^{d-2}}{r^{d-2}} \left(\frac{r_h^2}{L^2} - 1 \right), \quad (\text{A.55})$$

and as mentioned before, it has two positive real roots representing two horizons with radii which we labeled r_+ and r_- respectively.⁵

The computation parallels strongly the computation for a charged black hole described in [63] and we will not repeat the full details here. The contribution from the volume integral is most easily computed in the (r, v) and (r, u) coordinates and is given by:

$$\begin{aligned} I_{\text{bulk}} &= \frac{1}{16\pi G_N} \int (R - 2\Lambda) \sqrt{-g} d^{d+1}x = -\frac{d\Omega_{k,d-1}}{8\pi G_N L^2} \int dv dr r^{d-1} \\ &= -\frac{\Omega_{k,d-1}}{8\pi G_N L^2} \delta t r^d \Big|_{r_-}^{r_+}. \end{aligned} \quad (\text{A.56})$$

The joint terms are given by equations (3.36) of [63] without any modification:

$$I_{\text{jnt}} = \frac{\Omega_{k,d-1}}{16\pi G_N} \left(r^{d-1} \frac{df}{dr} \right) \Big|_{r_-}^{r_+} \delta t. \quad (\text{A.57})$$

Plugging the blackening factor and summing together eq. (A.56) and eq. (A.57) leads to:

$$\frac{\delta \mathcal{C}}{\delta t} = \frac{1}{\pi} \left(\frac{\delta I}{\delta t} \right) = 0 \quad (\text{A.58})$$

which implies that the growth rate vanishes for $r_h < L$. We would like to point out that this does not provide evidence for a discontinuity in the complexity growth rate as r_h approaches L since in this limit the black hole mass vanishes — see eq. (2.7).

A.4 Ambiguities in the Action Calculations

In this appendix, we recall that, as discussed in [63], the boundary terms on the null boundary surfaces (2.30) and null joints (2.34) may introduce some ambiguities in the

⁵By design, r_h in eq. (A.55) is one of the horizon radii and we set $r_+ = r_h$.

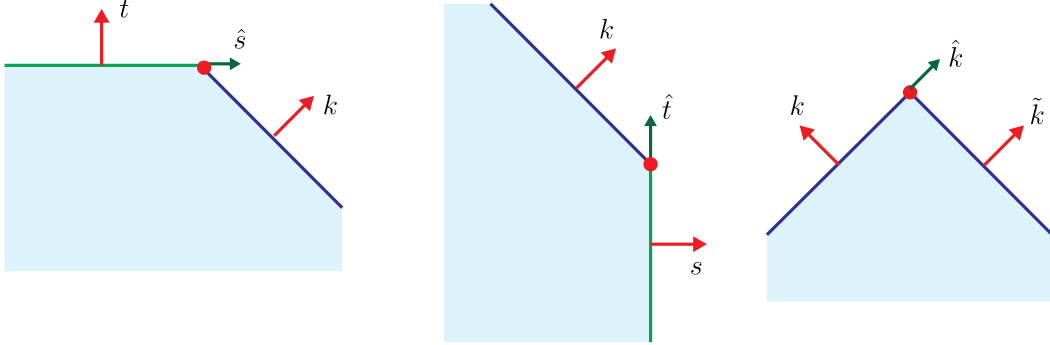


Figure A.6: Various possible null junctions appearing in our action calculations. We show k , t and s as outward-directed one-forms, following the convention of [65].

gravitational action. By construction, the variation of these boundary terms is well-defined and cancels the corresponding total derivative terms coming from the variation of the bulk action. However, evaluating the gravitational action for a particular spacetime geometry will generally yield different numerical values depending on different choices that can be made in constructing the boundary terms. In particular, κ in eq. (2.30) depends on an arbitrary choice of parameterization for the null generators. Further, in eq. (2.34), a depends on the arbitrary normalization of the null tangent k^α and in principle, we could add an additional function a_0 to a in eq. (2.34), which remains fixed when the action is varied. For convenience, we reiterate the expressions used to evaluate a :⁶

$$a = \begin{cases} \epsilon \log |k \cdot t| & \text{for spacelike-null joint with } \epsilon = -\text{sign}(k \cdot t) \text{sign}(k \cdot \hat{s}), \\ \epsilon \log |k \cdot s| & \text{for timelike-null joint with } \epsilon = -\text{sign}(k \cdot s) \text{sign}(k \cdot \hat{t}), \\ \epsilon \log |k \cdot \tilde{k}/2| & \text{for null-null joint with } \epsilon = -\text{sign}(k \cdot \tilde{k})\text{sign}(\hat{k} \cdot \tilde{k}). \end{cases} \quad (\text{A.59})$$

In the equation above, \hat{n} and \hat{s} (\hat{k}) are unit *vectors* (null *vector*) that are in the tangent space of the appropriate boundary region, orthogonal to the junction and pointing outward from the boundary region — see figure A.6. In this appendix, we will examine the influence of all these ambiguities on our results and show that except for the small hyperbolic black holes, our results are not effected by the different possible choices.

⁶Here we use the conventions introduced in [65].

A.4.1 Redefinition of the Function Defining the Null Hypersurface

It was argued in [63] that it is possible to introduce an ambiguity in the joint terms without redefining the null normal k_α . This is done by modifying the function Φ that describes the hypersurface (*i.e.*, with $\Phi(x) = 0$). In general $k_\alpha = \mu \partial_\alpha \Phi$ and therefore a in the joint action depends on both μ and Φ . We can however redefine $\Phi \rightarrow \bar{\Phi}(\Phi)$ (where also $\bar{\Phi}$ is required to vanish on the hypersurface) and choose $\bar{\mu} \equiv \mu d\Phi/d\bar{\Phi}$ in such a way that our normal vector is left unchanged:

$$k_\alpha = \mu \partial_\alpha \Phi = \bar{\mu} \partial_\alpha \bar{\Phi}. \quad (\text{A.60})$$

This implies that a is modified as follows:

$$a_{\text{new}} = a + a_0 = a + \log \left[\frac{d\Phi}{d\bar{\Phi}} \right]. \quad (\text{A.61})$$

In principle, there is no reason that a_0 should be the same on all the joints nor does it have to be a constant over a given joint.⁷ We will consider including a fixed constant a_0 for all joints as a simple test case. We will check how this addition influences our results.

We start from the joint contributions at infinity, eq. (2.37) will be modified by:

$$\Delta I_{\text{jnt,cut}} = I_{\text{jnt,cut}} = a_0 \frac{\Omega_{k,d-1}}{2\pi G_N} r_{\text{max}}^{d-1}. \quad (\text{A.62})$$

As discussed earlier (see eq. (2.13)), the difference in the cutoffs between vacuum AdS and the black hole background is of order δ^{d-1} . The leading order divergence near infinity is $r_{\text{max}} = L^2/\delta + \dots$, which implies that the subtraction of this term between the black hole and vacuum AdS spacetimes will result in an order δ contribution. Of course, we are assuming here that the same a_0 appears for both spacetimes.

Moving to the joint terms near the singularity we have that these are modified by

$$\Delta I_{\text{jnt,sing}} = I_{\text{jnt,cut}} = a_0 \frac{\Omega_{k,d-1}}{2\pi G_N} \epsilon_0^{d-1}, \quad (\text{A.63})$$

which vanishes in the limit $\epsilon_0 \rightarrow 0$. This implies already that most of the results presented in this thesis are left unchanged under such a modification of the joint terms.

⁷In principle, a_0 could be any scalar function with vanishing variation. Note however, that to maintain the additive character of the action, there are some restrictions that need to be imposed on a_0 for different kinds of joints — see section II.H of [63].

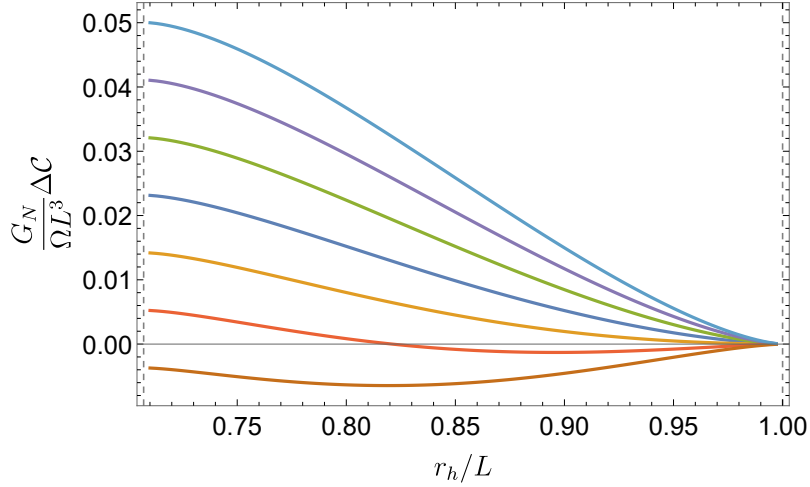


Figure A.7: Complexity of formation for the small hyperbolic black holes in $d = 4$ for different choices of a_0 ranging from $a_0 = -3$ (lowest line) to $a_0 = 3$ (highest line) in jumps of 1. We can observe that for certain values of a_0 the complexity becomes negative.

However, the small hyperbolic black holes are once again an exception. In this case we have also the joint terms at r_{meet} — see eq. (A.37). These will be modified by

$$\Delta I_{\text{jnt,meet}} = a_0 \frac{\Omega_{-1,d-1}}{4\pi G_N} r_{\text{meet}}^{d-1}. \quad (\text{A.64})$$

There is no equivalent contribution in vacuum AdS and so we will be left with a finite modification of the complexity of formation. The result for the small hyperbolic black holes in $d = 4$ with $a_0 = \{-3, -2, -1, 0, 1, 2, 3\}$ is shown in figure A.7.

A.4.2 Reparameterizations

In this subsection we demonstrate that our complexity of formation is invariant under a certain class of reparameterizations of the null generators $\lambda \rightarrow \bar{\lambda}(\lambda, \theta^A)$. The behavior of the various geometric quantities under reparameterizations was already studied in section II.C.4 of [63] and we briefly review it here. We use λ to denote the parameter along null generators and $\bar{\lambda}$ for the one associated to the new parameterization. We also define $e^{-\beta} = \partial \bar{\lambda} / \partial \lambda$. The normal vectors can be defined using the surface embedding functional $x^\alpha = x^\alpha(\lambda, \theta^A)$ where θ^A are the other intrinsic coordinates:

$$k^\alpha = \frac{\partial x^\alpha}{\partial \lambda}. \quad (\text{A.65})$$

Under a reparameterization, we have:

$$\bar{k}^\alpha = e^\beta k^\alpha, \quad \bar{\kappa} = e^\beta (\kappa + \partial_\lambda \beta). \quad (\text{A.66})$$

Let us look at the upper right normal in figure 4.1. In this case, the parametric representation of the null sheet reads $(t, r, \theta^A) = (v_\infty - r^*(r), r, \theta^A)$ where $\lambda = -r$ is the affine parameter along the null generators (oriented towards the future) and the null normal is given by the expression in eq. (2.32). We choose to look at a reparameterization with $e^\beta = g(r)$ for the upper right null sheet in figure 4.1. Applying the relations (A.66), we obtain:

$$\bar{k}_\mu dx^\mu = g(r) k_\mu dx^\mu = g(r) \left(dt + \frac{dr}{f(r)} \right), \quad \bar{\kappa} = -\frac{dg(r)}{dr}. \quad (\text{A.67})$$

Recall that we require our normal forms to be pointing outwards and so we will assume $g(r) > 0$ to maintain this condition. The other relevant normal forms are given by eqs. (2.25) and (A.29). The change in the action for the upper right null hypersurface of figure 4.1 is then:

$$\Delta I_{\text{null surface}} = -\frac{\Omega_{k,d-1}}{8\pi G_N} \int r^{d-1} \bar{\kappa} d\bar{\lambda} = \frac{\Omega_{k,d-1}}{8\pi G_N} \int_0^{r_{\max}} r^{d-1} \partial_r \log g(r), \quad (\text{A.68})$$

where the integral in the first equality is taken with integration limits from past ($r = r_{\max}$) to future ($r = 0$). The difference in the action due to joint terms is:

$$\Delta I_{\text{jnt}} = -\frac{\Omega_{k,d-1}}{8\pi G_N} r^{d-1} \log g(r) \Big|_0^{r_{\max}}. \quad (\text{A.69})$$

Summing the two contributions together, multiplying by four (assuming that we rescaled all our null normals with the same function $g(r)$) and using integration by parts we obtain:

$$\Delta I = -\frac{(d-1)\Omega_{k,d-1}}{2\pi G_N} \int_0^{r_{\max}} r^{d-2} \log g(r) dr. \quad (\text{A.70})$$

We recall that from this difference we are to subtract that of vacuum AdS, and so it will be enough for our purposes to demonstrate that the difference is independent of r_h in the limit $\delta \rightarrow 0$.

Let us now focus on the example of $\bar{\kappa}$ constant. This is achieved by choosing:

$$g(r) = 1 + \bar{\kappa}(r_{\max} - r). \quad (\text{A.71})$$

where we chose an additive constant to guarantee that the normalization condition $\bar{k} \cdot \hat{t} = \pm 1$ at the cutoff surface is maintained.

If we are to compare the different spacetimes, the nontrivial difference is in the r_{\max} dependence on the horizon radius. Since $g(r)$ is a known function, we can integrate eq. (A.70),

$$\begin{aligned} \bar{I}_{\bar{\kappa}} - I_{\kappa} = & -\frac{\Omega_{k,d-1} r^{d-1}}{2\pi G_N d(d+1)(\bar{\kappa} r_{\max} + 1)^2} \left[d r^2 \bar{\kappa}^2 {}_2F_1 \left(1, d+1; d+2; \frac{\bar{\kappa} r}{\bar{\kappa} r_{\max} + 1} \right) + \right. \\ & \left. (d+1)(\bar{\kappa} r_{\max} + 1)(\bar{\kappa} r + d(\bar{\kappa} r_{\max} + 1) \log(1 + \bar{\kappa}(r_{\max} - r))) \right] \Big|_0^{r_{\max}}. \end{aligned} \quad (\text{A.72})$$

This integral has a simple analytic expression for several dimensions. Since we know from eq. (2.13) that the difference in r_{\max} between the black hole and vacuum AdS is of order δ^{d-1} , the subtraction between the two spacetimes is of order $\delta \log \delta$,

$$\Delta I_{\text{BH}} - \Delta I_{\text{vac}} = \mathcal{O}(\delta \log \delta). \quad (\text{A.73})$$

Therefore, if the surface gravity changes to a constant value, the difference in the action between the two spacetimes can still be evaluated and the result is independent of $\bar{\kappa}$ in the limit $\delta \rightarrow 0$.⁸

A.4.3 Changing the Normalization Condition at the Boundary

The last source of ambiguity which we chose to explore is the possibility to normalize differently the null normals at the cutoff surface. Throughout chapter 3 we have normalized the null normal, *e.g.*, in eq. (2.32), at the asymptotic AdS boundary such that $\mathbf{k} \cdot \hat{\mathbf{t}} = 1$ where $\hat{\mathbf{t}} = \partial_t$. However, as suggested in [63], $\mathbf{k} \cdot \hat{\mathbf{t}} = c$ with c a positive constant would be an equally natural choice. Let us explore the consequences of choosing such a constant $c > 0$. This will lead to a rescaling of the null normal similar to the one in the previous subsection eq. (A.67). However, since in this case $g(r)$ is a constant, the surface gravity remains zero and the only contribution is of the form (A.69) with $g(r) = c$:

$$\Delta I_{\text{jnt}} = -\frac{\Omega_{k,d-1}}{8\pi G_N} r_{\max}^{d-1} \log c. \quad (\text{A.74})$$

We can now use again the fact that from eq. (2.13) the difference in r_{\max} between the black hole and vacuum AdS is of order δ^{d-1} . The expression (A.74) is therefore of order δ and vanishes when subtracting the two backgrounds. The small hyperbolic black holes are again different and will suffer ambiguities similar to those already discussed in subsection A.4.1.

⁸For small hyperbolic black holes, however, we have again an ambiguous result.

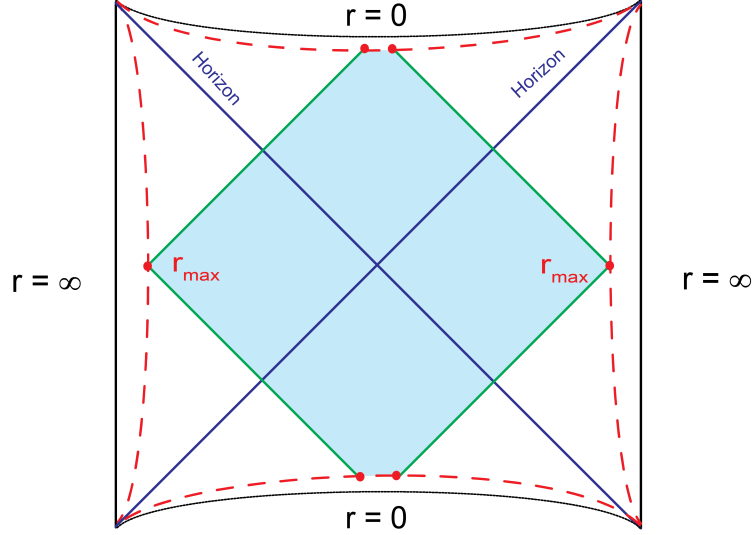


Figure A.8: Penrose diagram of a black hole in $d > 2$ representing a different way of regularizing the WDW patch. In this case we shoot the null rays from $r = r_{\max}$ and not from the boundary as in figure 4.1.

A.4.4 A Comment on the Cutoff Choice

We close this appendix with another nontrivial test of our results which is to check that they would not change for a certain modified regularization scheme. Suppose that instead of regularizing our action by a cutoff surface at $r = r_{\max}$ as we did in the text, we would bound our region by null rays which are emitted at $t = 0$ at $r = r_{\max}$, as depicted in figure A.8. In this appendix we demonstrate that our results do not change for such a choice. To be more precise, we show that the change introduced in the black hole action under our modified regularization scheme does not depend on r_h when taking the limit $\delta \rightarrow 0$ and so will cancel against that of vacuum AdS.

Let us start with the bulk contribution to the action. The sole modification to the integral (2.23) is that v_∞ would be replaced by:

$$\tilde{v}_\infty = r^*(r_{\max}) \tag{A.75}$$

which results in the following change of the bulk action:

$$\Delta I_{\text{bulk}} = -\frac{d\Omega_{k,d-1}}{2\pi G_N L^2} \int_0^{r_{\text{max}}} (\tilde{v}_\infty - v_\infty) r^{d-1} dr = -\frac{\Omega_{k,d-1} r_{\text{max}}^d}{2\pi G_N L^2} (\tilde{v}_\infty - v_\infty). \quad (\text{A.76})$$

Using the definition (2.14) of the tortoise coordinate:

$$\tilde{v}_\infty - v_\infty = -\int_{r_{\text{max}}}^\infty \frac{dr}{f(r)} = -\frac{L^2}{r_{\text{max}}} + \dots. \quad (\text{A.77})$$

This means that the bulk integral has a leading contribution proportional to r_{max}^{d-1} when r_{max} is large. Using again eq. (2.13) for the difference between the cutoffs of the black hole and vacuum AdS, we see that the r_h dependence of this expression is of order δ and vanishes in the limit $\delta \rightarrow 0$.

A similar argument holds for the surface contribution near the singularity (2.29) which is modified by:

$$\Delta I_{\text{GHY}} = \frac{d\Omega_{k,d-1} \omega^{d-2}}{4\pi G_N} (\tilde{v}_\infty - v_\infty). \quad (\text{A.78})$$

From eq. (A.77) we see that the difference $(\tilde{v}_\infty - v_\infty)$ has a leading $1/r_{\text{max}}$ contribution and goes to zero when we take the $\delta \rightarrow 0$ limit.

One last contribution which has to be considered is that of the right joint near the boundary (between the two null sheets):

$$I_{\text{jnt}} = \frac{r_{\text{max}}^{d-1} \Omega_{k,d-1}}{8\pi G_N} \log f(r_{\text{max}}). \quad (\text{A.79})$$

But notice that this (after a factor of 2 accounting for the two sides of the black hole) is exactly the same as in eq. (2.37) and so $\Delta I_{\text{jnt}} = 0$. This completes our argument that this different regularization scheme would give the same result for the complexity of formation.

Appendix B

Appendices to chapter 4

B.1 Details of Complexity=Action for BTZ Black Holes

In this appendix, we add some more details of the holographic complexity for the BTZ holes, using the complexity=action proposal. Much of these results are already summarized in section 4.2.1. The new results here include the derivation of our results for non-symmetric boundary times $\tau_L \neq \tau_R$ and their generalization for negative times.

B.1.1 General Boundary Times

We consider the BTZ metric, given in eq. (4.47):

$$ds^2 = -f(r) \frac{L^2}{R^2} d\tau^2 + \frac{dr^2}{f(r)} + r^2 d\phi^2, \quad \text{with } f(r) = \frac{r^2 - r_h^2}{L^2}. \quad (\text{B.1})$$

The boundary metric takes the form given in eq. (4.49) and so a constant time slice is simply a circle with circumference $2\pi R$. For general boundary times (τ_L, τ_R) ,¹ the WDW patch takes the form depicted in figure B.1. When the total time $\tau = \tau_L + \tau_R$ is positive $\tau > 0$ (or negative $\tau < 0$), the WDW patch does not reach the past (future) singularity and there is a past (future) corner represented by the dot in figure B.1. The radial coordinate r_m of this joint is given by

$$r_m(\tau_L, \tau_R) = r_h \tanh \frac{r_h |\tau_L + \tau_R|}{2LR} = r_h \tanh \frac{r_h |\tau|}{2LR}. \quad (\text{B.2})$$

¹Here, we do not assume $\tau_L = \tau_R$, but, of course, the result depends only on the total time $\tau = \tau_L + \tau_R$ due to the symmetry of the background.

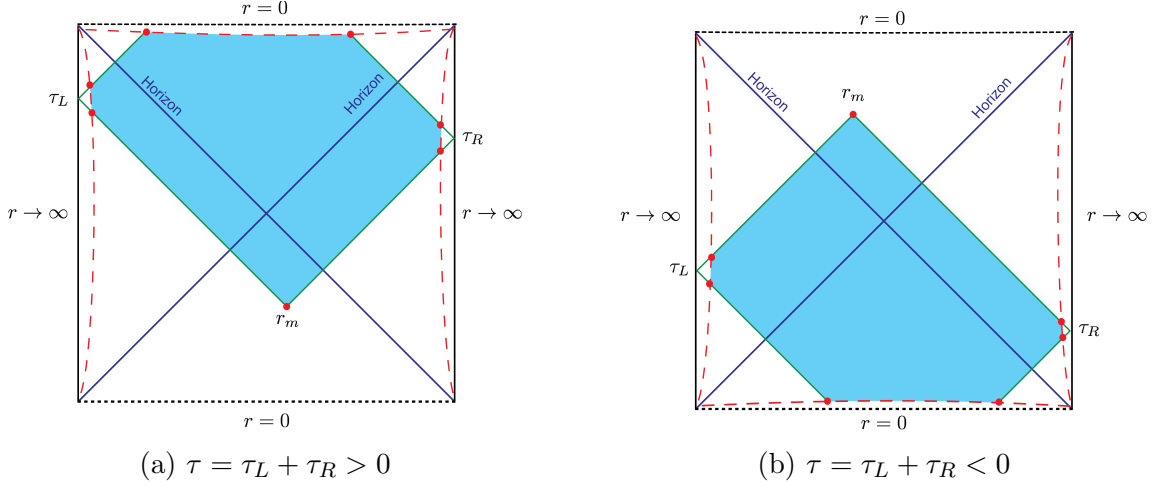


Figure B.1: The WDW patches in the BTZ black hole background. The dashed lines represent the cutoff surfaces. The left (right) panel illustrates the case in which $\tau = \tau_L + \tau_R > 0$ ($\tau = \tau_L + \tau_R < 0$).

The action for the WDW patch consists of a bulk term, surface terms and joint terms, as described in the main text:

$$I_{BTZ} = I_{\text{bulk}} + I_{\text{surf}} + I_{\text{jnt}}. \quad (\text{B.3})$$

The bulk term I_{bulk} is given by

$$I_{\text{bulk}} = -\frac{2LR}{G_N \delta} - \frac{r_h^2 |\tau|}{4G_N LR} + \frac{r_m}{2G_N}, \quad (\text{B.4})$$

where we used the cutoff $r = r_{\text{max}} = LR/\delta + r_h^2 \delta / (4LR)$ corresponding to the UV regulator $z = \delta$ in a Fefferman-Graham expansion (see also appendix A.1).

As in the text, we choose here an affine parametrization for the null generators. For this reason, the null surface terms vanish. Therefore the only nonvanishing surface contributions come from the surface at the future singularity and the UV cutoff surfaces. The contribution from the singularity is given by

$$I_{\text{surf},\text{sing}} = \frac{r_h^2 |\tau|}{4G_N LR}. \quad (\text{B.5})$$

The contribution from the cutoff surfaces is UV-divergent:

$$I_{\text{surf},\text{cut}} = \frac{2LR}{G_N\delta}. \quad (\text{B.6})$$

Thus, the total surface term is given by

$$I_{\text{surf}} = \frac{2LR}{G_N\delta} + \frac{r_h^2|\tau|}{4G_NLR}. \quad (\text{B.7})$$

The normalization of null vectors \mathbf{k}_L and \mathbf{k}_R are set to be the same as in the main text:

$$\mathbf{k}_L \cdot \hat{\tau}_L = \mathbf{k}_R \cdot \hat{\tau}_R = \pm\alpha \quad (\text{B.8})$$

where $\hat{\tau}_L = \partial_{\tau_L}$ and $\hat{\tau}_R = \partial_{\tau_R}$, and the sign is chosen as $+$ ($-$) for future (past) null surfaces. The joint contributions come from joints at $r = r_m$ and at $r = r_{\text{max}}$ and are given by

$$I_{\text{jnt},\text{cut}} = -\frac{LR}{G_N\delta} \log \frac{\alpha\delta}{L}. \quad (\text{B.9})$$

$$I_{\text{jnt},r_m} = -\frac{r_m}{4G_N} \log \left| \frac{L^2 f(r_m)}{\alpha^2 R^2} \right| = \frac{r_h}{2G_N} \tanh \frac{r_h|\tau|}{2LR} \log \left(\frac{\alpha R}{r_h} \cosh \frac{r_h\tau}{2LR} \right). \quad (\text{B.10})$$

Therefore, the total action reads

$$\begin{aligned} I_{BTZ} &= I_{\text{bulk}} + I_{\text{surf}} + I_{\text{jnt}} \\ &= \frac{r_h}{2G_N} \tanh \frac{r_h|\tau|}{2LR} \left[1 + \log \left(\frac{\alpha R}{r_h} \cosh \frac{r_h\tau}{2LR} \right) \right] - \frac{LR}{G_N\delta} \log \frac{\alpha\delta}{L}. \end{aligned} \quad (\text{B.11})$$

We can regularize it by subtracting twice the action of the WDW patch in the vacuum AdS space, following chapter 3. If we consider the Neveu–Schwarz vacuum of the boundary theory [144], *i.e.*, with the metric $f_0(r) = r^2/L^2 + 1$, the action of vacuum AdS space is given by a sum of eq. (2.42) and eqs. (B.6) and (B.9) which remain the same for the empty AdS background (but need to be multiplied by a factor of a half if we consider a single copy of empty AdS). We therefore obtain:

$$I_{AdS} = \frac{\pi L}{4G_N} - \frac{LR}{2G_N\delta} \log \frac{\alpha\delta}{L}. \quad (\text{B.12})$$

The regularized action is then given after the subtraction by:

$$I_{\text{reg}}(\tau_L, \tau_R) = I_{BTZ}(\tau_L, \tau_R) - I_{AdS}(\tau_L) - I_{AdS}(\tau_R) \quad (\text{B.13})$$

$$= -\frac{\pi L}{2G_N} + \frac{r_h}{2G_N} \tanh \frac{r_h|\tau|}{2LR} \left[1 + \log \left(\frac{\alpha R}{r_h} \cosh \frac{r_h\tau}{2LR} \right) \right]. \quad (\text{B.14})$$

The finite part of the holographic complexity from the CA conjecture is thus

$$\Delta\mathcal{C}_A(\tau_L, \tau_R) = \frac{I_{reg}}{\pi} = -\frac{L}{2G_N} + \frac{r_h}{2\pi G_N} \tanh \frac{r_h|\tau|}{2LR} \left[1 + \log \left(\frac{\alpha R}{r_h} \cosh \frac{r_h\tau}{2LR} \right) \right]. \quad (\text{B.15})$$

This result can also be written as

$$\Delta\mathcal{C}_A(\tau_L, \tau_R) = -\frac{c}{3} + \frac{2M}{\pi^2 T} \tanh(\pi T|\tau|) \left(1 + \log \left[\frac{\alpha}{2\pi LT} \cosh(\pi T\tau) \right] \right), \quad (\text{B.16})$$

where c is the central charge of the boundary CFT, given by $c = 3L/(2G_N)$, M is the mass of the BTZ black hole $M = r_h^2/(8G_N LR)$, and T is the temperature $T = r_h/(2\pi LR)$. We can think of this result as the complexity of formation of the thermofield double state, with general times τ_L, τ_R . Note that the temperature should satisfy $T > 1/(2\pi R)$ so that the BTZ black hole is the dominant saddle point for the gravitational theory in the bulk. In order to express $\Delta\mathcal{C}_A$ solely in terms of boundary quantities, choose the normalization constant $\alpha = L/\ell$, where ℓ is a new length scale in the boundary theory, as discussed in section 4.2 — see also [65].

The holographic complexity of the AdS vacuum is independent of time and hence taking the derivative of eq. (B.16) with respect to time $\tau = \tau_L + \tau_R$, yields the rate of growth appearing in eq. (4.53)

$$\frac{d\mathcal{C}_A}{d\tau} = \frac{2M}{\pi} \left(1 + \text{sech}^2(\pi T\tau) \log \left[\frac{\alpha}{2\pi LT} \cosh(\pi T\tau) \right] \right). \quad (\text{B.17})$$

We are assuming $\tau > 0$ here.

Unlike the higher dimensional case, $d\mathcal{C}_A/d\tau$ is finite at $\tau = 0$.² In fact, we have

$$\frac{d\mathcal{C}_A}{d\tau}(\tau \rightarrow 0^+) = \frac{2M}{\pi} \left(1 + \log \frac{\alpha}{2\pi LT} \right). \quad (\text{B.18})$$

At late times, we have

$$\frac{d\mathcal{C}_A}{d\tau}(\tau \rightarrow \infty) \sim \frac{2M}{\pi} \left[1 + 4 \left(\pi T\tau + \log \frac{\alpha}{4\pi LT} \right) e^{-2\pi T\tau} + \dots \right]. \quad (\text{B.19})$$

Noting the coefficient of the exponential is positive, we find that it approaches $2M/\pi$ from above. In figure 4.2, we see that $\frac{d\mathcal{C}_A}{d\tau}$ has a maximum at some time τ_{peak} . We can determine the latter by evaluating $\frac{d^2\mathcal{C}_A}{d\tau^2}(\tau_{peak}) = 0$ and we find

$$\tau_{peak} = \frac{1}{\pi T} \cosh^{-1} \frac{\sqrt{e} 2\pi LT}{\alpha}. \quad (\text{B.20})$$

²Recall the discussion for higher dimensional black holes around eq. (4.34).

At that time, $\frac{d\mathcal{C}_A}{d\tau}$ is greater than $2M/\pi$ with,

$$\frac{d\mathcal{C}_A}{d\tau}(\tau_{peak}) = \frac{2M}{\pi} \left[1 + \frac{1}{2e} \left(\frac{\alpha}{2\pi LT} \right)^2 \right] > \frac{2M}{\pi}. \quad (\text{B.21})$$

Hence $d\mathcal{C}_A/d\tau$ always exceeds the Lloyd bound and further the violation increases for smaller black holes, *i.e.*, smaller temperatures. Substituting the minimum temperature, $T = 1/(2\pi R)$, into eq. (B.21) yields

$$\frac{d\mathcal{C}_A}{d\tau}(\tau_{peak}) \Big|_{T=\frac{1}{2\pi R}} = \frac{2M}{\pi} \left[1 + \frac{1}{2e} \left(\frac{\alpha R}{L} \right)^2 \right]. \quad (\text{B.22})$$

Note that implicitly the above expressions require $2\pi LT \geq \alpha/\sqrt{e}$. Otherwise the maximum occurs at $\tau = 0$, *i.e.*,

$$\frac{d\mathcal{C}_A}{d\tau} \Big|_{max} = \frac{d\mathcal{C}_A}{d\tau}(\tau = 0) = \frac{2M}{\pi} \left(1 + \log \left[\frac{\alpha}{2\pi LT} \right] \right) \quad \text{for } 2\pi LT < \alpha/\sqrt{e}. \quad (\text{B.23})$$

We observe, however, that the details of the violation of Lloyd's bound depend on the normalization constant α , *i.e.*, whether or not the violation is large depends crucially on the choice of α .

B.1.2 Boundary Counterterm

We will now add the boundary counterterm to the action, which was introduced in [63] to make the action invariant under the reparametrizations of null boundaries of the WDW patch. As we see in appendix B.4.2, the counterterm for the affine parametrization $\lambda = r/\alpha$, which corresponds to the normalization of \mathbf{k}_L and \mathbf{k}_R in the previous subsection B.1.1, is³

$$\Delta I_{\Sigma}^{BTZ} = -\frac{1}{G_N} r_{max} \left(\log \frac{r_{max}}{\alpha \tilde{L}} - 1 \right) + \frac{1}{2G_N} r_m \left(\log \frac{r_m}{\alpha \tilde{L}} - 1 \right), \quad (\text{B.24})$$

where \tilde{L} is an arbitrary constant. Similarly the counter term for pure AdS₃ is given by

$$\Delta I_{\Sigma}^{AdS} = -\frac{1}{2G_N} r_{max}^{AdS} \left(\log \frac{r_{max}^{AdS}}{\alpha \tilde{L}} - 1 \right), \quad (\text{B.25})$$

³This expression holds for the general boundary size $2\pi R$.

where we assume that the arbitrary constant \tilde{L} is the same as that in BTZ. Subtracting this from eq. (B.24), we obtain the regularized counter term

$$\begin{aligned}\Delta I^{reg} &= \Delta I_{\Sigma}^{BTZ} - 2\Delta I_{\Sigma}^{AdS} = \frac{1}{2G_N} r_m \left(\log \frac{r_m}{\alpha \tilde{L}} - 1 \right) \\ &= \frac{r_h}{2G_N} \tanh \frac{r_h |\tau|}{2LR} \left[\log \left(\frac{r_h}{\alpha \tilde{L}} \tanh \frac{r_h |\tau|}{2LR} \right) - 1 \right].\end{aligned}\quad (\text{B.26})$$

Adding this result to eq. (B.14), the regularized BTZ action with the counter term is given by

$$I_{BTZ} = -\frac{\pi L}{2G_N} + \frac{r_h}{2G_N} \tanh \frac{r_h |\tau|}{2LR} \left[\log \left(\frac{R}{\tilde{L}} \sinh \frac{r_h |\tau|}{2LR} \right) \right].\quad (\text{B.27})$$

Note that α -dependence cancels out. We thus obtain the holographic complexity

$$\Delta \mathcal{C}_A(\tau_L, \tau_R) = \frac{I_{BTZ}}{\pi} = -\frac{L}{2G_N} + \frac{r_h}{2\pi G_N} \tanh \frac{r_h |\tau|}{2LR} \left[\log \left(\frac{R}{\tilde{L}} \sinh \frac{r_h |\tau|}{2LR} \right) \right]\quad (\text{B.28})$$

$$= -\frac{c}{3} + \frac{2M}{\pi^2 T} \tanh(\pi T |\tau|) \left(\log \left[\frac{R}{\tilde{L}} \sinh(\pi T |\tau|) \right] \right).\quad (\text{B.29})$$

Of course, the boundary counterterm introduces a new arbitrary length scale \tilde{L} . Hence we again encounter an ambiguity of the choice of the arbitrary length scale like in the choice of α without the counterterm or the ambiguous factor in the CV conjecture (3.42). The plots of eq. (B.29) for various R/\tilde{L} are shown in figure B.2.

The time derivative of the holographic complexity for $\tau > 0$ is

$$\frac{d\mathcal{C}_A}{d\tau} = \frac{2M}{\pi} \left[1 + \frac{\log\left(\frac{R}{\tilde{L}} \sinh(\pi T \tau)\right)}{\cosh^2(\pi T \tau)} \right].\quad (\text{B.30})$$

We show the plots for various choices of \tilde{L} in Fig. B.3. Unlike the case without the counter term, $d\mathcal{C}_A/d\tau$ is divergent at $\tau = 0$ with

$$\frac{d\mathcal{C}_A}{dt} \sim \frac{2M}{\pi} \log[\pi T \tau] \quad \text{for } 0 < T\tau \ll 1.\quad (\text{B.31})$$

This divergence might be comparable to that found for higher dimensional black holes at $t = t_c$, *i.e.*, see eq. (4.34). However, the complexity of formation (B.29) still has a finite value at $\tau = 0$, as

$$\Delta \mathcal{C}_A(0) = -c/3.\quad (\text{B.32})$$

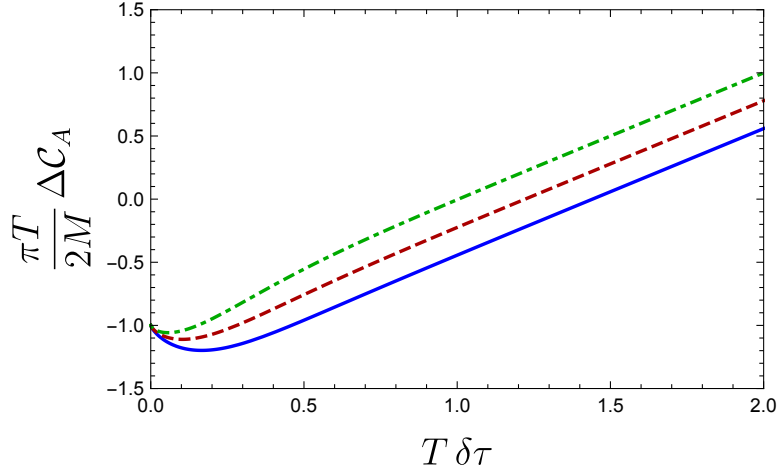


Figure B.2: Plot of $[\pi/(2M\beta)]\mathcal{C}_A(\tau)$ with $TR = \frac{1}{2\pi}$ for $R/\tilde{L} = 0.5$ (solid blue), $R/\tilde{L} = 1.0$ (dashed red) and $R/\tilde{L} = 2.0$ (dot-dashed green).

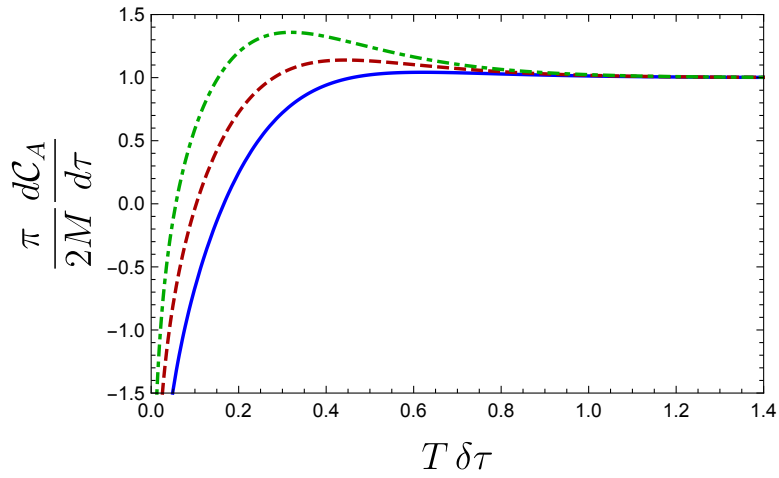


Figure B.3: Plot of $[\pi/(2M)]d\mathcal{C}_A/d\tau$ for $R/\tilde{L} = 0.5$ (solid blue), $R/\tilde{L} = 1.0$ (dashed red) and $R/\tilde{L} = 2.0$ (dot-dashed green). The curves diverge at $\tau = 0$ and approach to 1 from above at late times.

This matches the complexity of formation for Neveu-Schwarz vacuum found in chapter 3. At late times, $d\mathcal{C}_A/d\tau$ behaves as

$$\frac{d\mathcal{C}_A}{d\tau} \sim \frac{2M}{\pi} \left[1 + 4 \left(\pi T \tau + \log \frac{R}{2\tilde{L}} \right) e^{-2\pi T \tau} \right]. \quad (\text{B.33})$$

Thus, the rate of growth still approaches the universal limit $2M/\pi$ from above, for any choices of \tilde{L} .

B.2 Additional Examples of Time Dependence of Complexity

In eq. (4.27), we provided a general expression for the time rate of change of the holographic complexity of (neutral) AdS black holes using the CA conjecture. We examined some specific examples in section 4.2.1 for boundary CFTs with $d = 2$ and 4 — see also appendix B.1. Further, in eq. (4.71), together with eqs. (4.66) and (4.67), we provided an expression for the rate of change of complexity based on the CV conjecture, and examined numerically the cases of $d = 2$, and planar geometry with $d = 3, 4$ in subsection 4.3.2. In this appendix, we provide further examples of the time dependence of holographic complexity. We show that qualitatively the holographic complexity behaves in the same way in a different (odd) dimension, namely $d = 3$, using the CA conjecture. We also explore the influence of the choice of horizon geometry on the results of the CV conjecture in $d = 3$ and $d = 4$.

B.2.1 CA Results in $d = 3$

For the case of $d = 3$, we have the dimensionless tortoise coordinate $x^*(x, RT) = \frac{r_h}{L^2} r^*(r)$, where we have used the definition $x \equiv \frac{r}{r_h}$. This leads to

$$x^*(x, RT) = \frac{1}{\frac{kL^2}{r_h^2} + 3} \left[\log \left[\frac{|x-1|}{\sqrt{\frac{kL^2}{r_h^2} + x^2 + x + 1}} \right] + \frac{\left(\frac{2kL^2}{r_h^2} + 3\right)}{\sqrt{\frac{4kL^2}{r_h^2} + 3}} \tan^{-1} \left[\frac{2x+1}{\sqrt{\frac{4kL^2}{r_h^2} + 3}} \right] \right], \quad (\text{B.34})$$

and

$$x_\infty^* = \frac{\pi \left(\frac{2kL^2}{r_h^2} + 3\right)}{2 \left(\frac{kL^2}{r_h^2} + 3\right) \sqrt{\frac{4kL^2}{r_h^2} + 3}}. \quad (\text{B.35})$$

We can evaluate the critical time τ_c using eq. (4.40). This leads to

$$\tau_c = \frac{1}{4\pi T \sqrt{\frac{4kL^2}{r_h^2} + 3}} \left[\sqrt{\frac{4kL^2}{r_h^2} + 3} \log \left(\frac{kL^2}{r_h^2} + 1 \right) + \left(\frac{4kL^2}{r_h^2} + 6 \right) \tan^{-1} \left(\sqrt{\frac{4kL^2}{r_h^2} + 3} \right) \right]. \quad (\text{B.36})$$

We can apply these results to evaluate the rate of change of holographic complexity for spherical, planar and large hyperbolic black holes. By large hyperbolic black holes, we mean that $r_h/L \geq 1$ which implies that the mass is positive. Actually, we assumed here that $r_h > 2L/\sqrt{3}$ for the hyperbolic case with $k = -1$. In the regime $L \leq r_h \leq 2L/\sqrt{3}$, $f(r)$ has two additional negative real roots. While these do not indicate the existence of additional horizons, the tortoise coordinate is modified in this case and takes the form

$$x^*(x, RT) = \frac{1}{3 - \frac{L^2}{r_h^2}} \log \left(\frac{|x-1|}{\sqrt{-\frac{L^2}{r_h^2} + x^2 + x + 1}} \right) - \frac{\left(3 - \frac{2L^2}{r_h^2}\right)}{\left(3 - \frac{L^2}{r_h^2}\right) \sqrt{\frac{4L^2}{r_h^2} - 3}} \coth^{-1} \left(\frac{2x+1}{\sqrt{\frac{4L^2}{r_h^2} - 3}} \right) \quad (\text{B.37})$$

and the critical time for the hyperbolic black holes in this mass range reads

$$\tau_c = \frac{1}{4\pi T \sqrt{\frac{4L^2}{r_h^2} - 3}} \left(\sqrt{\frac{4L^2}{r_h^2} - 3} \log \left(1 - \frac{L^2}{r_h^2} \right) + \left(6 - \frac{4L^2}{r_h^2} \right) \tanh^{-1} \left(\sqrt{\frac{4L^2}{r_h^2} - 3} \right) \right). \quad (\text{B.38})$$

We present a plot of $\tau_c T$ as a function of the horizon radius in figure B.4.

After solving numerically for x_m , the results are presented in figure B.5 for $k = 0, 1$, and in figure B.6 for $k = -1$. The overall behaviour of the rate of change of complexity is very similar to the results shown in figure 4.4 for spherical and planar black holes in $d = 4$. We also present the integrated complexity in figures B.7 and B.8 to demonstrate that there is no divergence near $\tau = \tau_c$. That is, these figures show $\mathcal{C}_A(\tau) - \mathcal{C}_A(\tau_c) = \int_{\tau_c}^{\tau} d\tau \frac{d\mathcal{C}_A}{d\tau}$. Even though $d\mathcal{C}_A/d\tau$ diverges at the critical time (see eq. (4.34)), it is an integrable singularity and the complexity itself only shows a mild variation at this point. We have also included as the integration constant $\mathcal{C}_A(\tau_c)$ the complexity of formation. Recall that the complexity of formation is given by the complexity of the thermofield double state minus twice that of the vacuum state of the CFT, and so presents a natural finite value for the complexity for $|\tau| < \tau_c$. Again we found similar results for $d = 4$, although we do not explicitly show the corresponding figures here.

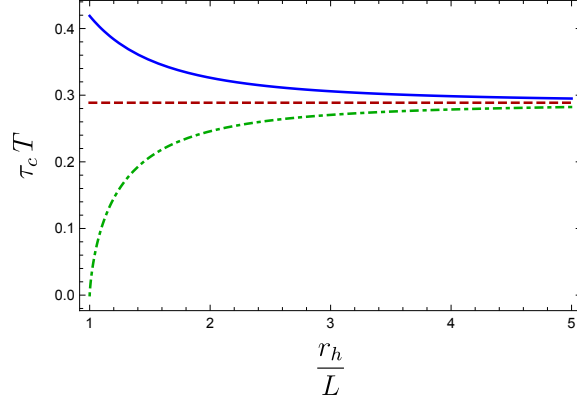


Figure B.4: Critical time as a function of the horizon radius for $d = 3$ for the various geometries – spherical $k = 1$ (blue, solid), planar $k = 0$ (red, dashed) and large hyperbolic $k = -1$, $r_h > L$ (green, dot-dashed).

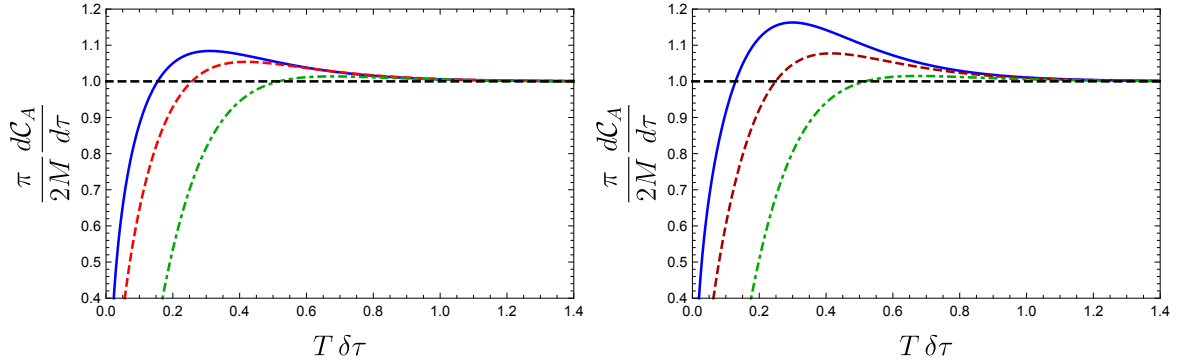


Figure B.5: Time derivative of complexity as a function of time for spherical (left) and planar (right) geometries in $d = 3$ boundary dimensions for various values of the horizon radius – $r_h = L$ (solid blue), $r_h = 1.5L$ (dashed red), $r_h = 3.5L$ (dot-dashed green). We present the plot as a function of the time coordinate in units of the thermal scale $\delta\tau T = (\tau - \tau_c) T$. We stress again that the complexity starts changing at τ_c and each of the curves presented has a different value of τ_c . For these parameters, the violation of the late time bound is clearly manifest.

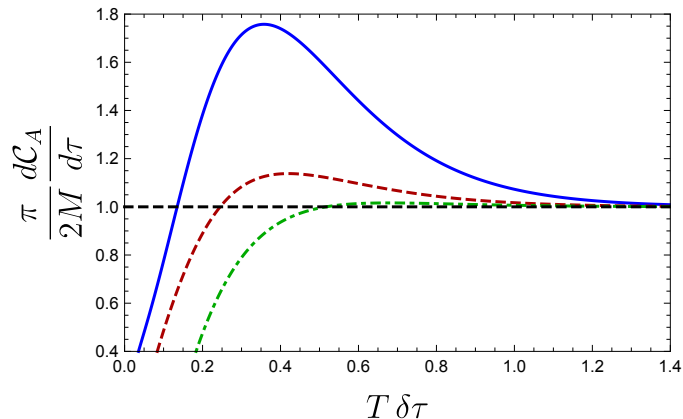


Figure B.6: Time derivative of complexity as a function of time for large hyperbolic black holes ($r_h > L$) in $d = 3$ boundary dimensions for various values of the horizon radius – $r_h = 1.1L$ (blue), $r_h = 1.5L$ (dashed red), $r_h = 3.5L$ (dot-dashed green). We present the plot as a function of the time coordinate in units of the thermal scale $\delta\tau T = (\tau - \tau_c) T$. We stress again that the complexity starts changing at τ_c and each of the curves presented has a different value of τ_c . For these parameters, the violation of the late time bound is clearly manifested.

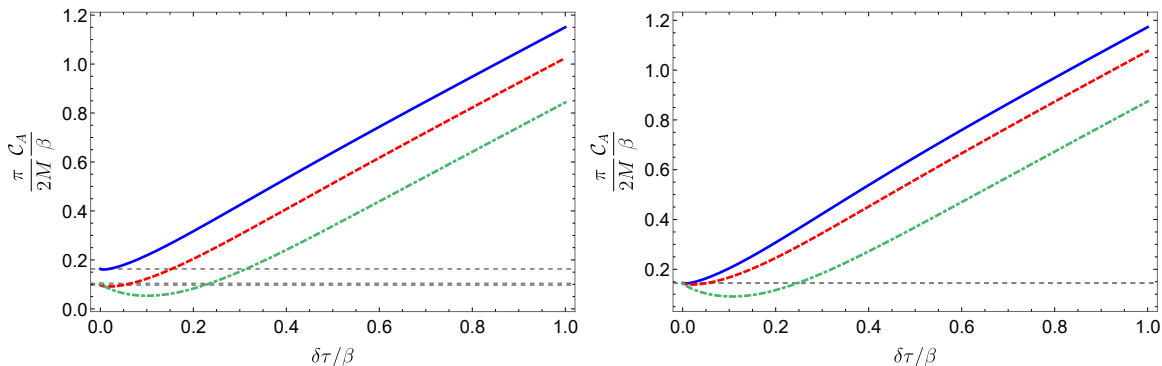


Figure B.7: Integrated complexity as a function of time for spherical (left) and planar (right) geometries in $d = 3$ boundary dimensions for various values of the horizon radius – $r_h = L$ (solid blue), $r_h = 1.5L$ (dashed red), $r_h = 3.5L$ (dot-dashed green). We see that it does not diverge at $\tau = \tau_c$ ($\delta\tau = 0$). The value at $\delta\tau = 0$ has been set according to the complexity of formation, see chapter 3.

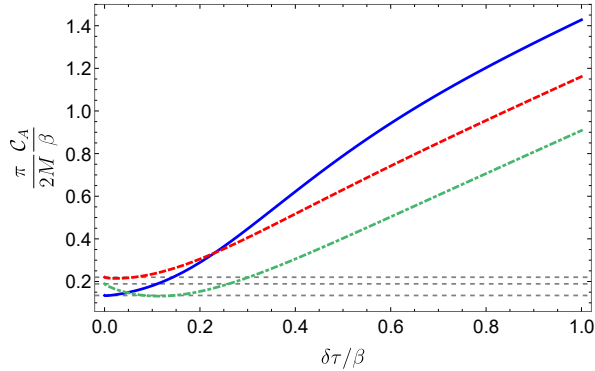


Figure B.8: Integrated complexity as a function of time for large hyperbolic black holes in $d = 3$ boundary dimensions for various values of the horizon radius – $r_h = 1.1L$ (blue), $r_h = 1.5L$ (dashed red), $r_h = 3.5L$ (dot-dashed green). We see that it does not diverge at $\tau = \tau_c$ ($\delta\tau = 0$). The value at $\delta\tau = 0$ has been set according to the complexity of formation, see chapter 3.

B.3 Complexity of Formation for Charged Black Holes

In this appendix, we evaluate the complexity of formation for charged black holes. The complexity of formation for uncharged black holes was examined in detail in chapter 3. There, the complexity of formation is defined as the additional complexity involved in preparing two copies of the boundary CFT in the entangled thermofield double state (1.21) (evaluated at $t_L = t_R = 0$) compared to preparing each of the CFTs in their vacuum state. Using the CA proposal,⁴ the bulk calculation consists of evaluating the gravitational action for the WDW patch (anchored at $t_L = t_R = 0$) in the (neutral) AdS black hole background and subtracting twice the action for the WDW in an appropriate vacuum of AdS space. A key aspect of this subtraction is that all of the UV (large r) divergences cancel, which as a consequence leaves a UV finite result.

Hence in the present charged case, the first question to settle is what is the appropriate reference state to compare to the charged thermofield double state (4.94). Here we recall that it was shown in [156] that at zero temperature and with a spherical boundary, the ground state for the fixed chemical potential ensemble is pure AdS for $\mu < \frac{gL}{2R\sqrt{2\pi G}}\sqrt{\frac{(d-1)}{(d-2)}}$ and an extremal black hole of the same chemical potential for $\mu > \frac{gL}{2R\sqrt{2\pi G}}\sqrt{\frac{(d-1)}{(d-2)}}$. It was

⁴Of course, an analogous calculation can also be performed using the CV proposal — see below.

also noted there that this extremal black hole may be unstable and decay by the emission of charged particles. For the planar boundary geometry (*i.e.*, $k = 0$) and the hyperbolic one (*i.e.*, $k = -1$), the ground state is always the extremal black hole.

Hence in evaluating the complexity of formation for the charged thermofield double state, one suggestion is to subtract the holographic complexity corresponding to an extremal black hole with the same chemical potential [34]. However, we find that the holographic complexity for an extremal black hole contains an additional infrared divergence and hence a meaningful comparison cannot be achieved by comparing a charged black hole to the corresponding extremal one. We will see that this IR divergence appears for both the CA and the CV conjectures. Therefore, we simply choose the uncharged vacuum ($\omega = q = 0$) as our reference state, *i.e.*, we subtract the holographic complexity of two copies of the corresponding AdS vacuum.

As in section 4.4, it is convenient to work with the dimensionless variables introduced in eq. (4.101). Recall

$$x \equiv \frac{r}{r_+}, \quad y \equiv \frac{r_-}{r_+}, \quad z \equiv \frac{L}{r_+}. \quad (4.101)$$

The first is a dimensionless radial coordinate, while the latter two can be defined in terms of boundary quantities, as in eq. (4.102). Further, in the following, we will focus on the case of $d = 4$, where that latter expressions are explicitly given in eq. (4.119). In principle then, we can invert these formula to write our results in terms of the boundary quantities, $\nu = \sqrt{C_J/C_T} \mu/T$ and RT . In the planar geometry, *i.e.*, $k = 0$, for $d = 4$ eq. (4.119) reads

$$\nu = \sqrt{\frac{C_J}{C_T}} \frac{\mu}{T} = \frac{3\pi}{\sqrt{10}} \frac{y\sqrt{y^2+1}}{(1-y^2)(2+y^2)}, \quad RT = \frac{1}{2\pi} \frac{(1-y^2)(2+y^2)}{z}. \quad (B.39)$$

Then the first of these equations can be inverted to obtain

$$y^2 = \frac{\sqrt{3}\sqrt{15\nu^2 - \pi\sqrt{80\nu^2 + 9\pi^2} + 3\pi^2}}{2\sqrt{5}\nu} - \frac{1}{2} \quad (B.40)$$

and for the second, we may write

$$z = \frac{1}{2\pi} \frac{(1-y^2(\nu))(2+y^2(\nu))}{RT}. \quad (B.41)$$

B.3.1 Complexity=Action

Using the CA proposal, the complexity of formation is given by:

$$\Delta\mathcal{C}_A = \frac{1}{\pi} [\Delta I_{\text{bulk}} + I_{\text{jnt}}] \quad (B.42)$$

where

$$\begin{aligned} \Delta I_{\text{bulk}} = & \frac{\Omega_{k,d-1}}{2\pi G_N} \int_{r_m}^{r_{\text{max}}} \left(-\frac{d}{L^2} + \frac{q^2(d-2)}{r^{2(d-1)}} \right) r^{d-1} (r_{\infty}^* - r^*(r)) dr \\ & + \frac{d\Omega_{k,d-1}}{2\pi G_N L^2} \int_0^{r_{\text{max}}^{\text{vac}}} r^{d-1} (r_{\infty,\text{vac}}^* - r_{\text{vac}}^*(r)) dr \end{aligned} \quad (\text{B.43})$$

and

$$I_{\text{jnt}} = -\frac{\Omega_{k,d-1}}{4\pi G_N} r_m^{d-1} \log \frac{L^2 |f(r_m)|}{R^2 \alpha^2}. \quad (\text{B.44})$$

The meeting point r_m is obtained by numerically solving (4.110) for $\tau = 0$, *i.e.*,

$$r^*(r_m) = r_{\infty}^*. \quad (\text{B.45})$$

Note that here the future and past meeting points are at the same value of the radial coordinate, *i.e.*, $r_m^1 = r_m^2 = r_m$. Further, r_{max} corresponds to the UV cutoff $z = \delta$ in the Fefferman-Graham expansion of the respective metric.

Planar $d = 4$

We proceed by analyzing charged planar black holes. Recall that with $q = 0$, the planar black holes produced $\Delta \mathcal{C}_A = S/(2\pi)$ where S is the entanglement entropy of the thermofield double state (1.21), as discussed in chapter 3. For the curved horizons, there were curvature corrections to this simple result, proportional to inverse powers of RT . Below, we will find that this expression receives corrections even with $k = 0$ in the charged case. Since the curvature vanishes, all of the nontrivial behaviour comes from the finite chemical potential.

As before, we redefine the tortoise coordinate (2.14) in terms of dimensionless variables

$$\begin{aligned} \tilde{f}(x, y) \equiv z^2 f(r) &= \frac{(x^2 - 1)(x - y)(x + y)(x^2 + y^2 + 1)}{x^4} \\ x^*(x, y) \equiv \frac{r^*(r)}{z^2 r_+} &= \int^x \frac{dx}{\tilde{f}(x, y)} = \frac{y^3}{4y^4 - 2y^2 - 2} \log \frac{|x - y|}{x + y} \\ &\quad - \frac{1}{2(y^4 + y^2 - 2)} \log \frac{|x - 1|}{x + 1} + \frac{(y^2 + 1)^{3/2}}{2y^4 + 5y^2 + 2} \tan^{-1} \left(\frac{x}{\sqrt{y^2 + 1}} \right). \end{aligned} \quad (\text{B.46})$$

This allows us to rewrite eq. (B.45) for the meeting points as

$$x^*(x_m, y) = x_{\infty}^* = \frac{\pi (y^2 + 1)^{3/2}}{4y^4 + 10y^2 + 4} \quad (\text{B.47})$$

where $x_m \equiv r_m/r_+$. Given eq. (B.40), we see that x_m is a function of ν only.

There is a subtlety in numerically solving for the meeting point for small values of the charge. The reason is that r_- approaches zero as $r_-^{d-2} = q^2/\omega^{d-2}$ and the tortoise coordinate peaks very sharply around r_- . The meeting point equation $r_\infty^* = r^*(r_m)$ solves for the point in which the asymptotic value of the tortoise coordinate intersects back with the curve. As a consequence of the special form of the curve for small values of r_- , this happens very close to r_- . In fact, in the limit that r_- (or equivalently y) approaches zero, the meeting point can be approximated by (see eq. (4.127) with $\tau = 0$ and $k = 0$):

$$x_m = y \left(1 + \exp \left(-\frac{\pi}{2y^3} + \mathcal{O} \left(\frac{1}{y} \right) \right) \right). \quad (\text{B.48})$$

This means that the corner contribution is nonvanishing in the $r_- \rightarrow 0$ limit despite the fact that r_m approaches zero. In our plots, we have used similar approximations for the cases of small ν .

Motivated by the results of chapter 3 for the neutral case, we will be interested in evaluating the ratio of complexity of formation over entropy. Using eq. (B.42) we find

$$\frac{\Delta \mathcal{C}_{\text{form}}}{S} = \frac{1}{\pi} \left[\frac{\Delta I_{\text{bulk}}}{S} + \frac{I_{\text{jnt}}}{S} \right] \quad (\text{B.49})$$

where

$$\frac{\Delta I_{\text{bulk}}}{S} = \frac{8}{\pi} \frac{x_{\text{max}}^3}{3} + \int_{x_m}^{x_{\text{max}}} \frac{4}{\pi x^3} (-2x^6 + y^4 + y^2) (x_\infty^* - x^*(x, y)) dx \quad (\text{B.50})$$

and

$$\frac{I_{\text{jnt}}}{S} = -\frac{x_m^{d-1}}{\pi} \log \frac{r_+^2 |\tilde{f}(x_m, y)|}{R^2 \alpha^2} = -\frac{x_m^{d-1}}{\pi} \log \left| \frac{g_2(x_m, y) L^2 T^2}{\alpha^2} \right|, \quad (\text{B.51})$$

where we have defined

$$g_2(x, y) = \frac{4\pi^2 (x^2 - 1) (x^2 - y^2) (x^2 + y^2 + 1)}{x^4 (y^2 - 1)^2 (y^2 + 2)^2} \quad (\text{B.52})$$

and the planar black hole complexity of formation is regularized at infinity by subtracting two copies of the vacuum as the construction in chapter 3. A meaningful comparison between the two spacetimes is achieved by placing the cutoff at $x_{\text{max}} \equiv r_{\text{max}}/r_+$ corresponding to $z = \delta$ in the Fefferman-Graham expansion of the respective metric (see *e.g.*, appendix

A.1). We see that the complexity of formation can be naturally split into a sum of two functions

$$\Delta\mathcal{C}_A \equiv \frac{S}{2\pi} \left(F(\nu) + G(\nu) \log \left(\frac{T^2 L^2}{\alpha^2} \right) \right), \quad (\text{B.53})$$

where S is the entropy of the charged AdS black hole, given in eq. (4.95); and $F(\nu)$ and $G(\nu)$ are universal functions that depend only on the ratio ν through their dependence on y as follows

$$\begin{aligned} G(\nu) = G(y) &= -\frac{2}{\pi} x_m^{d-1}, \\ F(\nu) = F(y) &= -\frac{2}{\pi} x_m^{d-1} \log |g_2(x_m, y)| + \frac{16}{\pi} \frac{x_{\max}^3}{3} \\ &\quad - \int_{x_m}^{x_{\max}} \frac{8}{\pi x^3} (2x^6 - y^4 - y^2) (x_{\infty}^* - x^*(x, y)) dx. \end{aligned} \quad (\text{B.54})$$

We note that our result for the complexity of formation depends on the arbitrary parameter α associated to the normalization of null normals. The two functions $G(\nu)$ and $F(\nu)$ are shown in figure B.9 as a function of $\nu = \sqrt{\frac{C_J}{C_T} \frac{\mu}{T}}$. Note that in the limit $\nu \rightarrow 0$, the complexity of formation agrees with the uncharged result found in chapter 3, *i.e.*, $F(\nu \rightarrow 0) \rightarrow 1$ and $G(\nu \rightarrow 0) \rightarrow 0$.

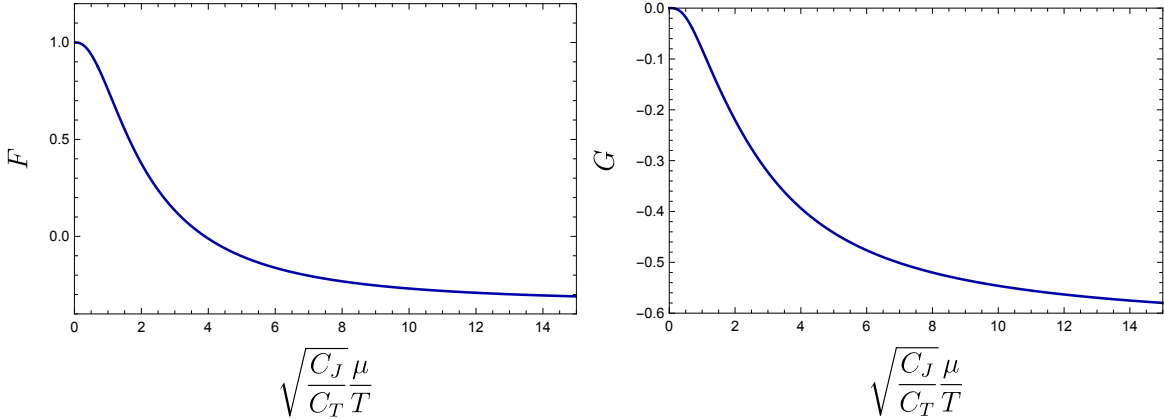


Figure B.9: The functions $F(\nu)$ and $G(\nu)$ defined in eq. (B.54) which appear in the complexity of formation (B.53) for charged planar AdS₅ black holes as a function of $\nu \equiv \sqrt{\frac{C_J}{C_T} \frac{\mu}{T}}$.

As we showed in section 4.4, we can write an expansion of the complexity of formation

for small charge as an expansion in the parameter y , which reads

$$\Delta\mathcal{C}_A = \frac{S}{2\pi} \left(1 + \left(\frac{20}{3\pi} + \frac{4}{\pi} \log \left[\frac{yz}{2} \frac{\alpha R}{L} \right] \right) y^3 + \dots \right). \quad (4.105)$$

In order to probe the limit of extremal black holes, *i.e.*, $T \rightarrow 0$ with μ finite, we investigate eq. (B.53) in this limit. The result is divergent in the $T \rightarrow 0$ limit. To see this we use the expansion for x_m near extremality

$$x_m = 1 - \frac{\epsilon}{2} + \frac{7}{12} \epsilon^2 \log \epsilon - \frac{8\sqrt{2}\pi + 3 + 28 \log(2) - 16\sqrt{2} \cot^{-1}\sqrt{2}}{24} \epsilon^2 + \dots, \quad (B.55)$$

where we have defined $y \equiv 1 - \epsilon$, and evaluate the complexity of formation

$$\Delta\mathcal{C}_A = \frac{2S}{\pi^2} \left(\log \left(\frac{\alpha}{LT} \right) + \frac{1}{3} - \log \left(\frac{\pi}{\sqrt{3}} \right) + \mathcal{O}(RT \log RT) \right). \quad (B.56)$$

Note that the limit $RT \rightarrow 0$ corresponds to the limit $\nu \rightarrow \infty$, so the correction, where we have left implicit a function of z , is in fact a function of ν only. We find that the result diverges logarithmically at low temperatures and the coefficient of the logarithmic divergence is proportional to the entanglement entropy of the system. The result also depends on the arbitrary length scale $\ell \equiv L/\alpha$ associated to the normalization of null normals. We will see in the next subsection that a similar divergence at low temperatures appears using the CV conjecture.

Spherical $d = 4$

The calculation of the complexity of formation for spherical charged black holes follows closely the one of the planar case. However, the two contributions from eq. (B.42) need to be evaluated using the appropriate blackening factor (4.92) with $k = 1$. We show the results for $d = 4$ in figure B.10 and note that again the complexity of formation diverges in the low temperature (near extremal) limit.

As in the planar case, we can find the leading behaviour when RT is small. The expansion for the meeting point reads

$$x_m = 1 - \frac{\epsilon}{2} + \frac{(3z^2 + 7) \epsilon^2 \log(\epsilon)}{4z^2 + 12} - \frac{\epsilon^2 \left(z^2(1 + 12 \log(2)) + 8(z^2 + 2)^{3/2} \tan^{-1}(\sqrt{z^2 + 2}) + 3 + 28 \log(2) \right)}{8(z^2 + 3)} + \mathcal{O}(\epsilon^3 \log \epsilon) \quad (B.57)$$

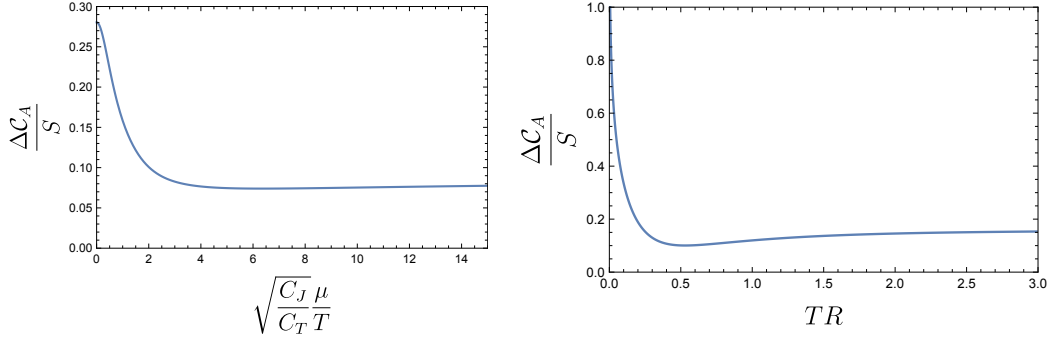


Figure B.10: Complexity of formation for spherical charged black holes in $d = 4$. In the left panel, we fix $RT = \frac{1}{2}$ and we show the dependence on the dimensionless boundary quantity ν . In the right panel, we fix the quantity $\sqrt{\frac{C_J}{C_T}} \mu R = \nu RT = 1$ and show the dependence on RT .

and that of the complexity of formation

$$\begin{aligned} \Delta C_A = & \frac{S}{3\pi^2(3+z^2)} \left(-9(z^2+2) \log\left(\frac{\pi RT z}{z^2+3}\right) - 3(z^2+3) \log\left(\frac{L^2(z^2+3)}{\alpha^2 R^2 z^2}\right) + z^2 \log 64 \right. \\ & \left. + (z^2+3)(3(\pi z-2)z^2+2) - 6z^2(z^2+2)^{3/2} \tan^{-1}(\sqrt{z^2+2}) + \mathcal{O}(RT \log RT) \right). \end{aligned} \quad (\text{B.58})$$

Notice that as $z \rightarrow 0$, we recover the planar result in eq. (B.56). However, unlike in the planar case, now the overall coefficient that controls the divergence for small temperatures depends on z , which in turn depends on the product of the boundary size and the chemical potential. The exact relation is obtained from eq. (4.119), which leads to the relation

$$z = \frac{3\sqrt{2}}{\sqrt{40 \left(\sqrt{\frac{C_J}{C_T}} \mu R \right)^2 - 9}}. \quad (\text{B.59})$$

where C_J and C_T are the coefficients in the two point function of stress tensors or currents, respectively, see eq. (4.100). The value of chemical potential for which z becomes imaginary in this expression exactly matches the value for which the extremal black holes cease to exist (see discussion at the beginning of this appendix). We stress once more that the conclusion that the complexity of formation diverges in the zero temperature limit holds also in the spherical geometry.

It is also interesting to write the first few terms in a small charge (small y) expansion. In fact, we will also expand our results for small z (large temperatures). In order to compare

the results for charged black holes to those of neutral black holes found in chapter 3, we express for spherical neutral black holes in $d = 4$, as an expansion in small z , (large horizon radius)

$$\left. \frac{\Delta \mathcal{C}_A}{S} \right|_{\mu=0} = \frac{1}{2\pi} + \frac{z^3}{\pi} - \frac{9z^4}{16\pi} + \mathcal{O}(z^6) = \frac{1}{2\pi} + \frac{1}{\pi^4} \frac{1}{(TR)^3} - \frac{9}{16\pi^5} \frac{1}{(TR)^4} + \mathcal{O}\left(\frac{1}{(TR)^6}\right). \quad (\text{B.60})$$

The dependence on z^3 in the expansion comes from the vacuum contribution to the complexity of formation for the spherical geometry, as can be seen from the $L^3 \delta_{k,1}$ dependence in equation (3.14). For charged black holes, a double expansion in y and z reads

$$\begin{aligned} \frac{\Delta \mathcal{C}_A}{S} &= \left(\frac{1}{2\pi} + \frac{z^3}{\pi} - \frac{9z^4}{16\pi} \right) - \left(\frac{9z^2}{8\pi} - \frac{3z^4}{16\pi} \right) y^2 \\ &+ \left(\frac{2}{3\pi^2} \left(5 + 3 \log \frac{R\alpha y z}{2L} \right) - \frac{z^2}{\pi^2} + \frac{z^4}{2\pi^2} \right) y^3 + \mathcal{O}(z^5, y^4). \end{aligned} \quad (\text{B.61})$$

We see by comparing this expression to (B.60) that the neutral limit is recovered in the zero charge limit $y \rightarrow 0$.

B.3.2 Small Hyperbolic Black Holes

We briefly comment below on the time evolution of uncharged small hyperbolic black holes as discussed in appendix A.3. For hyperbolic black holes with $r_h < L$, the mass parameter is negative, as can be seen from eqs. (2.4) and (2.7). In this case, the causal structure changes, with the appearance of an inner Cauchy horizon, and becomes similar to the one of charged black holes, as in figure 4.8. As was already pointed out in appendix A.3, the CA calculation indicates that for small uncharged hyperbolic black holes the complexity does not change with time. In this subsection, we present an alternative argument for that statement using the neutral limit of charged black holes.

Consider the late time limit of the rate of change in complexity in eq. (4.118). In general, the zero charge limit is obtained by the requirement that the chemical potential vanishes. For small hyperbolic black holes, this limit does not coincide with the one in which the variable y vanishes. The expression for the chemical potential in general d for $k = -1$ can be obtained from the multiplication of $h(y, z)$ and $\bar{h}(y, z)$ in eq. (4.103), and it vanishes for

$$\mu = 0 \quad \rightarrow \quad z = \sqrt{\frac{1 - y^d}{1 - y^{d-2}}}. \quad (\text{B.62})$$

Evaluating eq. (4.118) for this value of z , namely, at zero chemical potential, results in a vanishing time derivative of \mathcal{C}_A for small uncharged hyperbolic black holes.

B.4 Ambiguities in the Action Calculations

It was argued in [63] that the null boundary terms in eq. (2.10), associated with null boundary surfaces and null joints, introduce certain ambiguities in the numerical value of the gravitational action. In this appendix we consider the influence of these ambiguities on the time dependence of complexity of neutral black holes studied in section 4.1 using the CA conjecture. The influence of the various ambiguities on the complexity of formation was studied in appendix A.4 and we will follow the discussion there closely. In particular it was demonstrated there that a large class of ambiguities are essentially equivalent to adding a constant to the null joint term a . This amounts to changing a in eq. (2.10) to

$$a_{\text{new}} = a + a_0. \quad (\text{B.63})$$

This is indeed the effect of multiplying the function $\Phi(x)$, which determines the position of the null surface according to $\Phi(x) = 0$, by a constant. A similar effect is achieved by a constant rescaling of the parameter λ , which runs along the null generators. Finally, this is also equivalent to changing the normalization constant α , which fixes the null normal normalization at the asymptotic boundary according to $\hat{k} \cdot \hat{\tau} = \pm\alpha$. We reiterate here, that these ambiguities do not affect the late time rate of growth of holographic complexity. In subsection B.4.1 we explore the influence of a constant a_0 on the action calculation. In appendix B of [63] it was argued that the reparametrization ambiguity can be avoided by including a certain boundary counterterm. We explore this possibility in subsection B.4.2.

B.4.1 Influence of a Constant a_0

When a_0 is a fixed constant, the joint term at $r = r_m$ in our calculations in section 4.1 is modified by

$$\Delta I_{\text{jnt}} = a_0 \frac{\Omega_{k,d-1}}{8\pi G_N} r_m^{d-1}. \quad (\text{B.64})$$

Taking the time derivative and using eq. (4.23) yields

$$\Delta \left(\frac{d\mathcal{C}_A}{d\tau} \right) = -a_0 \frac{\Omega_{k,d-1}(d-1)}{16\pi^2 G_N} \frac{L}{R} r_m^{d-2} f(r_m). \quad (\text{B.65})$$

This shift in the corner term is equivalent to changing the normalization constant α in eq. (4.41) to $\alpha_N = e^{a_0/2} \alpha$. Note that the term in eq. (B.65) also vanishes in the late time limit since r_m approaches the horizon radius r_h there and so $f(r_m)$ vanishes as $\tau \rightarrow \infty$. The modification does however contribute to the rate of change of complexity at earlier

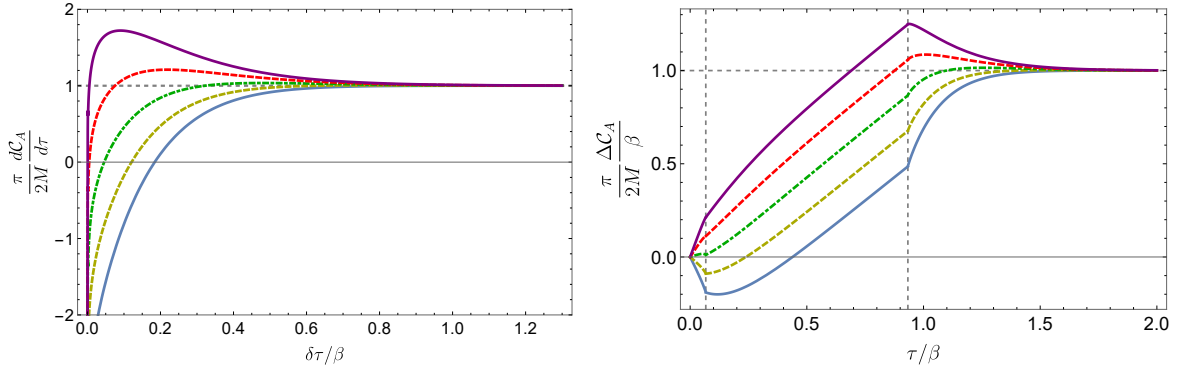


Figure B.11: The rate of change of the complexity (left) and its average value (right) as a function of time for spherical black holes ($k = 1$) in $d = 4$ with $r_h = 2L$ for different values of the constant a_0 – $a_0 = -4$ (blue, solid), $a_0 = -2$ (yellow, dashed), $a_0 = 0$ (green, dot-dashed), $a_0 = 2$ (red, dashed) and $a_0 = 4$ (purple, solid). We have set $\alpha = L/R$ for simplicity.

times. The influence of a constant a_0 on the rate of change of complexity and its average for a spherical black hole in $d = 4$ is studied numerically in figure B.11. We note that the averaging procedure suggested in eq. (4.35) somewhat reduces the effect of changing a_0 , however the bound is still approached from above at late times.

B.4.2 Boundary Counterterm

In this subsection we discuss the effect of adding the boundary counterterm suggested in appendix B of [63] for eternal black hole backgrounds (2.1) on the rate of change of complexity. This counterterm makes the action invariant under the reparametrization of null surfaces. For simplicity we set in this subsection $R = L$. The counterterm for each null surface is given by

$$\Delta I_\Sigma = \frac{1}{8\pi G_N} \int_\Sigma d\lambda d^{d-1} \sqrt{\gamma} \Theta \log(\tilde{L}|\Theta|), \quad (\text{B.66})$$

where γ_{AB} is the cross-sectional metric of a bundle of null generators, Θ is the expansion parameter given by $\Theta = \partial_\lambda \log \sqrt{\gamma}$ and \tilde{L} is an arbitrary length scale.⁵ We take for simplicity an affine parametrization

$$\lambda = \frac{r}{\alpha}. \quad (\text{B.67})$$

⁵The choice of the length scale corresponds to the ambiguous constant c in eq. (B4) of ref. [63].

However, keep in mind that the total action with the counterterm does not depend on the parametrization of null surfaces. In this parametrization, the expansion takes the form

$$\Theta = \frac{(d-1)\alpha}{r}. \quad (\text{B.68})$$

Taking into account that there are two future null boundaries and two past ones, the counterterm (B.66) at $t > t_c$ becomes

$$\begin{aligned} \Delta I_\Sigma &= \frac{(d-1)\Omega_{k,d-1}}{4\pi G_N} \int_0^{r_{max}} dr r^{d-2} \log \frac{(d-1)\alpha\tilde{L}}{r} + \frac{(d-1)\Omega_{k,d-1}}{4\pi G_N} \int_{r_m}^{r_{max}} dr r^{d-2} \log \frac{(d-1)\alpha\tilde{L}}{r} \\ &= \frac{\Omega_{k,d-1}}{2\pi G_N} r_{max}^{d-1} \left(\log \frac{(d-1)\alpha\tilde{L}}{r_{max}} + \frac{1}{d-1} \right) - \frac{\Omega_{k,d-1}}{4\pi G_N} r_m^{d-1} \left(\log \frac{(d-1)\alpha\tilde{L}}{r_m} + \frac{1}{d-1} \right). \end{aligned} \quad (\text{B.69})$$

The time derivative of the counterterm is then readily evaluated using the relation (4.23) and found to be

$$\frac{d\Delta I_\Sigma}{dt} = -\frac{(d-1)\Omega_{k,d-1}r_m^{d-2}}{8\pi G_N} f(r_m) \log \left(\frac{r_m}{(d-1)\alpha\tilde{L}} \right). \quad (\text{B.70})$$

If we take another parametrization of null surfaces, the expression (B.70) changes. However, the total action is invariant under reparametrization. The rate of change of complexity with the counterterm is given by the following expression for any parametrization:

$$\frac{d\mathcal{C}_A}{dt} = \frac{1}{\pi} \left(2M + \frac{\Omega_{k,d-1}(d-1)r_m^{d-2}f(r_m)}{16\pi G_N} \left[\log |f(r_m)| - 2 \log \left(\frac{r_m}{(d-1)\tilde{L}} \right) \right] \right). \quad (\text{B.71})$$

Note that the α -dependence which appeared in eq. (4.27) is totally canceled when including the boundary counterterm. We see from this expression that the counterterm does not resolve the divergence in $\frac{d\mathcal{C}_A}{dt}$ at times shortly after the critical time t_c which we observed in section 4.2 for $d > 2$. In fact, eq. (B.71) behaves shortly after t_c as

$$\frac{d\mathcal{C}_A}{dt} \sim \frac{\Omega_{k,d-1}d(d-1)\omega^{d-2}}{16\pi^2 G_N} \log r_m + \text{finite}, \quad (\text{B.72})$$

where r_m is very close to $r = 0$ at times right after t_c .

Appendix C

Appendices to chapter 6

C.1 Counterterm for the Null Boundaries

As originally discussed in [63], the contributions to the gravitational action from the null boundaries give rise to various ambiguities. In particular, I_{WDW} will depend on the parametrization of the null boundaries and so one must choose a ‘universal’ prescription which allows the comparison of this quantity evaluated for arbitrary boundary time slices in arbitrary bulk backgrounds. However, a simple alternative, which was also suggested in [63], is to add the following counterterm to the action on the null boundaries,

$$I_{\text{ct}} = \frac{1}{8\pi G_N} \int_{B'} d\lambda d^{d-1}\theta \sqrt{\gamma} \Theta \log(\ell_{\text{ct}} \Theta) , \quad (\text{C.1})$$

where ℓ_{ct} is some length scale, and Θ is the expansion scalar of the null boundary generators, *i.e.*,

$$\Theta = \partial_\lambda \log \sqrt{\gamma} . \quad (\text{C.2})$$

The expansion Θ only depends on the intrinsic geometry of the null boundaries and so this surface term (C.1) plays no role in producing a well-defined variational principle for the gravitational action (2.10). However, as shown in [63], this counterterm ensures that the action is independent of the parametrization of the null boundaries. While adding this surface term does not modify the key features of holographic complexity in stationary spacetimes, it was argued in chapter 5 and in the main text here that the counterterm is essential when applying the CA proposal to dynamical spacetimes.

Here we examine in detail the effect of adding the counterterm (C.1) to the gravitational action for the calculations in section 6.2. In particular, we will confirm that the inclusion

of this term removes the dependence on the parametrization of the null boundaries, *i.e.*, on the normalization of the null normal vectors. We also examine the role of the scale ℓ_{ct} appearing in eq. (C.1) in the UV divergences and in the transient behaviour in the growth of the holographic complexity.

Let us begin by reviewing¹ the computation of the expansion (C.2) on the past null boundary on the right side of the WDW patch, *i.e.*, the past boundary which crosses the shock wave in figure 6.1. Recall that the null normals are actually tangent vectors along the null boundaries, *i.e.*, $k^\mu \partial_\mu = \partial_\lambda$, and so Θ is determined by the normalization of these vectors. For the past boundary extending to the right asymptotic AdS boundary, we can write the null normal (6.37) as

$$k_\mu^p dx^\mu = H(r, v) \left(-dv + \frac{2}{F(r, v)} dr \right) \quad (\text{C.3})$$

where $F(r, v)$ is the metric function appearing in eq. (5.1) and $H(r, v)$ takes the form

$$H(r, v) = \alpha \mathcal{H}(r - r_s) + \tilde{\alpha} (1 - \mathcal{H}(r - r_s)) , \quad (\text{C.4})$$

Here \mathcal{H} denotes the Heaviside function and we leave $\tilde{\alpha}$ unspecified for now. Further, we have $dr/d\lambda = H(r, v)$ and hence the null expansion (C.2) becomes

$$\Theta = \frac{H(r, v)}{r^{d-1}} \frac{d}{dr} (r^{d-1}) = \frac{(d-1)H(r, v)}{r} . \quad (\text{C.5})$$

Hence the counterterm contribution (C.1) for $\mathcal{B}_{\text{past}}$ can be written as

$$I_{\text{ct}}^{(1)} = \frac{\Omega_{k,d-1}(d-1)}{8\pi G_N} \int_{r_{\min}}^{r_{\max}} dr r^{d-2} \log \left(\frac{(d-1)\ell_{\text{ct}}H(r, v)}{r} \right) , \quad (\text{C.6})$$

where we replaced $d\lambda = dr/H(r, v)$. The upper limit of the radial integral r_{\max} is the position of the UV regulator surface. We set the lower limit $r_{\min} = r_m$ where r_m is the position of the intersection of the two past null boundaries, with the understanding that we set $r_m = 0$ when these boundaries end on the past singularity. Hence using eq. (C.4), the integral in eq. (C.6) yields

$$\begin{aligned} I_{\text{ct}}^{(1)} &= \frac{\Omega_{k,d-1}}{8\pi G_N} r_{\max}^{d-1} \left[\log \left(\frac{(d-1)\alpha\ell_{\text{ct}}}{r_{\max}} \right) + \frac{1}{d-1} \right] \\ &\quad - \frac{\Omega_{k,d-1}}{8\pi G_N} r_m^{d-1} \left[\log \left(\frac{(d-1)\tilde{\alpha}\ell_{\text{ct}}}{r_m} \right) + \frac{1}{d-1} \right] + \frac{\Omega_{k,d-1}}{8\pi G_N} r_s^{d-1} \log \left(\frac{\tilde{\alpha}}{\alpha} \right) . \end{aligned} \quad (\text{C.7})$$

¹See section 5.1.3 for further details.

Upon substituting $\tilde{\alpha}$ as given in eq. (6.40), the above result becomes the expression given in eq. (6.49).

The future null boundary on the left side of the WDW patch also crosses the shock wave at early times, *i.e.*, for $t_L < t_{L,c2}$. Hence it is straightforward to carry out the above analysis with the corresponding null normal (6.42) and we find that the counterterm contribution becomes

$$I_{\text{ct}}^{(\text{II})} = \frac{\Omega_{k,d-1}}{8\pi G_N} r_{\text{max}}^{d-1} \left[\log\left(\frac{(d-1)\alpha\ell_{\text{ct}}}{r_{\text{max}}}\right) + \frac{1}{d-1} \right] + \frac{\Omega_{k,d-1}}{8\pi G_N} r_b^{d-1} \log\left(\frac{\hat{\alpha}}{\alpha}\right). \quad (\text{C.8})$$

Here we have assumed that we are only considering positive times when this boundary ends at $r = 0$ (*i.e.*, at the future singularity). Further, for $t_L > t_{L,c2}$, we would drop the second term above since this boundary no longer crosses the shock wave. Upon substituting $\hat{\alpha}$ from eq. (6.44), this result matches that given in eq. (6.50).

Of course, it is also straightforward to evaluate the counterterm contributions for the null boundaries which are parallel to the trajectory of the null shell — see figure 6.1. For the past null boundary extending to the left asymptotic AdS boundary, we find

$$I_{\text{ct}}^{(\text{III})} = \frac{\Omega_{k,d-1}}{8\pi G_N} r_{\text{max}}^{d-1} \left[\log\left(\frac{(d-1)\alpha\ell_{\text{ct}}}{r_{\text{max}}}\right) + \frac{1}{d-1} \right] - \frac{\Omega_{k,d-1}}{8\pi G_N} r_m^{d-1} \left[\log\left(\frac{(d-1)\alpha\ell_{\text{ct}}}{r_m}\right) + \frac{1}{d-1} \right], \quad (\text{C.9})$$

where again, we drop the second term for $t_L < t_{L,c1}$, *i.e.*, in the regime where this boundary ends on the past singularity. Finally, for the future null boundary on the right side of the WDW patch, we have

$$I_{\text{ct}}^{(\text{IV})} = \frac{\Omega_{k,d-1}}{8\pi G_N} r_{\text{max}}^{d-1} \left[\log\left(\frac{(d-1)\alpha\ell_{\text{ct}}}{r_{\text{max}}}\right) + \frac{1}{d-1} \right]. \quad (\text{C.10})$$

Here we have assumed that we are in a regime where this boundary surface ends at the future singularity, as with the left future boundary in eq. (C.8).

To confirm that the inclusion of the counterterm (C.1) removes the dependence on the parametrization of the null boundaries, we should combine the four counterterm contributions given above with the joint contributions for the corresponding WDW patch. In the main text, we have already evaluated the joint contributions at $r = r_s$, r_b and r_m in eqs. (6.39), (6.43) and (6.47), respectively. Here we are indicating the expressions for these

joint contributions before $\tilde{\alpha}$ and $\hat{\alpha}$ were fixed.² We must also include the joint contributions arising where the null boundaries intersect the UV regulator surface at $r = r_{\max}$,³ and using the prescription given in [63, 65], we find

$$I_{\text{joint}}^{\text{UV}} = -\frac{\Omega_{k,d-1}}{4\pi G_N} r_{\max}^{d-1} \left[\log \frac{\alpha}{\sqrt{f_1(r_{\max})}} + \log \frac{\alpha}{\sqrt{f_2(r_{\max})}} \right], \quad (\text{C.11})$$

where the first (second) term corresponds to the contribution from the UV joint at the left (right) asymptotic boundary.

Hence now combining the counterterm and the joint contributions, we find

$$\begin{aligned} I_{\text{ct}}^{\text{tot}} + I_{\text{joint}}^{\text{tot}} &= \frac{\Omega_{k,d-1}}{4\pi G_N} r_{\max}^{d-1} \left[\log \left(\frac{(d-1)^2 \ell_{\text{ct}}^2 \sqrt{f_1(r_{\max}) f_2(r_{\max})}}{r_{\max}^2} \right) + \frac{2}{d-1} \right] \\ &\quad - \frac{\Omega_{k,d-1}}{4\pi G_N} r_m^{d-1} \left[\log \left(\frac{(d-1) \ell_{\text{ct}}}{r_m} \sqrt{|f_1(r_m)|} \right) + \frac{1}{d-1} \right] \\ &\quad + \frac{\Omega_{k,d-1}}{8\pi G_N} r_s^{d-1} \log \left(\frac{f_1(r_s)}{f_2(r_s)} \right) - \frac{\Omega_{k,d-1}}{8\pi G_N} r_b^{d-1} \log \left(\frac{f_1(r_b)}{f_2(r_b)} \right). \end{aligned} \quad (\text{C.12})$$

Hence we see that the combined result is completely independent of the normalization constants appearing in the null normals, *i.e.*, α , $\tilde{\alpha}$ and $\hat{\alpha}$. Of course, this is simply an explicit verification that introducing the counterterm (C.1) eliminates the dependence of I_{WDW} on the parametrization of the null boundaries [63].

At this point, we reiterate that we have left $\tilde{\alpha}$ and $\hat{\alpha}$ arbitrary above, rather than fixing them with the conditions, in eqs. (6.40) and (6.44), that the null boundaries are affinely parametrized across the shock wave. Hence we emphasize that the elimination of these normalization constants in eq. (C.12) was independent of any particular choice we might make for the parametrization of the correspond boundaries. We might also note that if we choose $\tilde{\alpha} = \alpha$ and $\hat{\alpha} = \alpha$ (*e.g.*, as was done in [77, 78, 173]), the counterterm contributions at the two crossing points (*i.e.*, $r = r_s$ and $r = r_b$) vanish in eqs. (C.7) and (C.8). There remains a contribution at the meeting point $r = r_m$ coming from eqs. (C.7) and (C.9). However, at late times, these terms make a vanishing contribution to the growth rate and so with this choice (for $\tilde{\alpha}$ and $\hat{\alpha}$), the joint terms alone capture many of the essential

²Recall that for general values of the normalization constants, $\tilde{\alpha}$ and $\hat{\alpha}$, the joint contributions in eqs. (6.39) and (6.43) account for the fact that κ is nonvanishing as the corresponding null boundaries cross the shock wave as discussed in chapter 5.

³There is no contribution from the joints where the null boundaries terminate on the future or past singularities because the area of these joints at $r = 0$ vanishes.

features of the time evolution of the complexity growth, *e.g.*, as can be seen in comparing the results in [77] and [195].⁴ It is also straightforward to show in the present context of a shock wave propagating into an eternal black hole background, that the key results for the time evolution of the complexity are reproduced with $\tilde{\alpha} = \alpha = \hat{\alpha}$. However, the transient early time behaviour again exhibits some differences from the results in the main text where the counterterm is included.

UV divergences with counterterm

One of the interesting effects of adding the counterterm (2.11) to the action of the WDW patch is that it seems to change the structure of the UV divergences in the corresponding holographic complexity, as first noted in [190]. We would like to review these changes and the leading UV divergences carefully here because it is relevant for the comparison of the holographic complexity with the complexity evaluated in quantum field theories [38, 39]. The latter comparison is considered in more detail in the main text in section 6.3.

Of course, the action of the WDW patch diverges because this region of spacetime extends all the way to the asymptotic AdS boundaries, *e.g.*, as in figure 6.1. Hence we regulate our calculations as usual with a UV regulator surface at $r = r_{\max}$,⁵ *e.g.*, see [136, 137, 229] and also the discussion for holographic complexity in [65] and chapter 3. Of course, this radius can be expressed in terms of the short-distance cutoff δ in the boundary theory, *e.g.*, for the present Vaidya geometries (5.1), we have

$$r_{\max} = \frac{L^2}{\delta} \left(1 - \frac{k}{4} \frac{\delta^2}{L^2} + \dots \right). \quad (\text{C.13})$$

⁴Both references study the complexity growth rate in hyperscaling violating geometries, but [77] does not introduce the counterterm and makes the choice $\tilde{\alpha} = \alpha = \hat{\alpha}$, while [195] uses the counterterm.

⁵Let us add that there are number of variations of this regulator procedure that one might consider [65]. For example, one might: a) choose the null boundaries of the WDW patch to be anchored to the desired time slice on the UV regulator surface; b) choose the null boundaries to be anchored to the time slice on the asymptotic AdS boundary (*i.e.*, $r \rightarrow \infty$) but terminate the WDW patch at $r = r_{\max}$, including the GHY surface term on the small (timelike) portion of the regulator surface that becomes part of the boundary; and c) proceed as in (b) and also include the usual AdS boundary counterterms [229], as well as the GHY surface term, on the portion of the boundary at $r = r_{\max}$. These different choices will not change the universal features of the holographic complexity but we note that in fact, the UV divergences will agree for procedures (a) and (c). Further, we are implicitly using procedure (a) in the following, as in [65, 190].

Hence the leading UV divergences in the holographic complexity take the form [65]

$$\tilde{\mathcal{C}}_A^{\text{UV}} = \frac{I_{\text{grav}}^{\text{UV}}}{\pi} \simeq \frac{L^{d-1}}{4\pi^2 G_N} \frac{\mathcal{V}(\Sigma)}{\delta^{d-1}} \left[\log\left(\frac{L}{\alpha\delta}\right) - \frac{1}{d-1} \right] + \dots, \quad (\text{C.14})$$

where $\mathcal{V}(\Sigma)$ is the total volume of the boundary time slice Σ , *e.g.*, $\mathcal{V}(\Sigma) = 2\Omega_{k,d-1}L^{d-1}$, including both the left and right boundaries, for the constant time slices used in our calculations. The ellipsis indicates the subleading divergences which will involve integrals of geometric curvatures over the boundary time slice. Note that as indicated in eq. (C.14), we are only considering the contributions from eq. (2.10)⁶ and so we have adopted the notation of eq. (6.108) since we are not including the counterterm contribution. An interesting feature of the UV divergences in eq. (C.14) is the appearance of the normalization constant α in the logarithmic factor. We might add that this factor is essential for the interpretation of this result as holographic complexity since consistency demands that the sum of the contributions in eq. (C.14) must be positive in order for $\tilde{\mathcal{C}}_A$ to be positive [65].

However, the counterterm contributions must remove this α dependence in eq. (C.14). Indeed combining the leading contributions from eqs. (C.7–C.10), we find

$$[\mathcal{C}_A^{\text{UV}}]_{\text{ct}} = \frac{L^{d-1}}{4\pi^2 G_N} \frac{\mathcal{V}(\Sigma)}{\delta^{d-1}} \left[\log\left(\frac{(d-1)\alpha\ell_{\text{ct}}\delta}{L^2}\right) + \frac{1}{d-1} \right] + \dots, \quad (\text{C.15})$$

and then combining these UV contributions with eq. (C.14) yields

$$\mathcal{C}_A^{\text{UV}} = \tilde{\mathcal{C}}_A^{\text{UV}} + [\mathcal{C}_A^{\text{UV}}]_{\text{ct}} = \frac{L^{d-1}}{4\pi^2 G_N} \frac{\mathcal{V}(\Sigma)}{\delta^{d-1}} \log\left(\frac{(d-1)\ell_{\text{ct}}}{L}\right) + \dots. \quad (\text{C.16})$$

We emphasize that the counterterm removes the α dependence from this leading divergence but also from all of the subleading divergences, as is evident from eq. (C.12). However, the ambiguity which α introduced in eq. (C.16) has been replaced here by the ambiguity in specifying the counterterm scale ℓ_{ct} .⁷

Let us add that the AdS scale L appears in two places in eq. (C.16). The first factor, L^{d-1}/G_N , yields the central charge C_T of the boundary theory, *e.g.*, see [230]. However, the factor of L in the argument of the logarithm must be absorbed by ℓ_{ct} in order for the final result (which is a quantity in the boundary theory) to be independent of the AdS scale.⁸

⁶In particular, only the bulk integral and the joint at the cutoff surface are contributing to these UV divergences.

⁷We note that this ambiguity was implicitly fixed in [190] by setting $\ell_{\text{ct}} = L$.

⁸It is straightforward to confirm that this factor of L is the AdS scale, and not the boundary curvature scale, following the discussion in chapter 4 and [231].

C.2 Complexity=Action in Higher Dimensions

In this appendix, we examine higher dimensional examples of a shock wave in an eternal black hole geometry using the CA proposal. In section 6.2, we focused on the simple case of $d = 2$ in detail since much of the analysis could be carried out analytically. Here, we begin by examining the case of $d = 4$ (*i.e.*, five bulk dimensions) in detail. There will be some interesting differences when comparing the behaviour of the AdS₅ black holes here to the BTZ black holes in section 6.2, as the sign of $t_{c2} - t_{c1}$ in eq. (6.60) changes depending on the parameters t_w (how early the shock wave is inserted) and w (how heavy the shock wave is). As in section 6.2, we examine how the CA proposal is affected when we include or do not include the null surface counterterm (2.11) in the WDW action. We conclude the appendix by presenting some results for the complexity of formation (with and without the counterterm) for general d in the case of planar horizons (*i.e.*, $k = 0$).

From eqs. (6.7) and (6.12), the parameters describing the $d = 4$ boundary state dual to the AdS₅ black hole are

$$\begin{aligned} M &= \frac{3\Omega_{k,3}}{16\pi G_N} \omega^2, & \omega^2 &= r_h^2 \left(\frac{r_h^2}{L^2} + k \right), \\ T &= \frac{1}{2\pi r_h} \left(2 \frac{r_h^2}{L^2} + k \right), & S &= \frac{\Omega_{k,3}}{4G_N} r_h^3. \end{aligned} \quad (\text{C.17})$$

From eqs. (6.8) and (6.9), the blackening factor becomes

$$\text{for all } v_L \ \& \ v_R < -t_w : \quad F(r, v) = f_1(r) = \frac{r^2}{L^2} + k - \frac{\omega_1^2}{r^2}, \quad (\text{C.18})$$

$$v_R > -t_w : \quad F(r, v) = f_2(r) = \frac{r^2}{L^2} + k - \frac{\omega_2^2}{r^2}. \quad (\text{C.19})$$

Then following eqs. (6.13) and (6.14), the tortoise coordinates in the different regions of the black hole geometry become: for all v_L and $v_R < -t_w$,

$$\begin{aligned} r_1^*(r) &= \frac{L^2}{2(2r_{h,1}^2 + kL^2)} \left[2\sqrt{r_{h,1}^2 + kL^2} \tan^{-1} \left(\frac{r}{\sqrt{r_{h,1}^2 + kL^2}} \right) \right. \\ &\quad \left. - \pi \sqrt{r_{h,1}^2 + kL^2} + r_{h,1} \log \left(\frac{|r - r_{h,1}|}{r + r_{h,1}} \right) \right]; \end{aligned} \quad (\text{C.20})$$

and $v_R > -t_w$,

$$r_2^*(r) = \frac{L^2}{2(2r_{h,2}^2 + kL^2)} \left[2\sqrt{r_{h,2}^2 + kL^2} \tan^{-1} \left(\frac{r}{\sqrt{r_{h,2}^2 + kL^2}} \right) - \pi\sqrt{r_{h,2}^2 + kL^2} + r_{h,2} \log \left(\frac{|r - r_{h,2}|}{r + r_{h,2}} \right) \right]; \quad (\text{C.21})$$

Recall that the integration constants are chosen here such that $\lim_{r \rightarrow \infty} r_{1,2}^*(r) = 0$. Using the dimensionless coordinates in eq. (6.16), eq. (6.17), the ratios of the masses and entropies before and after the shock wave become in $d = 4$

$$\frac{M_2}{M_1} = w^4 \frac{(1 + kz^2)}{(1 + kz^2w^2)} \quad \text{and} \quad \frac{S_2}{S_1} = w^3. \quad (\text{C.22})$$

Early Time Analysis

One interesting difference for higher dimensional AdS black holes, with respect to (three-dimensional) BTZ black holes, is that the spacetime singularities ‘bow’ into the Penrose diagram [198]. As a result, when studying complexity=action for such (unperturbed) black holes (*i.e.*, with $d \geq 3$), there is an initial period during which the WDW patch touches both the future and past singularities and the holographic complexity remains constant, as discussed in [34] and chapter 4. This geometric property also produces some interesting new features in the early time evolution of the holographic complexity when we introduce shock waves in these higher dimensional black holes.

In section 6.2, we introduced two critical times in the evolution of the CA complexity for $t \geq 0$. The critical time t_{c1} in eq. (6.55) determines the time when the WDW patch lifts off of the past singularity (*i.e.*, when $r_m = 0$). Hence for $t > t_{c1}$, r_m is a dynamical variable. The critical time t_{c2} in eq. (6.58) determines the time when the point where the shock wave hits the future singularity just moves inside of the WDW patch (*i.e.*, when $r_b = 0$). That is, for $t > t_{c2}$, the (left) future null boundary of the WDW patch does not cross the shock wave and so r_b is a dynamical variable only for $t < t_{c2}$. For the BTZ black hole discussed in section 6.2, t_{c2} was always equal to $2t_w$ and the difference between the critical times $t_{c2} - t_{c1} > 0$ was always positive, which meant that there existed a regime with both r_m and r_b as dynamical variables. For the higher dimensional black holes, this is not always the case, and we will derive the relevant expressions below in this appendix.

Let us begin by evaluating the time derivative of the holographic complexity at $t = 0$. Note that from eq. (6.58), the condition that $t_{c2} > 0$ implies that $t_w > -2r_1^*(0)$. Therefore,

if the shock wave is not sent early enough (*i.e.*, the latter inequality is not satisfied), only r_s is a dynamical variable in the time derivative of complexity, which we will call regime (a). If $t_w > -2r_1^*(0)$, then we have to consider both r_b as well as r_s as dynamical variables. This was always the case for the BTZ black holes studied in section 6.2. Here we denote this regime by (b). The rate of change of the holographic complexity in these two regimes reads

$$\frac{d\mathcal{C}_A^{(a)}}{dt} = \frac{M_2}{\pi} - \frac{M_1}{\pi} \frac{f_2(r_s)}{f_1(r_s)} - \frac{M_2}{2\pi} \frac{r_s^{d-2}}{\omega_2^{d-2}} f_2(r_s) \log \frac{f_1(r_s)}{f_2(r_s)}, \quad (\text{C.23})$$

$$\begin{aligned} \frac{d\mathcal{C}_A^{(b)}}{dt} = & \frac{M_2}{\pi} \left(1 + \frac{f_1(r_b)}{f_2(r_b)} \right) - \frac{M_1}{\pi} \left(1 + \frac{f_2(r_s)}{f_1(r_s)} \right) + \\ & + \frac{M_1}{2\pi} \frac{r_b^{d-2}}{\omega_1^{d-2}} f_1(r_b) \log \frac{f_2(r_b)}{f_1(r_b)} - \frac{M_2}{2\pi} \frac{r_s^{d-2}}{\omega_2^{d-2}} f_2(r_s) \log \frac{f_1(r_s)}{f_2(r_s)}. \end{aligned} \quad (\text{C.24})$$

Now we consider the rate of complexity growth at $t = 0$ in more detail for AdS₅ spherical $k = 1$ black holes, with z defined in eq. (6.16) given by $z = 1/w$, which means that the smaller black hole with horizon radius $r_{h,1}$ has the smallest stable horizon radius, right at the Hawking-Page transition. Of course, the overall conclusions are independent of the specific value of z , but we will focus on this example for concreteness. In the left panel of figure C.1, we have a very light shock, with $w = 10^{-6}$, and we show the dependence on the perturbation time t_w . The vertical dashed line represents the time $t_w = -2r_1^*(0)$ (*i.e.*, $t_{c2} = 0$), which separates between regimes (a) and (b) in eqs. (C.23) and (C.24). When the shock wave is inserted at very early times (*i.e.*, for large values of t_w), the initial rate of change becomes the difference of masses $\frac{M_2 - M_1}{\pi}$ (represented by the horizontal dashed red line). The right panel in figure C.1 shows the analogous results for a heavier shock wave with $w = 2$. For the heavier shocks, the critical time t_{c2} grows in units of $1/T_2$ as w grows, and once again the early growth rate approaches $\frac{M_2 - M_1}{\pi}$ for early enough shock waves.

At $t_w \rightarrow 0$, r_s approaches the AdS boundary. Therefore, if we expand eq. (C.23) in inverse powers of r_s , we obtain

$$\left. \frac{d\mathcal{C}_A^{(a)}}{dt} \right|_{t \rightarrow 0} = \frac{M_2 - M_1}{2\pi} + \mathcal{O}\left(\frac{1}{r_s^4}\right). \quad (\text{C.25})$$

For both spherical and planar black holes, the leading order contribution from eq. (C.26) is simply $(M_2 - M_1)/2$. In contrast, for large t_w , it approaches the difference of masses as r_s and r_b approach $r_{h,2}$ and $r_{h,1}$ respectively,

$$\left. \frac{d\mathcal{C}_A^{(b)}}{dt} \right|_{t \rightarrow 0} = \frac{M_2 - M_1}{\pi} + \mathcal{O}\left(T_2 t_w e^{-T_2 t_w}\right). \quad (\text{C.26})$$

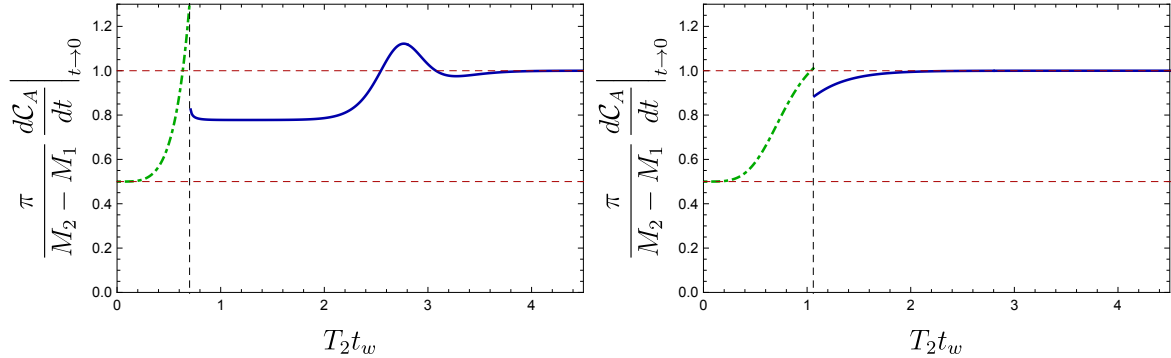


Figure C.1: The growth rate of the holographic complexity at $t = 0$ for an AdS_5 spherical black hole as a function of the perturbation time t_w . We choose $z = 1/w$ (as defined in eq. (6.16)) so that the smaller black hole is at the HP transition. The left and right panels show the results for $w = 1 + 10^{-6}$ and $w = 2$, respectively. The vertical dashed line indicates the transition from regimes (a) and (b) in eqs. (C.23) and (C.24). The rate of change starts at half of $(M_2 - M_1)/\pi$ (lower dashed red line), as expected from the expansion in eq. (C.26), and for large t_w the rate of $(M_2 - M_1)/\pi$ (indicated by the upper dashed red horizontal line) is reached.

Time evolution in AdS_5

We now turn our attention to the full time evolution in spherical AdS_5 black hole geometries with shock waves. As the previous early time analysis suggested, there are some interesting differences between the behaviour of higher dimensional black holes and the BTZ case discussed in section 6.2. It is still true that for large t_w , at first the complexity rate of change is approximately given by $(M_2 - M_1)/\pi$ for a period of time of the order of $2t_w$. This is followed by a transient period, and then the final rate of $(M_2 + M_1)/\pi$ is reached from above, analogously to the unperturbed case in chapter ???. However, there are two possible transient regimes depending on the sign of $t_{c2} - t_{c1}$, which we will analyze next.

As noted above, if the shock wave is sent early enough such that $t_w > -2r_1^*(0)$, the dynamics of the growth rate is parametrized by the positions r_b and r_s . Now, for light shocks, $t_{c2} - t_{c1}$ is positive, and therefore there is a regime with r_m , r_b and r_s contributing to the time derivative, as occurred for the BTZ black hole in section 6.2. However, for heavier shocks, $t_{c2} - t_{c1}$ can be negative. That is, r_b disappears into the future singularity before r_m becomes dynamical. This leads to a different transition between early and late time behaviours. Of course, the dividing line between these different regimes is determined

by solving $t_{c2} - t_{c1} = 0$ in eq. (6.60), which yields

$$r_1^*(r_s) = 2r_1^*(0). \quad (\text{C.27})$$

Because generally r_s approaches $r_{h,2}$ exponentially fast, and we are interested in a regime where $t_w > -2r_1^*(0)$, we can approximate the above equation as

$$r_1^*(r_{h,2}) \approx 2r_1^*(0). \quad (\text{C.28})$$

Despite having a simple form, it is still in general a transcendental equation. For AdS₅, the above expression can be explicitly written as

$$\sqrt{k w_c^2 z_c^2 + 1} \left(\pi + 2 \cot^{-1} \left[\frac{\sqrt{k w_c^2 z_c^2 + 1}}{w_c} \right] \right) - 2 \coth^{-1} w_c = 0, \quad (\text{C.29})$$

where we denote z_c and w_c the parameters at the transition between these regimes. For instance, if we denote $z = 1/w_c$ as in the previous discussion, then for $w > w_c$, $t_{c2} - t_{c1} < 0$. For $k = 1$ and $z_c = 1/w_c$, we find that $w_c \approx 1.00411$. In order to probe these two regimes, we solve for a very light shock wave and a heavy shock wave.

If $t_{c2} - t_{c1} > 0$, the three regimes to be considered are the same as those discussed in eq. (6.61). If instead $t_{c2} - t_{c1} < 0$, the time evolution passes through the three following regimes:

$$\begin{aligned} \text{I} &: -t_{c0} < t < t_{c2} && r_b, r_s \text{ exist; } r_m < 0 \\ \text{II} &: t_{c2} < t < t_{c1} && r_s \text{ exists; } r_b, r_m < 0 \\ \text{III} &: t > t_{c1} && r_s, r_m \text{ exist; } r_b < 0. \end{aligned} \quad (\text{C.30})$$

The rate of change of complexity for regime I is again given by eq. (6.62), and for regime III, by eq. (6.64). For regime II, it is now given by

$$\frac{d\mathcal{C}_A^{(\text{II})}}{dt} = \frac{M_2}{\pi} - \frac{M_1}{\pi} \frac{f_2(r_s)}{f_1(r_s)} - \frac{M_2}{2\pi} \frac{r_s^{d-2}}{\omega_2^{d-2}} f_2(r_s) \log \left[\frac{f_1(r_s)}{f_2(r_s)} \right]. \quad (\text{C.31})$$

Notice that because generally r_s approaches $r_{h,2}$ exponentially fast, the rate in the above expression will be approximately constant and equal to $\frac{M_2}{\pi}$.

Figure C.2 shows the evolution of the complexity growth rate in an AdS₅ spherical black hole geometry, with $z = 1/w$ for early shocks sent at $t_w = 6/T_2$, with a light energy of $w = 1 + 10^{-4}$ (left) and a heavy one with $w = 2$ (right). The lower dashed horizontal

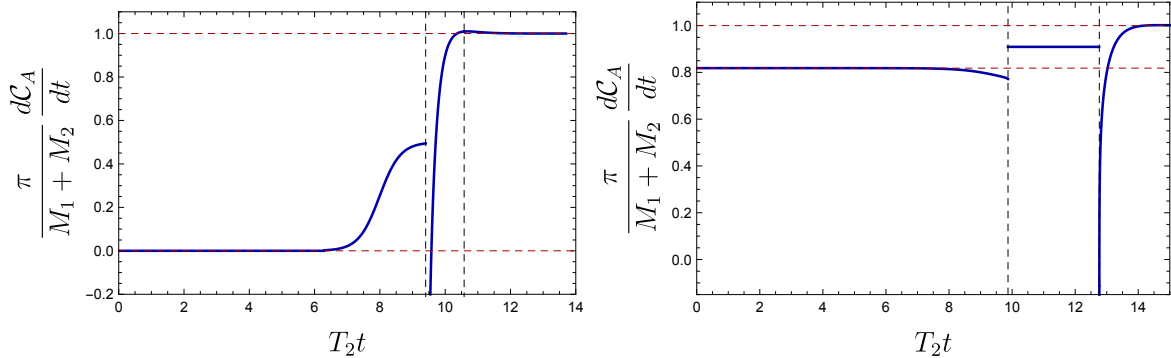


Figure C.2: Complexity growth rate for AdS₅ spherical ($k = 1$) black hole with $z = 1/w$, $t_w = 6/T_2$ and $\tilde{\ell}_{ct} = 1$, light shock wave $w = 1 + 10^{-4}$ to the left and heavy shock wave $w = 2$ to the right. For the heavy shock wave, r_b disappears into the future singularity before r_m emerges from the past singularity. Around $t = 0$, there is a long plateau where the rate is $(M_2 - M_1)/\pi$ (indicated by the lower dashed horizontal line). For the heavy shock wave, there is a transient regime ($t_{c2} < t < t_{c1}$) where the rate is approximately constant and given by M_2/π . In both examples, when r_m emerges from the past singularity (right dashed vertical line), there is a sharp negative peak, then the late time limit of $(M_2 + M_1)/\pi$ is approached from above (upper dashed horizontal line).

line indicates the limit $(M_2 - M_1)/\pi$, while the upper dashed line is $(M_2 + M_1)/\pi$, in this normalization. In the heavy shock wave example, for a long time, roughly of the order $2t_w$, the complexity growth rate is characterized by the difference of masses, then there is a transient regime (*i.e.*, $t_{c2} < t < t_{c1}$) with a constant growth rate proportional to M_2 , as predicted by eq. (C.31). For the light shock wave we have $t_{c1} < t_{c2}$, which means that the transient behaviour is analogous to the one that was studied for the BTZ black hole. At $t = t_{c1}$ (first vertical line in the left panel and second in the right panel), when r_m emerges from the past singularity, there is a sharp and negative peak in the rate of change. Finally, the late time limit is approached from above, and the rate is proportional to the sum of the masses.

Complexity of Formation

We now consider the complexity of formation for planar (*i.e.*, $k = 0$) black holes perturbed by a shock wave in asymptotically AdS₅ geometries. In chapter 3, we studied the complexity of formation for unperturbed eternal black holes and found that for planar black holes, $\Delta\mathcal{C}$ is proportional to the horizon entropy (*i.e.*, the entanglement entropy between the two

copies of the CFT in the thermofield double state).⁹ Using the CA proposal with $d = 4$ and $k = 0$, the unperturbed result reads

$$\Delta\mathcal{C}_A = \frac{S}{2\pi}. \quad (\text{C.32})$$

Since the complexity of formation for stationary planar Schwarzschild-AdS black holes had this simple expression, we will investigate how this quantity behaves in the presence of shock waves.

In order to evaluate the complexity of formation in the Vaidya geometry, we need to examine separately the two regimes, (a) and (b), introduced above. First we consider regime (a), with $r_b < 0$ at $t = 0$ (and hence there are no contributions from the counterterm that depends on r_b to $\Delta\mathcal{C}$). In this case, the contributions from the bulk integration are

$$\begin{aligned} \Delta I_{\text{bulk}}^{(a)} = & \left(\frac{\Omega_{k,d-1}}{16\pi G_N} \right) \left(-\frac{2d}{L^2} \right) \left[\int_{r_s}^{r_{\text{max}}} dr r^{d-1} (-2r_2^*(r)) + \int_0^{r_{\text{max}}} dr r^{d-1} (-2r_1^*(r)) + \right. \\ & \left. + \int_0^{r_s} dr r^{d-1} (t_w + 2r_1^*(r_s) - 2r_1^*(r)) \right] - 2I_{\text{bulk, vac}}. \end{aligned} \quad (\text{C.33})$$

The Gibbons-Hawking contributions from the future and past singularities are given in eqs. (6.33) and (6.35), respectively, resulting in

$$\Delta I_{GHY}^{(a)} = \frac{d\Omega_{k,d-1}}{16\pi G_N} [\omega_1^{d-2} (2r_1^*(r_s) - 4r_1^*(0)) - \omega_2^{d-2} (2r_2^*(r_s))]. \quad (\text{C.34})$$

There are no joint contributions using affine parametrization across the shock wave. With the inclusion of the counterterm to the null boundary that crosses the shock wave at r_s given by eq. (6.49) with $r_m = 0$, we have

$$\Delta I_{\text{ct}}^{(a)} = \frac{\Omega_{k,d-1}}{8\pi G_N} \left[r_s^{d-1} \log \left(\frac{f_1(r_s)}{f_2(r_s)} \right) \right]. \quad (\text{C.35})$$

Similarly, in the second regime (b), the contribution to the complexity of formation from the counterterm in the future boundary that crosses the shock wave at r_b is given by eq. (6.50),

$$\Delta I_{\text{ct}}^{(b)} = \frac{\Omega_{k,d-1}}{8\pi G_N} \left[r_b^{d-1} \log \left(\frac{f_2(r_b)}{f_1(r_b)} \right) \right]. \quad (\text{C.36})$$

⁹At high temperatures, $\Delta\mathcal{C}$ could be expressed for the $k = \pm 1$ cases as the entropy plus curvature corrections, in an expansion in inverse powers of LT , where here L stands for the curvature of the sphere in the boundary theory as discussed in chapter 3.

The complexity of formation in regime (a) is then the sum of the above contributions in eqs. (C.33), (C.34) and (C.35),

$$\Delta\mathcal{C}_A^{(a)} = \frac{\Delta I_{\text{bulk}}^{(a)} + \Delta I_{GHY}^{(a)} + \Delta I_{\text{ct}}^{(a)}}{\pi}. \quad (\text{C.37})$$

In the second regime (b), which occurs for larger values of t_w , the contributions to the complexity of formation are analogous to the expressions arising for the BTZ black hole discussed in section 6.2. That is, the result here is simply the sum of eqs. (6.89), (6.92), (C.35) and (C.36), now with $d = 4$.

In terms of the dimensionless coordinates (6.65), the final result for the complexity of formation for the perturbed planar ($k = 0$) AdS₅ black holes reads

$$\begin{aligned} \Delta\mathcal{C}_A^{(a)} = & \frac{S_1}{4\pi^2} \left[w^3 \log\left(\frac{x_s + 1}{x_s - 1}\right) - 2w^3 \tan^{-1}(x_s) + 2 \tan^{-1}(wx_s) + \pi(w^3 + 1) \right. \\ & \left. + 2w^3 x_s^3 \log\left(\frac{w^4 x_s^4 - 1}{w^4 (x_s^4 - 1)}\right) + \log\left(\frac{wx_s + 1}{wx_s - 1}\right) + 2 \log\left(\frac{wx_s - 1}{wx_s + 1}\right) \right], \end{aligned} \quad (\text{C.38})$$

for regime (a), while for regime (b), the expression becomes

$$\begin{aligned} \Delta\mathcal{C}_A^{(b)} = & \frac{S_1}{4\pi^2 w} \left[4w^4 \tan^{-1}\left(\frac{x_b}{w}\right) + 2w^4 \tan^{-1}(x_s) + 2w \tan^{-1}(wx_s) - 4 \tan^{-1}(x_s) \right. \\ & + 2wx_b^3 \log\left(\frac{x_b^4 - w^4}{x_b^4 - 1}\right) + (w^4 - 2) \log\left(\frac{x_s - 1}{x_s + 1}\right) + w \log\left(\frac{wx_s - 1}{wx_s + 1}\right) - 2x_b^4 \tan^{-1}\left(\frac{x_b}{w}\right) \\ & + (x_b^4 - 2w^4) \log\left(\frac{x_b + w}{w - x_b}\right) + 2w(x_b^4 - 2w^4) \tan^{-1}(x_b) + (2w^5 - wx_b^4) \log\left(\frac{x_b + 1}{1 - x_b}\right) \\ & \left. - \pi((w - 1)x_b^4 - 2w^5 + w^4 + w - 2) - 8w^4 x_s^3 \log(w) + 2w^4 x_s^3 \log\left(\frac{w^4 x_s^4 - 1}{x_s^4 - 1}\right) \right]. \end{aligned} \quad (\text{C.39})$$

Recall that the cross-over between these two regimes occurs at $t_w = -2r_1^*(0)$ with the tortoise coordinate given in eq. (C.20). Hence this transition occurs when

$$t_w = \frac{\pi L^2 \sqrt{r_{h,1}^2 + kL^2}}{2r_{h,1}^2 + kL^2}, \quad (\text{C.40})$$

which for $k = 0$, yields $t_w = \pi L^2 / (2r_{h,1}) = 1 / (2T_1)$.

Figure C.3 combines these expressions to illustrate the complexity of formation for different temperature ratios w (which for planar black holes is simply $w = \frac{T_2}{T_1}$). First,

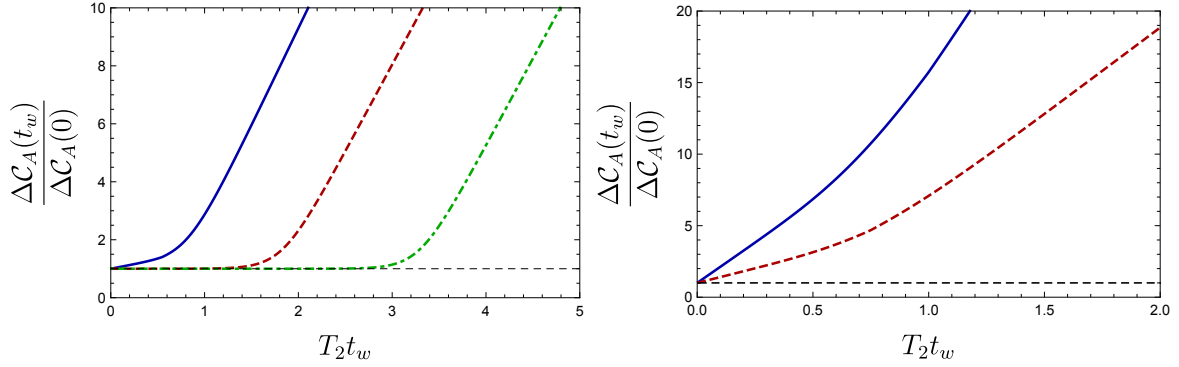


Figure C.3: The complexity of formation for planar AdS₅ black hole (*i.e.*, $k = 0$) as a function of the shock wave time t_w . We normalize by the complexity of formation of the unperturbed black hole in eq. (C.32). In the left panel, we show $\Delta\mathcal{C}_A(t_w)$ for light shock waves with $w = 1 + 10^{-1}$ (solid blue), $w = 1 + 10^{-4}$ (dashed red) and $w = 1 + 10^{-8}$ (green dot-dashed). For very light shocks, the complexity of formation remains close to the unperturbed value until times of the order of t_{scr}^* , then increases approximately linearly with t_w . In the right panel, we show $\Delta\mathcal{C}_A(t_w)$ for heavier shock waves, with $w = 2$ (solid blue) and $w = 1.5$ (dashed red). In these cases, the complexity of formation begins growing immediately as t_w moves away from zero.

we investigate the behaviour of light shock waves in the left panel, with $w = 1 + 10^{-1}$ (solid blue), $w = 1 + 10^{-4}$ (dashed red) and $w = 1 + 10^{-8}$ (green dot-dashed). We see a similar overall behaviour to the BTZ case in figure 6.7. The complexity does not change significantly from the unperturbed result until times of the order of the scrambling time t_{scr}^* , after which it grows approximately linearly with t_w . In the right panel of figure C.3, we show $\Delta\mathcal{C}_A$ for heavier shock waves. In this case, the complexity of formation starts growing immediately from the unperturbed value (C.32), but again we see that there are two distinct regimes.

To better understand the two regimes shown in figure C.3, we want then to investigate the rate of growth of $\Delta\mathcal{C}_A(t_w)$ from eqs. (C.38) and (C.39) for small and large values of t_w , respectively. One can find such slopes by differentiating eqs. (C.38) and (C.39) with respect to x_b and x_s , and finding the derivative of x_b and x_s with respect to t_w in eq. (6.22).

As a consequence, we have the simple expressions for the slopes as

$$\left. \frac{d \Delta \mathcal{C}}{d t_w} \right|_{t_w \rightarrow 0} = \frac{M_2 - M_1}{\pi}, \quad (\text{C.41})$$

$$\left. \frac{d \Delta \mathcal{C}}{d t_w} \right|_{t_w \rightarrow \infty} = \frac{2(M_2 + M_1)}{\pi}. \quad (\text{C.42})$$

Hence we see that the initial slope depends on the difference in the masses and hence is essentially zero for the very light shock waves. The expression in eq. (C.41) can be compared to that for the BTZ black holes in eq. (6.103), which contains an additional term proportional to $\log[M_2/M_1]$. Similarly, eq. (C.42) can be compared to the slope implied in eq. (6.104) for $d = 2$, and in this case, the two slopes for large values of t_w are identical.

In analogy to eq. (6.104) for $d = 2$, we find that the large t_w behaviour of the complexity of formation follows

$$\Delta \mathcal{C}_A = \frac{S_1}{2\pi} + \frac{2}{\pi} (M_1 + M_2) (t_w - t_{\text{del}}) + \mathcal{O}(T_2 t_w e^{-T_2 t_w}), \quad (\text{C.43})$$

with the delay time given by

$$t_{\text{del}} \equiv \frac{1}{6\pi T_2 (w^4 + 1)} \left[\pi(w^4 - 1) - 2(2w^4 - 1) \cot^{-1}(w) + 4\pi w - 2w \tan^{-1}(w) \right. \\ \left. + 8w^4 \log(w) - 2w^3(w + 1) \log\left(\frac{w^4 - 1}{8}\right) + (2w^4 + w - 1) \log\left(\frac{w + 1}{w - 1}\right) \right]. \quad (\text{C.44})$$

For light shock waves with $w = 1 + \epsilon$, the delay time agrees with the scrambling time at leading order,¹⁰

$$t_{\text{del}} = \frac{1}{2\pi T_1} \log\left(\frac{2}{\epsilon}\right) + \frac{1}{4T_1} + \mathcal{O}(\epsilon \log \epsilon) = t_{\text{scr}}^* + \frac{1}{4T_1} + \mathcal{O}(\epsilon \log \epsilon), \quad (\text{C.45})$$

which can be compared to eq. (6.106) for the BTZ case. For heavy shock waves, we have that the delay time approaches a constant proportional to $1/T_2$,

$$t_{\text{del}} = \frac{1}{6\pi T_2} \left[(\pi + 6 \log 2) - \frac{8}{w^3} \log w + \frac{3\pi + \frac{8}{3} + 6 \log 2}{w^3} \right] + \mathcal{O}\left(\frac{1}{T_2 w^4}\right), \quad (\text{C.46})$$

which can be compared to eq. (6.107) for the BTZ case. In figure C.4 we show how this characteristic time t_{del} in eq. (C.44) generally behaves as a function of w . Overall, this behaviour is very similar to that for the BTZ black hole in figure 6.9.

¹⁰Combining the expressions in eq. (C.17), we have $M \propto T^4$, $S \propto T^3$ and $M = \frac{3}{4} ST$ for the planar AdS₅ black holes (*i.e.*, $k = 0$). Then we have $4\epsilon \simeq E/M_1$ where E is the energy in the shock wave and so $2/\epsilon = S_1$ if we choose $E = 6T_1$.

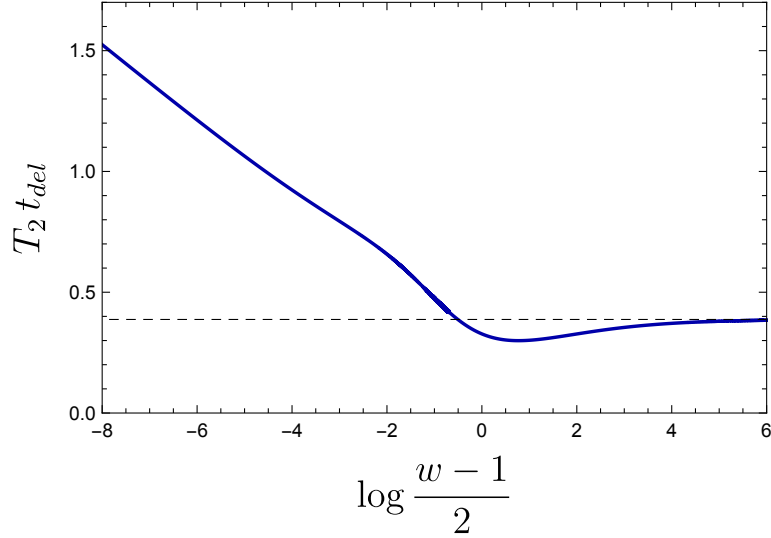


Figure C.4: The delay time in eq. (C.44) as a function of $\log((w-1)/2)$. The left part of the plot is linear with a slope minus one, as is characteristic of the scrambling time in eq. (C.45). For heavy shock waves, t_{del} approaches a constant at large w , as given in eq. (C.46).

We can also calculate the derivative of the complexity of formation with respect to t_w in order to show the transition between shock waves sent before and after the delay time defined in eq. (C.44). We show these results in figure C.5. For heavy shock waves, we can see that initially the derivative begins as

$$\frac{d\Delta\mathcal{C}_A}{dt_w} = \frac{M_2 - M_1}{\pi} + \mathcal{O}(x_s^{-4}) . \quad (\text{C.47})$$

Further, there is a more pronounced regime in which this derivative remains constant for small t_w , in comparison to the BTZ results in figure 6.8. However, this plateau is never very long as it ends before t_{del} , which we see from eq. (C.46) that becomes $T_2 t_{\text{del}} \simeq 0.39$ for large w . Another notable difference for the heavy shock wave is that the derivative has a discontinuity going from regime (a) to (b), given by eqs. (C.38) and (C.39).¹¹ It is given at leading order by

$$\left(\frac{d\Delta\mathcal{C}_A^{(b)}}{dt_w} - \frac{d\Delta\mathcal{C}_A^{(a)}}{dt_w} \right) \Big|_{t_w \rightarrow \frac{1}{2T_1}} = \frac{4(M_1 + M_2)}{\pi} \frac{\log w}{(1 + w^4)} . \quad (\text{C.48})$$

¹¹However, the complexity of formation is continuous, as can be seen from figure C.3.

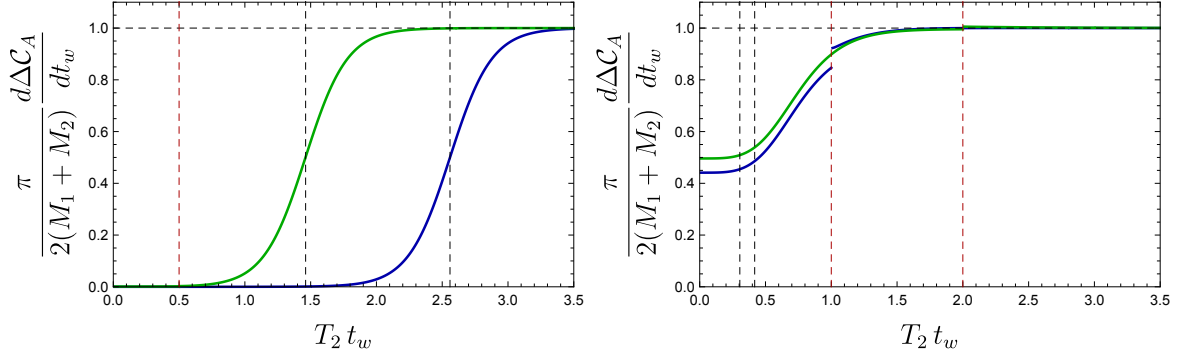


Figure C.5: The derivative of the complexity of formation with respect to the insertion time t_w , for planar AdS₅. In the left panel, we evaluate for a light shock waves with $w = 1 + 10^{-6}$ (blue) and $w = 1 + 10^{-3}$ (green), while in the right panel, we have heavier shock waves with $w = 2$ (blue) and $w = 4$ (green). The results for light shock waves resemble those for the BTZ black hole in figure 6.8, with a clear transition between two regimes at the scrambling time, indicated by the vertical dashed black lines. For the heavier shock waves, even though the complexity is a continuous function of t_w as the regime makes a transition between regimes (a) and (b), as in eqs. (C.38) and (C.39), the derivative has a non-zero jump proportional to $\log w$, as shown in eq. (C.48). The vertical dashed black line denotes the transition from regimes (a) to (b), while the dashed red line stands for the delay time in eq. (C.44). Notice that for heavy shock waves, there is a longer period with a constant derivative, in contrast to the BTZ result in figure 6.8. The profile for heavier shock waves is very similar to the $w = 4$ example.

As a consequence, the jump for light shock waves is close to zero, making it imperceptible in figure C.5.

Complexity without the counterterm

We briefly discuss the consequences of not adding eq. (2.11) to the WDW action for $d = 4$. The relevant rates of change of complexity in this regime were calculated and discussed in section 6.2.3. For instance, in the planar case with $k = 0$ and $d = 4$, the rate of change of complexity for very early shock waves in eq. (6.112) become

$$\left. \frac{d\tilde{\mathcal{C}}_A^{(1)}}{dt} \right|_{t_w \rightarrow \infty} = \frac{M_2 - M_1}{3\pi} + \mathcal{O}(T_1(2t_w - t)e^{-\pi T_1(2t_w - t)}) . \quad (\text{C.49})$$

It is proportional to $M_2 - M_1$ and not simply 0 as for the BTZ black hole. In addition, the late time growth of complexity from eq. (6.115) reads

$$\left. \frac{d\tilde{\mathcal{C}}_A^{(\text{III})}}{dt} \right|_{t \rightarrow \infty} = \frac{1}{\pi} \left(M_1 + \frac{M_2}{3} + \frac{5}{6} M_1^{3/4} M_2^{1/4} \right) + \mathcal{O}(T_1 t e^{-\pi T_1 (t-2t_w)}), \quad (\text{C.50})$$

which does not reproduce the expected late time behaviour with $d\mathcal{C}_A/dt \propto M_1 + M_2$. Further, if the shock wave is very light, with $M_1 \approx M_2$, we have

$$\left. \frac{d\tilde{\mathcal{C}}_A^{(\text{III})}}{dt} \right|_{M_1 \approx M_2, t \rightarrow \infty} = \frac{13}{6\pi} M_2, \quad (\text{C.51})$$

which does not recover the expected eternal black hole rate of $2M_2/\pi$. The behaviour here is similar to that discussed in the context of the order of limits of light shock wave, without the addition of the counterterm in section 6.2.3.

Let us also briefly consider the complexity of formation without the inclusion of the counterterm. The only contributions are from the bulk and Gibbons-Hawking-York boundaries in eqs. (C.33) and (C.34)

$$\Delta\tilde{\mathcal{C}}_A^{(a)} = \frac{S_1}{4\pi^2} \left[w^3 \log \left(\frac{x_s + 1}{x_s - 1} \right) - 2w^3 \tan^{-1}(x_s) + \log \left(\frac{wx_s - 1}{wx_s + 1} \right) + 2 \tan^{-1}(wx_s) + \pi(w^3 + 1) \right]. \quad (\text{C.52})$$

In the second regime, adding eqs. (6.89), (6.92) and (6.93) with $d = 4$, the complexity of formation reads,

$$\begin{aligned} \Delta\tilde{\mathcal{C}}_A^{(b)} = & \frac{S_1}{4w\pi^2} \left[-\pi((w-1)x_b^4 - 2w^5 + w^4 + w - 2) + (w^4 - 2) \log \left(\frac{x_s - 1}{x_s + 1} \right) \right. \\ & + w \log \left(\frac{wx_s - 1}{wx_s + 1} \right) - (2w^4 - x_b^4) \left(\log \left(\frac{w + x_b}{w - x_b} \right) + w \log \left(\frac{1 - x_b}{1 + x_b} \right) \right) + 2w \tan^{-1}(wx_s) \\ & \left. + 2(w^4 - 2) \tan^{-1}(x_s) + 2(2w^4 - x_b^4) \left(\tan^{-1} \left(\frac{x_b}{w} \right) - w \tan^{-1}(x_b) \right) \right]. \end{aligned} \quad (\text{C.53})$$

We show the complexity of formation without the addition of counterterm in figure C.6. In contrast to the complexity of formation of BTZ black holes (*i.e.*, $d = 2$) in figure 6.12, the overall behaviour of the complexity of formation, up to overall multiplicative constants, is similar to that with the inclusion of the counterterm in figure C.3.

Complexity of Formation for general dimensions (and $k = 0$)

We have shown how the growth rate of complexity behaves in certain regimes in general dimension d in section 6.2, with and without the null surface counterterm. It is also possible

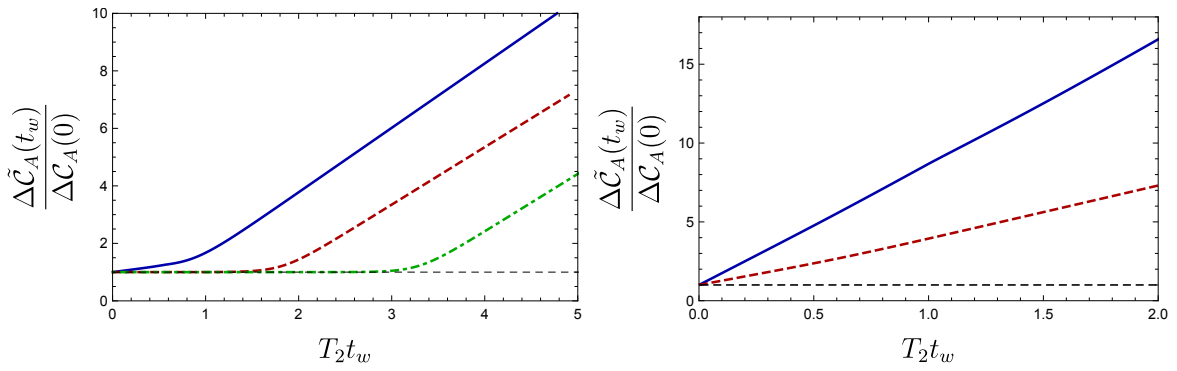


Figure C.6: The complexity of formation for planar AdS_5 black hole as a function of the shock wave time t_w , without the inclusion of the counterterm. We normalize by the complexity of formation of the unperturbed black hole in eq. (C.32). In the left panel, we show $\Delta \tilde{\mathcal{C}}_A(t_w)$ for light shock waves with $w = 1 + 10^{-1}$ (solid blue), $w = 1 + 10^{-4}$ (dashed red) and $w = 1 + 10^{-8}$ (green dot-dashed). For very light shocks, the complexity of formation remains close to the unperturbed value until times of the order of t_{scr}^* , then increases approximately linearly with t_w . In the right panel, we show $\Delta \tilde{\mathcal{C}}_A(t_w)$ for heavier shock waves, with $w = 2$ (solid blue) and $w = 1.5$ (dashed red). The overall behaviour is similar to the complexity of formation in figure C.3, with the inclusion of the counterterm. Therefore, it contrasts with the BTZ black hole results in section 6.2.3.

to derive the dependence of the complexity of formation on t_w for general dimensions if we consider planar horizons, *i.e.*, $k = 0$. In the case of planar black holes, we can use the tortoise coordinates derived for any dimension d given in chapter 3, which we rewrite here with the convention that r^* vanishes at infinity,

$$r_{\text{in},i}^*(r) = \frac{L^2}{r} \left[{}_2F_1 \left(1, -\frac{1}{d}; 1 - \frac{1}{d}; \left(\frac{r}{r_{h,i}} \right)^d \right) - 1 \right] - \frac{\pi L^2}{dr_{h,i}} \cot \left(\frac{\pi}{d} \right), \quad (\text{C.54})$$

$$r_{\text{out},i}^*(r) = -\frac{L^2}{(r^d - r_{h,i}^d)^{1/d}} {}_2F_1 \left(\frac{1}{d}, \frac{1}{d}; 1 + \frac{1}{d}; \frac{r_{h,i}^d}{r_{h,i}^d - r^d} \right).$$

In the first regime, we have $t_w < -2r_1^*(0)$, which for $k = 0$ and general d gives

$$t_w < \frac{1}{2 \cot \left(\frac{\pi}{d} \right) T_1}. \quad (\text{C.55})$$

We solve eqs. (C.33) and (C.34) using the tortoise coordinates given by eq. (C.54), which has a long but analytic expression,

$$\begin{aligned} \frac{\pi}{S_1} \Delta \tilde{\mathcal{C}}_A^{(a)} &= \frac{(d-2) \cot \left(\frac{\pi}{d} \right)}{d} - \frac{d}{\pi(d-1)} \left[\left(w^d x_s^d - 1 \right)^{\frac{d-1}{d}} {}_2F_1 \left(\frac{1}{d} - 1, \frac{1}{d}; 1 + \frac{1}{d}; \frac{1}{1 - (wx_s)^d} \right) \right. \\ &\quad \left. - w^{d-1} \left(x_s^d - 1 \right)^{\frac{d-1}{d}} {}_2F_1 \left(\frac{1}{d} - 1, \frac{1}{d}; 1 + \frac{1}{d}; -\frac{1}{x_s^d - 1} \right) \right] \\ &\quad + \frac{w^{d-1}}{2\pi} \frac{2x_s^d + d}{(x_s^d - 1)^{1/d}} {}_2F_1 \left(\frac{1}{d}, \frac{1}{d}; 1 + \frac{1}{d}; -\frac{1}{x_s^d - 1} \right) \\ &\quad + \frac{1}{2\pi} \frac{2(wx_s)^d - d}{((wx_s)^d - 1)^{1/d}} {}_2F_1 \left(\frac{1}{d}, \frac{1}{d}; \frac{1}{d} + 1; \frac{1}{1 - (wx_s)^d} \right). \end{aligned} \quad (\text{C.56})$$

Here we have begun with the complexity of formation evaluated without the null surface counterterm (2.11). If the shock wave is very light, and $t_w \ll t_{\text{scr}}^*$, the above expression simply reduces to

$$\Delta \tilde{\mathcal{C}}_A^{(a)} = \frac{(d-2) \cot \left(\frac{\pi}{d} \right)}{d\pi} S_1, \quad (\text{C.57})$$

which reproduces the complexity of formation for a planar boundary geometry in d dimensions found in chapter 3.

The second regime, with $t_w > -2r_1^*(0)$, consists of solving eqs. (6.89) and (6.92) with the general d tortoise coordinates in eq. (C.54), which results in

$$\begin{aligned}
\frac{\pi}{S_1} \Delta \tilde{\mathcal{C}}_A^{(b)} &= \frac{\Gamma\left(\frac{1}{d}-1\right)}{\pi d \Gamma\left(1+\frac{1}{d}\right)} \left[\left(\frac{1}{(wx_s)^d - 1} \right)^{\frac{1}{d}-1} {}_2F_1\left(\frac{1}{d}-1, \frac{1}{d}; 1+\frac{1}{d}; -\frac{1}{(wx_s)^d - 1}\right) \right. \\
&\quad \left. - \left(\frac{1}{(wx_s)^d - w^d} \right)^{\frac{1}{d}-1} {}_2F_1\left(\frac{1}{d}-1, \frac{1}{d}; 1+\frac{1}{d}; -\frac{1}{x_s^d - 1}\right) \right] \\
&\quad + \frac{dw^d - 2x_b}{2\pi x_b} \left[{}_2F_1\left(1, -\frac{1}{d}; \frac{d-1}{d}; \left(\frac{x_b}{w}\right)^d\right) - {}_2F_1\left(1, -\frac{1}{d}; \frac{d-1}{d}; x_b^d\right) \right] \\
&\quad + \frac{2(wx_s)^d - d}{2\pi w} \left[\left(\frac{w^d}{(wx_s)^d - 1} \right)^{1/d} {}_2F_1\left(\frac{1}{d}, \frac{1}{d}; 1+\frac{1}{d}; -\frac{1}{(wx_s)^d - 1}\right) \right. \\
&\quad \left. - \left(\frac{1}{x_s^d - 1} \right)^{1/d} {}_2F_1\left(\frac{1}{d}, \frac{1}{d}; 1+\frac{1}{d}; -\frac{1}{x_s^d - 1}\right) \right] + \frac{\cot\left(\frac{\pi}{d}\right)}{2dw} \left[2x^b + (d-4)w - w(2x_b - dw^d) \right]. \tag{C.58}
\end{aligned}$$

Of course, we can also evaluate the complexity of formation including the counterterm for general dimension and $k = 0$. We would simply add the contributions in eq. (C.35) to eq. (C.56)

$$\Delta \mathcal{C}_A^{(a)} = \Delta \tilde{\mathcal{C}}_A^{(a)} + \frac{S_1}{2\pi^2} \left[w^{d-1} x_s^{d-1} \log \left(\frac{((wx_s)^d - 1)}{w^d(x_s^d - 1)} \right) \right], \tag{C.59}$$

and eqs. (C.35) and (C.36) to eq. (C.58), which results in

$$\Delta \mathcal{C}_A^{(b)} = \Delta \tilde{\mathcal{C}}_A^{(b)} + \frac{S_1}{2\pi^2} \left[x_b^{d-1} \log \left(\frac{x_b^d - w^d}{x_b^d - 1} \right) + w^{d-1} x_s^{d-1} \log \left(\frac{((wx_s)^d - 1)}{w^d(x_s^d - 1)} \right) \right]. \tag{C.60}$$

Note that the additional contributions in eq. (C.59) do not modify the result in the limit $w \rightarrow 1$ and $t_w \ll t_{\text{scr}}^*$, *i.e.*, we still recover the expected result for the complexity of formation (C.57) without any shock wave perturbation.¹²

For large t_w , we can simply expand the expressions for $x_s = 1 + A \exp^{-2\pi T_2 t_w}$ and $x_b = 1 - B \exp^{-2\pi T_1 t_w}$, where A and B are constants that depend on the dimension, but that nonetheless are independent of t_w . In addition, we can evaluate the dependence on t_w when t_w is small, which means r_s is close to the boundary. Evaluating the complexity of formation without counterterm in eqs. (C.56) and (C.58), we find

$$\left. \frac{d\Delta \tilde{\mathcal{C}}_A}{dt_w} \right|_{t_w \rightarrow 0} = \frac{d-2}{d-1} \frac{M_2 - M_1}{\pi}, \quad \left. \frac{d\Delta \tilde{\mathcal{C}}_A}{dt_w} \right|_{t_w \rightarrow \infty} = \frac{d-2}{d-1} \frac{M_1 + M_2}{\pi}. \tag{C.61}$$

¹²We might note that the original calculations of the complexity of formation in chapter 3 were made without the counterterm (2.11).

Also, we can evaluate the complexity of formation with the addition of the counterterm in eqs. (C.59) and (C.60), which in these regimes give us the expected results

$$\left. \frac{d\Delta\mathcal{C}_A}{dt_w} \right|_{t_w \rightarrow 0} = \frac{(M_2 - M_1)}{\pi}, \quad \left. \frac{d\Delta\mathcal{C}_A}{dt_w} \right|_{t_w \rightarrow \infty} = \frac{2(M_1 + M_2)}{\pi}, \quad (\text{C.62})$$

e.g., compare to the CA results in eqs. (6.124) and (6.125). Of course, in the limit where M_2 is much larger than M_1 , we should recover the one sided result in chapter 5. Without the addition of the counterterm, the planar rate of change is just a constant (with the same d dependence), as can be seen in eq. (5.57). When the counterterm is added, the expressions also agree, with the initial rate of M_2/π and the late time rate of $2M_2/\pi$, as can be seen in eq. (5.76). In addition, the general d dependence in eq. (C.61) agrees with our analysis of the BTZ black hole in section 6.2.3, where the complexity of formation without the inclusion of the counterterm saturated to a constant in $d = 2$.